Developing Deep Eutectic Solvents as Sustainable Media for Homogeneous Catalysis and Energy Storage

Luis Mauricio Murillo Herrera

PhD

University of York

Chemistry

January 2022

Abstract

This thesis follows the green zeitgeist and describes the application of deep eutectic solvents (DESs) as potential green solvents in organometallic catalysis and the preparation of anthraquinones salts towards the development of redox-active DESs for energy storage applications. The first chapter reviews ionic liquids and DESs. Their differences and green attributes are discussed. The second chapter aims to detail the experimental and computational methodologies employed in this thesis. In the third chapter, two novel and affordable cross-coupling methodologies in DESs are described: a Suzuki reaction and a regioselective Negishi reaction. The Suzuki reaction was chemically robust and proceeded in DESs smoothly, whereas the Negishi reaction posed bigger challenges. Temperature was the most influential variable, and its careful control allowed to perform the Negishi reaction in DESs at open air, thus circumventing its need for protective atmosphere and dry solvents. With $Pd_3(OAc)_6$ pre-catalyst, the Negishi reaction exhibited good performance with iodoarenes functionalized at the *ortho*-position with metal-coordinating groups, whereas with $[Pd(OAc)_2(PPh_3)_2]$ pre-catalyst exhibited better performance with *meta*- or *para*-substituted iodoarenes. This feature was exploited in a regioselective Negishi reaction with methyl 2,3,5-triiodobenzoate that exhibited high selectivity for the *ortho*-monosubstituted product. The fourth chapter involves the preparation of 2-methylanthraquinone-based imidazolium, alkylammonium, pyrrolidinium and piperidinium salts, as potential candidates for redox-active DESs. The salts were fully characterized, and their redox properties studied using voltamperommetric and computational methods. Most of the alkyl ammonium salts decomposed under reducing conditions, while the imidazolium salts exhibited an electrochemically quasi-reversible one-electron two-step mechanism. It was concluded that the imidazolium-anthraquinone bromide salt was the best candidate to prepare a redox-active DES.

List of Contents

List of Tables

List of Figures

List of Schemes

List of Compounds

Compound number	Chapter II Structure
1	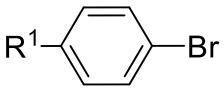 **a**, R^1 = H **b**, R^1 = OMe **c**, R^1 = COMe
2	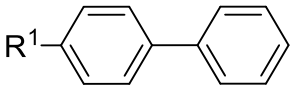 **a**, R^1 = H **b**, R^1 = OMe **c**, R^1 = COMe
3	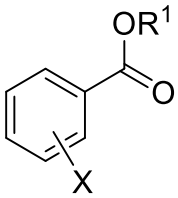 **a**, X = 2-I, R^1 = Me **b**, X = 2-I, R^1 = Et **c**, X = 4-I, R^1 = Me d, X = 2-Br R^1 = Me
4	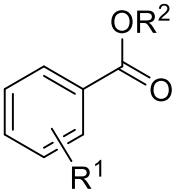 **a**, R^1 = 2-^{n}Bu, R^2 = Me **b**, R^1 = 2-^{n}Bu, R^2 = Et **c**, R^1 = 4-^{n}Bu, R^2 = Me **d**, R^1 = 2-Bn, R^2 = Me **e**, R^1 = 4-Bn, R^2 = Me
5	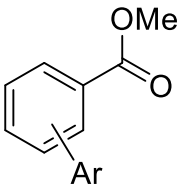 **a**, 2-Ar
6	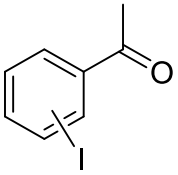 **a**, 2-I **b**, 4-I
7	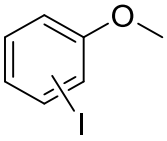 **a**, 2-I **b**, 3-I **c**, 4-I
8	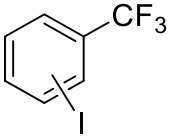 **a**, 2-I **b**, 3-I **c**, 4-I

9	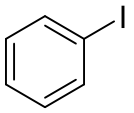	
10	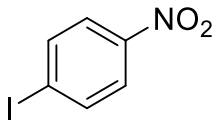	
11	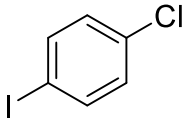	
12	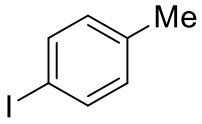	
13	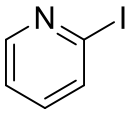	
14	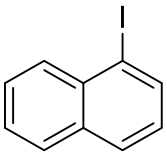	
15	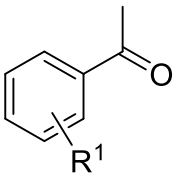	**a**, R^1 = 2-^{n}Bu **b**, R^1 = 4-^{n}Bu **c**, R^1 = 2-Bn **d**, R^1 = 4-Bn
16	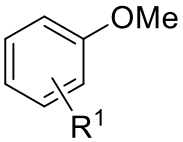	**a**, R^1 = 2-^{n}Bu **b**, R^1 = 3-^{n}Bu **c**, R^1 = 4-^{n}Bu **d**, R^1 = 2-Bn **e**, R^1 = 4-Bn
17	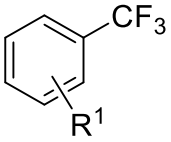	**a**, R^1 = 2-^{n}Bu **b**, R^1 = 3-^{n}Bu **c**, R^1 = 4-^{n}Bu
18	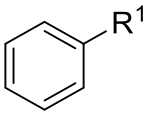	**a**, R^1 = ^{n}Bu **b**, R^1 = Bn
19	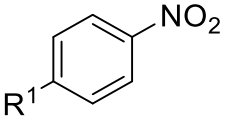	**a**, R^1 = ^{n}Bu **b**, R^1 = Bn

20	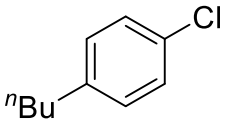	
21	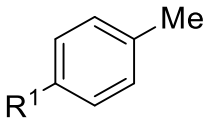	**a**, R^1 = ^{n}Bu **b**, R^1 = Bn
22	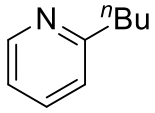	
23	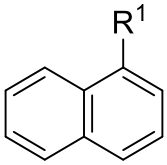	**a**, R^1 = ^{n}Bu **b**, R^1 = Bn
24	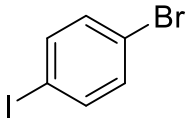	
25	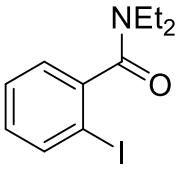	
26	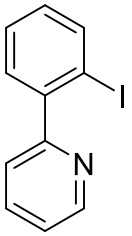	
27	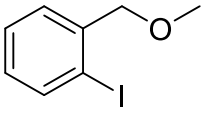	
28	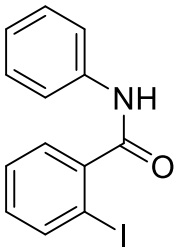	
29	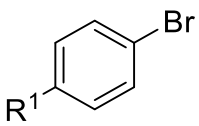	**a**, R^1 = ^{n}Bu **b**, R^1 = Bn

30	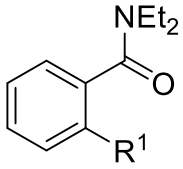	**a**, R^1 = ^{n}Bu **b**, R^1 = Bn
31	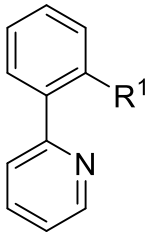	**a**, R^1 = ^{n}Bu **b**, R^1 = Bn
32	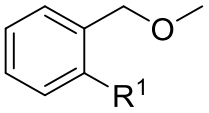	**a**, R^1 = ^{n}Bu **b**, R^1 = Bn
33	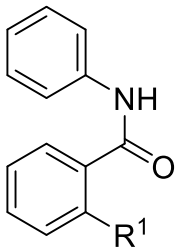	**a**, R^1 = ^{n}Bu **b**, R^1 = Bn
34	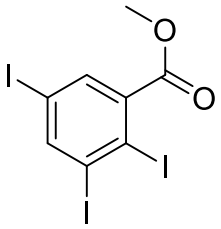	
35	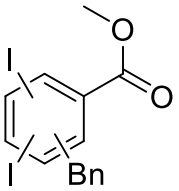	**a**, 3,5-I, 2-Bn **b**, 2,5-I, 3-Bn **c**, 2,3-I, 5-Bn
36	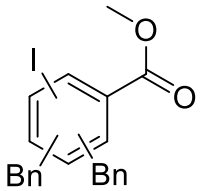	**a**, 2-I, 3,5-Bn **b**, 3-I, 2,5-Bn **c**, 5-I, 2,3-Bn
37	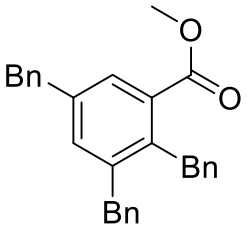	

SP1	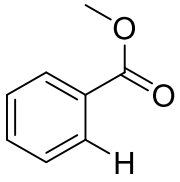
SP2	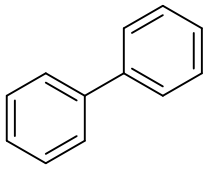
SP3	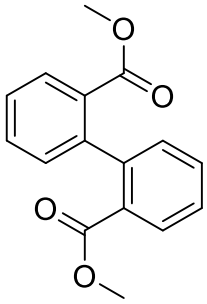
SP4	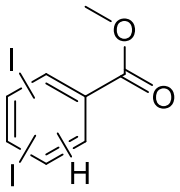
SP5	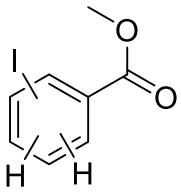

Chapter III

Compound number	**Structure**
38	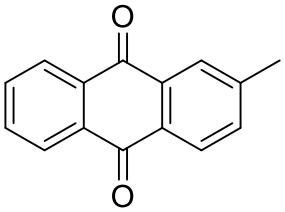
39	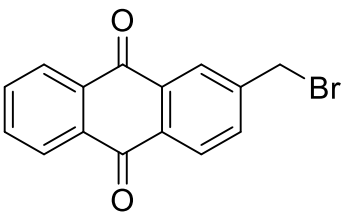

40

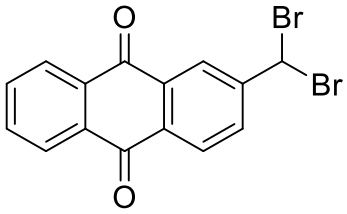

[41]

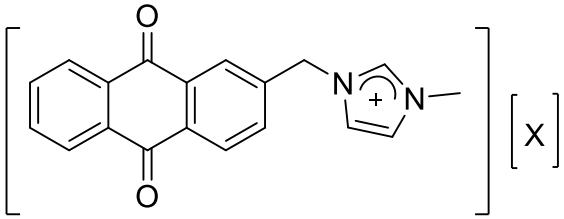

$X = Br^-, Tf_2N^-$

[42]

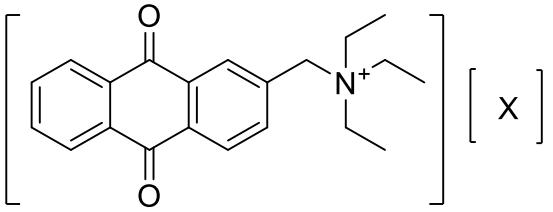

$X = Br^-, Tf_2N^-$

[43]

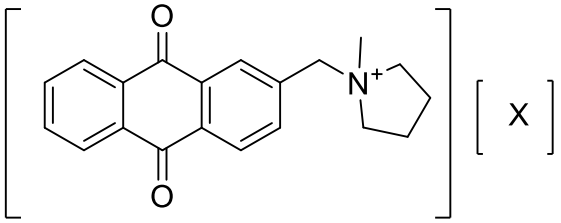

$X = Br^-, Tf_2N^-$

[44]

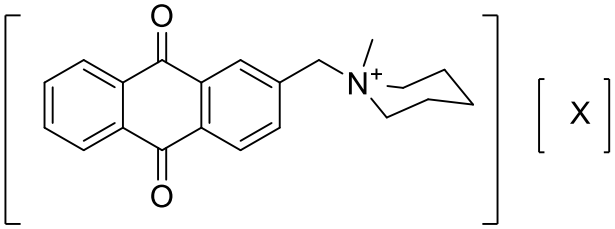

$X = Br^-, Tf_2N^-$

[45]

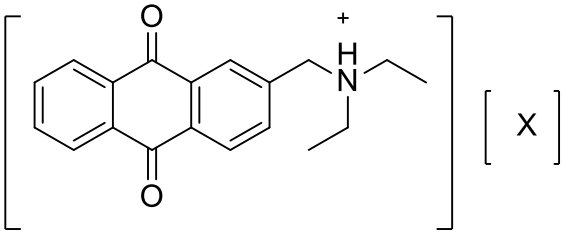

$X = Br^-, Tf_2N^-$

[46]

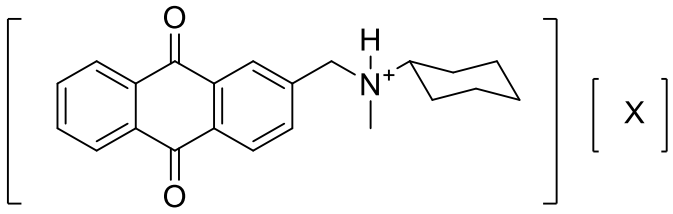

X = Br^-, Tf_2N^-

Acknowledgments

I would like to thank my supervisor Dr John Slattery for guiding this research project throughout these long 4 years, for always being available for questions or discussions whether it was a busy day or whether we were under lockdown due to the COVID-19 pandemic. I would also thank Dr Slattery and Dr Naomi Elstone for all the time spent reading this thesis and for his valuable suggestions.

I would like to thank the National Council of Science and Technology for funding the first three years of this research project as well as the University of York for the financial support given to me to undertake the continuation year of this project, which had to be extended due to the time lost during the COVID-19 lockdowns.

I would also like to thank Dr Adrain Withwood, Dr Scott Hicks, Dr Graeme McAllister, Dr Alex Heynam, Ms Heather Fish and Mr Karl Heaton for their valuable assistance and support with all the analytical techniques used in this thesis.

I would like to thank my lab mates from year 1, Chris, Rachel, Lewis, Nina and Martin for helping me to get adapted to a new country, a new culture and to a new weather. Of course, I would also thank the rest of the members of the JMS through the years, Bono, Aidan, Theo, Naomi, Harry and Christian for forming such a nice community. Special thanks to Harry and Christian with whom I worked in the synthesis and characterization of the anthraquinones, since at least, we could share the same feelings of despair when dealing with disappointing characterization data or weird cyclic voltammograms.

También me gustaría agradecer a mis amigos y compañeros de casa, Eduardo, Víctor y Cynthia por ser unos estupendos amigos y buenos cohabitantes, especialmente porque pasar los confinamientos del COVID con ellos fue incluso hasta divertido. Por supuesto también agradezco al resto de

los mexicanos en York, porque creamos una comunidad que hizo que la ciudad amurallada, a más 8500 km de distancia de casa, se sintiera familiar.

Quiero también agradecer a mis amigos en México, a Carlos, Alam, Fausto, Zazueta y a mi hermano Juan, porque a pesar de la distancia y la pandemia, siempre encontramos la manera de mantenernos en contacto y estar al día, a través de los videojuegos.

Quiero agradecer a Hannah por haber sido, a través de estos años, un gran fuerte de soporte y cariño, quien siempre ha está preocupada de que no trabaje más horas de las razonablemente sanas y que esté contento. Le agradezco también a su familia por su amabilidad y porque me han hecho sentir como parte suya.

Finalmente, quiero agradecer a mi papá Luis Murillo por su apoyo financiero al principio del proyecto doctoral, que me ayudó a estabilizar mi nueva vida, por su cariño y por siempre estar al pendiente cada mañana. A mi mamá Lulu Herrera por mandarme ropa calientita y paquetes salvavidas de comida mexicana, y junto con mis hermanos Juan y Paula y mi abuelita Elvira, también quiero agradecerles por su cariño, sus mensajes durante estos cuatro años y por hacerme sentir como si estuviera cerca de casa.

Authors Declaration

I declare that the research presented in this thesis is, to the best of my knowledge, original and was carried out under the supervision of Dr John Slattery in the Chemistry Department of the University of York, between February 2018 and January 2021. Contributions from other authors and co-workers are listed below and referenced in the appropriate chapters throughout this thesis.

- Mass spectrometry experiments were performed by Mr Karl Heaton
- X-Ray crystallography data was collected by, or with the assistance of, Dr Adrian Whitwood, Dr Rachel Parker and Mr Theo Tanner
- Elemental analyses were performed by Dr Graeme McAllister.
- The NMR experiments carried out in the 600 MHz Bruker Avance III HD spectrometer, presented in chapter II, were performed by Dr Alex Heynam.
- The gas chromatography experiments related to the second substrate scope from chapter II, were performed by Dr Scott Hicks.
- The concentration-dependent cyclic voltammetry experiment of 1-methyl-3-(2-methylanthraquinone)imidazolium bis(trifluoromethanesulfonyl)imide in acetonitrile, presented in chapter III, was performed by Mr Christian Hoffman.

Chapter I: Introduction to deep eutectic solvents

Solvents are the most ubiquitous substances in chemistry and in everyday life; they are used for transportation, cleaning, undergoing reactions, performing quantitative and instrumental analysis among other applications. Due to public concern over the environment, chemistry and society are moving towards newer, renewable, and sustainable (biodegradable, non-toxic, non-polluting, carbon-neutral, atmosphere-friendly, cheaper) solvents or even solvent-free processes. Such an example is the study and development of ionic liquids (ILs) as media for chemical reactions, extractions, gas capture, metal solubility and electrochemical devices. This project is focused upon an analogous group of liquids, the so-called deep eutectic solvents (DESs), which are strongly related to ILs in their composition and properties.

1.1 Molten salts and ionic liquids

Molten salts and ILs are materials formed solely by mixtures of cations and anions that are in the liquid state at a given temperature. Molten salts usually have hight melting points, for example: LiCl/KCl eutectic mixture (MP: 357 °C) or $NaNO_3$/KNO_3 (60%:40%, MP: 220 °C); these liquids conduct electricity, possess high volumetric heat capacity and are corrosive.[1] ILs are technically molten salts too, however, the term ILs is preferred nowadays for mixtures of ions which melting points are below 100°C. This is so, because unlike high temperature molten salts, ILs are made of low-charge, highly unsymmetrical and bulky ions. This combination of factors promotes weaker coulombic interactions between ions, more flexibility, ion-movement and packing constraints, thus smaller enthalpic and higher entropic contributions to the lattice energy which drives the melting points down.[2,3]

The cation in ILs is usually a bulky ion where the positive charge is formally located at a nitrogen or phosphorus atom. ILs can be characterized by the type of cation in heterocyclic, ammonium $[R^1R^2R^3R^4N]^+$, phosphonium $[R^1R^2R^3R^4P]^+$ and sulphonium $[R^1R^2R^3S]^+$ based cations. As a general trend, the more unsymmetrical and bulky the cation, the lower the melting point will

be. On the other hand, anions in ILs are usually non-oxidizing conjugate bases of some strong inorganic acids like halides, $[NO_3]^-$, $[BF_4]^-$, or $[PF_6]^-$. Other common anions are triflate, acetate, thiocyanate, amide & methanide-based, sulphates & phosphates (*Figure 1.1.1*).[4]

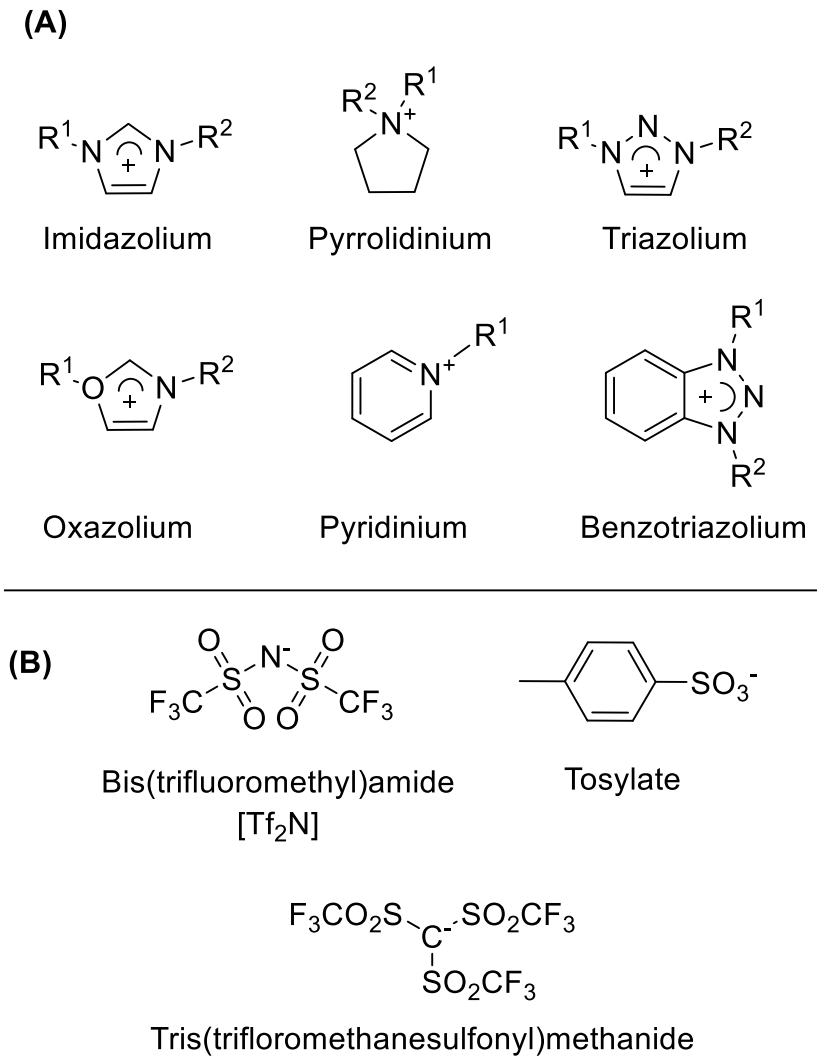

Figure 1.1.1: A: Cations & B: Anions used commonly in ILs synthesis

The strategies for synthesizing ILs can be divided into aprotic and protic. The cationic species in protic ILs is synthesised by protonation of an organic base with acids. The issues with these syntheses involve side-reactions of the pre-cationic species, easy decomposition of the IL through the inverse acid/base equilibrium and volatility due to unreacted pre-cationic species.[4]

The cationic species in aprotic ILs is synthesized by quaternisation of an organic base with alkylating reagents, like haloalkanes. The quaternisation of amines, phosphines or N-heterocyclic rings require a slight excess of haloalkane and can be carried out with or without solvent. The better the leaving group character of the halide the milder the reaction conditions. Chloroalkanes need reaction temperatures around 80 ^{o}C for several days, bromoalkanes require temperatures around 50 ^{o}C (*Scheme 1.1.1*). It is important to take into consideration that the longer the alkyl chain, the lower the reactivity due to steric constraints. The reaction does not require Schlenk conditions to be carried out, but these are desirable to avoid oxygen, which induces a pale-yellow coloration in the liquid. The halide salt formed can be purified by heating under vacuum to remove any excess of haloalkane when the alkyl chain is short and thus relatively volatile. When the haloalkane is not volatile, washes with organic solvents are required. Using a solvent in which the halide salt is not soluble is a good strategy to remove the unreacted starting materials.[5]

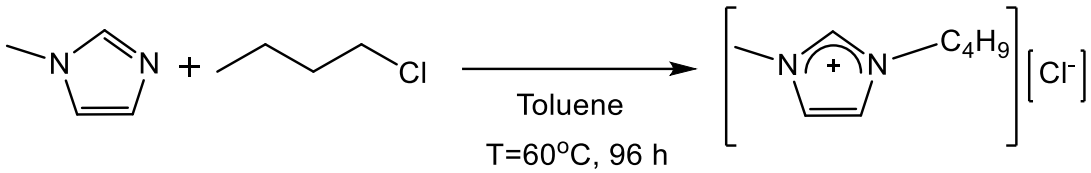

Scheme 1.1.1: Quaternisation of 1-methylimidazole by nucleophilic substitution over chlorobutane.

Other synthetic routes to prepare cations for ILs are alkylation with halogen-free alkylating reagents like alkylphosphates or alkylsulphates; *in-situ* generation of N-heterocyclic carbenes and further treatment with acids.[4]

The anionic species can be formed directly from the protonation or the quaternisation steps described before. However, if another anion is desired, it can be prepared by anion metathesis. Examples are metathesis of halide salts with a silver salt of the desired anion in water or methanol, which produces a silver halide precipitate and the IL. Another metathesis strategy involves lithium bis(trifluoromethanesulfonyl)imide Li[Tf_2N] in water, the IL product is

usually insoluble and forms a biphasic system that can be separated and washed. Other examples of anion exchange are reactions between halides salts and metal-based Lewis acids like $AlCl_3$, $FeCl_4/Fe_2Cl_7$, $VOCl_2$, *etc.* to form new anionic species.[5]

1.1.1 Ionic liquids' green attributes

In September 2015 the United Nations held a summit in New York City to discuss poverty, peace, prosperity and preservation of planet Earth. All the countries agreed upon adopting the 2030 Agenda for Sustainable Development, a plan of action to achieve a series of Sustainable Development Goals. Chemistry can be positively employed to achieve some of these goals such as #7: affordable and clean energy; #8: sustainable, inclusive and innovative industrialisation; #12: responsible consumption and production, 13#: climate action; #14 & 15: sustainable use and protection of aquatic and land ecosystems.[6]

Green chemists have been working on these problems actively since the 90's. Since then, many alternative and more environmentally friendly chemical processes have been published, which guided the scientific community towards the promulgation of the 12 principles of green chemistry[7]

According to these principles, a green chemical process is the one that maximises the use of all materials involved while reducing the amount of waste generated; when available, it should use catalytic strategies rather than stoichiometric reactions; its energy requirements should be minimised *e.g*. room pressure & temperature. It should not need auxiliary substances and derivatisation techniques in order to generate the minimum amount of waste. In terms of the starting materials and products, a green chemical process should use substances that are not harmful to health and the environment and the products should be degradable after their purpose has been fulfilled.

Over the past two decades, there has been a substantial interest in ILs in synthetic chemistry as replacement for traditional volatile organic solvents because ILs exhibit properties that make them suitable solvents such as

negligible vapour pressure, high heat capacity, good solubility for metals and ionic species, immiscibility with most organic solvents great potential for recyclability and flexibility of design.[8]

Welton pointed out that frequently in literature ILs are regarded as a green technology because of the negligible vapour pressure and the fact that these liquids can be designed *ad hoc* to be non-toxic to human health and biodegradable; nevertheless the author mentioned that criticism from other researchers exist, they affirm that the ions involved in ILs syntheses are often toxic and non-degradable.[7]

In a critical review on the assessment of the green credentials of ILs, Deetlefs and Seddon identified that the huge manipulability of the ILs structure to address different properties, can make them loose their green attributes. They affirmed that an ILs is only truly green when its chemical structure and its synthesis are both green.[9]

Deetlefs and Seddon suggested to evaluate the ILs preparation risk assessment using E-factors rather than atom economy since the second only takes into consideration whether all the starting material is incorporated to the product; it does not take into consideration whether a reaction gives side-products or has low yields. On the other hand, E-factor accounts for all generated waste.[9]

The authors concluded that a synthetic procedure for ILs is not green when excess of alkyl halide is needed, when solvents are employed for synthesis and washing up, when thermal conductivity from a heating source such as oil is used and drying of the ionic liquid is necessary. Instead, to make ILs green, they suggested syntheses assisted by microwave irradiation since reactions are faster and require less excess of alkyl halide. When further anion metathesis is involved, ILs need washing with organic solvents or water depending on the hydrophilicity of the salt, which can generate toxic waste and requires a high amount of energy.[9] Another topic of concern is the source of the starting materials, which are often derived from the petrochemical industry and which derivatisation require substantial energy investment.

In conclusion, even though ILs exhibit interesting green attributes like non-volatility, recyclability, thermal stability and “designer” capabilities, these are not sufficient features to classify ILs as a green technology *per se*; both the final product and its synthesis should follow the principles of green chemistry in order to be considered as green.

1.2 Description and synthesis of deep eutectic solvents

Eutectic mixtures are usually covered during early courses of physical chemistry at the undergraduate level. These mixtures are made of at least two components and possess the property of melting at considerably lower temperatures than the melting points of its pure components when mixed at a specific molar composition called eutectic point.

When two mixed solids reach the eutectic point, the molar fraction of the liquid components remains the same in both the solid and the liquid fractions as can be seen in a temperature vs composition diagram **Figure 1.2.1**.

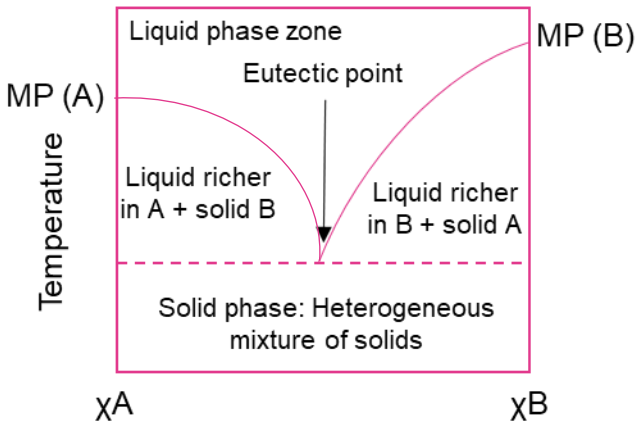

Figure 1.2.1*:* T vs χ diagram for a 2 immiscible-solids/miscible-liquids system

The first reference on the application of eutectic mixtures, now DESs, on the field of ILs and green solvents is by Abbot *et al.* at the University of Leicester in 2001.[10] The authors reported an IL composed of Zn and Sn chlorides with different quaternary ammonium salts as an alternative for overcoming water-sensitivity and costs of some ILs. The need for fixed molar ratios was

highlighted in the paper and the lower melting points of the mixtures with respect to those of the pure components were discussed.

Table 1.2.1: Classification of DES

Family	Formula	Example
I	Cat^+X^- $zMCl_x$, M=1st transition series or p-block metals	$ChCl/FeCl_3$
II	Cat^+X^- $zMCl_x*yH_2O$ (hydrated)	$ChCl/CoCl_2$ $6H_2O$
III	**$R_4N^+X^-$ zRZ**	ChCl/U (1:2)
IV	MCl_x+zRZ	$ZnCl_2$/U (1:3.5)

DESs are described as binary of tertiary mixtures of Lewis acids and bases, which are liquid at temperatures below 100 ºC. DESs can be represented by the general formula Cat^+X^-zY. Cat^+ is an ammonium, sulphonium phosphonium cation, X^- is the counterion which is usually a halide. *Y* is another molecule which interacts with the salt *CatX* through intermolecular interactions. It is the nature of *Y* the one that allows chemists to classify DES into families, (*Table 1.2.1*). Family I is composed of the cations mentioned above and non-hydrated metal chlorides. Family II is much like family I but consist of hydrated metal halides instead. This improves DESs water tolerance and reduces the price of the components.[11]

Family III is made of quaternary ammonium salts and hydrogen bond donors (HBD); this is the most popular DES family in synthetic chemistry due to the availability, cost, tuneability, biodegradability and low toxicity of the components. This because, Family III is usually made of choline cations and chloride (ChCl) or other ammonium derivatives while the HBDs could be natural metabolites, polyols or amides such as urea (U), glycerol (G), glucose (D-Glu), acetamide ($AcNH_2$), carboxylic acids, *etc*. Family IV is composed of transition metal halides and hydrogen bond donors, *Figure 1.2.2*. Through this thesis, the nomenclature to refer to DESs will be as follows: Lewis base/Lewis acid *e.g.*, a DES, made of 1 equivalent of ChCl and 2 equivalents of ethylene glycol (EG) will be referred as ChCl/EG. In cases where two or more DESs are made of the same components but with different stoichiometries, a third label

will be used to indicate it. A list of common DESs, the stoichiometry of their components and its melting points is showed in *Table 1.2.2*.

Table 1.2.2: Common DESs

DES	Ratio	HBA MP(ºC)	HBD MP(ºC)	DES MP(ºC)
ChCl/U[12]	1:2	302	133	12
ChCl/Gly[12]	1:2	302	18	-40
ChCl/$ZnCl_2$[12]	1:2	302	290	14
$ZnCl_2$/U[12]	1:3.5	290	133	24
$ZnCl_2$/$AcNH_2$	1:4	290	80	9
$ZnCl_2$/EG[12]	1:4	290	-13	-16
K_2CO_3/Gly[13]	1:4	891	18	-38

HBA: hydrogen bond acceptor. HBD: hydrogen bond donor. HBDs: U = urea, Gly = glycerol, AcNH2 = acetamide, EG = ethylene glycol

Choi *et al.* introduced the concept of "natural deep eutectic solvents" (NADES) as DESs formed from cell metabolites.[14] The researchers postulated the hypothesis that natural compounds existing in cells like sugars, small-chain carboxylic acids and ChCl, should form eutectic mixtures inside cells.

The authors carried out experiments to investigate the solubility in NADES of cell compounds which are not soluble in water nor lipids. The authors concluded that NADES could play significant roles in biosynthesis, and cell survivability in extreme temperature or drought environments. However, it is the opinion of this student that the term NADES is used arbitrarily nowadays in the field of green solvents since for example, the prototypical DES ChCl/U: 1 equivalent of ChCl, 2 equivalents of urea is technically made of components of the metabolism, nevertheless it is not regarded as NADES; other examples of DESs made of natural components and not always regarded as NADES are ChCl/G: 1 equivalent of ChCl, 2 equivalents of glycerol, ChCl/D-Glu: 1 equivalent of ChCl 2 equivalents of glucose or ChCl/AA: 1 equivalent of ChCl, 1 equivalent of acetic acid. For this reason, the term DES will be used for all eutectic mixtures discussed in this thesis.

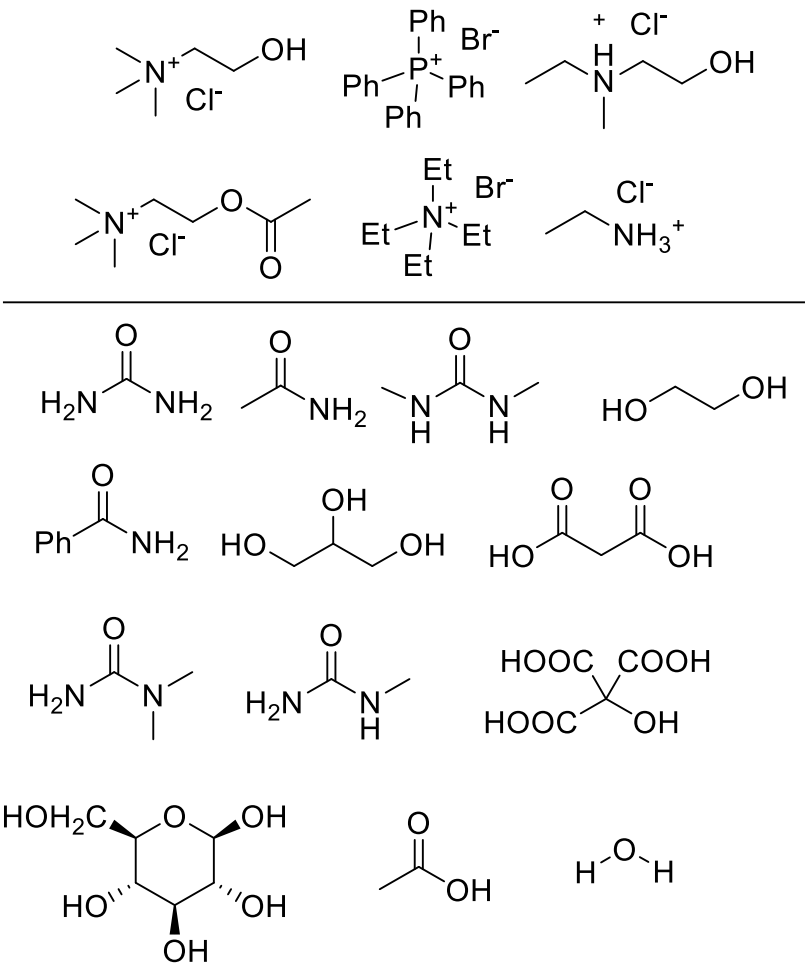

Figure 1.2.2: Common Salts and HBDs used for DES III Family

The synthesis of families II, III and IV DES is quite straightforward and does not require Schlenk techniques nor Argon glovebox. It is just matter of mixing the desired salt, also known as hydrogen bond acceptor (HBA) and the HBD in the correct molar proportion and stirring for periods no longer than 2 hours at temperatures between 60 ^{o}C to 80 ^{o}C. Since no solvent is required and all the starting material is consumed to form the new DES, the E-factor for these syntheses is virtually zero. Abbot's group recommends crystallization of the HBA salt from absolute ethanol with further filtration and drying under vacuum prior to use, while the HBD can be dried under vacuum before using.[15]

The characteristic depression of the melting point of the DESs is due to the interactions between Lewis acids and bases. In the case of DES families III & IV, the complexation of the HBD with the anion from the HBA promotes the

dissociation of the salt ions and disperse the charge localized in such species which lowers the lattice energy of the solids, *Table 1.2.2*. Abbot and co-workers pointed out that the lower the symmetry of the ions the lower the melting temperature at the eutectic point.[16]

It has been pointed out by many authors that for some mixtures a pure melting point is not observed.[13,17] Instead, a glass transition occurs. This is due to slow solidification kinetics and structure-reinforcing effects of the cation over the HBD that cause an extra investment in heat of fusion. This effect is characteristic of mixtures of HBD bearing hydroxyl functionalities like ethylene glycol with group 1 metal salts such as potassium carbonate or sodium chloride.

Francisco *et al*. prepared mixtures involving oxalic, malic and lactic acid with different amino acids and ChCl as HBA. All of their mixtures formed liquids at room temperature; however, they found glass transitions rather than true melting points. Then, they proposed to generalise the concept of DESs to low transition temperature mixtures (LTTM).[18]

1.3 DES at the molecular level

As discussed before, DESs are mixtures of at least two Lewis acids and bases. The molecular arrangement of the solvent depends on the type of intermolecular interaction occurring between its components: ionic, dipole-dipole Van der Waals, *etc*. It is complicated to generalise the knowledge generated by studying a particular DES system to the rest of the mixtures. Therefore, this chapter's review is narrowed to DESs formed by ChCl, as these are the primary focus of the thesis.

The prototypical ChCl/U DES was first described by Abbot *et al*. in 2003 alongside other DESs made of Ch derivatives and amides.[16] The eutectic point was found at a stoichiometry of 2 equivalents of urea per equivalent of ChCl.

The authors theorized the depression of the freezing point is caused by a hydrogen bond interaction between the urea's NH_2 protons and the chloride

anion. Their proposed structure is depicted in *Scheme 1.3.1*. They backed their hypothesis on the following experimental observations: the crystal structure of a choline oxalate/thiourea mixture showing atomic distances between the oxalate and the thiourea protons close enough to be considered as a hydrogen bonds; intense cross-correlation in ^{1}H-^{19}F NOESY 2D-NMR between F^- and protons from a NH_2 moiety in a choline fluoride/urea mixture; and ChCl/U FAB-MS experiments which showed a peak with a mass consistent with a complex between one chloride and two urea molecules.[16]

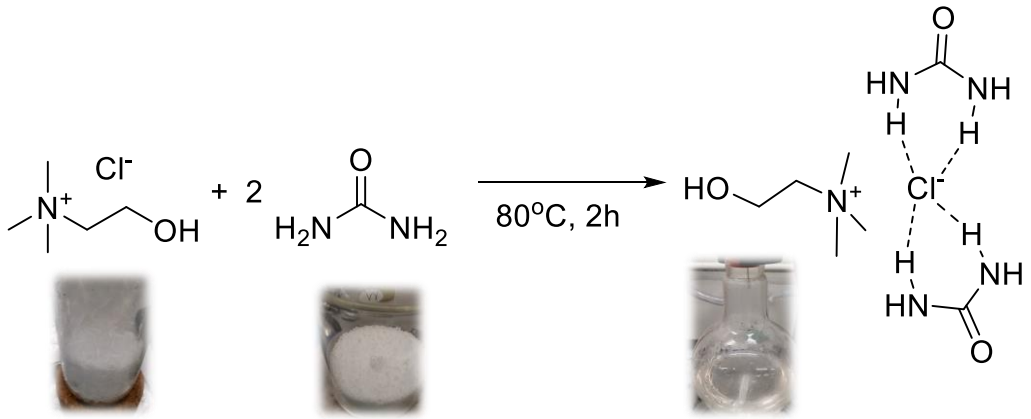

Scheme 1.3.1: Preparation of ChCl/U. Ion-complex proposed by Abbot *et al*.[16]

It is noteworthy that the authors found DESs between ChCl and different amides at the same stoichiometry, this is ChCl/Amide (1:2).[16] The cases of benzamide and acetamide are interesting since the stoichiometry would imply 2 molecules of amide per chloride but only one N-H fragment to provide hydrogen bonds which, if compared with ChCl/U leaves the chloride anion with vacant sites to coordinate to H-bond donors

Following this discovery, DESs between ChCl and carboxylic acids were reported in 2004 by Abbot *et al*.[19] They found the same stoichiometries and inferred that 2 molecules of acid have to coordinate to the anion in order to form the eutectic. The authors noted that when adding $NaHCO_3$, the salt remains unreacted and undissolved in the DES after several days with no relative effervescence observed. They interpreted this as an intense association between the acidic protons and the anion, which did not let them

undergo proton-transfer reactions to generate H_2CO_3, and thus, produce effervescence.

The model proposed by Abbot, now-called the ion-complex model, presumes to describe molecular organisation in the bulk DES. It suggests that the anion from the HBA disperses charge through a hydrogen bond interaction network.[20] Hence, the stronger and more numerous anion-HBD interactions, the larger the effect that charge delocalization has on the reduction of the transition temperature.[21] However, according to Hammond and Edler, the description of the molecular structure of DES in the bulk is specific for each mixture and cannot be generalised to other DESs in this way. For these authors, the ion-complex model provides fundamental understanding of the DES nanostructure, but a more personalised description of each DES structure should be done employing analytical techniques and computational chemistry. For example, at the expense of generalizing, the ion-complex model tends to undermine the HBD-HBD and cationic-anionic interactions.

The structure of DESs at the molecular level can be interrogated computationally or experimentally. Molecular dynamics (MD) is an interesting computational tool for simulating the bulk structure of DESs. It allows the researcher to model any desired stoichiometric mixture of DES either at constant volume and temperature (canonical ensemble) or constant pressure and temperature (isothermal-isobaric ensemble). MD use atomistic models; molecules are represented as spheres of fixed charge wired by bonds simulated as springs, the movement of these systems is described using classical mechanics and electromagnetism. The model requires to be provided with several parameters such as bond distances, spring restitution constants, bond angles and atomic sizes. These parameters alongside the equations that describe interactions between charges, dipoles, quadrupoles, etc. define a total potential energy function V=V(x,y,z) that depends on the Cartesian coordinates of all atoms, called the force field.[22] The minimization of V(x,y,z) through different approaches allows to obtain bulk structures and averaged physicochemical properties at equilibrium.

Sun *et al*. used MD to study hydrogen-bonding lifetimes and energy partitions in ChCl/U and other ChCl/U mixtures, through the analysis of the radial distribution functions (RDFs) obtained for each atom at equilibrium.[23] The authors found that in pure ChCl the ions create an alternating pattern of cation-anion-cation-anion, where Cl^- interacts mainly with the hydroxyl hydrogen (6) and the methyl hydrogen atoms (1-3) from choline (Ch^+), (*Figure 1.3.1-A*). According to the RDFs urea gets into the anion coordination sphere, around other cations and compete with methyl protons (1-3) for the interactions with the anion, which is repositioned farther from the ammonium centre and closer to the hydroxyl hydrogen (6). Interestingly, urea and Ch^+ were found to interact as well, through hydrogen bonds between the methyl and the methylene Ch^+ hydrogen atoms with urea's oxygen, although those interactions are less intense than urea-anion (*Figure 1.3.1-B*). The authors reported that when urea concentration increases, so does the urea-urea and anion-urea interactions; when urea reaches the eutectic composition the reduction of cation-anion interactions is balanced by increasing anion-HBD and HBD-HBD interactions. Additionally, all RDFs showed considerable noise and a lack of distinctive features when urea was added, which was interpreted as a disruption of the ChCl ordered structure.

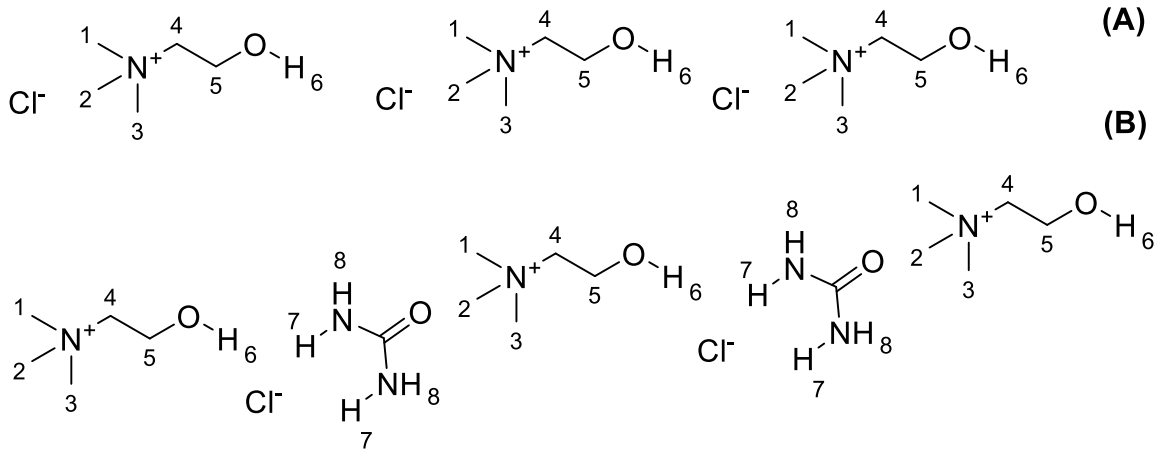

Figure 1.3.1: Molecular representation of radial distribution functions calculated for ChCl/U by Sun *et al.*[23] (A) Short atomic interactions in pure ChCl. (B) Short atomic interactions in ChCl/U mixtures.

Also, the study showed that the lifetime of all meaningful interactions is the smallest for this eutectic composition, which indicates higher mobility and can explain the lower melting point, the lifetime of various hydrogen bonds are showed in *Table 1.3.1*. With regards to energy partitioning, the simulations indicated that the energy related to the urea-anion interaction increases with concentration while cation-anion energy decreases, the eutectic point occurred when urea-anion interaction energy surpassed the ionic interaction energy. Also, at the eutectic point, urea induces the weakest interactions because at higher urea concentration, urea-anion interaction energies increases and hence, higher melting points are obtained.[23]

Table 1.3.1: Estimated ChCl/U H-bond lifetimes in ps.[23]

Bond	**Urea mol%**				
	0	25	50	67.7	75
OH(6)···Cl	18.8	18.4	12.3	12.6	16.4
NH(6)···Cl	-	4.6	2.8	2.4	4.1
NH(7)···O	-	14.7	4.0	3.0	4.3

Perkins *et al*. studied hydrogen-bonding in ChCl/U, ChCl/G, ChCl/EG and a DES made of 1 equivalent of ChCl and 1 equivalent of malic acid (ChCl/M) through MD and FTIR.[24] The methodology employed a similar force field to Sun's *et al*. The authors found the RDFs of all DESs follow similar patterns except for the ones accounting for anion-HBD interaction which depends on the HBD structure. All ChCl DES show a bimodal distribution for cation-anion distances, this appears to be typical for choline-based DES; the authors suggested this is due to 2 different Ch^+ binding orientations towards Cl^-. It's also noteworthy that urea interacts with chloride preferentially through the *trans* NH_2 hydrogen atom with respect to the oxygen atom. Overall, this study supported the ion-complex model since anion-HBD are the most important interactions, nevertheless, they acknowledged HBD-HBD interactions play an important role for ChCl-based DES.

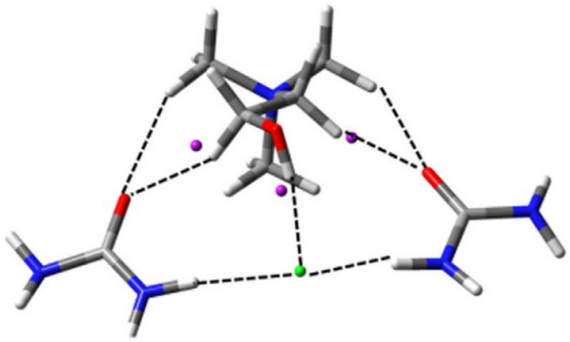

Figure 1.3.2: ChCl/U minima structure. Hydrogen bonds in dotted line. Cage critical point in purple. Cl^- in green. Adapted from García *et al*.[25]

García *et al*. studied the topological features of the electron density in some small clusters made of ChCl-based DES.[25] They discovered no correlations between DES melting point and the topology of the electron density involved in the HBD-anion interaction. They attributed this to the fact that many other interactions also help to keep the cage-like cluster structure together, therefore, the single description of the HBD-anion hydrogen bonds is not enough to explain such structure, *Figure 1.3.2*. Keeping this in mind, they looked for a feature which could include all the interactions present on the clusters rather than looking for each one separately. The cage critical point is an electronic topological feature which appears inside closed networks like the ones depicted in *Figure 1.3.2*. They found that the less electron density that is accumulated in these regions, the lower the melting point. This was explained in terms of charge delocalization through the hydrogen bonds, which promotes low-charge densities and thus low melting temperatures, due to weaker interactions between solvent components.

Overall, the three studies agree on the fact that urea disrupts the ChCl structure by moving Cl^- further from the cationic centre than in ChCl. The role of the HBD-anion interactions is under debate. For Sun *et al*. HBD-anion interactions are not the strongest nor the most long-lived interactions whereas for Perkins *et al*. HBD-anion interactions are the most numerous and strongest, which would support the ion-complex model. García *et al*. followed

the same trend by suggesting the charge delocalisation in the HBD-anion complex was responsible for the DES melting point depression.

Wagle *et al*. studied ChCl/U, ChCl/EG and a DES made of 1 equivalent of ChCl and 1 equivalent of malonic acid (ChCl/MA). They used a methodology combining experimental FTIR with electronic-structure calculations. The authors proposed some DESs cluster structures and a found good agreement between the calculated and experimental IR spectra. Afterwards, they performed bond-order analysis, charge-transfer analysis and studied the thermochemistry of the DES interactions.[26]

Table 1.3.2: Calculated total Bond Orders for the interactions between DES components.[26]

Species	Ch--Cl	HBD--Cl	HBD--Ch
ChCl	0.876	-	-
ChCl/U	0.937	0.300	0.288
ChCl/EG	0.196	0.428	0.511
ChCl/MA	0.648	0.479	0.058

The authors found a linear correlation between the Ch-Cl total bond order and the melting point. They highlighted the role of weak non-covalent interactions like CH···O through the hydroxyl lone pair on the stabilisation of both Ch-Cl and Ch-urea interactions; in fact, they found higher total bond orders for HBD-cation interactions compared to HBD-anion interactions in ChCl/EG and ChCl/MA, the calculated bond orders between DES components are shown in *Table 1.3.2*.

Nevertheless, for ChCl/U, the authors' findings agreed with the MD results discussed previously, this shows the complexity of DESs' bulk structure, where relationships between molecular interactions and physical properties are difficult to stablish even through a family of ChCl-based DESs.

The charge transfer analysis performed by Wagle *et al.* confirmed the ion-complex hypothesis which states that the charge is spread from the ions to the HBD through the hydrogen bond network. However, they also found Ch^+ contributed more significantly to the charge delocalization into the HBD than

Cl^-, in contrast with previous papers that concluded that HBD-cation interactions were weaker than HBD-anion interactions, *Table 1.3.3*.

Finally, the authors concluded that the reduction of the mixture melting point at the eutectic composition was enthalpy driven. Overall, the authors proposed a DESs structure model composed of a heterogeneous bulk with ordered regions of cage-like arrays dominated by HBD-cation and HBD-anion interactions.

Table 1.3.3: Charge comparison between DESs and pure components (dimers). [26]

Component	Ch^+	Cl^-	Urea	EG	MA
Pure ChCl	0.780	-0.780	0	0	0
ChCl/U	0.825	-0.781	-0.044	-	-
ChCl/EG	0.857	-0.689	-	-0.168	-
ChCl/MA	0.832	-0.723	-	-	-0.109

Charge in atomic units calculated at the DFT(M062x/6-31++G(d,p)) level of theory

Wagle *et al.* findings with regards to the more intense charge transfer process between HBD and cation compared to HBD and anion is at odds with the work supporting the complex-ion model, the debate focuses on whether this model fairly represents the DES bulk structure or if it exists only as aggregates inside a heterogeneous universe. García *et al*. and Wagle *et al*. chose their cluster structures by “chemical intuition” followed by structure optimisation. Two ways to reduce human bias in structure selection are MD starting from random positions or Monte Carlo generated molecular clusters. With regards to the optimisation, the calculations were done in the gas phase which could increase interaction distances compared to in solvent, and therefore, produce a different order for the trends of the charge transfer process in real systems.

Following Wagle *et al*. and García *et al*. research, Ashworth *et al*. published a comprehensive study of the possible Ch-Cl, Ch-urea, Cl-urea and urea-urea cluster structures in ChCl/U through the analysis of 172 different H-bonds, structural and energetic comparisons, the topology of the electron density around the hydrogen bonds and charge delocalisation through NBO analysis.[27] First, the authors highlighted the role double-ionic H-bonds play on

the stabilisation of molecular geometry in DESs. These non-traditional bonds are formed between the chloride and the methyl hydrogen atoms near to the ammonium centre. These bonds are overall weaker than the traditional OH···Cl bonds, however, when all their contributions in the most stable geometries are accounted, they arise as stronger than OH···Cl bonds.

Ashworth *et al*. found several sets of ChCl structures within a range no higher than 24 kJ/mol, which indicates that many geometries are available in the liquid phase. What could be highlighted is the fact that all the most stable ion-pairs show at least 2 double-ionic H-bonds and one linear O-H···Cl bond, all of which serve as medium for certain charge delocalisation between the ions, nevertheless, the authors conclude the ion pair still behaves like ions, not like neutral entities, due to the charge delocalisation *Figure 1.3.3*.[27]

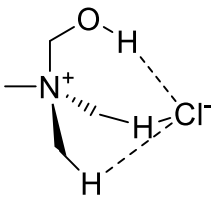

Figure 1.3.3: Example of a tripodal ChCl structure with 2 double ionic H-bonds, described by Ashworth *et al*.[27]

With regards to urea-urea and urea-Cl structures Ashworth *et al*. tested different urea-urea dimers and concluded there are at least 2 conformations available with hydrogen bonds similar in strength as OH···Cl. Afterwards, the authors tested the ion-complex hypothesis which suggest that charge delocalisation from Cl^- to urea through N-H_{trans} H-bonds is the main reason behind the DES melting point. They found that addition of urea to chloride in a chelating fashion as it has been proposed is certainly stabilising, however, in terms of energy, other structures like a dimer of urea linked to Cl^- through only one of the urea molecules or 3 urea molecules bonding directly to Cl^- are, for example, very similar in energy *Figure 1.3.4*. This means the proposed ion-complex is probably not the dominant geometry as others are almost equally competitive; even when comparing within urea-Cl-urea complexes, both

symmetrical and unsymmetrical variations are similar in energy. The authors also found the charge transfer from Cl^- to Urea is approximately 86% of the one found between choline and chloride, this means the urea-Cl complex disperse chloride's charge to a certain extent but, this is not likely to be the main cause of the DESs melting point depression. [27]

Finally, Ashworth *et al*. showed the importance of the Ch-urea interactions, often disregarded in other papers. They found the most intense H-bond is between choline's hydroxyl group and O_u. Again, many conformations lie within a threshold of 15 kJ/mol and interestingly, these conformations are equally competitive and stabilising as the formation of the ion-complex between 2 urea molecules and chloride. Based on this finding, the authors proposed the existence of a urea-Cl^----urea-Ch^+ cluster in which the charge is more diffuse than in the previously proposed urea-Cl-urea cluster.[27]

Overall, the work by Ashworth *et al*. is relevant because it highlights the role double-ionic H-bonds in the stabilisation of interactions where Ch is involved. It puts the proposed urea-Cl-urea ion-complex into perspective and concludes that it is probably not the dominant structure, also it redefines the role of urea in urea-ion interaction, which can hold and share small quantities of charge, but not enough to talk about a delocalised charge complex. Urea's role in the depression of melting point is not as a medium for charge delocalisation, but as charge separator and as inducer of intense entropic contributions. Urea can participate in hundreds of different interactions which enables a big number of competitive geometries. Ashworth *et al*. named this model of highly distorted molecular arrays holding a variety of different H-bonds with different energies and available geometries as "Alphabet Soup".

Zahn performed first-principles MD calculations for the ChCl/U DES.[28] the author discovered that the spatial distribution of both Cl^- and the oxygen from urea O_u, have similar features which indicate these species can interact with other DES components in a similar way. O_u appears closer to the ammonium methyl protons while the anion is closer to the hydroxyl group. Thus, Zahn supports the hypothesis that urea replaces chloride on the positions near the

ammonium centre. The melting point reduction is related then, to a balance of the old Ch-Cl interactions and the new urea-Ch interactions. The author also reported that HBD-anion NH-Cl hydrogen bonds have smaller lifetimes in comparison with OH···Cl bonds or other NH···O_u bonds. The authors proposed this fast NH···Cl hydrogen bonds could imply quick hydrogen bond hopping with other urea molecules, which could promote high mobility for the anion, which in turn could explain the melting point depressions. Also, the author investigated cluster dynamics, discovering cluster lifetimes between 20 to 100 ps. However, the analysis shows the molecules forming these clusters are unlikely to migrate together. Zahn concluded that ChCl/U bulk is composed of molecules rattling together in long-living cages rather than clusters far from each other in a heterogeneous media.

Finally, following Zahn's and Ashworth's findings, Stefanovic *et al*. published a QM/MM dynamic study linking viscosities and melting points in ChCl/U ChCl/EG and ChCl/G with their hydrogen-bonding capabilities.[27–29] The authors showed ChCl/U behaves differently compared to ChCl/EG and ChCl/G. In ChCl/U, urea has interactions with Cl^- and other urea molecules through its *trans* and *cis* hydrogen atoms respectively; this allows it to keep its bulk structure partially while effectively putting both ions apart, thus

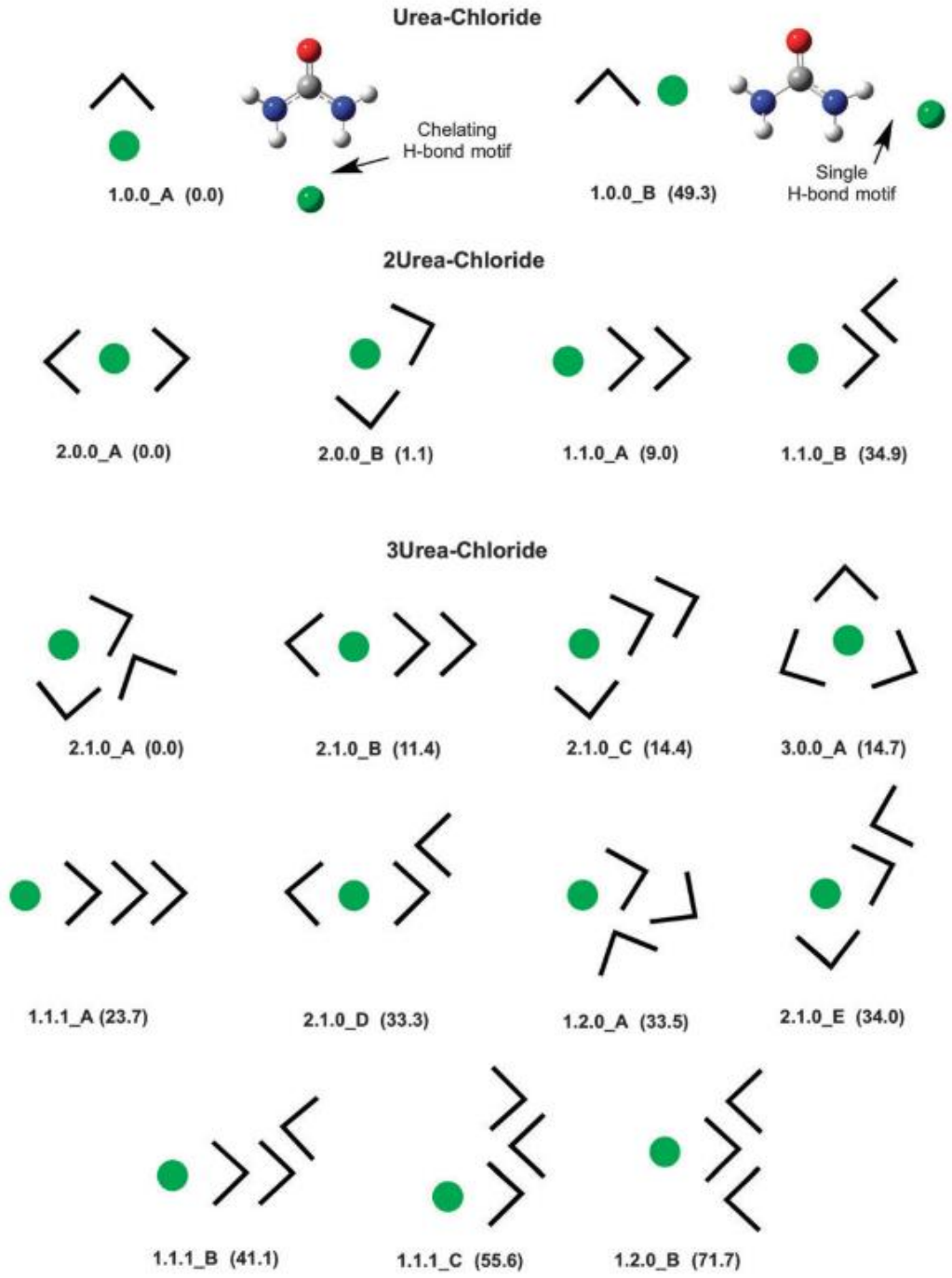

Figure 1.3.4: Various Urea-Cl clusters. The arrow represents the NH_2-C(O)-NH_2 urea structure. Energies in brackets relative to the most stable monourea-Cl complex in kJ/mol. Adated from Ashworth *et al*.[27]

reducing the electrostatic interaction between them; interestingly, the O-H···Cl interaction between choline and chloride remained almost as in the crystal

structure after adding urea which led the authors to suggest this interaction is not involved in the DES formation.

On the experimental side, D'Agostino *et al*. studied self-diffusion coefficients of choline and the HBD in ChCl/U, ChCl/EG, ChCl/G and ChCl/MA by ^{1}H-Pulse Field Gradient NMR.[30] Overall the study found choline diffuses more slowly than urea, ethylene glycol and glycerol. The authors attributed this to the size of the cation with respect to the anion. The same goes for the obtained activation energies, which measure how much energy a molecule requires to move to an adjacent position. The same trend was found for chloride, and it was explained likewise. In the case of malonic acid, it was found choline diffuses faster, which is attributed to the formation of stronger dimer interactions between the acid moieties of the HBD as compared to other DESs. Based on diffusion and viscosity data, the authors proposed that molecular movement in DES can be explained by a hopping mechanism where molecules move only when there is an adjacent void to occupy. For this model, nevertheless, the authors assumed total ChCl dissociation and formation of the ion-complex, which they justify with the ^{1}H-^{19}F-NOESY experiments discussed at the beginning of the chapter.

Wagle *et al*. studied the diffusion of molecular components in ChCl/G by quasielastic neutron scattering (QUENS). This technique allows the study of localised molecular movement, since the neutron wavelengths used are of comparable size to the intermolecular distances found in DESs, on the other hand, pulsed-NMR techniques inform us on long-range molecular diffusion.[31] The authors found that in contrast to the long-range phenomena studied by D'Agostino *et al*., Ch^{+} diffuses faster in the nanometre scale compared to glycerol. To explain this, the authors invoked a heterogeneous environment with ordered regions of cage-like aggregates hypothesis. When DES components are confined in localised regions, Ch^{+} exhibits faster diffusive motion even though its hydrodynamic radius is bigger than glycerol, because glycerol interacts more tightly with chloride. Glycerol is tied up through its H-bonds and diffuses slower inside the transient molecular cage.

The first experimental direct measurement of DESs structure was reported by Hammond *et al*. who performed neutron diffraction experiments on the liquid phase of ChCl/U.[32] The authors found high correlation for the HBD-anion interactions in agreement with the computational studies; urea tends to form four strong H-bonds with chloride through its *trans* hydrogen atoms of 2.2 Å on average, and a series of weak H-bonds through the *cis* hydrogens atoms with average bond lengths of 4 Å. Urea then, competes with Ch^+ for the H-bond interactions with chloride. With regards to Ch-urea interactions, the authors reported that the strongest interaction occurs between choline's hydroxyl proton and one nitrogen in urea, at slightly closer distances compared to $NH_{trans}\cdots Cl$, in contrast to what has been reported previously in MD studies. Nevertheless, the authors concluded that the position of Ch^+ near urea is mostly located around the $C{=}O_u$ bond axis and doesn't seem to be driven by the $OH\cdots N$ interaction. Instead, it is suggested that urea and Ch hold together due to weak H-bonds between choline's methyl and methylene protons with the electronegative urea atoms. With regards to the Ch-Cl interactions, the authors reported a strong H-bond between choline's hydroxyl proton with chloride and a smaller interaction between chloride and the ammonium centre. This explains the bimodal shape in cation-anion RDFs observed computationally for most Ch-based DES. Also, this confirms the hypothesis that when urea is added, chloride tends to abandon the cationic centre to reposition close to choline's hydroxyl group. The authors reported that the Ch-Ch correlations appeared at a distance of 6 Å on average, forming a solvation shell of 7 Ch cations around each other. Finally, the authors found strong urea-urea correlations trough $NH\cdots O_u$ in agreement with Ashworth *et al*. and Zahn *Figure 1.3.5*.[27,28]

Based on these results Hammond *et al*. proposed a structure model for ChCl/U of concentric solvation shells centred on chloride no bigger than 10 Å with many available structural conformations. The cage possesses localised charge neutrality with strong close-range interactions driven by the HBD, where each chloride is solvated by 1 Ch^+ and 2 urea molecules that are located near the ammonium centre. The structure is stabilised by a synergistic activity

of the OH···Cl, NH···Cl, OH···N H-bonds and weaker H-bonds and electrostatic interactions, which agrees with the "Alphabet Soup" model.[20,27,32]

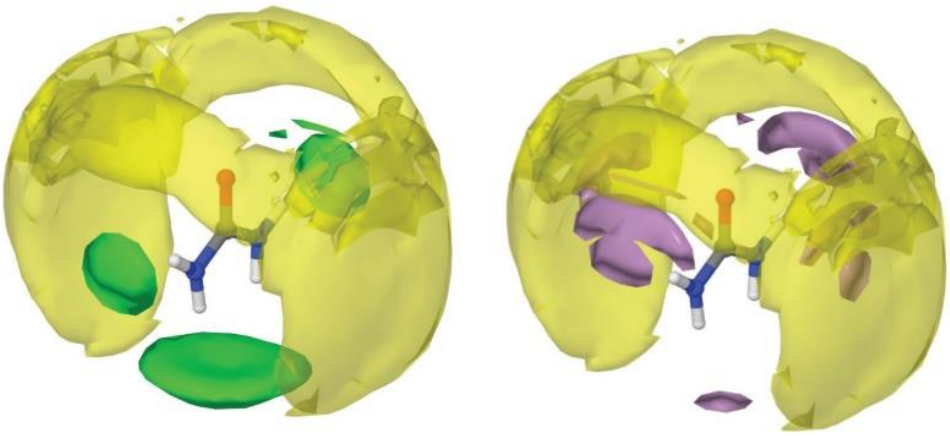

Figure 1.3.5: Spatial distributions functions centred on urea showcasing the cage-like structure of ChCl/U. Yellow surface: Ch probability. Green Surface: Ch probability. Purple surface: Urea probability. Adapted from Hammond *et al*.[32]

The revision of the last 15 years of publications regarding DESs bulk structure show that the first hypotheses trying to explain DES structure and its properties pointed towards the formation of a complex between the salt's anion and the HBD or complexing agent (depending on the DES family). Nevertheless, through years of computational and experimental research, particularly on family III ChCl-based DESs, the understanding of the bulk structure shifted from a complex-ion model to an "Alphabet Soup" of intermolecular interactions. Overall, ChCl-based DES bulk structures can be understood as a mixture of H-bonds, non-covalent and electrostatic interactions between cations, anions, HBA and HBD; which give rise to a plethora of disordered conformations with localised ordered regions of cage-like structures.

1.3.1 Are DES ILs?

To answer this question one has to be more precise. DES families I and II can be regarded as a subset of ILs based on ammonium salts, since the mixture of the salt and the metal chlorides generates a new salt exhibiting a depression of its melting point with respect to the original components, *Scheme 1.3.2*. In fact, these salts made of ammonium, sulphonium or phosphonium cations with

metal chlorides such as $AlCl_3$ or $ZnCl_2$ are analogous to haloaluminate ILs described in the fifties from reaction of salts like imidazolium halides and species like $ZnCl_2$ or $AlCl_3$.[5,10]

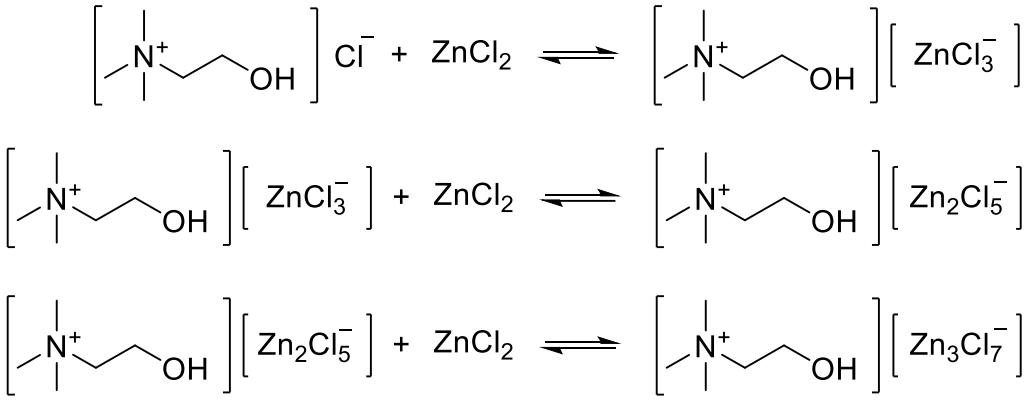

Scheme 1.3.2: Series of equilibria occurring in the mixture of a model DES from family II.

On the other hand, DESs from family III, which is undoubtedly the one that gathers most attention currently, and family IV, are not ILs because these are mixtures made of ions and neutral components, while ILs are composed of ions only.[21]

1.4 DES sustainability

DES are often regarded as green solvents because of their low-vapour pressure, non-flammability, cheap and simple synthetic methods, tolerance to moisture and the fact they are made from components that are not harmful to human health and that are biodegradable.

We developed a Strengths, Weaknesses, Opportunities and Threats (SWOT) analysis for the preparation of most ChCl-based DES, inspired by the work by Deetlefs and Seddon for the preparation of imidazolium-based ionic liquids *Figure 1.4.1*.[9]

These DES can be prepared directly by mixing ChCl and the desired HBD without prior purification (as received from the supplier). However, for studies of their properties or fundamental behaviour, it is recommended to first recrystallize ChCl from ethanol, followed by further drying under vacuum. In a

similar way, the HBD is commonly dried under vacuum at 40 ºC to get rid of as much moisture as possible.[16]

DES components can be mixed under room atmosphere or under inert atmosphere depending on how much moisture control is desired for the final application. The synthesis possesses an E-factor of 0 or 100% atom economy because all of the reagents are used for the eutectic mixture preparation and no further purification is required. We have observed that ChCl-based DES require stirring for 1 or 2 hours in an oil bath at 60ºC to achieve a homogeneous transparent liquid. With regards to storage, we keep our DES at room temperature in capped round-bottom flasks. We have observed that our DESs made of amide HBDs solidify as homogeneous oily solids. These require heating and stirring for 20 minutes to achieve a homogeneous transparent liquid again. Our DESs made of polyol HBDs do not solidify overnight but, after storing them for several days without further use, some ChCl crystallizes from the liquid matrix.

With regards to toxicity, DESs components are often biodegradable and harmless to human health. In fact, many of them are naturally present like urea, glucose, acetic acid or choline chloride. However, there is little data about their toxicity once mixed. Based on this we present the SWOT analysis as in *Figure 1.4.1*:

Figure 1.4.1: Strengths, Opportunities, Weaknesses & Threats analysis for ChCl-bases DES. Vectorial background: vecteezy.com

Yang reviewed the work done on toxicity and biodegradability of ChCl-based DESs. Most DESs show moderate to high toxicity to bacteria, fungi and protozoa. The mechanism depends heavily on DES concentration in water, the nature of the anion and HBD. Overall toxicity increases with: DES concentration, lipophilicity of the HBD, acidity when the HBD is an organic acid and charge delocalisation. The disruption mechanisms are not well understood but it is believed DESs can cross the cell wall and modify pH and ion-balance in the insides. DESs can interact with the cell wall as well, accumulating and disrupting it. Cell dehydration has been observed to be an important cause of death as well. In animals, it has been observed that DESs possess low to moderate toxicity, causing liver and muscular damage on models. DESs toxicity depended on the cell line since for some of them, DESs are more toxic than its components and for other lines the opposite is true. Data suggest those DESs made of metabolic components are less toxic than those which are not. Overall, DESs showed more toxicity than their pure components. On the other hand, biodegradability tests suggest all ChCl-based DESs are readily degradable; when the HBD is an organic acid or possess big

carbon chains, the degradability is lowered. The mechanisms for this are not well understood.[33]

1.5 Project general aims

The popularity of DESs has increased in the last 10 years for their use in a wide range of applications: from metal electrodeposition to extractions, from organic transformations to catalysis, processing of biomass, *etc*. Great efforts have been made recently on the elaboration of new sustainable protocols for carrying out organic transformations by the application of DESs as solvent media and sometimes as catalyst and reagent as well. The improvements due to DES are not only limited to the replacement of common volatile organic solvents, but also by enabling milder reactions conditions, wide functional group tolerance, and catalysis.[34,35] Despite the increasing popularity of DESs in organic synthesis, only a small number of reports have been published on the application of DESs as solvent media for cross-coupling reactions. On the other hand, the implementation of DESs in energy storage devices like redox-flow batteries has been limited as solvent/electrolyte for copper or iron redox-active salts.[36–38] The objective of this research project was to study the application of DESs in two areas of relevance for sustainable development: catalysis and energy storage.

The aim of the second chapter was to describe the chromatographic methodology employed to determine the outcome of the catalytic reactions carried-out in DESs and the experimental and computational techniques used to study the electrochemical properties of some redox-active organic salts. The aim of the third chapter was to implement Pd-catalysed Suzuki and Negishi cross-coupling reactions in DESs, and to analyze how the reaction conditions impact the selectivity of the Negishi reaction. The aim of the fourth chapter was to synthesize and characterise twelve redox-active anthraquinone salts, and to study their electrochemical properties to assess their usefulness as components or redox-active DESs or ILs for applications in energy storage.

Chapter II: Methodology

2.1 Chapter aims

As described in Chapter I, the main objectives of this research project were to study the implementation of cross-couplings in DESs, and to synthesize, characterise and analyze the electrochemical properties of a series of anthraquinone salts to evaluate their potential use in redox-active DESs or ILs

One of the aims of this chapter was to introduce gas chromatography and to the describe the methodology developed to determine the conversion to products from the catalytic reactions implemented in DESs, that were discussed in chapter III. The other aim from this chapter was to introduce and describe the electroanalytical and computational techniques that were used in chapter IV, to study the electrochemical properties of anthraquinone-based organic salts.

2.2 Gas chromatography

2.2.1 Introduction to gas chromatography

Chromatography is a technique designed to separate the components from mixtures by dissolving a sample in a mobile phase, which in the case of gas chromatography (GC), could be hydrogen, acetylene, helium, or nitrogen among others. The mobile phase is passed through a stationary phase, which can be solid or liquid. The separation is based on the different affinities exhibited by the components for both phases. As such, the stronger the interaction is between a component and the stationary phase, the slower the component moves through the stationary phase. A measure of how strongly an analyte interacts with the stationary phase is given by the distribution constant (*Equation 2.2.1*).[39]

$$K_c = \frac{c_s}{c_m}$$

Equation 2.2.1: Distribution constant of an analyte between the stationary and mobile phases. C_s is the concentration of the analyte in the stationary phase and C_m is the concentration of the analyte in the mobile phase.

At the end of the stationary phase, the analyte is directed into a detector, which generates a response linearly dependent to the analyte concentration in the mobile phase. The flame ionization detector (FID) is the most used detector in GC, and it was the equipment used in this research project. The FID is composed by an air-hydrogen-flame burner and an electrode. The FID is a suitable detector for organic compounds that generate radical and charged species after pyrolysis at the air-hydrogen flame.[39] The charged species are detected by the electrode and as a result, a plot of detector response signal vs time called chromatogram is obtained (*Figure 2.2.1*).

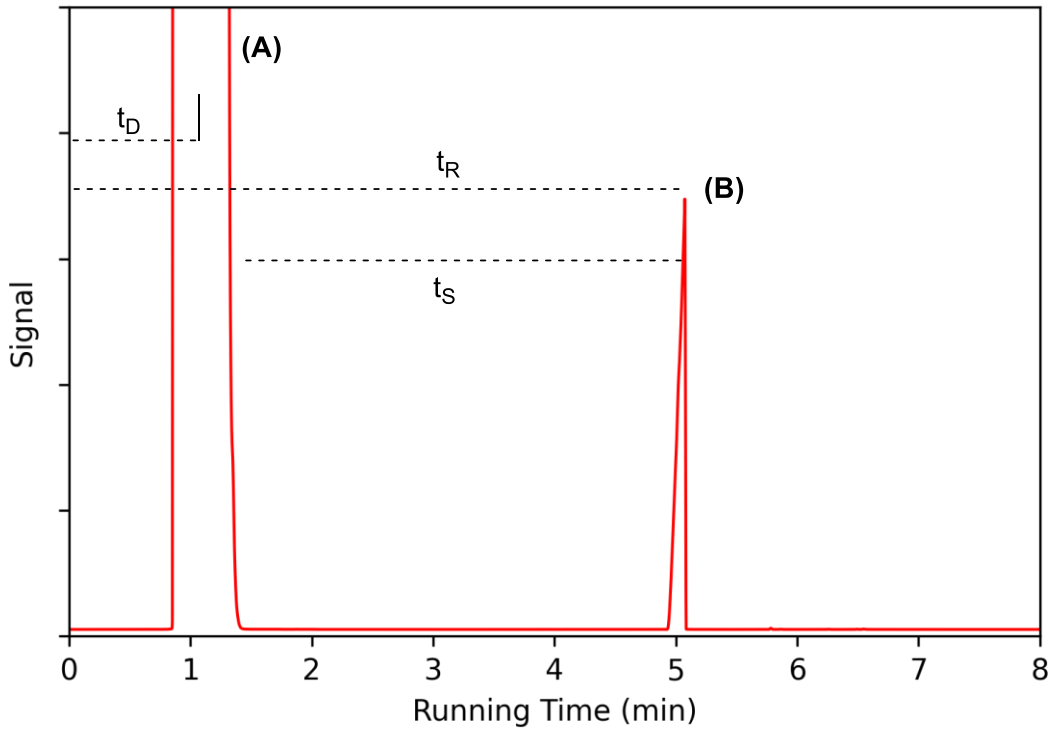

Figure 2.2.1: Example of a chromatogram from a pure sample of biphenyl dissolved in dichloromethane. (A): Unretained peak corresponding to dichloromethane. (B) Analyte peak

Two important parameters obtained from the chromatogram are the retention time t_R and the dead time t_D The retention time is defined as the time that it takes for the analyte to travel from the injection point to the detector, going through the stationary phase. The dead time is the time that it takes for species that does not interact with the stationary phase to travel the same path. In GC, it is better to calculate the retention volume V_R rather than the retention times, to accurately account for the effects of pressure and temperature on the mobile phase. The retention volumes also depend on the mobile phase flow rate according to *Equation 2.2.2*. This equation shows how the retention times of different species can be controlled by modifying the stationary phase temperature and the mobile phase flow rate.

$$V_R = t_R F \frac{T_c}{T}$$

Equation 2.2.2: Retention volume equation. t_R is the retention time and F is the mobile phase flow rate (cm^3/min), T_c is the stationary phase temperature and T is the temperature at the flow meter apparatus.

Another important parameter that can be obtained from a chromatogram is the peak area. The concentration of the respective analyte can be calculated by analytical methodologies like external calibration curve or internal standard addition, which allow to obtain response factors to transform the peak area units into concentration (*Equation 2.2.3*).

$$RF_A = \frac{[A]}{A_{pA}}$$

Equation 2.2.3: Response factor from an analyte A of known concentration [A]. A_{pA} is the analyte's peak area.

2.2.2 Gas chromatography methodology employed in chapter III

In this research project, GC was used to separate and analyze all the components of the crude reaction mixtures obtained from the catalytic reactions implemented in DESs. The amount of unreacted starting material

and the conversion to products and side-products were determined from their concentrations in the crude reaction mixtures.

First, stock solutions of each compound and an internal standard (naphthalene or *n*-decane) were prepared and used to determine their GC response factors according to *Equation 2.2.3.* Then, the relative response factor of each compound with respect to the response factor of the internal standard were calculated according to *Equation 2.2.4*

$$RRF_A = \frac{RF_A}{RF_{STD}}$$

Equation 2.2.4: Relative response factor the analyte A. RF_{STD} is the response factor of the internal standard employed.

The unknown concentration of the analytes was calculated according to Equation *2.2.5* from the chromatograms of the crude reaction mixtures, by adding a known amount of internal standard.

$$[\mathrm{A}] = \frac{A_{pA}}{A_{\mathrm{pSTD}}} \frac{[\mathrm{STD}]}{\mathrm{RRF_A}}$$

Equation 2.2.5: Calculation of the concentration of an analyte. A_{pA} is the analyte's peak area. A_{pSTD} is the internal standard peak area. [STD] is the known internal standard concentration and RRF_A is the analyte's relative response factor.

When the chemical response of the internal standard at the FID does not completely reproduce the chemical response of the analytes (starting materials, product, and side-products), a mass balance different of 100% can be obtained. For experiments in which a mass balance > 100% was obtained, the masses of the analytes detected in the chromatogram were normalised to 100%. For cases in which mass balance < 100%, the data was not normalised since it is not possible to determine if the result was due to the response of the analytes and the standard at the FID or due to mass loses alongside the methodology steps.

The response factors of the Suzuki and Negishi cross-coupling products were assumed to be equal to the response factor of a known reference sample of similar structure. The response factors of the dehalogenated arenes, which are side-products from the cross-coupling reactions, were assumed to be equal to a known reference of similar structure The response factors of the products from the homocoupling side-reaction of the organozinc reagents involved in the Negishi cross-coupling, were assumed to be equal to the response factor of biphenyl. The response factors of the products from the homocoupling side-reaction of the starting materials from the Negishi cross-coupling reaction, were assumed to be equal to the response factor of biphenyl. Naphthalene or *n*-decane were used as internal standards in all the experiments.

2.3 Voltamperommetric methods

2.3.1 Introduction to voltamperommetric methods

Voltamperommetric methods are part of electroanalytical chemistry and study the dependence of the current detected at the electrode with respect to the applied potential for a given electrochemical cell. Voltamperommetry can be used to quantitatively measure the concentration in solution of redox-active analytes, electron-transfer kinetics or mechanisms of reactions involving changes in oxidation states of reactants.

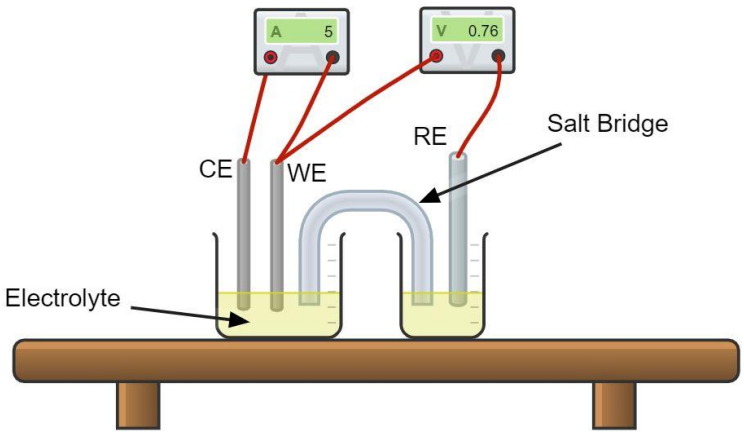

Figure 2.3.1: Schematic Representation of a three-electrode cell used in voltamperommetric measurements

The electrochemical cell in voltamperommetry consists of an array of three electrodes, a working electrode (WE), a counter electrode (CE) and a reference electrode (RE). WE and CE are submerged in an electrolyte solution containing the redox-active analyte. The RE is usually separated from the analyte solution to avoid contamination or perturbation of the chemical system that originates the electrode potential (*Figure 2.3.1*). The potential of the cell is measured by connecting a voltammeter to the wire between WE and RE, whereas the current is measured with an ammeter connected to the wire between WE and CE.[40]

In voltamperommetry, the electrochemical equilibrium is perturbed by the application of potential, which in consequence generates electric current caused by an electron exchange with the analyte. The current is then measured and received by a second electrode submerged in the solution to close the system. If the second electrode is the RE, then it is polarised by the current, causing unwanted potential fluctuations. The CE solves this problem by allowing the current to flow and close the electrochemical system. In this way the electrochemical equilibrium at the RE remains unaltered.

Although the potentials of redox processes like $[Fe(H_2O)_6]^{3+}(aq) + e^- \rightarrow [Fe(H_2O)_6]^{2+}(aq)$ are usually reported for the half-reaction of the reduction of the species, experimentally it is necessary to compare the potential of a given redox-process against the potential of a reference redox reaction. Following the previous example, the reduction potential of hexaaquoiron (III) to hexaaquoiron (II) is expressed as E= -0.77 V vs SHE, where SHE is the standard hydrogen electrode potential. This potential has been assigned as 0 V by convention and is based on the reaction $2H^+(aq) + e^- \rightarrow H_2(g)$ at 25 ^oC and 1 atm.

Table 2.3.1: Selected standard potentials of reference electrodes.

Ref. electrode	Half-reaction	E (V) vs SHE
Ag/AgCl (NaCl, 3 M)	$AgCl(s) + e^- \rightarrow Ag(s) + Cl^-$	0.209
$Hg/HgCl_2$ (KCl, sat.)	$HgCl_2(s) + 2e^- \rightarrow 2Hg(liq) + 2Cl^-$	0.244
Ferrocene ($LiClO_4$ 0.2 M in MeCN)	$Cp_2Fe^+ + e^- \rightarrow Cp_2Fe$	0.554

The SHE is experimentally a complicated reference electrode with which to work, therefore other reference electrodes are more popular in the literature. A list of potentials for the redox reaction of some reference electrodes are displayed in *Table 2.3.1*. IUPAC suggests reporting potentials for organic molecules and inorganic molecules in non-aqueous solvents referenced to the ferrocenium/ferrocene potential, measured separately under the same conditions.[41]

In voltamperommetry, the potential is a dynamic independent variable and can be applied to the system in different ways: constant rate *e.g*. linear sweep voltamperommetry, cyclic voltamperommetry (CV) or pulsed rate, *e.g*. differential pulse voltamperommetry (DPV). In CV, a potential is applied and increased linearly with respect to time, up to a certain value called the switching potential, after which the potential is reverted at the same rate (*Figure 2.3.2 left*). The current is measured at every potential and plotted in a potential (E) *vs* current (i) diagram called cyclic voltammogram (CV). In DPV, the potential is increased in a series of pulses of fixed amplitude, which are superimposed over a linear increasing potential (*Figure 2.3.2 right*). In DPV, the current is measured before and after the pulse increment t_2-t_1 and reported as a difference. The E vs i plot in DPV can be thought of as the plot of the first derivative of the E vs i curve obtained from a linear sweep in CV.

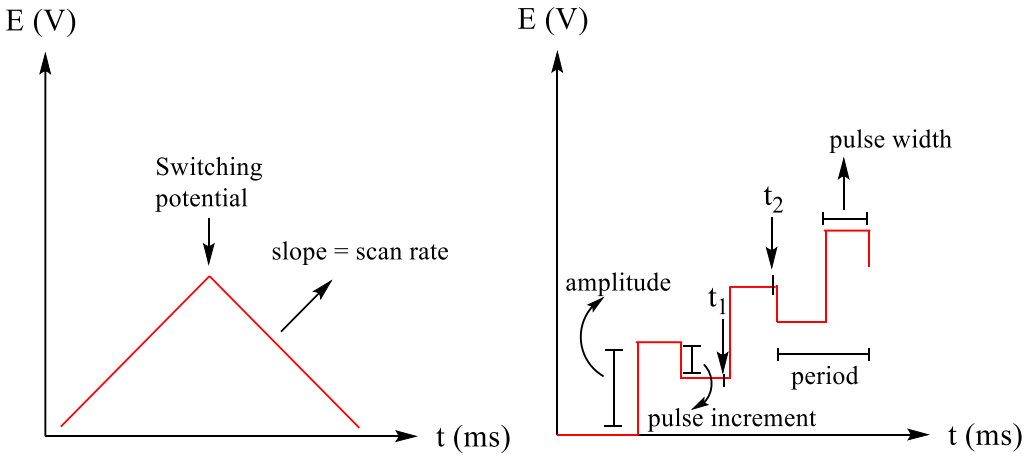

Figure 2.3.2: Application of potential over time in voltamperommetry. Left: cyclic voltammetry. Right: Differential pulse voltammetry

The ratio between the concentration of oxidized and reduced species of the analyte close to the electrode will be determined by the applied electrode potential according to the Nernst equation (*Equation 2.3.1*)

$$E = E' + \frac{RT}{nF} ln \left(\frac{[ox]}{[red]}\right)$$

Equation 2.3.1: Nernst equation. *R* is the ideal gas constant, *T* is temperature, *n* is the number of exchanged electrons, *F* is the Faraday constant and *E*' is the formal potential of the half-reaction studied at the experimental conditions.

In CV, the formal potential for electrochemical reversible processes is calculated as the average of the voltage of the cathodic and anodic peaks. The height of the current peaks derived from electrochemically reversible process variates linearly with the square root of the voltage scan rate according to Randles-Sevcik equation (*Equation 2.3.2*).

$$i_p = 0.446nFAC\left(\frac{nF\upsilon D}{RT}\right)$$

Equation 2.3.2: Randles-Sevcik equation. *A* is the electrode surface area, *C* is the analyte bulk concentration, *D* is the analyte diffusion coefficient and υ is the scan rate.

Instead, the current derived from electrochemical processes of electrode-adsorbed species depends linearly on the scan rate and the surface concentration of the to *Equation 2.3.3*.[40,42]

$$i_p = \frac{n^2F^2}{4RT}\upsilon A\Gamma$$

Equation 2.3.3: Peak current when redox species is adsorbed to the electrode. *Γ* is the surface concentration of the analyte.

In an electrochemical reversible process, the electron transfer between electrode and analyte is faster than the rate at which the analyte moves from

the bulk to the electrode surface. Consequently, these processes are limited by the analyte's diffusion.

Some key features of reversible processes include:

- The height of the reduction and oxidation peaks is $Ip_c/Ip_a = 1$
- The peak-to-peak distance is of 57/n mV at 25 ^oC, where n is the number of electrons exchanged as predicted by *Equation 2.3.1*
- The width of the redox waves is 59 mV
- Equation *2.3.2* is satisfied.

Electrochemically irreversible processes are characterised by slow electron exchange kinetics, which means overpotentials are needed for electron transfer to occur. Other sources of electrochemical irreversibility include chemical instability of the redox-active species.

2.3.2 Electrochemical methodology employed in chapter IV

The electrochemical performance of the AQ salts was characterised using CV. All voltamperommetric experiments were performed at a scan rate100 mV/s unless otherwise stated.

Tetrabutylammonium hexafluorophosphate 0.1 M was used as electrolyte in acetonitrile (0.0075 % m/m water on average) and dimethyl sulfoxide (0.255 % m/m water on average). ($[C_2Mim][Tf_2N]$) dried under vacuum (0.045% m/m water content on average) was used as solvent/electrolyte (details of the IL preparation can be found in *section 5.2.2*). The three electrolyte solutions were used to prepare 2 mM solutions of **38a** and salts **[41-46]Br** and **[41-46][Tf_2N]**. All the electrochemical measurements were performed using analyte concentrations of 2 mM unless otherwise stated.

The electrochemical cell consisted of a three-electrode setup, where a glassy carbon electrode (3 mm diameter) was used as WE, a Pt wire was used as CE and a Innovative Instruments Inc. leak-free Ag/AgCl electrode was used as RE For the electrochemical experiments involving the protic anthraquinone salts,

a BASi Pt disk electrode (3 mm diameter) was used as WE. The potentiostat used was a PalmSens EmStat[3].

The glassy carbon electrode was chosen over the Pt disk electrode as WE in acetonitrile for the study of the imidazolium and aprotic ammonium salts, because it exhibited a wider electrochemical window. However, the protic anthraquinone salts exhibited broad redox waves in acetonitrile with the glassy carbon electrode. For these protic salts, the Pt disk electrode was used as WE in dimethyl sulfoxide.

2.4 Electronic structure calculations

2.4.1 Introduction to electronic structure calculations.

The structure and some electronic properties of the anthraquinone salts prepared in chapter IV were modelled computationally using density functional theory (DFT). The calculation and modelling of the electronic structure properties of atoms and molecules is based on the postulates of quantum mechanics, described as follows:[43]

1. A state made of N particles is described by a wave-function $\Psi(q_1,q_2,\ldots,q_n, t)$ where q_n represents the Cartesian coordinates of each particle and t, time. The quantity $\Psi^*\Psi$ is proportional to the probability of finding each of the N particles in the volume space q_n+dq_n at a given time.
2. For every observable (measurable) property of a system, there is a corresponding linear Hermitian operator $\hat{H}$
3. If the wave-function of a system is an eigenfunction of certain operator $\hat{H}$ associated with an observable such that the eigenvalue equation *Equation 2.4.1 is* satisfied, then the eigenvalue equation will return a number “E” which is called the eigenvalue of the operator $\hat{H}$. The eigenvalue can be obtained experimentally, after measuring the observable associated with the operator.

$$\hat{H}\Psi = E\Psi$$

Equation 2.4.1: Eigenvalue equation.

4. If the wave-function is not an eigen-function of the operator, then instead of obtaining the associated eigenvalue when measuring an observable, a distribution of results is obtained.
5. The evolution over time for a state described by a wave-function is dictated by *Equation 2.4.2*, also known as the Schrödinger equation where $\hat{H}$ is known as the Hamiltonian operator and $\hbar$ is Planck's constant

$$\hat{H}\Psi = i\hbar\frac{\partial\Psi}{\partial t}$$

Equation 2.4.2: Time-dependent Schrödinger equation.

The Schrödinger equation is a second-order differential equation that, as described in the first postulate of quantum mechanics, depends on the Cartesian coordinates of each particle contained in the system and time. The Hamiltonian is the operator associated with the total energy of a system, which is divided into kinetic and potential components. For a molecule, the Hamiltonian is defined as *Equation 2.4.3*.

$$\hat{H} = T_q + T_N + V_{Nq} + V_{qq} + V_{NN}$$

Equation 2.4.3: Kinetic and potential energy components of the Hamiltonian.

T_q in *Equation 2.4.3*. is the electronic kinetic energy, T_N is the nuclear kinetic energy, V_{qq} is the potential energy experienced between electrons (repulsive), V_{NN} is the potential energy experienced between nuclei (repulsive) and V_{Nq} is the potential energy experienced between electrons and nuclei.

There are two key approximations that simplify electronic structure calculations. The first is the Born-Oppenheimer approximation, which is based

on the fact that nuclei in molecules are much heavier, larger and slower than electrons, thus they can be treated as fixed points of charge. In this way, the kinetic energy associated with the nuclei can be omitted. The second approximation involves defining a Hamiltonian operator independent of time, which is the case for the calculations performed in this project. The time-independent Hamiltonian under the Born-Oppenheimer approximation is depicted in (*Equation 2.4.4*) where the indices *q* & *j* represent electrons and *N* the nuclei. The first term of the Hamiltonian is the electronic kinetic energy operator, the second term is the potential energy operator accounting for the interaction between electrons and nuclei, with Z_N the atomic number of a given nucleus, the third term is the potential energy between electrons and the fourth term is the potential energy from the nuclei-nuclei interaction which can be calculated from the nuclei positions and is treated as a constant.

$$\hat{H}_{electronic} = -\frac{\hbar^2}{2m}\sum_q \nabla^2 - \sum_q \sum_N \frac{Z_N e^2}{r_{qN}} + \sum_q \sum_{q>j} \frac{e^2}{r_{qj}} + V_{NN}$$

$$\nabla^2 = \frac{\partial^2}{\partial x^2} + \frac{\partial^2}{\partial y^2} + \frac{\partial^2}{\partial z^2}$$

Equation 2.4.4: Above: electronic Hamiltonian. Below: Laplacian operator.

If the Hamiltonian is defined as being independent of time, then the wave-function can be simplified as the product of two functions, one that depends on the spatial coordinates (q_n) and one that depends on time (t).[22] When this approximations are plugged into Schrödinger equation (*Equation 2.4.2*), the time-independent Schrödinger equation is obtained (*Equation 2.4.5*)

$$(-\frac{\hbar^2}{2m}\sum_q \nabla^2 - \sum_q \sum_N \frac{Z_N e^2}{r_{qN}} + \sum_q \sum_{q>j} \frac{e^2}{r_{qj}} + V_{NN})\Psi(q_n) = E\Psi(q_n)$$

Equation 2.4.5: Time-independent Schrödinger equation.

The time-independent Schrödinger equation for a single electron is said to be complete when it is described by two functions, one which depends on the

spatial coordinates (q_n) and one that is function of the spin coordinate (s) (*Equation 2.4.6*). These single-electron time-independent wave-functions are also known as spin-orbital functions.

$$\Psi = \varphi(q_n)\sigma(s)$$

Equation 2.4.6: Single-electron time-independent Schrödinger equation or spin-orbital function.

Considering that electrons are fermions, then the Schrödinger equation must be antisymmetric with respect to the exchange of electron coordinates. These features can be easily mathematically represented using determinants in which every column represents a spin-orbital and every row represents an electron. The representation of multiel-ectronic wave-functions as determinants is known as the Slater determinant expansion. Since each spin-orbital is defined for a single electron, the Slater determinants model electrons independently, and the influence of the other electrons is considered as its average. For example, the ground-state wave-function of Helium has two electrons in a $1s^2$ configuration and can be written as a Slatter determinant, as shown in *Equation 2.4.7*, where the term $\frac{1}{\sqrt{q}}$ is a normalisation constant with q the number of electrons.[43]

$$He\ 1s^2 = \frac{1}{\sqrt{2}}\begin{vmatrix} 1s(1)\alpha(1) & 1s(1)\beta(1) \\ 1s(2)\alpha(2) & 1s(1)\beta(1) \end{vmatrix}$$

Equation 2.4.7: Slater determinant expansion of the Helium atom

The Schrödinger equation possess analytical solutions only for hydrogenic systems, *i.e*. systems with only one electron. For multi-electron systems, approximate solutions can be obtained through the Hartree-Fock method. The wave-functions used in the Hartree-Fock method are built as Slater determinants, in which the spatial function of each spin-orbital can be approximated using atomic orbitals [22] The Hatree-Fock equations are obtained by replacing the Hamiltonian operator with a new expression that describes

the electronic interaction of a given electron with the rest, as an average, called the one-electron Fock operator. Mathematically it is built by three terms, (h) which is a sum of the electronic kinetic energy for electron 1 plus the potential energy between electron 1 and the array of nuclei, J_j is the Coulombic term and K_j is the exchange term.[22]

$$\hat{F}(1) = h(1) + \sum_{j=1}^{N/2} [2J_j(1) - K_j(1)]$$

Equation 2.4.8: Fock operator energy components

The new exchange operator is a consequence of the Pauli Exclusion Principle, which dictates that two fermions cannot be described by the same quantum numbers. The exchange operator thus, calculates a repulsive energy component that brings electrons away from each other.

$$\varphi(1) = \sum_{s-1}^{b} C_{s,i} X_s$$

Equation 2.4.9: Molecular orbital description

The molecular orbitals can be approximated as linear combinations of single-electron functions X_s called basis sets (*Equation 2.4.9*). An exact representation of an orbital in terms of basis sets would require an infinite set of functions. In practice, a finite number of functions must be used.

The variational theorem states that the exact energy of a system is only obtained from the analytical and unknown form of the wave-function, it also states that guess functions will always give equal or higher energies. The Hartree-Fock method consist of looking for the coefficients $C_{s,i}$ which allows orbitals to be built as linear combinations of functions that minimize the electronic energy of the system, calculated according to *Equation 2.4.10.*

$$\hat{F}\Psi = \varepsilon\Psi$$

Equation 2.4.10: Hartree-Fock eigenvalue equation

The Hartree-Fock equations need to be solved in an iterative manner because the components of the Fock operator depend upon the orbitals, which at the same time, depend on the coefficients used to build the linear combination of basis sets, which are unknown. This iterative method is called the self-consistent field approach. It begins with an estimated selection of orbital coefficients to build an approximate wave-function from which the energy is obtained, then the coefficients are modified to obtain a new function to recalculate the energy until two subsequent iterations give the same energy, within pre-defined tollerances.[22,44]

Hohenberg and Kohn proved in 1964 that the electronic properties of a system can be also derived from the electronic density of the system. This means that properties such as the ground-state energy are functions of a function of the electron density (functionals) (*Equation 2.4.11*). [45]

$$E_{elec} = E[\rho] = \bar{\bar{T}}_q[\rho] + \bar{\bar{V}}_{Nq}[\rho] + \bar{\bar{V}}_{qq}[\rho]$$

Equation 2.4.11: Components of the electronic energy functional.

This approach called density functional theory (DFT) is very interesting because while the Hartree Fock method works with the wave-function of the system, which depends on three spatial coordinates plus the spin coordinate of each particle, the function of the electron density depends only on three spatial coordinates. *Equation 2.4.11* shows that the potential energy functional for the interaction between nuclei and electrons $\bar{\bar{V}}_{Nq}[\rho_0]$ can be built as the volume integral of the product of the electron density function and the sum of Coulombic interactions between electrons and nuclei. The kinetic energy functional $\bar{\bar{T}}_q[\rho]$ and the potential energy functional for the electronic interactions $\bar{\bar{V}}_{qq}[\rho]$ are unknown but can be approximated variationally as in the Hartree-Fock method (*Equation 2.4.12*).

$$\bar{\bar{T}}_q[\rho] + \bar{\bar{V}}_{Nq}[\rho] + \bar{\bar{V}}_{qq}[\rho] \geq E[\rho]$$

Equation 2.4.12: Variational estimation of the kinetic and potential energy functionals

The problem with *Equation 2.4.12* is that the exact mathematical description of the functional $E[\rho]$ is also unknown. In 1965 Kohn and Sham proposed an approach to find the electron density based on a reference system of similar electron density to the real system. This allowed them to define a wave-function composed of non-interacting one-electron orbitals, which would be capable of rebuilding the electron density of the reference system.[22]

The wave-function can be plugged into the eigenvalue equation to calculate the energy of the reference system. The difference between the kinetic energy component of the real molecule and the non-interacting system can be written as *Equation 2.4.13*.

$$\Delta T[\rho_{ref}] = \bar{\bar{T}}_q[\rho] - T_{ref}[\rho_{ref}]$$

Equation 2.4.13: Difference between the real-system electron density and the reference system electron density.

Through a series of algebraic manipulations, the energy of the real system can be rewritten in terms of the reference system as *Equation 2.4.14*, from which the ΔT and V_{qq} are still unknown and are grouped in a new expression called the exchange-correlation functional $E_{xc}[\rho]$. The correlation term, which originates from the difference between a real system and a non-interacting system, describes how the movement of one electron is influenced by the rest. The exchange term originated from the antisymmetric requirement as is found in Hartree-Fock theory.

$$E[\rho] = T_{ref}[\rho_{ref}] + \bar{\bar{V}}_{Nq}[\rho_{ref}] + V_{qq}[\rho_{ref}] + \Delta T[\rho_{ref}]$$

Equation 2.4.14: Energy functional of the real system written in terms of the reference system.

To solve this expression the electron density of the ground-state needs to be found first, and the non-interacting wave functions can be used to derive it as a first iteration, as long as an expression for $E_{xc}[\rho]$ is given. Since exact form of the $E_{xc}[\rho]$ is not known, different approaches to this functional have been proposed.

The local density approach (LDA) is based on an ideal “gas” of non-interacting electrons evenly distributed, and it is a suitable model for molecules where the electron density variates subtly over the space. In this approach, the exchange-correlation functional depends only on the electron density.[22]

An improvement on the LDA approach called the generalized gradient approximation (GGA), involves describing the exchange-correlation functional both in terms of the electron density and its first derivative, the gradient of the electron density, which helps to correct for electron density variations. Examples of GGA exchange functionals are Becke88 (B88) or Perdew-Burke-Ernzerhof97 (PBE) . Examples of correlations functionals are Lee-Yang-Parr (LYP) or Perdew86 (P86). $E_{xc}[\rho]$ is then built by combining an exchange functional with a correlation functional.[22] Further improvement can be achieved by adding the second derivative of the electron density, these are called meta-GGA approximations.

A third approach involves creating linear combinations of GGA or meta-GGA functionals with exchange or correlation terms coming from different approaches like Hartree-Fock or LDA. These functionals are called hybrid functionals, and the coefficients from each term of the linear combination are parametrised empirically to fit specific experimental results, like bond distances in organic molecules, electronic affinities of metals, *etc*. Some famous examples are the three-parameter Becke88 Lee-Yang-Parr (B3LYP) functional, which includes 20% of Harttee-Fock exchange energy, or Perdew-Burke-Ernzerhof (PBE0), which mixes 25% of Hatree-Fock exchange with 75% PBE exchange.[22]

2.4.2 Computational methodology employed in chapter IV

All electronic structure calculations were performed under the DFT formalism using Gaussian09 package. The stationary state geometries of the fully oxidised anthraquinone cations were optimised using the GGA BP86 functional with the double-zeta split-valence basis set with polarization functions on all atoms except hydrogen, developed by Ahlrichs and co-workers (def-SV(P)).[46] This GGA functional provides a good compromise between accuracy and speed for optimisation and vibrational frequency calculations of closed shell molecules, and has been recently employed independently by Tavan and co-workers, Krossing and co-workers and Aubry and co-workers for calculations involving quinones and ammonium salts.[47–49]

The molecular orbitals and the energy values from the different oxidation states of every anthraquinone, were obtained by single point calculations using the fully oxidised optimised stationary geometries. The single point calculations were performed using the PBE0 hybrid functional with the second generation triple-zeta split-valence basis set with two sets of polarization functions for all atoms, developed by Ahlrichs and co-workers (def2-TZVPP).[50–56] Hybrid functionals like PBE0 or B3LYP accompanied of triple-zeta basis sets have been widely used in the literature to accurately predict the energies of quinone radical ions and fully reduced close shell anionic species.[57–59]

The optimisation of the anthraquinone cations molecular structures and the single point calculations performed on the optimised structures, included implicit solvent effect corrections, calculated with the Solvent Model Density method (SMD), using the dielectric constant of acetonitrile at 298 ^{o}C, ε = 37.5.

Chapter III: Development of simple, selective protocols for the implementation of cross-couplings in DESs.

3.1 Introduction

Most chemical processes are carried out in solvent: syntheses, extractions, purifications, measurement of bulk physical properties, valorisations, *etc*. Their role is not only restricted to being a medium for reactions to occur in and to prevent overrunning risks; solvents can modify chemical kinetics or induce selectivity. Reactions require solvents in huge excess relative to reagents and products; many of them like hexane, toluene or benzene, are petroleum-based and hence non-renewable. Most of traditional volatile organic solvents tend to be harmful to the atmosphere, carcinogenic or non-degradable. Therefore, one of the main objectives of green chemistry is the replacement of processes involving traditional volatile organic solvents with greener alternatives. An ideal green solvent should be non-toxic to human health and the environment, non-flammable, of low vapor pressure, high heat capacity and inexpensive. Our ideal solvent should also reduce the number of synthetic steps, lessen the rate of side-reactions and facilitate the purification process. With this in mind, DESs arise as promising candidates for carrying out the chemistry of the future.[60]

In the last ten years there has been an increased interest in the application of DESs to organic transformations. DESs were involved as innocent solvents, catalysts or even as solvent/reagent. DESs have been successfully used as solvents for organocatalysed aldol reactions[61,62], Michael additions[63–66] and other conjugate additions[6768], Knoevenagel condensations[69], Friedel-Crafts alkylations[70], redox reactions of alcohols, sulfides, aldehydes or for the bromination of anthraquinones.[71–74] A relevant paper by Brenna *et al*., reported a stereoselective Michael addition in ChCl/U, ChCl/U/H_2O, ChCl/Fructose/H_2O and ChCl/Gly DESs and observed that different DESs exerted diverse rates of stereo control due to different 3D configurations between HBA and HBDs.[62] Overall, these reports coincide in that reactions proceeded smoothly and

better yields were obtained in the DES, when compared to traditional solvents. Recyclability of DESs for further reactions was possible in most cases by simple extraction of the products.

On the other hand, DESs have been used as organocatalysts or as both solvent and organocatalysts for Diels-Alder reactions[75,76], Pictet-Spengler cyclizations[77], Fischer indole synthesis[78], Clauson-Kaas[79] and Paal-Knorr cyclizations[80,81] or Mannich reactions[82] among others. Overall, these examples show that DESs can promote H-bond catalysis, Lewis-acidic catalysis or even Brønsted acid-base catalysis depending on the HBD and the DES 3D molecular arrangement.[34,35]

3.1.1 DES applied to polar-organometallic chemistry

One of the main issues that needs to be addressed when analyzing the feasibility of applying ChCl-based DESs to reactions involving polar-organometallic reagents like Grignard (RMg), organolithium (RLi) or organozinc (RZn) is the high hygroscopicity, and thus high water content of DESs. This may impact on the life expectancy of the organometallic species due to hydrolysis reactions with water or the protic components of the DES. Meng *et al*. measured the change in water content of a sample of ChCl/U stirred at 21^{o}C for three weeks.[83] The researchers found that ChCl/U absorbed approximately 1150 ppm of water per hour until an equilibrated concentration of 18-20% wt was reached. Although at first glance the water content of protic DESs might seem an issue that denies their involvement as solvents for polar-organometallic chemistry, there is evidence that suggests that despite their protic components and inherent moisture, DESs do allow these reactions to proceed and could even act synergistically to enhance the reactivity of the organometallic reagent. In 2003, Kuo *et al*. reported that water had a positive effect in the enantioselective alkylation of compound ***a*** in *Scheme 3.1.1* with LDA in toluene, a key step of the synthesis of an anticancer drug called Lonafarnib.[84] Surprisingly, the authors found that careful elimination of moisture from the reaction reduced both the yield and the enantiomeric excess

(ee). On the contrary, addition of 1 equivalent of water optimised the reaction outcome, allowing them to increase the yield to 95% with 95% ee.[84]

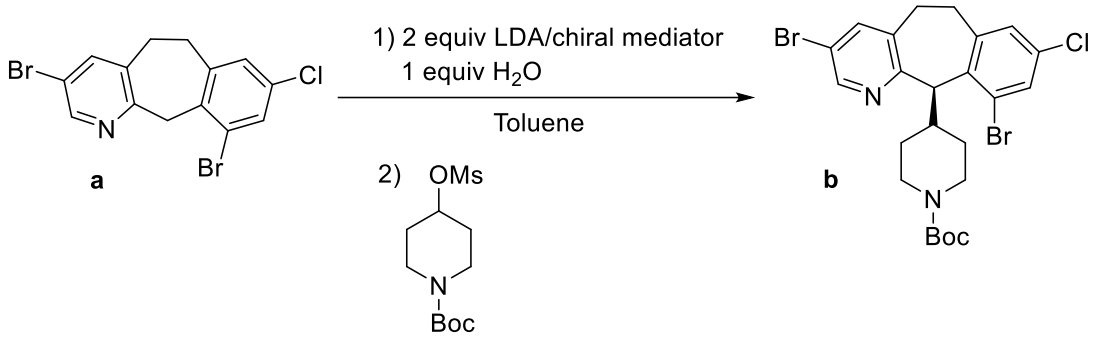

Scheme 3.1.1: Key enantioselective alkylation step in the synthesis of Lonafarnib promoted by water as reported by Kuo *et al*.[84]

Another example of how protic additives can improve the reactivity of moisture-sensitive organometallic reagents is the work by Osztrovsky, Holm and Madsen.[85] The authors studied the nucleophilic addition of Grignard reagents to carbonyl compounds in ethereal solvents in the presence of water.[85] The authors discovered that under these conditions, the rate of addition of allylmagnesium bromide to acetone was higher than the rate of Grignard reagent hydrolysis, thus achieving a 91% yield of addition. Interestingly, when the experiments were repeated with alcohols instead of water, the yields were reduced by 37% on average, even though water is expected to be more acidic than alcohols.

The authors suggested this is due to an intermolecular water scavenging effect exerted by the same Grignard reagent. Water can coordinate more effectively to the magnesium core than alcohols, thus reducing its reactivity towards protonolysis of the organometallic reagent. The faster kinetics of addition over hydrolysis were only observed for allyl- and benzylmagnesium bromide, with butylmagnesium bromide favouring hydrolysis. To prove the scavenging effect hypothesis, the reactions were repeated in the presence $MgBr_2$. This modification promoted a quantitative formation of the correspondent tertiary alcohol.[85]

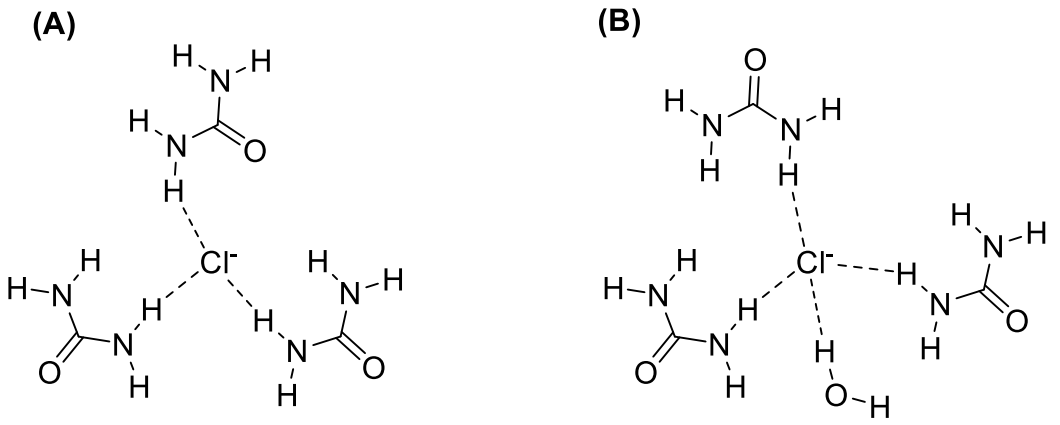

Figure 3.1.1: Examples of environments around Cl^-. (A) Neat ChCl. (B) wet ChCl/U described by Fetisov *et al.*[86]

The work by Ostrozvsky, Holm and Madsen is very important in the discussion of polar-organometallic chemistry in DESs because it showed that when water is already committed to strong intermolecular interactions, its reactivity towards protonolysis of the organometallic reagent is reduced. This opens a window of opportunity to perform fast reactions in the presence of water. Such is the case for wet ChCl-based DESs where water interacts tightly with the DES components.

Fetisov *et al*. analyzed the structure of an equimolar mixture of ChCl/U and water using MD.[86] According to their study, the neat DES showed a heterogeneous ordering with regions made of organised aggregates, *Figure 3.1.1*. In these aggregates, the *trans* hydrogen atoms from urea interact predominantly with chloride, while the *cis* hydrogen atoms interact with oxygen atoms from other urea molecules, or with choline to a lesser extent. Moreover, chloride showed closer and stronger interactions with choline's hydroxyl hydrogen when compared with the hydrogen atoms from urea. When water was added, it disrupted the ion-complex structure by increasing the distance between urea and chloride and in consequence, reducing the coordination number of chloride, *Figure 3.1.1*. Also, water engaged in short interactions with the *cis* protons from urea. Water replaced around half of the hydrogen bonds between chloride and the hydroxyl group in choline, although, the orientation of chloride around the positive region of Ch was not modified. The authors

concluded that the changes in the solvation of the anion by new H-bonds with water increased the mobility of all the other species which was reflected in a reduction of viscosity.

Hammond *et al*. used neutron scattering experiments to study the changes in the bulk structure of ChCl/U upon addition of up to 30 equivalents of water.[87] The authors observed that addition of up to 10 equivalents of water did not disturb the DES cluster array but slightly enhanced the hydrogen-bonding web. Interestingly, water was allocated preferentially in interstitial holes around choline. According to the authors, when the water content reached 42% wt., the DES structure was replaced by a new regime *i.e.*, from "water-in-DES" to "DES-in-water". In DES-in-water regime, the number of water molecules of solvation around choline was reduced and the ions were brought closer. After this point, the mixture can be understood as a solution of DES in water.

Sapir and Harris shed more light on the transition between water-in-DES to DES-in-water.[88] They studied mixtures of ChCl/U and water from dry DES to 30% wt of water, using a MD with a force field especially suited to reproduce experimental DESs properties like viscosity and density. The authors studied RDFs using a deconvolution technique, which allowed them to elucidate different molecular structures and their contributions to the RDFs. The authors discovered an interplay between two basic conformations. The first basic conformation is related to the DES cluster: the authors found that water molecules were inserted between DES components without significantly distorting the molecular array in agreement with the experimental observations by Hammond *et al*. (water-in-DES regime).[87,88] When water concentration increased, it sequestered chloride by replacing the old Cl-Urea interactions. This generated the second basic conformation. This conformation is composed of Cl/water/Cl chain-like aggregates, *Figure 3.1.2*. The length of the chain-like structure increased with water concentration, in agreement with Hammond *et al* (DES-in-water regime).[87,88] When water concentration exceeded 30% wt., a third basic conformation emerged, where water solvated both choline and chloride and brought the ions closer. In this way, the changes

on DES viscosity and density were correlated with the appearance of DES-in-water aggregates.

Overall, these studies showed how water interacts with the DES components and how the 3D DES arrangement changes with water concentration. These water-DES interactions resemble the water scavenging effect exerted by Mg salts described by Ozstrovsky, Holm and Madsen.[85] These observations suggest that despite their high hygroscopicity and inherently protic nature, DESs can be used as solvents for reactions involving air and water-sensitive polar organometallic reagents.

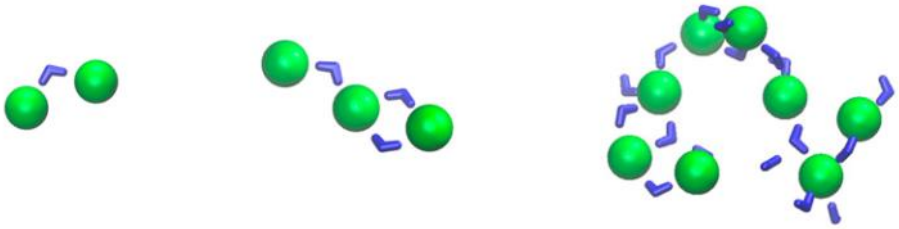

Figure 3.1.2: Chain-like Water-Cl clusters extracted from a 10% wt water concentration MD simulation. Water is depicted with blue arrows, Cl by green spheres. Adapted from Sapir and Harris.[88]

A paper published in 2012 by Zong *et al*. demonstrated the effectiveness of tetrabutylammonium halides and donor ligands such as diglyme as additives to improve the yield of addition reactions between Grignard reagents and ketones by reducing the amount of enolization and β-hydride elimination side-reactions.[89] The authors proposed that the ammonium salt promoted the displacement of the Grignard reagent's Schlenk equilibrium to the side of the dimeric alkylmagnesium species by bridging the monomers through the halide from the ammonium salt (*Scheme 3.1.2-A*). On the other hand, it was proposed the donor ligand increased the nucleophilicity of the Grignard reagent in a similar fashion to Lewis-basic solvents like THF. The dimeric alkylmagnesium species would favour addition over enolization and β-hydride elimination by accessing a six-member transition state (*Scheme 3.1.2-B*).

These observations were pointing towards the potential application of choline-based DESs as solvents in polar-organometallic chemistry.

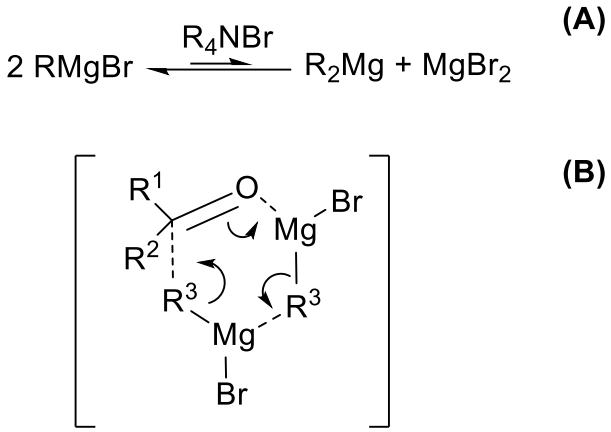

Scheme 3.1.2: (A) Influence of tetraalkylammonium halides on the Schlenk equilibrium of Grignard reagents. (B) Six-membered transition state for the addition of dimeric Grignard reagents to ketones.[89]

Inspired by the previous discoveries, in 2014, Vidal *et al*. reported the first addition of organolithium and Grignard reagents to ketones in ChCl-based DES.[90] Surprisingly, the authors found that additions of organolithium and organomagnesium reagents to aliphatic and aromatic ketones proceed in good yields and with good chemoselectivety, since no side-products were found, *Scheme 3.1.3.* The best results were obtained for ChCl/G and ChCl/H_2O DESs. The authors reported that the organometallic reagents reacted with the carbonyl group from urea when the reaction was performed in ChCl/U. Moreover, all attempts to perform the reaction in the absence of choline reduced the yields considerably. It is noteworthy that Vidal *et al*. reported to be unable to prepare the organometallic reagents *in situ* and that the volume of organic solvent (THF or hexane) used to dissolve the organometallic reagent, almost equalled the volume of DES employed in these reactions. As such, the solvent system would be better described as DES/organic suspension. The addition of Grignard reagents without co-solvent still produced the desired ketone although in lower yields. The exception was the addition of neat lithium acetylide to 2-petanone in ChCl/H_2O

which gave the correspondent tertiary alcohol in 84%. This same reaction in water produced the tertiary alcohol in only 7%. [90]

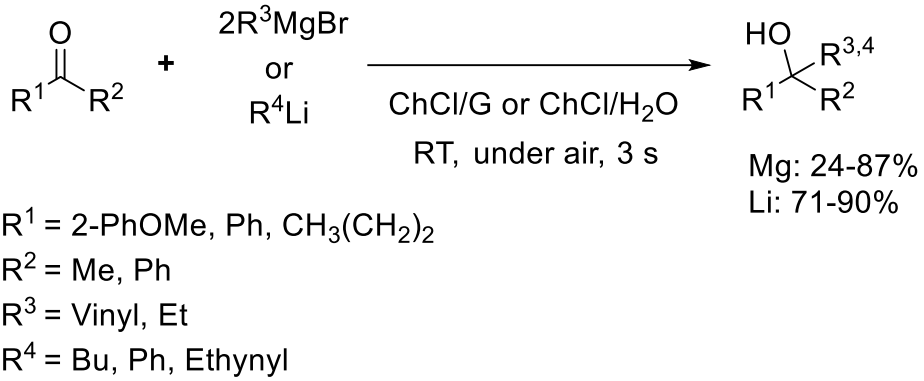

Scheme 3.1.3: Addition of polar-organometallic to Ketones in DES reported by Vidal *et al*.[90]

Vidal *et al*. shed light to the "enhancement-by-ammonium" hypothesis by synthesizing and isolating crystals of a [{Nbu_4}][{$(THF)MgCl_2(CH_2SiMe_3)$}] and by analyzing the mixtures of organolithium reagents and tetrabutylammonium chloride in deuterated THF.[90] Based on their observations, the authors proposed that the formation of a highly nucleophilic magnesiate anion with the ammonium counterion could be the responsible for the faster kinetics and superior chemoselectivety observed, acting synergistically with the HBD to activate the carbonyl through H-bond interactions. Even though crystals of the lithiate-ammonium salts couldn't be isolated, 2D-NMR studies of the sample pointed towards the formation of similar anionic species.

Cicco *et al*. followed Vidal *et al*. findings on the addition of polar-organometallic reagents to ketones in DESs and reported a methodology to prepare functionalized tetrahydrofurans in ChCl/G and ChCl/D-Fru DESs.[91] Their methodology consisted of a one-pot two-step addition of Grignard and organolithium reagents to γ-chloroketones, and the further use of NaOH to enolize the addition product *in situ,* which undergone an intramolecular nucleophilic substitution, *Scheme 3.1.4*. The authors found that DESs enhanced the basic nature of the organolithium reagent over its nucleophilic nature, thus favouring enolization over addition. Moreover, the authors

reported that DESs containing acids as HBDs, were not suitable for these reactions due to complete hydrolysis of the organometallic reagent. By adding an excess of 3 to 6 equivalents or the organometallic reagent, Cicco *et al*. were able to successfully replace the DESs with water. Methanol was demonstrated to be a bad solvent for this reaction, despite being able to solubilize all the reagents. The authors proposed that the reactions should take place at the aqueous/organic interface, which might explain why their yields were sensitive to different stirring speeds. Reactions occurring at interfaces benefit from bigger surface areas, *i.e*., higher stirring speeds. The authors observed a small drop in yields (8% on average) when repeating the control reaction in D_2O. With this in mind, and the unsuitability of methanol (which, is more limited in terms of H-bonds), the authors suggested these reactions might be catalysed by the protic solvent through *trans*-face itinerant H bonding interactions.[91]

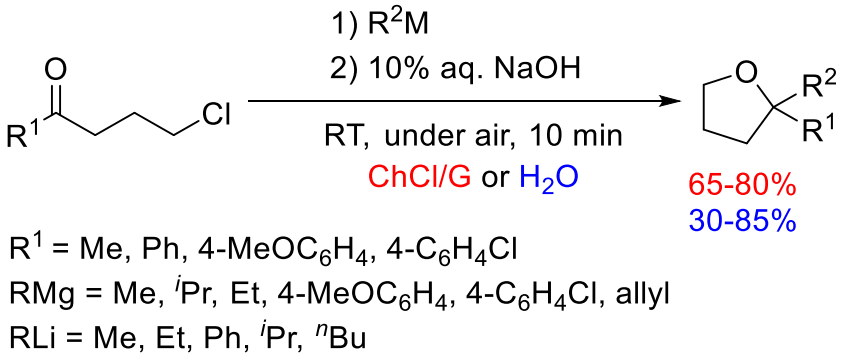

Scheme 3.1.4: Synthesis of substituted tetrahydrofuranes by addition of organolithium reagents to γ-chloroketones by Cicco *et al*.[91]

In the same year, Mallardo *et al*. reported the *ortho*-directed lithiation of diaryl-substituted THF derivatives in ethereal solvents by organolithium reagents.[92] DESs were involved in a subsequent step, where the lithiated intermediate was reacted with electrophiles to obtain the corresponding adducts in good yields, *Scheme 3.1.5-A*.

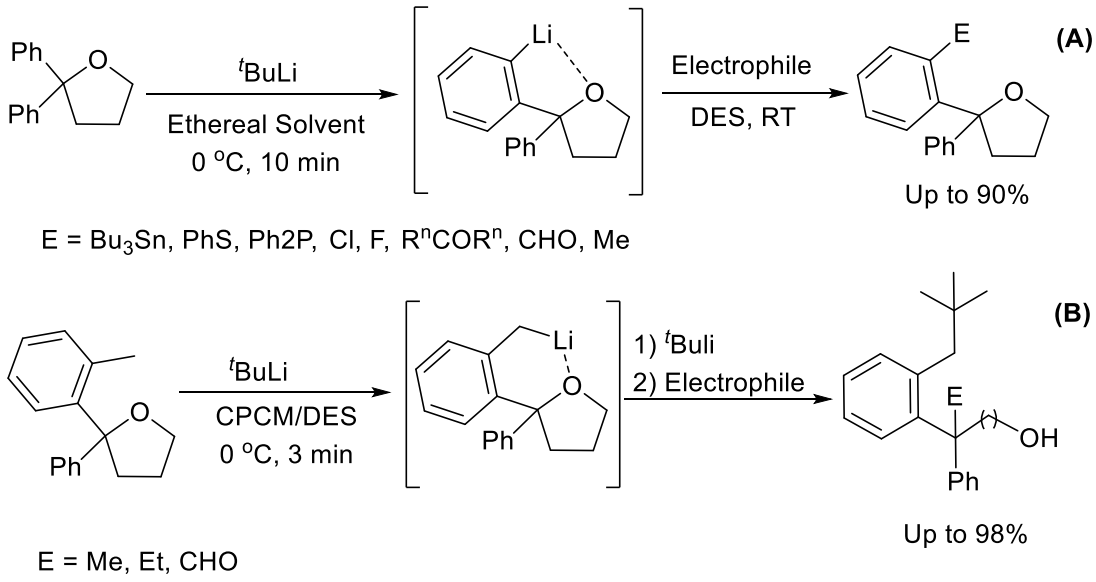

Scheme 3.1.5: A) Electrophilic quenching of an organolithium prepared through THF-directed *ortho*-lithiation as reported by Mallardo *et al*.[92] B) THF-directed lateral lithiation through organolithium intermediate formed *in-situ* in DES reported by Sassone *et al*.[93]

Adding to these findings, Sassone *et al*. disclosed the THF-directed lateral lithiation of benzylic derivatives followed by electrophilic quenching promoted by organolithium bases.[93] The reaction was proposed to occur through an organolithium intermediate prepared *in situ* in a cyclopenthylmethyl ether (CPCM)/ChCl/G DES mixture, *Scheme 3.1.5-B.*

Expanding their previously reported methodology, Vidal *et al*. reported the addition of organolithium reagents to imines and quinolines in ChCl/G and ChCl/H_2O.[94] The authors highlighted how even nucleophilic additions to less-reactive electrophiles with bulky organolithium compounds, seemed to be competitive against protonolysis in DESs. Imines underwent rapid additions with organolithium reagents without prior activation by Lewis-acids, rendering only the addition product and starting material, without formation of enolization of reduction products, *Scheme 3.1.6-A*.

(A)

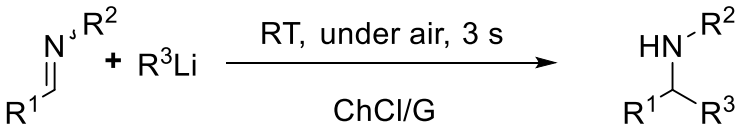

73-95%

R^1 = Ph, 4-PhOMe, 4-PhBr
R^2 = Ph, ^{t}Bu, 4-PhOMe, 4-PhBr, 4-Tol
R^3 = Me, ^{n}Bu, ^{s}Bu, ^{t}Bu, Ph

(B)

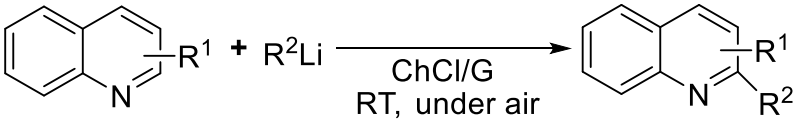

30-52%

R^1 = 4-Me, H
R^2 = Me, Ph, ^{s}Bu, ^{t}Bu

(C)

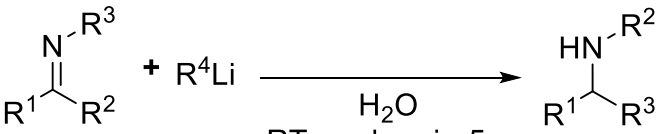

60-96%

R^1, R^2 = H, ^{t}Bu, pentyl, Ph, 4-C_6H_4OMe, 4-C_6H_4Cl
R^3 = ^{t}Bu, Ph, Bn
R^4 = Me, ^{n}Bu, ^{s}Bu, ^{t}Bu, Ph

(D)

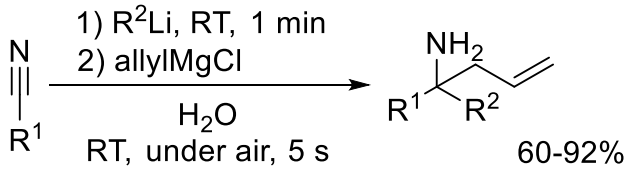

60-92%

R^1 = Ph, Pr, Bn, Ph, 4-C_6H_4OPh, 2,5-C_6H_3ClF
R^2 = ^{s}Bu, ^{n}Bu, Et, Me, Ph

(E)

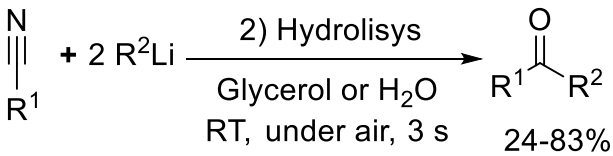

24-83%

R^1 = Ph, 4-C_6H_4OMe, 4-C_6H_4F, 4-C_6H_4Br, 4-Tol, 2-Tol
R^2 = Ph, 3-Tol, 2-C_6H_4OMe, 3-C_6H_4F, 3,5-$C_6H_3(CF_3)_2$

Scheme 3.1.6: Application of DESs as solvents for addition of polar organometallic reagents to nitrogenated electrophiles. [A,B]Vidal *et al*.[94], [C,D]Dilauro *et al*.[95], [E]Rodríguez-Álvarez *et al*.[96]

Quinolines underwent addition in lower yields, but selectively at position 2, *Scheme 3.1.6-B*. The protocol exhibited both functional group tolerance and robustness with regards to electronic effects since imines holding both electron-withdrawing groups (EWGs) and electron-donating groups (EDGs) were transformed in good yields. Surprisingly, the authors reported a set of optimised reaction conditions with a smaller excess of organolithium reagent (1.4 equivalents) compared to their previous work on ketones (2.0 equivalents), although the scope was limited to organolithium reagents only.

Dilauro *et al*. expanded the previous work on imines in DESs by reporting the addition of organolithium reagents to imines and nitriles "on water".[95] The authors reported the reactions proceeded faster and more chemoseletively than in organic solvents. Imines reacted moderately with 1.4 equivalents of some of the organolithium reagents, better yields were achieved with 3.0 equivalents *Scheme 3.1.6-C*. Nitriles underwent a double addition in a one-pot two-step process to generate primary amines with a tertiary carbon substituent. The best set of reaction conditions consisted in adding 3 equivalents of the respective organolithium reagent first, and a minute after, 3 equivalents of allylMgCl. The scope of the second addition resulted limited only to allylMgCl *Scheme 3.1.6-D*. The improvements reported for the addition of polar-organometallic reagents to imines and nitriles compared to organic solvents was attributed to *trans*-face proton-transfer reactions between the aqueous phase and the reagents, in contrast with their previous work where *trans*-phase hydrogen-bonding was invoked.[91] This hypothesis was based on a more significant isotopic effect between reactions on D_2O and H_2O which rendered a reduction in yield from 96% to 57%.

Following similar procedures, García-Álvarez *et al*. reported the nucleophilic addition of organolithium reagents to nitriles in glycerol and water.[96] The researchers found that glycerol and water improved the reaction yield by 15% compared to ChCl/G, and reported that better results were obtained when the nitrile was less soluble and the stirring speed maximized, *Scheme 3.1.6-E.* The authors proposed that enhanced activity could be due to *trans*-phase hydrogen-bonding by glycerol ("on-glycerol" effects). Interestingly, when the

authors replaced glycerol with water, they were not able to reproduce Dilauro *et al*. results on the addition of *n*-butyllithium to nitriles to obtain primary amines in high yields, since the first addition could only produce the butylated ketone in 37%.[95,96]

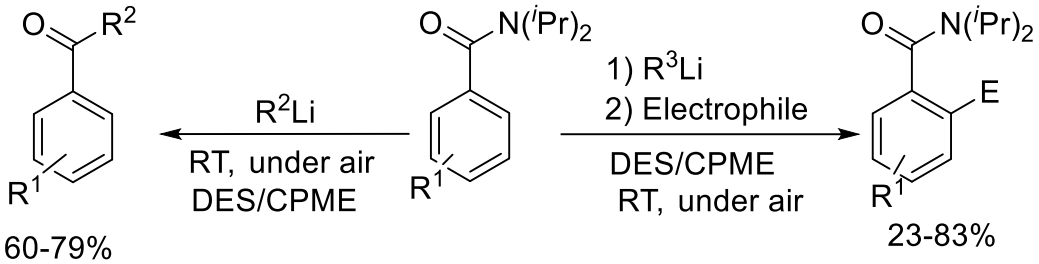

DESs: ChCl/G, ChCl/U, ChCl/H_2O
R^1 = 3-Me, 4-Cl, 4-OMe, indol
R^2 = ^{n}Bu, Me, Ph, ^{n}Hex
R^3 = ^{t}Bu
Electrophile: CHO, Br, I, SMe, PhCO, CO_2H

Scheme 3.1.7: Direct ortho-Metalation and nucleophilic addition mediated by organolithium reagents in DES adapted from Ghinato *et al*.[97]

Ghinato *et al*. exploited the high reactivity of organolithium reagents to perform C(sp^2)-H bond activation through the direct *ortho*-metalation (DoM) of benzamide derivatives in DES/ethereal mixtures, *Scheme 3.1.7*.[97] The authors were able to tune the outcome of their reactions by modifying the size of the organolithium reagents. Bulky alkyllithiums behaved like bases in the DES environments, thus allowing them to achieve DoM chemoselectively, while, in contrast, less bulky alkyllithiums underwent nucleophilic addition to the carbonyl group, *Scheme 3.1.7*. The authors suggested that the DES polar environment helped to promote the nucleophilic acyl substitution by stabilizing the tetrahedral intermediate formed after the nucleophilic addition of the organolithium, thus avoiding the formation of the corresponding alcohol. It is noteworthy that the authors reported that higher yields were obtained when adding the organometallic reagent in a single addition. Also, the authors performed kinetic studies in order to measure the half-life period of *t*-BuLi in ChUr and ChGly, finding an average period of 6 seconds.

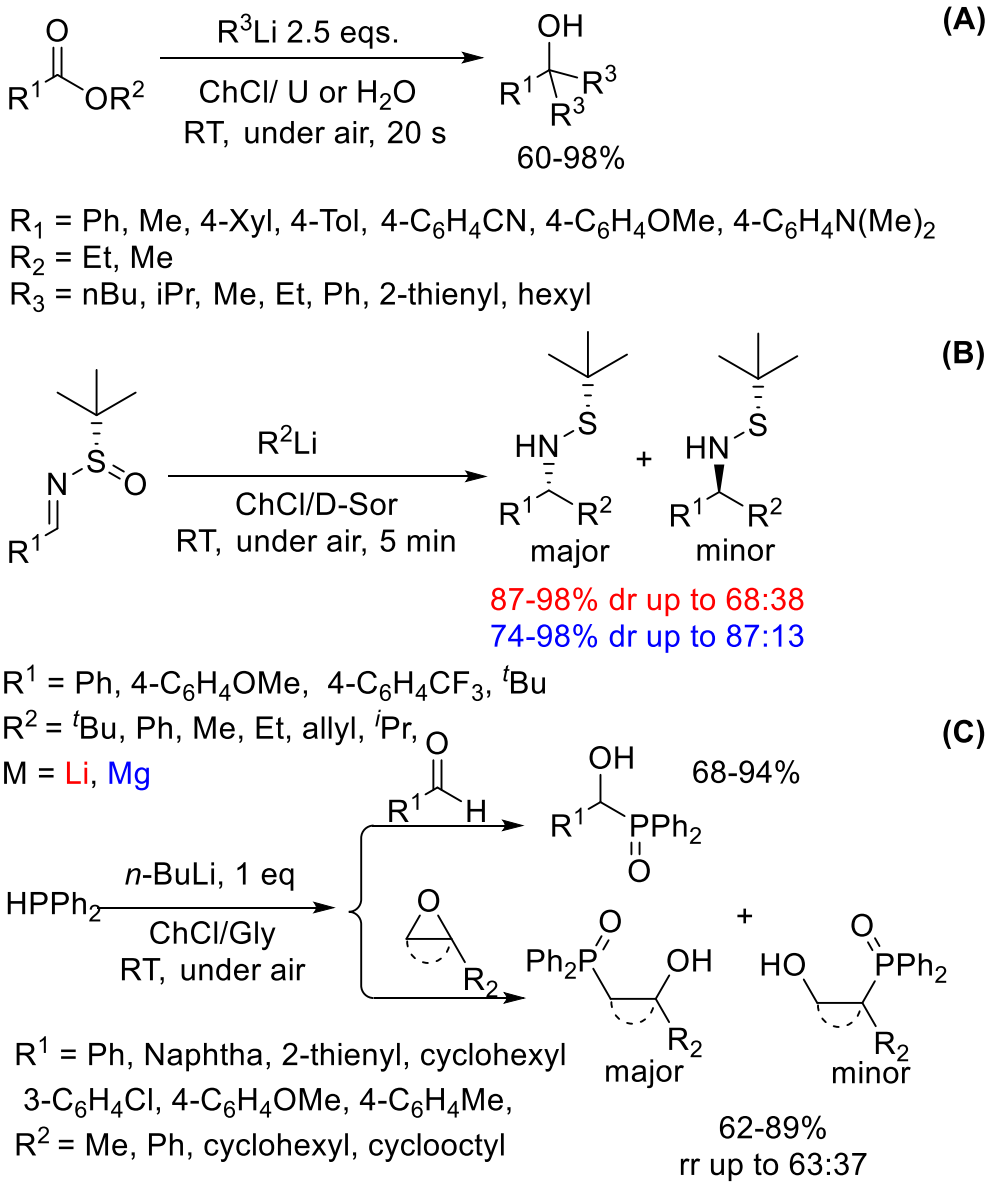

Scheme 3.1.8: Addition of lithium organometallics to esters.[98] B) Addition of lithium and magnesium organometallics to sulfinyl imines by Cicco *et al*.[99] C) Preparation of lithium phosphide organometallics in DESs and addition to aldehydes and epoxides.[100]

More recently, Quivelli *et al*. reported the addition of organolithium reagents to esters in DESs, thus increasing the set of electrophiles that have been studied.[98] The researchers followed a similar strategy to previous reports, by adding a solution of the respective organolithium reagent to a vigorously stirred DES/ester suspension. The reaction exhibited good functional group tolerance and robustness, since electrophiles decorated with both EWG and EDGs were transformed satisfactorily, *Scheme 3.1.8-A*. The researchers found that

ChCl/U, ChCl/G, glycerol, and water were effective solvents for this reaction. Interestingly, no addition of the organometallic reagent to urea was observed, in contrast to previous reports on the unsuitability of ChCl/U due to parasitic additions reactions with the organometallic reagent.[90] Another interesting recent example, is the nucleophilic addition of organolithium or Grignard reagents to sulfinyl imines as electrophiles in a ChCl/D-Sor DES by Cicco *et al*.[99] These reactions proceeded with good conversions but only moderate diasteroselectivities. In this case, the sugar-based DES provided better conversions than water (98% vs 87%) with equal diasteroselectivity (dr 65:35), *Scheme 3.1.8-B.*

So far, all the research reviewed here on the application of DESs as solvents in reactions involving polar-organometallic reagents has focused on alkyllithium and Grignard reagents. Recently, Cicco *et al*. reported the preparation of lithium phosphides in DESs and their reactivity against aldehydes and epoxides.[100] Astonishingly, the researchers were able to prepare metalated phosphides *in situ*, using ChCl/G as solvent by reacting a secondary phosphine with *n*-butyllithium, sodium hydride or potassium hydride. The formation of the phosphide was followed by addition to the desired electrophile with high yields. The reaction tolerated aldehydes decorated with both EWGs and EDGs and showed good regioselectivity for the less substituted carbon when tested with asymmetric epoxides, *Scheme 3.1.8-C*.

In most of these experiments, the organometallic reagent was used as a solution in ethereal/hydrocarbon solvents, which implies the reactions take place in a heterogeneous environment. Also, the organic electrophiles are not always soluble in the DES employed. Nevertheless, it is striking that, as pointed out by Vidal and Cicco *et al*., these heterogenous protic environments seem to enhance the reactivity of the organometallic reagent (or perhaps the electrophile or both), since reactions occur at faster speeds and with higher chemoselectivety than same experiments in traditional dry solvents.[90,91] From this observation, it is obvious that DESs play a non-innocent role. It has been

suggested by Vidal *et al*. that the ammonium-based cations can form anionic complexes with the organometallic species.

The *trans*-face hydrogen-bonding catalysis hypothesis has also been proposed as a reason for the enhanced reactivity observed in different organic transformations mediated by DES, as reviewed by García-Alvarez, Hevia and Capriati, and Alonso *et al*.[35,101] This hypothesis suggest that reactions taking place in aqueous/organic biphasic systems can be catalysed by hydrogen-bonding interactions between hydrogen-donors in the aqueous/protic phase and hydrogen-acceptors in the organic phase.

Overall, in the last 7 years the feasibility of DESs as solvent systems for nucleophilic additions, C-H bond activation and acid/base reactions involving water-sensitive organometallic reagents has been demonstrated. Many systems have to be classified as heterogeneous mixtures of DESs with organic solvents since the organometallic reagent is usually provided in solution by chemical suppliers.

3.1.2 Introduction to cross-couplings

Cross-couplings are a set of organic reactions between electron-deficient organic species, and activated coupling partners, catalysed by transition metals, in which new C-C bonds are formed. The first coupling reaction was reported in 1855 by Wurtz, the author performed the homocoupling of two haloalkanes in the presence of elemental sodium to yield a new alkane. On the other hand, the first cross-coupling reactions catalysed by transition metals ($CuCl_2$) were reported independently in 1939 and 1941 by Meerwin and Kharasch. The first was a cross-coupling between diazonium salts and α,β-unsaturated esters or carboxylic acids and the second one, a cross-coupling between aryl halides and Grignard reagents.[102]

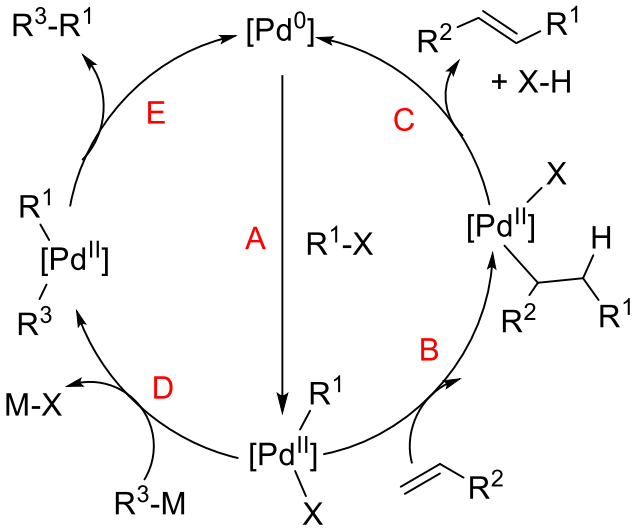

Scheme 3.1.9: Simplified mechanism for Pd-catalysed cross-coupling reactions. Left side of the manifold: Suzuki-Miyaura, Corriu-Kumada, Stille and Negishi, reactions. Right side of the manifold: Mizoroki-Heck reaction. R^1: Usually aryl or vinyl, R^2: Usually an EWG. R^3: $C(sp^3)$, $C(sp^2)$ or C(sp), X: halides or pseudohalides.

Nowadays, most cross-coupling reactions are done between organic halides (mainly aryl or vinyl compounds) or pseudohalides (triflates, sulfonates, mesylates) and activated nucleophilic hydrocarbons, catalysed by Pd or Ni complexes. As a general mechanism, all palladium catalysed cross-coupling reactions first undergo activation of the catalyst by generation of a Pd(0) species and subsequent addition of the organic halide (electrophile) to Pd(0) through an oxidative addition step *Scheme 3.1.9-A*.[103] All the reactions represented in the left side of the manifold of *Scheme 3.1.9* have in common that once the catalyst and the electrophile had undergone oxidative addition, a transmetalation with a coupling partner, which is usually an organometallic compound, occurs, *Scheme 3.1.9-D*. *Table 3.1.1* shows the organometallic reagents employed in the most popular Pd catalysed cross-coupling reactions seminal papers. The transmetalation step is followed by a reductive elimination of the cross-coupling product, *Scheme 3.1.9-E.* The Heck reaction on the right side of the manifold of *Scheme 3.1.9* follows a different path since no organometallic reagent is required. The reaction proceeds through the formation of a π-complex between the Pd(II) complex and the activated alkene by means of EWGs, followed by a regioselective *syn*-insertion of the activated

alkene, *Scheme 3.1.9-B.* Then, the new adduct coordinated to Pd, suffers a β-hydride elimination to form the coupling product and regenerate the catalyst with the assistance of base, *Scheme 3.1.9-C*.[103]

Table 3.1.1: Seminal papers from most popular cross-coupling reactions.

Coupling	Year	Nucleophile	Electrophile	Metal
Korriu-Kumada[104]	1972	Organomagnesium	Aryl Halides	Ni
Mizoroki-Heck[105]	1972	Activated alkene	Aryl Halides	Pd
Sonogashira[106]	1975	Copper Acetylide	Aryl Halides	Pd &Cu
Negishi[107]	1976	Alkenylalanes	Alkenyl Halides	Pd & Ni
Stille[108]	1979	Organotin	Aryl & Benzyl Halides	Pd
Suzuki-Miyaura[109]	1979	Alkenylboranes	Alkenyl Halides & Alkynyl Halides	Pd

3.1.3 Pd catalyst speciation in cross-coupling reactions

Although the catalyst speciation in Pd-catalysed cross coupling reactions is very system-dependent, the generally accepted mechanism involves a Pd(II)/Pd(0) redox manifold composed by three main steps as the one depicted in *Scheme 3.1.9*. The most common Pd precatalyst sources are Pd(II) compounds like $Pd_3(OAc)_6$, $PdCl_2$ or $[Pd(OAc)_2(PPh_3)_2]$, as these tend to be bench-stable and commercially available. However Pd(0) complexes like $[Pd^0(PPh_3)_4]$, $[Pd^0(P\textit{t}\text{-}Bu_3)_2]$ or $[Pd_2(dba)_3]$ are also common Pd(0) precatalyst sources. The first step in these kind of reactions is the formation of a Pd(0) catalytically-active species from the precatalyst which can be a Pd(II) or Pd(0) complex. The reduction of Pd(II) complexes to Pd(0) is very flexible and can be achieved under diverse reaction conditions, *e.g*. by oxidation of amines, alkenes, polyols or phosphines among other reagents, or by organometallic compounds like organoboron, organolithium or organozinc reagents through transmetalation and reductive elimination reactions (*Scheme 3.1.10*).[110–113]

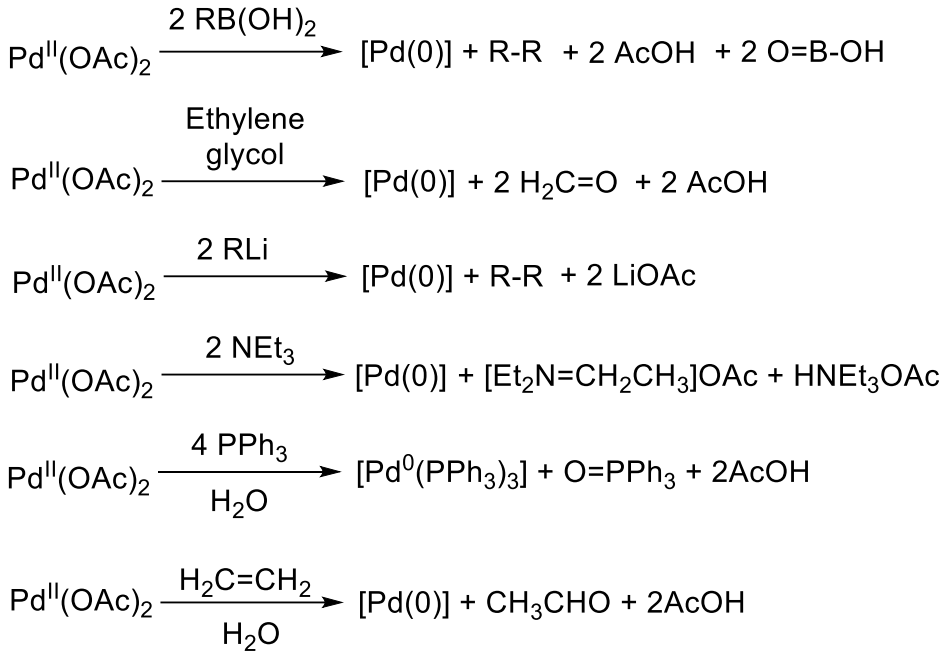

Scheme 3.1.10: Reduction of Pd acetate under different reaction conditions

$Pd_3(OAc)_6$, is commercially available as a trimer bridged by acetate ligands, the cleavage of the trimer to generate monomeric fragments of $Pd(OAc)_2$, which are the ones that undergo reduction to Pd(0), has been correlated with the polarity of the solvent and the presence of protic functional groups.[114]

When Pd(II) salts like $Pd_3(OAc)_6$ or $PdCl_2$ are reduced without supporting ligands under cross-coupling reaction conditions, they form unstable Pd(0) species that tend to aggregate into colloidal Pd, Pd nanoparticles or black Pd aggregates.[115] In 1996, Tuyet Jeffery discovered that $Pd_3(OAC)_6$ can be used as pre-catalyst for Heck-type cross-coupling reactions without the need for supporting ligands, to form Pd nanoparticles, when tetraalkylammonium salts were used as phase-transfer stabilizers in ethereal solvents.[116] Later, similar conditions were developed to perform other cross-coupling reactions, including Suzuki-Miyaura and Negishi reactions, under ligand-free conditions.[117–119] In this regard, it has been proposed that under ligand-free conditions, ChCl might provide electrostatic stabilization of the catalytically-active Pd species in resemblance to Jeffery catalytic conditions.[120,121]

The nature of the catalytically-active Pd species under heterogeneous ligand-free cross-coupling conditions depends on the reaction conditions employed. For example, Fairlamb and co-workers reported that $Pd_3(OAc)_6$ tends to form nanoparticles between 1.8 and 4 Å. when it is used as pre-catalyst under "ligand-free" conditions in polar-aprotic solvents. The authors found that under such conditions, Pd(0) species leaching from the nanoparticles are probably the responsible species for the catalytic reaction.[122] Nevertheless, the authors also showed that if appropriate conditions are used, *i.e,* polyvynilpyrolidone-supported Pd(0) nanoparticles in polar solvents, a truly heterogeneously-catalysed Suzuki reaction can be carried out.[123] In separate work, Corma and co-workers performed Heck, Sonogashira, Stille and Suzuki cross-couplings using Pd(II) salts as precatalysts to generate Pd(0) nanoparticles in N-methylpyrrolidone as solvent at temperatures above 100 ^{o}C.[124] The authors found that the oxidative addition of bromoarenes to Pd nanoparticles was the origin of the leaching of atomic Pd from larger clusters. Moreover, the authors identified that under basic reaction conditions, three- and four- atom Pd nanoclusters were formed and were the dominant catalytically-active Pd species.[124]

On the other hand, when Pd precatalysts supported by ancillary ligands like phosphines or N-heterocyclic carbenes (NHC), among others are used, homogeneous reaction conditions can be achieved. Several experimental and computational studies have shown that halides can react with [Pd(0)] complexes to generate anionic Pd complexes, or even dinuclear Pd(I) species with bridging halides.[125,126] Pd-ate complexes are believed to increase the efficiency of the catalyst by stabilising the oxidative addition transition state and by destabilising the intermediate leading to the reductive elimination step.[127] Besides, it has been suggested that coordination of halides to low-valent [Pd(0)] complexes prevent their decomposition due to oligomerisation.[128,129] Moreover, Amatore and Jutand have suggested that in the presence of halides, the oxidative addition of an aryl halide to [Pd(0)] would form a pentacoordinate Pd(II) anionic species with halides involved as ligands. These species were postulated to be more reactive under catalytic conditions

than the traditional square planar Pd(II) species.[130] In a chloride-rich environment like DESs, the formation of such anionic Pd complexes seems feasible and has been proposed a reason for the enhanced reactivity of Pd catalysts in Negishi cross-couplings in DES (section).[121] In this regard, it has been reported that the less electron-rich the Pd complex is, the more likely it is to form anionic complexes with halides.[131]

Pd(I) compounds have been found to be the catalytically-active Pd species under certain homogeneous reaction conditions when $[Pd(OAc)_2(PPh_3)_2]$ was used as precatalyst. This Pd phosphine complex can be reduced *in situ* by an intramolecular cleavage of a phosphine, as described in *Scheme 3.1.11-A*. Amatore, Jutand and M'Barki proposed the product was a reactive and unstable low-valent Pd(0) species, which was not characterised.[132] Recently, Scott *et al*. determined that when the reduction is carried out in THF, the product is a dinuclear Pd(I) species bridged by one acetate and one phosphine (*Scheme 3.1.11-B*).[133]

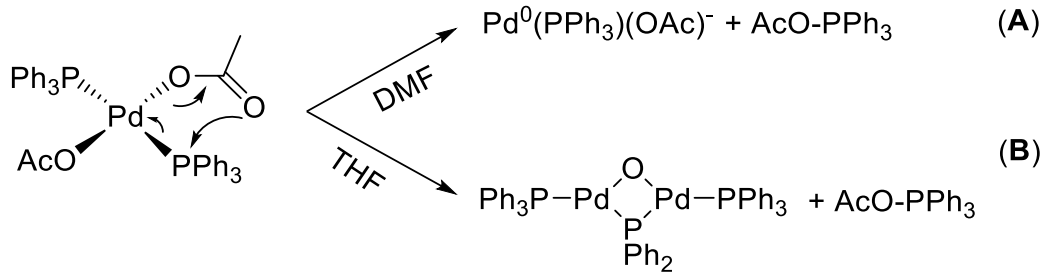

Scheme 3.1.11: Speciation of $Pd(OAc)_2(PPh_3)_2$

A similar catalytically-active Pd(I) dimer bridged by bromide was prepared by Colacot and co-workers through the reduction of $Pd(cod)Br_2$ and 1 equivalent of P(*t*-Bu_3) with base in methanol as solvent.[134] Later, Colacot, Schoenebeck and co-workers shed light into the mechanism for the reduction of Pd(II) by finding that the reduction can be carried out without cod, from $PdCl_2$ and by describing a hexabromo-Pd(II) dimeric anion, which is a key side product that provides a thermodynamic driving force for the reduction to take place.[135]

3.1.4 The Suzuki-Miyaura cross-coupling reaction in alternative solvents

The Suzuki-Miyaura coupling is the most popular cross-coupling reaction nowadays. This process involves C-C bond formation between alkyl, aromatic, acyl or vinylic halides with organoboranes, catalysed by Pd and promoted by inorganic bases like sodium carbonate.[102]

In their seminal work, Suzuki and co-workers used alkenylboranes as the activated C(sp^2) species, which were obtained *via* hydroboration of vinyl compounds.[109] Nowadays, new organoboron compounds have become the preferred choice when performing Suzuki couplings *e.g*. organoboronic acids, organotrifluoroborates, organoboron esters, *etc*. The use of boronic acids has certain advantages, as these compounds increase the activation of the C_α towards transmetalation in comparison to alkenylboranes. However, some inconveniences arise, in aprotic solvents boronic acids behave like proton donors but, in protic media boronic acids tend to form boronate species, which are susceptible to protodeboronation leading to decomposition. Another important issue to consider is the tendency of organoboronic acids to undergo homocoupling under reaction conditions.[136]

The Suzuki-Miyaura reaction is the most robust coupling methodology due to the organoboron compounds superior compatibility with protic solvents, therefore, it is no surprise the reaction has been successfully implemented both at laboratory and industrial scale in water or biomass-derived solvents like 2-MeTHF, γ-valerolactone, *etc*.[137–139] Nevertheless, the aim of this literature review will be focused on its implementation in Ils and DESs.

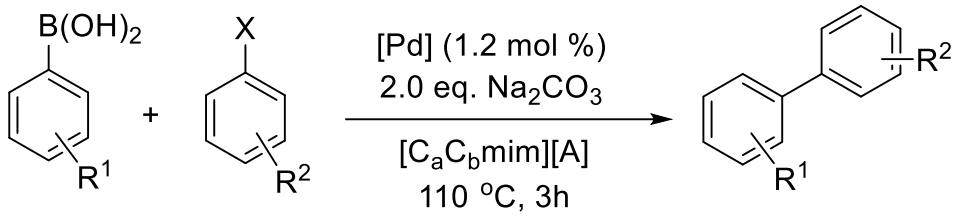

R^1 = H, 4-Me, 2-Me, 4-OMe, 4-COMe
R^2 = H, Cl, $COCH_3$, 4-Me, OCH_3
X = I, Br, Cl
a = 2, 4, 6
b = 1, 4
[A] = BF_4, PF_6, SbF_6, Tf_2N, OTf
[Pd] = $Pd(PPh_3)_4$, $(MeCN)_2PdCl_2$, $(MeCN)_2PdCl_2$/4mim

Scheme 3.1.12: Suzuki couplings in imidazolium-based ILs by Mathews, Smith and Welton.[140,141]

The first report of a Suzuki-Miyaura coupling in ILs was published in 2000 by Mathews, Smith and Welton.[140] The researchers designed a Suzuki reaction in $[C_4C_1im][BF_4]$ IL catalysed by $Pd(PPh_3)_4$. The reaction showed moderate to good conversions, with little to no homocoupling side products, *Scheme 3.1.12*. The IL increased the tolerance of the catalyst to air and moisture and allowed the recyclability of the solvent/catalyst phase without losses in reactivity. Then, the researchers developed a catalyst supported by *N*-substituted imidazolium derivatives as ligands. Initially, the catalyst was tested in dioxane, toluene, THF and water. Although haloarenes were consumed almost quantitatively and no homocoupling of the boronic acids was observed, the catalyst suffered total decomposition after the reaction. The researchers tried a different strategy consisting of replacing molecular solvents for ILs. All Pd pre-catalyst showed a slightly reduced catalytic activity in ILs, with appearance of homocoupling products (<5%). Nevertheless, the decrease in reactivity was accompanied by an enhanced stability, which allowed for recyclability of the catalyst/IL. Through speciation studies, the authors attributed the increased stability to an *in situ* NHC-Pd complex, formed with either imidazolium added as ligand or the IL cation, once aqueous sodium carbonate was added.[141–144]

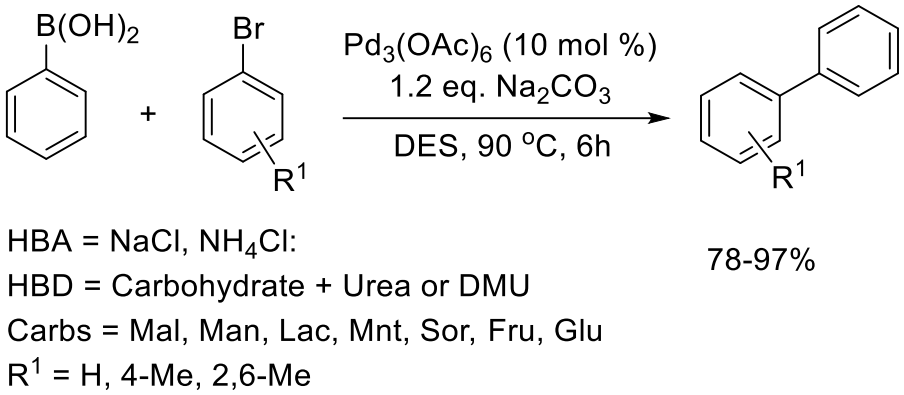

Scheme 3.1.13: Pd-catalysed Suzuki coupling reaction in carbohydrate-based DESs reported by Imperato *et al*.[145]

The first application of DESs as solvents for Pd-catalysed Suzuki-Miyaura coupling reactions was reported in 2006 by Imperato *et al*.[145] The researchers reported a series of DESs made of urea or dimethyl urea (DMU) and carbohydrates as HBDs with ammonium chlorides as HBA. The DESs were tested in a "ligand-free" Pd acetate-catalysed Suzuki-Miyaura reaction between phenylboronic and bromobenzene derivatives, *Scheme 3.1.13*. Good yields were obtained and no phenylboronic acid homocoupling nor hydrodeboronation were observed. Moreover, the authors did not report any proof of catalyst decomposition.

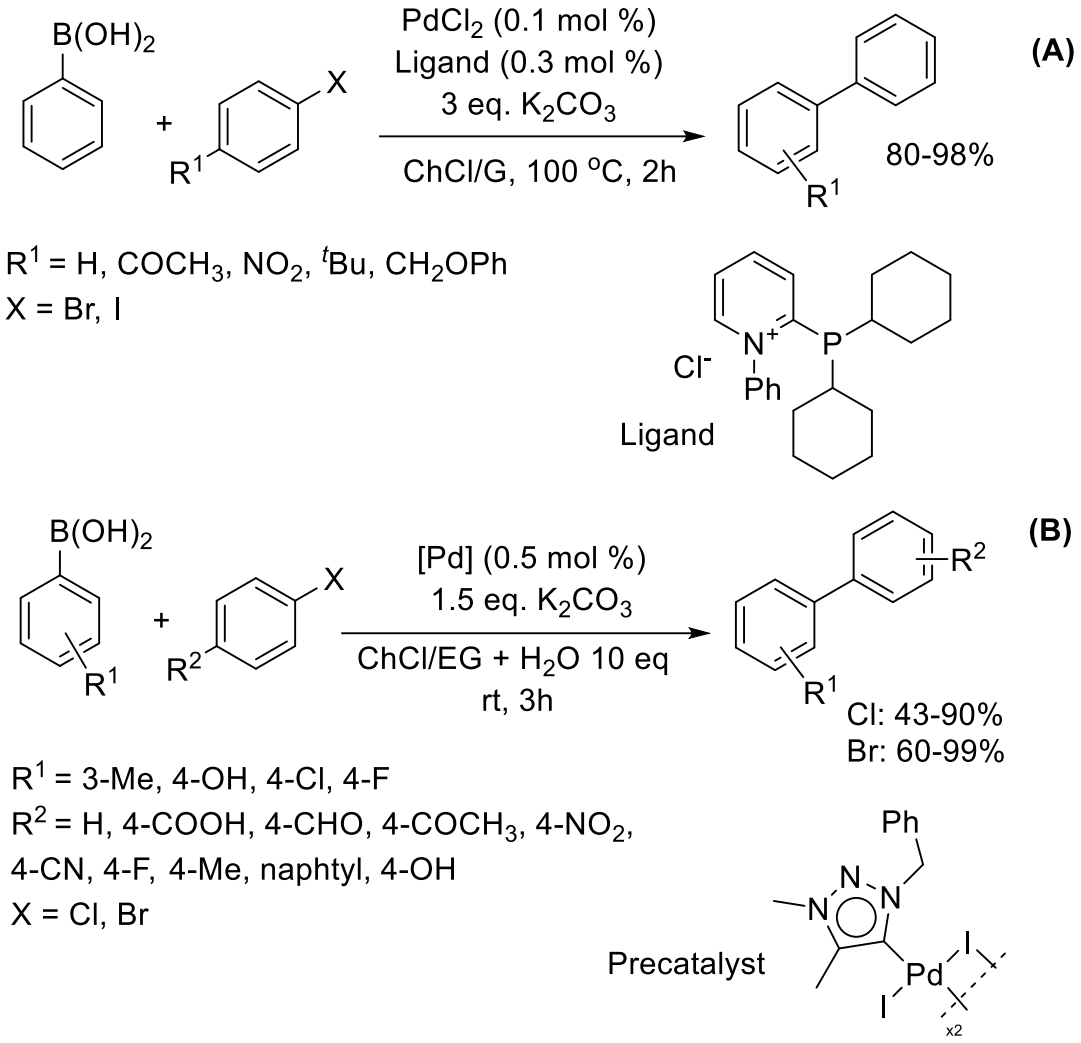

Scheme 3.1.14: Suzuki couplings in DESs with *ad hoc* Pd pre-catalysts[146,147]

Eleven years after this, Marset *et al*. reported a cationic piridiniophosphine chloride ligand, specifically designed for Pd-catalysed cross-couplings in DESs.[146] This ligand was designed to improve the solubility of the Pd complex in DESs and to prevent the formation of black Pd aggregates. The authors tested their DES-compatible ligand in Pd-catalysed Suzuki-Miyaura, Heck and Sonogashira cross-coupling reactions using ChCl/U, ChCl/EG and ChCl/G DESs. With regards to the Suzuki reaction, the authors reported excellent yields and good recyclability of the DES/catalyst mixture, with up to 5 cycles of re-use tested, *Scheme 3.1.14-A*. The new Pd complex, formed with 3 equivalents of ligand, proved to be more effective than unsupported sources of Pd(II) like $PdCl_2$ and $Pd_3(OAc)_6$ or even, Pd(II) complexes with PCy_3 and

CyJohnPhos. Both unsupported and phosphine-supported pre-catalysts gave conversions no higher than 25%, whereas the cationic phosphine-supported Pd pre-catalyst gave conversions between 80 and 98% for bromo-and iodoarenes, and 46% for chloroarenes. With regards to the solvent, the best results were obtained in ChCl/EG and ChCl/G followed closely by ChCl/U. The authors did not observe black palladium aggregates nor homocoupling products after the reactions were complete.

The same year, Dilauro *et al*. disclosed a Suzuki coupling in the aforementioned DESs using $Pd_3(OAc)_6$ as pre-catalyst without any supporting ligands and potassium aryltrifluoroborates instead of arylboronic acids, obtaining good to excellent yields, *Scheme 3.1.15*.[148] The authors reported that arylboronates showed better stability towards hydrolysis than boronic acids; in fact, the authors found that switching to borates as coupling partners improved their yields and allowed them to use less catalyst.

They also assessed the recyclability of the catalyst/ChCl/G system by increasing the pre-catalyst loading to 5 mol%. Good yields were obtained for the firsts 5 cycles, followed by a significant decrease in isolated yield on the sixth cycle. Pd particles were identified during the reactions, however, the high yields of up to 98% let the authors think that ChCl/G was playing certain stabilizing role to support the Pd active species. When repeating the recyclability experiments with 1% mol catalyst, the DES/catalyst mixture gave good yields but only up to the fourth cycle. These results suggests a gradual degradation of the catalyst through each cycle, and that 1 mol % catalyst loading was more than needed for the first cycles.

Later, Marset *et al*. reported a mesoionic Pd pre-catalysts supported by an abnormal NHC ligand for cross-coupling reactions in DESs, *Scheme 3.1.14-B*.[147] A NHC ligand is classified as abnormal when the imidazolium ring is metalated at positions C4 or C5. These ligands tend to be better σ-donors than classic NHC ligands. [147] The authors theorized an abnormal NHC ligand would increase the electron density of the metal centre when compared to phosphines. The new pre-catalyst showed higher activity than the one

supported by cationic phosphine ligands. The reactions proceeded at room temperature with improved conversion for chloroarenes and good tolerance for arenes decorated with EWGs and EDGs. Interestingly, the authors reported that they obtained poor yields when running the Suzuki coupling in water or dry ChCl/EG, but that the reactivity dramatically increased when they used mixtures of ChCl/EG with up to 10 equivalents of water, *Scheme 3.1.14-B*. This suggests a synergistic effect of water and DES in this reaction.

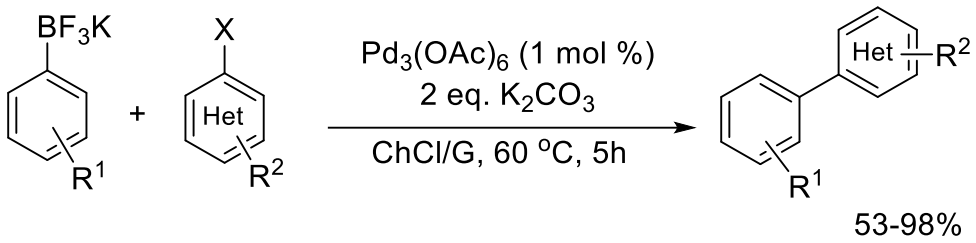

R^1 = H, NO_2, OMe
R^2 = 2-NO_2, 4-CO_2Et, 3-CO_2Me, 2-CO_2H, 3-CO_2H, 2-OMe, 4-OMe, 4-CH_2CN, 2-Cl, 4-Cl, 2-NH_3, 4-CHO, 3-Et, 4-OH
Heterocycles: indol, pyrdine, thiazol

Scheme 3.1.15: "Ligand-free" Suzuki coupling with $Pd_3(OAc)_6$ in DESs[148]

DESs have also proved to be good solvents for transformations involving biomolecules, since the DESs 3D structure provides enhanced protein thermal stability and good reversibility for folding/unfolding processes depending on the HBA employed. DESs have been also used to dissolve nucleic acids while preventing their denaturation.[149] Paris *et al*. reported a process that involves the coexistence of Pd-TPPTS catalysed Suzuki-Miyaura couplings with either alcohol dehydrogenase or amine transaminase catalysed bioreductions in DESs/buffer systems.[150,151] This process allowed the authors to prepare biaryls decorated with ketones, which then undergo bioreduction to generate enantiopure alcohols and amines holding biaryl motifs. A different approach to Suzuki-Miyaura couplings was demonstrated by Chakraborty *et al*. who prepared metallized DNA fragments with Pd(II) salts and Fe_3O_4 in ChCl/EG in an effort to generate a nanobiocatalyst with superior recyclability compared to molecular catalysts.[152] The authors reported that ChCl/EG resulted the best

solvent for the metallization because it allowed the process to be carried out in one pot, it prevented the loss of the DNA 3D helical structure and it reduced Pd(II) to Pd(0), due to the presence of ethylene glycol. Afterwards, ChCl/EG was used as solvent for the Suzuki coupling of boronic acids with aryl halides functionalized with EWGs or EDGs, giving nearly quantitative conversion of the starting materials with good selectivity for the productive coupling products. Moreover, the authors reported the DES/nanobiocatalyst system was able to be recycled 6 times, with conversions ranging from 97% to 81%.

Overall, it has been demonstrated that the Suzuki-Miyaura cross-coupling is compatible with IL's and type III DESs formed with a variety of HBD. It has been observed that in many of these reactions, Pd aggregates form visible black particles, but this phenomenon does not seem to affect the catalyst activity since in most examples, good yields were obtained. In some cases, the DES/catalyst systems were able to be recycled a number of times. It has been proposed that ChCl might provide electrostatic stabilization of the catalytically-active Pd species in resemblance to Jeffery catalytic conditions reported in molecular solvents with tetraalkylammonium as additives.[153]

3.1.5 The Negishi cross-coupling reactions in alternative solvents.

The Negishi cross-coupling is a reaction between organohalides or pseudohalides with Zn-based organometallic reagents to create new C-C bonds, which is often catalysed by Pd or Ni, depicted in red in *Scheme 3.1.16*. This reaction has found many applications in the synthesis of natural products, drugs, or organic electronic materials.[154–157] The biggest competitive advantage of this cross-coupling reaction against other popular methodologies like Suzuki-Miyaura, Corriu-Kumada or Stille couplings lies in the reactivity of the Zn organometallic used as the transmetalation reagent.

As a moderately electronegative metal, Zn exhibits high functional group tolerance, this enables the preparation of organozinc reagents with a more covalent C-Zn bond, functionalized with esters, cyanides, ethers, amines, *etc*., which in turn, are compatible with a wide range of functionalized organic halides as coupling electrophiles, such as ketones, nitriles, nitro-compounds,

esters, amides, *etc*.[158] The reduced basicity of Zn reagents as compared to Mg and Li reagents improves its involvement in catalysed cross-couplings by having a reduced reactivity against Pd under catalytic conditions. More basic reagents tend to poison the metal catalyst by formation of organopalladate species, as suggested by Negishi.[159,160] On the other hand, organozinc reagents undergo cross-coupling reactions faster than organoboron and organotin reagents, by means of faster transmetalations, due to the more nucleophilic character of the organozinc reagent, which allows for faster reactions with potentially less-reactive substrates like chloroarenes.[161,162] Thus, Negishi couplings offer a good balance between selectivity, functional group tolerance and reactivity and as such, are highly attractive for small-molecule synthesis.

Negishi couplings presents some important challenges: the presence of unwanted reactivity, leading to organozinc homocoupling and reductive dehalogenation of the electrophile through a β-hydride elimination mechanism (represented with the involvement of a generic species holding β hydrogen atoms), or from an Zn complex coming from a second transmetalation step shown in blue in *Scheme 3.1.16*. In addition, and in contrasts to reactions like the Suzuki coupling, Negishi couplings require to be performed in rigorously dried, non-protic solvents, with protection from atmospheric moisture during the reaction, to avoid protonolysis of the organozinc reagent. This latter limitation is particularly relevant to industrial settings and in laboratories lacking a glovebox and Schlenk equipment, where Negishi couplings may be deemed infeasible.

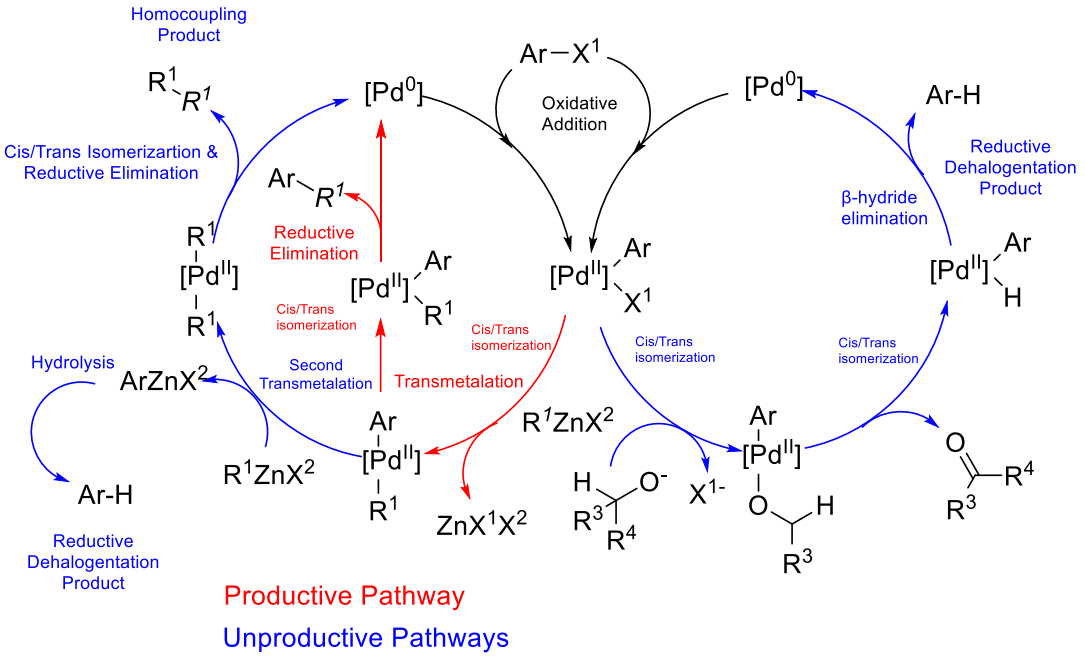

Scheme 3.1.16: General mechanism for Pd-catalysed Negishi couplings showing both productive and non-productive pathways.

The unproductive cycles shown in blue in *Scheme 3.1.16*, leading to organozinc homocoupling and reductive dehalogenation products, can be partially controlled by strategies that increase the rate of the productive oxidative addition and reductive elimination steps, over the unproductive pathways. Some examples are the employment of bulky and electron-rich phosphines as supporting ligands for the Pd catalyst *e.g.,* Xphos, Amphos, HandaPhos, *etc.*, the use of slightly hindered electrophiles or the use of bulky organozinc reagents.[163,164] In this regard, it has been reported that *ortho*-substituted aryl electrophiles tend to slow down the rate of oxidative addition[165,166] Nevertheless, Dai and Fu as well as Çalimsiz *et al*. reported independently Negishi coupling protocols for preparing highly functionalised, and therefore severely hindered, biaryls from *ortho*-functionalized haloarenes without the need for harsh reaction conditions.[167,168]

Due to the air- and moisture-sensitive nature of organozinc reagents, the use of alternative and green solvents for Negishi couplings have not been explored as extensively as for Suzuki-Miyaura couplings. In 2000, Sirieix *et al*. reported the application of $[C_4Mim]BF_4$ IL for a Negishi couplings between aromatic and

benzylic zinc organometallic reagents with aromatic and alkenyl halides catalysed by Pd supported by cationic phosphines holding 1-butyl-3-methylimidazolium groups.[169] Good yields were obtained and good recyclability observed up to the third cycle. It is noteworthy that the researchers did not report the use of protective atmosphere, although it is implied, since the reactions were carried in Schlenk flasks and the Pd precursor loaded in a dry Toluene solution, *Scheme 3.1.17*.

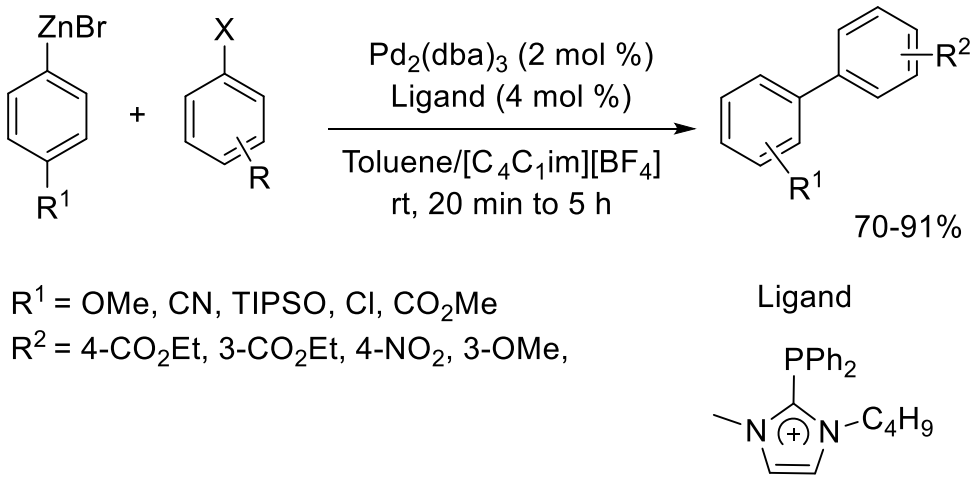

Scheme 3.1.17: Negishi coupling in IIs by Sirieix *et al*.[169]

Krasovsky, Duplais and Lipshutz disclosed a different approach to Negishi couplings in green solvents by the development of Negishi-like reactions "on water", with the assistance from micelles formed by non-ionic surfactants.[170–172] It was postulated as a Negishi-like process because, instead of adding a RZnX or R_2Zn species to a mixture of organic halide and catalyst, the Zn reagent was prepared *in situ* in the hydrophobic phase, by insertion of Zn^0 into an alkyl halide mediated by TMEDA as an additive, which is believed to both activate the Zn surface and stabilize the organometallic complex. The synthesis of the Zn organometallic reagent was compatible with ketones and esters and selective for C-Br over C-Cl bonds. The structure of the surfactant was found to be crucial to reduce the amount of reductive dehalogenation and homocoupling products, since with bigger micelle sizes, better yields and selectivities were obtained. After Pd pre-catalyst optimisation, the authors chose $PdCl_2(AmPhos)_2$ pre-catalyst, which showed superiority with respect to

traditional phosphine ligands. The cross-coupling proceeded at room temperature over periods of 48 h and showed good tolerance for C(sp^2) halides functionalized with ketones, esters and methoxy groups, Scheme *3.1.18*. Nitriles, amides and alcohols were not tolerated. The scope of this methodology included the coupling of aryl and alkenyl halides with C(sp^3)-Zn reagents. One of the major problems encountered was the reductive dehalogenation of the C(sp^2) halides, which forced the authors to work with an excess of electrophile. Interestingly, Lipshutz and co-workers did not observe β-hydride elimination nor isomerisation when using secondary alkyl Zn reagents. Moreover, when using alkenyl bromides as electrophilic coupling partners, the cross-coupling showed good retention of stereochemistry.

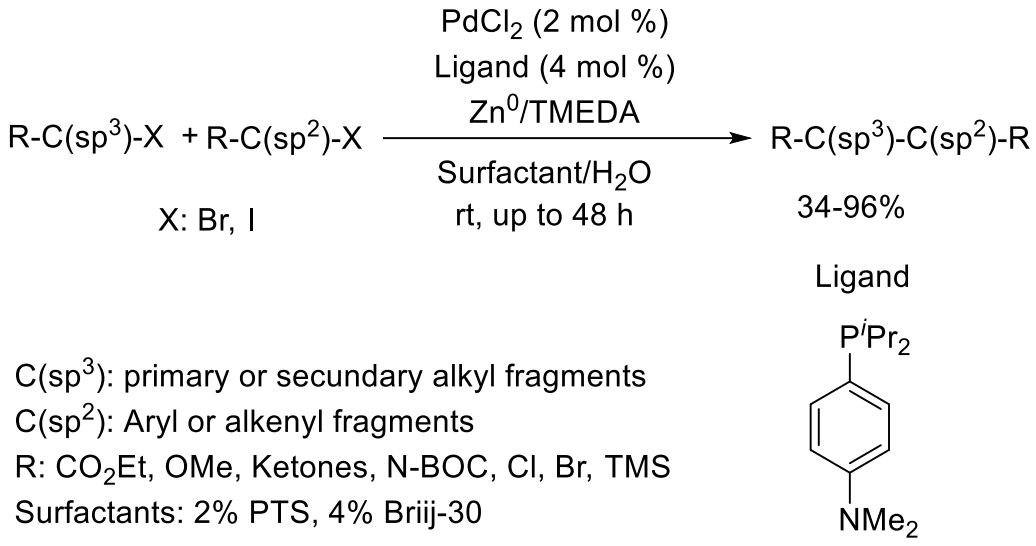

Scheme 3.1.18: Negishi-like cross-couplings "on water", under Lipshutz conditions.[170–172]

As discussed in *section 3.1.1*, many studies have shown that ChCl-based DESs can be used as solvents for reactions involving air- and moisture-sensitive polar-organometallic reagents, despite the protic and hygroscopic nature of the neoteric solvent. It has also been suggested that the role of DESs in metal-mediated reactions is not merely as solvent media, but as a non-innocent and crucial participant that enhances the reactivity of the organometallic reagents and the organic electrophiles. The difference in reactivity of polar-organometallic reagents in DESs compared to volatile

organic solvents has been attributed to water engaging with the complex DES 3D structure through hydrogen-bonding interactions, which promotes a similar scavenging effect to that described previously with magnesium-halide-mediated nucleophilic additions.[89,101] Also, cholinium-based DESs usually have chloride as counter-anion and it has been proposed that chloride can coordinate to the organometallic reagent to form anionic complexes with enhanced nucleophilicity of the organometallic, while at the same time, the hydrogen-bond donor component of the DES can activate the electrophile through hydrogen-bonding catalysis. *Trans*-phase hydrogen-bonding and *trans*-phase acid-base reactions in between the heterogeneous DES/organic systems have also been invoked to explain the enhanced reactivity in DESs.[173,174] Thus, a major aim of the work presented in this thesis was to explore the use of highly reactive organometallic reagents in Pd-catalysed cross-coupling reactions in DESs.

During the course of the PhD studies reported here, some papers emerged describing early results of Pd-catalysed couplings using highly reactive reagents in DESs. Dilauro *et al*. published the first cross-coupling reaction between aryl bromides and organolithium reagents catalysed by $Pd[P(t\text{-}Bu)_3]_2$ in a water/NaCl mixture and DESs.[120] Interestingly, this cross-coupling reaction generated mainly dehalogenation products when performed in ChCl/U and ChCl/G. The authors replaced the ChCl-based DESs by water/NaCl. The authors suggested chloride might have a similar role as in ChCl-DESs, to enhance the nucleophilicity of the organolithium reagent and the Pd catalyst *via* the formation of anionic complexes and by narrowing P-Pd-P angles. The authors reported that a NaCl concentration of 0.2 M was critical to achieve good yields and so was the rate of addition of the organometallic reagent. Adding the organolithium solution quickly to a vigorously stirred reaction mixture gave 98% conversion, while dropwise additions reduced the conversion to 45%, *Scheme 3.1.19*. The cross-coupling protocol showed an outstanding recyclability of 10 cycles and good tolerance to changes in the reactivity of the aryl halides, induced by EWGs and EDGs bonded to the aromatic ring.

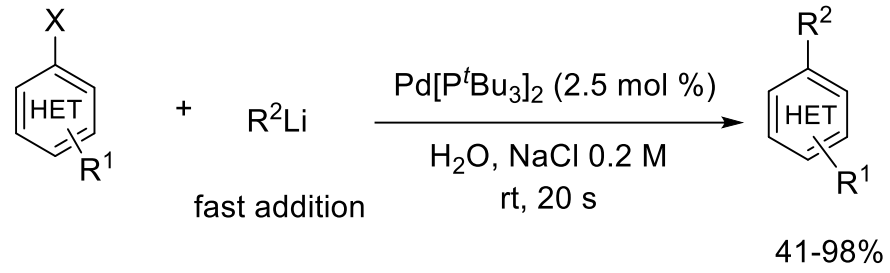

R^1 = 4-OMe, 4-Cl, 4-F, 4-CF_3, 2-Alkyl, 4-Benzyl
R^2 = Me, Et, ^{s}Bu, ^{i}Pr, Ph, Me_3SiCH_3, PhC_2,^{n}Bu
X: Br, I
Heterocycles: Indole, isoquinoline, thiophene

Scheme 3.1.19: Cross-coupling involving organolithium reagents "on water".[120]

In 2021, Dilauro *et al*. disclosed the first Negishi coupling in DESs or water/NaCl mixtures by following a similar strategy.[121] The organozinc reagents underwent cross-coupling satisfactorily in both ChCl/U DES and "on water" with NaCl as additive, *Scheme 3.1.20*. It is noteworthy ChCl/U was found to be a better solvent than water/NaCl for substrates bearing acidic C-H bonds *e.g.*, amines, carboxylic acids and alcohols, since these haloarenes were not able to undergo Negishi coupling "on water". As expected, the Negishi coupling in DESs or "on water" exhibited superior functional group tolerance compared to the cross-coupling with organolithium reagents, and in agreement with Krasovsky, Duplais and Lipshutz, when secondary alkylzinc reagents were used as coupling partners, Dilauro *et al*. found no undesired isomerisation leading to linear products due to competing β-hydride elimination. The authors found their Negishi coupling reaction conditions to be very sensitive to the pre-catalyst loading and the use of supporting ligands since for example, $PdCl_2$ and $Pd_3(OAc)_6$ were not able to catalyse this reaction satisfactorily without support from phosphine ligands. Interestingly, when the reaction was tried "on water" without NaCl or in glycerol without ChCl, the cross-coupling product could only be isolated in small yields, which indicated that chloride anions may play a key role in this transformation.

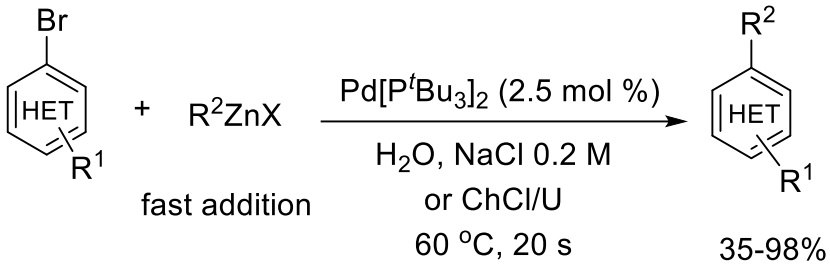

R^1 = CHO, COMe, Cl, CO_2Me, CN, NO_2, OH, CO_2H, NH_2
R^2 = ^{n}Bu ^{s}Bu, ^{i}Pr, Ph, Me_3SiCH_3, Hexyl, $EtO_2C_4H_8$, C_4H_8CN, Pyr
Heterocycles = Benzofuran, napthalene, quinoline, azaindole
indole, thiazole
X: Br, Cl

Scheme 3.1.20: Negishi coupling in ChCl/U DES and "on water".[121]

The work by Dilauro *et al*. on the applications of DESs in cross-couplings involving organolithium and organozinc reagents represented a breakthrough in the field. Their research, which was published during the development of this PhD project, showed that DESs are promising alternative solvents for some reactions involving reactive organometallic compounds. However, the range of reactions demonstrated so far, and their scope is still very limited. Only one previous example of Pd-catalysed Negishi coupling in DES has been reported. There remains a need to establish methodologies for these reactions in DESs using simple, cheap and readily available Pd catalysts, e.g. $Pd_3(OAc)_6$, in order to maximise their utility in a range of settings. The development of regioselective Negishi couplings in DES is also still an unmet challenge. This PhD project differentiates from the previous work because it presents methodologies that address both of these challenges, whilst maintaining the ability to perform the cross-coupling reactions in wet solvents with no protective atmosphere.

3.1.6 Negishi cross-coupling reactions under "ligand-free" catalytic conditions.

In 2008, Liu *et al*. disclosed a Negishi cross-coupling reaction between C(sp^3), C(sp^2) and C(sp) organozinc reagents with aryl iodides bearing EWGs and

EDGs and $Pd_3(OAc)_6$ as pre-catalyst under Jeffery conditions, *i.e.,* Pd supported by tetrabutylammonium bromide as phase-transfer stabilizer, in THF without the involvement of phosphine ligands, *Scheme 3.1.21*.[119] The authors reported that in the absence of supporting ligands, palladium acetate tended to form aggregates, which were believed to be catalytically-inactive. Nevertheless, when the phase-transfer stabilizer additive was employed, the Negishi couplings ran smoothly at room temperature with quantitative formation of products with very low catalyst loadings. A problem with the "ligand-free" Negishi conditions in ethereal solvents, was the poor selectivity when secondary organozinc reagents were investigated, since significant amounts of linear products were formed due to undesired β-hydride elimination.

Kinetic studies carried by Liu *et al*. showed that the reactions did not proceed if phosphine ligands were added and that the reaction was not first order in pre-catalyst, which was reported to be a clear indication of the heterogeneous nature of the active catalyst.[119] Other trials without phase-transfer additives showed equally satisfying yields, however, at lower reaction rates with an increased tendency of Pd to degrade into inactive black aggregates. Based on these results, the researchers suggested that when $Pd_3(OAc)_6$ pre-catalyst is reduced to Pd^0 it may be forming catalytically-active palladium nanoparticles (PdNPs).

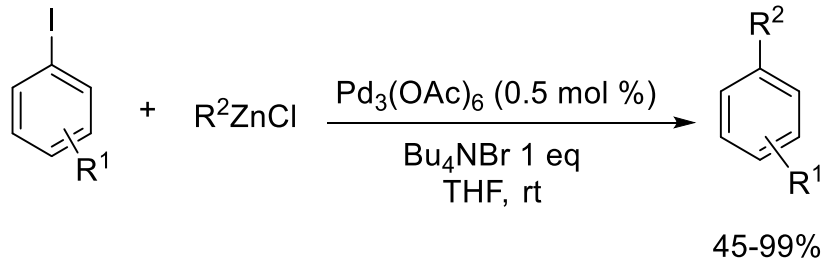

R^1 = 2-CO_2Me, 4-CO_2Me, 4-OMe
R^2 = Primary & secondary alkyl fragments, aromatic fragments

Scheme 3.1.21: Negishi coupling in THF catalysed by Pd under "ligand-free" conditions

The work of Liu *et al*. is of significant relevance to this PhD project, since ChCl is also an ammonium salt, therefore, ChCl-based DESs were considered to be potential reaction media for this type of “ligand-free” coupling, as they might exert a stabilizing effect on the catalytically-active Pd species during the reaction. This hypothesis would be in agreement with the observations by Dilauro *et al*. and Imperato *et al*. on the conserved activity of the catalyst across several recycling steps in “ligand-free” Pd-catalysed Suzuki-Miyaura cross-couplings in DESs, even though black Pd was observed in their first reaction cycles.[145,148]

3.2 Chapter aims

DESs have emerged in the last decade as promising alternatives to conventional solvents due to the low-prices of their components, atom-economical syntheses, biodegradability and high tunability. ChCl-based DESs have been introduced as viable solvents for C-C bond formation reactions promoted by air- and moisture-sensitive organometallic reagents such as organomagnesium, organolithium and organozinc reagents. It has been shown that DESs not only acts as an innocent solvent, but can also speed-up the reactions through mechanisms that are not fully understood

A key objective of the project reported in this chapter, was to implement simple and affordable protocols for Suzuki and Negishi cross-coupling reactions in DESs, without the need for protective atmospheres and Schlenk conditions and where possible, without the addition of complex or expensive supporting ligands. Specific aims were:

- To develop conditions for the Suzuki-Miyaura reaction between phenylboronic acid bromoarenes in DESs, in open air with $Pd_3(OAc)_6$ as pre-catalyst and no supporting ligands.
- To study the Negishi reaction in DESs taking as a starting point the results obtained for the Suzuki reaction.
- To determine an optimised set of reaction conditions for the Negishi coupling.

- To study the different reactivities exhibited by the catalysts against certain substrates and to develop a regioselective Negishi methodology by exploiting these differences in reactivity.

3.3 Results and Discussion.

5 DESs were prepared and stored in open air as described in *section 5.1.2* and labelled as "wet" DESs: ChCl/G, ChCl/EG ChCl/U, ChCl/DMU and ChCl/$AcNH_2$. In the case of ChCl/G and ChCl/U, an extra batch was prepared employing Schlenk conditions and stored under protective N_2 atmosphere with the objective to minimize its water content. These were labelled as "dry" DESs. The water content of the DESs employed was measured by Karl-Fisher titration. The wet DESs were left to equilibrate with the lab atmosphere for a week prior to water content measurement.

The results were reported in *Table 3.3.1*. For all wet DESs, the water content in molar fraction ranged from 13% to 46%, which is an indication of the relatively higher proportion of water present in the eutectic mixtures compared to the content in polar aprotic organic solvents. The water content observed for ChCl/U equilibrated with the laboratory atmosphere resulted in agreement with the reported values by Meng *et al*.[83]

The water content in wet DESs tended to correlate with the number of H bonds that the HBD species can form, *e.g*., ChCl/$AcNH_2$ < ChCl/EG < ChCl/G < ChCl/U. Unexpectedly though, ChCl/DMU resulted the most hygroscopic DESs.

Table 3.3.1: Determination of water content of DESs by Karl Fischer titration

Entry	DES	Water (ppm)	X_{H2O} (%)
1	ChCl/U[a]	28571	29.7
2	ChCl/U[b]	382	0.5
3	ChCl/EG[a]	17737	20.5
4	ChCl/G[a]	24720	31.3
5	ChCl/G[b]	317	0.6

6	ChCl/DMU[a]	46535	46.0
7	ChCl/AcNH$_2$[a]	10420	13.1

[a] Wet: equilibrated with the lab atmosphere for a week. [b] Kept under N_2 atmosphere.

3.3.1 Suzuki-Miyaura reaction

It was decided to begin this investigation with the study of the Suzuki coupling between phenylboronic acid **1a** and bromobenzene **2a** in wet DESs in open air as a model reaction. $Pd_3(OAc)_6$ pre-catalyst was chosen as a Pd(II) source without supporting ligands and K_2CO_3 as base, *Scheme 3.3.1*. The model reaction was examined in three wet ChCl-based DESs prepared according to the procedures described in *section 5.1.3*: ChCl/G, ChCl/EG and ChCl/U. Different temperatures, pre-catalyst loadings and reaction times were assessed.

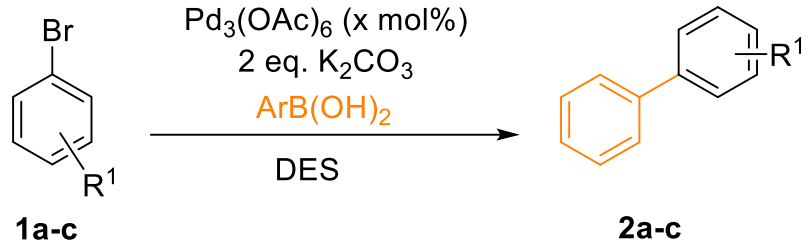

1a-c **2a-c**

1a, 2a: R^1 = H
1b, 2b: R^1 = 4-OMe
1c, 2c: R^1 = 4-COMe

Scheme 3.3.1: Suzuki-Miyaura reaction in DESs under "ligand-free" conditions

K_2CO_3, **1a** and phenylboronic acid were mixed in the corresponding DES at room temperature for 10 minutes and then, $Pd_3(OAc)_6$ was added to the reaction mixture. K_2CO_3 was insoluble in all DESs tested. In ChCl/EG and ChCl/G, the pre-catalyst was solubilized at room temperature to form a yellow translucent solution. $Pd_3(OAc)_6$ was not soluble in ChCl/U at room temperature and remained suspended in the DES mixture. No black aggregates were observed to form at room temperature in any of the DES mixtures after stirring for 10 extra minutes.

Figure 3.3.1: Left: Suzuki-Miyaura reaction mixture in ChCl/U after stirring for 10 minutes at 100 ^{o}C. Right: Suzuki-Miyaura reaction mixture in ChCl/G after stirring for 10 minutes at 100 ^{o}C

When the reaction mixtures were heated, intense and quick formation of Pd black aggregates was evident in the ChCl/G and ChCl/EG mixtures once the temperature was raised above 50-60 ^{o}C. Few black aggregates were observed in ChCl/U mixture, but most of the Pd acetate remained suspended even at 100 ^{o}C, Figure *3.3.1*.

Under the studied reaction conditions *i.e.*, ChCl/G, ChCl/EG and ChCl/U DESs, $Pd_3(OAc)_6$, no supporting ligands, involvement of phenylboronic acid; there are two possible routes to achieve the formation of the catalytically-active Pd(0) species from $Pd_3(OAc)_6$: reduction by the homocoupling of 2 equivalents of phenylboronic acid per equivalent of Pd (*-A)*, and reduction mediated by polyols, as discussed in *section 3.1.3*. [111–113,152] It is important to mention that the release of $Pd_3(OAc)_6$ monomer correlates with the polarity of the solvent, more polar solvents induce a higher proportion of $Pd(OAc)_2$ in solution to undergo reduction.[114,115]

Phenylboronic acid was found to be a good transmetalating partner, which allowed us to isolate **2a** from **1a** in a 75% yield in 6 hours with 10 mol% of $Pd_3(OAc)_6$ in ChCl/G as solvent *Table 3.3.2*, *entry 1*. Interestingly, when the catalyst loading was reduced to 1 mol%, **1a** was converted in **2a** nearly quantitatively in ChCl/G and ChCl/EG, *Table 3.3.2*, *entries 2-3*. This seems to indicate that an excess of $Pd_3(OAc)_6$ is detrimental to the formation of the

catalytically-active Pd(0) species. A possible explanation for this observation is that high concentrations of pre-catalyst might favour the formation of unreactive Pd aggregates. Moreover, only traces of **2a** were detected when the reaction was performed in ChCl/U, *Table 3.3.2*, *entry 4*. These observations suggested that, under the studied conditions, the low solubility of pre-catalyst in ChCl/U is not allowing the reduction of Pd, or that the most favourable mechanism of Pd(II) reduction might be the one mediated by polyols, over the one mediated by boronic acids.

Table 3.3.2: Summary of results from Suzuki-Miyaura reaction conditions optimisation in DESs.

Entry	ArBr	[Pd] (x mol)%	T (ºC)	t (h)	Solvent	Yield (%)
1[a]	**1a**	10	100	6	ChCl/G	75
2[a]	**1a**	1	100	6	ChCl/G	97
3[a]	**1a**	1	100	6	ChCl/EG	99
4[a]	**1a**	1	100	6	ChCl/U	0
5[a,b]	**1a**	1	100	6	ChCl/U	0
6[a]	**1a**	1	50	6	ChCl/EG	81
7[a]	**1a**	1	50	6	ChCl/U	0
8[a]	**1a**	1	100	3	ChCl/G	79
9[a]	**1a**	1	100	2	ChCl/G	61
10[a]	**1a**	1	100	3	ChCl/EG	77
11[a]	**1a**	1	100	6	Glycerol	73
12[a]	**1a**	1	100	3	Glycerol	96
13[a]	**1a**	1	100	6	Ethylene Glycol	87
14[a]	**1b**	1	100	6	ChCl/G	87
15[a]	**1c**	1	100	6	ChCl/G	81

Typical conditions: In a round-bottom flask, 5 cm^3 of solvent, phenylboronic acid (1.5 mmol) and **1a-c** (1mmol) were mixed at rt and open air for 10 min. $Pd_3(OAc)_6$ was added and mixed

at rt for 10 min, then heated to desired temperature. The reaction was quenched with 10 cm^3 of aqueous NH_4Cl 2 M. Reactions performed once. [a] Isolated yields of products purified by column chromatography. [b] $[Pd(OAc)_2(PPh_3)_2]$ used as pre-catalyst.

A fast formation of black Pd(0) aggregates was spotted at the beginning of the reactions in ChCl/G and ChCl/EG, with the consequent excellent cross-coupling yields, whereas in ChCl/U no reaction was observed even though both reactions were carried out with the same quantities of phenylboronic acid and the same temperatures. It is important to note that these results are in contrast to the Suzuki reaction reported by Dilauro *et al*. on the Suzuki reactions with aryltrifluoroborates in DES, since under similar conditions, the authors obtained a poor yield of **2a** in ChCl/EG, but 96% of isolated yield in ChCl/U after 24 hours at 60 ^oC.[148]

The formation of black Pd aggregates at the beginning of the reactions was observed to correlate with good yields of biphenyl **2a** in ChCl/EG and ChCl/G. These results are in agreement with the reports by Jeffery, Liu *et al*. and Dilauro *et al*. on the stabilization of catalytically-active Pd(0) nanoparticles by tetraalkylammonium salts, in Heck, Negishi and Suzuki cross-couplings respectively.[119,148,153] In the DESs experiments, the stabilising role might be played by choline ChCl as discussed in *section 3.1.6*. With the observations made so far and the amount of data gathered, it is not possible to determine the nature of the catalytically active Pd species when $Pd_3(OAc)_6$ was used under “ligand-free” conditions in DESs. Nevertheless, it was evident from the results that good yields were obtained when intense black Pd formation was observed at the beginning of the reactions, after the temperature was raised above 50-60 ^oC.

To investigate if a different Pd(II) source could be used to address the poor reactivity observed in ChCl/U, $[Pd(OAc)_2(PPh_3)_2]$ was used as a pre-catalyst with the same reaction conditions. Only the intact starting material was recovered and no improvements with respect to the “ligand-free” protocol were observed, *Table 3.3.2*, *entry 5*.

Different temperatures and reaction periods were assessed to find if less harsh reaction conditions would be able to promote the Suzuki coupling with similar success to *entries 2 & 3* in *Table 3.3.2*. It was found that reducing the temperature to 50 ^{o}C still promoted the cross-coupling in ChCl/EG to some extent, but the reaction did not reach to completion in 6 hours, *Table 3.3.2*, *entry 6*. Moreover, when the reaction time was halved or reduced to 2 hours at 100^{o}C, the reactions once again did not run to completion in ChCl/G, *Table 3.3.2*, *entries 8-10*.

The Suzuki coupling was also tried in glycerol and ethylene glycol, to compare the behaviour of the reaction in DESs against the HBAs only, *Table 3.3.2*, *entries 11-13*. These solvents have also been used as benign solvents for Suzuki couplings with heterogeneous Pd/C catalysts.[175] The formation of black Pd(0) aggregates was spotted at the beginning of the heating process as before. The reactions in glycerol were quite intriguing. When the reaction was set-up for 6 hours, 73% isolated yield of **2a** was obtained. Nevertheless, when the experiment was repeated under the same conditions, but the reaction quenched after 3 hours, 96% isolated yield of **2a** was obtained, *Table 3.3.2*, *entries 11-12.* These results show that the reaction can proceed in the absence of ChCl as potential stabilizer, but due to the counterintuitive results observed, *i.e*. obtaining 96% yield with a reaction period of 3 hours, but 73% yield in a different reaction of 6 hours, no conclusions can be drawn, and more experiments are required to assess the reproducibility of these ChCl-free systems.

A small substrate scope with aryl bromides decorated with EWGs (ketone) and EDGs (methoxy and methyl) was carried out with the reaction conditions from *entry 2* in *Table 3.3.2*. Interestingly, the yield of 4-bromoanisole **1b** into biphenyl **2b** resulted in higher yield than the yield of 4-bromoacetophenone **1c** into **2c,** despite 4-bromoanisole **1b** being the most electron-rich haloarene, *Table 3.3.2*, *entries 14-16.* Pd-catalysed cross-coupling reactions tend to give better results with electron-deficient substrates; therefore, this unusual result was attributed to the fact that 4-bromoanisole **1b** is a liquid partially soluble in ChCl/G, which formed colloids. 4-bromotoluene **1c** is an insoluble solid in

ChCl/G, which formed suspensions. As such, the surface of contact of **1c** is smaller than **1b**, which can potentially reduce the speed of the reaction by generating a suspension of aryl bromides, base and Pd aggregates on ChCl/G.

Finally, the recyclability of the ChCl/G/Pd(0) system was assessed under the reaction conditions of *entry 2* in *Table 3.3.2*. Instead of quenching the reaction with aqueous ammonium chloride, the mixture was cooled to room temperature and extracted 5 times with 10 mL ethyl acetate, by adding the solvent to the round-bottom flask, followed by vigorous stirring, and decanting of the solvent. It was found the system is not very recyclable using this approach, since the first cycle yielded 97% of isolated **2a**, then the second cycle 59% and by the third cycle only traces of **2a** were detected.

It has been demonstrated that ChCl/G and ChCl/EG are suitable solvents for the “ligand-free” Suzuki coupling, between phenylboronic acid and aryl bromides, with $Pd_3(OAc)_6$, provided that the haloarenes are soluble in DESs. These results are in contrast with a previous report by Dilauro *et al*. in which the $Pd_3(OAc)_6$-mediated Suzuki coupling between phenylboronic acid and iodobenzene gave no cross-coupling products in ChCl/EG, but good yields were obtained in ChCl/U. The evolution of black Pd aggregates at the beginning of the heating of the reactions was observed in every successful cross-coupling experiment. ChCl might have a role in the stabilization of the catalytically-active Pd(0) species. More experiments are required to understand the role of ChCl in these catalytic reactions.

3.3.2 Negishi reaction in DESs

3.3.2.1 Optimisation of reaction conditions.

The preliminary results obtained for the Suzuki-Miyaura cross-coupling in DESs were as expected, since these reactions have been previously reported in protic solvents, at open air and under mild conditions. On the other hand, at the beginning of this research project Negishi reactions had not been reported in DESs. The implementation of Negishi reactions in protic solvents posed a

big challenge due to the air- and water sensitivity of the zinc organometallic reagents, which would push the to the limit what DESs can support.

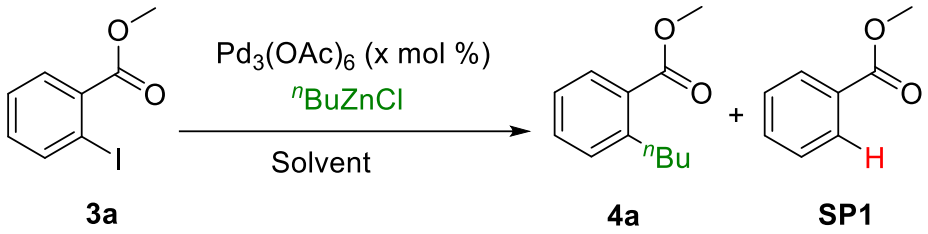

3a **4a** **SP1**

Scheme 3.3.2: Negishi coupling under "ligand-free" conditions in DESs

The reaction conditions were based on the preliminary conditions obtained from the Suzuki coupling in DESs, and a report by Liu *et al*. on the implementation of fast (less than 2 minutes) "ligand-free" Negishi couplings supported by tetrabutylammonium bromide in THF (*Scheme 3.3.2*).[119] These results suggested that a "ligand-free" Negishi methodology may be feasible in ChCl-based DESs, since fast reactions involving polar organometallic reagents have been shown to be compatible with DESs. Moreover, the absence of phosphine ligands and the fact that the stabilizer is part of the solvent, reduce solubility inconveniences and improve the E-factor of the process.[101]

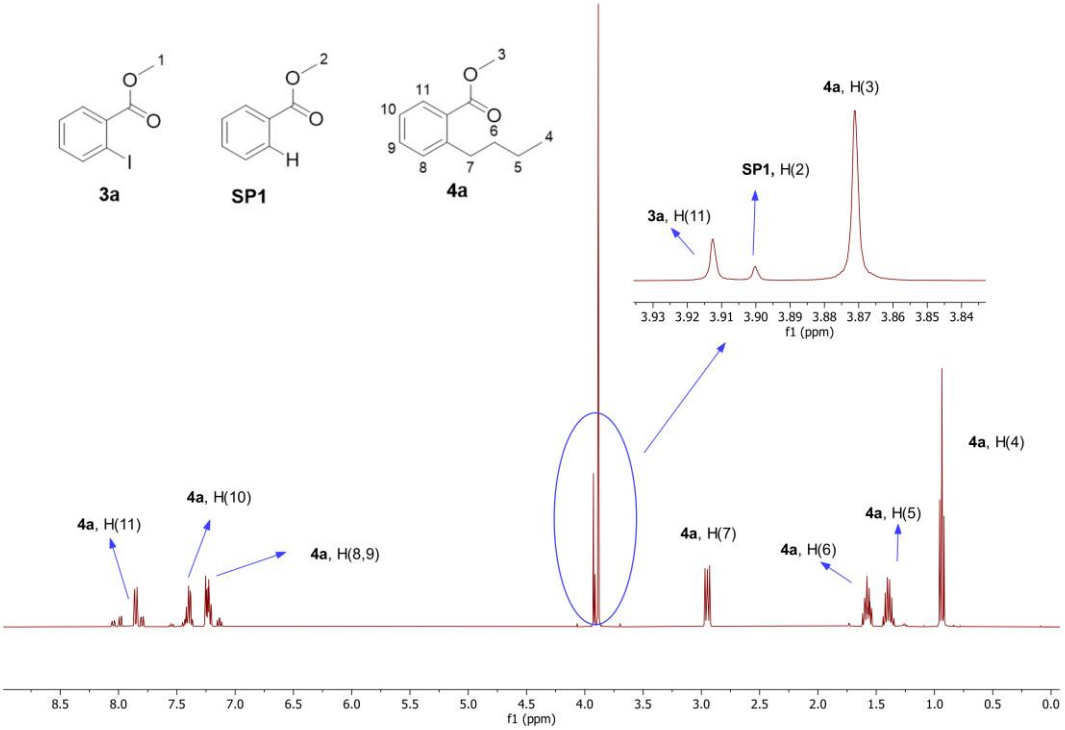

Figure 3.3.2: ^{1}H-NMR spectrum of a mixture of **3a**, **4a** and **SP1**, showcasing the proton resonances from the methyl groups linked to the ester functional groups of each compound.

The Negishi cross-coupling between methyl 2-iodobenzoate **3a** and *n*-butylzinc chloride, with $Pd_3(OAc)_6$ as pre-catalyst was used as model reaction for optimisation in DESs, *Scheme 3.3.2*. *n*-Butylzinc chloride (^{n}BuZnCl) was prepared by transmetalation between $ZnCl_2$ and *n*-butyllithium in dry THF.

Table 3.3.3: Summary results from the optimisation of the C(sp^3)-C(sp^2) Negishi reaction.

Entry	Solvent	Solvent wet/dry	T. (^{o}C)	[Pd] (mol %)	^{n}BuZnCl (equiv.)	RZn rate of addition	Conv. to **4a** (%)	Conv. to **SP1** (%)
1[a]	ChCl/G	wet	40	0.5	2.0	dropwise	6	0
2[a,c,d]	ChCl/G	wet	40	0.5	2.0	dropwise	0	0
3[a,d]	ChCl/G	dry	40	1	1.6	dropwise	0	0
4[a]	ChCl/U	dry	40	1	1.6	dropwise	88	10
5[a]	ChCl/U	dry	40	2	1.6	dropwise	90	6
6[a]	ChCl/U	dry	40	2	2.0	f/s	31	10
7	ChCl/U	wet	40	1	1.6	dropwise	27	3
8	ChCl/U	wet	40	1	2.0	f/s	46	8
9	ChCl/U	wet	40	2	2.0	dropwise	55	5
10	ChCl/U	wet	40	2	2.0	f/s	46	8

11	ChCl/U	wet	50	2	2.0	dropwise	58	7
12[a]	ChCl/U	dry	60	1	2.0	dropwise	87	12
13[e]	ChCl/U	wet	60	1	2.0	dropwise	80(59)	5
14[f]	ChCl/U	wet	60	2	2.0	dropwise	97(83)	0
15[g]	ChCl/U	wet	60	2	2.0	dropwise	80	-
16	ChCl/U	wet	60	2	2.0	f/s	70	7
17[h]	ChCl/U	wet	60	2	2.0	dropwise	68	4
18[i]	ChCl/U	wet	60	2	2.0	dropwise	25	3
19[a,b]	THF	dry	40	2	2.0	dropwise	84	1
20[j]	ChCl/DMU	wet	80	2	1.5	dropwise	14	1
21[j]	ChCl/$AcNH_2$	wet	80	2	1.5	dropwise	14	1
22[k]	ChCl/U	wet	60	0	2.0	dropwise	0	0
23[k]	ChCl/U	wet	60	2	0	-	0	0

Typical conditions: In a round-bottom flask, 5 cm^3 of solvent, **3a** (1.0 mmol) and $Pd_3(OAc)_6$ were mixed at the desired temperature for 10 min or until the reaction mixture became orange. A solution of ^{n}BuZnCl (2 mmol) in dry THF was added to **3a** and the reaction mixture stirred for 5 min at 1000 rpm. The reaction was quenched with 10 cm^3 of aqueous NH_4Cl 2 M. The conversion was determined by ^{1}H-NMR analysis of the crude reaction mixture. f/s stands for fast and single addition of Zn reagent. are averages. [a] Schlenk line and protective N_2 atmosphere used. [b] $[Bu_4N]Br$ added as additive. [c] 10 cm^3 of DES. [d] Reaction mixture stirred for 12 hours. [e] Conversion in brackets is an average over 5 runs. [f] Conversion in brackets is an average over 6 runs. [g] Isolated yield. [h] With $PdCl_2$. [i] With $Pd(PPh_3)_4$. [j] Conversion determined by GC using a DB5 column. [k] In the absence of Pd. [k] In the absence of **4a**, reaction time 12 h.

The preparation of the organozinc reagent required Schlenk conditions and a protective N_2 atmosphere, in order to avoid decomposition of the zinc organometallic. A detailed description of this preparation is shown in *section 5.1.4*. Although it was chosen to prepare the organozinc reagent for these experiments, a number of these reagents are available from commercial suppliers as ethereal solutions in SureSeal-type bottles for those who do not wish to prepare the zinc reagents themselves.

The conversion of **3a** into product **4a** and side-product **SP1** was determined through the analysis of the crude reaction mixture by ^{1}H-NMR. The proton resonances corresponding to the ester methyl groups of **3a** (3.92 ppm in $CDCl_3$), **4a** (3.87 ppm in $CDCl_3$) and **SP1** (3.90 ppm in $CDCl_3$) were integrated and compared as shown in *Figure 3.3.2*.

The reaction was firstly studied in dry ChCl/G under protective atmosphere with $Pd_3(OAc)_6$ as pre-catalyst, following the previous results from the Suzuki couplings. Temperature was set to 40 ^oC to avoid fast evaporation of the THF used as solvent media to prepare the organozinc reagent, and to reduce the viscosity of the DES. A pre-catalyst loading of 0.5 mol % was chosen following the optimised reaction conditions reported by Liu *et al*., whereas a stoichiometry of 1.6 or 2.0 equivalents of the organozinc reagent were chosen following the optimised reaction conditions reported by Liu *et al*. and Sirieix *et al*., respectively (*Table 3.3.3, entries 1-3*).[119,169] The results indicated that ChCl/G was not a suitable solvent for this reaction, since conversions to **4a** of only 6% max. were only achieved regardless of whether wet or dry ChCl/G were used. During this experiments the formation of a grey precipitate was observed, however it was not characterised, future experiments would be required to determine the nature of this precipitate, which is likely to be a zinc salt.

ChCl/G was replaced by ChCl/U, since it was rationalized that replacement of glycerol with urea could allow the organozinc reagent to survive long enough to take part in the catalytic cycle, due to the absence of OH groups from the polyol HBD. The model reaction was first investigated in dry ChCl/U under protective N_2 atmosphere with dropwise addition of the organozinc reagent to a mixture of **3a**, $Pd_3(OAc)_6$ and DES stirred at 1000 rpm (*Table 3.3.3, entry 4)*. Evolution of black Pd was observed during the dropwise addition. After quenching, **3a** was converted into **4a** at 88%, with significant conversion to **SP1** at 10%. The reaction was repeated with a pre-catalyst loading of 2 mol %, a similar conversion to **4a** of 90% was obtained, while the conversion to **SP1** was reduced to 6%, (*Table 3.3.3, entry 5*)

Capriati and co-workers reported that cross-couplings involving organolithium and organozinc reagents taking place “on water” or “on DES” rendered better yields when the addition of the organometallic reagent was done in a fast and single fashion. The authors argued these heterogeneous reactions benefited from a bigger organic phase surface area.[95,121,174] If the transmetalation between the oxidative addition ArPdI complex and ^{n}BuZnCl takes place in the

organic phase (*Scheme 3.1.16*), a single addition of ^{n}BuZnCl would provide more THF than a dropwise addition to extract the oxidative addition Pd complex from the DES phase at the beginning of the reaction. When the reaction was repeated with fast addition of ^{n}BuZnCl, the conversion to **4a** was reduced to 31%, despite observing an intense evolution of black Pd at the beginning of the reaction, (*Table 3.3.3, entry 6*). This result indicates a fast addition of the organozinc reagent is not compatible with the "ligand-free" Pd catalysed Negishi coupling in dry ChCl/U.

The next step was to investigate the model reaction in wet ChCl/U and in open air, *i.e.*, without Schlenk line or glovebox. The first experiment was carried out with the same reaction conditions as in *entry 4*, however, the conversion to **4a** dropped drastically to 27%, (*Table 3.3.3, entry 7)*. Increasing the stoichiometry of ^{n}BuZnCl from 1.6 equivalents to 2.0 and doubling the catalyst loading to 2 mol % proved only partially effective in raising the conversion to **4a**, (*Table 3.3.3, entries 8-10*). Interestingly, once again, when comparing dropwise to fast/single rates of addition in wet ChCl/U, dropwise addition allowed for a higher conversion to **4a**.

The impact of the temperature in the outcome of the model Negishi reaction in ChCl/U was then investigated. Increasing the temperature from 40 ^{o}C to 50 ^{o}C with 2 equivalents of ^{n}BuZnCl and 2 mol % catalyst raised the conversion to **4a** to nearly 60%, (*Table 3.3.3, entry 11*). When the model reaction was tried at 60 ^{o}C with 1 mol % of $Pd_3(OAc)_6$, conversions to **4a** of 87% and 80% were obtained for experiments carried out in dry DES/N_2 atmosphere and wet DES/open air respectively, (*Table 3.3.3, entries 12-13*). These results indicated that an increase of 20 ^{o}C allows the catalytic reaction to run smoothly in the absence of protective atmosphere and in wet ChCl/U. A possible explanation for this observation could be related to the decrease in viscosity of ChCl/U, which accompanies an increase of temperature. A lower viscosity accounts for higher diffusion rates, higher degree of wetting of the DES to the organic phase, better solubility of reactants/catalysts and faster reaction kinetics. It is also important to point out that at 60 ^{o}C, the THF that was used to dissolve the organozinc reagent would evaporate, which in consequence

could create a form of THF-enriched atmosphere above the reaction mixture. This could aid to prevent the hydrolysis of the organozinc reagent. The reproducibility of the experiment in wet ChCl/U also improved with respect to the experiments at 40 ^{o}C in both dry and wet ChCl/U, with an average across 5 runs of 59% and a standard deviation of 20%. However, the variability in the observed conversions between different runs still resulted in a reaction methodology that was far from reliable.

In an attempt to improve the reproducibility of the model reaction in wet ChCl/U, the catalyst loading was increased to 2 mol % with the rest of reaction conditions same as *entry 13.* In this way it was possible to obtain nearly quantitative conversion to **4a** in wet ChCl/U in open air while reducing the conversion to side-product **SP1**, (*Table 3.3.3, entry 14*). Moreover, the reproducibility of the reaction improved significantly with an average of 83% across 7 runs and a standard deviation of 9%. The reaction was repeated at double scale, fully worked up with product isolation after column chromatography to determine an isolated yield of **4a** of 80% after work up, (*Table 3.3.3, entry 15*). When these reaction conditions were interrogated under a fast and single regime of addition of ^{n}BuZnCl, the conversion to **4a** suffered a decrease to 70%, (*Table 3.3.3, entry 16*).

After the stoichiometry of ^{n}BuZnCl and temperature were analyzed, the source of Pd was studied. The model reaction was repeated under conditions from *entry 14* with $PdCl_2$ as and $Pd(PPh_3)_4$ instead of $Pd_3(OAc)_6$, (*Table 3.3.3, entries 17-18*). $PdCl_2$ showed good solubility in ChCl/U and evolution of black Pd was observed during the addition of ^{n}BuZnCl, although the obtained conversion to **4a** was inferior to the one obtained with $Pd_3(OAc)_6$ pre-catalyst. On the other hand, the solubility of $Pd(PPh_3)_4$ was poor in ChCl/U and resulted in poor conversion to **4a** under conditions from *entry 14*. No black Pd was observed in this case.

The model reaction was also studied in other DESs made from dimethylurea (ChCl/DMU) and acetamide (ChCl/$AcNH_2$) as HBDs, (*Table 3.3.3, entries 20-21*). These DESs improved the solubility of **3a** when compared to ChCl/U, in

which the aryl iodide was only partially soluble and tended to form suspensions. It was observed that **3a** was almost entirely consumed during the reactions, but in both cases, the conversion to **4a** was only 14% with substantial amount of side-products coming from reactions between **3a** and the solvent, mediated by the organozinc reagent, *Figure 3.3.3*.

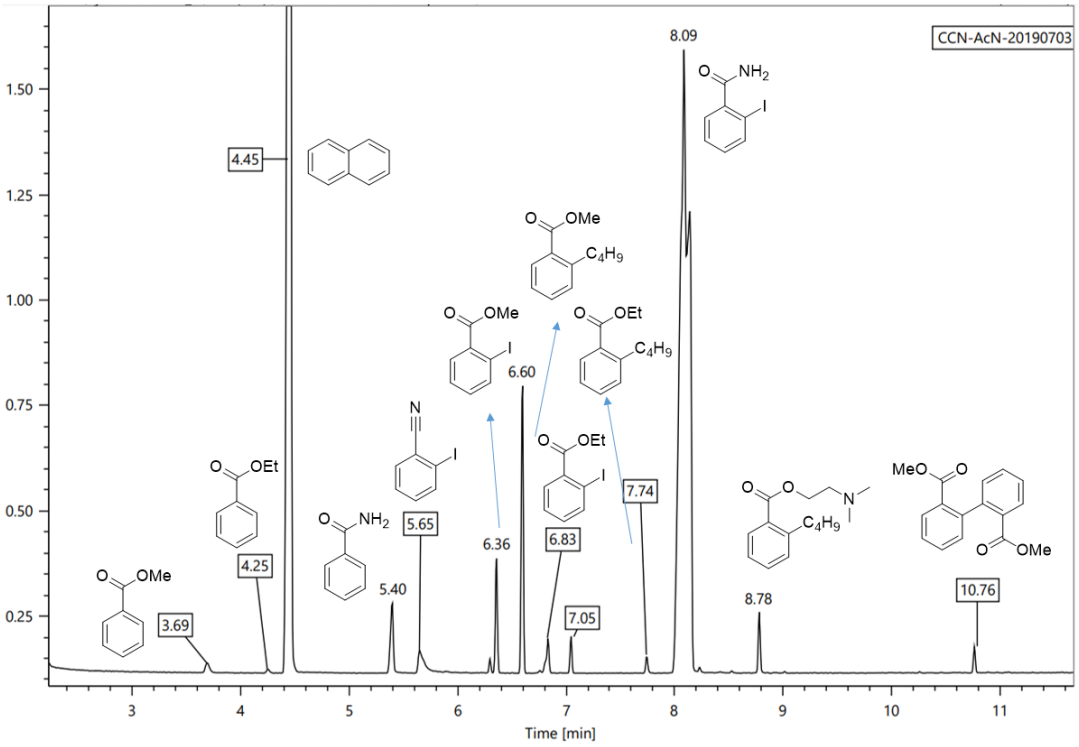

Figure 3.3.3: GC/MS chromatogram of the crude reaction mixture in ChCl/AcNH$_2$

The set of reaction conditions from *entry 14* in *Table 3.3.3* represents the simplest and at present most affordable protocol reported for a Negishi coupling in ChCl/U. The optimised reaction conditions in DESs were tested in dry THF under protective N_2 atmosphere at 40 ^oC to avoid the evaporation of THF. The reaction proceeded smoothly but rendered an inferior conversion to **4a** when compared to ChCl/U, altough **SP1** formation was observed only in 1%, (*Table 3.3.3, entry 19*). Finally, control reactions in ChCl/U under optimised reaction conditions, in the absence of $Pd_3(OAc)_6$ or ^{n}BuZnCl led to no conversion to either **4a** or **SP1**, confirming that Pd is crucial for the formation of **4a** and that no reductive dehalogenation product **SP1** is formed if there is no organozinc reagent. This confirmed that under the optimised

reaction conditions in ChCl/U, Pd acetate is reduced by homocoupling of ^{n}BuZnCl to trigger the catalytic reaction. (*Table 3.3.3, entry 20-21*.)

Despite the common assumption discussed in the introduction that organolithium reagents are very air- and water-sensitive, Hevia and co-workers demonstrated that these reagents can survive in ChCl/G or glycerol long enough to undergo addition to poorly reactive electrophiles when the substrate is added after the organometallic reagent. They were able to isolate the addition product in 68% and 42% after waiting for 1 and 2 minutes before adding the electrophile.[94,96]

Table 3.3.4: Negishi coupling with inverted order of addition.

Entry	Time (s)	Conv. (%)
1	10	56
2	30	38
3	60	12
4	120	1

The conversion was determined by GC analysis of the crude reaction mixture using a DB5 column.

A similar experiment was designed to assess the resistance of ^{n}BuZnCl towards protonolysis in ChCl/U. The model cross-coupling reaction between **3a** and ^{n}BuZnCl was repeated using an increased loading of 5 mol % Pd acetate to push the reaction forward under harsh reaction conditions. ^{n}BuZnCl was added in a fast and single addition to a mixture of DES/Pd, **3a** was added in a single addition after a given period. The results are shown in *Table 3.3.4*.

A conversion to **4a** of 56% was detected when adding **3a** 10 seconds after ^{n}BuZnCl, and almost total decomposition of the organozinc reagent was found with only 1% conversion to **4a** after a 2-minute delay between addition of the zinc reagent and the substrates to DES solution. These results shown that the protonolysis of ^{n}BuZnCl in wet ChCl/U is not an instantaneous process, however, the reduction in the Negishi reaction conversion to products due to decomposition of the organozinc reagent occurred faster than for the addition

reactions reported by Hevia and co-workers. This can be attributed to the Negishi reaction mechanism, because under catalytic conditions, ^{n}BuZnCl does not intervene in the reaction until the oxidative addition Pd complex is formed. Overall, this suggests that the rate of protonolysis of the organozinc reagent in wet ChCl/U is fast, but that of productive catalysis is faster under DES conditions, which allows these solvents to be used for this reaction, provided that the organozinc reagent is added last.

Table 3.3.5: Recyclability of a "ligand-free" Negishi Coupling in wet ChCl/U

Cycle	Conv. to **4a** (%)	Conv. to **SP1** (%)
1	83	14
2	64	11
3	56	7

The conversion was determined by ^{1}H-NMR analysis of the crude reaction mixture

The recyclability of the model Negishi reaction between **3a** and ^{n}BuZnCl in wet ChCl/U under optimised conditions was studied. The reaction was carried out as before, but instead of quenching the reaction with aqueous NH_4Cl, **4a**, **SP1** and any remaining **3a** were directly extracted from the round-bottom flask with organic solvents, while leaving the Pd catalyst in the DES. A detailed description of the procedure is described in *section 5.1.8*., the results are shown in *Table 3.3.5*. It can be seen that the "ligand-free" DES/Pd system exhibited a similar behaviour as in the Suzuki-Miyaura experiments, in which a decrease in the activity of Pd was seen throughout the cycles. Thus, compared to some other reported reactions catalysed by Pd complexes supported by phosphines or NHC ligands in IL/DES, the protocol described in here is not recyclable.[120,121,144,146,148]

A summary of the results from the optimisation of the "ligand-free" C(sp^3)-C(sp^2) Negishi coupling between **3a** and ^{n}BuZnCl in ChCl/U is represented in the radar diagram of *Figure 3.3.4*. Each polygon vertex represents a variation in the reaction conditions *e.g.,* temperature T (^{o}C), Pd loading (mol %), addition regime (**D**ropwise or **S**ingle) and stoichiometry of organozinc reagent

(equivalents). Each contour line in the diagram represents a conversion (%). The figure plotted over the radar diagram symbolises the conversion to **4a** of an experiment carried out under the set of reaction conditions of a given vertex. As such, the figure is expanded towards the vertices associated with the reaction conditions that have the bigger positive influence in the conversion to **4a**.

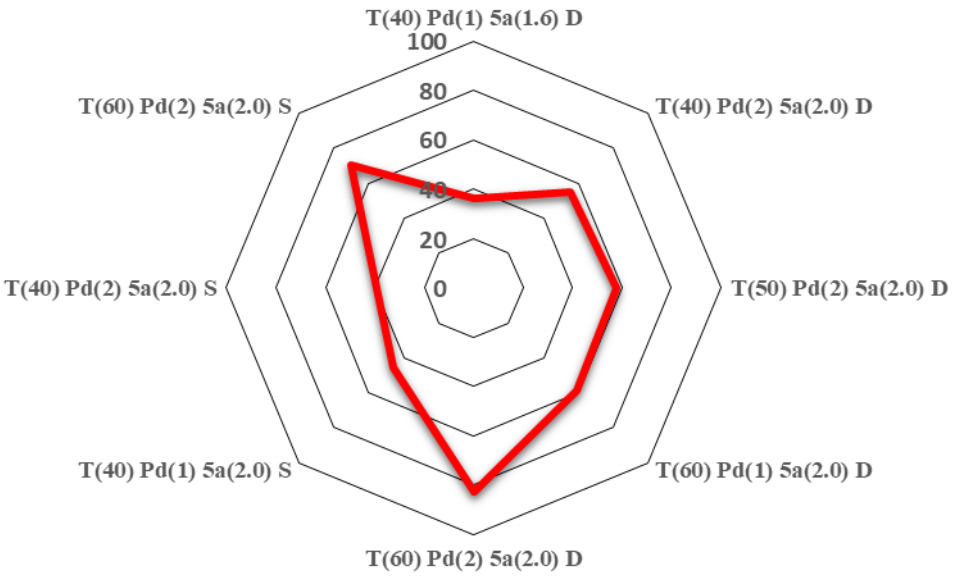

Figure 3.3.4: Summary of influence of reaction conditions in the outcome of the model Negishi coupling from *Scheme 3.3.2* In ChCl/U

As can be appreciated in *Figure 3.3.4,* the increase in Pd loading or the organozinc reagent equivalents added, have a small impact in the outcome of the reaction when these changes are implemented individually. At 40 ^{o}C, dry ChCl/U in N_2 outperformed wet ChCl/U in air, but at higher temperatures, the water content and the wet atmosphere no longer pose a significant obstacle for the Negishi reaction. According to *Figure 3.3.4,* temperature was the most critical variable, an increase of 20 ^{o}C helped to raise the conversions and to improve the reproducibility of the reaction. Moreover, it can be appreciated from the figure that those experiments under a fast and single regime of addition of ^{n}BuZnCl gave poorer results overall. Finally, the experiments in ChCl/DMU and ChCl/$AcNH_2$, in which the solubility of **3a** was improved compared to ChCl/U, showed lower selectivity, which allowed side-reactions

to be predominant. It appeared the system benefits from a reduced solubility of the substrate because this prevents it from reacting with the DES components and the organozinc reagent. On the other hand, the solubility of the Pd source in the DESs seemed critical for a good performance, given the poor conversions observed when the insoluble $Pd(PPh_3)_4$ was used as catalyst.

It is important to remark that the success of the reaction was correlated with the observation of black Pd aggregates during the addition of ^{n}BuZnCl, since only reactions in which a fast formation of black Pd was observed, led to good conversions. However, not all reactions in which formation of black Pd was seen, gave good conversions to **4a**. Based on these observations, the formation of catalytically-active Pd aggregates stabilized by alkylammonium halides, in this case, choline chloride as suggested by Liu *et al*. is a feasible hypothesis, but more research to determine the catalyst speciation under DES conditions is required.[119]

With the optimised reaction conditions for the $C(sp^3)$-$C(sp^2)$ Negishi coupling in mind, the $C(sp^2)$-$C(sp^2)$ version of the reaction was investigated. The cross-coupling between **3a** and phenyl-zinc halides with $Pd_3(OAc)_6$ as pre-catalyst was chosen as model reaction, *Scheme 3.3.3*. All attempts to optimize the model reaction to maximise the conversion to **5a** were unsuccessful. The results are displayed in *Table 3.3.6*.

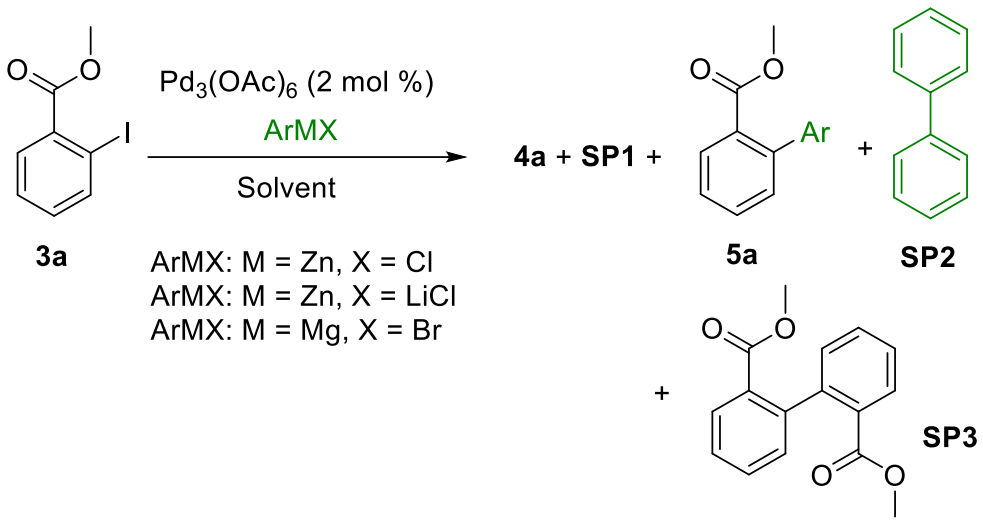

Scheme 3.3.3: Model "ligand-free" C(sp^2)-C(sp^2) Negishi coupling in DESs

Phenyl-zinc chloride was prepared by a halogen exchange reaction between bromobenzene and *n*-butyllithium followed by Zn/Li metathesis with $ZnCl_2$. A detailed procedure is described in *section 5.1.4*. When the model reaction was carried out under the C(sp^3)-C(sp^2) optimised reaction conditions, substrate **3a** was consumed in 65%, but the reaction showed poor selectivity for phenyl-zinc chloride, with significant conversion to side products **SP1**, **SP2** and **4a**. *Table 3.3.6*, *entry 1*. **SP1** could be generated through β-hydride elimination or by hydrolysis of a Zn-**3a** complex generated after a second transmetalation step between phenyl-zinc chloride and ArPd-**3a** complex, *Scheme 3.1.16*. **SP2** could be produced from the unproductive homocoupling pathway between 2 equivalents of phenyl-zinc chloride. Interestingly, some **4a** was detected in the GC chromatogram of the crude reaction mixture. It may have been produced by the cross-coupling between unreacted *n*-butyllithium and **3a**, or by *n*-butylzinc chloride formed by Zn/Li metathesis of unreacted *n*-butyllithium and $ZnCl_2$. Traces of **SP3** were detected in the GC chromatogram, its origin could be the previously mentioned Zn-**3a** complex, which can instead undergo transmetalation with either ArPd-**3a** coming from the productive first transmetalation step or the oxidative addition complex PdI-**3a**, *Scheme 3.1.16*.

Table 3.3.6: Summary results from the attempted optimisation of the "ligand-free" C(sp^2)-C(sp^2) Negishi reaction in DESs.

Entry	DES	RZn	Conv. (%)				
			3a	**5a**	**4a**	**SP1**	**SP2**
1	ChCl/U	PhZnCl	35	33	10	21	18
2	ChCl/U	PhZn*LiCl	65	3	0	42	18
3	ChCl/U	PhMgBr	67	0	0	4	1
4	ChCl/DMU	PhZnCl	14	2	1	2	16
5	ChCl/$AcNH_2$	PhZnCl	81	0	1	2	1
6	ChCl/$AcNH_2$	PhMgBr	1	25	0	1	1

Typical conditions: In a round-bottom flask, 5 cm^3 of solvent, **3a** (1.0 mmol) and $Pd_3(OAc)_6$ were mixed at the desired temperature for 10 min or until the reaction mixture become orange. A solution of phenyl-zinc (2 mmol) prepared by different methods in dry THF was added dropwise to **3a**, and the reaction mixture stirred for 5 min at 1000 rpm. The reaction was quenched with 10 cm^3 of 2 M aqueous NH_4Cl. The conversion was determined by GC of the crude, using a DB5 column.

A phenyl-zinc bromide complex was prepared by direct insertion of activated elemental Zn to bromobenzene with lithium chloride as additive to circumvent the need for *n*-butyllithium. The phenyl-zinc bromide reagent was then reacted with **3a**, *Table 3.3.6*, *entry 2*.[176,177] Although **4a** was not detected in the crude reaction mixture, the conversion to **5a** was reduced drastically with an increase of the dehalogenation side-product **SP1**. This result indicated that the phenyl-zinc bromide reagent prepared by direct insertion produced a less reactive catalytic reaction, this could be due to a faster hydrolysis of the organometallic reagent or changes in the speciation of the catalyst due to presence of bromide.

The organozinc reagent was replaced by phenylmagnesium bromide to perform a Corriu-Kumada-like cross-coupling reaction, *Table 3.3.6*, *entry 3*. Under these reaction conditions, the conversion to product **5a** was completely silenced and **3a** was recovered mostly intact from the crude reaction mixture. Further attempts to perform this reaction in ChCl/DMU and ChCl/$AcNH_2$ rendered equally disappointing results, although in these cases, **3a** was consumed and new GC peaks were observed in the crude reaction mixture, which indicated that the substrate reacted with the DES in a process mediated by the organometallic reagents, *Table 3.3.6*, *entries 4-6, Figure 5.1.7 in section*

5.1.13.1. No further attempts to optimise the outcome of these reactions were done.

Results from *Table 3.3.6* indicate that either the transmetalation of the model C(sp^2) organozinc reagents is slower than that observed for the model C(sp^3)-Zn reagent or, that the tolerance of phenyl-zinc to hydrolysis by the DES environment is lower than that exhibited by ^{n}BuZnCl. Therefore, under these reaction conditions, the pathways leading to the dehalogenation of **3a** became dominant. Despite this, complete consumption of **3a** to generate side-product **SP1** in high yields was not observed in any of the experiments. This suggested that under these reaction conditions, either the main pathway to **SP1** is through the hydrolysis of the Zn-**3a** complex discussed before, or that the kinetics of the β-hydride elimination cycle leading to **SP1** are not fast enough to consume most of **3a** before the reaction is quenched, *Scheme 3.1.16*. If, on the other hand, the main pathway to **SP1** is through hydrolysis of Zn-**3a**, then it is reasonable not to expect a high conversion due to a more competitive hydrolysis of phenyl-zinc**.**

3.3.2.2 Substrate scope for the C(sp^3)-C(sp^2) Negishi coupling in ChCl/U DES.

The experiments carried out to determine the optimal reaction conditions required to perform the “ligand-free” C(sp^3)-C(sp^2) Negishi coupling in DESs, showed that ChCl/U was the best solvent to host the reaction, from a set of DESs. No reaction conditions could be found to enable effective C(sp^2)-C(sp^2) Negishi couplings in DESs studied.

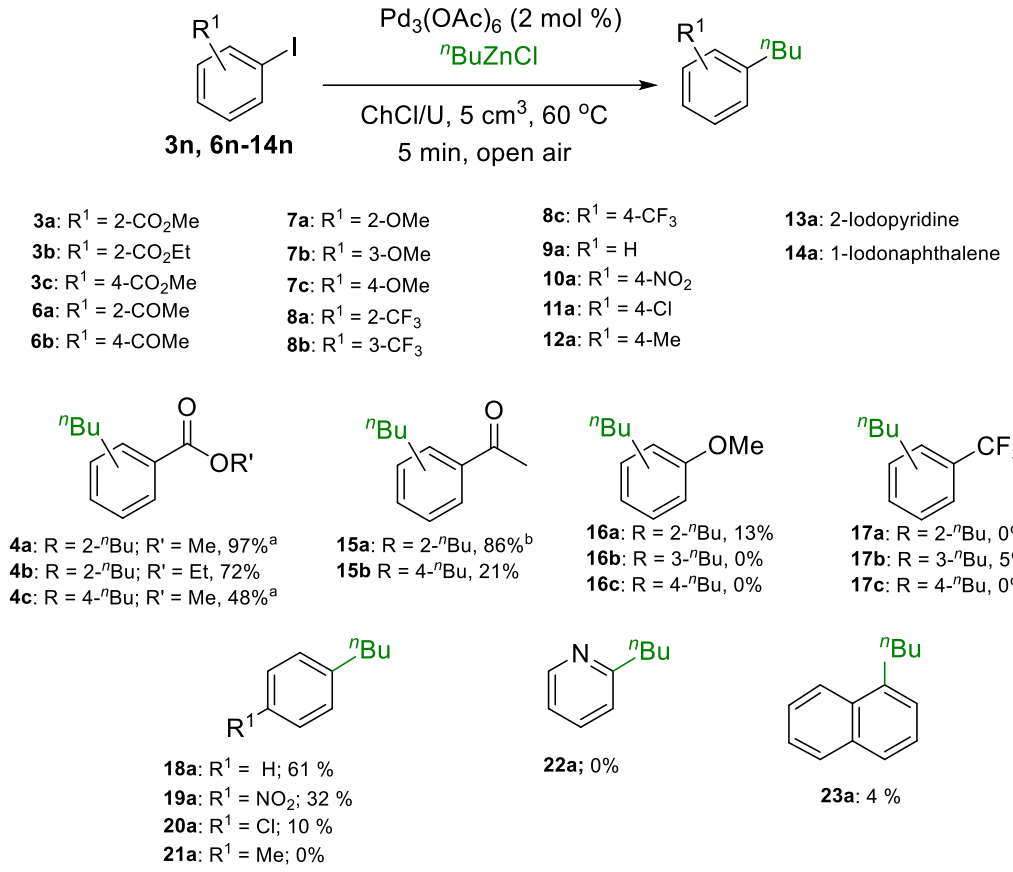

Scheme 3.3.4: Previous work involving cross-couplings with air- and moisture-sensitive polar organometallic reagents in DESs. Reaction conditions 2 mmol of R^2ZnX in 2 cm^3 dry THF was added dropwise to 1.0 mmol ArI and $Pd_3(OAc)_6$ (2 mol % Pd) in 5 cm^3 "wet" ChCl/U at 60 °C while stirring at 1000 rpm. The reaction was stirred for 5 minutes before work up. Conversions determined by gas chromatography. [a] Conversion determined by ^{1}H-NMR, [b] $Pd_3(OAc)_6$ (5 mol % Pd). Details of side product conversion are found in *Table 5.1.6 in section 5.1.13.2.*

Using the optimised methodology, a preliminary substrate scope was investigated. The outcome of the C(sp^3)-C(sp^2) Negishi coupling was evaluated considering two main variables: the electronics of the aromatic ring and functional group tolerance. The reaction was carried out with a range of aryl halides decorated with EWGs and EDGs at different positions of the aromatic ring. The results are condensed in *Scheme 3.3.4*. For those compounds where only traces of cross-coupling product were found, the starting material was recovered intact with no detectable signals of side-

products, as can be appreciated in the corresponding GC chromatograms, *Figure 5.1.9* in *section 5.1.13.2.*

The initial experiments resulted in poor conversions to the desired products in many cases, although interesting trends emerged from the analysis of the different aryl halide conversions, which allowed for further adjustments in the strategy. In general, under the optimal "ligand-free" reaction conditions, iodoarenes substituted at the *meta* and *para* positions delivered poor conversions, regardless of the electronics of the ring. Among a single family of compounds, it was observed that reactions involving iodoarenes **3a**-**b**, **6a** and **7a**, functionalized at the *ortho* position with ester and ketone functional groups, rendered higher conversions to products **4a-b**, **15a** and to some extend **16a** than *meta*- or *para*-substituted iodoarenes **3c**, **6b**, **7b-c**. A notable exception to this trend was iodobenzene **9a** which was converted to butylbenzene **18a** in 61%. Despite being a strong EWG, 2-iodobenzotrifluoride **8a**, did not react under these conditions and was recovered intact. In the case of the iodoanisole family **7a-c,** the results were particularly counterintuitive. It was expected that a strong EDG would deactivate *ortho* and *para* positions of the ring by resonance, therefore a higher conversion was expected at the *meta* position, nevertheless, 2-iodoanisole **7a** rendered the highest conversion among its family, *Scheme 3.3.4*.

Iodoarenes having electron-poor aromatic rings usually undergo oxidative addition to Pd more easily than electron-rich iodoarenes, due to a more polarised C-I bond and the enhanced electrophilicity of the *ipso* carbon. When the reactivity of electron-rich iodoarenes against electron-poor iodoarenes was compared, it became evident that electronic effects were not as determinant as expected. The results showed that iodoarenes holding strong EWGs *e.g.*, ester **3a-c**, ketone **6a-b** and nitro **10a**, gave moderate to good conversions to products **4a-c**, **15a-b** and **19a**. On the other hand, iodoarenes functionalized with EDGs *e.g.,* methoxy **7a-c**, chloride **11a** and methyl **12a**, resulted in low conversions to products **16a-c**, **20a** and **21a**. However, exceptions to this trend were found. The iodobenzotrifluoride family **8a-c** showed a very poor reactivity, despite the strong electron-withdrawing nature of the CF_3 group.

Moreover, 2-iodopyridine **13a** was converted into **22a** only in trace amounts, despite having a more electron-poor aromatic ring compared to iodobenzene **9a**. Interestingly, after the success obtained with **9a**, it was expected that 1-iodonaphtalene **14a** would undergo cross-coupling as readily, nevertheless, conversion to **23a** was observed in only 4%.

When it comes to the methodology's functional group tolerance, iodobenzoates **3a-c**, iodoacetophenones **6a-b** and 4-nitrobenzene **10a** did not suffer from functional group decomposition, due to reactions with the ^{n}BuZnCl reagent.

Overall, the optimised reaction conditions successfully promoted the Negishi coupling of substrates **3a-b**, **6a** and **9a** only. It appeared that the rest of the iodoarenes cannot undergo oxidative addition to Pd(0) quickly enough to generate the ArPdI organometallic species required for the transmetalation with ^{n}BuZnCl. The rate of formation of these species is important, as transmetalation is in competition with hydrolysis of the organozinc reagent in the DES. Thus, fast oxidative addition and fast transmetalation are required to out-compete the degradation pathway of the organozinc reagent.

The experiments suggested that the electronic effects were not the dominant driving force guiding the reactivity observed among different iodoarenes. The substitution pattern of the functional groups in the iodoarenes, which influences the electronics of the aromatic ring, did not explain the observed conversions either. What seemed clear is that *meta*- and *para*- substituted iodoarenes were not suitable substrates for the "ligand-free" Negishi coupling under these reaction conditions. However, for *ortho*-substituted iodoarenes, it was observed that those decorated with Lewis-basic functional groups, capable of coordinating to Pd *e.g.,* CO_2R (**3a-b**), C(O)R (**6a-b**) and to some extent OMe (**7a**), were successfully converted into products **4a-b**, **15a** and **16a**, whereas 2-iodobenzotrifluoride **8a,** which exhibits similar electronic properties to the benzoates and the acetophenones, but lacks the Lewis-basicity, did not react.

Based on these observations, it was proposed that methyl 2-iodobenzoate **3a** and 2-iodoacetophenone **6a** and 2-iodoanisole **7a**, might promote the oxidative addition to Pd by means of a coordinating interaction between the oxygen from the carbonyl groups and Pd, *Scheme 3.3.5*. This interaction could delocalise electron density from the oxygen to Pd, making the metal more nucleophilic while the ring becomes more electrophilic. This could facilitate the oxidative addition considering also, that if the iodoarenes exhibited an *ortho*-coordinating mode, they could add to Pd through a chelated transition state. A bidentate transition state would be more stable due to the chelate effect and would also generate a more stable bidentate oxidative addition complex intermediate.

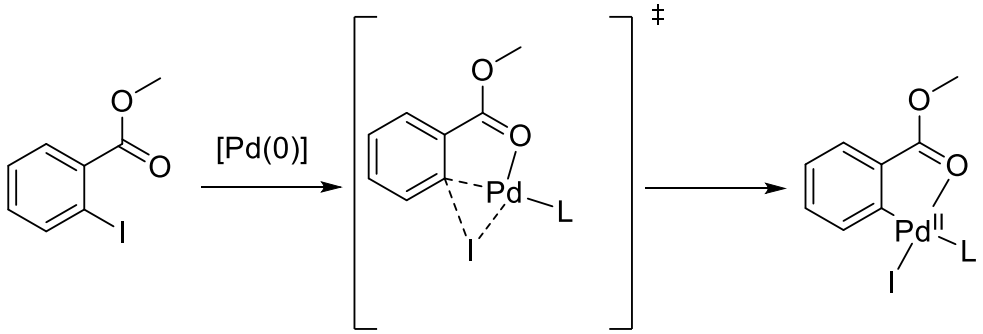

L: AcO^-, Cl^-, $HO\text{-}(CH_2)_2NMe_3^+$, $O{=}C(NH_2)_2$

Scheme 3.3.5: Example of the proposed *ortho*-coordinating interaction between **3a** and a hypothetical low-valent Pd monoacetate species.

To the test the "*ortho*-coordinating" hypothesis, the previous optimised reaction conditions from *Table 3.3.3, entry 14* were revisited and the range of substrates bearing functional groups with donor atoms at the *ortho* positions was expanded. Additionally, new reaction conditions were investigated to enable the Negishi coupling of *meta*- and *para*- substituted iodoarenes. Although a recent study has demonstrated that $[Pd(PtBu_3)_2]$ is able to successfully promote coupling for this type of substrate in DESs, the focus of this study was on developing a methodology that was able to utilize the cheapest, most readily available catalyst precursors and ligands/additives,

ideally with no additional ligands added, which is complementary to the approach recently reported by Dilauro *et al*.[121]

It was thought that those substrates without *ortho*-coordinating functional groups were not adding to the catalytically-active [Pd] species quickly enough. For reactions involving those substrates, Bis(triphenylphosphine)palladium(II) diacetate [$Pd(OAc)_2(PPh_3)_2$] was used as pre-catalyst. This Pd complex, supported by triphenyl phosphine exhibits a more nucleophilic character. It was expected that this would compensate for the lack of *ortho*-directing interactions, to achieve a faster oxidative addition with *meta*- and *para*-substituted iodoarenes.

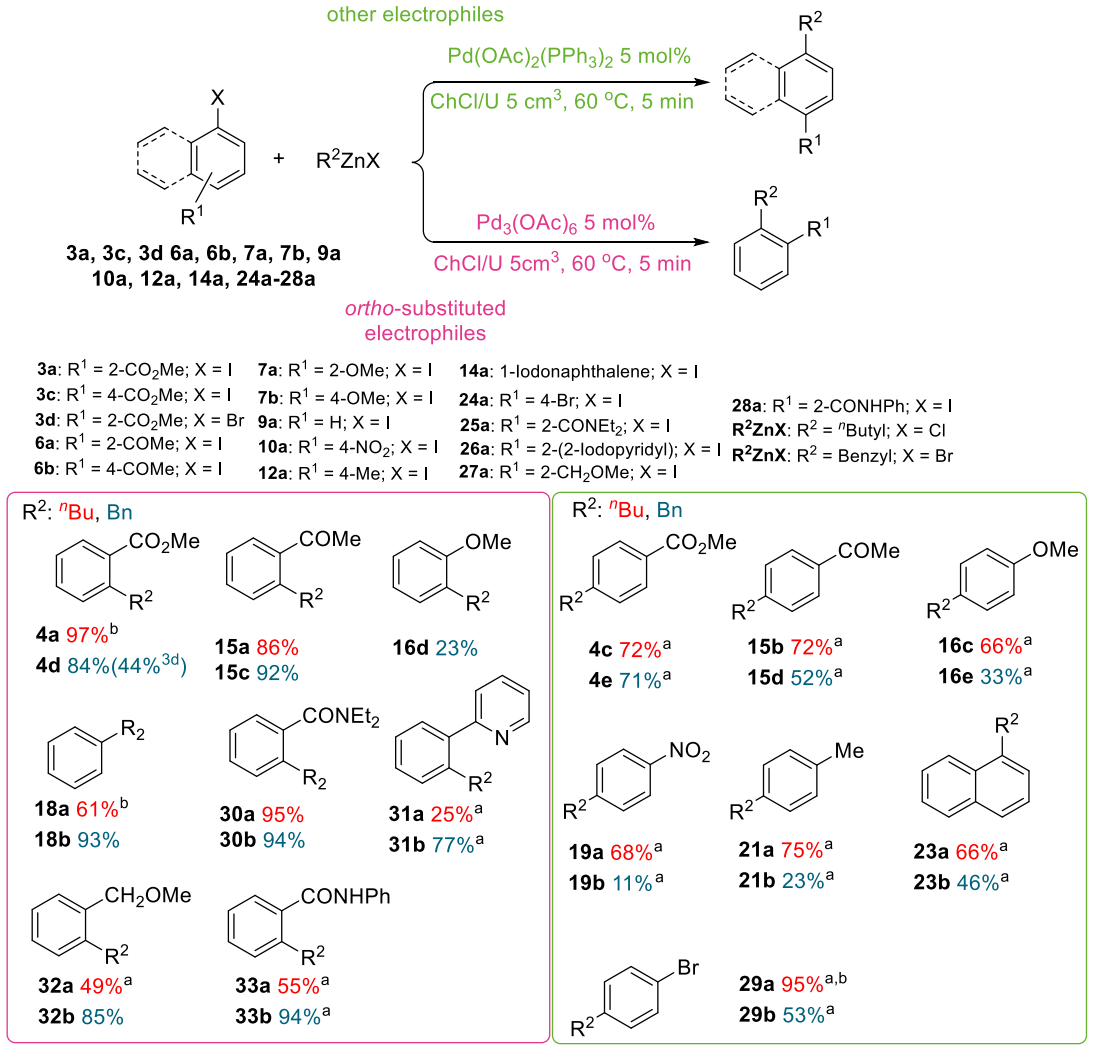

Scheme 3.3.6: Final substrate scope results for *ortho*-coordinating and *meta*- or *para*-substituted iodoarenes. Reaction conditions: R^2ZnX (1 mmol, 2 equiv.) in 2 cm^3 dry THF was added dropwise to ArI (0.5 mmol, 1 equiv.) and $Pd_3(OAc)_6$ (5 mol % Pd) in 5 cm^3 of "wet"

ChCl/U at 60 °C. The reaction was stirred for 5 minutes before workup. [a] 3 equiv. of R^2ZnX. [b] $Pd_3(OAc)_6$ (2 mol %). Conversions determined by GC. Conversions in red belong to cross-coupling products with ^{n}BuZnCl, conversions in blue belong to cross-coupling products with BnZnBr. Details of conversions are found in the *Table 5.1.8* in *section5.1.13.3.*

Following a similar approach to the one described previously, the catalyst loading was increased from 2 mol % to 5 mol % to maximize the availability of the oxidative addition complex ArPdI ready to transmetalate with the organozinc reagent. The new experiments were carried out with ^{n}BuZnCl and additionally with benzyl-zinc bromide (BnZnBr).

The synthesis of BnZnBr reagent was first tried by metal-halogen exchange between benzyl bromide and *n*-butyllithium with subsequent transmetalation with $ZnCl_2$, nevertheless this synthetic route proved unsuccessful for the Negishi reaction under DES conditions. Instead, it was decided to prepare BnZnBr by reductive replacement directly from elemental Zn, as reported by Knochel and co-workers.[177,178]

For iodoarenes holding functional groups with donor atoms at the *ortho* position, $Pd_3(OAc)_6$ was used as pre-catalyst. Conversely for other substrates $[Pd(OAc)_2(PPh_3)_2]$ was used as pre-catalyst. The results from the final substrate scope are condensed in *Scheme 3.3.6*.

When *ortho*-coordinating substrates reacted with ^{n}BuZnCl and BnZnBr under catalytic conditions with $Pd_3(OAc)_6$, moderate to excellent conversions to the respective cross-coupled products were obtained, *Scheme 3.3.6 pink box*. Iodoarenes **3a** and **6a**, showed the best conversions to cross-coupled products **4a**, **4d**, **15a** and **15c**. Surprisingly, when methyl 2-bromobenzoate **3d** was reacted with BnZnBr under *ortho*-coordinating reaction conditions, the conversion to product **4d** could be detected in 44%. During the optimisation of the reaction conditions, it was thought that bromoarenes were too challenging substrates, which is the reason this study was mainly focused in iodoarenes. However, it appears that some reactivity is possible with bromoarene substrates. Substrates **3a-d** and **6a** have in common a carbonyl group

attached to the *ortho* position which can coordinate Pd to generate a 5-membered palladacycle oxidative addition complex.

Interestingly, increasing the pre-catalyst loading did not significantly improve the outcome of the reaction between 2-iodoanisole **7a** and BnZnBr to produce **16d** when compared with previous reactions with ^{n}BuZnCl and 2 mol % of $Pd_3(OAc)_6$. Although the methoxy group has an oxygen atom capable of coordinating to Pd, the palladacycle would be less stable, due to the formation of a 4-membered ring, which is probably why this substrate does not exhibit the same reactivity as esters and ketones. This result also suggests that the proposed "ligand-free" Negishi reaction conditions in ChCl/U are still not appropriate for electron-rich iodoarenes, which are expected to undergo oxidative addition to Pd more slowly than electron-deficient haloarenes.

Under the reaction condition for *ortho*-coordinating iodoarenes, iodobenzene **9a** and BnZnBr showed an excellent conversion to diphenylmethane **18b,** following the same reactivity observed when **9a** was reacted with ^{n}BuZnCl to obtain **18a** under the previously optimised conditions with 2 mol % $Pd_3(OAc)_6$.

When *ortho*-coordinating iodoarenes **26a-28a,** capable of forming 5-membered palladacycles, were used as substrates for the Negishi reactions in ChCl/U, the first results with 2 equivalents of organozinc reagent, only gave moderate conversions to products **31-33**. By increasing the stoichiometry of the zinc reagents to 3 equivalents, the reactions with organozinc BnZnBr showed good conversions to cross-coupled products **31-33**. It was observed that in these 3 cases, the conversions to products involving ^{n}BuZnCl, were systematically lower than the BnZnBr equivalents.

Table 3.3.7: Negishi couplings of *ortho*-substituted haloarenes with $[Pd(OAc)_2(PPh_3)_2]$ as pre-catalyst.

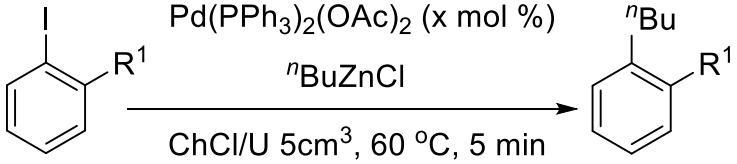

Entry	ArI	Pre-catalyst (x mol %)	Conversion [%]

1	**3a**	5	25
2	**3d**	5	5
3	**6a**	10	28

Typical reaction conditions: Reaction conditions 1 mmol of ^{n}BuZnCl in 2 cm^3 dry THF was added dropwise to 0.5 mmol ArI and $Pd_3(OAc)_6$ (5 mol % Pd) in 5 cm^3 of "wet" ChCl/U at 60 ^{o}C. The reaction was stirred for 5 minutes before workup.

In the reactions with BnZnBr, the homocoupling of the zinc reagent appeared ubiquitous and in ranges from 4 to 10%. It was suspected that the formation of octane as homocoupling product of ^{n}BuZnCl was occurring as well, but its presence was not detected in GC as it may be getting obscured by the solvent signals during the first 2 minutes of elution, *Figure 5.1.10* & *Figure 5.1.11* in experimental *section 5.1.13.3.*

The reactions involving iodoarenes functionalised at the *ortho* position exhibited poor conversions when $[Pd(OAc)_2(PPh_3)_2]$ was used as pre-catalyst for the Negishi coupling in agreement with the proposed hypothesis, *Table 3.3.7*. This phenomenon could be due to steric hindrance between the phosphine ligands and the *ortho*-functional groups, which would destabilise the transition states, and in consequence slow down the oxidative addition.[165]

On the other hand, the Negishi coupling in ChCl/U with *meta*- and *para*-substituted iodoarenes was substantially improved with respect to the previous experiments when $[Pd(OAc)_2(PPh_3)_2]$ was used as pre-catalyst, *Scheme 3.3.6 green box*. However, it was observed that the distribution of results was different from the experiments with *ortho*-substituted haloarenes. The difference in conversion to products between electron-rich and electron-poor iodoarenes was not as significative as for the "ligand-free" methodology. In consequence, when the reaction was carried out with ^{n}BuZnCl, the conversions to all products ranged from between 66% to 95%. This could be caused by a more nucleophilic Pd core, due to the electron density provided by the phosphine ligands. Moreover, it has been proposed by Jutand and co-workers, that in chloride-rich environments, chloride tends to bind to Pd and

push the phosphines, which narrows the P-Pd-P bite angle, which was observed to speed up the rate of oxidative addition of iodobenzene.[127,128]

In contrast to the “ligand-free” methodology, the phosphine-supported Pd methodology showed systematically lower conversions when BnZnBr was employed compared to ^{n}BuZnCl, excepting methyl 4-benzoate **3c**, which was converted to product **4e** in 71%. It was expected that the conversion of 4-iodoacetophenone **6b** to **15b** would give similar results with BnZnBr, given the similar electronic properties of substrates **3c** and **6b**. Nevertheless, the cross-coupled product with BnZnBr **15c** was detected only in 52% even with 3 equivalents of organozinc reagent. 4-iodoanisole **7b**, 1-iodonaphthalene **14a** and 4-bromo-1-iodobenzene **24a**, showed similar lower conversions to cross-coupled products with BnZnBr **16e**, **23b** and **29b,** between 35 and 53%. Strikingly, despite the nitro group being a strong electron-acceptor, 4-nitroiodobenzene **10a** could only be converted to product **19b** in 11%, whereas the moderate electron-rich 4-iodotoluene **12a** was converted to product **21b** in 23%, whereas the cross-coupled products with ^{n}BuZnCl conversions were higher.

If the observed reactivity in the “ligand-free” experiments, which favoured reactivity of ^{n}BuZnCl over BnZnBr is considered alongside the drastic reductions in conversions to products **4d** and **15c** with $[Pd(OAc)_2(PPh_3)_2]$, the contrasting reactivity between **10a** and **12a** and the overall poorer conversions obtained when BnZnBr was involved with $[Pd(OAc)_2(PPh_3)_2]$, it becomes clear that a more complex mechanistic picture than the traditional Negishi cross-coupling cycle mechanism may be taking place within the DES.

It is important to take into consideration that ^{n}BuZnCl was prepared by transmetalation of an organolithium reagent with $ZnCl_2$, whereas BnZnBr was prepared by direct Zn(0) insertion to benzyl bromide with LiCl as additive. It has been reported that when salts are introduced to the reaction in molecular solvents, a wide range of favouring and disfavouring effects on the speed of the reaction arise. ZnX_2 salts have been observed to reduce the speed of Pd-catalysed Negishi couplings involving alkylzinc reagents, but to speed up

those reactions involving arylzinc reagents. Conversely, lithium halides have been shown to increase the activity of the catalyst.[179,180]

Similar observations on the behaviour of the two studied organozinc reagents in the second substrate scope, have been made by Böck *et al*.[129] The authors reported kinetic experiments for Negishi couplings in THF catalysed by $Pd_3(OAc)_6$ supported by 2 equivalents of SPhos in which the rate of reaction showed no significant dependence on the concentration of the involved organozinc reagents. Nevertheless, when comparing between different organozinc reagents, the authors noted that the Negishi coupling proceeded faster for PhZnBr>BuZnBr>BnZnBr. The authors identified the rate limiting step was the oxidative addition, and attributed the reactivity dependence on the organozinc, to the formation a LPd-ZnRL adduct which then undergoes oxidative addition.

Although the observed trend in the experiments with *para*- and *meta*-substituted experiments seem to correlate with the results by Böck *et al*., the experiments with *ortho*-substituted iodoarenes gave opposite results. This, nevertheless, could reinforce Böck *et al*. hypothesis, since the involvement of the supporting ligands is crucial in the proposed Pd-Zn adduct. The lack of supporting ligands in the experiments with *ortho*-substituted iodoarenes could give rise to different adducts with different reactivities.

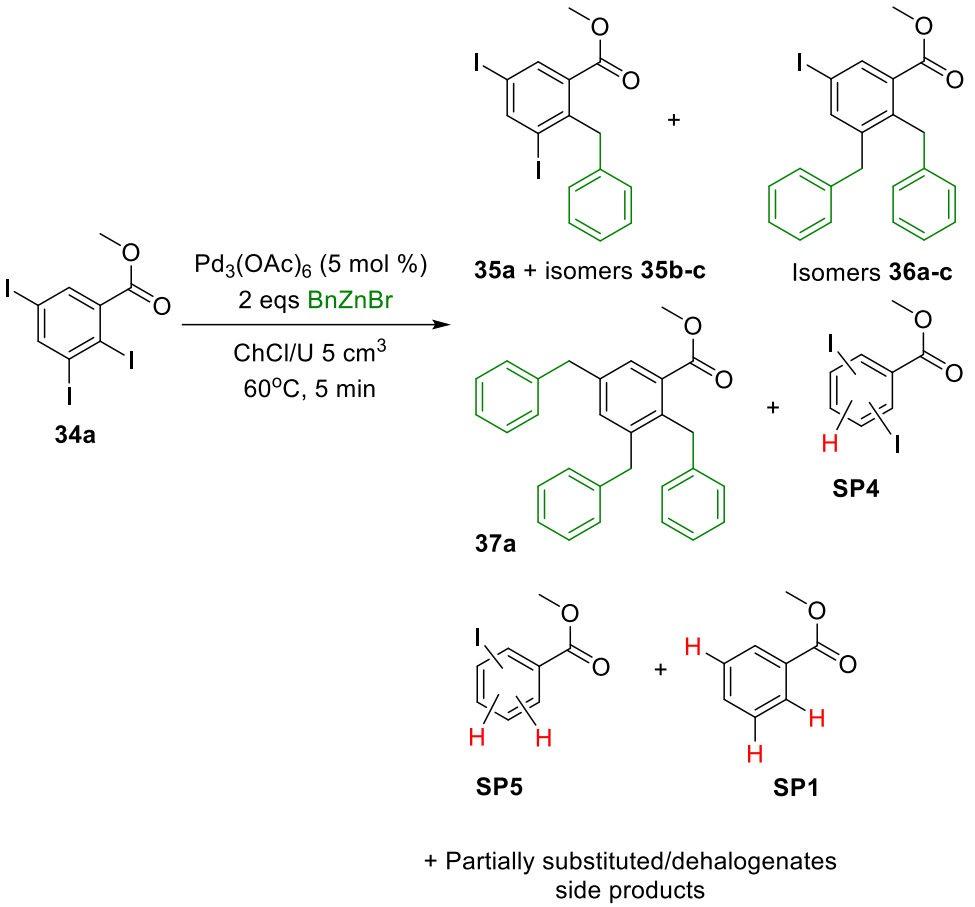

Scheme 3.3.7: Regioselective Negishi coupling under reaction conditions from the methodology devised for ortho-substituted iodoarenes.

In 2008, Houpis *et al*. reported a regioselective Suzuki-Miyaura cross-coupling in which 2,5-dibromobenzoic acid exerted an *ortho*-directing effect to selectively couple arylboronic acid in the *ortho* position of the bromoarene when $Pd_2(dba)_3$ was used as catalyst.[181] These observations and the results obtained after the last substrate scope showed in *Scheme 3.3.6*, inspired us to investigate the regioselectivity in a Negishi coupling between methyl 2,3,5-triiodobenzoate **34a** and BnZnBr, under the reaction conditions for *ortho*-substituted iodoarenes in ChCl/U DES.

Interestingly, the reaction proceeded in a different way compared to the successful reactions with other *ortho*-substituted electrophiles. Since **34a** was an insoluble solid in ChCl/U, an opaque pale orange suspension was formed upon addition of the substrate. Dropwise addition of BnZnBr dissolved in THF

solubilized **34a** and formed a translucent orange mixture. In contrast with other reactions, intense evolution of black Pd was not observed with the addition of the first drops of zinc reagent, nor white or grey aggregates, which are a characteristic feature of zinc reagent hydrolysis. The only appreciable change was the change in colour to a darker orange solution. 5 seconds after finishing the dropwise addition of BnZnBr, an intense and abrupt evolution of black Pd aggregates was observed.

The reaction proceeded smoothly at 60 ^{o}C and 5 mol % loading of $Pd_3(OAc)_6$. The crude reaction mixture was analyzed by GC and GC/MS. **34a** was consumed in 97%, with 71% conversion to the monosubstituted product at the *ortho* position **35a,** whilst 3% conversion was observed for the other monosubstituted isomers **35b** and **35c**. Some formation of disubstituted isomers **36a-c** and trisubstituted **37a** cross-coupling products were observed in 7% and 5% conversions respectively. Monodehalogenated side products **SP4** and fully dehalogenated starting material **SP1** accounted for 2% of consumed starting material with no doubly-dehalogenated product **SP5** being observed. Finally, a combination of partially substituted products with different degrees of dehalogenation were produced in 11% conversion. An excess of 2% in the final mass balance was acknowledged and attributed to the internal standard inability to fully reproduce the chemical response of every product in the FID.

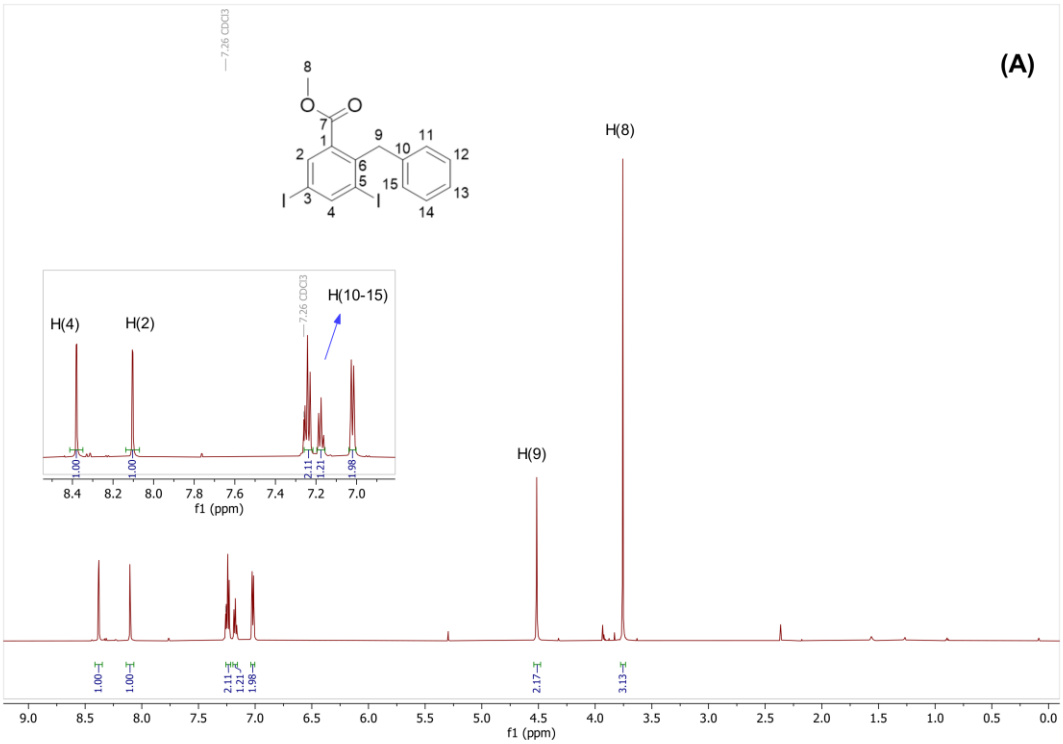
(A)
H(8)
H(10-15)
H(4)
H(2)
H(9)
f1 (ppm)

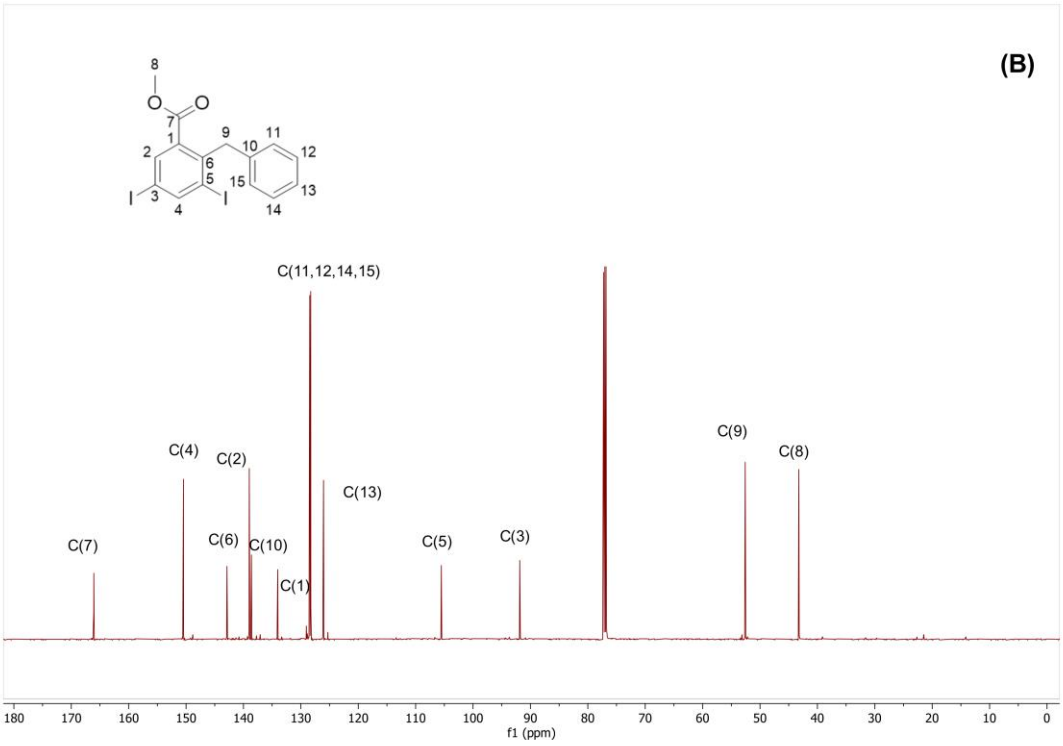
(B)
C(11,12,14,15)
C(4)
C(2)
C(9)
C(8)
C(13)
C(7)
C(6)
C(10)
C(5)
C(3)
C(1)
f1 (ppm)

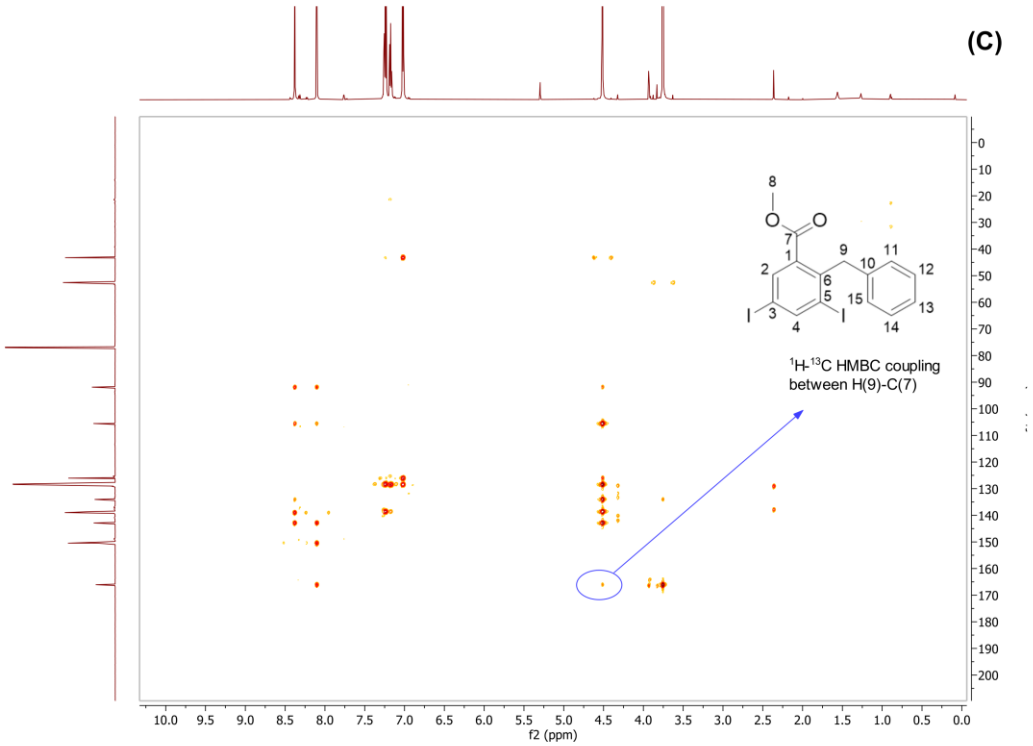

Figure 3.3.5: NMR characterization of major isolated product from the regioselective Negishi coupling experiment. A) ^{1}H-NMR. B) ^{13}C-NMR. C) ^{1}H-^{13}C-HMBC NMR featuring determinant interaction between C7 and C9. A complete characterization can be consulted in the section *5.1.13.3*

To confirm the connectivity of the major monosubstituted species, the product was isolated by column chromatography and analyzed by NMR, *Figure 3.3.5*. The major isolated species showed a characteristic proton chemical shift of δ 8.37, *Figure 3.3.5 A*. This very deshielded chemical shift is consistent with the proton being surrounded by two *ortho*-iodine atoms. The only connectivity pattern which could account for such a displacement downfield of the chemical shift is the one in which the new C-C bond was formed at the *ortho* position of the ring, leaving the two iodine atoms at *meta* positions intact. Moreover, a distinctive multiple-bond correlation between the methylene protons in the benzylic bridge and the carbonyl carbon was detected. In the *meta*-substituted isomers, the distance between the aforementioned atoms would be of 5 bonds, such correlation is unlikely to appear in an HMBC experiment *Figure 3.3.5 B & C*. Both features were indicative proof of the *ortho*-substituted product as the major species.

3.4 Summary and conclusions

It has been demonstrated that DESs can be used as solvents for cross-coupling reactions without need for protective N_2 atmosphere and in the presence of substantial amounts of water in the solvent. The Suzuki-Miyaura cross-coupling between arylboronic acid and bromoarenes was revisited in DESs with $Pd_3(OAc)_6$ as pre-catalyst, without supporting ligands. It was shown that the reaction can be accomplished with excellent yields in ChCl/G and ChCl/EG, while poor results were obtained in ChCl/U. The reaction could be carried out in glycerol and ethylene glycol with good yields, but the results suggested the catalytically-active Pd(0) species is less stable in these systems compared to reactions ran in DESs. The solubility of the substrates and catalyst was found to be key for achieving good cross-coupling yields. In all the cases, successful experiments correlated with the fast formation of black Pd at the beginning of the reactions. This "ligand-free" methodology in DESs showed poor recyclability with rapid decrease of isolated yields through the cycles.

The first example of a "ligand-free" $C(sp^3)$-$C(sp^2)$ Negishi coupling was successfully implemented in ChCl/U under mild reaction conditions. Temperature was found to be a variable of critical influence in the outcome of the reaction and running the experiments at 60 ^oC allowed the Negishi coupling to proceed in the absence of protective atmosphere and water-free conditions. No optimal reaction conditions were found for $C(sp^2)$-$C(sp^2)$ Negishi couplings in wet DESs in open air.

Two reaction methodologies were proposed based on the kind of substrate involved. When the Negishi reaction was performed with iodoarenes substituted at the *ortho* position with Lewis-basic functional groups, which are capable of coordinating to Pd, the best results were obtained when $Pd_3(OAc)_6$ was used as pre-catalyst. Iodoarenes with other substitution patterns showed better results when $[Pd(OAc)_2(PPh_3)_2]$ was used as pre-catalyst. The observed reactivity between $Pd_3(OAc)_6$ and *ortho*-coordinating iodoarenes, has been attributed to the formation of stable chelated 5-membered palladaycles as

oxidative addition products. $[Pd(OAc)_2(PPh_3)_2]$ showed poor results with *ortho*-subsituted iodoarenes, this was attributed to steric hindrance between the phosphine ligands and the functional groups from the aromatic ring. Iodoarenes exhibiting other substitution patterns do not suffer from steric hindrance when the catalyst approximate and can benefit from the more nucleophilic Pd core provided by the phosphine ligands. Important variations in the outcome of the Negishi coupling were observed between *n*-butylzinc chloride and benzylzinc bromide. The first organozinc gave better results with $[Pd(OAc)_2(PPh_3)_2]$ whereas benzylzinc bromide worked better with $Pd_3(OAc)_6$.

Finally, the "ligand-free" Negishi methodology showed high regioselectivity for the *ortho*-position of methyl 2,3,5-triiiodobenzoate, producing the monosubstituted product in 71%. This represents a unique case of solvent-mediated selectivity, in which the solvent decomposes one of the reagents, and the selectivity is dictated by the rate of productive catalysis against the rate of decomposition. In other words, rather than promoting one reaction pathway over others by stabilizing transition states or intermediates, the DES set up a threshold that separates the fast reaction pathways that can take place before the hydrolysis of the organozinc reagent from those slower pathways. The faster pathways occurred with *ortho*-coordinating iodoarenes, which were proposed to undergo oxidative addition through potentially more stable 5-membered chelated transition states than the monocoordinated oxidative addition transition states, accessed by iodoarenes with no coordinating groups next to the iodinated positions.

3.5 Future work

The application of green solvents in Suzuki-Miyaura reactions has gathered attention in the last 5 years. Since then, several works by Ramón, Capriati, König and co-workers have explored the limits of this reaction in DESs. On the other hand, there is only one paper, which was published this year with regards to the application of DESs in Negishi coupling in DESs by Capriati and co-workers.

The work published so far and the experiments discussed in here demonstrated the compatibility of ChCl/U with Negishi cross-couplings and opened the door for further research on fundamental mechanistic questions and methodology optimisation to enable the Csp^2-Csp^2 Negishi coupling under "ligand-free" conditions in DESs.

Several questions regarding mechanism are waiting to be addressed:

- Why was the Negishi reaction unable to proceed in ChCl/G DES?
- Are C(sp^2)-Zn reagents incompatible with the disclosed methodology? Why?
- What is the rate limiting step under these reaction conditions?
- What are the catalytically-active Pd species?
- Can *ortho*-coordinating iodoarenes form 5-membered palladycles?
- Has ChCl a non-innocent role in this reaction? Does it stabilize the catalytically-active Pd species?
- How the organozinc reagents influences the catalyst speciation under DES conditions, depending on their preparation and structure?
- Can the selectivity observed in these systems be harnessed in the synthesis of complex organic scaffolds?

A starting point for the future work would be to study why the Negishi reaction did not work in ChCl/G. For this it would be desirable to understand how tightly water molecules are bonded to Cl^- in comparison with ChCl/U. An series of experiments that would help to determine this can be FT-IR measurements of both DESs and pure water, to study the H-O-H angle bending vibrational mode. Recent work by Bonn and co-workers has found that the analysis of this vibrational mode, can offer information about the average intermolecular interactions that characterise the hydrogen-bonding network of water under different conditions. A second experiment to answer this question would be to characterise the chemical structure of the grey precipitates formed during the Negishi reaction in ChCl/G DES. Understanding the chemical composition of these salts, specially the counterion could help to determine what was causing the decomposition of the zinc reagent.

An approach to answer questions related to the rate-limiting step, the speciation of the catalyst, the role of ChCl in these reactions, etc. can be through the development of kinetic experiments. However, a problem that was encountered during the optimisation stage was that reactions finished too quickly to take aliquots to carry kinetic measurements. This problem can be solved by measuring the concentration of the species involved in the reaction *in situ*, through microelectrochemical measurements or time-resolved IR spectroscopy. Each elementary step could be studied stoichiometrically to determine rate constants from each elemental step and to study the influence of each variable considered on the optimisation stage. The nature of the catalytically-active Pd species can be studied by microscopic characterization of the Pd aggregates formed after each reaction, ESI-MS analysis of the crude reaction mixture to detect molecular Pd in solution under DESs conditions, catalyst poisoning experiments, *etc*.

With a deeper knowledge of the influence the DES has on the catalyst speciation and on the reaction mechanism, a new DES designed *ad hoc* for cross-coupling reactions involving air- and moisture-sensitive organometallic reagents can be proposed. The solubility of the reagents and the catalyst will be a crucial factor to consider. The experiments demonstrated the solubility of the catalyst and the starting material is necessary to some extent. Moreover, an ideal DES should not react with the organometallic reagent or the catalysis, as was observed when ChCl/DMU and ChCl/$AcNH_2$ were used.

There is also room for optimisation of the catalyst. During these experiments, $Pd_3(OAc)_6$ and $Pd(OAc)_2(PPh)_2$ were chosen as pre-catalysts to find the most affordable reaction conditions possible, *i.e.* no added ligands or the cheapest phosphine-Pd complex available. A first attempt could be to work with the ligands designed by Ramón and co-workers to perform Suzuki and Heck reactions in DESs.[146,182] Further research could be done on replacing Pd with a cheaper transition metal like Ni or Fe.

Finally, it is known that biological macromolecules like DNA fragments and proteins show good solubility in DES without losing their 3D structure. This

could be exploited to elaborate protocols for cross-coupling reactions between air- and moisture-sensitive organometallic reagents and biomolecules, which have not been possible due to the insolubility of such biomolecules in organic solvents and the incompatibility of the organometallic reagents with water.

Chapter IV: *En route* to the development of a redox-active DES for energy storage

4.1 Introduction

4.1.1 Viscosity and conductivity of ChCl-based DESs

Since DESs are made of salts, they possess ionic conductivity, although it tends to be lower than molecular solvents due to the inherently high viscosity of DESs caused by the size of the ionic components and the strong hydrogen bond networks they exhibit.[11] For example, ChCl-based DESs with ethylene glycol as HBD are among the least viscous DESs and tend to exhibit ionic conductivities of around 7-10 mS/cm, whereas for example, the ionic conductivity of sea water is of 5 S/cm. The ionic conductivities of other DES are shown in *Table 4.1.1.*

Table 4.1.1: Ionic conductivities of selected DESs at specific temperatures.[12,183]

Solvent	Base:Acid Ratio	χ(mS/cm)
ChCl/U	1:2	0.20 (40 ºC)
ChCl/G	1:2	1.05 (20 ºC)
ChCl/EG	1:2	7.61 (20 ºC)
$ChCl/ZnCl_2$	1:2	0.06 (42 ºC)
$ChCl/CF_3CONH2$	1:2	286 (40 ºC)
$[C_4mim][BF_4]$	-	3.5 (25 ºC)

Viscosity and conductivity are inversely proportional and can be tuned by modification of the ionic hydrodynamic radius of the salt components, the number of functionalities capable of donating H-bonds, by increasing the HBD tendency to dimerize or by allowing a certain percentage of hydration or other co-solvents.[11,30,87]

It is very common to model DESs viscosities as a function of temperature. This dependence usually has the form of an exponential decay that follows the Vogel-Fulcher-Tammann empirical model from *Equation 4.1.1.*

$$\eta = \eta_0 exp(\frac{B_\eta}{T\text{-}T_0})$$

Equation 4.1.1: Vogel-Fulcher-Tammann model. η_0, T_0 and B_η are empiric parameters that are adjusted by fitting the equation with the experimental data and are related to the energy barriers that arise when molecules try to move.

Conductivity is inversely proportional to viscosity since ion mobility is also determined by the availability of adjacent holes. Hole theory states that the concentration of appropriately sized holes is more important than the charge carrier concentration. Because of this, molar conductivities ($\Lambda^\infty = \kappa = \lambda^+ + \lambda^-$) in DESs usually correlate linearly with fluidity.[184] The limiting scenario is supposed to occur at an infinite dilution regime, hole theory assumes holes are akin to molecules in ideal gases with uncorrelated movement. Under this assumption, ionic conductivity can be calculated with the Einstein-Stokes model in *Equation 4.1.2.*[184]

$$\kappa = \frac{z_1 z_2 Fe\rho}{6\pi\eta M_w}(R_+^{-1} + R_-^{-1})$$

Equation 4.1.2: Einstein-Stokes model. z_1 and z_2 are the ion charges, "F" is the Faraday constant, "e" is the electron charge, "ρ" is the density, "M_w" is the DES's molecular mass, "η" is the viscosity and "R" are the ionic radii.

4.1.2 Electrochemical stability of ChCl-based DESs.

In this section, the electrochemical window of ChCl-based DESs and the stability of ammonium salts like choline chloride under reductive conditions is briefly discussed. Alongside conductivity and viscosity, determining the stability of DESs under reductive or oxidative conditions is important for the assessment of their application as solvent/electrolytes in electrochemical devices.

The electrochemical window of a solvent indicates a range of electrode potentials at which the solvent does not intervene in redox reactions at the

electrode surface. Wider electrochemical windows are desirable because they enable redox processes that take place at more extreme potentials.

Silva and co-workers performed cyclic voltammetry experiments in ChCl/U, ChCl/EG DES using a mercury WE and silver wire as pseudo-reference, and in ChCl/G DES using a glassy carbon WE and silver wire as pseudo-reference. The authors found electrochemical windows of -1.25 V to 0.2 V for ChCl/U, -1.5 V to 0.1 V for ChCl/EG and -1.2 V to 0.5 V for ChCl/G. The reduction barriers were attributed to the HBDs. In the case of ChCl/G, irreversible waves appeared a few mV before the DES redox barriers and were attributed to reduction of transient water and the oxidation of glycerol mediated by water. Moreover, the researchers noted that increasing the temperature narrowed the electrochemical window of the DESs. No hydrogen evolution reaction was detected despite the protic nature of the solvents. These values indicate DESs exhibit similar electrochemical windows as water, and narrower than common organic solvents used in electrochemistry like acetonitrile or dichloromethane.[185,186]

Quaternary ammonium salts are key components of ChCl-based DESs as the ones used in this thesis. Their electrochemical robustness was tested in ILs, and it has been found that these cations tend to be more stable than imidazolium-cations under reductive potentials, showing stabilities up to -3 V vs SHE, whereas in acetonitrile, these cations get reduced at potentials around -1.9 V vs SHE with Pt electrodes.[187] These results are relevant to the application of ammonium-based DESs as solvents/electrolytes because they establish at which limits, one of their key components is electrochemically decomposed.

Haerens *et al*. studied the cathodic decomposition of choline chloride in ChCl/EG during metal deposition experiments.[188] The researchers applied electrolysis currents between 0.5 and 3.0 A for up to 192 h. They were able to detect cholinium decomposition in the cathode and formation of chlorinated products at the anode.[188]

The authors proposed a cholinium cathodic degradation mechanism which involves Hofmann elimination of the ethanolic chain by hydroxide anions generated due to the reduction of water. Additionally, the authors proposed a single-electron-transfer process that can generate a choline radical which decomposes into either triethylamine and ethanol radical or dimethylaminoethanol and methyl radical. The radical can accept another electron to generate basic carbanions and subsequently attack other cholinium cations or suffer proton-transfer reactions. The authors proposed the formation of trichloride anion Cl_3^- at the anode, with which the alkyl radicals can react *via* single-electron transfer to generate chlorinated hydrocarbons since no Cl_2 gas formation was observed during the experiments.[188]

4.1.3 Electrochemical and spectroscopical properties of 9,10-anthraquinones and their applications in energy storage

9,10-anthraquinones (AQ) are polycyclic aromatic hydrocarbons derived from anthracene with two keto functional groups located on the central ring. AQs tend to be more chemically stable than other quinones, due to the higher degree of charge delocalisation provided by the aromatic rings. *Figure 4.1.1*.

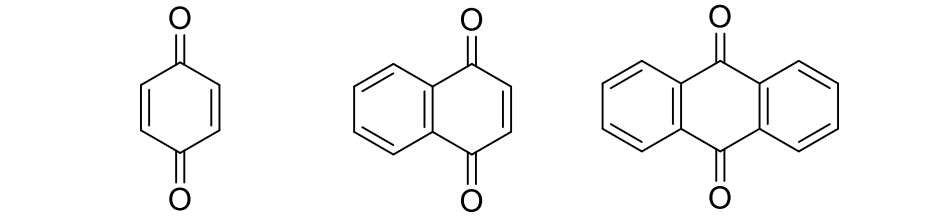

Figure 4.1.1: Quinones are a family of organic redox materials.

AQ exhibits 3 minor and 1 dominant allowed π to π* electronic transitions characterised by light absorption bands between 225 and 400 nm.[189] Non-polar solvents like dichloromethane, carbon tetrachloride or cyclohexane exert an hypsochromic effect on the electronic transitions, whereas polar aprotic solvents like acetonitrile or protic solvents like ethanol have a bathochromic effect (positive solvatochromism).[190–192] The functionalization of the

anthraquinone ring scaffold can cause modifications of its electronic properties. EWGs tend to have a little impact the on the electronics of AQs, whereas EDGs tend to cause bathochromic shifts on the absorption wavelengths, increments in the molar absorption coefficient of the least energetic electronic excitations, and the appearance of a new large band in the visible region of the spectrum due to a charge transfer transition from the EDG to the carbonyl group in the quinone ring.[189,192,193]

The electrochemistry of quinones, naphthoquinones and anthraquinones is characterised by two electron exchange processes, one per carbonyl group. The fully reduced AQ species is doubly charged and has a greater basic character than both the radical anion and the oxidized forms, therefore, in aqueous media or in the presence of proton donors, their redox reactions tend to be coupled with hydrogen bonding or proton-transfer equilibria.[194,195]

At low pH, the electron-transfer is coupled with proton-transfer and the redox reaction proceeds through a two-electron one-step mechanism (concerted. E_r, *Scheme 4.1.1-A*). Conversely, in aqueous environments at neutral pH or in non-protic solvents, the redox reaction proceeds through a one-electron two-step process (step-wise, E_rE_r, *Scheme 4.1.1-B & Scheme 4.1.1-C*).

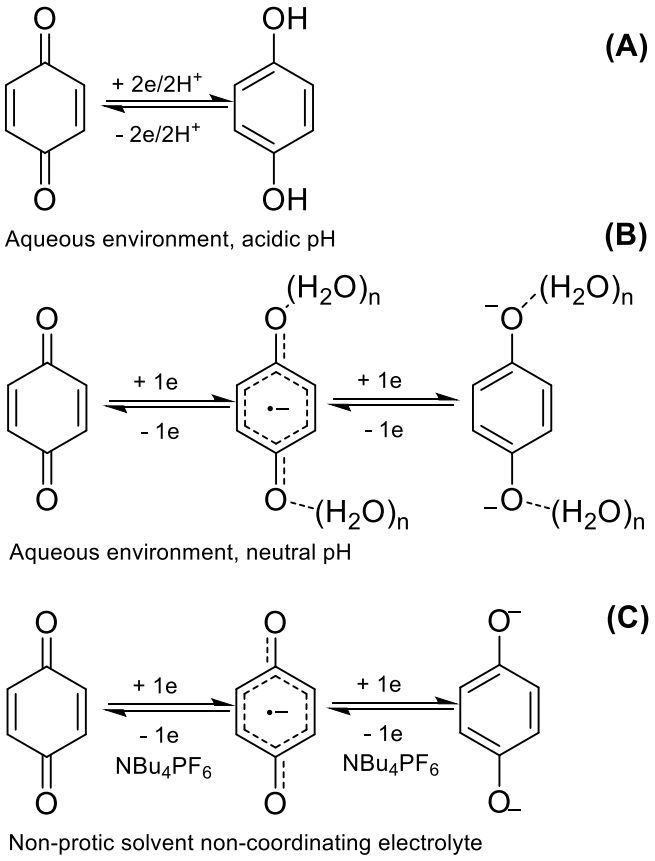

Scheme 4.1.1: Redox mechanisms of quinones in protic and non-protic solvents

According to the mechanism depicted in *Scheme 4.1.1-C*, in dry polar aprotic solvents, quinones exhibit a two-step one-electron mechanism characterised by a cyclic voltammogram composed of two cathodic waves and two anodic waves as the one shown in *Figure 4.1.2*.

The shape of the second redox wave of quinone-related compounds in polar aprotic solvents, which corresponds to the reduction of the quinone radical anion intermediate to the quinone dianionic species has been matter of debate among electrochemists, since it does not seem to perfectly correlate with the mechanism depicted in *Scheme 4.1.1*, from which equal peak heights for every process are expected. In contrast, it is often reported in the literature that the second redox wave exhibits lower peak heights than those of the first redox wave. This is an indication of the fact that there are more electrochemical or chemical equilibria taking place.[195]

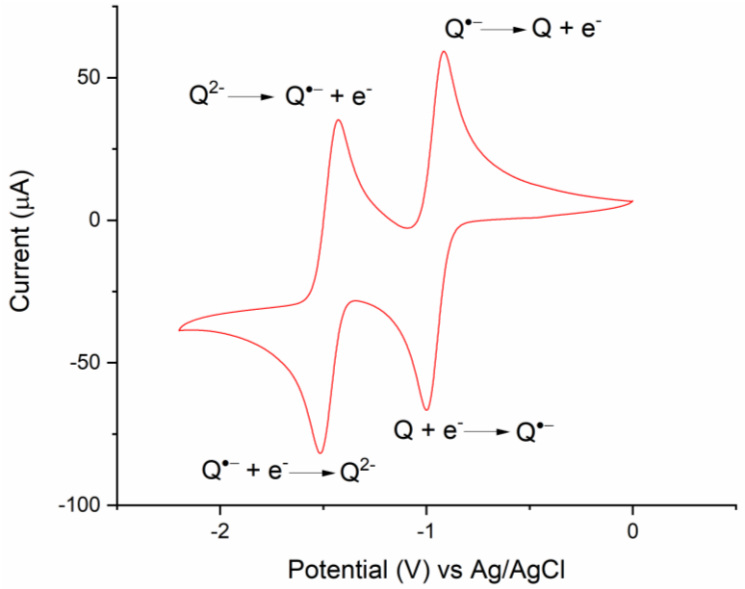

Figure 4.1.2: Example of the cyclic voltammogram of a quinone in polar aprotic solvent.

Gupta and Linschitz studied how the pKa of the AQ (and quinones) radical intermediate and the fully reduced dianionc species affects the electron transfer process in polar aprotic solvents, considering that the basicity of the quinone ring increases by 8 to 10 pKa units for every electron accepted.[194,196] The authors found that in the presence of weak proton donors of higher pKa values than the singly or doubly reduced AQ species, increments in the concentration of the protic additive were followed by shifts to cathodic potentials of the second redox wave of the quinones, without losing reversibility. The authors also observed that the peak heights of the first redox wave increased at the expense of the second redox wave. The authors attributed this phenomena to a dismutation of the radical anion to form the fully oxidised the fully reduced AQs, favoured by hydrogen-bonding interactions, since no spectroscopic evidence was found for the formation of protonated quinone species (*Scheme 4.1.2)*.[194]

$$2\ AQ^{\bullet -} \rightleftharpoons AQ + AQ^{2-}$$

Scheme 4.1.2: Proposed disproportionation mechanism by Gupta and Linschitz.[194]

Gupta and Linschitz also observed that in the absence of protic additives, the height of the second redox wave peaks were lower than the first redox wave peaks. Moreover, the cathodic/anodic peak height ratios for the second redox wave of the studied AQs were between 0.8 to 0.9 The authors explained the differences between the redox waves with a mechanism involving the formation of a redox-inactive complex between an equivalent of the fully oxidised AQ and an equivalent of the fully reduced AQ (*Scheme 4.1.3*). The formation of this complex would scavenge AQ molecules at the potentials in which the dianion is formed, thus provoking a decrease in the height of the second wave.

$$AQ + AQ^{2-} \rightleftharpoons [AQ\text{--}\pi\text{--}AQ]^{2-}$$

Scheme 4.1.3: Proposed dimerization by Gupta and Linschitz.[194]

The behaviour observed by Gupta and Linschitz, in which the second anodic wave was larger than the second cathodic wave has been also reported by Macías-Ruvalcaba and Evans for other quinones.[197] The authors proposed an explanation which also involves the formation of a π-adduct, but instead they proposed a redox-active dimer between two radical anion species, which would have a similar redox behaviour as the monomeric radical anion, but since its formation requires two equivalents, the current peak height would be lower (Scheme *4.1.4*).[197] Afterwards, the dimer would break at cathodic potentials beyond the second reduction potential to regenerate the doubly reduced species, thus not only explaining why the second redox wave is lower than the first redox wave, but also why the second anodic wave is larger than the second cathodic wave.

$$AQ^{\bullet-} + AQ^{\bullet-} \rightleftharpoons [AQ\text{--}\pi\text{--}AQ^{\bullet}]^{2-}$$

$$[AQ^{\bullet}\text{--}\pi\text{--}AQ^{\bullet}]^{2-} + e^{-} \rightleftharpoons [AQ^{\bullet}\text{--}\pi\text{--}AQ]^{3-}$$

Scheme 4.1.4: Formation of a redox-active π-dimer between two AQ radical anion species.[197]

In contrast, Staley *et al*. noted that in some specific cases where the quinone ring is functionalised with strong EWGs or proton-donor groups, the dimerization might be reasonable, however, it cannot explain the observed CV shapes in other contexts. The authors demonstrated that the peak current differences and the appearance of broad signals or shoulders were exacerbated when the AQ concentration was reduced.[196]

Since the formation of adducts is not favoured under dilute conditions, this indicated that the formation of adducts was unlikely the general explanation for these phenomena. Instead, Staley *et al*. suggested that for those cases where dimerization cannot explain the experimental CVs, a third hypothesis is viable. It involves acidic groups like phenols or carboxylic acids, which are formed on the glassy carbon electrode surface as a consequence of polishing in air.[196]

The AQ radical anion or the dianion would be capable of undergoing an acid-base exchange reaction with protic species generated at the electrode surface. The newly protonated radical would carry its respective redox processes at more positive potentials. This would give rise to small currents near to the original peaks corresponding to the formation of the fully reduced hydroquinone species, which can form hydrogen-bonding interactions with a second equivalent of radical anion, which would be responsible for the decrease of the second wave peak heights and the appearance of new broad signals belonging to the reduction of the hydrogen-bonding dimer.[196]

The functionalisation of AQ scaffolds is a field that have gathered significant attention due to their applications in energy storage because these organic molecules tend to be cheaper than metal redox-active salts, which are the most widespread redox-active material in batteries. Moreover, quinones can undertake two electron-transfer processes, which means that higher energy densities can be achieved at lower concentrations.[198–201] The biggest disadvantage of AQs is their poor solubility in organic solvents and their insolubility in water.[202] A common strategy to increase the solubility in polar solvents is to introduce charged functional groups like sulphonium or

ammonium groups into the AQ motif. Introducing the ionic functional groups away from the carbonyls improves the solubility.[203]

The redox potentials of the AQs can be controlled by functionalising the aromatic rings with EDGs or EWGs, where EDGs shift the redox potentials to more negative values, while EWGs have the opposite effect. The biggest impact on the redox potential is made when the functionalization is done close to the carbonyl groups.[203]

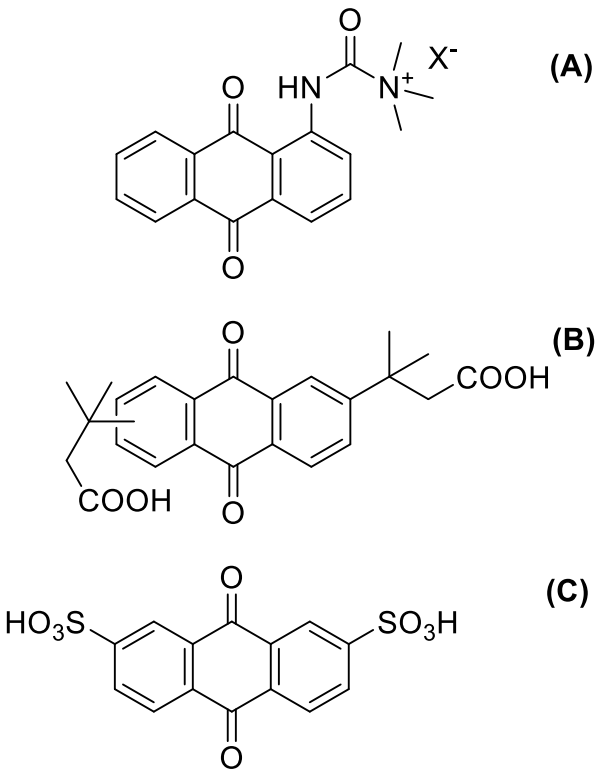

Figure 4.1.3: Designer anthraquinones for energy storage applications.[198,201,204]

The high tunability of the AQ backbone allows for its application in both aqueous and non-aqueous solvents. As an example of the non-aqueous design philosophy Zhen *et al*. recently disclosed a cationic AQ functionalised with amides holding quaternary ammonium salts, paired with Tf_2N^-, PF_6^- or BF_4^- anions (*Figure 4.1.3-A*).[204]

The authors proposed that the introduction of the amide group could help to extend the conjugation of the system to improve the stability of the reduced species. The introduction of a bulky quaternary ammonium group had the objective of inhibiting the dimerization of the AQ radical anion intermediate and improving the solvation of the redox-active species. The authors reported they were able to achieve a reversible E_rE_r redox process at a concentration of 0.91 M in acetonitrile when Tf_2N^- was used as counter anion.[204]

On the other hand, as an example of the aqueous design philosophy, Aziz and co-workers published a series of functionalised AQs designed to work at acid or basic pH.[198,201] The AQ designed to work at basic pH was functionalised with an alkyl chain bonded to a carboxylic group (*Figure 4.1.3-B*). The authors were able to achieve concentrations of up to 0.74 M. Under these conditions, the AQ exhibited a reversible two-electron one-step mechanism (E_r). At pH=12 the authors identified the disproportionation of the AQ dianion into fully-oxidised AQ and anthrone, which could be converted back to AQ by air oxidation. The AQ designed to work under acidic conditions (pH=0) was functionalised with a sulfonium group (*Figure 4.1.3-C*). Under these conditions the authors achieved a 1 M concentration of AQ in aqueous electrolyte. An inconvenience found with this sulphonic-AQ is that the strong electron-withdrawing effect caused by the sulphonium groups caused a shift of the AQ redox potentials towards more positive values.

The ammonium-AQ halide from *Figure 4.1.3-A* by Zahn *et al.* is a potential good candidate to prepare family III RADESs, since the AQ salt can potentially take the role of the ChCl as HBA. On the other hand, AQs functionalised with acidic functional groups shown in *Figure 4.1.3-B* & *Figure 4.1.3-C* can potentially be good HBDs for acidic RADESs.

4.1.4 Chapter aims

AQs are interesting organic redox materials for energy storage applications due to their reversible electrochemistry and chemical stability. These compounds tend to be cheaper than other redox-active materials and their

operation impose fewer toxicity risks. Since anthraquinones can exchange up to two electrons, these materials potentially allow higher energy densities than commercial redox-active materials like vanadium salts, iron and copper complexes, which exchange only one electron.

Although in the last 10 years, a diverse set of AQ scaffolds has been applied as cathode redox-active materials in energy storage devices like redox-flow batteries, these organic salts were implemented in aqueous or polar-aprotic solvents. In both systems, concentrations of around 1 M were reported. Moreover, for applications in aqueous media, the AQ redox-active core has to be functionalised to reduce their redox potentials in order to fit within the electrochemical window of water, thus reducing the potential of the device. On the other hand, despite polar-aprotic solvents exhibiting wider electrochemical windows, which allows to design more electron-rich AQ scaffolds, the commercialization of these electrolytes has not been consolidated due to operation and environmental hazards. Up to this date, no family III RADESs have been prepared and applied in energy storage.

The objective of this project was to synthesise organic salts based on the anthraquinone scaffold, which could be used to prepare family III RADESs. The specific aims were:

- To prepare and fully characterise a family of tetraalkylammonium and imidazolium halides substituted with 2-methylanthraquinone.
- To prepare and fully characterise a family of tetraalkylammonium and imidazolium bis(trifluoromethanesulfonyl)imide salts substituted with 2-methylanthraquinone.
- To study the redox properties of the AQ salts using voltamperommetric methods to obtain information about their redox mechanisms, with special focus on electrochemical and chemical reversibility.
- To model the AQ cationic structures in acetonitrile solution and the molecular orbitals involved in the electron-exchange reactions, using electronic structure calculations, to gain insight into the structure of the

AQs in solution, and the electronic stability of the different molecular oxidation states.

- To discuss which AQ salts were the most suitable candidates to prepare family III RADESs.

4.2 Results and discussion

4.2.1 Synthesis of 2-bromomethylanthraquinone

2-methylanthraquninone (**38a**) was chosen as the starting material because it is a readily available and cheap scaffold that permits functionalization of the AQ structure without the introduction of substantial modifications to the electronic properties of the aromatic system. A Wohl-Ziegler radical bromination was employed to replace one of the benzylic hydrogen atoms with bromine, to obtain 2-bromomethylanthraquinone **39a**. By introducing a new C-Br bond, the AQ scaffold obtains a good leaving group for later functionalization through nucleophilic substitution reactions.

Since Wohl-Ziegler reactions have been traditionally carried out in carbon tetrachloride or benzene, a greener approach to the α-bromination of ketones by Reddy *et al*. was tested to reduce the protocol's impact on health and environment.[205] The reaction conditions involved the use of refluxing methanol, N-bromosuccinimide (NBS) and silica gel 60-120 mesh as a catalyst.

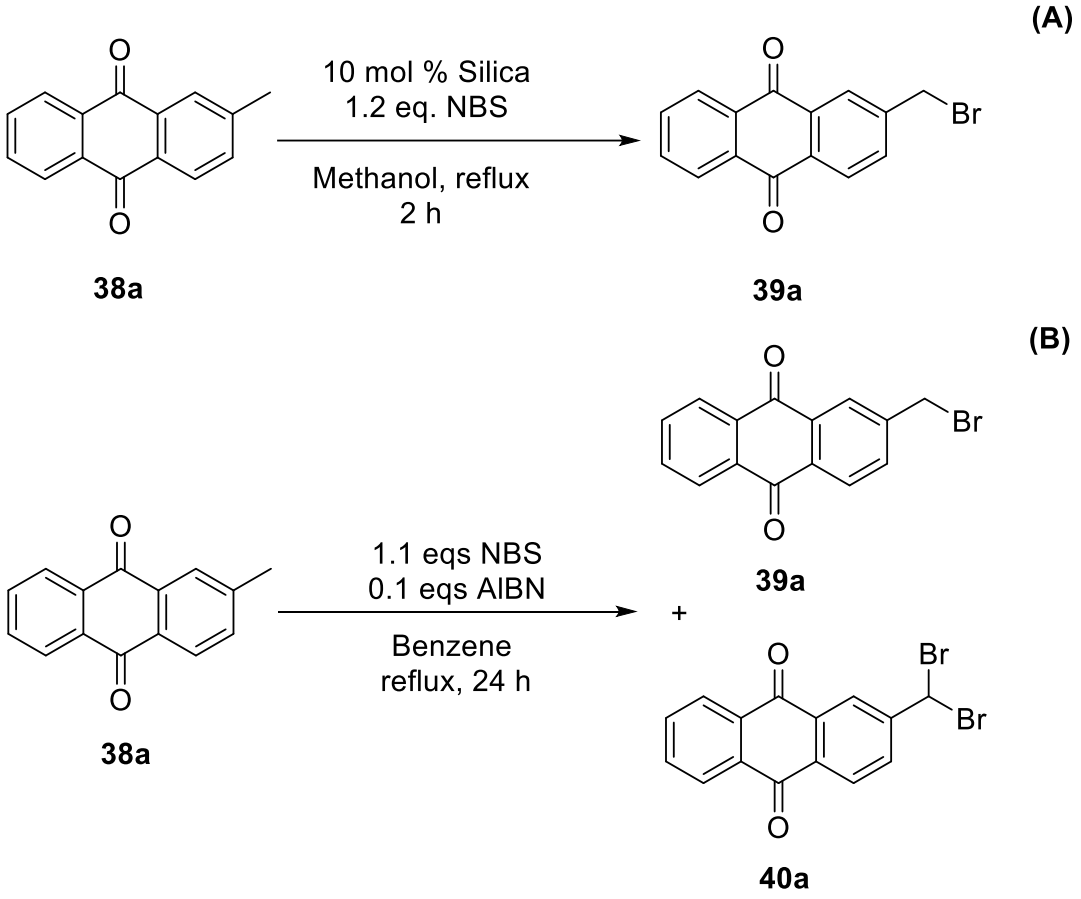

Scheme 4.2.1: Synthesis of 2-bromomethylanthraquinone **39a** attempted by different methods.

These reaction conditions were implemented for the benzylic bromination of **38a** as reported, except for the silica catalyst particle size, which was increased to 70-240 mesh (*Scheme 4.2.1 A*). A detailed reaction procedure can be found in *section 5.2.2*. Unfortunately, these reaction conditions proved unsuccessful to generate product **39a**. The reaction was repeated with acetophenone instead of **38a** but the α-brominated product was again not formed. It was concluded that the silica particle size might be not adequate to generate bromide radicals to trigger the reaction. Instead, a traditional Wohl-Ziegler approach was tried, involving NBS as bromide source and azobisisobutyronitrile (AIBN) as the radical propagator in benzene, based on the reaction conditions reported by Crozet *et al*. and Zheng *et al*. in carbon tetrachloride.[206,207] Later, the methodology was updated by Mr Harry Vincent, another PhD student in the research group. The reaction was reoptimized to

use acetonitrile as solvent and benzoyl peroxide as the radical propagator, with a similar outcome as in benzene.

The crude product was purified by recrystallization from boiling ethyl acetate. **39a** was obtained in 70% yield as a yellow solid of 94% purity as analyzed by ^{1}H-NMR. The impurities consisted of starting material **38a** in 5% and dibrominated product **40a** in 0.7 %, no traces of NBS or succinimide were found. Recrystallization was chosen over flash column chromatography, which was found to be an appropriate purification method in this system on small scales, because it offered similar purity without significant product loses and was significantly more convenient when the synthesis was scaled up.

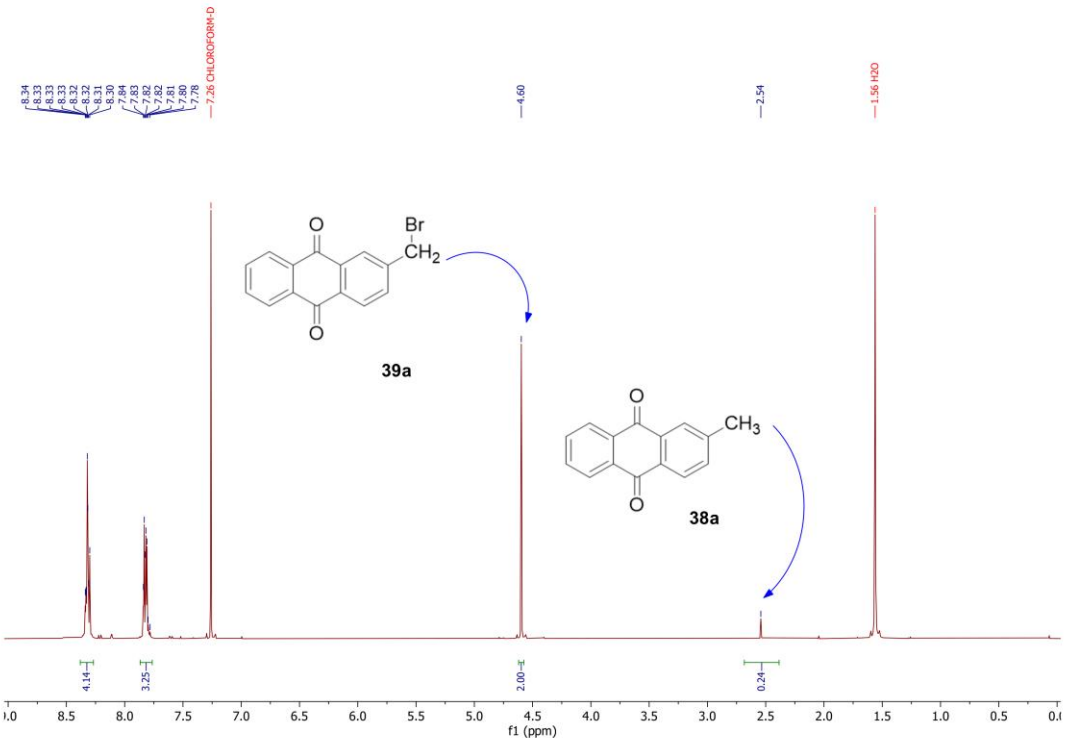

Figure 4.2.1: ^{1}H-NMR spectrum of **39a** after recrystallization in $CDCl_3$

Figure 4.2.1 shows the ^{1}H-NMR spectrum of the recrystallized **39a.** The chemical shift of the aromatic and methyl protons were in agreement with the reported NMR data in the literature.[206,207] The characteristic methyl protons signals from **38a** (δ=2.54 ppm), **39a** (δ=4.60 ppm), **40a** (δ=6.75 ppm) were normalised to determine the purity of **39a** in the recovered solid. The

introduction of bromide into **38a** caused a merge of the well-defined aromatic peaks into two broad signals for **39a**.

4.2.2 Synthesis of anthraquinone salts

The synthesis of AQ salts was divided into two methodologies: for protic and aprotic salts. The aprotic salts consisted of tetraalkylammonium salts prepared by quaternisation of tertiary amines. On the other hand, the protic salts consisted of alkylammonium salts prepared by neutralization of tertiary amines with Brønsted acids to yield salts in which the cations have an acidic proton their structure.[208]

The synthesis of the aprotic AQ bromide salts **[41-44]Br** was performed by quaternisation of 1-methylimidazole, triethylamine, N-methylpyrrolidine and N-methylpiperidine with compound **39a** in toluene, (*Scheme 4.2.2-A*). Then, products **[41-44]Br** were used in anion metathesis reactions with lithium bis(trifluoromethanesulfonyl)imide (Li[Tf_2N]) to generate salts **[41-44][Tf_2N]**, *Scheme 4.2.2-B*. The synthetic procedures were based on those reported by Wasserscheid *et al*. for the preparation of imidazolium-based ILs with some modifications to the anion metathesis conditions. (See *section 5.2.2*).[209]

The AQ bromide salts were obtained in good yields with 1-methylimidazole promoting the best conversion to product **[41]Br** in 92% (*Table 4.2.1 entry 1*). N-methylpyrrolidine and N-methylpiperidine reactions produced compounds **[43]Br** and **[44]Br** in similar yields (*Table 4.2.1 entries 3 & 4*) while product **[42]Br** with triethylamine was only formed in 41% (*Table 4.2.1 entry 2*).

The yields of isolated products do not follow the nucleophilicity trend for amines by Mayr and co-workers where N-methylpyrrolidine > N-methylpiperidine > triethylamine > 1-methylimidazole.[210,211] Instead, an explanation for the obtained yields could be related to the solubility of the cationic products in toluene. The higher conformational rigidity of the imidazolium, piperidinium and pyrrolidinium moieties compared to triethylammonium, may reduce the solubility of the salts thus easing its recovery. After evaporating the mother liquor from the reaction of *entry 2*,

unreacted **39a** was detected. Adding an excess of up to 5 equivalents of amine did not significantly improve the yield. The impurities were removed by recrystallization of the crude product.

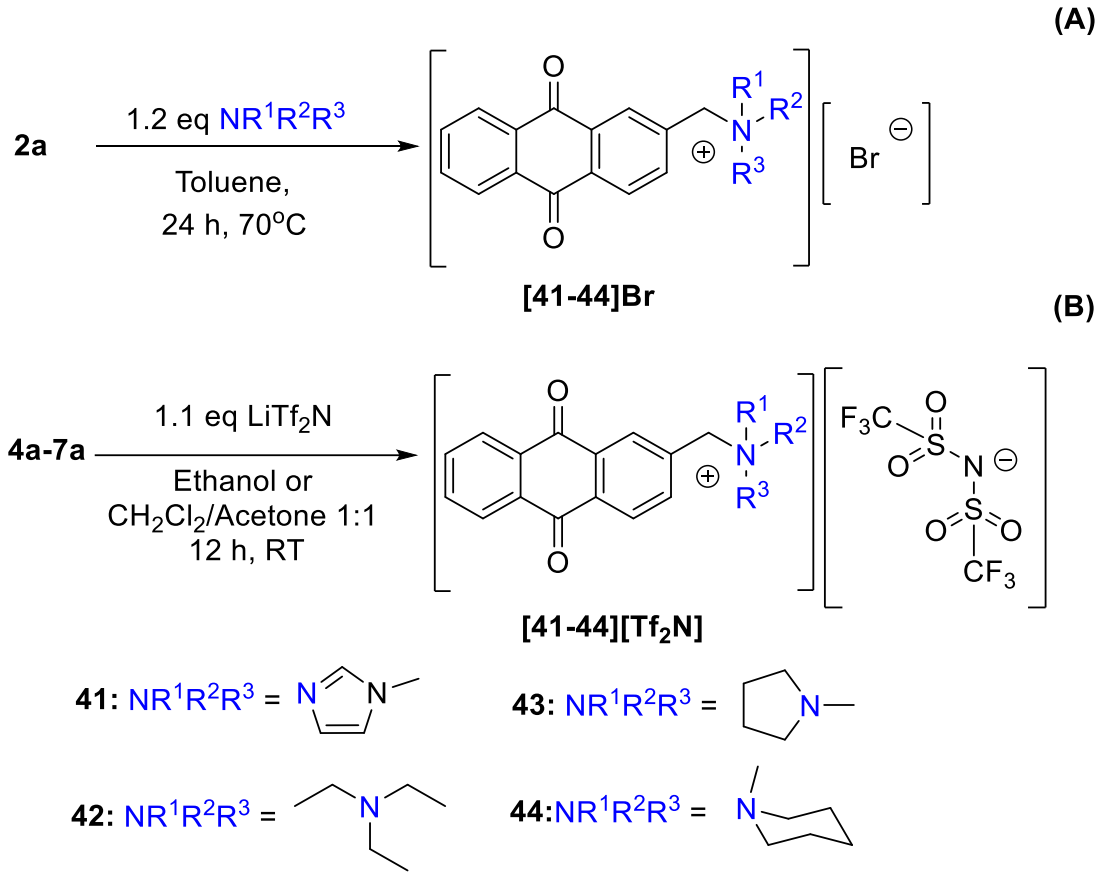

Scheme 4.2.2: Synthesis of anthraquinones salts functionalised with ammonium or imidazolium groups. (A) Bromide salts, (B) Tf_2N^- salts

[41-44]Br were used as starting materials for anion metathesis reactions. **[41]Br** showed good solubility in ethanol and after adding Li[Tf_2N], **[41][Tf_2N]** precipitated from solution as a yellow product. On the other hand, salts **[42-44]Br** showed poor solubility in ethanol, in these cases a dichloromethane/acetone solution was used. The metathesis products **[42-44][Tf_2N]** did not crash from solution and were washed with water. All [AQ][Tf_2N] salts were washed between 3 & 4 times with 10 cm^3 of water until AgBr precipitate was no longer observed using the $AgNO_3$ test. This test is used to detected halide impurities because silver nitrate reacts with them to form silver halides, which are insoluble in water.

Table 4.2.1: Isolated yield of aprotic anthraquinone salts

Entry	AQ	Isolated yield (%)	AQ/H_2O CHN Analysis Model	Water content (ppm)	Melting Point (ºC)
1	**[41]Br**	92	2/3	43	236-239
2	**[42]Br**	41	1/2	93	214-216
3	**[43]Br**	89	1/1	58	265-268
4	**[44]Br**	78	2/3	43	233-235
5	**[41][Tf_2N]**	54	1/0	2	171
6	**[42][Tf_2N]**	83	1/0	14	118
7	**[43][Tf_2N]**	77	1/0	4	162
8	**[44][Tf_2N]**	81	1/0	17	146

The melting point of all the salts was first measured with a Stuart SMP30 apparatus. Only the melting points of the Tf_2N^- salts were confirmed by DSC because the bromides showed thermal decomposition at their melting points.

A possible explanation for the smaller yield of reaction obtained for **[41][Tf_2N]** compared to **[42-44][Tf_2N]** (*Table 4.2.1 entry 4 vs entries 6-8*) is that product the **[41][Tf_2N]** could exhibit certain solubility in methanol, in which case the precipitation would not be quantitative, thus reducing the yield. **[42-44][Tf_2N]** were obtained by evaporating the organic phase after the washes, which ensured maximum recovery at the expense of purity.

For all AQ salts elemental analysis experiments results were within a range of 0.5% of the values obtained from the theoretical calculations, (See *section 5.2.2*). Different AQ/H_2O ratios were considered to calculate the theoretical composition of the solids, and the proportion which best reproduced the experimental data is reported in *Table 4.2.1* alongside the water contents of each AQ salt, measured by Karl-Fisher titration.

The bromide anion was expected to increase the hygroscopic nature of the new AQ salts compared to **38a**. Among the studied bromides, imidazolium **[41]Br** and piperidinium **[44]Br** salts registered the smallest water content (*Table 4.2.1 entries 1 & 3*) with pyrrolidinium **[43]Br** standing in a middle ground and triethylammonium **[42]Br** having the highest water content (*Table 4.2.1 entries 5 & 6*). On the other hand, Tf_2N^- anion undoubtedly provided a

more hydrophobic character to the AQ cations, since significantly less water was found in these compounds (*Table 4.2.1 entries 5 & 8*).

Salts **[41]Br**, **[42]Br** and **[44]Br** showed decomposition at the melting temperature and changed from yellow to brown. On the other hand, salt **[43]Br** turned black and degraded before melting (*Table 4.2.1 entries 1-4*). All Tf_2N^- salts showed significantly lower melting points due to the size and asymmetry of the anions. They were also seen to melt cleanly, without decomposition. This allowed their thermal properties to be characterised using DSC. Interestingly, the trend observed in the melting points of the different Tf_2N^- salts was different to that of the bromides. **[41][Tf_2N]** was observed to have the highest melting point, followed by the two cyclic ammonium salts **[43][Tf_2N]** and **[44][Tf_2N]**. In both cases, the triethylammonium salts **[42]Br** and **[42][Tf_2N]** had the lowest melting points, probably due to a higher entropic contribution from the ethyl chains as compared to the heteroatomic rings which have lower degrees of freedom to move (*Table 4.2.1 entries 5-8*).

The synthesis of protic AQ bromides was performed using diethylamine for **[45]Br**, and N-methylcyclohexylamine for **[46]Br**, following a similar procedure as the one used in the previous syntheses plus an extra protonation step with hydrobromic acid (*Scheme 4.2.3 A*). The preparation of the Tf_2N^- salts from the AQ bromides through anion metathesis reactions with Li[Tf_2N] was more challenging, because the products obtained were not pure after recrystallization according to the elemental analysis, which showed systematically higher proportions of carbon than expected. Column chromatography was attempted as an alternative purification method, but the AQ salts degraded on acidic silica, neutral silica and basic alumina.

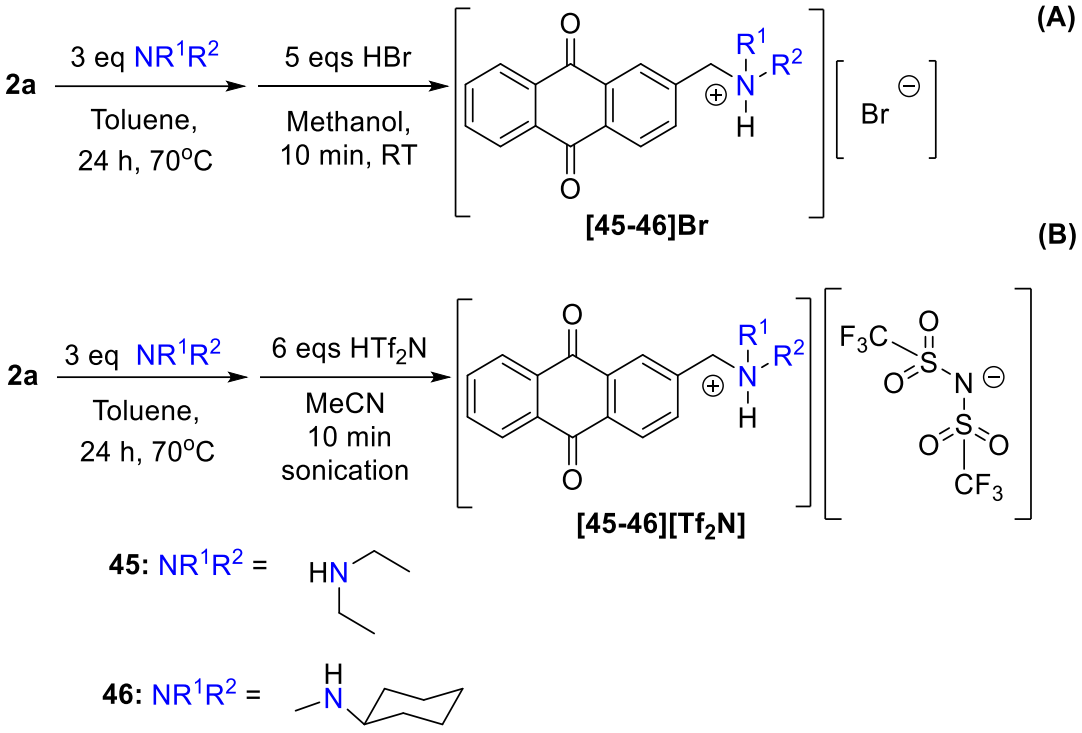

Scheme 4.2.3: Synthesis anthraquinones salts functionalised with protic ammonium groups. (A) Bromide salts, (B) Tf_2N^- salts

Instead, the Tf_2N^- salts were prepared by reacting **39a** with diethylamine and N-methylcyclohexylamine, as before, but the free amine was then protonated directly with $H[Tf_2N]$ to generate the protic [AQ][Tf_2N] salt (*Scheme 4.2.3-B*) (A detailed experimental description can be found in *section 5.2.2*).

Table 4.2.2: Isolated yields of protic anthraquinone salts

Entry	AQ	Isolated yield (%)	AQ/H_2O CHN Analysis	Water content (ppm)	Melting Point (ºC)
1	**[45]Br**	79	3/1	67	218-220
2	**[46]Br**	85	3/2	18	257-259
3	**[45][Tf_2N]**	78	3/1	8	145
4	**[46][Tf_2N]**	83	3/1	14	159

The melting point of all the salts was first measured with a Stuart SMP30 apparatus. Only the melting points if the Tf_2N^- salts were confirmed by DSC because the bromides showed thermal decomposition at their melting points.

The isolated yield of the protic AQ bromide salts was comparable to the yields for the aprotic AQ bromides, although for these reactions, 3 equivalents of amine had to be used to compensate for the lower nucleophilicity of the protic amines and the fact that the amine also works as the base to generate the corresponding tertiary amines functionalised with the AQ motif (*Table 4.2.4 entries 1 &2*).

The salt/water content ratio that best fit the experimental elemental analysis of salts **[45]Br** and **[46]Br** did not correlate with the water content obtained from the Karl-Fisher titrations. According to the elemental analysis, the **[45]Br**/H_2O and **[46]Br**/H_2O ratios were 3/1 and 3/2 respectively, which was interpreted as **[46]Br** being more hygroscopic. Nevertheless, according to the Karl-Fisher titrations, **[46]Br** exhibited lower water content than **[45]Br**, 18 ppm vs 67 ppm. The high hygroscopic nature of the bromide anion can cause the disparity between measurements, since the samples were exposed to the atmosphere for several days in between the elemental analysis experiments and the Karl-Fisher titrations. This means that the salts might have absorbed moisture at different rates during this period.

The protic salts **[45][Tf_2N]** and **[46][Tf_2N]** showed elemental analyzes that did not correlate with the theoretical value corresponding to the pure dry salts, which were observed for the aprotic salts **[41-44][Tf_2N]**. Instead, a salt/water ratio of 3:1 appeared to reproduce the atomic proportions observed in the elemental analysis from both **[45][Tf_2N]** and **[46][Tf_2N]**. This moisture can be caused by strong H-bond interactions with the acidic protons in the cations.

As reported for the aprotic AQ bromide salts, **[45]Br** and **[46]Br** decomposed on melting. **[45][Tf_2N]** showed a lower melting point than **[46][Tf_2N]** as observed for the aprotic salts (*Table 4.2.2* entries 3 & 4).

4.2.3 Structural characterization of anthraquinone salts.

The AQ salts were characterised by ^{1}H-NMR, ^{13}C-NMR, ESI-MS, and single-crystal X-Ray diffraction data was obtained for salts **[41]Br**, **[41][Tf_2N]**, **[42][Tf_2N]**, **[43][Tf_2N]**, **[44][Tf_2N]**, **[46][Tf_2N] and [46][Tf_2N]**. The AQ cationic

structures were modelled computationally at the DFT(BP86)/def-SV(P) to obtain insight into the molecular conformation of the salts in solution. The electronic structure of the salts was assessed through single point calculations at the DFT(PBE0)/def2-TZVPP level of theory including SMD solvation corrections to the energy (Acetonitrile, ε= 37.5 at 298 K) using Gaussian09 package. Full ^{1}H-NMR, ^{13}C-NMR and ^{19}F NMR characterization of the salts can be found in *section 6*

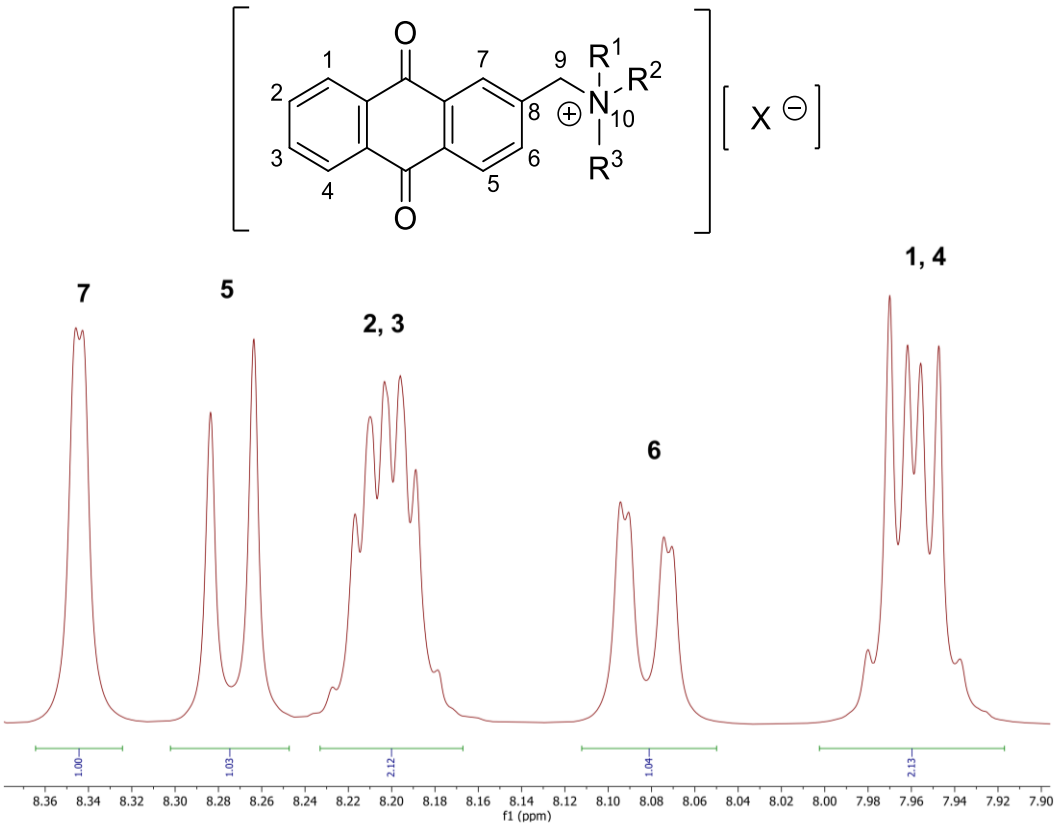

Figure 4.2.2: Example of the aromatic region from the ^{1}H-NMR spectrum of **[42]Br**.

The different proton environments from the aromatic region of the AQ motifs in the^{1}H-NMR spectrum became distinguishable again after replacing the C-Br bond with a C-N bond (in **39a**, all the aromatic environments coalesced into two broad signals, (*Figure 4.2.1*)). In all AQ salts, the most deshielded proton environments from the AQ motif corresponded to position 7 in *Figure 4.2.2* (doublet, small J^{4} due to *meta* H-H coupling) and 5 (doublet, big J^{3} due to *ortho* H-H coupling), followed by protons in positions 2 & 3 (multiplet), position 6

(doublet of doublets due to *ortho* and *meta* H-H couplings) and finally, 1 & 4 (multiplet), (*Figure 4.2.2*).

The chemical shift from the methylene bridge protons in position 9, behaved differently across the AQ salts. Their values are displayed in *Table 4.2.3*. Regardless of the solvent, the methylene bridge protons of the AQ salts appear further downfield compared with the starting material **39a** (*Table 4.2.3 entry 1*). This displacement can be a consequence of a strong inductive effect exerted by the new imidazolium and ammonium fragments through the C(15)-N(1) bond. Among studied AQs, **[41]Br** and **[41][Tf$_2$N]**, which contain an imidazolium fraction, exhibited significantly more deshielded methylene bridge protons compared with the rest of the salts (*Table 4.2.3 entries 1 & 6*). This contrast between **[41]Br** and **[41][Tf$_2$N]** with the rest of the salts could be due to the magnetic field induced by the imidazolium aromatic ring, which vector points perpendicularly to the imidazolium ring.

Table 4.2.3: Methylene bridge protons ^{1}H-NMR chemical shifts.

Entry	AQ	δ (ppm)
1[a]	**39a**	4.60
2[b]	**[41]Br**	5.73
3[b]	**[42]Br**	4.90
4[b]	**[43]Br**	4.91
5[c]	**[44]Br**	4.98
6[b]	**[45]Br**	4.61
7[b]	**[46]Br**	4.47-4.28
8[d]	**[41][Tf$_2$N]**	5.91
9[d]	**[42][Tf$_2$N]**	4.95
10[d]	**[43][Tf$_2$N]**	5.08
11[d]	**[44][Tf$_2$N]**	5.07
12[d]	**[45][Tf$_2$N]**	4.93
f13[d]	**[46][Tf$_2$N]**	4.65-5.15

^{1}H-NMR chemical shifts recorded in a 400 MHz spectrometer. [a]$CDCl_3$. [b]d_6-DMSO. [c]D_2O/d_6-acetone 1:1. [d]d_6-Acetone.

The molecular structure of the AQ cations were modelled in acetonitrile using DFT. The analysis of the optimised structures displayed in *Figure 4.2.3* showed that the imidazolium AQ cation exhibited the shortest C(9)-N(10) bond (1.49 Å) (*Figure 4.2.3-A*), a shorter C-N bond would draw more electron

density from the methylene protons, hence explaining the higher deshielding observed in NMR (*Table 4.2.4 entry 1*).

Table 4.2.4: Optimised C-N bond distances and methylene bridge angles for aprotic AQ cations

Entry	AQ cation	C(9)-N(10) Bond (Å)	C(8)-C(9)-N(10) Angle (º)
1	**41**$^+$	1.49	112.9
2	**42**$^+$	1.55	116.3
3	**43**$^+$	1.55	116.0
4	**44**$^+$	1.54	115.2
5	**45**$^+$	1.54	112.4
6	**46**$^+$	1.54	112.4

41$^+$: 1-methyl-3-(2-methylanthraquinone)imidazolium, **42**$^+$: N,N,N-triethyl(2-methylanthraquinone)ammonium, **43**$^+$: 1-Methyl-1-(2-methylanthraquinone)pyrrolidinium, **44**$^+$: 1-Methyl-1-(2-methylanthraquinone)piperidinium, **45**$^+$: N,N-Diethyl(2-methylanthraquinone)ammonium and **46**$^+$: N-cyclohexyl-N-methyl(2-methylanthraquinone)ammonium. The atom numbering is the same as the one used for the NMR spectrum in *Figure 4.2.2*

The protic ammonium cations exhibit the sharpest C(8)-C(9)-N(10) angles (112.4º) closely followed by the imidazolium cation (112.9º). (*Figure 4.2.3-E & F*) (*Table 4.2.4*. entries 5 & 6). Sharper angles for the methylene bridge were expected for the protic AQs since exchanging one alkyl chain for a proton reduces the steric hindrance around the ammonium group which allows the methylene carbon to better recover tetrahedral bond angles as compared to the aprotic AQs.

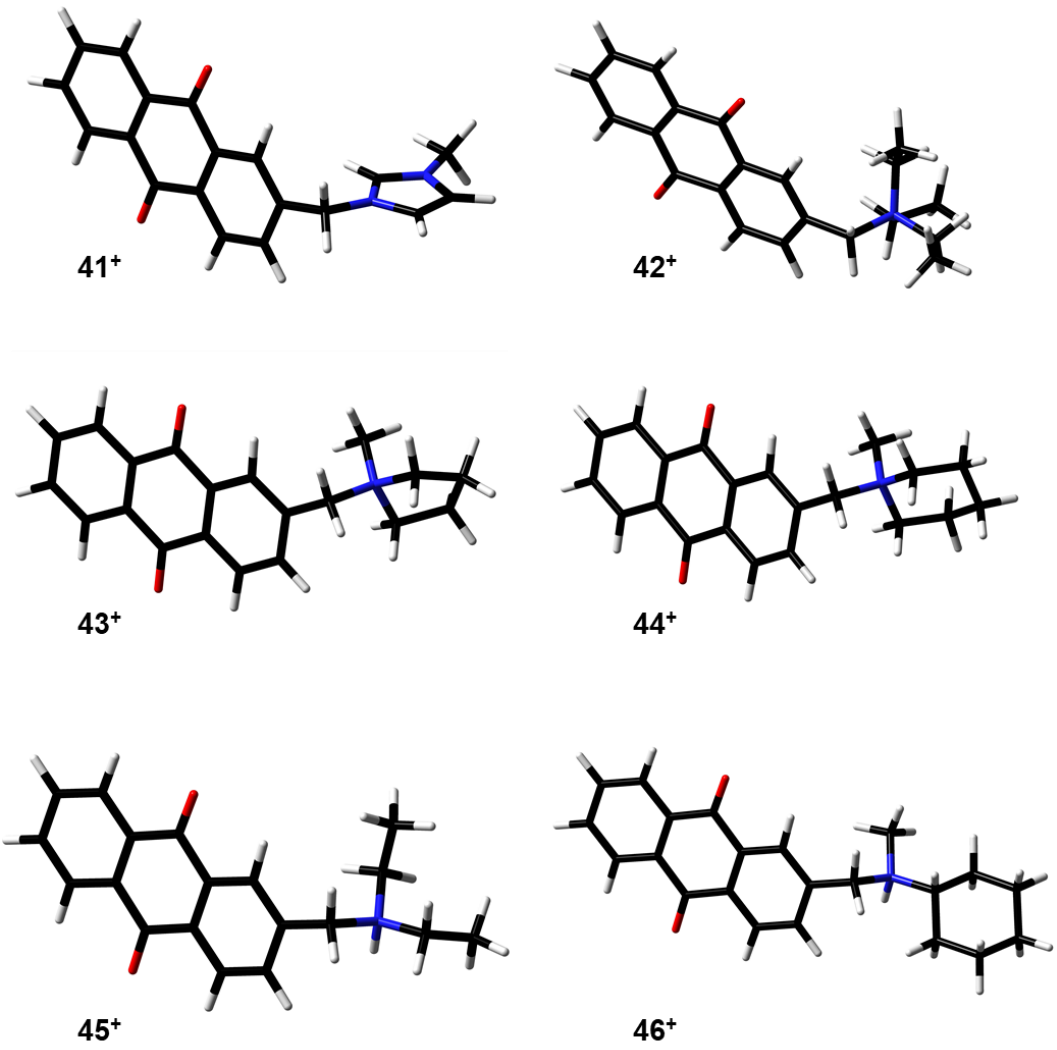

Figure 4.2.3: Optimised structures of aprotic AQ cations at the BP86/def-SV(P) level of theory. Each colour represents an atom, black: carbon, white: hydrogen, red: oxygen, blue: nitrogen. **41**$^{+}$: 1-methyl-3-(2-methylanthraquinone)imidazolium, **42**$^{+}$: N,N,N-triethyl(2-methylanthraquinone)ammonium, **43**$^{+}$: 1-Methyl-1-(2-methylanthraquinone)pyrrolidinium, **44**$^{+}$: 1-Methyl-1-(2-methylanthraquinone)piperidinium, **45**$^{+}$: N,N-Diethyl(2-methylanthraquinone)ammonium and **46**$^{+}$: N-cyclohexyl-N-methyl(2-methylanthraquinone)ammonium.

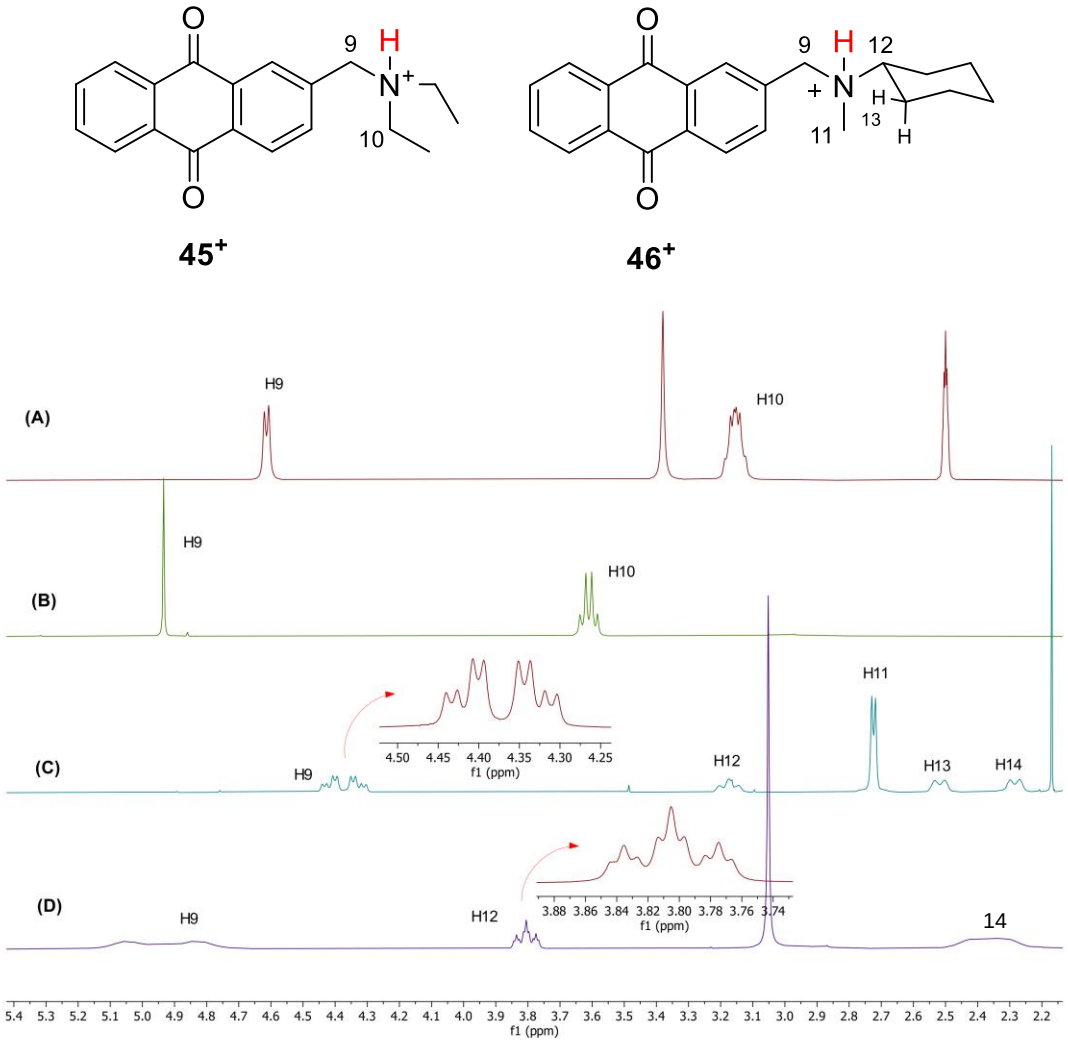

Figure 4.2.4: ^{1}H-NMR spectra of salts (A) **[45]Br** in d_6-DMSO, (B) **[45][Tf$_2$N]** in 1:1 D_2O/d_6-Acetone, (C) **[46]Br** in d_6-Acetone, (D) **[46][Tf$_2$N]** in d_6-Acetone featuring the peaks corresponding to the hydrogen atoms in the C-H positions alpha to the ammonium centre.

The ^{1}H-NMR spectrum of the hydrogen atom on the C-H positions alpha to the ammonium centre in the protic AQ bromides show interesting features that indicate that those protons are coupled to the acidic proton resting on N. Peak 9 in ^{1}H-NMR spectra (A) and (C) from *Figure 4.2.4* correspond to the methylene bridge hydrogen atoms from salts **[45]Br** and **[46]Br**. In the case of **[45]Br**, peak 9 is a doublet with a J^3 = 5.5 Hz that corresponds to a three bond coupling with the acidic proton, peak 10 which corresponds to the methylene hydrogen atoms from the ethyl chain, also coupled to the acidic proton with a similar J value, J^3 = 5.5 Hz.

The case of **[46]Br** (*Figure 4.2.4-C*) is more complicated, since peak 9 corresponding to the methylene bridge protons showed a multiplicity that seemed like a doublet of doublets of doublets although with wrong relative intensities. Each segment of the multiplet integrates for 1 hydrogen, the coupling constant between each small doublet is J = 5.4 Hz, the coupling constant between the two doublets of each segment is J = 13.3 Hz and the coupling in each segment is J = 37.3 Hz. These coupling values could represent the coupling of the methylene bridge hydrogen atoms with the acidic hydrogen, a class of *trans*-diaxial coupling and a geminal coupling respectively. Nevertheless, a ^{1}H-^{1}H COSY 2D-NMR experiment did not show any other coupling interactions involving the methylene bridge hydrogen atoms aside from with the acidic proton (*see Appendix I*) The methylene bridge hydrogen atoms, which are enantiotopic in **39a**, became diasterotopic when the free amine was protonated to obtain the ammonium salt. This turned the two methylene bridge hydrogen atoms chemically inequivalent and hence, detectable separately with ^{1}H-NMR.

Doublet 11 in spectrum (C) which corresponds to the methyl peak hydrogen atoms of **[46]Br**, reveals an interaction with the acidic proton through a J^{3} = 4.6 Hz coupling. Also, the broad triplet 12 reveals the axial hydrogen atom interacts with the acidic proton, with a J^{3} of approximately 2.5 Hz which suggest an axial-equatorial conformation. The broadening is likely caused because the other vicinal equatorial hydrogen atoms from the cyclohexane are coupled to the axial hydrogen 12, with similar coupling constant values. Although not shown for clarity, both spectra (A) and (C) from *Figure 4.2.4* show a peak corresponding to the acidic protons with chemical shifts of 9.88 ppm and 11.84 ppm respectively.

The ^{1}H-NMR spectra from the protic salts **[45][Tf$_2$N]** and **[46][Tf$_2$N]** depicting the hydrogen atoms in the C-H positions alpha to the ammonium centre are shown in *Figure 4.2.4-B & Figure 4.2.4-D* respectively. In the case of **[45][Tf$_2$N]**, peaks 9 and 10 suggest the coupling to the acidic proton is missing, since the doublet 9, from spectrum (A) and the quartet of doublets 10, from spectrum (A) become a singlet and a quartet respectively in spectrum (B).

The spectrum (D) of **[46][Tf_2N]** also suggest that the coupling to the acidic proton is missing, but in this case, the methylene bridge hydrogen atoms appeared as broad doublet with a J = 86.3 Hz, and the equatorial hydrogen atoms 13 and 14 from the cyclohexane ring went from two distinguishable doublets to a broad signal. The axial hydrogen 12 became a clear triplet of triplet, suggesting it lost the coupling to the acidic proton, which was broadening the triplet, while peak 11 corresponding to the methyl group hydrogen atoms became a singlet but neither of these two peaks were broadened. In both **[45][Tf_2N]** and **[46][Tf_2N]**, the peaks corresponding to the acidic protons were not detected. Hydrogen exchange with the d_6-acetone seems unlikely as a cause for the disappearance of the acidic proton peak. Even though the acidic hydrogen atoms were not detected in ^{1}H-NMR, the protonation and ion-paring of the free amines to obtain **[45][Tf_2N]** and **[46][Tf_2N]** was confirmed by elemental analysis and ESI-MS (See *section 5.2.2*).

While DFT modelling and NMR can provide information on the molecular structure of the AQ salts in solution, single-crystal structures offer information about the conformational arrangements the salts encounter when densely packed in the solid-state. Through these studies, the impact on the solid-state structure caused by replacing the AQ cationic moiety and the anion can be assessed, and a general picture of the most important intermolecular interactions displayed by these salts can be acquired. It was possible to grow single crystals and obtain single-crystal X-Ray diffraction data (XRD) from salts **[41]Br, [46]Br, [41-44][Tf_2N] and [46][Tf_2N]**. No XRD data from structures **[42-45]Br** and **[45][Tf_2N]** were obtained because the quality of the obtained crystals was not adequate.

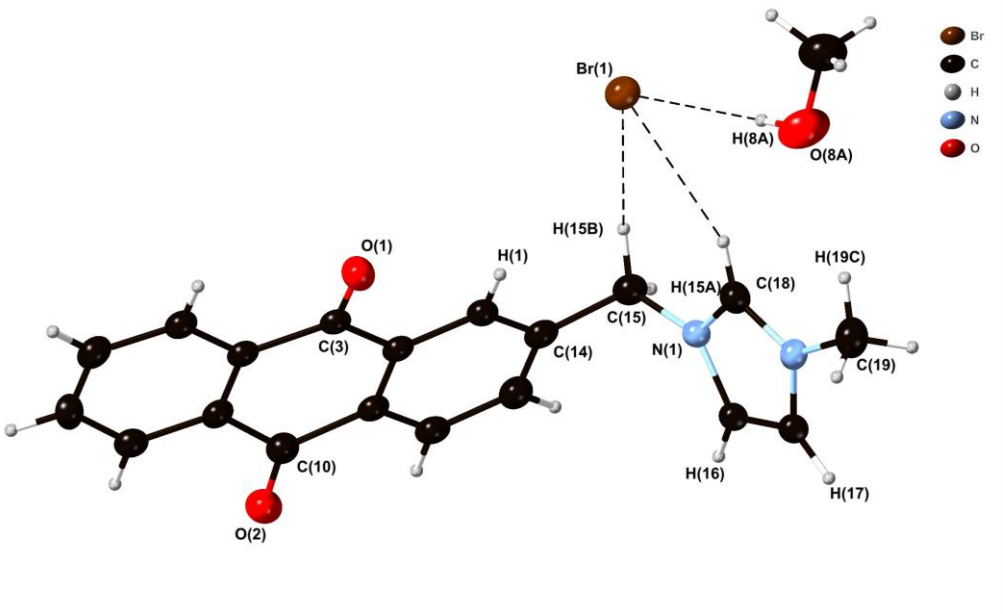

Figure 4.2.5: Single-crystal XRD structure of **[41]Br•**MeOH, ellipsoids at 50% probability. Selected bond lengths (Å) and angles (°), Atoms indicated with ‘, e.g. H(15B’) are associated with other molecules in the crystal lattice. Intermolecular interactions ranging between 2.5 and 3.3 Å were regarded as short contacts. O(1)-C(3) 1.219, O(2)-C(10) 1.221(6), N(1)-C(15) 1.476(6), Br(1)-C(15) 3.992, Br(1)-C(18) 3.992, C(14)-C(15)-N(1) 112.80, C(14)-C(15)-N(1)-C(18) -116.29. Angle between planes of AQ motif and imidazolium ring 62.1°. π-stacking interaction between AQ motifs: Distance from AQ centroid to the next closest AQ centroid 3.749 Å, distance from AQ centroid to next closest AQ plane 3.172 Å, interplanar angle 4.5°.

The crystal structures of **[41]Br** (*Figure 4.2.5*) and **[41][Tf$_2$N]** (*Figure 4.2.6*) showed some small differences in the AQ scaffold. While **[41][Tf$_2$N]** AQ scaffold is completely planar, in **[41]Br** the C_6 rings of the AQ motif are bent in a “v” shape of 8°. All C=O bonds lengths are the same (~ 1.23 Å on average) as the C=O bond lengths found for **38a**’s solid structure[212], which confirms that the functionalization methodology did not alter the aromaticity of the AQ significantly. Moreover, the AQ ring does not interact significantly with the anions through hydrogen-bonding. The interactions between different AQs motifs were dominated by π-stacking. In both salts, the stacking showed a small parallel displacement.

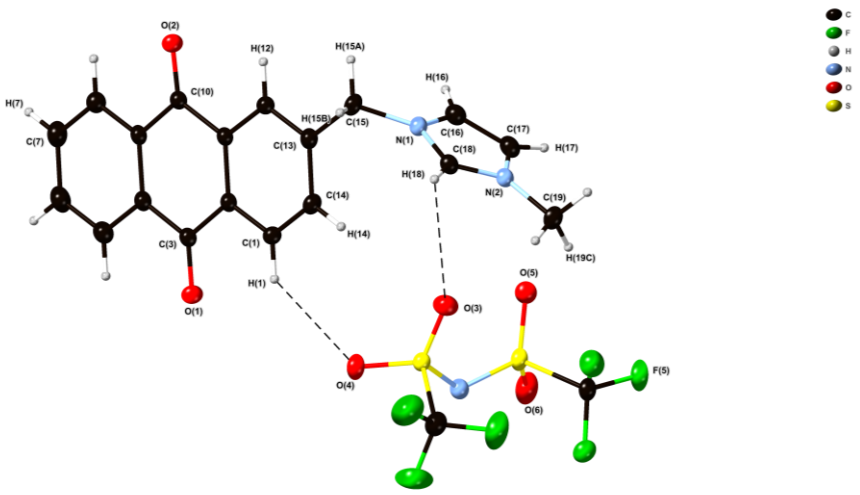

Figure 4.2.6: Single-crystal XRD structure of **[41][Tf_2N]**, ellipsoids at 50% probability. Selected bond lengths (Å) and angles (º), atoms indicated with ‘, e.g. H(15B’) are associated with other molecules in the crystal lattice. Intermolecular interactions ranging between 2.5 and 3.3 Å were regarded as short contacts. O(1)-C(3) 1.225, O1-C(15’) 3.227, O(2)-C(10) 1.226, O(2)-C(16’) 3.439, O(3)-C(18) 3.210, O(3)-N(2) 3.253, O(4)-C(1) 3.362, O(4)-C(17’) 3.419, O(5) -C(15’) 3.550, O(5)-C(7’) 3.506, O(5)-C(18’) 3.467, O(6)-C(14’) 3.254, C(15)-N(1) 1.473, C(13)-(C15)-N(1) 110.74, C(13)-(C15)-N(1)-C(18) -105.12,. Angle between planes of AQ motif and imidazolium ring 91.1º. π-stacking interaction between AQ motifs: Distance from AQ centroid to the next closest AQ centroid 3.789 Å, distance from AQ centroid to next closest AQ plane 3.438 Å, interplanar angle 0º.

In **[41]Br** the AQ layers are closer in the Z axis but the parallel displacement resulted more pronounced than in **[41][Tf_2N]**. The methylene bridge proton H(15A) in **[41]Br** exhibits a short and directional hydrogen-bonding interaction with the bromide (2.302 Å, 171º), whereas in **[41][Tf_2N]**, the methylene bridge protons interact with oxygen atoms from the quinone ring and Tf_2N^-. The Tf_2N^- fragment has three short contacts with the imidazolium ring protons, two through its oxygen atoms and one through fluorine (2.609 Å on average), among which O(4)-H(17’) hydrogen bond stands out for having an angle close to 180º and the shortest bond distance (2.496 Å).

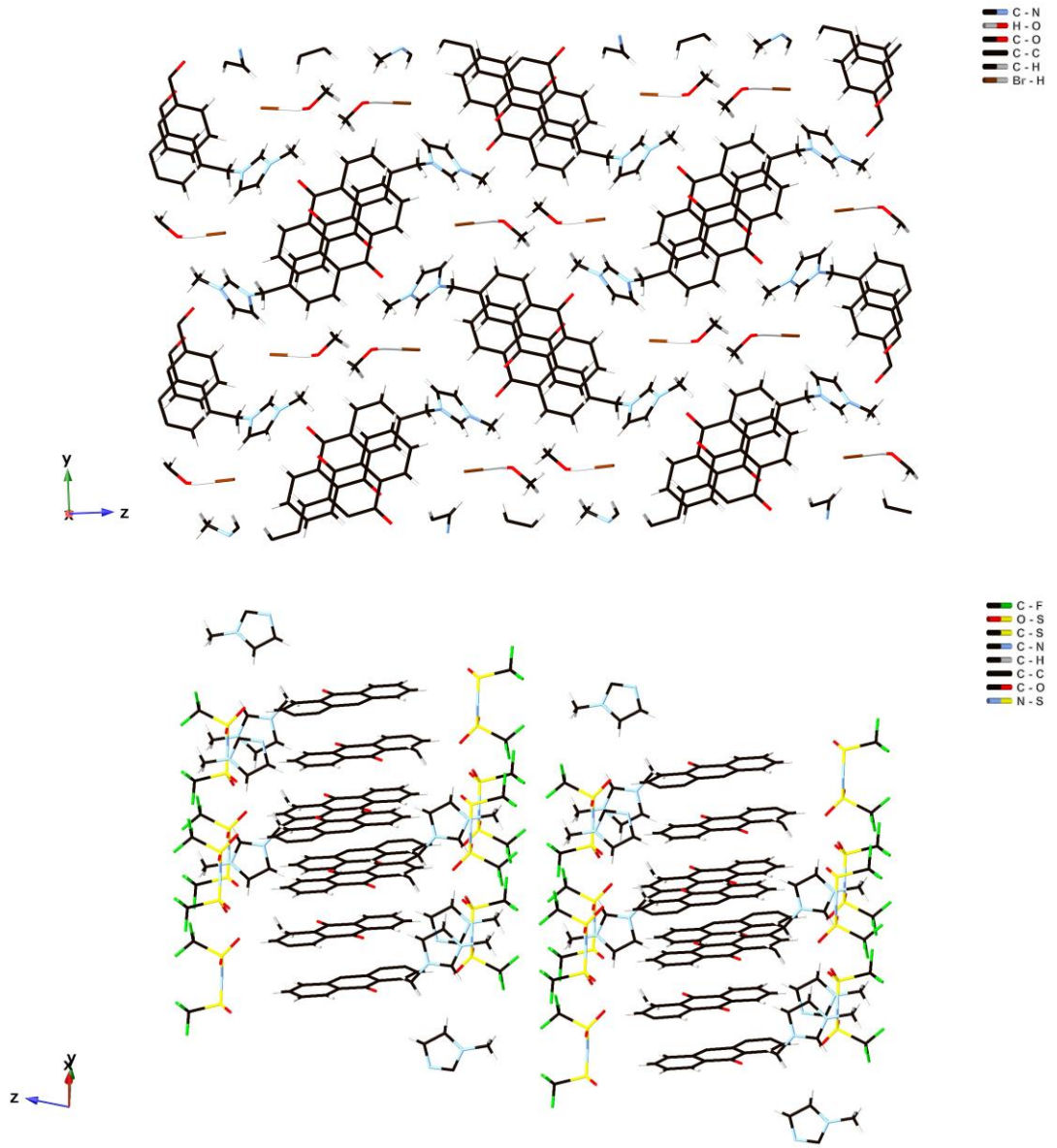

Figure 4.2.7: (Above) packing in the solid-state structure of **[41]Br**. (Below) packing in the solid-state structure of **[41][Tf_2N]**.

The cation/anion orientation was observed to be heavily dependent on the anion. In **[41]Br**, the bromide was located within voids in between two AQ layers, in close contact with the imidazolium ring, which displays hydrogen-bonding interactions through its ring protons and the methyl chain protons to Br. This orientation creates concentric zones dominated by ionic interactions between imidazolium fragments, bromide anions and solvent molecules surrounded by stacked AQs. (*Figure 4.2.7-above*). On the other hand, in

[41][Tf$_2$N], the imidazolium ring and the Tf_2N^- intercalate to the sides of stacked AQ layers, forming adjacent ionic planes surrounding another plane formed by stacked AQs . (*Figure 4.2.7-below*).

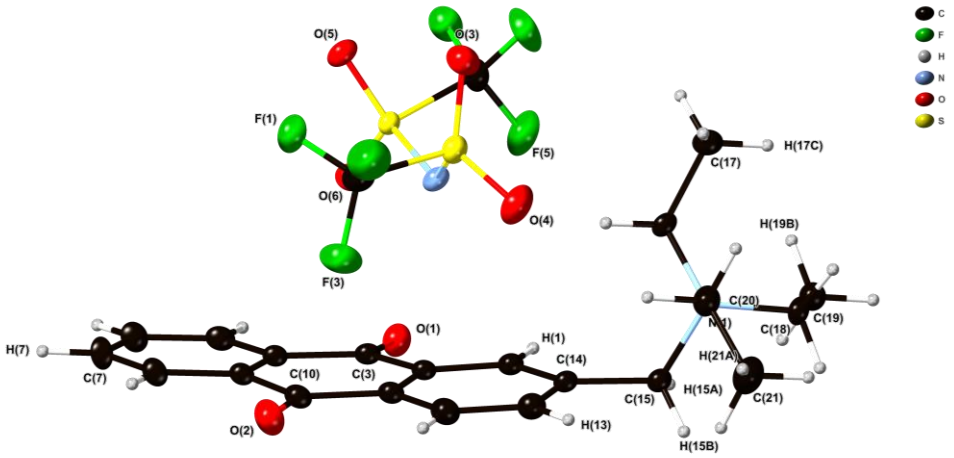

Figure 4.2.8: Single-crystal XRD structure of **[42][Tf$_2$N]**, ellipsoids at 50% probability. Selected bond lengths (Å) and angles (º), Atoms indicated with ‘, e.g. H(15B’) are associated with other molecules in the crystal lattice. Intermolecular interactions ranging between 2.5 and 3.3 Å were regarded as short contacts. O(1)-C(3) 1.218, O(1)-C(19’) 3.662, O(2)-C(10) 1.221, O(2)-C(21’) 3.287, O(3)-C(18’) 3.451, O4-C(20’) 3.498, O(5)-C(15’) 3.013, O(6)-C(7’) 3.511, C(15)-N(1) 1.524, C(14)-C(15)-N1 116.25. π-stacking interaction between AQ motifs: Distance from AQ centroid to the next closest AQ centroid 3.818 Å, distance from AQ centroid to next closest AQ plane 3.446 Å, interplanar angle 0º.

The solid-state structure from AQ salt **[42][Tf$_2$N]** shows that the Tf_2N^- anion is displaced from the lateral ionic plane observed in **[41][Tf$_2$N]** (*Figure 4.2.7 below*) to a new position closer to the AQ π-system (*Figure 4.2.8*). Another difference observed between **[41][Tf$_2$N]** and **[42][Tf$_2$N]** resides in the C-N bond length form the methylene bridge, in which the imidazolium salts have shorter bond distances than the alkylammonium salt (1.476 Å in **[41]Br**, and 1.502 Å in **[41][Tf$_2$N]** vs 1.524 Å in **[42][Tf$_2$N]**).The Tf_2N^- anion in **[42][Tf$_2$N]** appeared in a staggered conformation as opposed to the eclipsed conformation observed in **[41][Tf$_2$N]**, this maximises the interactions with the ethyl chains from the ammonium motif and the aromatic protons from the AQ ring. Tf_2N^- exhibits 1 short contact with aromatic protons through its oxygen

atoms and 2 contacts through its fluorine atoms. Tf_2N^- shows three short contacts with the methylene bridge protons, two through oxygen atoms and one through fluorine atoms, these contacts are very directional, close to 180º. The ethyl chain hydrogen atoms also have 4 short interactions with Tf_2N^-, but only through its oxygen atoms (2.625 Å on average). The π-stacking in **[42][Tf₂N]** is weaker than in **[41][Tf₂N]**, and it is characterised by a longer distance between AQ layers. The packing in **[42][Tf₂N]** shows Tf_2N^-occupying U shaped voids between three AQ cations, induced by the bulkiness of the ammonium substituent (*Figure 4.2.9*).

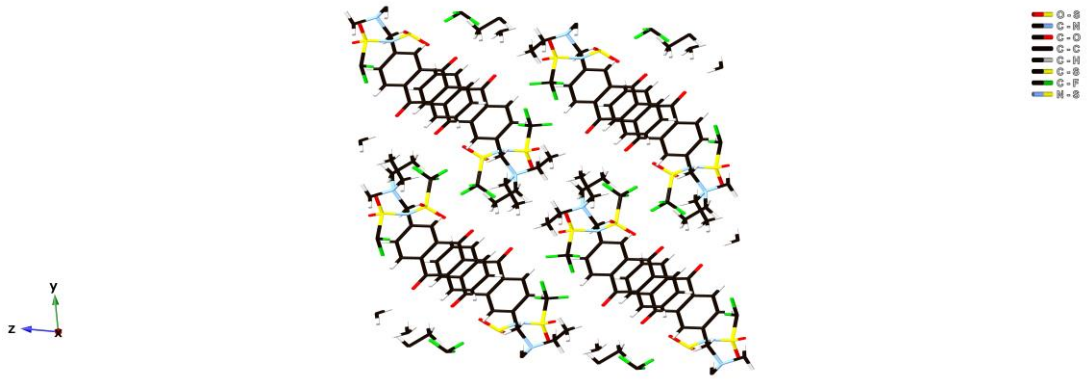

Figure 4.2.9: Packing in the solid-state structure of **[42][Tf₂N]**.

The solid-state structure of **[43][Tf₂N]** presents two AQ ion pairs per asymmetric unit, with a bigger intervention of the quinone oxygens in the hydrogen bond network. The interactions between O(3)-H(1A) and O(1)-H(27) stand-out from the others because they produce a distortion of 4º on the C=O(3) bond angle in the first case, and a bending of 2º on the C_6H_4 ring to which H(27) belongs (*Figure 4.2.10*). The Tf_2N^- anion in the **[43][Tf₂N]** solid-state structure has 10 short contacts with C-H hydrogen atoms from the pyrrolidinium motif (2.512 Å on average), which are shorter than the ones exhibited between the ammonium motif and the anion in **[42][Tf₂N]**. The amido nitrogen atoms from Tf_2N^- play a more significant role in the hydrogen bond network than the one observed for salts **[41][Tf₂N]** and **[42][Tf₂N]**, by

exhibiting highly directional contacts with the pyrrolidinium ring protons. As opposed to previous structures, fluorine atoms were relegated to a secondary role in which only interactions with one aromatic proton per AQ per Tf_2N^- were observed.

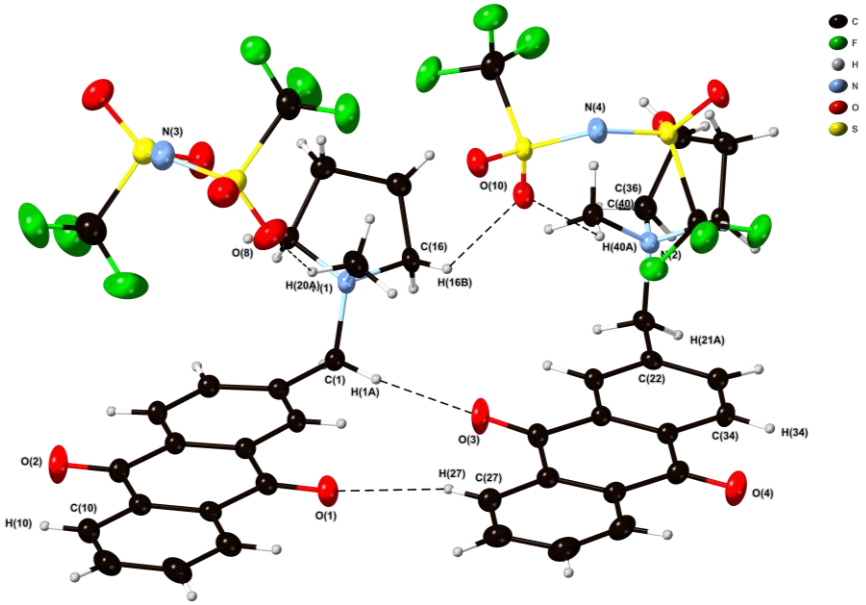

Figure 4.2.10: Single-crystal XRD structure of **[43][Tf_2N]** (two ion pairs are present in the asymmetric unit), ellipsoids at 50% probability. Selected bond lengths (Å) and angles (º), Atoms indicated with ‘, e.g. H(15B’) are associated with other molecules in the crystal lattice. Intermolecular interactions ranging between 2.5 and 3.3 Å were regarded as short contacts. O(1)-C(5) 1.222, O(1)-C(27) 3.214, O(2)-C(12) 1.219, O(2)-C(34’) 3.127, O(3)-C(25) 1.221, O(3)-C(1) 3.298, O(4)-C(32) 1.221, O(4)-C(10’) 3.492, N(1)-C(1) 1.517, O(10)-C(16) 3.319, O(10)-C(40) 3.181, N(3)-C(36’) 3.406, C(2)-C(1)-N(1) 113.51º, C(22)-C(21)-N(2) 114.00º. π-stacking interaction between anthraquinone motifs: Two stacking modes detected. Mode (1): Distance from AQ centroid to the next closest AQ centroid 3.628 Å, distance from AQ centroid to next closest AQ plane 3.357 Å, interplanar angle 0.0º. Mode (2) distance from centroid in one AQ C_6H4 ring to C_6H_3 ring centroid on the next closest AQ 3.520 Å, distance from AQ centroid on one ion to AQ plane on the next closest ion 3.382 Å, interplanar angle 0º

[43][Tf_2N] presents two π-stacking modes: the classical mode in which the centroid from the AQ motifs is aligned (with certain parallel displacement) and a new one in which the centroid of the AQ aligns better with the centroid from the C_6H_3 ring on the next AQ (*Figure 4.2.11-above*). Despite the differences in

the asymmetric unit of **[43][Tf_2N]** with respect to salts **[41][Tf_2N]** and **[42][Tf_2N]**, its packing in the solid-state structure resembles the arrangement of ionic and non-polar planes observed for AQ **[41][Tf_2N]**. These are formed from intercalating pyrrolidinium motifs and Tf_2N^- molecules on the sides, with the ionic planes adjacent to each other (*Figure 4.2.11-below*).

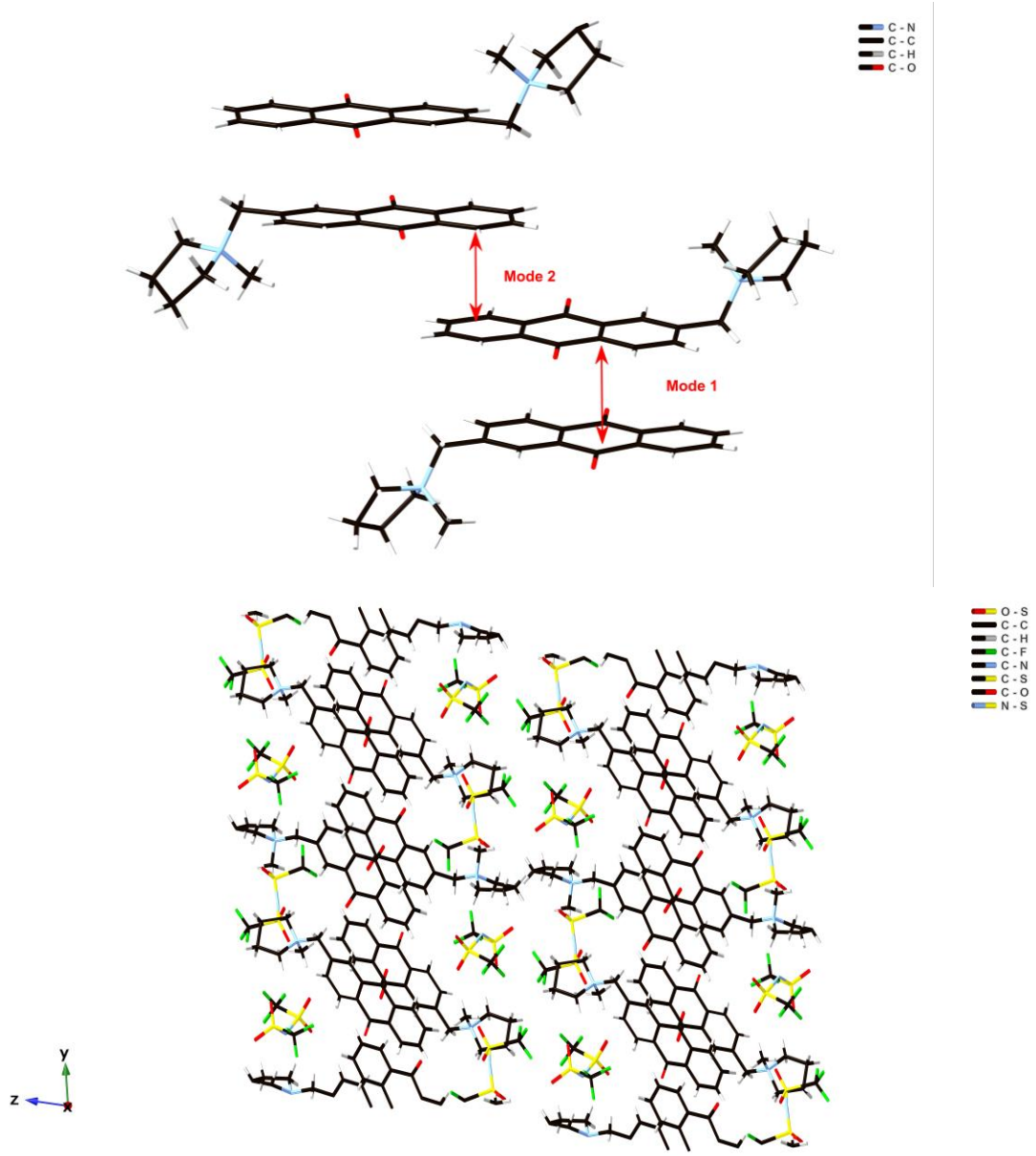

Figure 4.2.11: (Above) π-stacking modes observed in **[43][Tf_2N]** solid-state structure. (Below) Packing in the solid-state structure of **[43][Tf_2N]**

The asymmetric unit of **[44][Tf_2N]** shows a deformed AQ fragment in which the C_6H_3 ring is bent by approximately 5º with respect to the quinone ring and

the C_6H_4 ring by 1º. The deformation is caused by a series of short contacts between the aromatic protons with the quinone oxygen atoms from either other AQs or Tf_2N^-, which in this case lies closer to the C_6H_4 ring (*Figure 4.2.12*). This deformation from planarity could be responsible for reducing the aromaticity of the AQ and the absence of π-stacking.

The Tf_2N^- anion appeared opposite to the quaternary ammonium salt in the asymmetric unit from the solid-state structure of **[44][Tf$_2$N]**. Nevertheless, the anion intervenes in series of short contacts through its oxygen atoms, with the hydrogen atoms from the piperidinium fragments of other AQs (5 contacts, 2.579 Å on average) and aromatic hydrogen atoms from the AQ motif (3 contacts, 2.656 Å on average) (*Figure 4.2.12*).

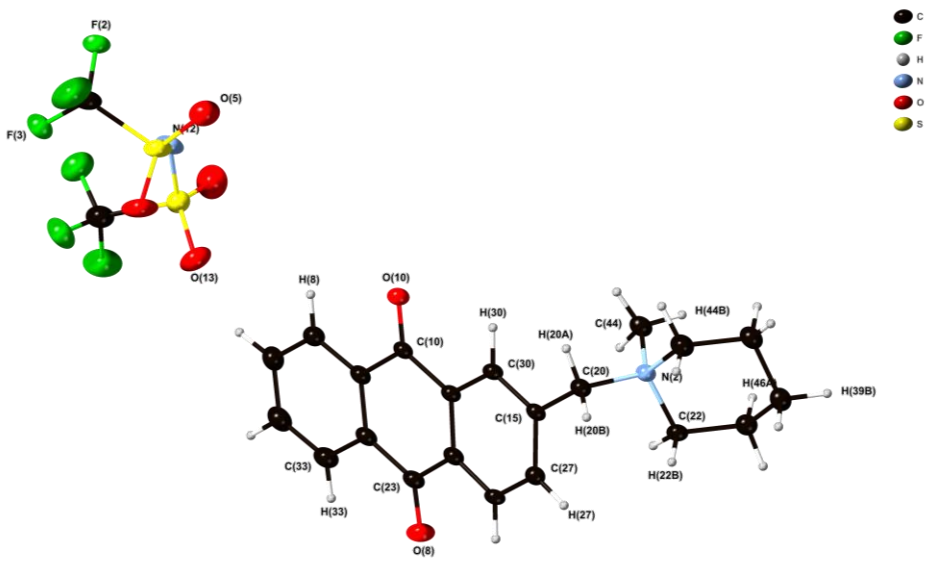

Figure 4.2.12: Single-crystal XRD structure of **[44][Tf$_2$N]**, ellipsoids at 50% probability. Selected bond lengths (Å) and angles (º), Atoms indicated with ‘, e.g. H(15B’) are associated with other molecules in the crystal lattice. Intermolecular interactions ranging between 2.5 and 3.3 Å were regarded as short contacts. O(4)-C(22’) 3.094, O(4)-C(27’) 3.433, O(8)-C(20’) 3.345, O(8)-C(23) 1.224, O(8)-C(30’), 3.383, O(10)-C(10) 1.222, O(10)-C(33’) 3.366, O(13)-C(20’) 3.355, N(2)-C(20) 1.528, 2.531, O(13)-H(20B’) 2.501, N(12)-C(44’) 3.328, C(15)-C(20)-N(2) 113.51o. π-stacking is not evident in this structure.

As observed in the solid-state structure **[43][Tf$_2$N]**, the CF_3 groups are relegated to a secondary role. On the other hand, the amide nitrogen is

involved in an intermolecular interaction with the piperidinium methyl group proton H(44B), but without the directionality observed in previous structures.

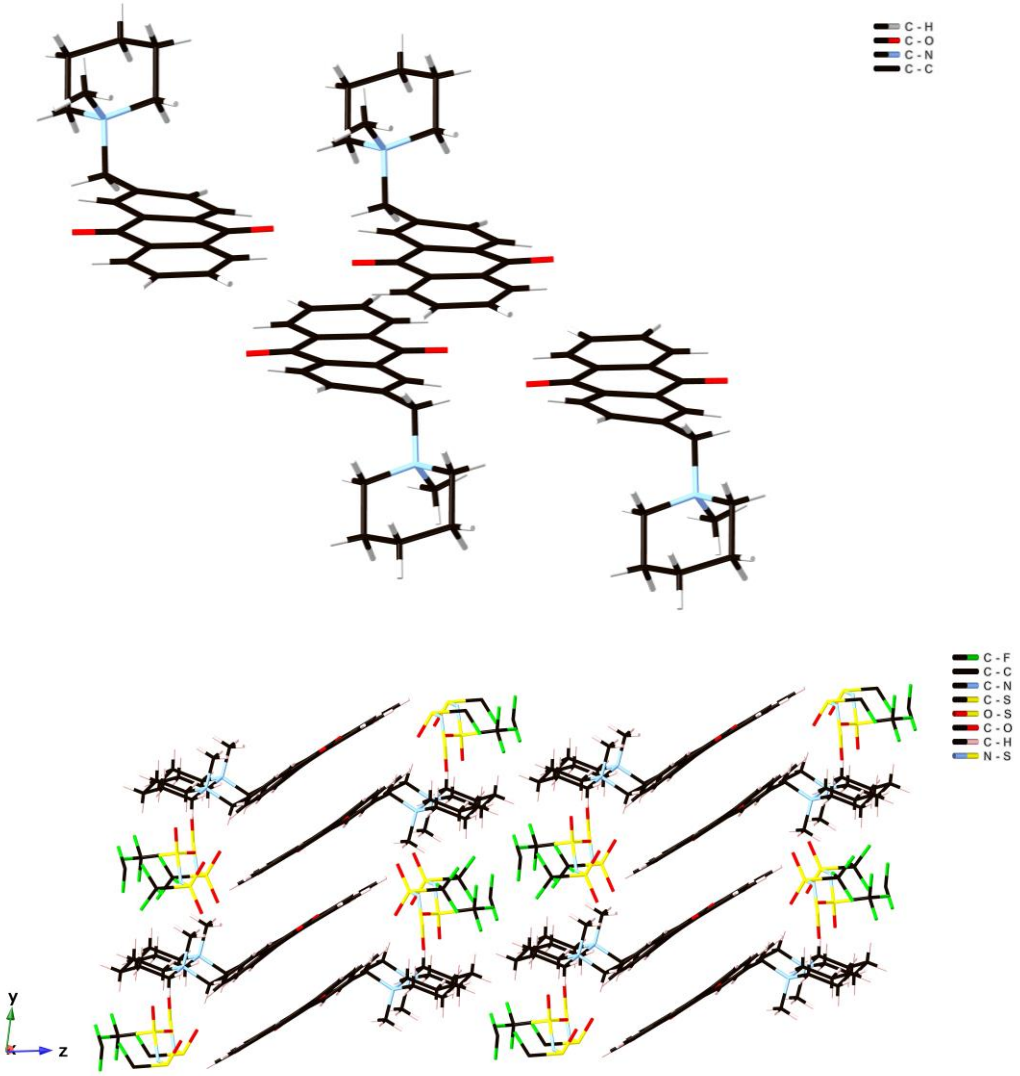

Figure 4.2.13: (Above) π-stacking modes observed in **[44][Tf$_2$N]** solid-state structure. (Below) Packing in the solid-state structure of **[44][Tf$_2$N].**

The packing in the solid state of **[44][Tf$_2$N]** was not observed to exhibit effective π-overlapping between AQs, due to a high degree of lateral displacement between consecutive AQ layers (*Figure 4.2.13-above*). Despite not having π-overlapping interactions, the AQ motifs in **[44][Tf$_2$N]** assembled in layers with comparative interplanar distances to the rest of the solid-state structures studied (3.639 Å) (*Figure 4.2.13-below*). Also, regardless of the lack of stacking, the AQ ion-pairs display a similar ordering as the one observed in

structures **[41][Tf_2N]** and **[43][Tf_2N]**, where non-polar planes made of AQ motifs are surrounded by ionic planes made of intercalated Tf_2N^- and piperidinium motifs.

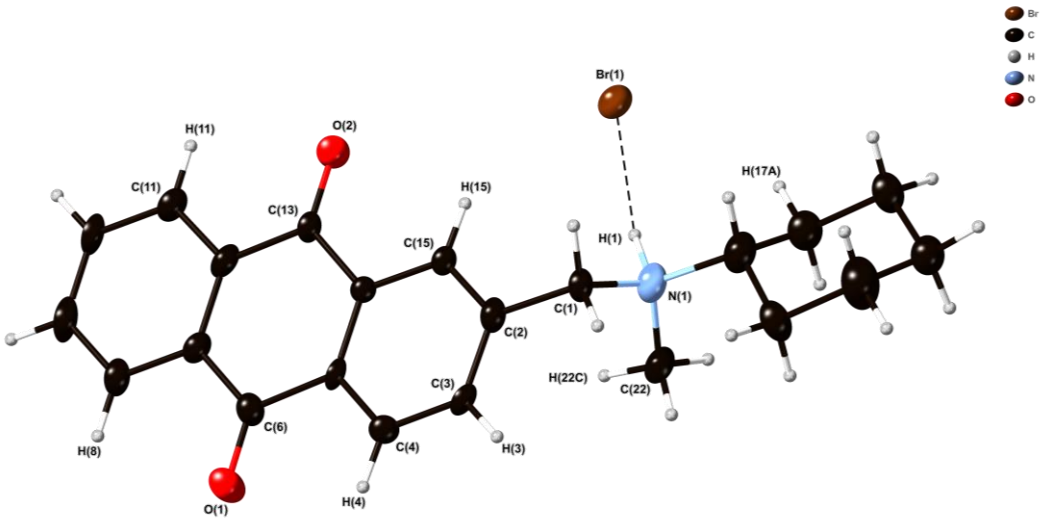

Figure 4.2.14: Single-crystal XRD structure of **[46]Br**, ellipsoids at 50% probability. Selected bond lengths (Å) and angles (º), Atoms indicated with ‘, e.g. H(15B’) are associated with other molecules in the crystal lattice. Intermolecular interactions ranging between 2.5 and 3.3 Å were regarded as short contacts. O(1)-C(6) 1.220, O(1)-C(11’) 3.266, O(2)-C(13) 1.214, O(2)-C(4’) 3.204, N(1)-C(1) 1.476, Br(1)-N(1) 3.295, Br(1)-C(3’) 3.910, Br(1)-C(15) 3.787, Br(1)-C(22’) 3.667, C(2)-C(1)-N(1) 112.91. π-π stacking interaction between AQ motifs: Distance from AQ centroid to next closes AQ centroid 4.078 Å, distance from AQ centroid to centroid from C_6H_4 ring belonging to next closes AQ 3.552 Å, distance from AQ centroid on one ion to AQ plane on the next closest ion 3.462 Å, interplanar angle 0º.

The solid-state structure from protic salt **[46]Br**, shows that quinone oxygen atoms participate in the network of intermolecular interactions only with aromatic hydrogen atoms from other AQs. In the aprotic salt **[41]Br**, the bromide sat close to the imidazolium ring and displayed short contacts with the methylene bridge hydrogen atoms and a molecule of solvent. In **[46]Br**, the presence of the acidic proton H(1) brought the bromide away from the methylene bridge through a short (2.297 Å) and directional (162º) hydrogen bond (*Figure 4.2.14*).

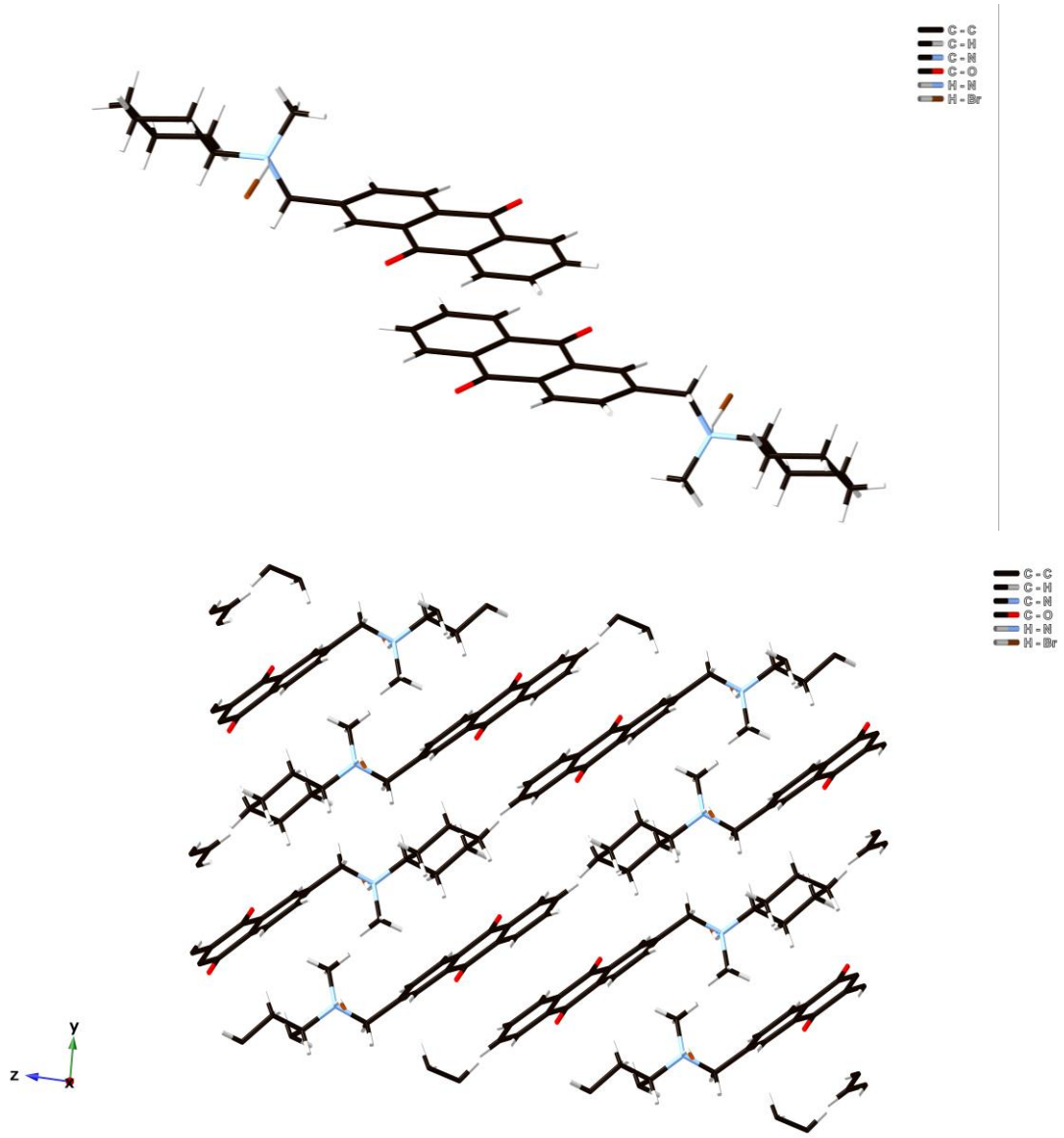

Figure 4.2.15: (Above) π-stacking observed in **[46]Br** solid-state structure. (Below) Packing in the solid-state structure of **[46]Br**

The bromide also interacted with the hydrogen atoms from the methyl and cyclohexyl groups, although with slightly longer contacts (5 contacts, 2.941 Å on average). **[46]Br** exhibits π-stacking between AQ layers although the next closest layer was displaced in such a way that the centroid from one AQ motif matches the centroid from the C_6H_4 ring of the next closest layer (*Figure 4.2.15 above*).

The solid-state packing of **[46]Br** shows the bromide anions sitting close to ammonium fragments. In this case the polar/non-polar layering is not present. Despite this, the ionic fragments are aligned to some extent, while the AQ rings and the cyclohexane rings are preferentially located to the side of the ionic regions in an alternating fashion. The ionic regions are not adjacent to each other because the cyclohexane ring prefers to sit closer to an AQ motif, (*Figure 4.2.15-below*).

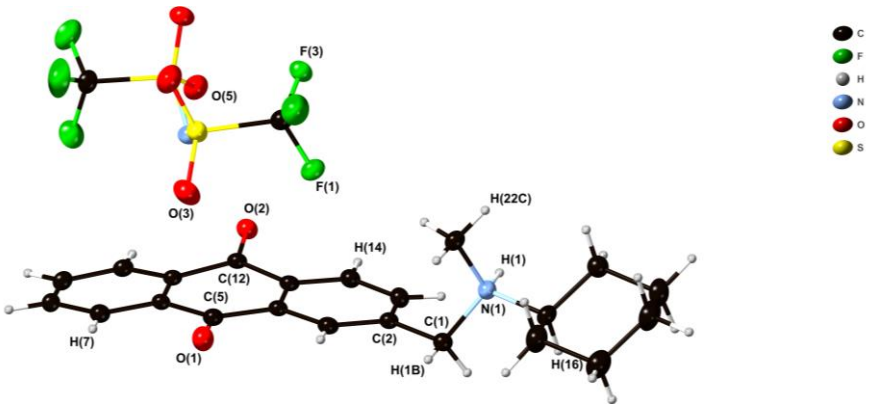

Figure 4.2.16: Single-crystal XRD structure of **[46][Tf$_2$N]**, ellipsoids at 50% probability. Selected bond lengths (Å) and angles (°), Atoms indicated with ‘, e.g. H(15B’) are associated with other molecules in the crystal lattice. Intermolecular interactions ranging between 2.5 and 3.3 Å were regarded as short contacts. O(1)-C(5) 1.216, O(2)-C(12) 1.223, O(2)-N(1’) 2.929, O(3)-C(1’) 3.508, O(5)-N(1’) 2.996, O(5)-C(16’) 3.097, O(6)-C(7’) 3.159, N(1)-C(1) 1.504, C(2)-C(1)-N(1) 112.87. O(2) is pulled out of the AQ plane by 8.06° due to a strong hydrogen-bonding interaction with H(1). π-stacking interaction between AQ motifs: Distance from AQ centroid to next closes AQ centroid 4.877 Å, distance from AQ centroid to centroid from C6H3 ring belonging to next closes AQ 3.923 Å, distance from AQ centroid on one ion to AQ plane on the next closest ion 3.554 Å, interplanar angle 0°.

The solid-state structure of salt **[46][Tf$_2$N]** presents the most deformed quinone ring among the studied structures with O(2) being held out of plane of the AQ motif by 8°. This deformation is caused by a strong hydrogen-bonding interaction between O(2) and the acidic proton H(1) from the ammonium fragment of a neighbouring cation, which although not very directional (141°) represents the shortest hydrogen bond detected among the studied AQ salts (2.170 Å). The structure **[46][Tf$_2$N]** also presents the longest inter-planar distance between AQ motifs.

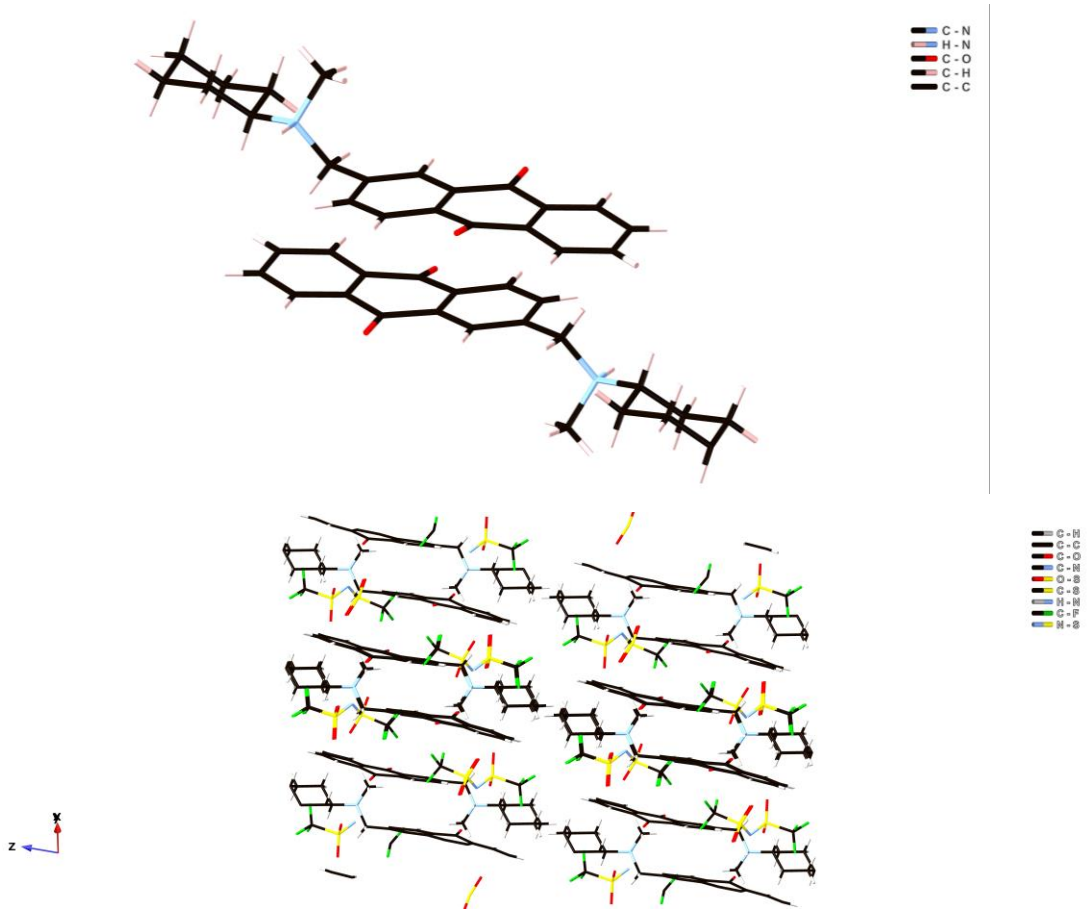

Figure 4.2.17: (Above) π-stacking observed in **[46][Tf$_2$N]** solid-state structure. (Below) Packing in the solid-state structure of **[46][Tf$_2$N]**

The Tf_2N^- in **[46][Tf$_2$N]** sits closer to the AQ motif, as observed with triethylammonium Tf_2N^- salt **[42][Tf$_2$N]** due to the bulkiness of the ammonium substituents. This arrangement allows it to interact with the acidic proton of neighbouring AQ cations while avoiding the cyclohexane ring. The Tf_2N^- anion interacts with the methylene bridge protons through its O(3) atom, although the number of interactions between these two fragments is smaller compared to the aprotic salts. The Tf_2N^- displays five other short contacts with the AQ motif, the methyl group hydrogen atoms, and the cyclohexane ring hydrogen atoms through their oxygen atoms (2.598 Å on average) and fluorine atoms (2 contacts of 2.620 Å on average).

The π-stacking present in structure **[46][Tf_2N]** exhibits a more pronounced parallel displacement compared for example to structure **[42][Tf_2N]**. This causes the centroid from an AQ layer to align better with the centroid of the C_6H_3 ring from the next closest AQ, rather than with the next closest AQ centroid. Alongside the deformation described on the quinone ring, this displacement produces a longer interplanar distance compared to other similar structures like **[42][Tf_2N]** and **[46]Br**. The packing in **[46][Tf_2N]** resembles the one observed in structure **[42][Tf_2N]**, in which rather being organised in ionic and non-polar planes, the anion sits in voids between AQ layers to maximise ionic interactions with other anions and with the acidic proton from the ammonium fragment.

4.2.4 Summary of the synthetic section

Overall, the study of the AQ salts in solution by means of ^{1}H-NMR showed that the chemical shift of the aromatic hydrogens from the AQ ring remained unaltered regardless of the cationic substituents and the anion. On the other hand, the chemical shift of the methylene bridge hydrogen atoms showed more variability depending on the salt. Among the AQ bromides analyzed in the same NMR solvent (d_6-DMSO), the deshielding of the methylene bridge hydrogen atoms followed the trend **[41]Br** > **[43]Br** ≈ **[42]Br** > **[45]Br** > **[46]Br**. Similarly, the deshielding of the methylene bridge hydrogen atoms from the Tf_2N^- salts (analyzed in d_6-acetone), followed the trend **[41][Tf_2N]** > **[43][Tf_2N]** ≈ **[44][Tf_2N]** > **[42][Tf_2N]** ≈ **[45][Tf_2N]** > **[46][Tf_2N]**.

The imidazolium salts were observed to exhibit the most deshielded methylene bridge hydrogens, this was partially a consequence of a deshielding effect between the magnetic field of the hydrogen atoms and the magnetic field of the imidazolium aromatic ring. The displacement of the chemical shift was also a consequence of intermolecular interactions between the methylene bridge hydrogen atoms and either the anions or carbonyl oxygen atoms from other AQs. Therefore, the observed trends indicate the extent to which the anions or the carbonyl oxygen atoms from other AQs remain close to the methylene bridge hydrogen atoms and the cationic centre. As such, these trends also

indicate the degree of steric hindrance introduced by the ammonium fragments.

The solid-state structures from the AQ bromide salts **[41]Br** and **[46]Br** showed that the bromide anion was located close to the positive nitrogen atom and the methylene bridge hydrogen atoms. In **[46]Br**, the presence of the acidic hydrogen pulled in the bromide. In both salts, the anion was surrounded by cationic fragments, while the AQ ring fragments were located outside of these ionic domains. On the other hand, in the [AQ][Tf_2N] salts, the anion preferred to be located farther from the methylene bridge region due to its larger size. Depending on the steric hindrance caused by the cation alkyl substituents, the anion sat closer to the AQ ring or to the alkyl groups. In salts **[41][Tf_2N]**, **[43][Tf_2N]**, **[44][Tf_2N]** the Tf_2N^- anion was observed to sit close to the ammonium or imidazolium fragments, which generated arrays of adjacent layers composed of alternating cationic/anionic fragments, and non-polar layers composed only of AQ fragments. Conversely, in salts **[42][Tf_2N]** and **[46][Tf_2N]**, the anion was located close to the AQ motifs due to steric hindrance with the cation alkyl substituents. Consequently, in these two cases, the polar/non-polar layering was lost.

The carbonyl functional groups of the AQ salts studied remained mostly unaltered when compared to starting material **38a**, except for **[46][Tf_2N]**. In all cases, the carbonyl oxygen atoms interacted mainly with aromatic hydrogen atoms or the methylene bridge hydrogen atoms from neighbouring AQ fragments. These interactions do not significantly modify the C=O bond length, which remained relatively constant alongside the series (around 1.23 Å) nor the angle between the C=O bond and the AQ plane (≈ 0^o). In **[46][Tf_2N]** one of the carbonyl oxygen atoms exhibited a strong interaction with the acidic hydrogen atom bonded to the ammonium centre of a neighbouring cationic fragment. This hydrogen-bonding interaction pulled the oxygen atom out of the AQ plane and distorted the AQ ring but did not disrupt the π-stacking.

Salts **[41]Br**, **[41][Tf_2N]**, **[42][Tf_2N]**, and **[46]Br** exhibited flat AQ ring motifs in their solid-state structures, while salts **[43][Tf_2N]**, **[44][Tf_2N]** and **[46][Tf_2N]**

showed certain distortions. In salts, **[43][Tf_2N]**, **[44][Tf_2N]** lateral aromatic rings were bent due to interactions of their aromatic protons with oxygen atoms coming from either neighbouring carbonyl groups or Tf_2N^- anions, the distortion was more pronounced in the case of **[44][Tf_2N].** As mentioned previously, the quinone ring of **[46][Tf_2N]** was distorted by a strong hydrogen-bonding interaction between one of the carbonyl oxygen atoms and a neighbouring acid hydrogen atom. Despite this distortion, all AQ salts but **[44][Tf_2N]** showed π-stacking with different degrees of lateral displacement. The absence of π-stacking in **[44][Tf_2N]** was attributed to the high degree of distortion of the C_6H_3 ring.

4.2.5 Electrochemical characterization of anthraquinone salts

4.2.5.1 Electrochemical studies of 2-methylanthraquninone and the imidazolium salts

The cyclic voltammetry of compound **38a** in acetonitrile was obtained first to compare its curve shape, potential and current parameters with the AQ salts to determine how the functionalization of the AQ affects their electrochemical behaviour.

$$1)\ AQ + e^- \rightleftharpoons AQ^{\bullet -}$$

$$2)\ AQ^{\bullet -} + e^- \rightleftharpoons AQ^{2-}$$

Scheme 4.2.4: One-electron two-step electrochemical redox mechanism of AQs

The CV of starting material **38a** is displayed in *Figure 4.2.18*. The cyclic voltammogram showed two reduction and oxidation waves $\mathbf{I_c/I_a}$ corresponding to the first redox process and $\mathbf{II_c/II_a}$ corresponding to the second redox process described in *Scheme 4.2.4*, which are separated by a few hundred mV. **38a** exhibited a quasi-reversible stepwise two-electron reduction to generate a radical anion intermediate in the first step, and a dianionic species in the second step according to *Scheme 4.2.4*.

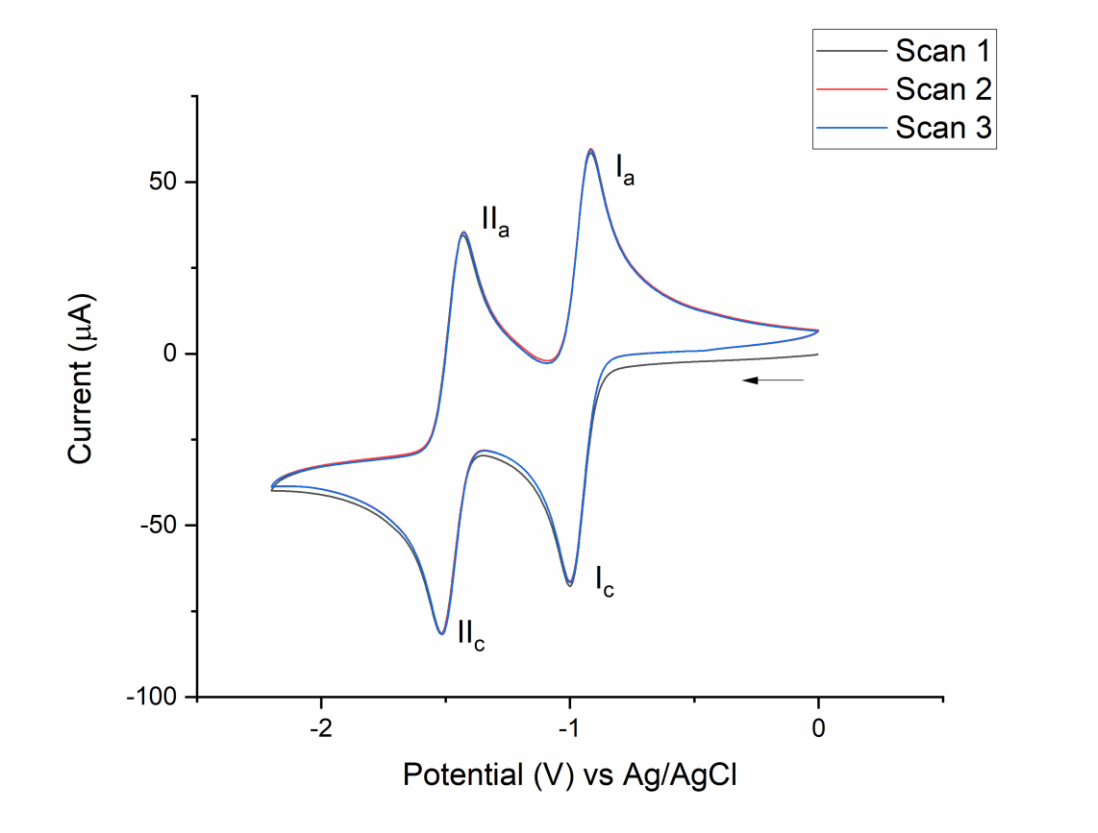

Figure 4.2.18: Cyclic voltammogram of **38a** in acetonitrile/NBu_4PF_6 0.1 M

Table 4.2.5: Electrochemical parameters of **38a** and the imidazolium salts.

Entry	AQ	$E_{1/2}$(1) (V vs Ag/AgCl)	$E_{1/2}$(2) (V vs Ag/AgCl)	ΔEp (I) (mV)	ΔEp (II) (mV)	Ip_c/Ip_a (I)	Ip_c/Ip_a (II)
1[a]	**38a**	-0.96	-1.47	84	88	1.04	0.85
2[a]	**[41]Br**	-0.82	-1.23	82	78	1.13	0.83
3[a]	**[41][Tf_2N]**	-0.82	-1.29	98	114	0.94	0.74
4[b]	**[41][Tf_2N]**	-0.49	-0.80	234	122	1.21	0.66

CV parameters: Ip_c (cathodic current peak height) Ip_a (anodic current peak height. [a]Experiment conducted in acetonitrile and 0.1M NBu_4PF_6. [b]Experiment conducted in [C_2Mim][Tf_2N] IL

The cathodic and anodic current peak heights from the first redox wave $\mathbf{I_c/I_a}$ were almost equal (*Table 4.2.5 entry 1*), which alongside a peak-to-peak separation of 84 mV, indicated that the reduction from the neutral AQ to the radical anion is quasi-reversible. On the other hand, the cathodic and anodic peaks from the second redox wave exhibited an Ip_c/Ip_a ratio of 0.85 while the peak-to-peak difference was of 88 mV. This suggested that the second redox

process, corresponding to the reduction of the radical anion to generate a dianion is less reversible than the first process.

It was observed that the CV of **38a** was in agreement with the previous research discussed in the introduction that reported that the second redox-wave peak heights were lower than the first redox wave peak heights, with Ip_c/Ip_a ratios < 1.[194,196,197]

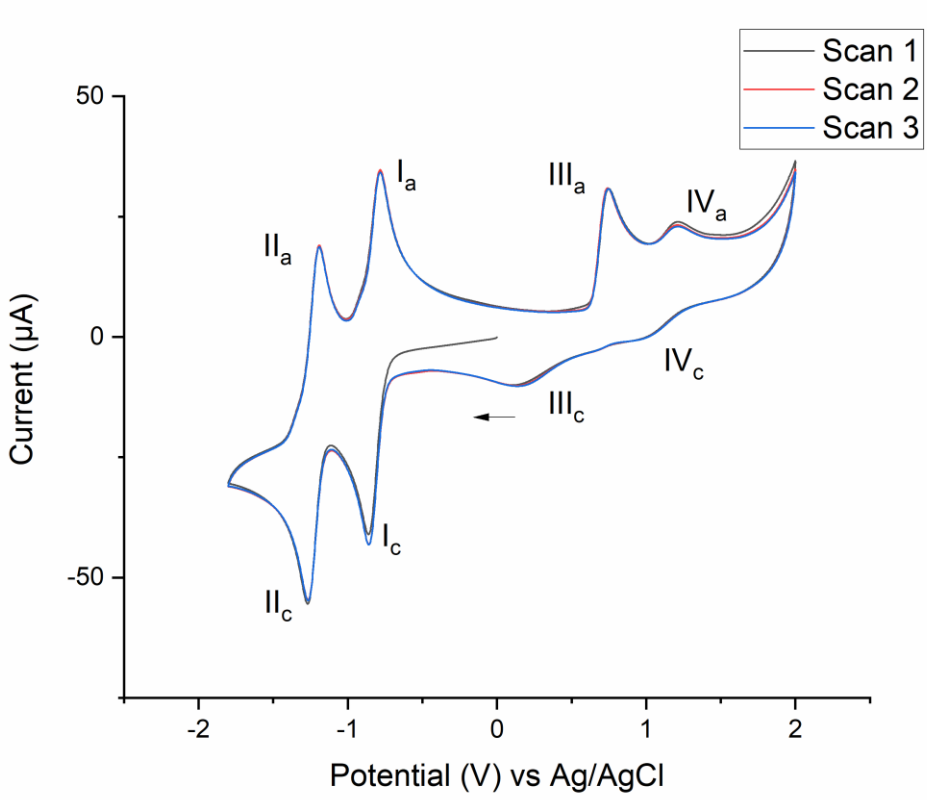

Figure 4.2.19: Cyclic Voltammogram of **[41]Br** in acetonitrile/NBu_4PF_6 0.1 M

The CV from salt **[41]Br** showed two more redox waves **IIIc/IIIa** and **IVc/IVa** at positive potentials in addition to the two redox processes associated with the AQ motif (*Figure 4.2.19*). These new redox waves exhibited sluggish and electrochemically irreversible processes characterised by two anodic peaks **III_a** and **IV_a**, separated by 440 mV, accompanied by two reductions peaks separated by 830 mV. These waves are associated with the redox process of the bromide anion. The first and highest anodic peak **III_a** corresponds to the oxidation of bromide to form tribromide, while the second process has been

attributed to the oxidation of the trihalide to generate Br_2 (*Scheme 4.2.5*, Figure *4.2.20*).[213]

$$3Br^- \rightleftharpoons Br_3^- + 2e^-$$

$$2Br_3^- \rightleftharpoons 3Br_2 + 2e^-$$

Scheme 4.2.5: Electrochemical redox mechanism of bromide anion.[213]

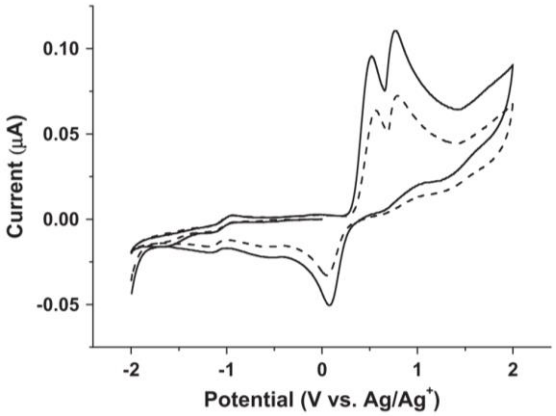

Figure 4.2.20: Cyclic voltammogram of $[C_4mim]Br$ (solid line) and Bu_4NBr (dash line) in $[C_4Mim]PF_6$, recorded with a Pt electrode. Adapted from Ju, Yin and Chen.[213]

The cyclic voltammetry experiments developed by Chen and co-workers exhibited in *Figure 4.2.20* also revealed that the $[C_4mim]Br$ imidazolium salt does not undergo any redox processes at potentials between -1.5 V and 0.0 V and that the cathodic limit of this ionic liquid occurs at potentials near -2.0 V vs Ag/AgCl when a Pt electrode is used as WE. In different research, voltamperommetric experiments of the C_2Mim^+ imidazolium cation carried out by Xie and Riechel in acetonitrile/tetrabutylammonium perchlorate using a glassy carbon electrode as WE, found similar results in which the imidazolium cation did not exhibit any redox processes at potentials between -1.5 V and 0.0 V.[214] In this regard, these evidences confirm that the imidazolium fragment of **[41]Br** should not undergo any redox processes at the working potentials and that the two sets of redox waves observed between -1.5 V and -0.7 V in

the CV of **[41]Br** (*Figure 4.2.19*), were due to the redox processes undergone by the AQ fragment.

The two AQ redox waves were separated by 410 mV and appeared at more anodic potentials than **38a,** which means that **[41]Br** possess a higher electron affinity and can better stabilize the received charge (*Table 4.2.5 entry 2)*. Moreover, the peak-to-peak gaps for the first and second waves of 82 and 78 mV respectively, alongside similar peak-to-peak distances for both processes suggested that the redox processes from **[41]Br** are slightly more electrochemically reversible than in **38a**.

The reasons for the shifting of the redox potentials from **[41]Br** to more positive potentials compared to **38a** is not well understood. A possible explanation could be that the introduction of the imidazolium group modified the AQ redox-active core by pulling electron density from the AQ aromatic system, thus increasing the AQ's the electron affinity. Another explanation could be that the introduction of a positively charged group stabilizes the negatively charged singly and doubly reduced species, by electrostatic charge stabilisation. A combination of both phenomena is also likely.

To investigate if the electronic structure of the AQ redox-active core was modified with the introduction of the imidazolium fragment, the electronic structure of the fully oxidized species **38a** and $\mathbf{41^{+}}$, as well as the singly and doubly reduced species $\mathbf{41^{\bullet}}$ and $\mathbf{41^{-}}$ were calculated using DFT including solvent corrections for acetonitrile (The computational methodology was detailed in *section 2.3.2*). *Figure 4.2.21* compares the highest occupied molecular orbitals (HOMO) singly occupied molecular orbitals (SOMO) and lowest unoccupied molecular orbitals (LUMO) of compounds **38a** and the AQ-imidazolium fragments $\mathbf{41^{+}}$, $\mathbf{41^{\bullet}}$ and $\mathbf{41^{-}}$. The electronic stability of every species can be qualitatively compared by analyzing the shape of the HOMO or SOMO orbital, which shows the location of the valence-shell electrons. A more dispersed orbital is indicative of higher stability.[204,215] On the other hand, the energy of the LUMO correlates with the electron affinity of the species.[204,215]

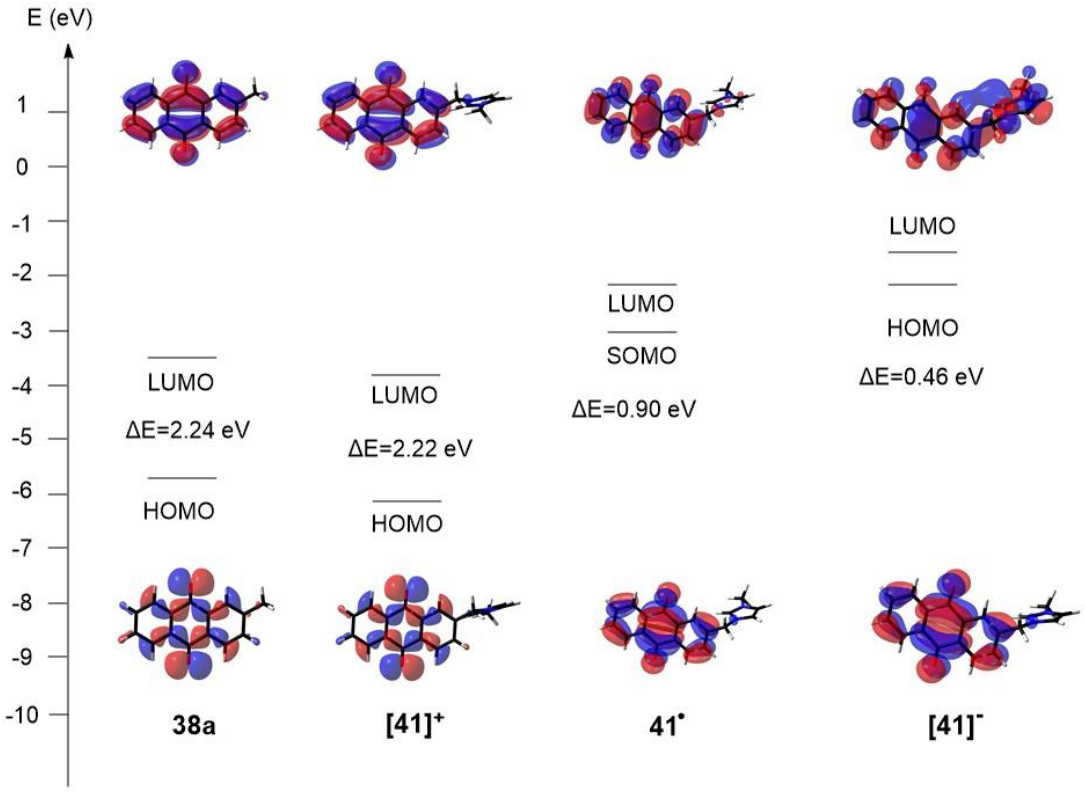

Figure 4.2.21: Calculated HOMO, SOMO and LUMO energy levels of compound **38a** and AQ-imidazolium motif **41⁺** different oxidation states at the PBE0/def2-TZVPP level of theory in acetonitrile.

As can be appreciated in *Figure 4.2.21*, both of the HOMOs from compounds **38a** and **41⁺** are geometrically similar and dispersed over the AQ ring motif only. The LUMO from **41⁺** is lower in energy (-3.82 eV) than the LUMO from **38a** (-3.64 eV), which agrees with the observed first reduction of **[41]Br** appearing at more anodic potentials. The SOMO from radical **41•** suggest the new electron is located within the aromatic AQ ring, while the HOMO in **41⁻** remains focused in the AQ motif with little contribution from the methylene and the imidazolium ring.

Although the functionalization induced some electron density localization into the imidazolium ring, as observed for the HOMO of the singly and doubly reduced species, the shape of the HOMOs did not significantly change. However, their energies did change, and the orbitals became more stable.

Both **38a** and **[41]Br** exhibited smaller cathodic redox half-waves for the second reduction compared to the first reduction, and in both cases the second redox wave Ip_c/Ip_a ratio was < 1. This observation is in agreement with the previous reports by Gupta and Linschitz, Macías-Ruvalcaba and Evans, and Staley *et al*. [194,196,197] The Ip_c/Ip_a ratio < 1 indicates that there was more doubly reduced AQ species available at the electrode surface, than the singly reduced radical anion AQ species.

A hypothesis to explain the depletion of the concentration of the singly reduced radical intermediate species at the electrode surface, could be due to the reversible formation of a redox-inactive dimer between two molecules of the singly reduced radical, formed after the reduction process $\mathbf{I_c}$, which then disproportionates at more cathodic potentials to generate the fully oxidised species and the doubly reduced species, as depicted in *Scheme 4.2.6* for $\mathbf{41^+}$. This hypothesis was proposed by Gupta and Linschitz when they studied the electrochemistry of AQs in the presence of hydrogen-bonding additives, as covered in the introduction.[194] These reactions would need to occur faster or at least at competitive speeds with the electron-exchange reactions.

$$2\ \mathbf{(41^{\bullet})} \rightleftharpoons \mathbf{41—41}$$

$$\mathbf{41—41} \rightleftharpoons \mathbf{41^+} + \mathbf{41^-}$$

Scheme 4.2.6: Proposed dimerization-disproportionation mechanism to explain the second redox wave of $\mathbf{41^+}$.

Alternatively, the behaviour observed for the second redox wave of **38a** and **[41]Br**, in which the second anodic wave is larger than the second cathodic wave could be explained by invoking the hypothesis by Macías-Ruvalcaba and Evans, about the formation of a redox-active dimer between two equivalents of the singly reduced radical intermediate (*Scheme 4.2.7*).[197] Since two equivalents of the radical intermediate would be involved in the formation of the dimer, the current peak height for the second reduction would be lower.

However, more studies are required to assess if the mechanisms proposed in these hypotheses correctly model the electrochemical behaviour of **[41]Br**.

$$\mathbf{41^{\bullet}} + \mathbf{41^{\bullet}} \rightleftharpoons [\mathbf{41^{\bullet}}\text{--}\pi\text{--}\mathbf{41^{\bullet}}]$$

$$[\mathbf{41^{\bullet}}\text{--}\pi\text{--}\mathbf{41^{\bullet}}] + e^{-} \rightleftharpoons [\mathbf{41^{\bullet}}\text{--}\pi\text{--}\mathbf{41}]^{1-}$$

Scheme 4.2.7: Formation of a redox-active π-dimer between two **41•** radical species.[197]

The hypothesis of Staley *et al*. discussed in the introduction, related to the protonation of the singly or the doubly reduced AQ species by protic groups formed on the electrode surface could explain the nature of the anodic shoulder observed on the second anodic peak $\mathbf{II_a}$ of **38a** in *Figure 4.2.18*. However, no broad signals or shoulders were observed in between the redox waves associated with the AQ motif of **[41]Br**. Therefore, the dimerization and comproportionation/disproportionation hypotheses seemed more likely. More electrochemical studies to determine the rate constant for the electron-exchange reactions and the equilibrium constants of dimerization and comproportionation would be required to narrow the number of plausible mechanisms.

The CV of **[41]Br** was also recorded at different scan rates to gain insight into the nature of the electron-exchange (*Figure 4.2.22*). The peak currents correlated linearly with the square root of the scan rate, which suggest that the electrochemical process is governed by the free diffusion of the AQ-imidazolium cation to the electrode surface according to the Rendles-Sevcik equation (Equation *2.3.2*).

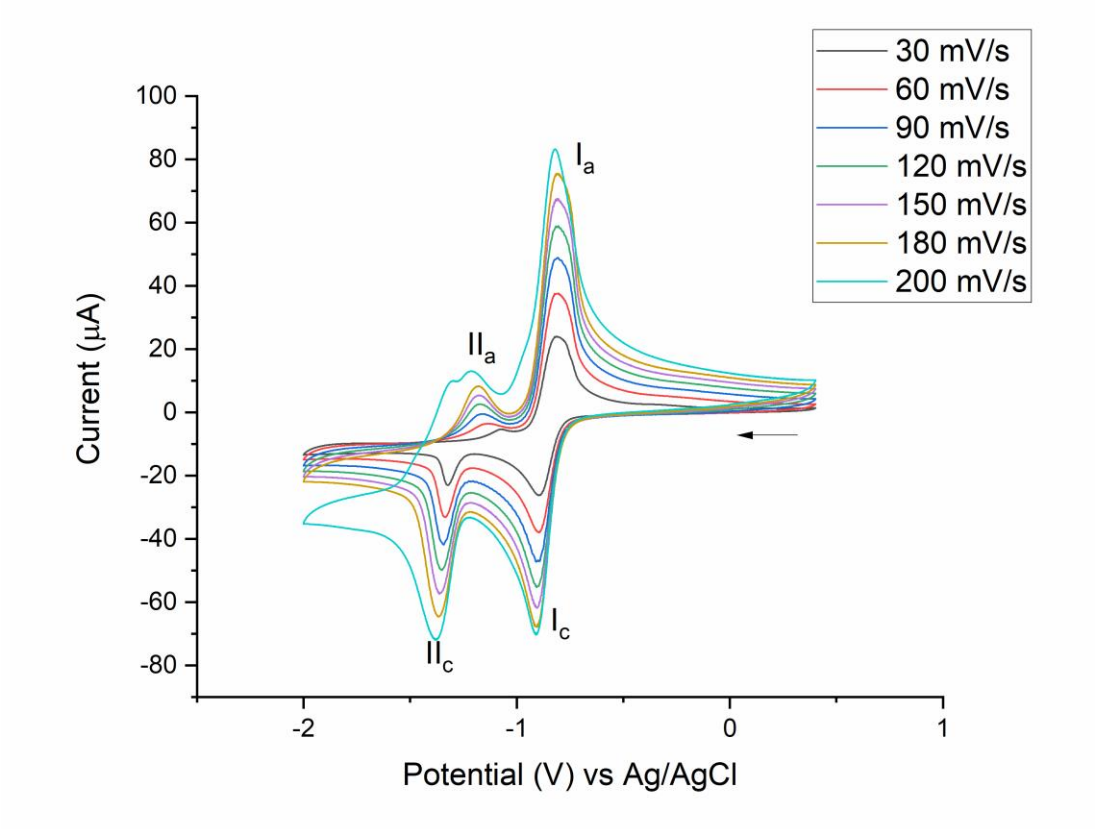

Figure 4.2.22: Cyclic voltammogram of **[41]Br** in acetonitrile/NBu_4PF_6 0.1 M recorded at different scan rates.

Interestingly, at a scan rate of 200 mV/s the second redox wave developed a new behaviour characterised by a residual cathodic current after the second reduction $\mathbf{II_c}$ and a bimodal oxidation peak at slightly more cathodic potentials than the potential where the oxidation of $\mathbf{41^-}$ to $\mathbf{41^\bullet}$ would be observed normally. These features could suggest a short-lived chemically reversible π-complex involving $\mathbf{41^-}$, which is only appreciable at fast scan rates.

The CVs from the AQ-imidazolium Tf_2N^- salt **[41][Tf_2N]** in acetonitrile and in [C_2Mim][Tf_2N] IL are shown in Figure *4.2.23*. The replacement of bromide by Tf_2N^- anion was evidenced by the disappearance of the two irreversible waves associated with redox processes undergone by the bromide anion.

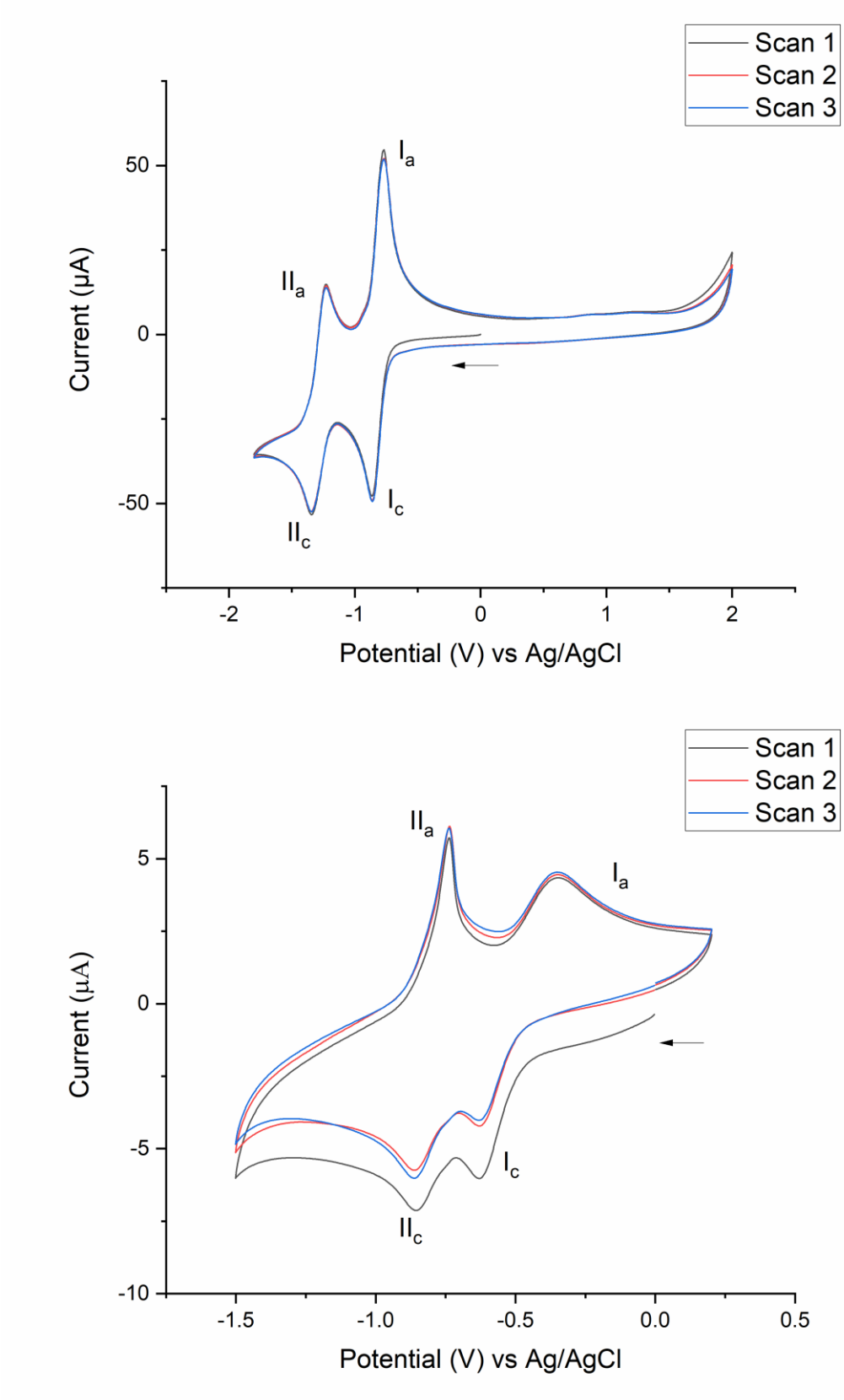

Figure 4.2.23: Cyclic voltammogram of **[41][Tf_2N]**. (Above) in acetonitrile NBu_4PF_6 0.1 M. (Below) in [C_2Mim][Tf_2N]

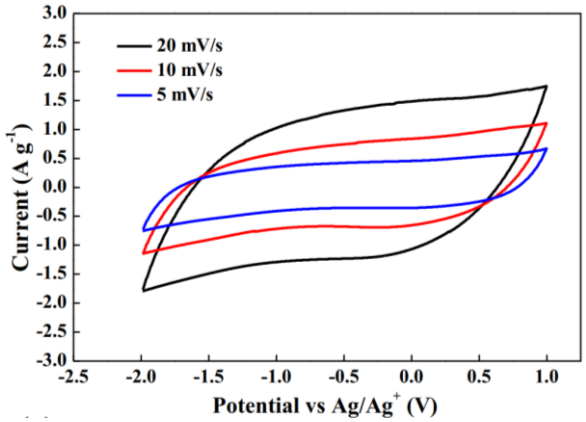

Figure 4.2.24: Cyclic voltammograms of [C_3Mim][Tf_2N] Adapted from Mahanta *et al*.[216]

Figure 4.2.24 shows a cyclic voltammogram of [C_3Mim][Tf_2N] performed by Mahanta *et al.* using a glassy carbon electrode that confirms that neither the imidazolium ring nor the Tf_2N^- anion undergo any redox processes between –2.0 V to 1.0 V vs Ag/Ag^+.[216] Moreover, linear sweep voltammetry experiments performed by Tatsumi and co-workers, confirmed that [C_2Mim][Tf_2N] did not exhibit any redox processes at potentials between -2.0 V to 2.0 V vs Fc/Fc^+.[217] Therefore the redox processes observed in the cathodic region of **[41][Tf_2N]** can be attributed to the AQ ring motif, while the absence of redox current in the anodic region of the CV from **[41][Tf_2N]** was in agreement with the literature reports.

The data suggest that the Tf_2N^- anion makes both redox steps less electrochemically reversible (*Table 4.2.5 entries 2 & 3*). This is because the peak-to-peak distances in **[41][Tf_2N]** are larger than **[41]Br**, which means that higher overpotentials are required to promote the redox reaction. In contrast with **[41]Br**, the second redox wave associated with the AQ motif of **[41][Tf_2N]** exhibited a Ip_c/Ip_a ratio < 1 ($\mathbf{II_{pa}}$ = 36.1 μA and $\mathbf{II_{pc}}$ = -26.8 μA), similarly as observed in the CV of **38a**. Therefore, the shape of the second redox wave suggests that **[41][Tf_2N]** exhibits a similar mechanism to the one proposed for **38a** and **[41]Br** and in agreement with the observations by Gupta and Linschitz, Macías-Ruvalcaba and Evans, and Staley *et al* (Scheme *4.2.6* and *Scheme 4.2.7*).[194,196,197] More studies are required to understand the chemical

and electrochemical equilibria in which the singly and doubly reduced AQ species are involved, the diffusion constants of the redox-active species need to be obtained and the rate of electron transfer constants calculated.

The CV of **[41][Tf_2N]** in the IL [C_2Mim][Tf_2N] displays currents significantly lower than in acetonitrile, despite performing the experiments with the same analyte concentration. This was associated with a slow diffusion of the AQ cation from the bulk to the electrode in the IL. The CV shows a first electrochemically irreversible redox process characterised by a small reduction peak $\mathbf{I_c}$ and a broad oxidation peak $\mathbf{I_a}$ with a significant peak-to-peak distance of 234 mV and a peak height ratio Ip_c/Ip_a of 1.21. The second redox process is also electrochemically irreversible, characterised by peak-to-peak distance of 120 mV and higher anodic current, Ip_c/Ip_a = 0.66, (*Table 4.2.5 entry 4*). Moreover, the two redox processes of **[41][Tf_2N]** were brought closer (310 mV distance) compared to **[41][Tf_2N]** in acetonitrile (475 mV) and **[41]Br** in acetonitrile (410 mV).

The peak broadening has been associated with slow electron exchange kinetics.[218] Considering that the water content is an order of magnitude higher in the IL compared to the water content in the acetonitrile (0.045 % vs 0.0075 %), the shape and height of the second anodic current peak can be attributed to a stabilisation of the anion $\mathbf{41^-}$.

Hydrogen-bonding with water or the IL components has been found to stabilise the fully reduced quinone ring. This causes a displacement of the second oxidation peak-to more positive potentials, but since the interaction with water is less favourable for the fully oxidised AQ, the overall effect is that both redox waves are brought closer together. Also, the peak height of the second wave increases until eventually a single reversible two-electron wave is obtained at high water concentrations.[219]

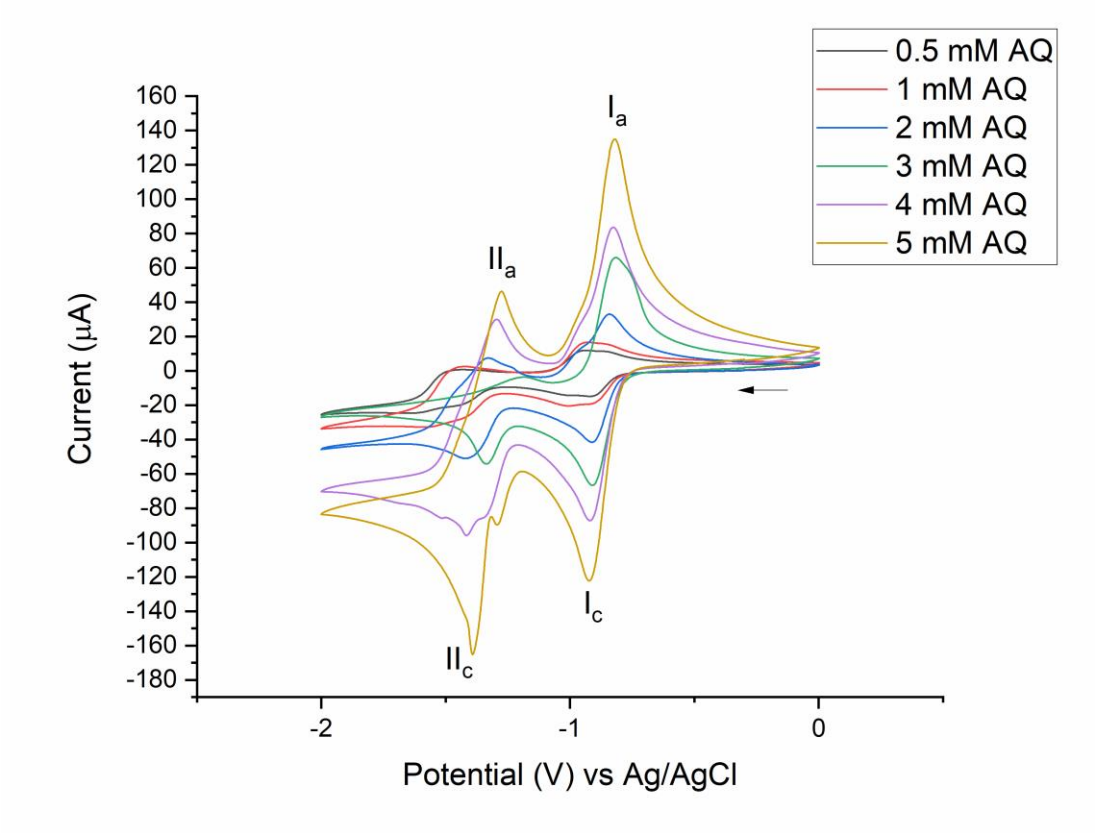

Figure 4.2.25: Cyclic voltammogram of **[41][Tf$_2$N]** at different concentrations in acetonitrile/NBu_4PF_6 0.1 M, recorded by Mr Christian Hoffman.

To gain more insight into the electrochemical and chemical equilibria involved in the AQ-imidazolium cation speciation, Christian Hoffman, a Master's student in our research group, recorded a CV of **[41][Tf$_2$N]** at different concentrations (*Figure 4.2.25*). It was noted that the redox peaks at concentrations below 2 mM are broad, which was in agreement with the observations by Staley *et al*., attributed to hydrogen-bonding interactions between protic groups generated by oxidation of the glassy carbon electrode surface and the AQs. As in the research by Staley *et al*. this behaviour was more evident at low AQ concentrations.[196] At concentrations above, 2 mM, the peaks get sharper and the observed smaller size of the second wave compared to the first becomes more evident. At a concentration of 4 mM and above, small new shoulders appeared at anodic potentials, next to the second reduction peak **II$_c$**. The first redox process remained unaltered aside from the appearance of a shoulder in the first oxidation peak **I$_a$**. Considering the high

concentration, these features are likely caused by the dimerization of the radical **41•**.

[41]Br arises as the most promising candidate to prepare a RADESs for energy storage applications, among the two imidazolium salts, because the bromide salt exhibited an slightly more reversible electrochemical behaviour than **[41][Tf$_2$N]**, and because the bromide anion, as the other halides, is a better HBA than the Tf_2N^- anion. A disadvantage of **[41]Br** is that it is more hygroscopic than the Tf_2N^-. The high-water content of DESs is commonly identified as the reason why they exhibit narrower electrochemical windows than ILs. However, the hygroscopicity of the bromide anion should not necessarily represent a problem, since the electrochemical windows of DESs incorporating hygroscopic halides are of around 2 to 2.5 V, which is still higher than water. Besides, water or small-chain alcohols are commonly used as additives to reduce the DESs viscosity in energy storage devices like redox-flow batteries.[220] A different approach that could be tried is to couple **41$^+$** with less hygroscopic anions, like large carboxylates or negatively charged amino acid, as it is done to prepare hydrophobic DESs.

Summarizing the results from the imidazolium-based AQ salts, it was observed that both salts were characterized by a one-electron two-step redox process in acetonitrile. The bromide salt exhibited slightly more electrochemically reversible redox reactions than the Tf_2N^- salt. The second redox wave of both salts showed that these redox reactions were coupled to a chemical equilibrium that was responsible for depleting the concentration of either **41•** and **41$^-$** at the electrode surface. Nevertheless, these side-reactions did not seem to affect the overall electrochemical reversibility the quinone.

4.2.5.2 Electrochemical studies of the aprotic ammonium salts

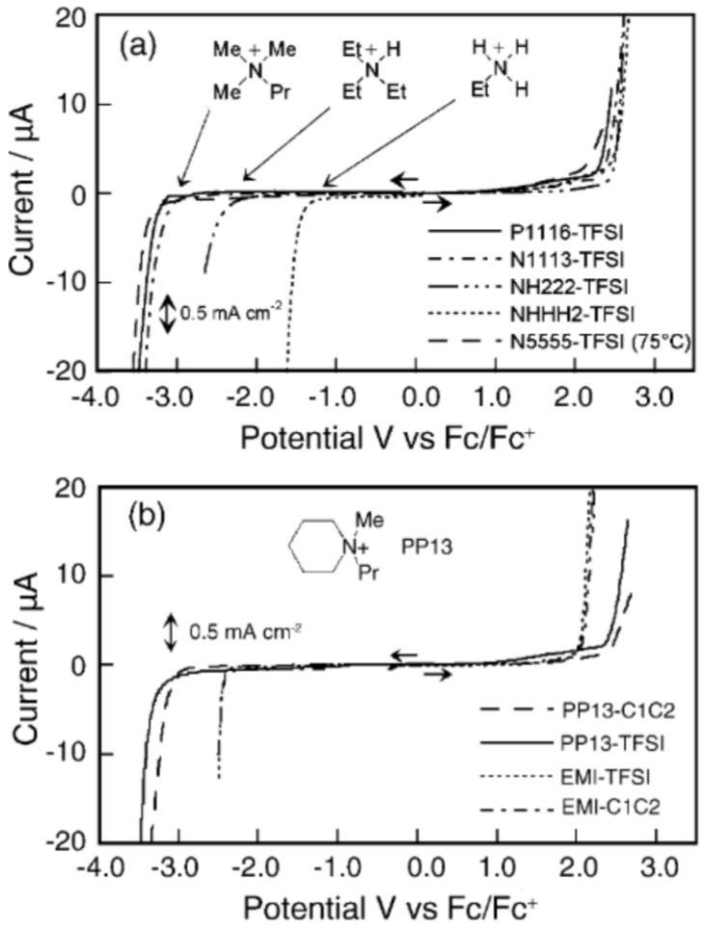

Figure 4.2.26: Linear sweep voltammograms of (a) aprotic and protic alkylammonium-based ionic liquids and (b) piperidinium-based ionic liquids. Adapted from Tatsumi and co-workers.[217]

The redox properties of the AQ salts based on the triethylammonium cation (**[42]Br** and **[42][Tf$_2$N]**), the N-methylpyrrolidinium cation (**[43]Br** and **[43][Tf$_2$N]**), and the N-methylpiperidinium cation (**[44]Br** and **[44][Tf$_2$N])**, were studied in acetonitrile. *Figure 4.2.26* exhibits a series of linear sweep voltammograms of various protic and aprotic tetraalkylammonium-based ionic liquids and a cyclic piperidinium-based ionic liquid performed by Tatsumi and co-workers using a glassy carbon electrode as WE.[217] The anodic stability of these redox-active salts depends on the oxidation of the anion, whereas the cathodic stability depends on the reduction of the cation. It can be appreciated that the linear and cyclic ammonium cations are more stable than the

imidazolium cations under reductive conditions. Based on the work by Tatsumi and co-workers, no reductive degradation of the "onium" fragments, nor oxidation of the Tf_2N^- anion were expected at potentials between -1.8 V to 1.5 V.[217] Only oxidation of the bromide anion was expected, as observed previously for **[41]Br**.

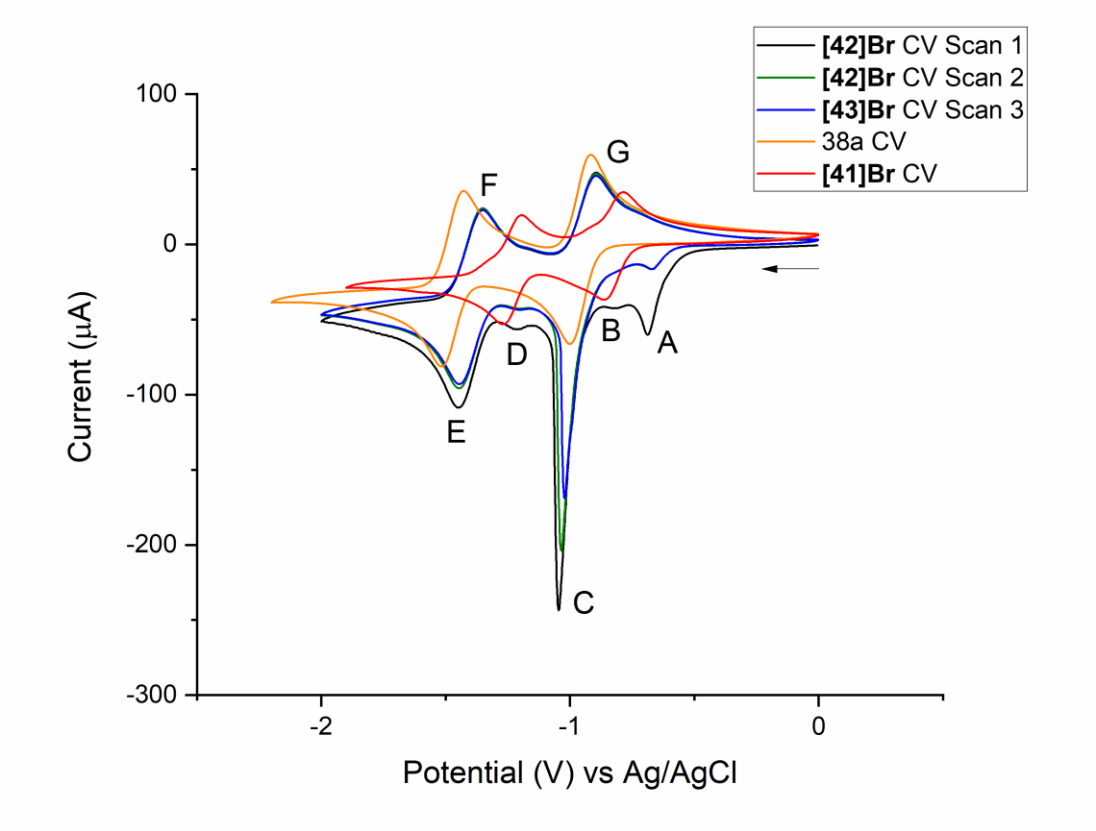

Figure 4.2.27: Cyclic voltammogram in acetonitrile//[NBu_4][PF_6] 0.1 M of **[42]Br**. The CVs of **38a** and **[41]Br** were obtained from another experiment.

A complicated CV for **[42]Br**, which differs from the well-documented one-electron two-step process, was obtained and displayed in *Figure 4.2.27*. At positive potentials, the CV only exhibited the redox waves associated with the bromide anion, similarly to **[41]Br**. Considering this, the discussion of **[42]Br** was narrowed to the cathodic region, which showed five cathodic peaks (**A-E**) and two anodic peaks (**F** & **G**). Peak **A** (-0.66 V) appeared at more anodic potentials than the first half-wave of reduction $\mathbf{I_a}$ (-0.86 V) from the imidazolium-based salt **[41]Br**. The electrochemical species that gives rise to Peak **A, B** and **D** suffered a chemically irreversible reaction during the first

scan, because their peak height current was considerably reduced in the second scan.

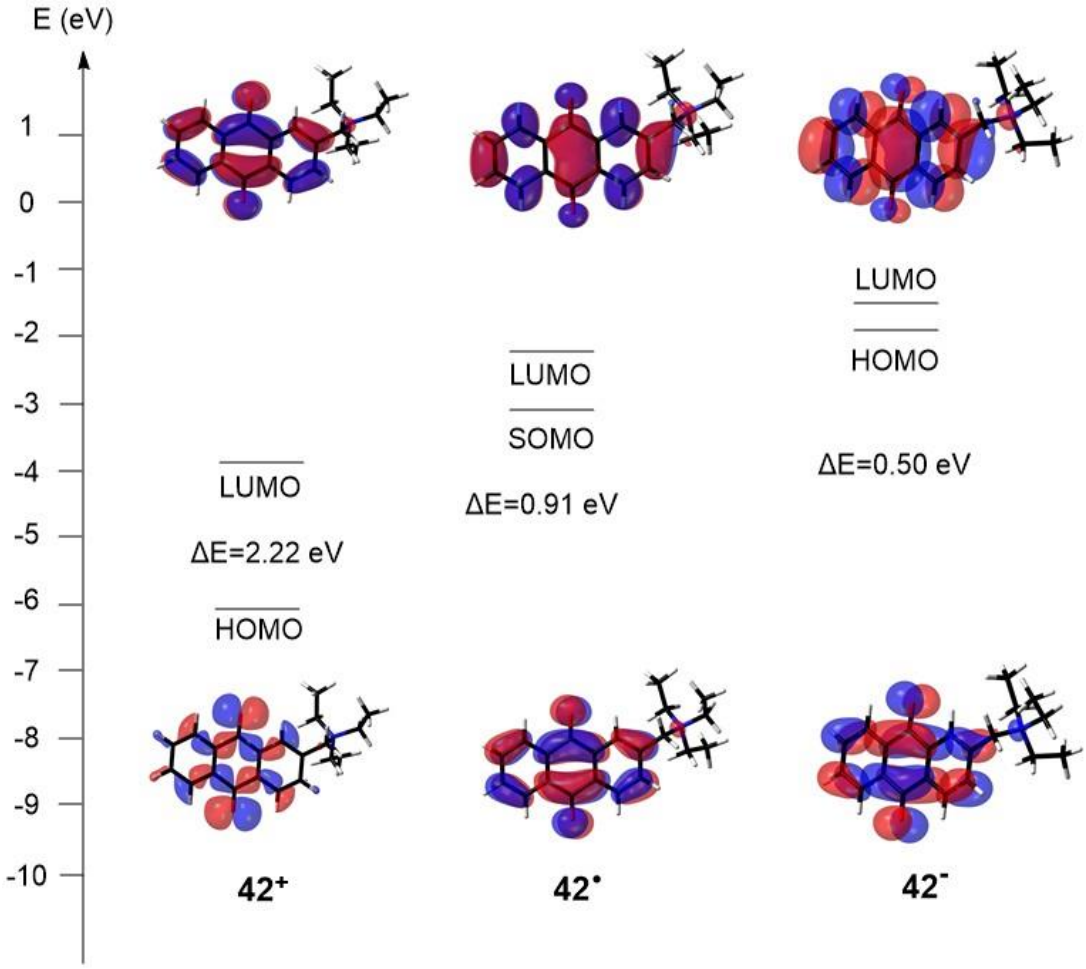

Figure 4.2.28: Calculated HOMO, SOMO and LUMO energy levels of the AQ-triethylammonium motif **42⁺** different oxidation states at the PBE0/def2-TZVPP level of theory in acetonitrile.

To shed some light into the possible electrochemical reactions that **42⁺** could suffer, the HOMO, SOMO and LUMO orbitals from the different redox states of the cation **42⁺** were calculated using DFT in acetonitrile. It was found that the LUMO energies of **41⁺** and **42⁺** were nearly equal, (-3.82 eV and -3.81 eV) (*Figure 4.2.28*). Based on these results, the stability of the reduced species associated with both cations would be expected to be similar, and in consequence, their reduction reactions should occur at similar potentials.

It was also observed that the ammonium centre has a small contribution to the HOMO and LUMO orbitals, which suggest that it can accumulate electron density because of the electron-transfer processes. In contrast to the imidazolium fragment, which can delocalise the electron density on its ring through resonance, the triethylammonium cation cannot delocalise the electron density. Therefore, reductive degradation of the ammonium centre is likely, although it was not expected at such mild reductive potentials.

Based on the analysis of the electronic structure of **42^{+}**, it is likely that peaks **B** and **D** were related to the two reduction reactions of **42^{+}** into **42$^{\bullet}$** and **42^{-}** respectively, since these cathodic waves appeared at similar potentials to those of **[41]Br**. The nature of peak **A** is unclear, its concentration at the electrode surface changed in a similar pattern to peaks **B** and **D**, and its cathodic wave appeared at more anodic potentials than those expected for the first reduction of the AQ. It was proposed that it could be a positively charged degradation product associated to **42^{+}**.

Peak **C** appeared at -0.99 V and was characterised by a very sharp cathodic current peak (156 μA). This electrochemical behaviour is characteristic of the reduction of a species adsorbed on the electrode surface.[218] The potential of peak **C** was very similar to the potential of the first cathodic half-wave of 2-methylanthraquinone **38a** (-1.01 V). Therefore, it was proposed that this peak could be related to the reduction of **38a**, or the reduction of an AQ species of similar electronic structure like the neutral **AQ-NEt$_2$**, which would be generated by the reductive degradation of **[42]Br** (*Scheme 4.2.8-A*).

The cathodic peak **E** and the anodic peak **F** appeared at more positive potentials than the second redox wave of **38a**. These two peaks seemed to be related to the same redox process as their peak-to-peak distance was 94 mV and their Ip_c/Ip_a ratio was 0.89. These electrochemical parameters are in the range of expected values for the second redox wave of an AQ-based species. These peaks could belong to the second reduction of an AQ radical species that exhibits more electron affinity than **38a** but smaller electron affinity than **41$^{\bullet}$**, for example, the radical anion **AQ-NEt$_2^{\bullet -}$.**

The potential of the anodic peak **G** (-0.90 V) was very similar to the potential for the first anodic half-wave of **38a** (-0.92 V). Therefore, both peaks **C** and **G** could be related to the first redox wave of **38a** or **AQ-NEt$_2$**, which could have been generated by the decomposition of **42$^+$** (*Scheme 4.2.8-A*).

It is not clear why **42$^+$** would suffer reductive degradation at mild negative potentials. These degradation reactions are not expected at low cathodic potentials, in fact, ILs based on linear and cyclic ammonium salts are very electrochemically stable and only begin to exhibit reductive degradation at potentials between -2.7 to -4.0 V vs Ag/AgCl.[188,221,222] However, when quaternary ammonium salts are dissolved in acetonitrile, cathodic decomposition of the salts has been observed at -1.9 V vs Ag/AgCl using Pt electrodes. This process appeared to be triggered by the reduction of the solvent to generate the CH_2CN^- base, which then attacked the quaternary ammonium cation.[187]

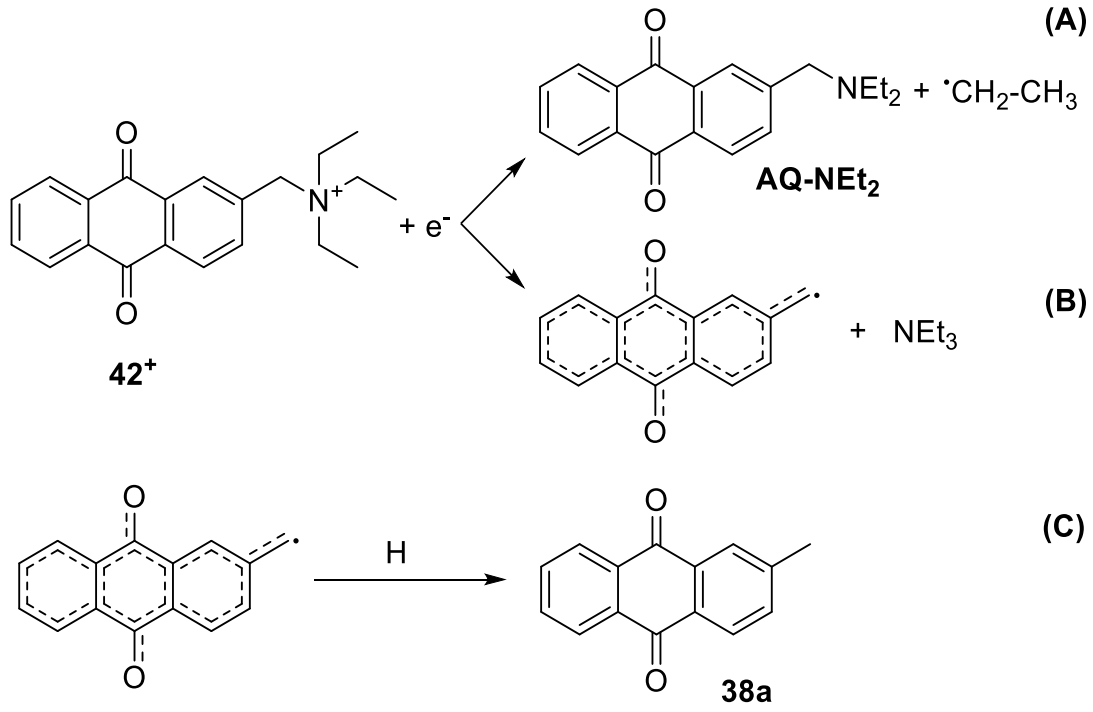

Scheme 4.2.8: Proposed reductive degradation mechanism of **42$^+$**

The electrochemical degradation mechanism of **42$^+$** could be initiated by an irreversible one-electron transfer to the ammonium cation, which would cause

a radical cleavage of one of the ammonium C-N bonds to generate an alkyl radical and a tertiary amine (*Scheme 4.2.8-A*). If the C-N bond cleavage occurred between the AQ motif and the ammonium centre, the alkyl radical could be stabilized by the AQ aromatic system (*Scheme 4.2.8-B*). Such stabilization of the radical intermediate could be the driving force for the unexpected early decomposition of **42⁺**. The examination of the LUMOs suggested that the radical cleavage of the C-N bond between the AQ and the ammonium centre of **42⁺** or **42•** may be possible, since the nitrogen atom exhibits a small contribution to the orbitals.

The AQ alkyl radical can abstract an H-atom from adventitious water, the electrolyte or any mildly acid C-H bond to yield **38a** (*Scheme 4.2.8-C*). Another possibility is that an ethyl radical generated from the homolytic C-N bond cleavage of one of the ethyl chains of the ammonium centre, undergoes a second reduction to generate a basic carbanion. This base could deprotonate another ammonium ion promoting Hofmann elimination and formation of a **AQ-NEt₂** (*Scheme 4.2.9*).[223–225] The Hofmann degradation is enabled by the presence of hydrogen atoms in the C-H β positions to the ammonium centre.

It is important not to forget that basic species like OH^- or NBu_3 can be generated after the H-atom abstraction that saturates the alkyl radical proposed in *Scheme 4.2.8-C.* These bases can effectively trigger the Hoffman degradation of **[42]Br** or the electrolyte $[NBu_4][PF_6]$ (*Scheme 4.2.9*).

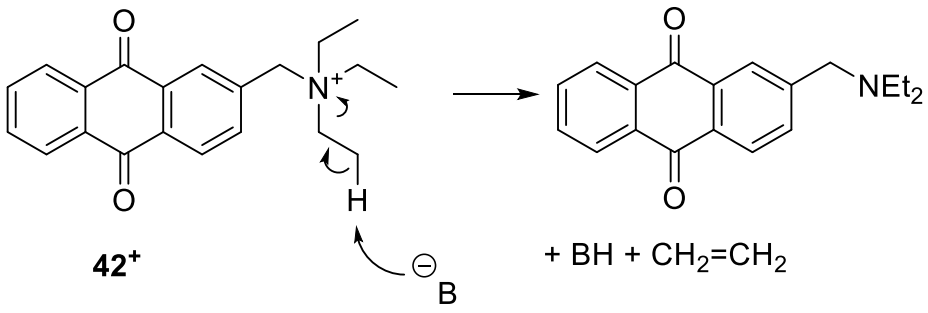

Scheme 4.2.9: Hoffman degradation of **[42]Br**

The shape of peak **C** could be a consequence of the degradation of **[42]Br**, which creates a local region enriched with basic species around the WE. These bases can attack the electrolyte cation NBu_4^+. Gamboa-Valero *et al*. demonstrated that the Hoffman elimination product of the tetrabutylammonium cation can interact with quinones and force their precipitation at the electrode surface, thus explaining the high reduction peak currents.[218]

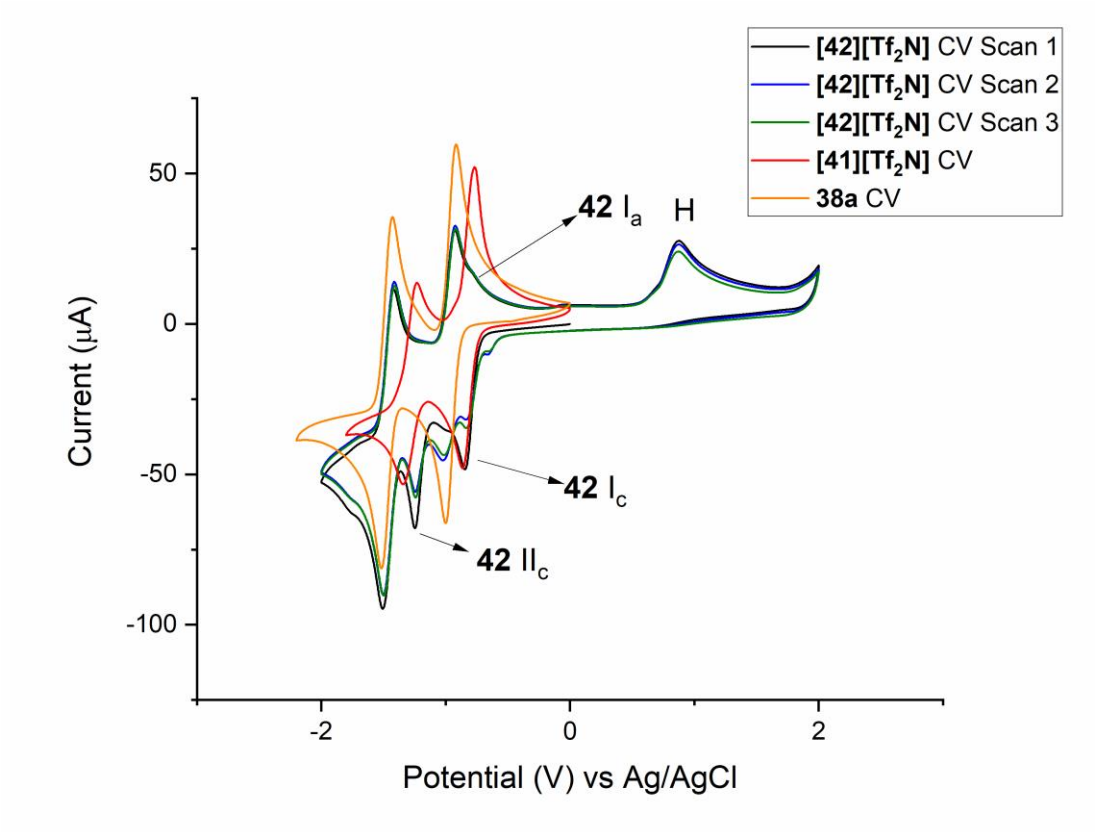

Figure 4.2.29: Cyclic voltammogram in acetonitrile/$[NBu_4][PF_6]$ 0.1 M of **[42][Tf$_2$N]**. The CV of **38a** was obtained from another experiment.

After analyzing the electrochemical behaviour of **[42]Br**, the CV of **[42][Tf$_2$N]** was obtained in acetonitrile and displayed in *Figure 4.2.29* alongside the CVs from starting material **38a** and the imidazolium-based **[41][Tf$_2$N]**. The anodic region of the CV exhibited an oxidation half-wave (peak **H**) at 0.88 V, that appeared ubiquitously in all the ammonium based Tf_2N^- salts, but not in **[41][Tf$_2$N]**. When the CV was performed cycling between potentials from -0.5 V to 1.67 V, *i.e*. more positive potentials than any reduction peaks associated

with the AQ salt, peak **H** did not appear. However, when the cathodic turning point of the CV was set to -1.1 V, to only allow the first reduction of **[42][Tf_2N]** to take place, peak **H** was spotted. This could indicate that peak **H** is related to the oxidation of the side-product from the first reduction of **[42][Tf_2N]**. Also, this experiment suggested that the oxidation of this species is mediated, or only takes place, in the presence of the Tf_2N^- anion.

Although the potential at which the tribromide anion oxidises to generate bromide is similar to the potential of peak **H**, its origin due to bromide impurities can be ruled out. The tribromide anion shows a characteristic electrochemically irreversible one-electron two-step redox mechanism instead of a single electron-transfer process. Also, the silver nitrate test performed during the work-up of the Tf_2N^- salts, their elemental analyses and their -ve ESI-MS did not suggest the presence of bromide impurities. Besides, peak **H** was also observed in the protic Tf_2N^- salts (see below), which were synthesized directly from their neutral amines with H[Tf_2N] without involving metathesis of the bromide anion.

Table 4.2.6: Electrochemical parameters of the aprotic AQ salts

Entry	AQ	E (I_c) (V vs Ag/AgCl)	E (II_c) (V vs Ag/AgCl)	E (I_a) (V vs Ag/AgCl	I_c (μA)	II_c (μA)
1	**[42]Br**	-0.69	-	-	-48	-
2	**[42][Tf_2N]**	-0.84	-1.24	-0.78	-43	-34
3	**[43]Br**	-0.84	-1.29	-0.80	-41	-41
4	**[43][Tf_2N]**	-0.84	-1.30	-0.80	-43	-43
5	**[44]Br**	-0.83	-1.18	-0.78	-33	-32
6	**[44][Tf_2N]**	-0.83	-1.27	-0.76	-44	-44

Peak currents taken from the first scan.

The first cathodic half-wave **I_c** of **42^+** in **[42][Tf_2N]**, occurred at -0.84 V, similarly to peak **B** in the CV of **[42]Br**, and the first cathodic waves of **[41]Br** and **[42][Tf_2N]**. **I_c** of **[42][Tf_2N]** displayed a peak current of 43 μA, similarly to **[41][Tf_2N]**, (*Table 4.2.6*, entry 1). However, the CV suggested that **[42][Tf_2N]** was involved in a chemically irreversible reaction that depleted its concentration at the electrode between the first and the third scans. The first

half-wave of oxidation $\mathbf{I_a}$ (-0.78 V) of $\mathbf{42^+}$ was detected as shoulder of a bigger anodic wave (*Table 4.2.6*, *entry 1*). The peak height of $\mathbf{I_a}$ remained small and constant throughout the scans. The second half-wave of reduction $\mathbf{II_c}$ that generates $\mathbf{42^-}$ from $\mathbf{42^\bullet}$ was detected at -1.25 V, and just as $\mathbf{I_c}$, its peak height current was reduced throughout the scans. The returning oxidation wave $\mathbf{II_a}$ of $\mathbf{42^-}$ was not detected in the CV, which suggests that $\mathbf{42^-}$ is almost completely consumed in another chemical equilibrium or degraded at the studied cathodic potentials. This can explain why the half-wave $\mathbf{I_a}$ is small (*Figure 4.2.29*).

The redox wave $\mathbf{I_a/I_c}$ and $\mathbf{II_a/II_c}$ from **38a** were detected in the CV of **[42][Tf$_2$N]**. The third redox wave detected in the CV from **[42][Tf$_2$N]** was shifted 14 mV to anodic potential with respect to the expected redox wave $\mathbf{II_a/II_c}$ of **38a**, (*Figure 4.2.29*). According to the potentiostat's user manual, for a range of 4 V, the uncertainty of the measurement is of ± 8 mV. Therefore, the difference between the peaks is significant. However, it was assumed that the species giving rise to the third wave of **[42][Tf$_2$N]** was indeed **38a**, which could have been generated by reductive degradation.

It was observed that only the peak height current of the first cathodic wave $\mathbf{I_c}$ of **38a** increased throughout the scans. In the first scan $\mathbf{I_c}$ is present as a small shoulder and by the third scan, the redox wave is larger than the first cathodic wave of $\mathbf{42^+}$. Moreover, according to *Table 4.2.6*, entry 1, the current of $\mathbf{II_c}$ was 21% smaller than $\mathbf{I_c}$, which suggests that a certain amount of $\mathbf{42^\bullet}$ was degraded in between both waves.

Based on these observations a degradation mechanism was proposed as follows: $\mathbf{42^+}$ first underwent reduction to generate $\mathbf{42^\bullet}$ which suffered a reductive degradation to generate the alkyl radical $\mathbf{38a^\bullet}$. This radical was quickly quenched by an H-atom abstraction from another molecule in the system (electrolyte, solvent, substrate) to generate **38a**, which then underwent its first reduction to produce the radical anion $\mathbf{38a^{\bullet-}}$. Then, the remaining $\mathbf{42^\bullet}$ underwent its second reduction and suffered complete reductive degradation at further cathodic potentials to generate the radical anion $\mathbf{38a^{\bullet-}}$**,** which added

up to the previously generated **38a$^{\bullet-}$**. Finally, **38a$^{\bullet-}$** underwent its second reduction and the returning oxidation steps. This mechanism would explain why the current associated with the half-waves **I_a**, **II_c** and **II_c** of **38a** remained constant throughout the different scans while **I_c** grew after the first scan. However, the CV suggested that **38a** was mostly generated by degradation of **42^{-}**, (*Figure 4.2.29*).

It is not clear why **[42]Br** produced a different cathodic CV compared to **[42][Tf_2N].** Based on the second redox wave of the degradation products in both CVs**,** it is probable that the main degradation product of **[42]Br** is a neutral AQ amine like **AQ-NEt_2**, while the main degradation product of **[42][Tf_2N]** is **38a**. An AQ-based degradation product of similar electronic properties as **38a**, would be expected to exhibit a very similar first redox wave to that of **38a**, because the redox potential of the fully oxidised species is less sensible to subtle electronic changes in the redox-active core. More studies are required to understand what is favouring each degradation product. It also not fully understood what caused the large currents observed for the first cathodic half-wave of the degradation product of **[42]Br**. The Hoffman elimination of the electrolyte has been postulated as a reason for these currents, but it is not clear why this phenomenon was not observed in **[42][Tf_2N]**.

The CVs from the AQ-methylpyrrolidinium salts **[43]Br** and **[43][Tf_2N]** in acetonitrile showed similar features in the anodic region as **[42]Br** and **[42][Tf_2N]** respectively. This is the reason why the discussion of their CVs was focused on the cathodic region only (*Figure 4.2.30*).

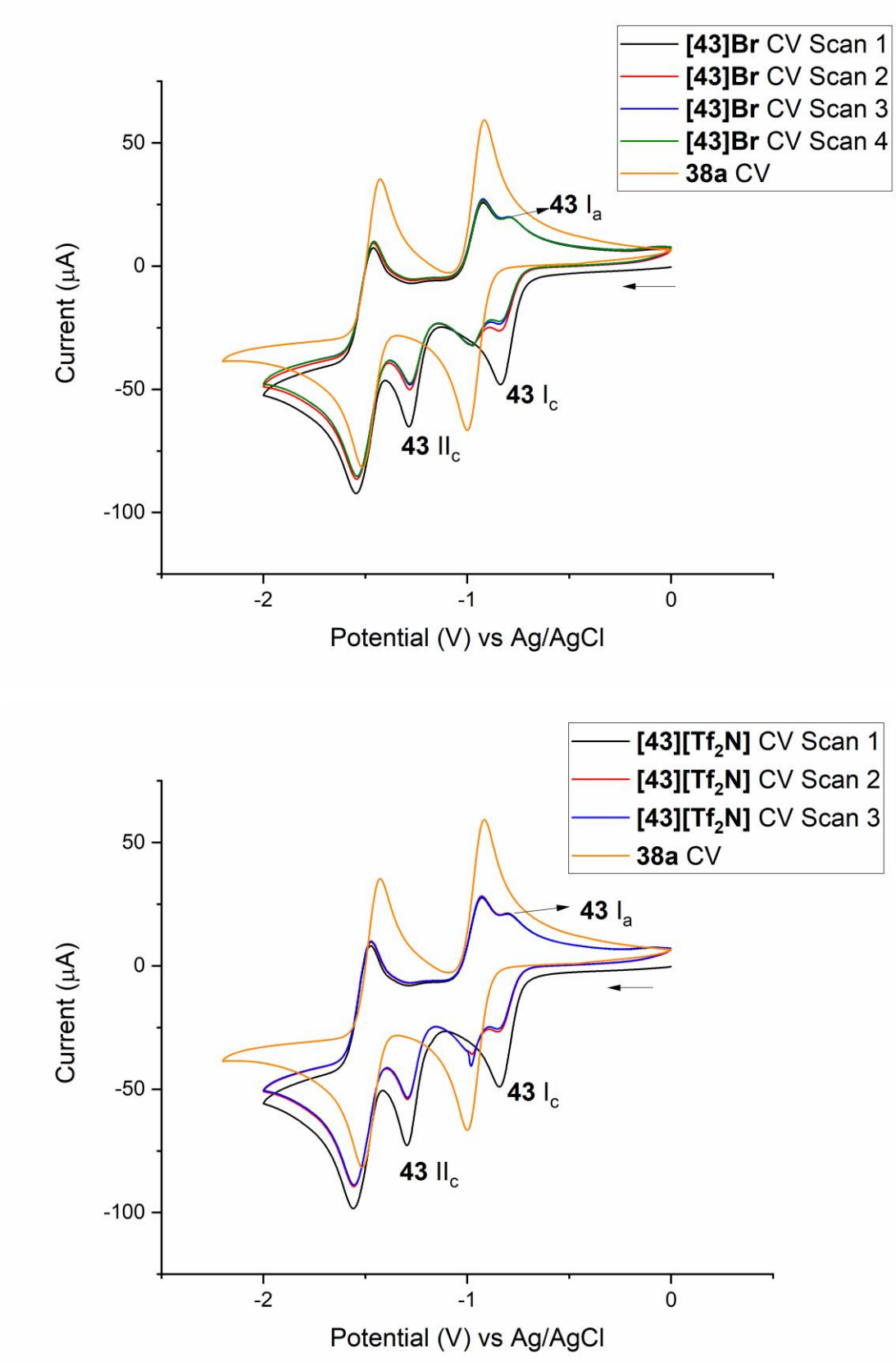

Figure 4.2.30: Cyclic voltammogram in acetonitrile/[NBu_4][PF_6] 0.1 M of **[43]Br** (above) and **[43][Tf_2N]** (below). The CV of **38a** was obtained from another experiment.

The CV of **[43]Br** showed a similar behaviour to the one observed for **[42][Tf$_2$N]** (*Figure 4.2.30-above*). The potential of the first cathodic half-wave **I$_c$** of both methylpyrrolidinium salts (-0.84 V) was equal to **[42][Tf$_2$N]** (*Table 4.2.6, entry 2 & 3*). On the other hand, the second cathodic half-wave **II$_c$** (-1.29 V for **[43]Br** and -1.30 V for **[42][Tf$_2$N]**) suggested that **43$^+$** has a slightly lower electron affinity value than **42$^+$**, but both ammonium cations had higher electron affinity than the imidazolium cation **41$^+$**, for which the second reduction occurred at more cathodic potentials, (*Table 4.2.6, entry 3 & 4).*

Contrary to the first cathodic half-wave, the potential of the second cathodic half-wave **II$_c$** associated with the aprotic AQ-salts, exhibited high variability even among salts of the same cation. This observation is in agreement with previous research on the electrochemistry of quinones, which reported that the second redox wave of the quinones is more sensitive to intermolecular interactions involving the redox-active core.[226]

The only important difference observed between cations **43$^+$** and **42$^+$** was that the first anodic wave **I$_a$** of **43$^+$** exhibited a higher current peak height, at a slightly more cathodic potential (-0.80 V). This suggests that **[43]Br** is slightly more resistant to reductive degradation than **[42][Tf$_2$N]**.

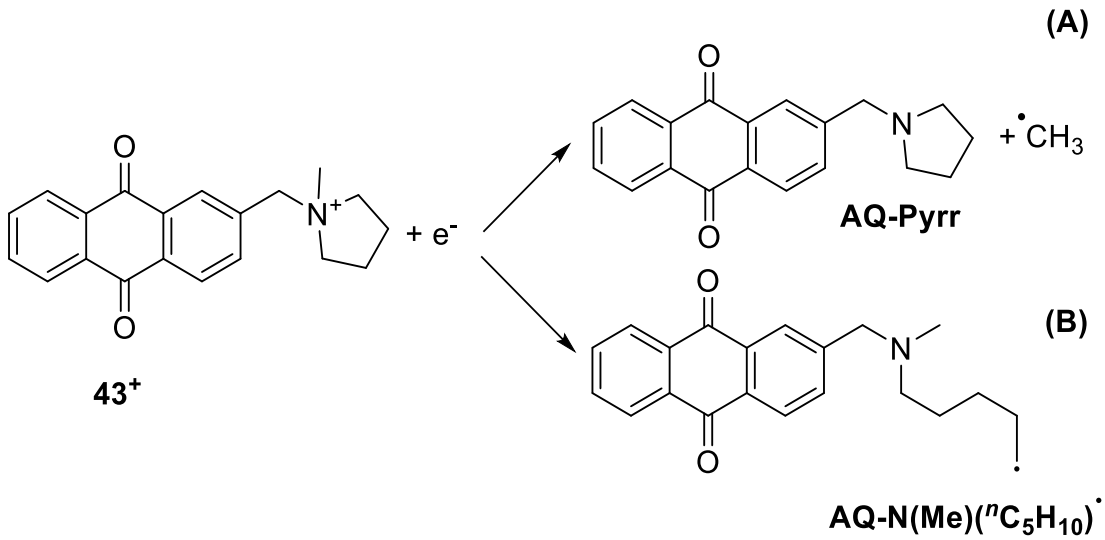

Scheme 4.2.10: Reductive degradation of **43$^+$**

The degradation process of **[43]Br** and **[42][Tf_2N]** was also similar according to their CVs. However, some differences arose. The first cathodic wave $\mathbf{I_c}$ of the degradation product from the CV of **[43]Br** was not detected in the first scan, it appeared until the second scan. Also the current peak height of the second cathodic wave of **[43]Br** was equal to the first cathodic half-wave, suggesting no reductive degradation of **43$^{\bullet}$** during the first scan.

The first reduction half-wave associated with the degradation product was shifted 17 mV to cathodic potentials with respect to the expected first cathodic wave $\mathbf{I_c}$ of **38a** (*Figure 4.2.30-above*). The second cathodic wave $\mathbf{II_c}$ of the degradation product from the CV of **[43]Br** was shifted 29 mV to anodic potentials with respect to the expected $\mathbf{II_c}$ of **38a**. These differences are slightly bigger than in **[42][Tf_2N]**, therefore, it is not clear whether the degradation product is **38a** or an AQ species of very similar electronic properties.

One of the possible degradation products is **AQ-Pyrr**, which can be generated by single-electron transfer to **43^{+}**, followed by homolytic C-N bond cleavage of the methyl group to generate a neutral cyclic amine, (*Scheme 4.2.10-A*). The other possible degradation product is the alkyl radical **AQ-N(Me)(${}^{n}C_5H_{10}$)$^{\bullet}$**, which can be produced if the homolytic C-N bond cleavage breaks the pyrrolidinium ring instead, thus obtaining a linear amine (*Scheme 4.2.10-B*). The radicals obtained by reductive degradation of **43^{+}** can either be quenched by a H-atom abstraction or receive a second electron to form carbanions. As discussed previously, carbanions can then trigger Hoffman elimination of other ammonium salts.

The HOMO, SOMO and LUMO orbitals of the AQ-methylpyrrolidinium fragment **43^{+}** were calculated with DFT in acetonitrile. Their shape and energies are similar to the ones obtained for fragments **41^{+}** and **42^{+}** The methylene bridge in **43^{+}** has a similar contribution to the HOMOs and LUMOs to that of the triethylammonium fragment, which indicates that the reductive cleavage C-N bond of the methylene bridge is likely (*Figure 4.2.31*).

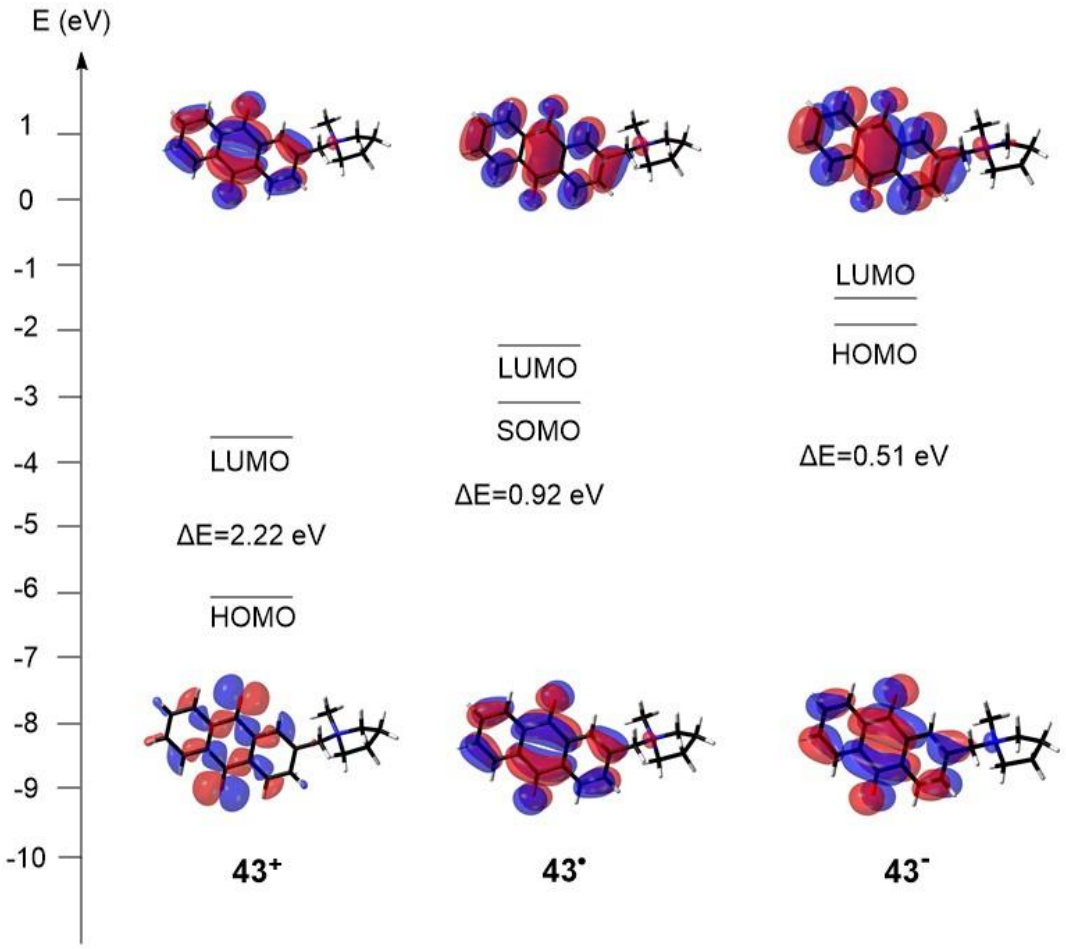

Figure 4.2.31: Calculated HOMO, SOMO and LUMO energy levels of the AQ-methylpyrrolidinium motif **43**$^{+}$ different oxidation states at the PBE0/def2-TZVPP level of theory in acetonitrile.

The redox properties of the methylpiperidinium-based AQ salts **[44]Br** and **[44][Tf$_2$N]** were analized by CV in acetonitrile (*Figure 4.2.32*). Both salts exhibited similar degradation redox waves as **[43]Br**, **[42][Tf$_2$N]** and **[43][Tf$_2$N]**. No signs of species adsorbed at the electrode were detected. The potential of the first cathodic wave of the salts based on the cation **44**$^{+}$ (-0.83 V) were in agreement with the previous aprotic salts and the imidazolium salts, except for **[42]Br**, which suffered a different degradation process (*Table 4.2.6, entry 5 & 6*). The electronic structure of the different oxidation states of the cation **44**$^{+}$ were calculated with DFT in acetonitrile.

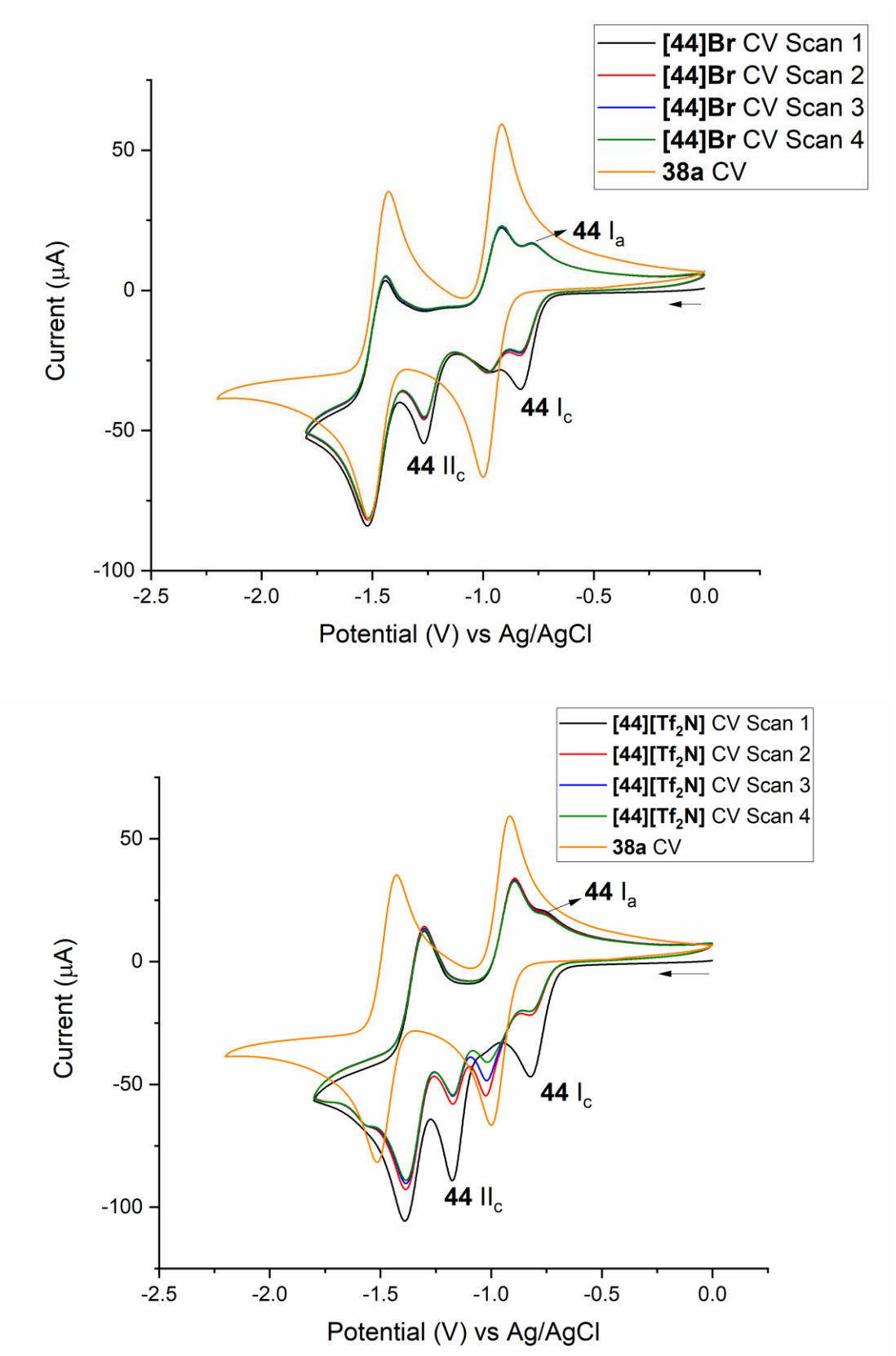

Figure 4.2.32: Cyclic voltammogram in acetonitrile/[NBu_4][PF_6] 0.1 M of **[44]Br** (above) and **[44][Tf_2N]** (below). The CV of **38a** was obtained from another experiment.

As observed previously, the second cathodic half-wave $\mathbf{II_c}$ of the aprotic AQ salts exhibited higher variation than the first half-wave. Salts **[44]Br** and **[44][Tf$_2$N]** exhibited a shift of 90 mV, the major variation between salts of the same cation (*Table 4.2.6, entry 5 & 6*). This indicates that **[44][Tf$_2$N]** was involved in a certain type of interaction that increased the electron density of the quinone core, thus reducing its electron affinity compared to **[44]Br**.

The degradation process of **[44]Br** showed similarities to the one of **[42][Tf$_2$N]** to their CVs, since **38a** appeared to be also the degradation product of **[44]Br**. However, in contrast to **[42][Tf$_2$N]**, all the current peak heights of the redox-waves associated with **38a** remained constant throughout the CV, in agreement with the salts based on the cation $\mathbf{43^+}$ (*Figure 4.2.32*-above). Also, the current peak heights of both redox waves of **[44]Br** remained equal during the first scan, which suggest that the reductive degradation process took place after the second reduction of the AQ salt (*Table 4.2.6, entry 5 & 6*).

The electronic energies and orbital shapes of $\mathbf{44^+}$ were very similar to $\mathbf{43^+}$ and led to the conclude that, as previously, the homolytic C-N bond cleavage of the methylene bridge is possible. The HOMO-LUMO diagrams of the different oxidation states of $\mathbf{44^+}$ can be found in *section 6.2*

In contrast to **[44]Br**, the degradation process of **[44][Tf$_2$N]** appeared to generate a different AQ species to **38a**, since the second redox wave of the degradation product was shifted 200 mV to anodic potentials with respect to the expected potential for the second redox wave of **38a**. The probable mechanism could be as previously discussed, single-electron transfer to the ammonium fragment followed by homolytic C-N bond cleavage to generate the neutral cyclic amine AQ-Pip (*Scheme 4.2.11-A*), or the radical AQ-N(Me)(^{n}C$_6$H$_{12}$) produced by the breaking of the piperidinium cycle due to homolytic C-N bond cleavage (*Scheme 4.2.11-A*). As in the case of **[44]Br**, the current peak heights of the two redox waves associated with **[44][Tf$_2$N]** remained equal during the first scan, which suggest that the reductive degradation took place after the second scan.

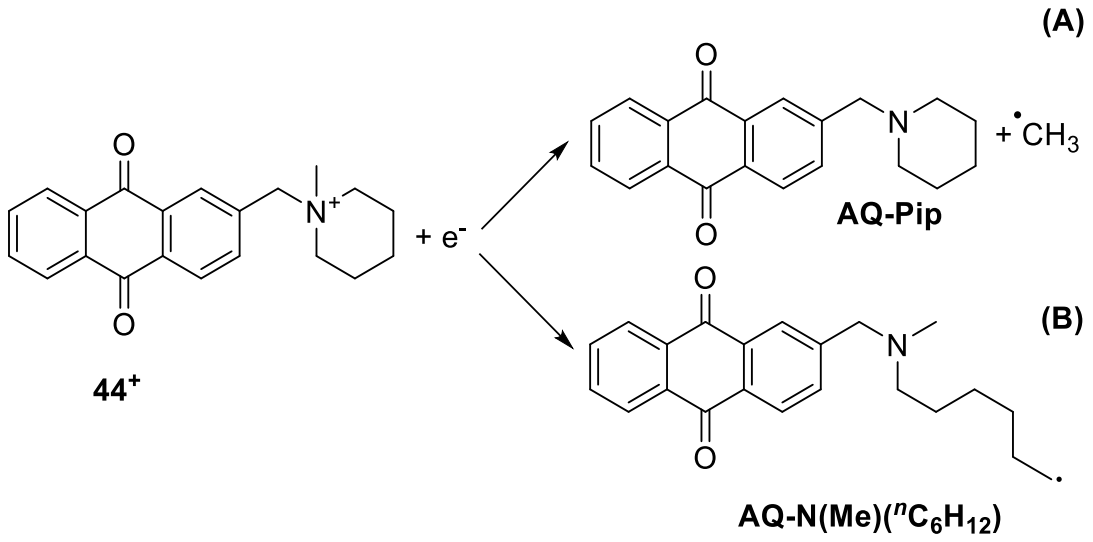

Scheme 4.2.11: Reductive degradation of **44⁺**

As discussed previously, it has been reported that in acetonitrile the degradation of quaternary alkylammonium salts occurred at cathodic potentials around -2.1 V vs Ag/AgCl.[187] The degradation was attributed to Hoffman elimination of the ammonium salt by a basic species, which was generated through the reduction of acetonitrile. Taking this into consideration, the CV of **[44][Tf₂N]** was obtained in dimethyl sulfoxide/[NBu_4][PF_6] 0.1 M with a Pt disk electrode in an attempt to also rule out that the decomposition of the aprotic ammonium salts was related to solvent or electrode effects (*Figure 4.2.33*). In general, the electron-transfer reactions between the AQ salt and the electrode were slower in dimethyl sulfoxide compared to acetonitrile.

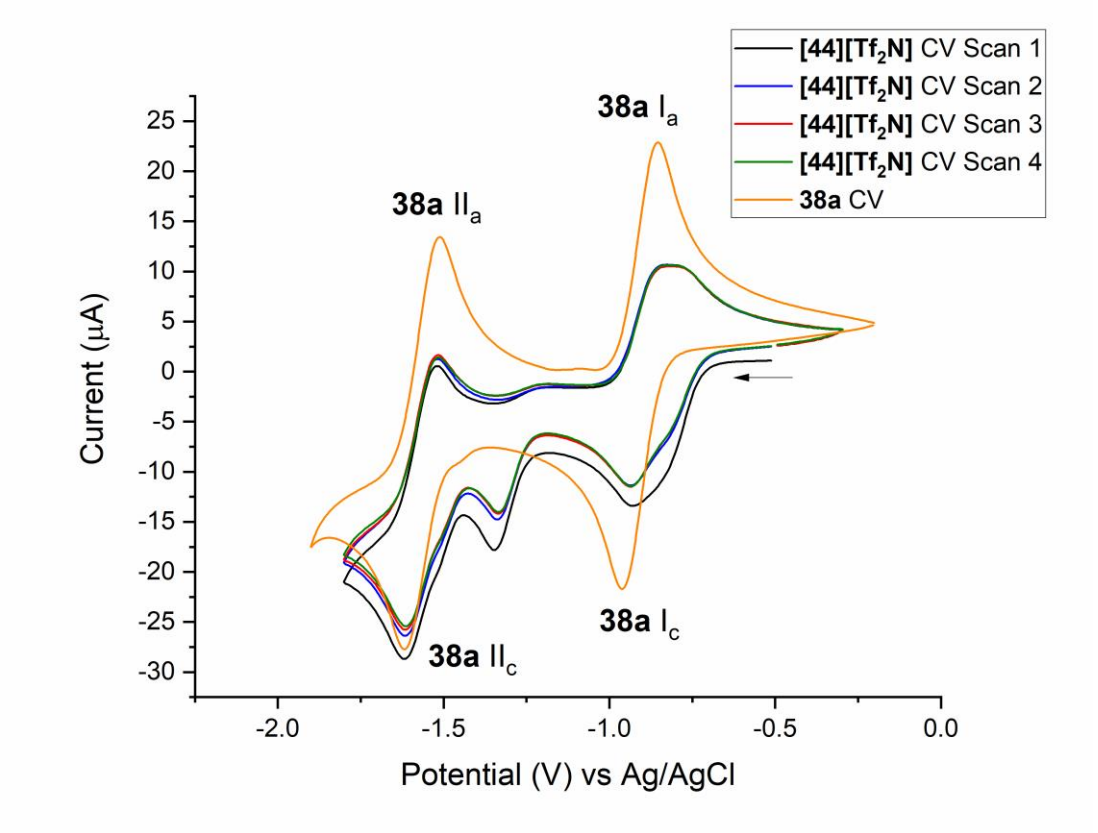

Figure 4.2.33: Cyclic voltammogram in dimethyl sulfoxide/[NBu_4][PF_6] 0.1 M. The CV of **38a** was obtained from another experiment.

From *Figure 4.2.33* it was observed that **[44][Tf$_2$N]** still underwent reductive degradation in dimethyl sulfoxide, nevertheless, the first cathodic half-wave of the aprotic salt was not as evident as it was in the CVs obtained in acetonitrile. It appeared that the first cathodic wave of **[44][Tf$_2$N]** was shifted to cathodic potentials and overlapped with the first cathodic wave of the degradation product. This hypothesis could be supported by the appearance of a small shoulder on the first reduction wave of the degradation product at -0.81 V.

Interestingly, while in acetonitrile, the second redox wave associated with the degradation product was shifted to anodic potentials with respect to **38a**, in dimethyl sulfoxide, both cathodic waves coincided. This could be a coincidence, or may suggest that in this system, **38a** is the ultimate reductive degradation product. From these results it was confirmed that the degradation

of the aprotic ammonium salts appears to occur in both acetonitrile and dimethyl sulfoxide, and with both the glassy carbon and the Pt disk electrodes.

Summarizing the results from the aprotic ammonium-bases AQ salts, it was observed that in contrast with imidazolium-based salts, these salts suffered reductive degradation processes, which generated different redox-active species at the electrode surface. The nature of the degradation products is not understood. In all cases, the potential of the first redox wave of the degradation products closely coincided with the first redox wave of **38a**. Nevertheless, the potential of the second redox wave of the degradation products showed different degrees of variation. Based on these redox waves, it was hypothesised that for **[42][Tf$_2$N]**, **[43]Br**, and **[44]Br**, **38a** is likely to be the main degradation product, while for salts **[42]Br [43][Tf$_2$N]** and **[44][Tf$_2$N]** a different degradation product was obtained. For these cases, it was proposed that neutral AQ-amines produced by homolytic C-N bond cleavage of one of the alkyl chains of the ammonium centre, were the degradation products giving rise to the new redox waves. These neutral AQ species would exhibit more similar electronic properties to those of **38a** than its ionic counterparts, thus explaining why similar redox waves were observed. However, more studies are required to determine the chemical structure of the degradation products

4.2.5.3 Electrochemical studies of the protic ammonium salts

The electrochemical behaviour of the salts **[45]Br**, **[45][Tf$_2$N]**, **[46]Br** and **[46][Tf$_2$N]** was studied in acetonitrile/0.1 M [NBu$_4$][PF$_6$] using the glassy carbon electrode, as with the aprotic ammonium salts (*Figure 4.2.34*). However, all the protic salts showed more complicated CVs, characterized by a new cathodic half-wave **J** composed of two peaks that appeared very close to each other at -0.61 V, and a new very irreversible anodic half-wave **K** at -0.23 V. Moreover, as seen in the CVs from the aprotic ammonium salts, all the protic salts exhibited a high degree of reductive degradation and formation of **38a.** Other experiments in acetonitrile, but employing a Pt disk electrode as WE, showed similar results.

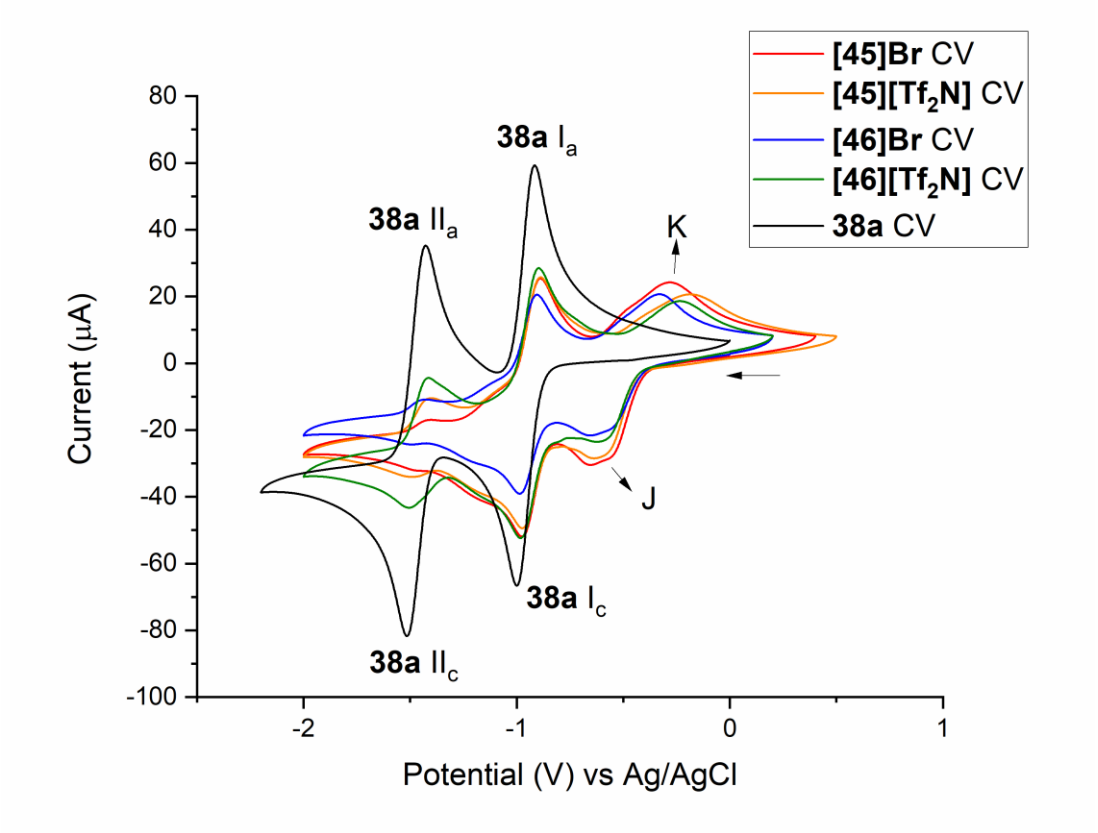

Figure 4.2.34: Cyclic voltammogram in in acetonitrile/[NBu4][PF_6] 0.1 M of the protic ammonium salts

In principle, the presence of the relatively acidic N-H proton in these salts makes the reductive degradation mechanism of the protic AQ ammonium salts more complicated, since the singly and doubly reduced AQ redox-cores are basic enough to abstract an acidic proton (*via* either inter- or intramolecular reactions). This can potentially generate new protonated AQ species, which according to the independent work by Smith and co-workers,[195,196,219] and González and co-workers,[227,228] usually leads to the appearance of significant residual current in between the redox waves of the major species, as seen in the CVs from *Figure 4.2.34*.

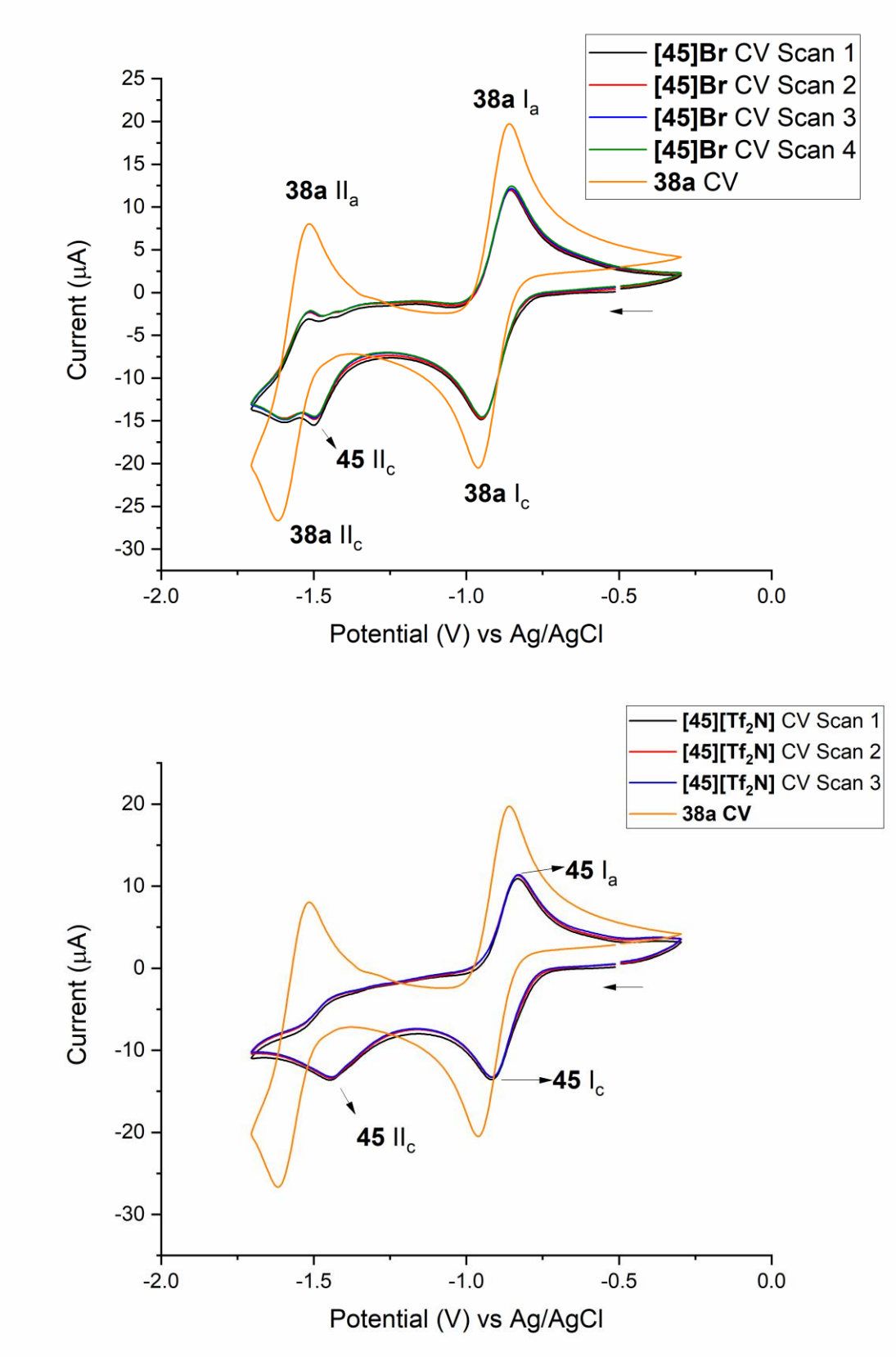

Figure 4.2.35: Cyclic voltammogram in dimethyl sulfoxide/[NBu_4][PF_6] 0.1 M of **[45]Br** (above) and **[45][Tf_2N]** (below). The CV of **38a** was obtained from another experiment.

As with **[44][Tf_2N]**, the CVs of the protic salts **[45]Br** and **[45][Tf_2N]** were also obtained in dimethyl sulfoxide/[NBu_4][PF_6] 0.1 M to obtain more insight into the reductive degradation mechanisms of the protic salts (*Figure 4.2.35*). As observed in the CV of **[44][Tf_2N]** in dimethyl sulfoxide, **[45]Br** also exhibited a reductive degradation process in which the first cathodic half-wave associated with the reduction of $\mathbf{45^+}$ overlapped with the first cathodic half-wave of the degradation product. It was assumed that both reduction steps occurred at very similar potentials, because the presence of a small but perceptible second half-wave of reduction of $\mathbf{45^{\bullet}}$ was observed at -1.50 V. As discussed for the aprotic salts, no returning oxidation half-wave for the doubly reduced species $\mathbf{45^-}$ was detected in the CV, which suggested that after the neutral radical was reduced, the newly formed anion $\mathbf{45^-}$ degraded at further cathodic potentials (*Figure 4.2.35*-above).

The potential of the first and second cathodic half-waves associated with the degradation product almost coincided with the expected potentials for the redox waves of **38a** in dimethyl sulfoxide. The cathodic peaks of the degradation product were shifted by 14 mV to anodic potentials with respect to the expected potentials of the reduction peaks of **38a**. However, $\mathbf{II_a}$ from the degradation product and $\mathbf{II_a}$ from **38a**, occurred at the same potential. Therefore, it is probable that under the cathodic potentials studied, **[45]Br** underwent a single-electron transfer to the ammonium centre that produced a homolytic C-N bond cleavage, which generated **38a** as major degradation product.

Surprisingly, the CV of **[45][Tf_2N]** suggested that the salt is electrochemically stable towards reductive degradation under the potentials studied (*Figure 4.2.35*-below). Its electrochemical behaviour was described by a one-electron two-step mechanism, characterized by a quasi-reversible first redox step ($E_{1/2}$ = -0.890, ΔEp = 84 mV, Ip_c/Ip_a = 1.11), and an electrochemically irreversible second redox step, in which the reduced species $\mathbf{45^-}$ was coupled to a chemical process that consumed it, causing no anodic peak associated with its re-oxidation to be observed.

The current peak height from the second cathodic half-wave was half the size of the first cathodic half-wave $\mathbf{I_c}$ = -12 μA *vs* $\mathbf{II_c}$ -6 μA. In principle, both half-waves should be the same size, hence, this suggested that the neutral radical **45•** was involved in some chemical reaction, which consumed part of it and depleted its concentration at the electrode surface. Moreover, the second anodic half-wave was only evident at faster scan rates. This suggests that **45⁻** was involved in a chemical reaction at the electrode surface. A hypothesis that was previously proposed to explain why the second anodic wave was smaller than second cathodic wave in **[41]Br**, was that the doubly reduced species **45⁻** could be involved in a comproportionation reaction with the fully oxidized species **45⁺** to generate **45•** (*Scheme 4.2.12*). Although this would explain the small current of $\mathbf{II_a}$, this hypothesis would be in contrast with the fact that $\mathbf{II_c}$ was half the size of $\mathbf{I_c}$. If **45•** was being formed by comproportionation of **45⁺** and **45⁻**, a higher half-wave $\mathbf{II_c}$ associated with the reduction of **45•**, prior to the comproportionation reaction, would be expected.

$$\mathbf{45^-} + \mathbf{45^+} \rightleftharpoons 2\ \mathbf{(45^\bullet)}$$

Scheme 4.2.12: Comproportionation hypothesis to explain the absence of the re-oxidation wave of **45⁻**

To gain insight into the chemical reactions accompanying the one-electron two-step redox mechanism of **[45][Tf₂N]**, the CV was obtained at different scan rates (*Figure 4.2.36-above*). The analysis of the Ip vs $\upsilon^{1/2}$ plots showed that the half-waves $\mathbf{I_c}$, $\mathbf{II_c}$ and $\mathbf{I_a}$ were close to linearity (*Figure 4.2.36-below*). This was interpreted as that for these redox steps, the electron-transfer processes were limited by the diffusion of the electroactive species to the electrode surface only.

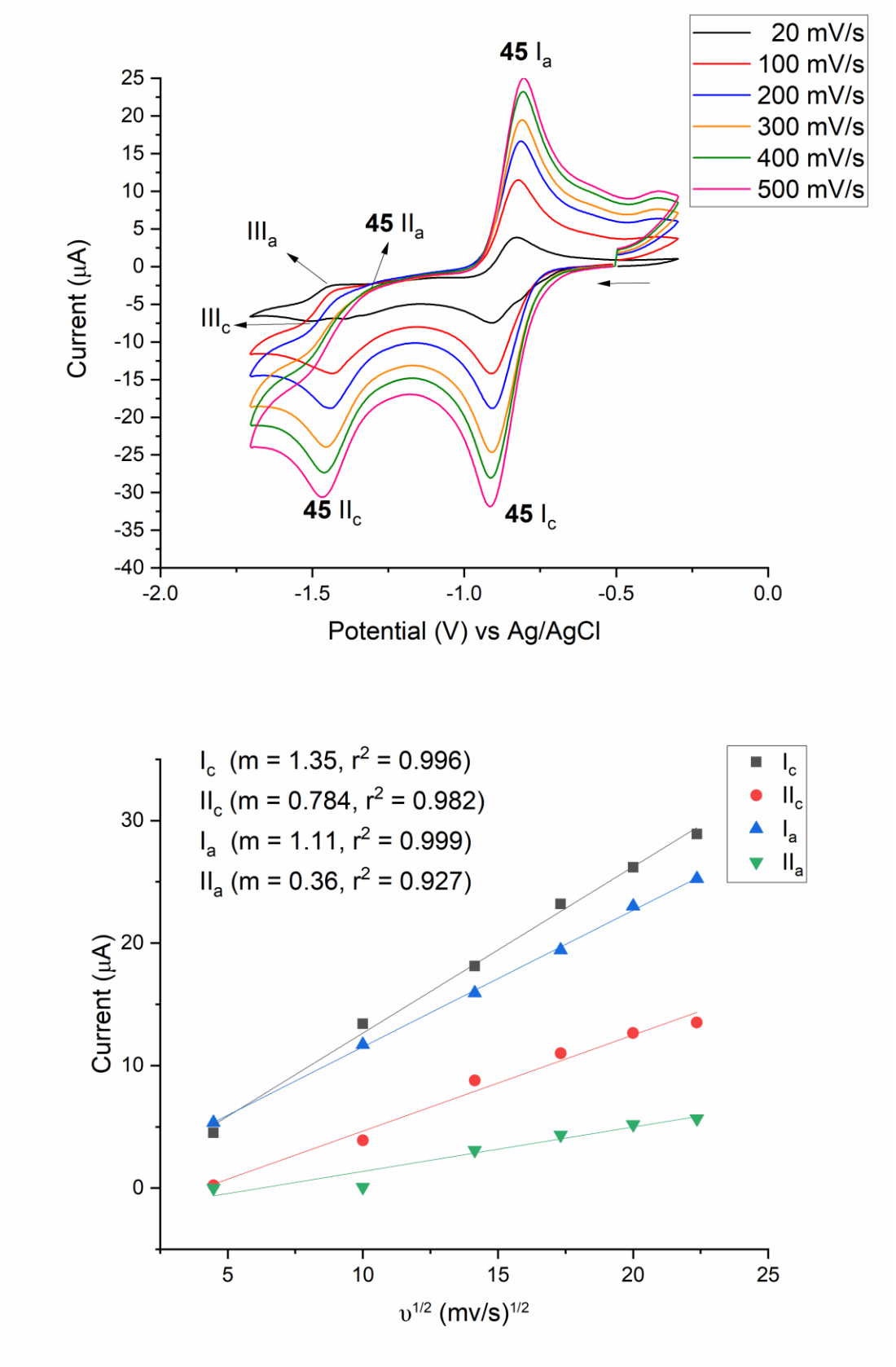

Figure 4.2.36: Cyclic voltammogram in dimethyl sulfoxide/[NBu$_4$][PF$_6$] 0.1 M of **[45][Tf$_2$N]** at different scan rates**.** (above). I vs $\upsilon^{1/2}$ plot of **[45][Tf$_2$N]** (below)

The fact that **II_c** appeared to be limited only by the diffusion of **$45^{\bullet}$** from the surroundings of the electrode to the electrode surface, suggested that the chemical process responsible for depleting it, is faster than the diffusion of **$45^{\bullet}$** and takes place before this species reaches the electrode surface. On the other hand, **II_a** showed more deviation from linearity which confirms that the chemical process responsible for consuming **45^{-}** takes place at similar rates to the electron-exchange reaction.

At scan rates ≤ 100 mV/s a new redox wave **III_c/III_a** was observed at $E_{1/2}$ = -1.471 V, which did not coincide with the second redox process of **38a,** therefore, it corresponds to the second redox process of a different AQ-related species. At scan rates between 100 mV/s and 300 mV/s, **III_c/III_a** wave faded, but some residual current remained visible, while at faster scan rates the residual current was no longer perceptible.

It is important to highlight that **III_c/III_a** was not followed by new anodic waves on the returning scan, which suggested that upon oxidation, the species associated with the new redox wave, generates back the neutral radical **$45^{\bullet}$**, which then undergoes oxidation to **45^{+}** at the same potential regardless of the scan rate.

At slow scan rates, the current peak heights of the half-waves **II_c** and **III_c** only added up to 20% the total current of wave **I_a**. Besides, despite the redox wave **III_c/III_a** disappeared at scan rates above 100 mV/s, the current associated with **II_a** from the oxidation of the doubly reduced anion **45^{-}** did not experience a more pronounced increase. This suggest that there are at least two chemical transformations responsible for the depletion of **45^{-}** at the electrode surface. One which generates **III_c/III_a** and that is only active at slow scan rates, and one which is active all the time and it is responsible for most of the depletion of the concentration **45^{-}** at the electrode surface.

The formation of a redox-inactive complex involving **$45^{\bullet}$** could explain why **II_c** is smaller than **I_c**. This complex would have to decompose at potentials

between -1.483 V and -0.83 V to regenerate the neutral radical, which then would undergo its oxidation to **45^{+}** at -0.83 V, thus explaining why the current peak height of the first anodic wave **I_a** was almost equal to I_c. This could also explain the small size of **II_a**. However, it is not clear what is causing the **III_c/III_a** wave at slow scan rates only.

Another hypothesis to explain the small size of **II_a** and its broadness, is that once the doubly reduced anion species **45^{-}** is generated, it rapidly catches a proton from another ammonium cation or from water in the solvent, which would cause a large shift of the second anodic half-wave to positive potentials, up to a point where **I_a** and **II_a** would merge into a single two-electron oxidation half-wave. However, if this was the case, the current peak height of **I_a** would be expected to be twice the size of **I_c**, which was not observed. More studies are required to determine their origin of the chemical transformations involved.

Finally, the CVs of the N-methylcyclohexylammonium-based AQ salts **[46]Br** and **[46][Tf$_2$N]** were obtained in dimethyl sulfoxide with the Pt disk electrode as WE (*Figure 4.2.37*). It was found that **[46]Br** exhibits a similar electrochemical behaviour to that of **[45]Br**. **[46]Br** showed a reductive degradation process in which the first cathodic half-wave of **46^{+}** appeared overlapped with the first cathodic wave of the degradation product (*Figure 4.2.37-above*).

The potentials at which the AQ-based degradation product underwent its two reduction steps were shifted by 14 mV to positive potentials with respect to the expected reduction potentials of **38a**, but the potential of the second anodic half-wave of the degradation product, coincided with the potential of the second oxidation of **38a**, exactly as observed previously in the CV of **[45]Br.** Therefore, it was concluded that **[46]Br** also exhibited reductive degradation to form **38a**.

An important difference between the reductive degradation processes exhibited by the protic and the aprotic ammonium salts, is that the current peak heights associated with the reduction steps of the aprotic salts were smaller in

the second and third scans compared to the first. This was interpreted as that the degradation took place at cathodic potentials equal or beyond to the potential of the reduction of the corresponding neutral radical. On the other hand, the current peak heights associated with the reduction steps of the protic salts remained constant throughout the different scans. This suggests that their degradation process took place at potentials before the first reduction of the protic salt. Again, ammonium salts were not expected to be degraded at potentials above -1.0 V vs Ag/AgCl. More studies are needed to understand the electrochemical and chemical processes occurring with the ammonium salts.

The CV of **[46][Tf_2N]** in dimethyl sulfoxide was similar to its diethylammonium counterpart, since as observed previously, the Tf_2N^- salt did not exhibit reductive degradation reactions, characterized by the appearance of more than two redox waves, at similar potentials to those at which **38a** undergoes its redox reactions (*Figure 4.2.37-above*).

The electrochemical behaviour of **[46][Tf_2N]** was in agreement with a one-electron two-step mechanism, characterized by a quasi-reversible first redox wave ($E_{1/2}$ = -0.83, ΔEp = 84 mV, Ip_c/Ip_a = 1.15) and an electrochemically irreversible second redox step, in which the reduced species **46$^-$** was coupled to a chemical process that reduced its concentration at the electrode surface.

As observed in the previous Tf_2N^- salt, no anodic half-wave **IIa** was detected in the CV of **[46][Tf_2N]** at 100 mV. Instead, a new small anodic half-wave was detected at more negative potentials (-1.46 V). Besides, the current peak height of $\mathbf{II_c}$ accounted only for 50% of the current peak height of $\mathbf{I}_a$, as observed previously for **[46][Tf_2N]**. This suggest that in **[46][Tf_2N]** a similar mechanism that reduces the concentration of **46$^\bullet$** at the electrode surface takes place.

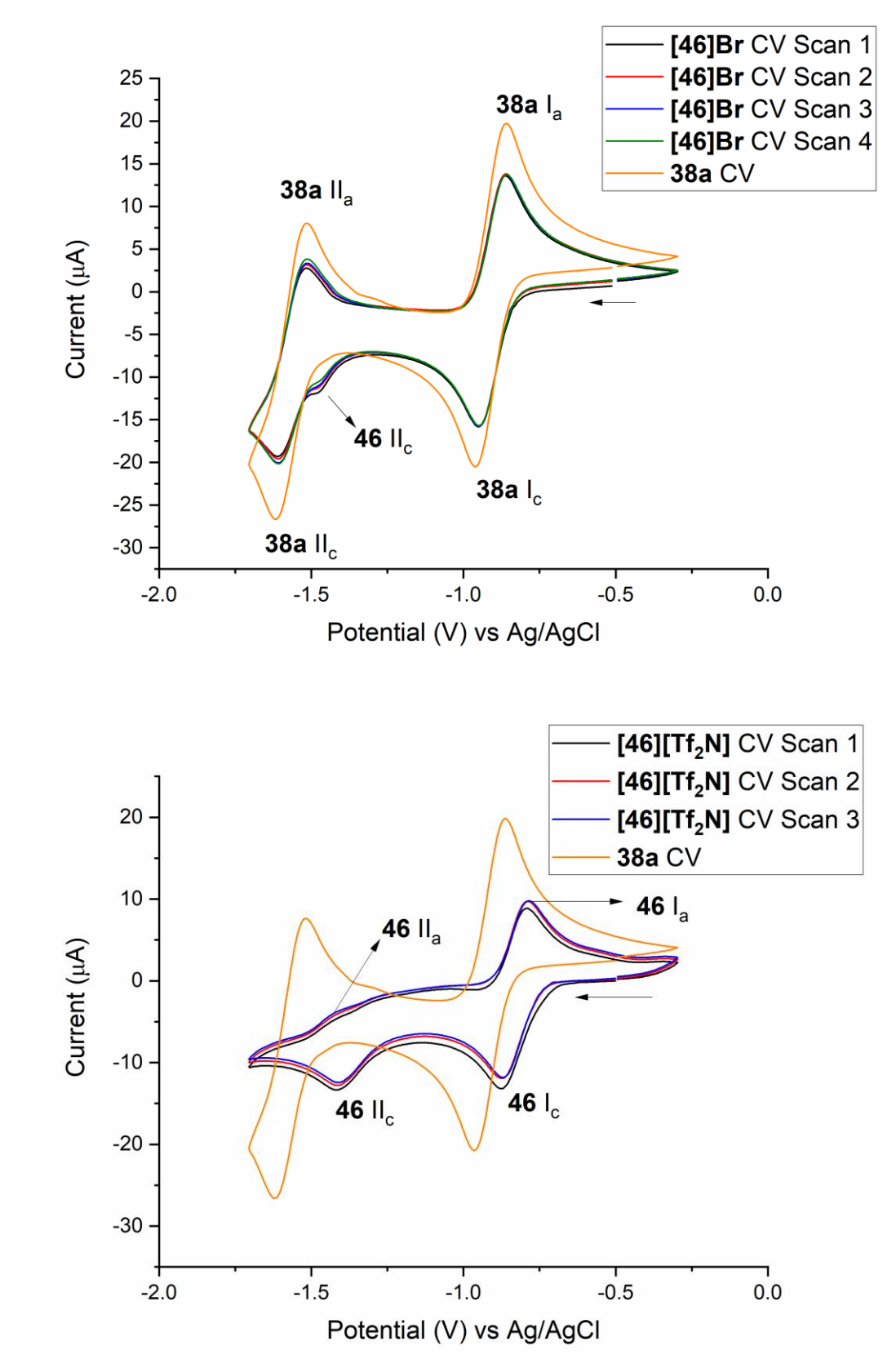

Figure 4.2.37: Cyclic voltammogram in dimethyl sulfoxide/[NBu_4][PF_6] 0.1 M of **[46]Br** (above) and **[46][Tf_2N]** (below). The CV of **38a** was obtained from another experiment.

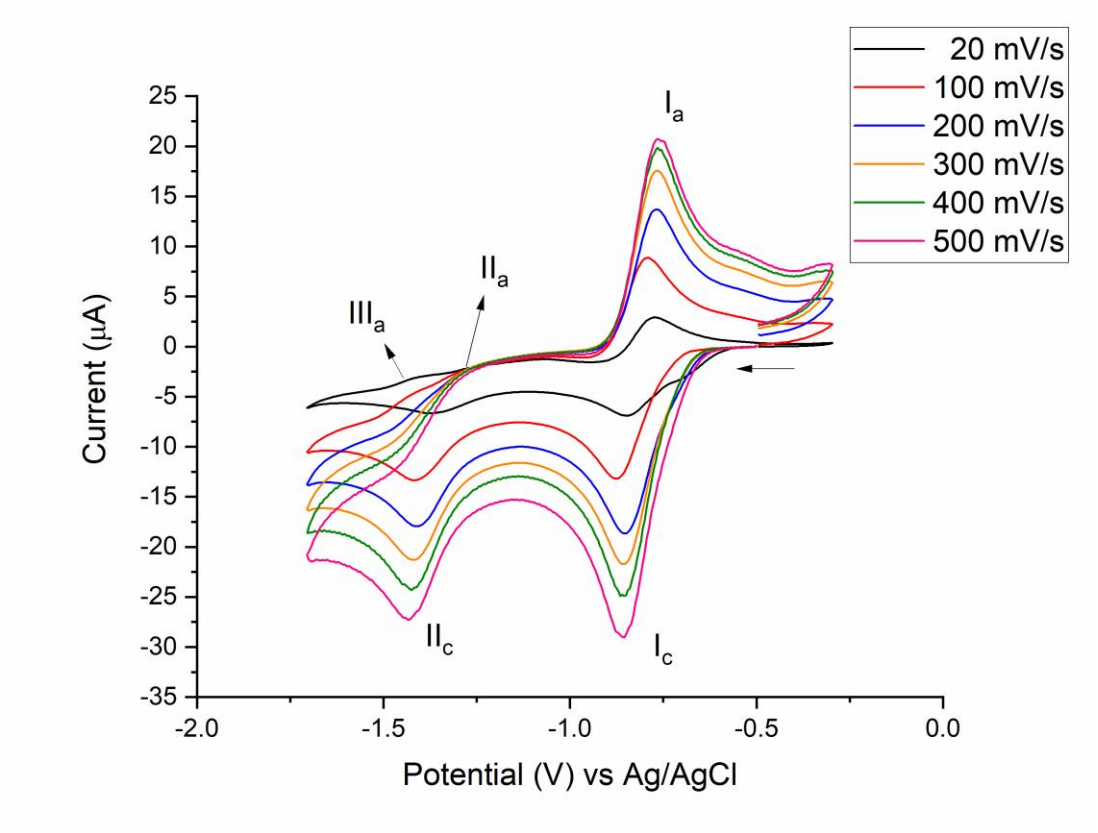

Figure 4.2.38: Cyclic voltammogram in dimethyl sulfoxide/[NBu_4][PF_6] 0.1 M of **[46][Tf_2N]** at different scan rates.

The third wave was not due to reductive degradation of the salt to generate **38a** as the oxidation potential of both waves did not coincide, and no reduction half-wave was observed in the cathodic scan. As discussed previously, the nature of this wave is not clear.

The CVs of **[46][Tf_2N]** obtained at various scan rates showed a similar behaviour of the cathodic and anodic waves as discussed previously (*Figure 4.2.38*). While $\mathbf{I_c}$, $\mathbf{I_a}$ and $\mathbf{II_c}$ exhibited a good linear correlation with the square root of the scan rate ($r^2 \leq 0.98$), $\mathbf{II_a}$, showed higher deviation from linearity ($r^2 = 0.90$), This means that $\mathbf{I_c}$, $\mathbf{I_a}$ and $\mathbf{II_c}$ are limited only by the diffusion of the electroactive species to electrode, while for $\mathbf{II_a}$ there is an interplay of chemical transformations conditioning the redox reaction.

The electrochemical analysis of the protic AQ salts showed that **[45][Tf_2N]** and **[46][Tf_2N]** were characterized by a one-electron two-step mechanism, with no

reductive degradation observed at the Pt disk electrode in dimethyl sulfoxide. It is not clear why the electrochemical behaviour of these salts became reversible and resistant to degradation when the solvent and the WE were replaced. Based on these results, it seems that the protic alkylammonium AQ salts were benefited by a more protic environment, since dimethyl sulfoxide had a water content around two orders of magnitude higher than acetonitrile. Considering that DESs exhibit a similar protic environment, it would be expected that **[45][Tf_2N]** and **[46][Tf_2N]** would exhibit a similar electrochemical behaviour as in dimethyl sulfoxide. However, more studies are needed to characterize the electrochemical stability of these salts.

Summarising, the electrochemical studies of the protic alkylammonium AQ salts using the glassy carbon electrode in acetonitrile showed that these species suffered reductive degradation and exhibited slow electron-exchange reactions characterized by broad redox waves and the appearance of residual current in between the major redox processes. However, the protic ammonium salts exhibited more electrochemically reversible redox processes in dimethyl sulfoxide and with a Pt disk electrode. The electrochemical behaviour of **[45]Br** and **[46]Br** was characterized by exhibiting high degradation from the beginning of the experiment. The Tf_2N^- salts **[45][Tf_2N]** and **[46][Tf_2N]** did not appear to show reductive degradation, since their CVs showed two main redox waves. The CVs of the Tf_2N^- salts showed that the electrochemical reactions were coupled to chemical reactions that depleted the concentration of the neutral radical species and the doubly reduced anionic species. However, as occurred with the imidazolium-based salts, these coupled chemical reactions did not affect the electrochemical reversibility of the whole redox process.

4.3 Summary and conclusions

The synthesis of six AQ bromide salts functionalised with ammonium and imidazolium ionic fragments from 2-methylanthraquinone was carried out by halogenation of the methyl position of the starting material *via* Wohl-Ziegler bromination and subsequent nucleophilic substitution of the C-Br bond with

the corresponding amine. The Tf_2N^- salts **[41-44][Tf$_2$N]** were prepared by anion metathesis with Li[Tf_2N] while the Tf_2N^- salts of the protic cations **45$^+$** and **46$^+$** were prepared by acid/base reaction of the corresponding neutral amine with H[Tf_2N]. All twelve AQs were characterised by means of multinuclear NMR, ESI-MS and elemental analysis, the solid-state structure of salts **[41]Br**, **[46]Br**, **[41-44][Tf$_2$N]** and **[46][Tf$_2$N]** was obtained by single-crystal XRD and their molecular and electronic structures modelled with DFT.

The chemical shift of the aromatic protons remained consistent throughout the family of salts with the most deshielded environments being the hydrogen atoms from the C_6H_3 ring located at the *ortho* position of the quinone rings. The solid-state structures show the quinone and the aromatic AQ system bonding distances and angles remained overall unperturbed, with deviations from planarity of the lateral aromatic rings no greater than 4º. The only exception was salt **[46][Tf$_2$N]**, where one of its C=O bonds from the quinone ring severely pulled out of the ring plane by an intense hydrogen-bonding interaction with the acidic proton from the ammonium group of a neighbouring cation. The packing in the solid-state structures of the AQ motifs was dominated by parallel-displaced π-stacking interactions except for salt **[44][Tf$_2$N]**, which did not exhibit AQ π-stacking. Salts **[41][Tf$_2$N]**, **[43][Tf$_2$N]**, **[44][Tf$_2$N]** and **[46]Br** prefer to arrange in a way that leads to separated ionic and non-polar planes, while in salts **[41]Br**, **[42][Tf$_2$N]** and **[46][Tf$_2$N]** the anions prefer to occupy voids between pairs of AQ layers.

The imidazolium-based AQ salts exhibited a reversible one-electron two-step redox mechanism in acetonitrile with a glassy carbon electrode as WE. The redox waves associated with the AQ motif of salts **[41]Br** and **[41][Tf$_2$N]** appeared at more positive potentials than the starting material **38a**, which suggested that the introduction of the charged imidazolium ring stabilized the reduced AQ species. It was observed that **[41]Br** displayed a slightly more electrochemically reversible behaviour than **[41][Tf$_2$N]**, as its redox waves were characterized by smaller peak-to-peak separations. The second redox step of **38a** and both imidazolium salts **[41]Br** and **[41][Tf$_2$N]** exhibited smaller

cathodic half-wave peak currents than the first redox wave, and Ip_c/Ip_a ratios < 1, which suggested that the singly reduced species of these compounds were coupled to a chemical equilibrium that was reducing its concentration at the electrode surface. However, these chemical equilibria were reversible, since the reduced species were regenerated during the anodic scan, as evidenced by an Ip_c/Ip_a ratio of the first redox wave close to 1. This electrochemical behaviour was consistent with other AQ derivatives used in electrochemical energy storage.

The electrochemical behaviour of **[41][Tf_2N]** was also characterized in [C_2Mim][Tf_2N], but in contrast to what was observed in acetonitrile, the redox waves of the AQ salt were characterized by larger peak-to-peak separations and larger half-wave areas, which is an indication of electrochemical irreversibility due to slow electron-exchange kinetics.

The CVs of the aprotic alkylammonium salts in acetonitrile showed new redox waves that appeared at potentials near to the expected redox waves of the starting material **38a**. It was hypothesised that either **38a**, or an AQ-based degradation product of similar electronic structure to that of **38a**, was being formed through a single-electron transfer to the ammonium cation, followed by homolytic C-N bond cleavage of one of the alkyl chains of the ammonium salt. This could either generate a tertiary amine substituted with a 2-methylanthraquinone fragment or **38a**. All salts showed major degradation at cathodic potentials beyond their second reduction, only **[42][Tf_2N]** showed a small degradation peak after its first reduction in the first scan. The case of **[42]Br** was different, because the first reduction peak associated with the degradation product presented larger current peak heights than the rest of the redox half-waves. This was attributed to the adsorption of the degradation product to the electrode surface.

The protic alkylammonium salts also showed reductive degradation in acetonitrile, but in these cases, their redox reactions were also electrochemically irreversible, as demonstrated by large redox waves areas and long peak-to-peak distances. The protic salts exhibited faster electron-

exchange kinetics in dimethyl sulfoxide and with a Pt disk electrode as WE, which facilitated their electrochemical characterization. **[45]Br** and **[46]Br** showed very similar CVs, both salts presented new redox waves at potentials near to those of **38a**. As opposed to what was observed with the aprotic salts, these new redox waves were seen since the first cathodic scan of the bromide salts and their current peaks heights remained constant throughout the experiments. **[45][Tf_2N]** and **[46][Tf_2N]** also showed very similar CVs, but in contrast with the bromide salts, the Tf_2N^- salts were characterized by only two redox waves that occurred at more positive potentials than those of **38a**. This suggested that the Tf_2N^- protic salts did not suffer reductive degradation under the potentials studied.

In both protic Tf_2N^- salts the second cathodic wave was characterized by smaller current peak heights than the first redox wave, and by presenting very small and broad anodic peaks corresponding to the second oxidation. It was observed that the electrochemical processes were coupled to chemical reactions that depleted the concentration of both the singly reduced neutral radical and the doubly reduced anion at the electrode surface. However, these reactions appeared to be reversible because the neutral radical species was regenerated during the anodic scan, since the current peak height of the first oxidation was similar to that of the first reduction.

From the electrochemical studies performed, it was concluded that **[41]Br** was the best candidate to prepare a RADES, because the imidazolium-based salts exhibited the most electrochemically reversible reactions and showed no reductive degradation at the potentials studied. The bromide salt was chosen over the Tf_2N^- salt because the halides are better HBA than the Tf_2N^- anion, which would make the preparation of the RADESs potentially easier.

4.3.1 Future Work.

The electrochemical studies of the alkylammonium salts left some questions unanswered with regards to the chemical nature of the reductive degradation products. To address this problem, the next steps could involve:

- To quantitatively reduce the AQ-salts at cathodic potentials beyond -1.5 V vs Ag/AgCl.
- To characterize the degradation products by LC-MS and NMR.

With regards to **[41]Br**, **[41][Tf_2N]**, **[45][Tf_2N]** and **[46][Tf_2N]**, more studies are required to determine the mechanism of the electrochemical and chemical coupled reactions involved in the depletion of the concentration of the singly and doubly reduced species at the electrode. To do so, it is necessary to determine the following parameters:

- The diffusion constants of every redox state for every salt. These can be obtained by amperometric methods.
- The rate of every electron-transfer reaction.
- Different chemical equilibria can be proposed, and their equilibrium constants estimated by modelling the CVs computationally with the experimental data obtained previously.

Alongside the electrochemical studies, the preparation of a RADES with **[41]Br** as HBD can be tried using glycerol or ethylene glycol as HBDs. Besides, a long-chain carboxylic acid like decanoic acid can be used as HBD to analyze if a more hydrophobic HBD could reduce the water content of the RADES.

Chapter V: Experimental Section

5.1 Chapter III experimental information

5.1.1 General methods

All reagents were purchased from commercial sources unless their preparation is described. THF was refluxed over sodium wires for 3 days and stored over 4 Å molecular sieves, its water content was confirmed to be lower than 10 ppm by Karl Fischer analysis. Anhydrous $ZnCl_2$, Zn^0, LiCl and $[Pd(OAc)_2(PPh_3)_2]$ were stored in a dinitrogen-filled glovebox and used without further purification. For the synthesis of the electrophiles, hydrogen and carbon nuclear magnetic resonance spectra were recorded on a JEOL EXC400 spectrometer (operating at 400 MHz for ^1H and 100.5 MHz for ^{13}C). For the analysis of the monosubstituted cross-coupling product of methyl 2,3,5-trisubstituted benzoate and benzyl zinc, a 600 MHz Bruker Avance III HD spectrometer equipped with a room temperature broadband probe was used (operating at 600 MHz for 1H and 150 MHz for ^{13}C). All chemical shifts were reported in parts per million and were referenced using the chemical shifts of residual protio solvent resonances to internal solvent peaks. The chemical shifts are consecutively reported as position (δ), relative integral, multiplicity (s=singlet, d=doublet, t=triplet, q=quartet, br=broad,), coupling constant (J in Hz) and assignment. The isolated yield of selected samples was obtained by purification of the reaction mixture through flash column chromatography with Silica gel 60 Å 220-440 mesh.

Gas chromatography experiments were performed in a ThermoScientific Trace 1300 GC equipped 2 columns: a) DB5 general purpose column, nonpolar (5% Phenyl)methylpolysiloxane (30 cm x 0.25 mm x 0.25µm) and b) Rxi-17 mid polarity column (50% Phenyl)methylpolysiloxane (30 cm x 0.25 mm x 0.25µm); autosampler, detector: FID, carrier gas: Hydrogen, samples diluted in dichloromethane. Method: Run time between 15 and 21 min, splitless injections at 280 ^oC, column flow 1.5 mL/mim. Ramp: Starting temperature: 50 ^oC holded for 0.5 min, then ramp at 100^oC/min to 90 ^oC, then ramp at 15 ^oC/min

to 300 ºC, holded for 6 min. FID: 330 ºC. GC-MS experiments were done in a JEOL AccuTOF GCx plus mass spectrometer, GC: Agilent 7890B GC, ionization method: EI.

5.1.2 Preparation of DESs.

Choline chloride was recrystallized from ethanol in a Schlenk tube, the solvent was removed by cannula filtration and the crystals dried under vacuum. The amides and polyols were dried under vacuum at 100 ºC for 30 minutes. Acetyl choline chloride was used as purchased. For all wet-DESs the components were added to a round-bottom flask at the corresponding stoichiometry shown in *Table 5.1.1*, stirred and heated to 80 ºC for 30 minutes or until a homogeneous liquid was formed. For all dry-DESs, the components were added to an oven-dried Schlenk tube using protecting N_2 atmosphere.

Table 5.1.1: Employed DES

Entry	DES	Ammonium Salt	Hydrogen Bond Donor	NR_4X/HBD Stoichiometry
1	ChCl/U	Choline chloride	Urea	1:2
2	ChCl/Gly	Choline chloride	Glycerol	1:2
3	ChCl/EtGly	Choline chloride	Ethylene glycol	1:2
4	ChCl/DMU	Choline chloride	Dimethylurea	1:2
5	ChCl/$AcNH_2$	Choline chloride	Acetamide	1:2
6	AcOChCl/U	Acetyl choline chloride	Urea	1:1

5.1.3 Procedure for the Suzuki-Miyaura experiments in DESs

A round-bottom flask was loaded with the respective bromoarene (1 mmol, 1 equivalent), phenylboronic acid (183 mg, 1.5 mmol, 1.5 equivalents), $Pd_3(OAc)_6$ (4.5 mg, 2 mol%) and 5 cm^3 of DES. The mixture was stirred for 10 minutes at room temperature and then heated to the desired temperature for 2 to 6 hours. After this, the reaction mixture was quenched with 10 cm^3 of 2 M aqueous solution of ammonium chloride, extracted with dichloromethane

(3x15 cm^3), washed with 30 cm^3 of deionized water and 30 cm^3 of brine, dried over $MgSO_4$ and filtered. The product was purified by flash column chromatography with hexane/ethyl acetate 4:1 as eluent.

5.1.4 Preparation of Zn reagents.

n-Butylzinc chloride: In an oven-dried Schlenk tube under nitrogen atmosphere, *N*-benzylbenzamide (105.58 mg, 0.5 mmol) was dissolved in dry THF and cooled to -40 ^oC in a mixture of liquid nitrogen and acetone to titrate a commercial solution of *n*-butyllithium in hexanes, the equivalence point was reached when the solution in the Schlenk tube became electric blue. In a separate oven-dried Schlenk tube under nitrogen atmosphere, $ZnCl_2$ (276 mg, 2.0 mmol) was dissolved in 2 cm^3 of anhydrous THF. The mixture was cooled to -78 ^oC with a dry ice/acetone bath and a solution of *n*-butyllithium in hexanes was added dropwise (2.0 mmol). The mixture was stirred for 30 minutes at -78 ^oC and then allowed to reach room temperature for 30 min before its usage. The reagent was employed without further characterization.

Phenyl-zinc chloride: In an oven-dried Schlenk tube under nitrogen atmosphere, bromobenzene (211 µL, 2 mmol) was dissolved in 2 cm^3 of anhydrous THF and cooled to -78 ^oC. Then a titrated solution of *n*-butyllithium in hexanes was added dropwise (, 2 mmol) and stirred at -78 ^oC for 30 min. In a second oven-dried Schlenk tube under nitrogen atmosphere, $ZnCl_2$ (276 mg, 2 mmol) was dissolved in 2 cm^3 of anhydrous THF cooled to -78 ^oC and stirred for 30 minutes. Then, the phenyllithium mixture was added dropwise to the $ZnCl_2$ mixture at -78 ^oC and stirred for 30 minutes. Then, the phenyl-zinc reaction mixture was allowed to reach room temperature for 30 minutes before its usage. The reagent was employed without further characterization.

Phenyl-zinc*LiCl: Prepared according to a literature method.[176,177] Anhydrous LiCl (429.4 mg, 10 mmol) was placed in an oven-dried Schlenk tube, dried for 20 minutes at 150 ^oC under vacuum. Zn powder (325 mesh, 915.3 mg, 1.4 mmol) was added to LiCl and dried for another 20 minutes. 10 cm^3 of anhydrous THF were added to the mixture and Zn activated *in situ* by dibromoethane (60 µL, 5 mol %) and trimethylsilyl chloride (17.8 µL, 1 mol %).

After that, iodobenzene (1.1 cm^3, 1 mmol) was added at room temperature and the mixture stirred for 24 h. The organozinc solution was titrated by dissolving I_2 (127 mg, 0.5 mmol) in a previously prepared anhydrous solution of LiCl in THF 0.5 M. The titration was carried out in an ice bath. The equivalence point was reached when the iodine mixture became colourless. The reagent was employed without further characterization.

Benzylzinc bromide: Prepared according to a literature method.[177,178] An oven-dried Schlenk tube under nitrogen atmosphere was loaded with Zn^0 powder (325 mesh) (1.34g, 21 mmol) and 2 cm^3 of dry THF. In a second oven-dried Schlenk tube benzyl bromide freshly distilled under nitrogen (1.7 cm^3, 14 mmol) was dissolved in 7 cm^3 of dry THF. The Zn mixture was cooled to 0 ^oC and the benzyl bromide solution was added dropwise with a rate of 1 drop per 10 seconds. After the addition, the reaction was stirred for 18 hours at 0 ^oC under nitrogen. Finally, the excess of Zn was filtrated, and the benzylzinc solution stored in an ampule at 4 ^oC. The organozinc solution was titrated by dissolving I_2 (127 mg, 0.5 mmol) in a previously prepared anhydrous solution of LiCl in THF 0.5 M. The titration was carried out in an ice bath. The equivalence point was reached when the iodine mixture became colourless. The reagent was employed without further characterization.

5.1.5 Preparation of *ortho*-substituted electrophiles

N'N-diethtyl-2-iodobenzamide: This product was prepared according to a literature method with slight modifications.[229] Reaction conditions: 2-iodobenzoic acid (2g, 8.1 mmol, 1 equivalent) was placed into an oven-dried two-neck round-bottom flask equipped with a magnetic stirred bar under N_2 atmosphere. The acid was dissolved in 16 cm^3 of dry dichloromethane (0.5 M solution) and 5 drops of dry dimethylformamide. Then, the reaction mixture was cooled to 0 ^oC and oxalyl chloride (820 µL, 9.7 mmol, 1.2 equivalents) was added dropwise. Gas evolution was observed. Afterwards, the reaction was allowed to reach room temperature and stirred for 3 hours. After this, the solvent removed under vacuum and the crude redissolved in 16 cm^3 of dry dichloromethane. The reaction mixture was cooled to 0 ^oC and diethylamine

(3.3 cm^3, 32.24 mmol. 4 equivalents) was added dropwise. The reaction was allowed to reach room temperarture and stirred for 3 h. Work up: The reaction was quenched with 16 cm^3 of deionised water. The aqueous phase was extracted with dichloromethane (2x10 cm^3) and the organic phases as well as the initial reaction solvent combined and washed with HCl 1M (2x10 cm^3) and brine (1x15 cm^3). The crude was concentrated under vacuum and purified by column chromatography eluent, Hexane/Ethyl acetate 3:2. A yellow transparent oil was obtained 88% yield.

2-Iodobenzanilide**:** Prepared according to a literature method with slight modifications.[229] Reaction conditions: 2-iodobenzoic acid (4g, 0.016 mol, 1 equivalent) was placed was placed into an oven-dried two-neck round-bottom flask equipped with a magnetic stirred bar under N_2 atmosphere. The acid was dissolved in 30 cm^3 of dry dichloromethane (0.5 M solution), 10 drops of dry dimethylformamide were added. Then, the reaction mixture was cooled to 0 ^oC and oxalyl chloride (1.640 cm^3, 0.019 mol, 1.2 equivalents) was added dropwise. Gas evolution was observed. Afterwards, the reaction was allowed to reach room temperature and stirred for 3 hours. After this, the solvent was removed under vacuum and the crude dissolved in 30 cm^3 of dry dichloromethane. The reaction mixture was cooled to 0 ^oC and aniline (5.9 cm^3, 0.064 mol 4 equivalents) was added dropwise. The reaction was allowed to reach room temperature and stirred for 3h. Work up: The reaction was quenched with 30 cm^3 of deionised water. The aqueous phase was extracted with dihcloromethane (2x10 cm^3) and the combined organic phases were washed with HCl 1M (2x10 cm^3) and brine (1x15 cm^3). The crude product mixture was concentrated under vacuum and purified by recrystallization from boiling dichloromethane. White needles were obtained, 69% yield.

2-(2-iodophenyl)pyridine**:** Prepared according to a literature method with slight modifications.[230] Reaction conditions: 2-phenylpiridine (2.55 cm^3, 2.761 g, 0.0178 mol), *N*-iodosuccinimide (8 g, 0.0178 mol) and $Pd_3(OAc)_6$ (200 mg 0.00089 mol) were added to a 250 cm^3 roundbottom flask and dissolved in 175 cm^3 of acetonitrile to achieve a 0.1M concentration of pyridine. A condenser was settled and the reaction stirred at 100 ^oC for three

days. A purple-pink heterogeneous mixture was obtained. The acetonitrile was removed under vacuum, and the product purified by flash column chromatography. First, the purple non-polar impurities were removed with hexanes as eluent and then the product was separated from the starting material using 10% EtOAc in hexanes as eluent. A yellow oil was obtained, yield 35%.

1-iodo-2-(methoxymethyl)benzene**:** Prepared according to literature method with slight modifications.[231] Reaction conditions: The synthesis was carried out under inert atmosphere. In an oven-dried Schlenk tube, NaH (492 mg, 20.5 mmol) was dissolved in 15 cm^3 of dry THF. In a second oven-dried Schlenk tube, a solution of 2-iodobenzyl alcohol (4g, 17 mmol) in 15 cm^3 of dry THF was prepared. The iodoarene solution was then added dropwise to the NaH solution at 0 ^oC. Aftwerwards, the reaction mixture was stirred for 0.5 h at 0 ^oC. After this, iodomethane (1.3 cm^3, 21 mmol) was added dropwise to the reaction mixture at 0 ^oC. The reaction mixture was then stirred for 4 h and allowed to reach room temperature during this period. Work up: The reaction was quenched with 30 cm^3 of deionized water; the aqueous mixture was extracted with dichloromethane (3x20 cm^3). Then, the organic layer was dried over $MgSO_4$ and concentrated under reduced pressure. The product was purified by flash column chromatography, eluent: 10% EtOAc in hexane. A colourless oil was obtained, 85% yield.

Methyl 2,3,5-triiodobenzoate: 2,3,5-triiodobenzoic acid (5g, 0.01 mol) was placed in a round-bottom flask equipped with a magnetic stirrer bar. The acid was dissolved in 60 cm^3 of methanol and 0.11 cm^3 of concentrated sulfuric acid (20 mol %) added. A condenser was installed and the reaction refluxed for 6h. After this, the solvent was removed under vacuum and the crude product dissolved in 30 cm^3 of dichloromethane. The organic solution was washed with saturated $NaHCO_3$ aqueous solution (5x30 cm^3), and dried over $MgSO_4$ and concentrated under vacumm. An orange powder was obtained, yield 68%

5.1.6 Procedure for the C(sp^3)-C(sp^2) Negishi coupling optimisation experiments

A round-bottom flask was loaded with $Pd_3(OAc)_6$ (0.5 to 2 mol %) and 5 cm^3 of the respective DES, the mixture was heated and stirred to the desired temperature until the solution turned orange (around 10 minutes). After palladium has been solubilized, the respective iodoarene (1.0 mmol) was added and stirred at 1000 rpm for 10 minutes. Then, the organozinc solution was added in a single portion or dropwise (1 drop every 3 seconds approximately) to the Pd/arene mixture. The reaction mixture was stirred at 1000 rpm for 5 min at the desired temperature. Then, the reaction was quenched with 15 cm^3 of 2 M aqueous solution of ammonium chloride, extracted with dichloromethane (3x15 cm^3), washed with 30 cm^3 of deionized water and 30 cm^3 of brine, dried over $MgSO_4$ and filtered. The crude product was concentrated on a rotary evaporator under reduced pressure and weighed. The crude product was then analyzed by ^{1}H-NMR. The crude yield was estimated by integration of the characteristic proton signals from the methyl groups linked to the ester functionality on the product, the aryl halide and the dehalogenated side-product. The crude products of the reactions performed in ChCl/DMU and ChCl/$AcNH_2$ DESs were analyzed by GC.

5.1.7 Procedure for the C(sp^2)-C(sp^2) Negishi coupling optimisation experiments

A round-bottom flask was loaded with $Pd_3(OAc)_6$ (4.5 mg, 2 mol %) and 5 cm^3 of the respective DES, the mixture was heated to at 60 ^oC and stirred at 1000 rpm until the solution turned orange (around 10 minutes). After palladium has been solubilized, the respective iodoarene (1.0 mmol) was added and mixed for 10 minutes at 1000 rpm. After this, the organozinc mixture added dropwise (1 drop every 3 seconds approximately. The reaction mixture was stirred for 5 min at the desired temperature. Then quenched with 15 cm^3 of a 2 M aqueous solution of ammonium chloride, extracted with dichloromethane (3x15 cm^3), washed with 30 cm^3 of deionized water and 30 cm^3 of brine, dried over $MgCl_2$ and filtered. After that, the crude reaction mixture was diluted to 50 cm^3 of

dichloromethane in a volumetric flask with a known amount of internal standard. The crude reaction mixture was analyzed by GC.

5.1.8 Procedure for the Negishi coupling recycling experiment.

A round-bottom flask was loaded with $Pd_3(OAc)_6$ (11.23 mg, 5 mol %), methyl 2-iodobenzoate (147 µL, 1 mmol, 1 equivalent) and 5 cm^3 of ChCl/U, the mixture was heated to 60 ºC and stirred at 1000 rpm until the solution turned orange (around 10 minutes). Then, a solution of *n*-butylzinc chloride in dry THF (2 mmol, 2 equivalents) prepared as described previously was added dropwise (1 drop every 3 seconds approximately). The reaction mixture was stirred at 1000 rpm for 5 min at 60 ºC. Then, the products were extracted from ChCl/U with dichloromethane (5x10 cm^3) by adding the solvent directly to the round-bottom flask and stirring vigorously for a minute and decanting the dichloromethane. All the organic phases were collected, dried over $MgSO_4$ and concentrated under vacuum. The remaining organic solvent was removed from the DES by heating under vacuum. The reaction mixture was reloaded with methyl 2-iodobenzoate and the procedure repeated two more times. Hexamethylbenzene was added to the crude reaction mixture as internal standard, and the crude analyzed by ^{1}H-NMR to determine conversion.

5.1.9 Procedure for the first C(sp^3)-C(sp^2) substrate scope

A round-bottom flask was loaded with $Pd_3(OAc)_6$ (4.5 mg, 2 mol %) and 5 cm^3 of ChCl/U, the mixture was heated to at 60 ºC and stirred at 1000 rpm until the solution turned orange. After palladium has been solubilized, the respective iodoarene (1.0 mmol) was added and mixed for 10 minutes. After this, *n*-butylzinc chloride was added in a dropwise fashion (1 drop every 3 seconds approximately) to the Pd/arene mixture. The reaction mixture was stirred at 1000 rpm for 5 min at 60 ºC. Then, quenched with 15 cm^3 of 2 M aqueous solution of ammonium chloride, extracted with dichloromethane (3x15 cm^3), washed with 30 cm^3 of deionized water and 30 cm^3 of brine, dried over $MgSO_4$ and filtered. The crude reaction mixture was analyzed by GC.

5.1.10 Procedure for the s C(sp^3)-C(sp^2) Negishi coupling optimisation and substrate scope involving *ortho*-coordinating iodoarenes and other substitution patterns.

A round-bottom flask was loaded either $Pd_3(OAc)_6$ (5.5 mg, 5 mol %) or $[Pd(OAc)_2(PPh_3)_2]$ (18.7 mg, 5 mol %) and 5 cm^3 of ChCl/U. The mixture was stirred at 1000 rpm at 60 ^oC until the pre-catalyst was completely dissolved and the solution turned orange (around 10 minutes). Then, the respective iodoarene (0.5 mmol) was added and stirred for another 10 minutes. After this, the respective organozinc reagent was added in a dropwise fashion (1 drop every 3 seconds approximately). The reaction mixture was stirred at 60 ^oC for 5 minutes, then quenched with 15 cm^3 of a 2 M solution of ammonium chloride, extracted with dichloromethane (3x15 cm^3), washed with 30 cm^3 of deionized water and 30 cm^3 of brine, dried over $MgSO_4$ and filtered. The crude reaction mixture was analyzed by GC.

5.1.11 Procedure for the Negishi coupling reaction between methyl 2,3,5-triiodobenzoate and benzylzinc bromide.

A round-bottom flask was loaded either $Pd_3(OAc)_6$ (11.23 mg, 5 mol %), methyl 2,3,5-triiodobenzoate (513 mg, 1 mmol, 1 equivalent) and 5 cm^3 of ChCl/U. The mixture was stirred at 1000 rpm at 60 ^oC until solution turned orange (around 10 minutes). Then, a solution of benzylzinc in dry THF 1.2 M (1.7 cm^3, 2 mmol, 2 equivalents) was added in a dropwise fashion (1 drop every 3 seconds approximately). The reaction mixture was stirred at 1000 rpm at 60 ^oC for 5 minutes, then quenched with 15 cm^3 of a 2 M solution of ammonium chloride, extracted with dichloromethane (3x15 cm^3), washed with 30 cm^3 of deionized water and 30 cm^3 of brine, dried over $MgSO_4$ and filtered. The crude reaction mixture was analyzed by GC. Then, the internal standard was removed from the crude by flash column chromatography in silica gel 220-440 mesh using Hexane/Ethyl Acetate 99:1 as eluent. The crude was then further purified using a ConbiFlash Rf system equipped with a RediSep Rf silica column for 20 mg to 0.4 g sample, using a flow rate of 18 mL/min and a gradient of dichloromethane in hexane from 0% to 5% in 20 minutes. The

major product was not fully isolated but a sufficient amount for NMR analysis was obtained pure.

5.1.12 Suzuki-Miyaura reaction experimental data

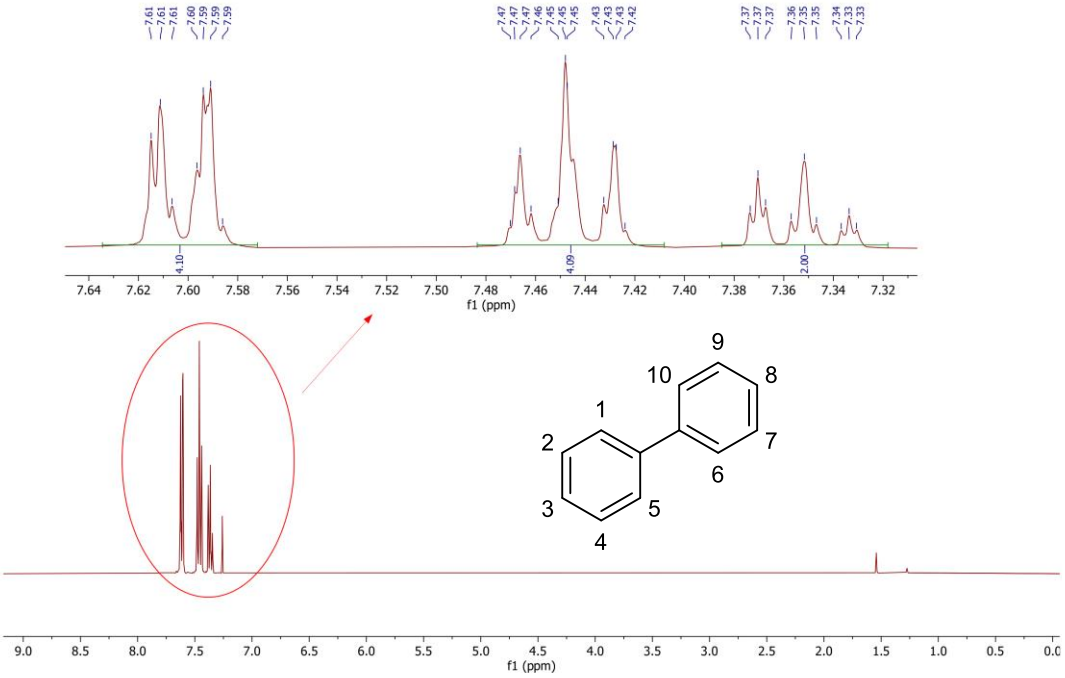

Figure 5.1.1*:* ^{1}H-NMR Biphenyl **2a**

Compound isolated by flash column chromatography from Suzuki-Miyaura experiments between phenylboronic acid and bromobenzene **1a** in DESs. ^{1}H-NMR ($CDCl_3$, 400 MHz). δ 7.61 (dt, *J* = 1.8, 8.0 Hz, 4H, (1, 5, 6, 10)), 7.46 (tt, *J* = 1.8, 7.5 Hz, 4H, (2, 4, 7, 9)), 7.36 (tt, *J* = 1.2, 7.5 Hz, 2H, (3, 8)), 7.04

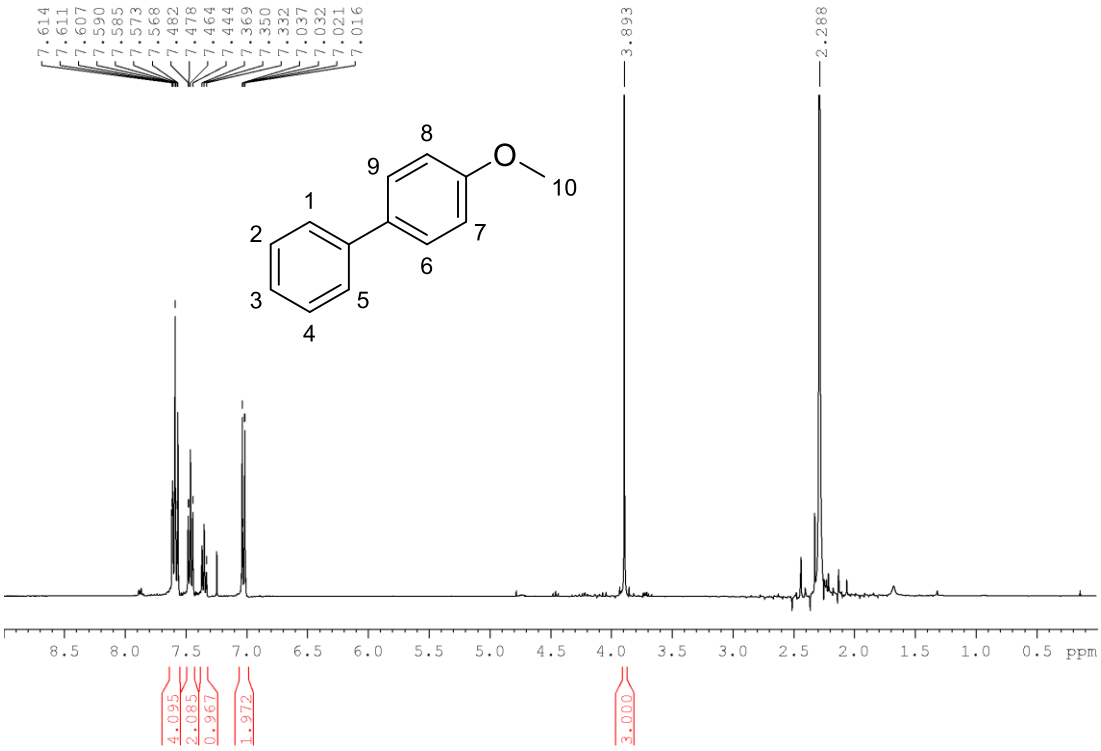

Figure 5.1.2: ^{1}H-NMR 4-methoxybiphenyl **2b**

Compound isolated by flash column chromatography hexane/ethyl acetate 4:1 from Suzuki-Miyaura reaction between phenylboronic acid and 4-bromoanisole **1b** in ChCl/G. Hexamethylbenzene added as internal standard. ^{1}H-NMR ($CDCl_3$, 400 MHz). δ 7.59 (m, 4H, (1, 5, 6, 9)), 7.46 (tt, *J* = 1.7, 7.5 Hz, 2H, (2, 4)), 7.35 (tt, *J* = 1.2, 7.5 Hz, 1H, (3)), 7.03 (dt, *J* = 2.1, 8.9 Hz, 2H, (7, 8)), 2.29 (s, 3H, (10))

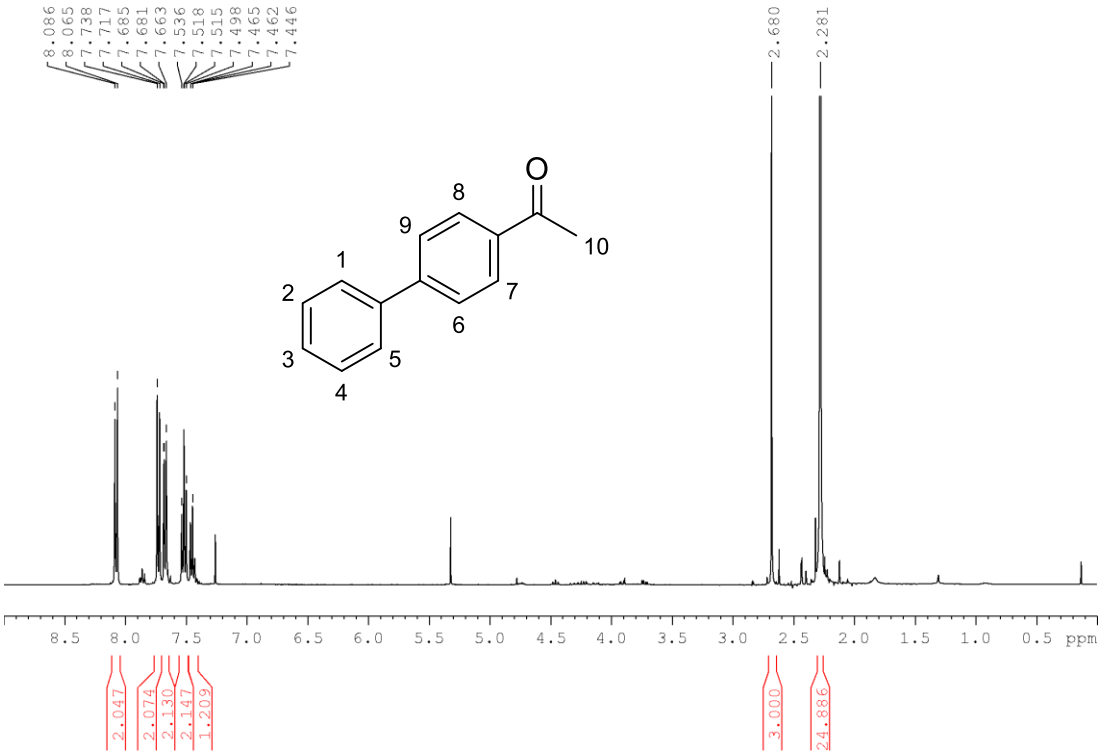

Figure 5.1.3: ^{1}H-NMR 4-acetylbiphenyl **2c**

Compound isolated by flash column chromatography hexane/ethyl acetate 4:1 from Suzuki-Miyaura reaction between phenylboronic acid and 4-bromacetophenone **1c** in ChCl/G. Hexamethylbenzene added as internal standard. ^{1}H-NMR ($CDCl_3$, 400 MHz). δ 8.08 (dt, *J* = 1.8, 8.5 Hz, 2H, (1, 5)), 7.72 (dt, *J* = 1.8, 8.5 Hz, 2H, (6, 9)), 7.67 (dt, *J* = 1.6, 7.4 Hz, 2H, (7, 8)), 7.52 (tt, *J* = 1.8, 7.8 Hz, 2H, (2, 4)), 7.45 (tt, *J* = 2.2, 7.4 Hz, 1H, (3)), 2.68 (s, 3H, (10))

5.1.13 Negishi coupling reaction experimental data

5.1.13.1 Csp^3-Csp^2 optimisation of reaction conditions

This section gathers the results from the optimisation of the reaction conditions of the Negishi coupling between methyl-2-iodobenzonate **3a** and ^{n}BuZnCl.

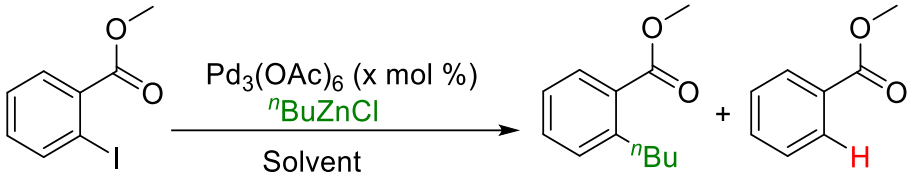

3a **4a** **SP1**

Table 5.1.2 Compendium of optimisation results

Entry	Solvent	Solvent wet/dry	T. (°C)	[Pd] (mol %)	^{n}BuZnCl (equiv.)	RZn rate of addition	Conv. to **4a** (%)	Conv. to **SP1** (%)
1[a]	ChCl/G	wet	40	0.5	2.0	dropwise	6	0
2[a,c,d]	ChCl/G	wet	40	0.5	2.0	dropwise	0	0
3[a,d]	ChCl/G	dry	40	1	1.6	dropwise	0	0
4[a]	ChCl/U	dry	40	1	1.6	dropwise	88	10
5[a]	ChCl/U	dry	40	2	1.6	dropwise	90	6
6[a]	ChCl/U	dry	40	2	2.0	f/s	31	10
7.1	ChCl/U	wet	40	1	1.6	dropwise	27	3
7.2	ChCl/U	wet	40	1	1.6	dropwise	20	2
8	ChCl/U	wet	40	1	2.0	f/s	46	8
9	ChCl/U	wet	40	2	2.0	dropwise	55	5
10	ChCl/U	wet	40	2	2.0	f/s	46	8
11	ChCl/U	wet	50	2	2.0	dropwise	58	7
12[a]	ChCl/U	dry	60	1	2.0	dropwise	87	12
13.1	ChCl/U	wet	60	1	2.0	dropwise	80	5
13.2	ChCl/U	wet	60	1	2.0	dropwise	40	4
13.3	ChCl/U	wet	60	1	2.0	dropwise	38	4
13.4	ChCl/U	wet	60	1	2.0	dropwise	51	6
13.5	ChCl/U	wet	60	1	2.0	dropwise	87	12
14.1	ChCl/U	wet	60	2	2.0	dropwise	97	0
14.2	ChCl/U	wet	60	2	2.0	dropwise	90	10
14.3	ChCl/U	wet	60	2	2.0	dropwise	77	8
14.4	ChCl/U	wet	60	2	2.0	dropwise	80	8
14.5	ChCl/U	wet	60	2	2.0	dropwise	78	5
14.6	ChCl/U	wet	60	2	2.0	dropwise	91	8
15[e]	ChCl/U	wet	60	2	2.0	dropwise	80	-
16	ChCl/U	wet	60	2	2.0	f/s	70	7
17[f]	ChCl/U	wet	60	2	2.0	dropwise	68	4

18[g]	ChCl/U	wet	60	2	2.0	dropwise	25	3
19[a,b]	THF	dry	40	2	2.0	dropwise	84	1
20[h]	ChCl/DMU	wet	80	2	1.5	dropwise	14	1
21[h]	ChCl/$AcNH_2$	wet	80	2	1.5	dropwise	14	1
22[i]	ChCl/U	wet	60	0	2.0	dropwise	0	0
23[j]	ChCl/U	wet	60	2	0	dropwise	0	0

Typical conditions: In a round-bottom flask, 5 cm^3 of solvent, **3a** (1.0 mmol) and $Pd_3(OAc)_6$ were mixed at the desired temperature for 10 min or until the reaction mixture became orange. A solution of ^{n}BuZnCl (2 mmol) in dry THF was added to **3a** and the reaction mixture stirred for 5 min at 1000 rpm. The reaction was quenched with 10 cm^3 of aqueous NH_4Cl 2 M. The conversion was determined by ^{1}H-NMR analysis of the crude. f/s stands for fast and single addition of ^{n}BuZnCl. Conversions in brackets are averages. [a] Schlenk line and protective N_2 atmosphere used. [b] .[Bu_4N]Br added as additive. [c] 10 cm^3 of DES. [d] Reaction mixture stirred for 12 hours [e] Isolated yield. [f] With $PdCl_2$. [g] With $Pd(PPh_3)_4$. [h] Conversion determined by GC using a DB5 column. [i] In the absence of Pd. [j] In the absence of ^{n}BuZnCl, reaction time 12 h.

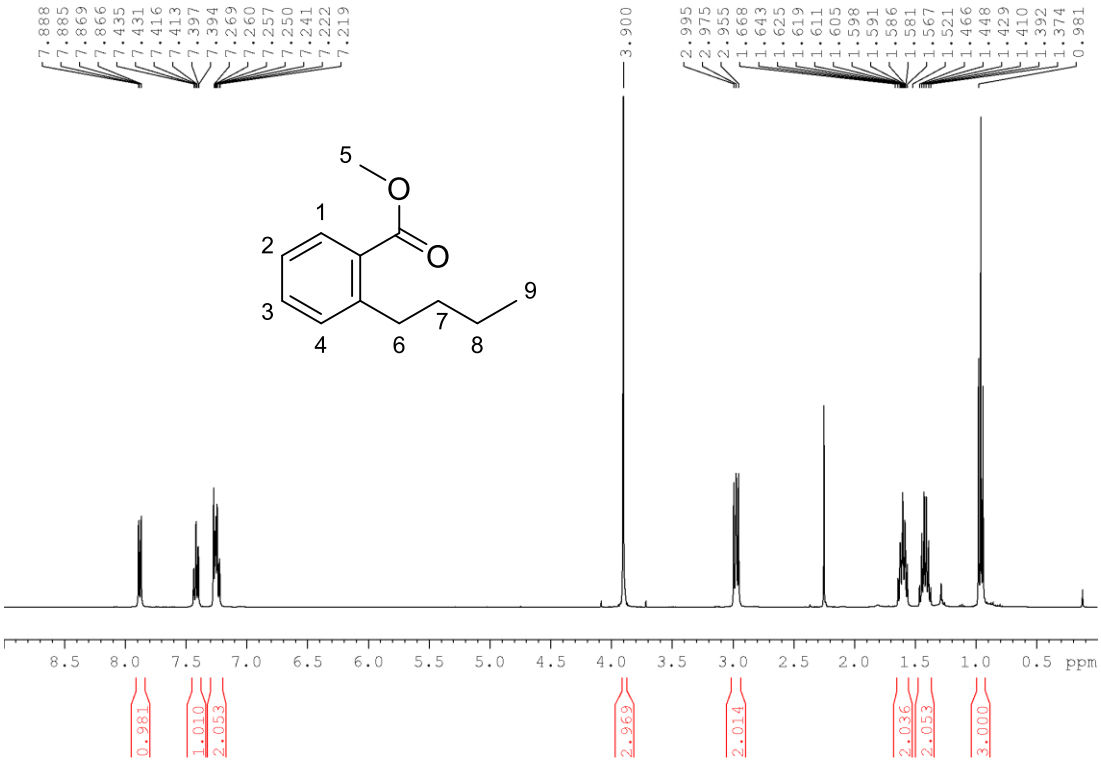

Figure 5.1.4: ^{1}H-NMR Methyl 2-butylbenzoate **4a**

Table 5.1.2 entry 15: **4a** isolated by flash column chromatography hexane/ethyl acetate 98:2 from the crude reaction mixture of Negishi coupling between methyl 2-iodobenzoate **3a** and ^{n}BuZnCl in ChCl/U with

hexamethylbenzene as internal standard. ^{1}H-NMR ($CDCl_3$, 400 MHz). δ 7.86 (dd, *J* = 1.1, 7.8 Hz, 1H, (1)), 7.41 (td, *J* = 1.2, 7.5 Hz, 1H, (2)), 7.25 (m, 2H, (6, 7)), 3.90 (s, 3H, (5)), 2.99 (td *J* = 7.7 Hz, 2H, (6)), 1.61 (quintet, *J* = 7.7 Hz, 2H, (7)), 1.42 (sextet, *J* = 7.4 Hz, 2H, (8)), 0.96 (t, *J* = 7.3 Hz, 3H, (9))

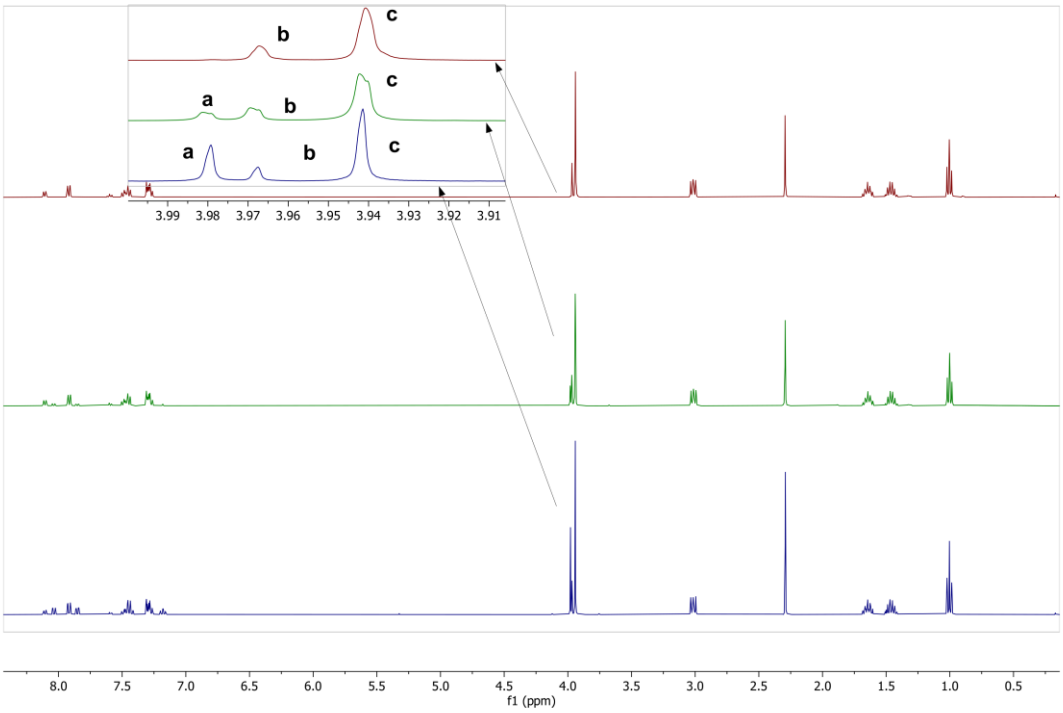

Figure 5.1.5: Stacked crude ^{1}H-NMR spectra from the Negishi coupling recycling experiments between benzoate **3a** and ^{n}BuZnCl catalysed by Pd acetate in DES. Red: first cycle, green: second cycle, blue: third cycle. a) Methyl peak from starting material, b) methyl peak from dehalogenated side product, c) methyl peak from cross-coupling product.

Table 5.1.3: Negishi coupling recycling experiment

Entry	Analyte	Integral Analyte	Integral Std	Conversion (%)	Cycle
1	**4a**	2.9789	1.9279	80	Cycle1
2	**SP1**	0.7414	1.9279	14	Cycle1
3	**3a**	0.039	1.9279	1	Cycle1
4	**4a**	2.8813	2.2658	64	Cycle2
5	**SP1**	0.7356	2.2658	12	Cycle2
6	**3a**	0.4699	2.2658	14	Cycle2
7	**4a**	3.007	2.4256	56	Cycle3
8	**SP1**	0.5898	2.4256	8	Cycle3
9	**3a**	1.3596	2.4256	34	Cycle3

^{1}H NMR integrals from characteristic methyl protons from cross-coupling product, dehalogenated side product and starting material, and its respective NMR conversion based on hexamethylbenzene as internal standard.

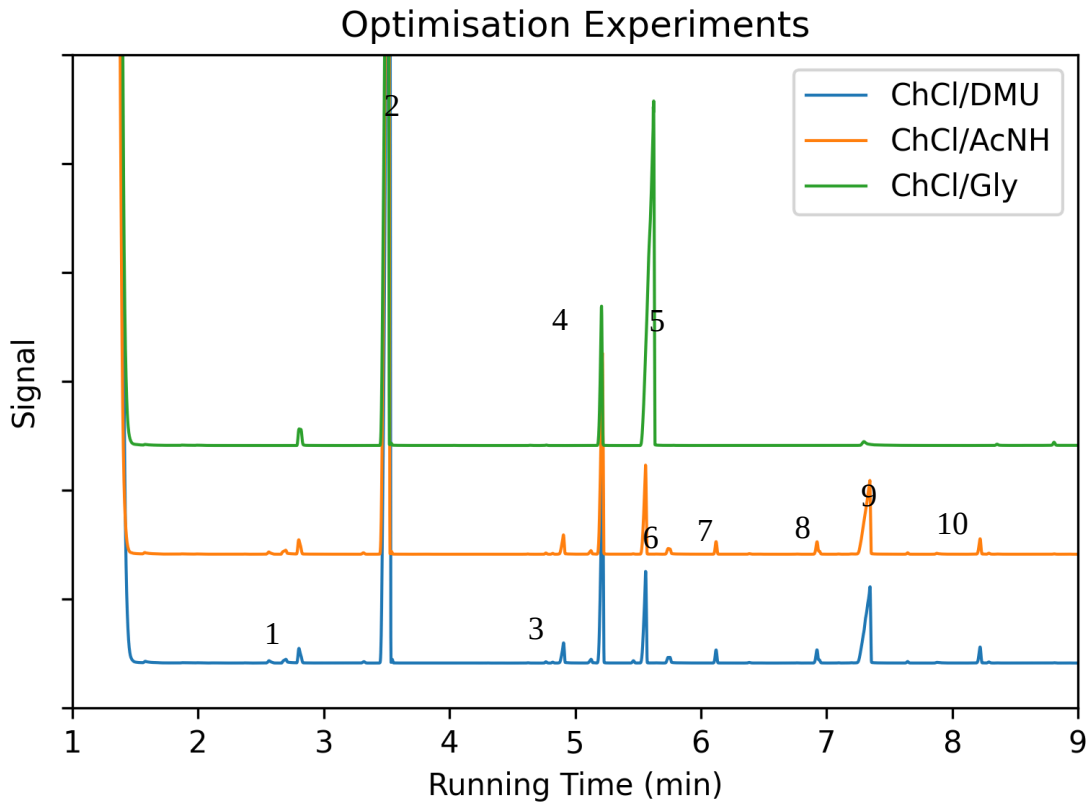

Figure 5.1.6: GC chromatographs from the crudes of the Negishi coupling between methyl 2-iodobenzoate and n-butylzinc chloride in ChCl/DMU, ChCl/AcNH and ChCl/Gly DESs. Al experiments were run using a DB5 column. The structure of the compounds associated with the peaks is outlined in *Table 5.1.4*

Table 5.1.4: Chemical Structure of the compounds associated with the chromatograms plotted in Figure *5.1.6*

GC Peak	Formula	Structure
1	$C_8H_8O_2$	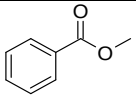
2	$C_{10}H_8$	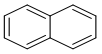
3	C_7H_7NO	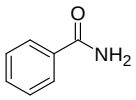

4	$C_{12}H_{16}O_2$	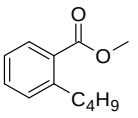
5	$C_8H_7IO_2$	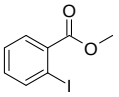
6	$C_9H_9IO_2$	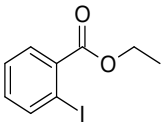
7	$C_{11}H_{15}NO$	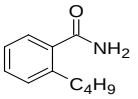
8	$C_{15}H_{23}NO_2$	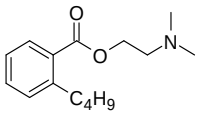
9	C_7H_6INO	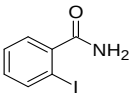
10	$C_{16}H_{14}O_4$	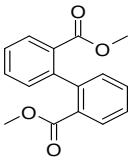

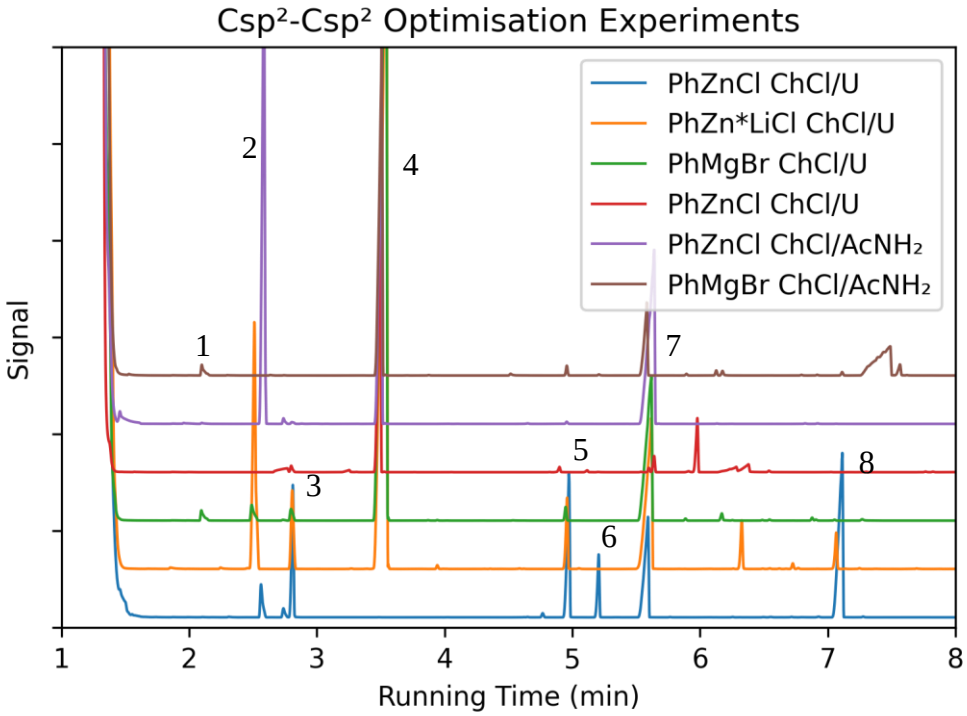

Figure 5.1.7: GC chromatograms of the crudes from Csp²-Csp² optimisation reactions. All experiments were run using a DB5 column. The structure of compounds associated with the peaks is outlined in Table 5.1.5

Table 5.1.5: Chemical structure of the compounds associated with the chromatograms plotted in *Figure 5.1.7*

GC Peak	Formula	Structure
1	C_6H_5Br	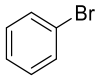
2	$C_8H_8O_2$	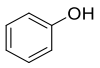
3	C_7H_7NO	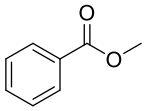
4	$C_{10}H_8$	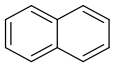
5	$C_{12}H_{10}$	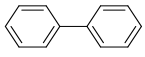
6	$C_{12}H_{16}O_2$	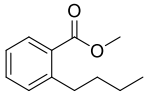
7	$C_8H_7IO_2$	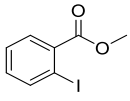

8	$C_{14}H_{12}O_2$	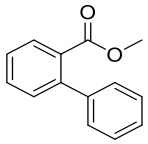	

5.1.13.2 Csp³-Csp² first substrate scope

Table 5.1.6: Csp^3-Csp^2 Negishi cross-coupling reaction conversions

Entry	Electrophile	Ar-^{n}Bu Conv. (%)	Ar-H Conv. (%)	Ar-I Recov. (%)
1[a]	4-Bromoanisole	0	-	100
2[b]	Bromobenzene	0	-	100
3[b]	Iodobenzene	62	-	38
4[b]	4-Chloro-1-iodobenzene	10	-	68
5[b]	2-Iodoanisole	5		85
6[b]	Ethyl-2-iodobenzoate	72	9	19
7[a]	Methyl 2-iodobenzoate	97	3	0
8[c]	Methyl-4-benzoate	48	15	17
9[a]	1-Iodonaphthalene	4	4	92
10[a]	3-Iodoanisole	0	0	100
11[b]	4-Iodoacetophenone	21	8	71
12[ad]	2-iodoacetophenone	86	1	11
12[b]	4-Iodotoluene	0	-	94
13[a]	4-Iodonitrobenzene	32	8	45
14[b]	4-Iodobenzotrifluoride	0	-	100
15[b]	2-Iodopyridine	0	-	100
16[b]	2-Iodobenzotrifluoride	0	-	100
17	3-Iodobenzotrifluoride	0	-	75
18	4-Iodobenzotrifluoride	0	-	100

Conversions obtained by GC analysis of the crudes of reaction using a DB-5 column. [a] Decane was used as internal standard. [b] Naphthalene was used as internal standard. Conversion determined by ^{1}H-NMR. [d] $Pd_3(OAc)_6$ 5 mol %

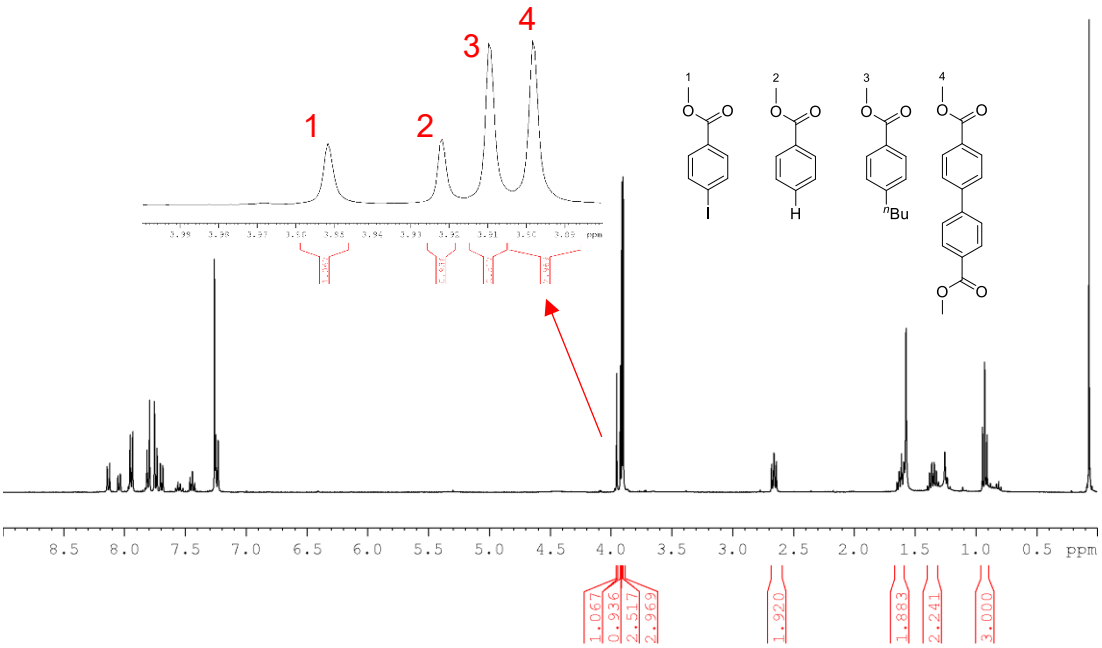

Figure 5.1.8: ^{1}H-NMR spectrum from the crude reaction mixture from *Table 5.1.6 entry 8* showcasing the peaks taken as reference to estimate the ratio between starting material, productive coupling product dehalogenation product and homocoupling product.

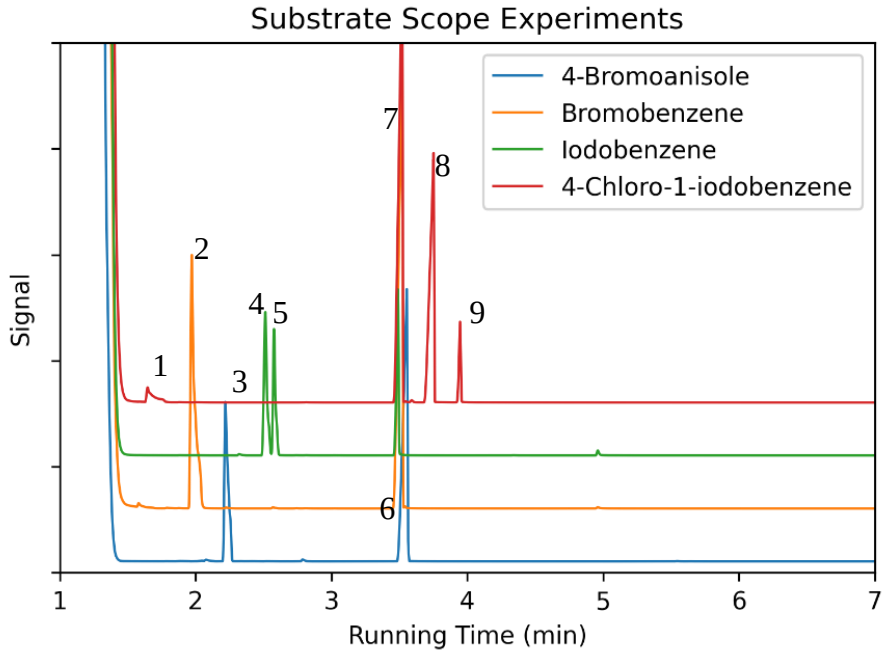

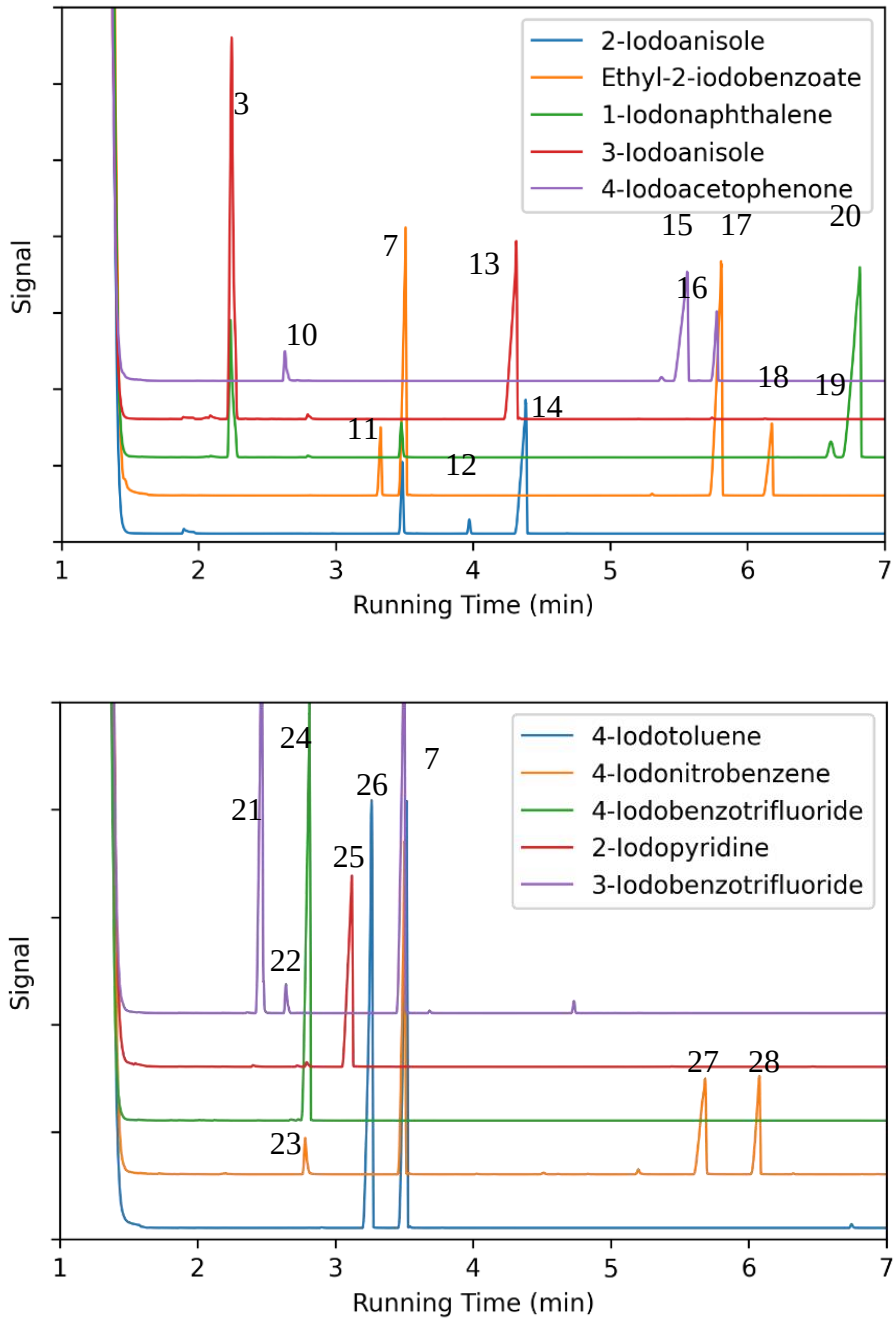

Figure 5.1.9: Csp^3-Csp^2 substrate scope. GC chromatograms from the crudes of reaction. All experiments were run using a DB5 column. The structure of the compounds associated with the peaks is outlined in *Table 5.1.7*

Table 5.1.7: Chemical structure of the compounds associated with the chromatograms plotted in *Figure 5.1.9*

GC Peak	Formula	Structure

1	C_6H_5Cl	
2	C_6H_5Br	
3	$C_{10}H_{22}$	
4	$C_{10}H_{14}$	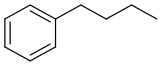
5	C_6H_5I	
6	C_7H_7BrO	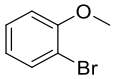
7	$C_{10}H_8$	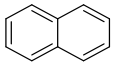
8	C_6H_4ICl	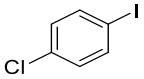
9	$C_{10}H_{13}Cl$	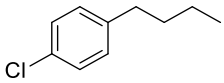
10	C_8H_8O	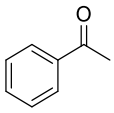
11	$C_9H_{10}O_2$	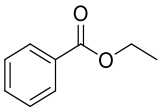
12	$C_{11}H_{16}O$	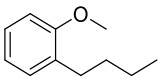
13	C_7H_7IO	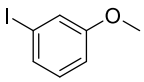
14	C_7H_7IO	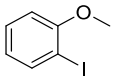
15	C_8H_7IO	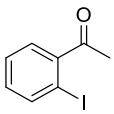
16	$C_8H_{16}O$	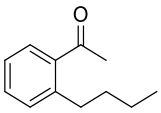
17	$C_{13}H_{18}O_2$	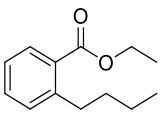

18	$C_9H_9IO_2$	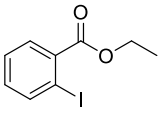
19	$C_{10}H_{16}$	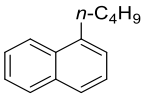
20	$C_{10}H_7I$	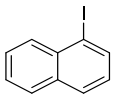
21	$C_7H_4IF_3$	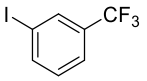
22	$C_{11}H_{13}F_3$	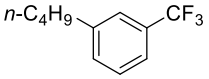
23	$C_6H_5NO_2$	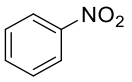
24	$C_7H_4IF_3$	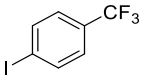
25	C_5H_4IN	
26	C_7H_7I	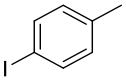
27	$C_6H_4INO_2$	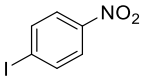
28	$C_{10}H_{13}NO_2$	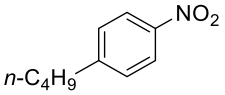

5.1.13.3 Csp^3-Csp^2 reaction conditions and substrate scope for *ortho*-coordinating iodoarenes and other substitution patterns.

Table 5.1.8: GC conversions for the substrate scopes with *ortho*- and para or meta- substituted iodoarenes.

Entry	Electrophile	RZn (equiv)	Ar-R^2 Conv. (%)	Ar-H Conv. (%)	Ar-I Recov. (%)	Ar-Ar Conv. (%)

1[ac]	Iodobenzene	^{n}BuZnCl (2)	61	-	37	2
2[a]	Iodobenzene	BnZnBr (3)	93	-	7	0
3[a]	2-(2iodophenyl)pyridine	^{n}BuZnCl (3)	25	13	33	12
4[a]	2-(2iodophenyl)pyridine	BnZnBr (3)	77	7	13	2
5[a]	N,N-Diethyliodobenzamide	^{n}BuZnCl (2)	96	0	4	0
6[b]	N,N-Diethyliodobenzamide	BnZnBr (2)	94	1	5	0
7[a]	Methyl-2-iodobenzoate	^{n}BuZnCl (2)	97	3	0	0
8[a]	Methyl-2-iodobenzoate	BnZnBr (2)	84	2	14	0
9[b]	1-Iodo-2-(methoxymethyl)benzene	^{n}BuZnCl (3)	49	7	32	0
10[b]	1-Iodo-2-(methoxymethyl)benzene	BnZnBr (2)	85	1	14	0
11[b]	2-Iodobenzanilide	^{n}BuZnCl (3)	55	19	26	0
12[b]	2-Iodobenzanilide	BnZnBr (3)	94	4	2	0
13[a]	2-Iodoacetophenone	^{n}BuZnCl (2)	86	1	11	2
14[b]	2-Iodoacetophenone	BnZnBr (2)	92	1	5	0
15[b]	Methyl-4-iodobenzoate	^{n}BuZnCl (3)	72	6	0	14
16[b]	Methyl-4-iodobenzoate	BnZnBr (3)	71	16	13	0
17[b]	4-Iodoacetophenone	^{n}BuZnCl (3)	72	6	0	11
18[b]	4-Iodoacetophenone	BnZnBr (3)	52	5	44	0
19[b]	4-Iodoanisole	^{n}BuZnCl (3)	66	13	0	7
20[b]	4-Iodoanisole	BnZnBr (3)	33	20	47	0
21[b]	4-Iodotoluene	^{n}BuZnCl (3)	75	-	0	22
22[b]	4-Iodotoluene	BnZnBr (3)	23	-	67	0
23[a]	1-Iodonaphthalene	^{n}BuZnCl (3)	66	17	9	0
24[b]	1-Iodonaphthalene	BnZnBr (3)	46	5	27	0
25[a]	4-Bromo-1-iodobenzene	^{n}BuZnCl (3)	95	2	1	0
26[b]	4-Bromo-1-iodobenzene	BnZnBr (3)	53	4	43	0
27[b]	4-Iodonitrobenzene	^{n}BuZnCl (3)	68	5	2	25
28[b]	4-Iodonitrobenzene	BnZnBr (3)	11	40	9	0
29[b]	Methyl 2-bromobenzoate	^{n}BuZnCl (2)	44	3	53	0

GC conversions for the substrate scopes with *ortho*- and *para* or *meta*- substituted iodoarenes with ^{n}BuZnCl and BnZnBr. [a] GC column DB-5 [b] GC column Rxi-17. [c] $Pd_3(OAc)_6$ (2 mol %).

Csp^3-Csp^2 Negishi Couplings with *ortho*-substituted iodoarenes

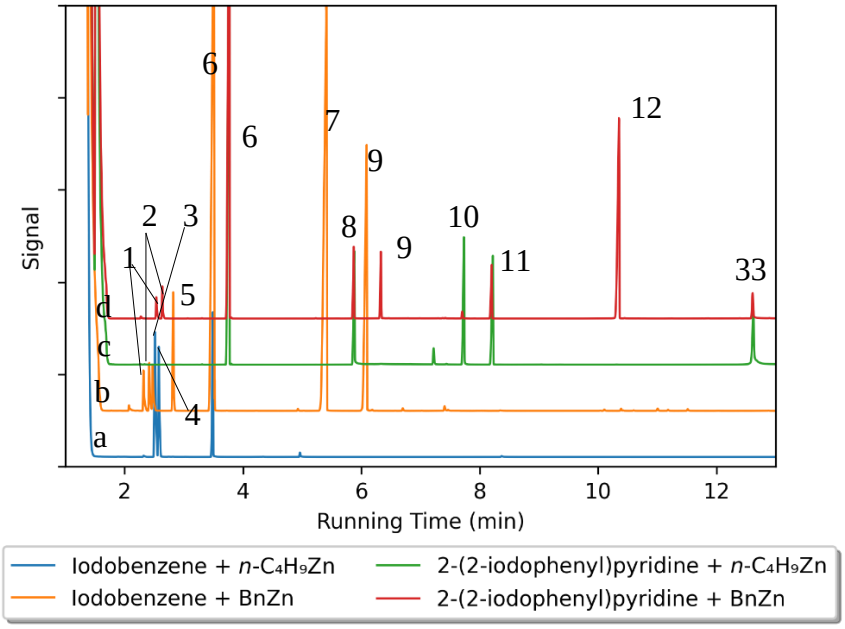

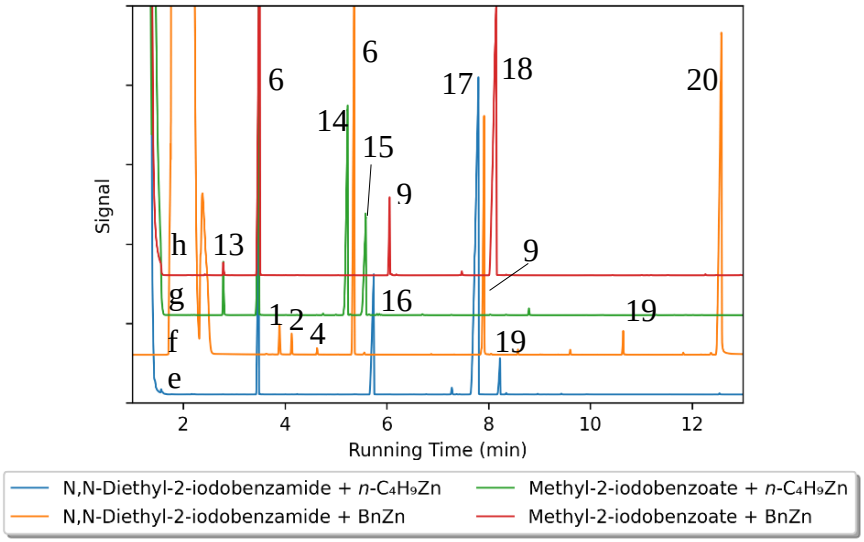

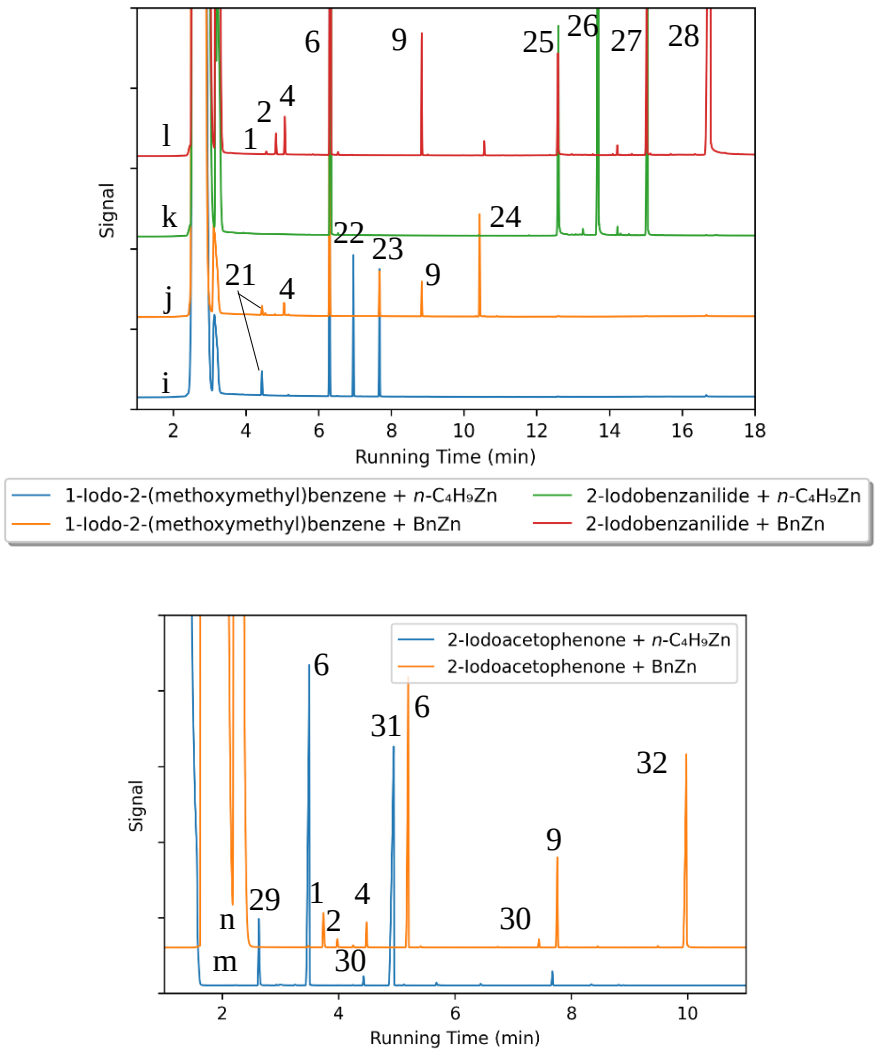

Figure 5.1.10: GC chromatograms from the crudes of reactions between iodobenzene & *ortho*-substituted iodoarenes with Csp^3 Zn reagents. Experiments a, b, c ,d, e, g, h & m were run using a DB5 column; f, i, j, k, l & n, using a Rix-17 column. The structure associated with the peaks is outlined in *Table 5.1.9*

Table 5.1.9: Chemical structure of the compounds associated with the chromatograms plotted in *Figure 5.1.10*

GC Peak	Formula	Structure
1	C_7H_7Cl	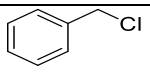
2	C_7H_8OH	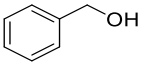

3	C_6H_5I	
4	$C_{10}H_{14}$	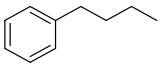
5	C_7H_7Br	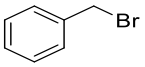
6	$C_{10}H_8$	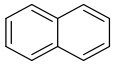
7	$C_{13}H_{12}$	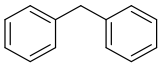
8	$C_{11}H_9N$	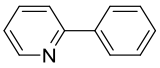
9	$C_{14}H_{14}$	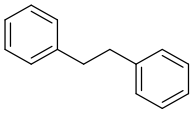
10	$C_{15}H_{17}N$	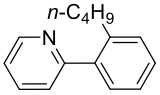
11	$C_{11}H_8IN$	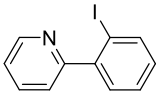
12	$C_8H_{15}N$	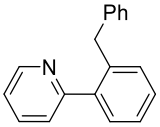
13	$C_8H_8O_2$	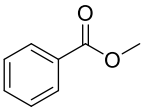
14	$C_{12}H_{16}O_2$	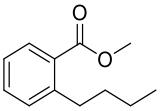
15	$C_8H_7IO_2$	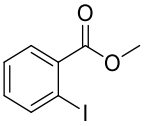
16	$C_8H_{15}NO$	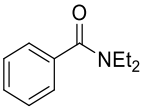
17	$C_{15}H_{23}NO$	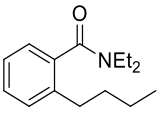

18	$C_{15}H_{14}O_2$	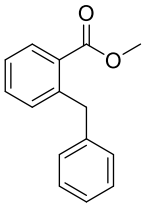
19	$C_{11}H_{14}INO$	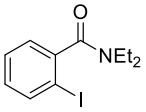
20	$C_{18}H_{21}NO$	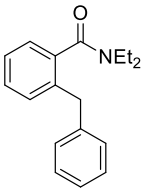
21	$C_8H_{10}O$	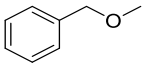
22	$C_{12}H_{18}O$	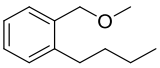
23	C_8H_9IO	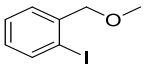
24	$C_{15}H_{16}O$	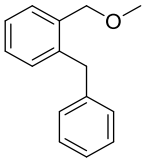
25	$C_{13}H_{11}NO$	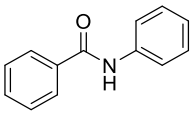
26	$C_{17}H_{19}NO$	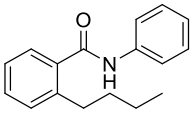
27	$C_{13}H_{10}INO$	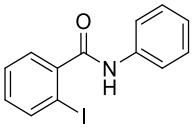
28	$C_{20}H_{17}NO$	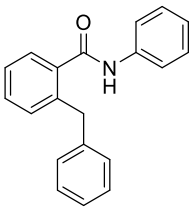
29	C_8H_8O	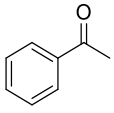

30	C_8H_7IO	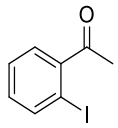
31	$C_{12}H_{16}O$	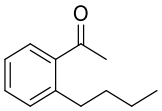
32	$C_{12}H_{16}O$	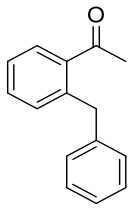
33	$C_{22}H_{16}N_2$	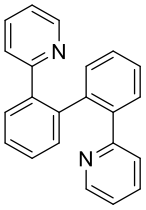

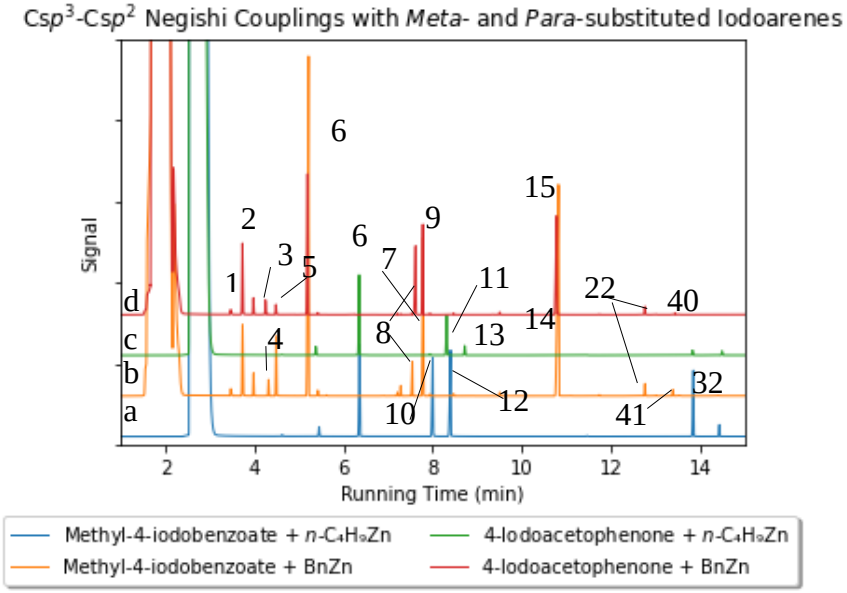

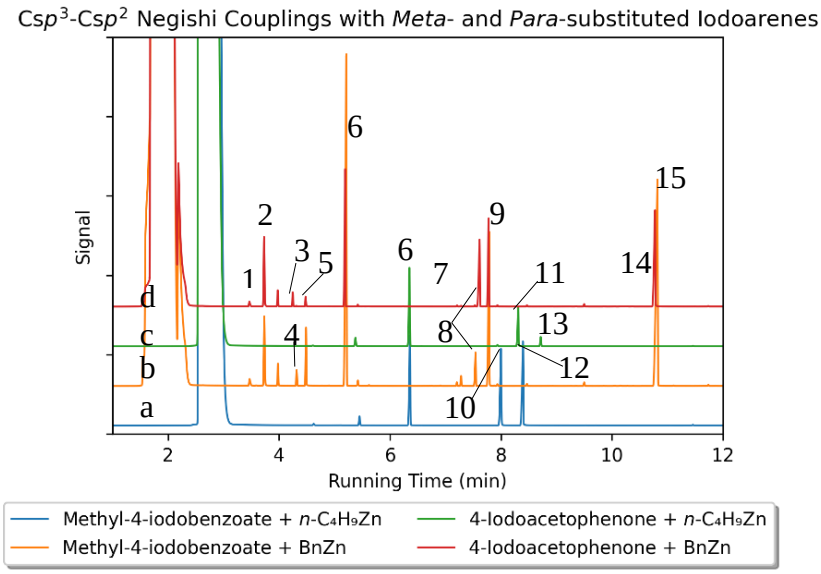
Csp³-Csp² Negishi Couplings with Meta- and Para-substituted Iodoarenes
Signal
Running Time (min)
Methyl-4-iodobenzoate + n-C4H9Zn
Methyl-4-iodobenzoate + BnZn
4-Iodoacetophenone + n-C4H9Zn
4-Iodoacetophenone + BnZn

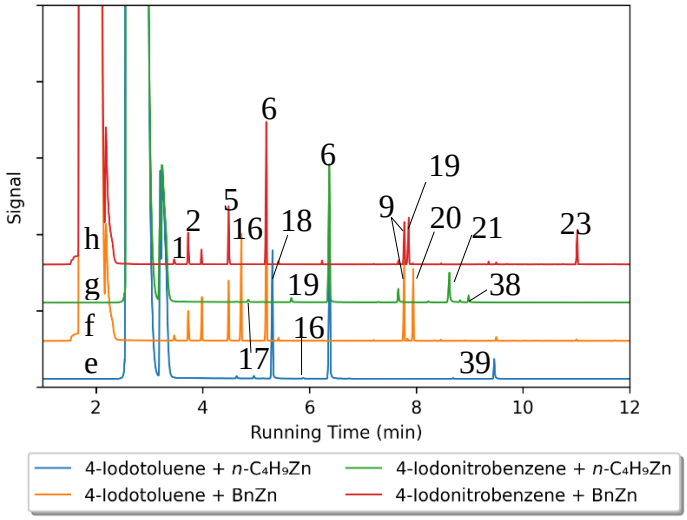
Signal
Running Time (min)
4-Iodotoluene + n-C4H9Zn
4-Iodotoluene + BnZn
4-Iodonitrobenzene + n-C4H9Zn
4-Iodonitrobenzene + BnZn

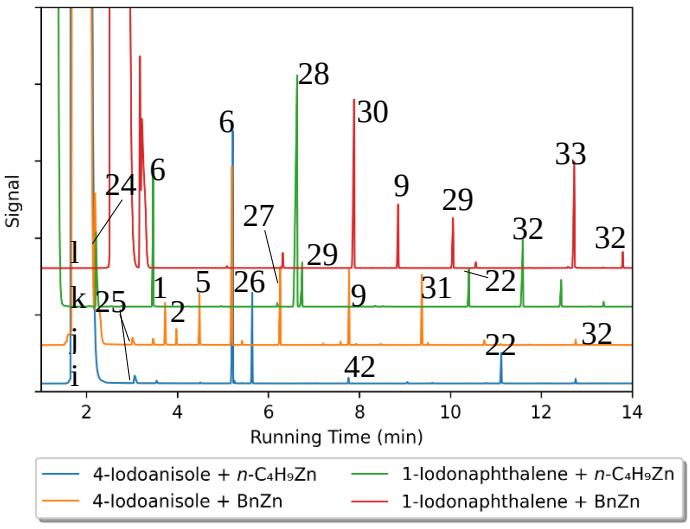
Signal
Running Time (min)
4-Iodoanisole + n-C4H9Zn
4-Iodoanisole + BnZn
1-Iodonaphthalene + n-C4H9Zn
1-Iodonaphthalene + BnZn

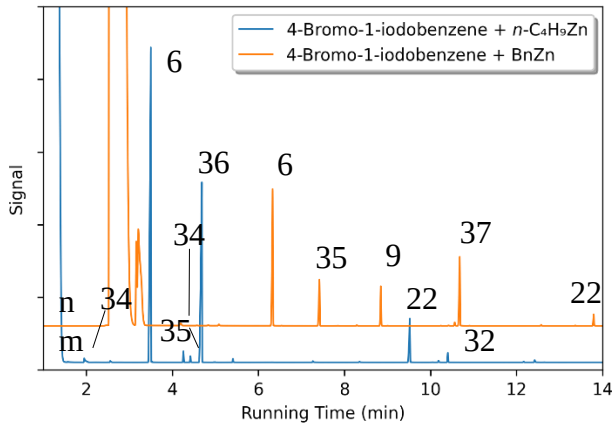

Figure 5.1.11: GC chromatograms from the crudes of reactions between *para* and *meta*-substituted iodoarenes with Csp^3 Zn reagents. Experiments a, b, c ,d, e, f, g, h, i, j, l & n were run using a Rix-17 column; k & m using a DB5 column. The structure associated with the peaks is outlined in *Table 5.1.10*

Table 5.1.10: Chemical structure of the compounds associated with the chromatograms plotted in *Figure 5.1.11*

GC Peak	Formula	Structure
1	C_7H_7Cl	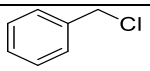
2	C_7H_8OH	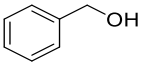
3	C_8H_8O	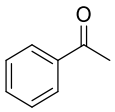
4	$C_8H_8O_2$	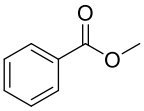
5	C_7H_7Br	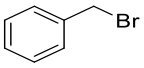
6	$C_{10}H_8$	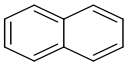
7	$C_8H_7IO_2$	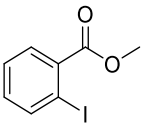

8	C_8H_7IO	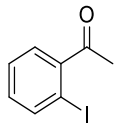
9	$C_{14}H_{14}$	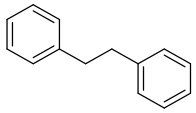
10	$C_{12}H_{18}$	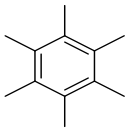
11	$C_{12}H_{16}O$	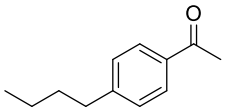
12	$C_{12}H_{16}O_2$	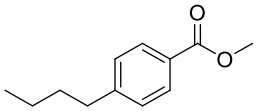
13	C_8H_7IO	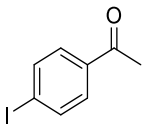
14	$C_{15}H_{14}O$	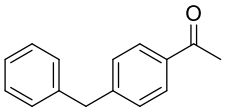
15	$C_{15}H_{14}O_2$	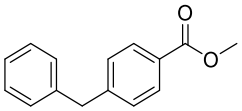
16	C_7H_7I	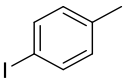
17	$C_6H_5NO_2$	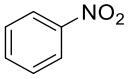
18	$C_{11}H_{16}$	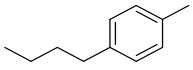
19	$C_6H_4INO_2$	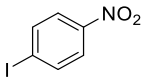
20	$C_{14}H_{14}$	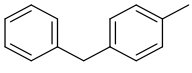
21	$C_{10}H_{13}NO_2$	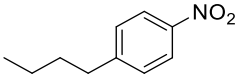
22	$C_{18}H_{15}P$	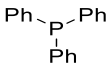

23	$C_{13}H_{11}NO_2$	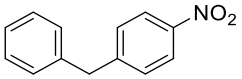
24	$C_{10}H_{22}$	
25	C_7H_8O	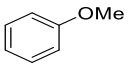
26	$C_{11}H_{16}O$	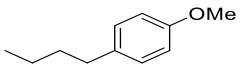
27	C_7H_7IO	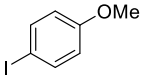
28	$C_{14}H_{16}$	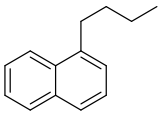
29	$C_{10}H_7I$	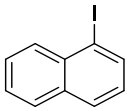
30	$C_{12}H_{10}$	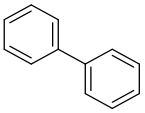
31	$C_{14}H_{14}O$	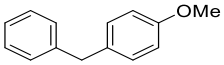
32	$C_{18}H_{15}OP$	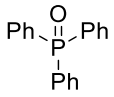
33	$C_{17}H_{14}$	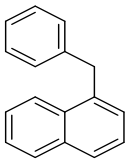
34	C_6H_5Br	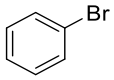
35	C_6H_4IBr	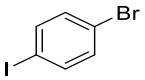
36	$C_{10}H_{13}Br$	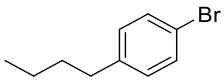
37	$C_{13}H_{11}Br$	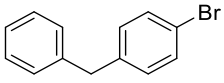
38	$C_{12}H_8N_2O_4$	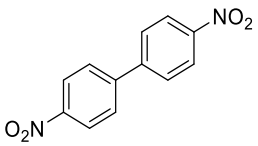

39	$C_{10}H_{14}$	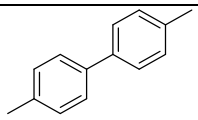
40	$C_{16}H_{14}O_2$	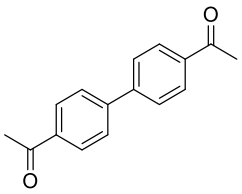
41	$C_{16}H_{14}O_4$	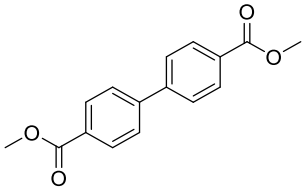

Table 5.1.11: GC conversions for regioselective Negishi coupling with methyl 2,3,5triiodobenzoate **34a**

Entry	Electrophile	Conversion (%)
1[a]	Methyl 2,3,5-triiodobenzoate	3
2	Monodehalogenated species+ Fully dehalogenated species	2
4	Monosubstituted product at *ortho* position	71
	Monosubstituted products at *meta* position	3
5	Disubstituted product	7
6	Trisubstituted product	5
7	Partially substituted/dehalogenated products	11

Crude analyzed with a Rxi-17 column. [a] (%) of starting material detected

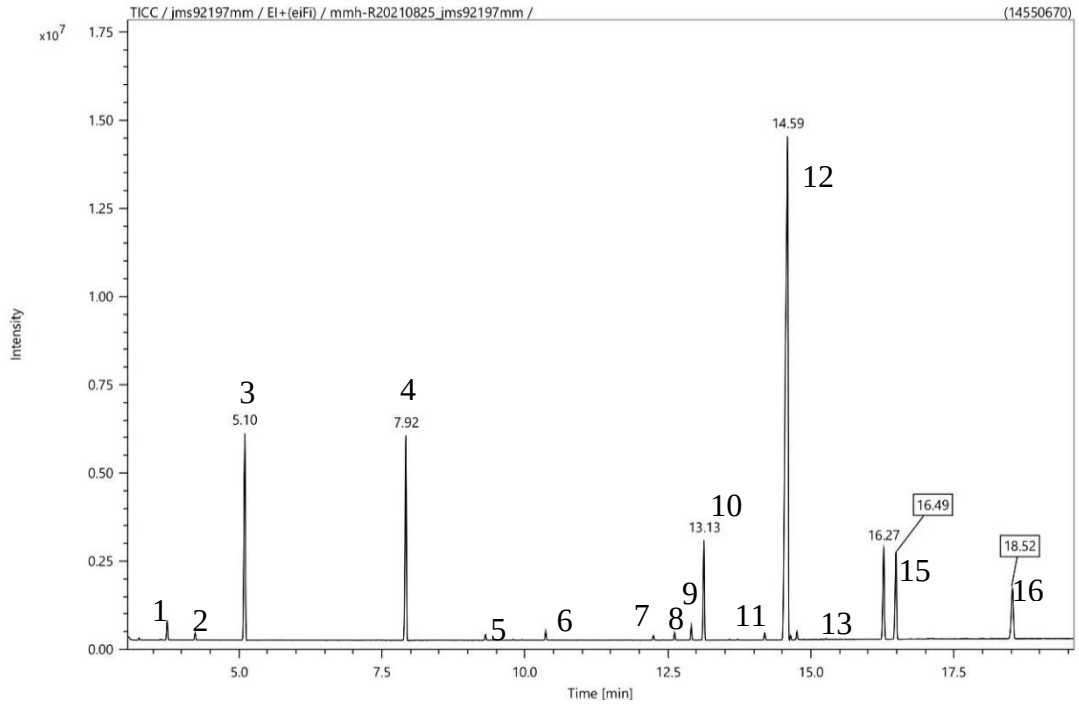

Figure 5.1.12: GC chromatogram from the crude reaction mixture between methyl 2,3,5 triiodobenzoate and BnZnBr catalysed by Pd acetate in DES. The Experiment was run using a Rix-17 column. The structure associated with the peak numbers is outlines in *Table 5.1.12*

Table 5.1.12: Chemical structure of the compounds associated with the chromatograms plotted in *Figure 5.1.12*

GC Peak	Formula	Structure
1	C_7H_8OH	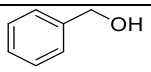
2	$C_8H_8O_2$	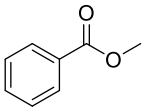
3	$C_{10}H_8$	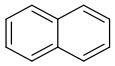
4	$C_{14}H_{14}$	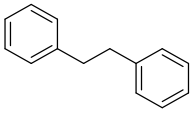
5	$C_{14}H_{14}O$	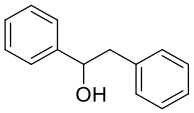

6	$C_8H_8I_2O_2$	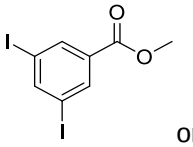 or isomers
7	$C_{15}H_{13}IO_2$	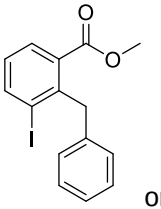 or isomers
8	$C_{15}H_{13}IO_2$	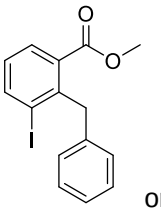 or isomers
9	$C_{15}H_{13}IO_2$	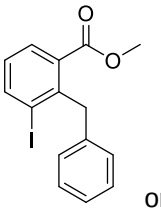 or isomers
10	$C_8H_5I_3O_2$	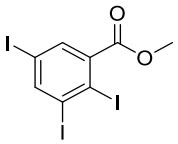
11	$C_{15}H_{12}I_2O_2$	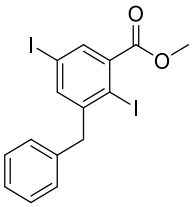 or isomer
12	$C_{15}H_{12}I_2O_2$	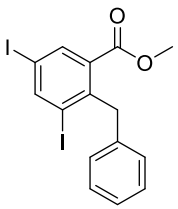
13	$C_{15}H_{12}I_2O_2$	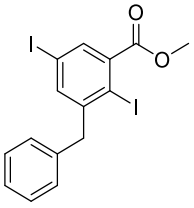 or isomer

14	$C_{22}H_{19}IO_2$	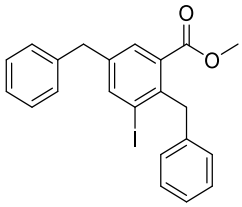 or isomer
15	$C_{22}H_{19}IO_2$	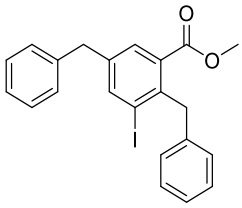 or isomer
16	$C_{29}H_{26}O_2$	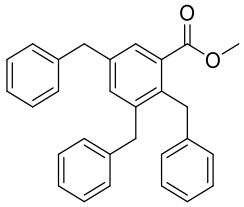

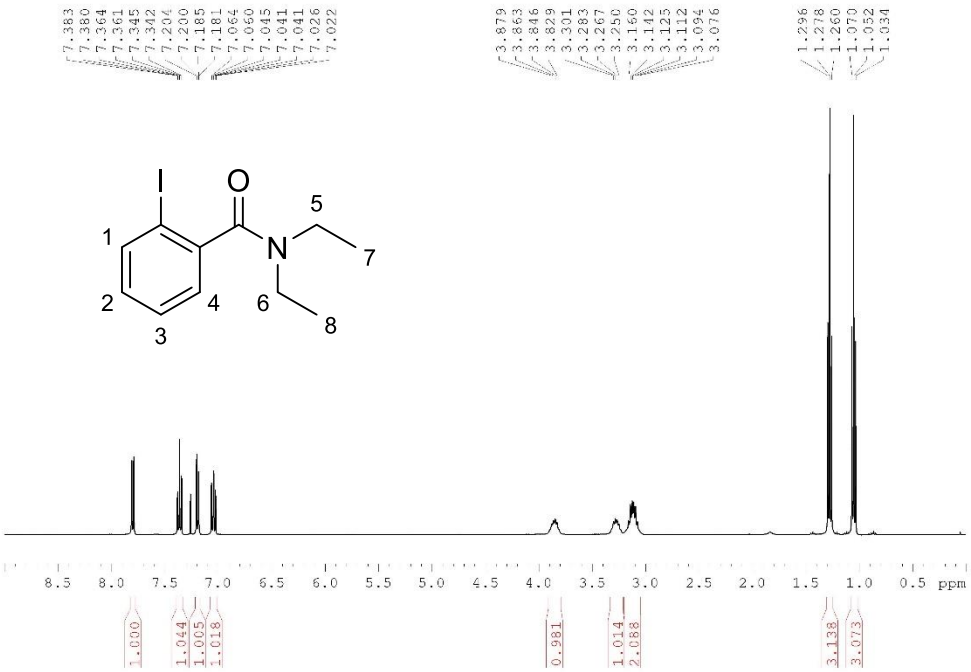

Figure 5.1.13 ^{1}H-NMR N'N-diethtyl-2-iodobenzamide **25a**

^{1}H-NMR ($CDCl_3$, 400 MHz). δ 7.80 (dd, *J* = 1.0, 8.1 Hz, 1H, (4)), 7.36 (td, *J* = 1.2, 7.6 Hz, 1H, (2)), 7.19 (dd, *J* = 1.7, 7.6 Hz, 1H, (1)), 7.04 (td, *J* = 1.7, 7.7 Hz, 1H, (3)), 3.86 (m, 1H), 3.28 (m, 1H) 3.13 (m, 2H), 1.28 (t, *J* = 7.1 Hz, 3H), 1.05 (t, *J* = 7.1 Hz, 3H).

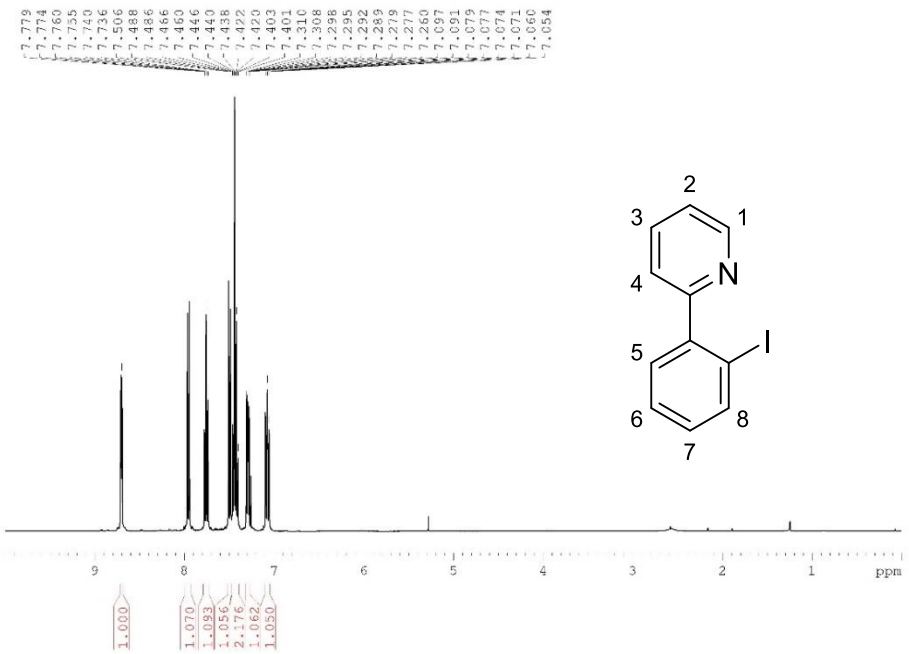

Figure 5.1.14: ^{1}H-NMR 2-(2-iodophenyl)pyridine **26a**

^{1}H-NMR ($CDCl_3$, 400 MHz). δ 8.70 (dq, *J* = 0.9, 5.0 Hz, 1H, (1)), 7.98 (dd, *J* = 1.1, 8.0 Hz, 1H, (5)), 7.76 (td, *J* = 1.8, 7.8 Hz, 1H, (3)), 7.50 (dt, *J* = 1.1, 7.9 Hz, 1H (4)), 7.46 (dd, *J* = 2.2, 7.7 Hz, 1H, (8)), 7.43 (td, *J* = 1.1, 7.8 Hz, 1H, (7)), 7.32 (ddd, *J* = 1.1, 5.0, 7.7 Hz, 1H, (2)), 7.08 (ddd, *J* = 2.2, 6.4, 8.0 Hz, 1H (6)).

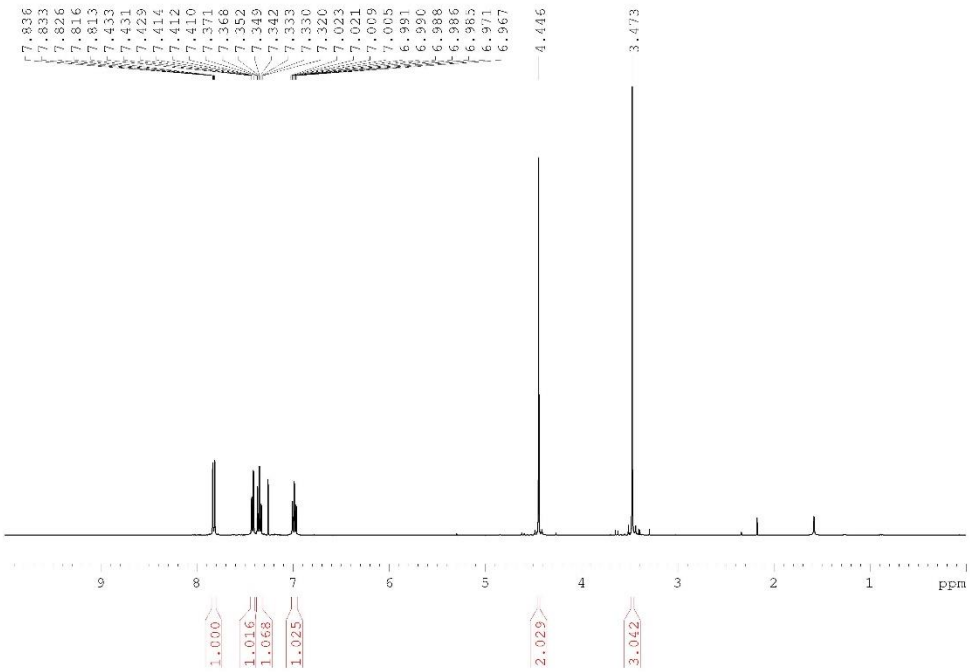

Figure 5.1.15: 1-iodo-2-(methoxymethyl)benzene **27a**

^{1}H-NMR ($CDCl_3$, 400 MHz). δ 7.83 (dd, *J* = 1.2, 7.9 Hz, 1H, (1)), 7.42 (dd, *J* = 1.7, 7.6 Hz, 1H, (4)), 7.35 (td, *J* = 1.2, 7.4 Hz, 1H, (3)), 6.99 (dt, *J* = 1.8, 7.55 Hz, 1H, (2)), 4.45 (s, 2H (5)), 3.47 (s, 3H, (6))

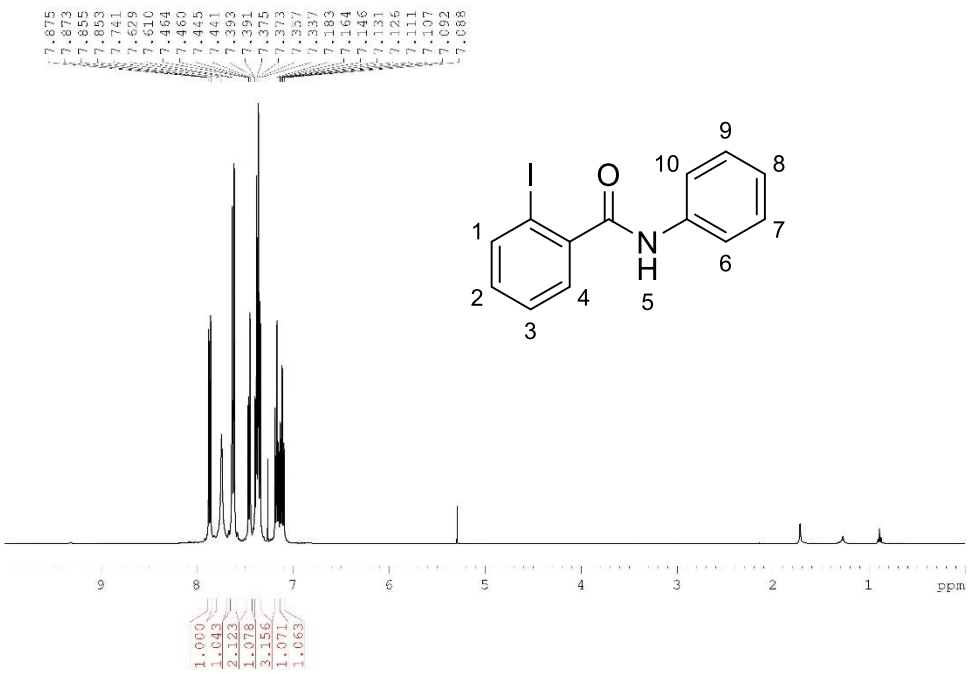

Figure 5.1.16: ^{1}H-NMR 2-Iodobenzanilide **28a**

^{1}H-NMR ($CDCl_3$, 400 MHz). δ 7.86 (dd *J* = 0.8, 8.1 Hz, 1H (4)), 7.74 (s, 1H, (55)), 7.62 (m, 2H, (6 & 10)), 7.45 (dd, *J* = 1.6, 7.6 Hz, 1H, (1)), 7.37 (m, 3H, (2, 7 & 9)), 7.16 (tt, *J* = 1.7, 7.7 Hz, 1H (8)), 7.11 (td, 1.7, 7.7, 1H, (3)).

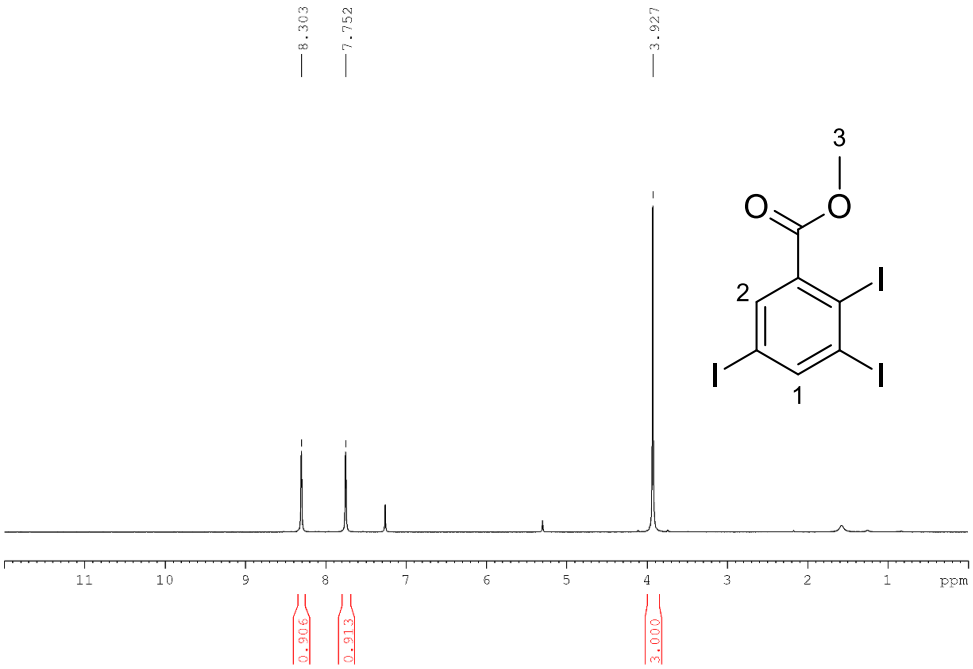

Figure 5.1.17: ^{1}H-NMR Methyl 2,3,5-triiodobenzoate **34a**

^{1}H-NMR ($CDCl_3$, 400 MHz). δ 8.30 (s, 1H, (1)), 7.75 (s, 1H, (2)), 3.93 (s, 1H, (3)).

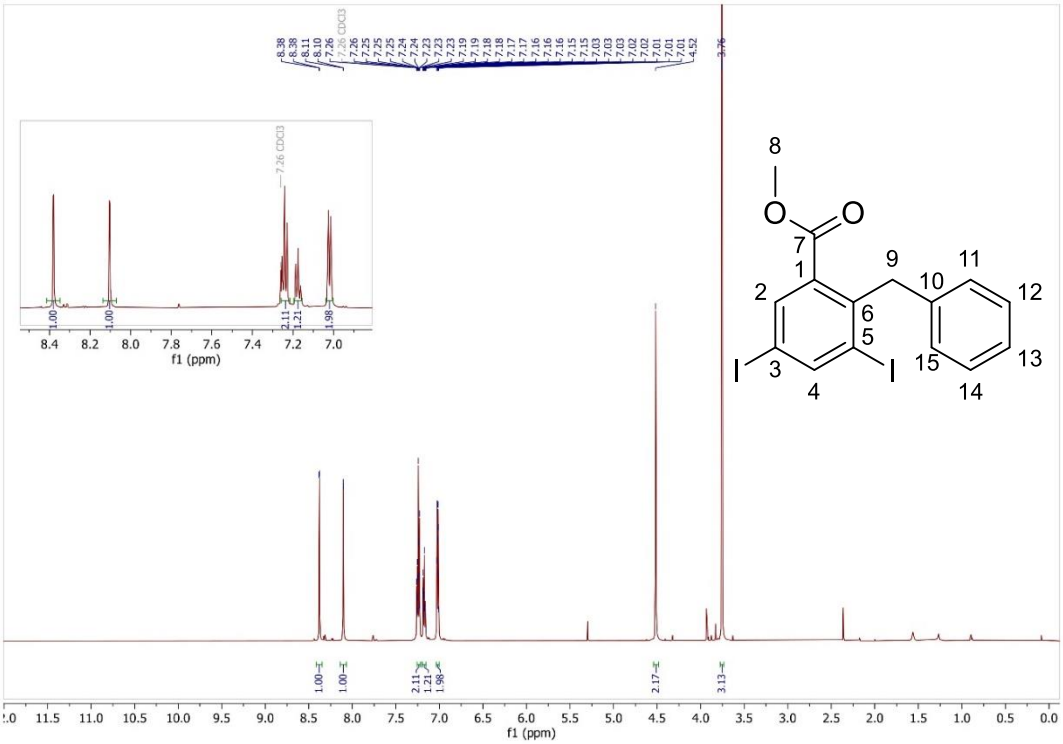

Figure 5.1.18: ^{1}H NMR spectrum of major product **35a**

Characterization of major monosubstituted cross-coupling product: ^{1}H-NMR ($CDCl_3$, 600 MHz). δ 8.37 (d, *J* = 1.9 Hz, 1H, (4)), 8.10 (d, *J* = 1.9 Hz, 1H, (2)), 7.24 (tt, *J* = 7.7, 1.7 Hz, 2H, (12, 14)), 7.17 (tt, *J* = 7.4, 1.8 Hz, 1H (10)), 7.02 (tt, *J* = 7.2, 1.1 Hz, 2H, (11, 15)), 4.52 (s, 2H, (9)), 3.76 (s, 1H, (8)).

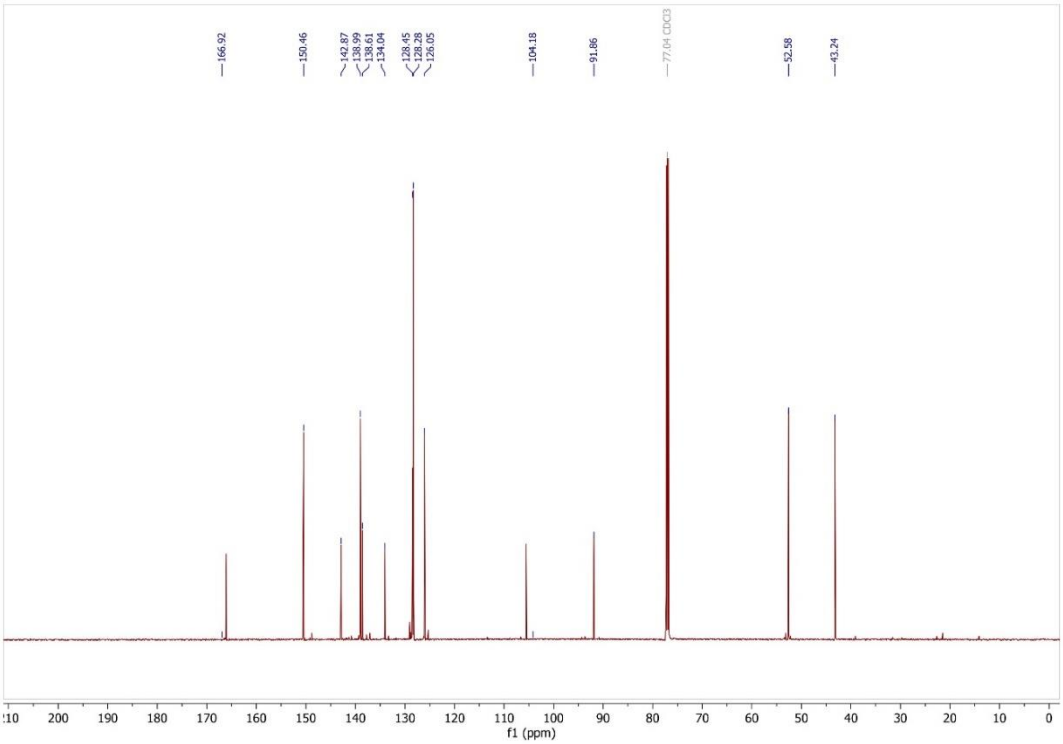

Figure 5.1.19: ^{13}C NMR spectrum of major product **35a**

$^{13}C\{^{1}H\}$-NMR ($CDCl_3$, 150 MHz). δ 166.1 (7), 150.5 (4), 142.9 (6), 138.9 (2), 138.6 (10), 134.0 (1), 128.5 (11, 15), 128.3 (12, 14), 125.9 (13), 105.5 (5), 91.9 (3), 52.3 (9), 42.3 (8).

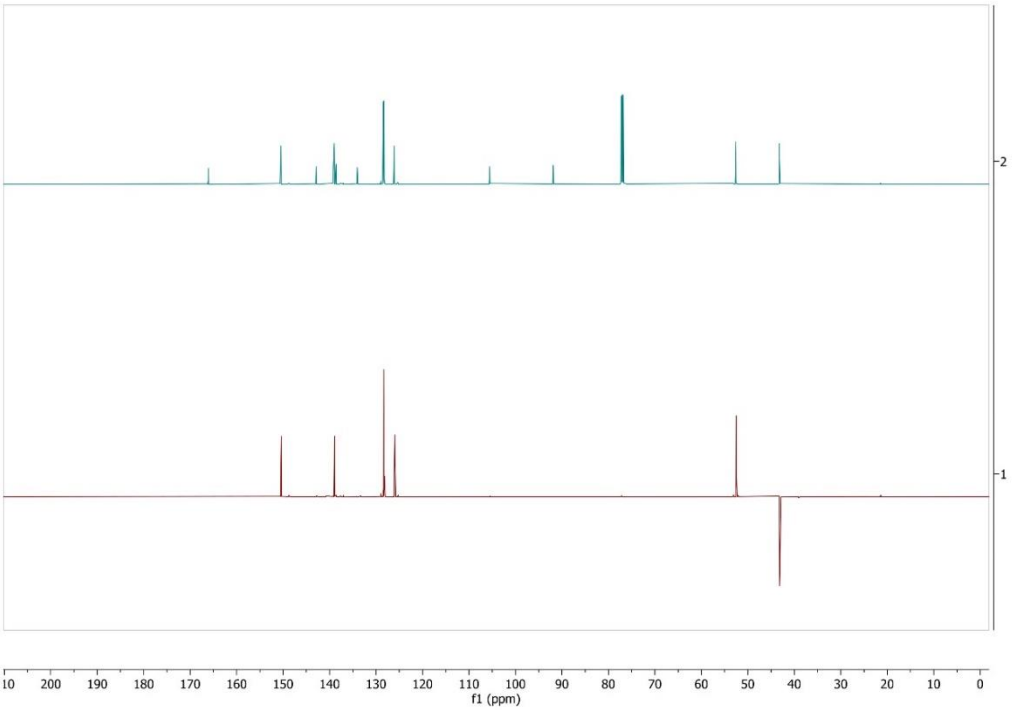

Figure 5.1.20: DEPT-135 experiment contrasted against ^{13}C spectrum of major product **35a**

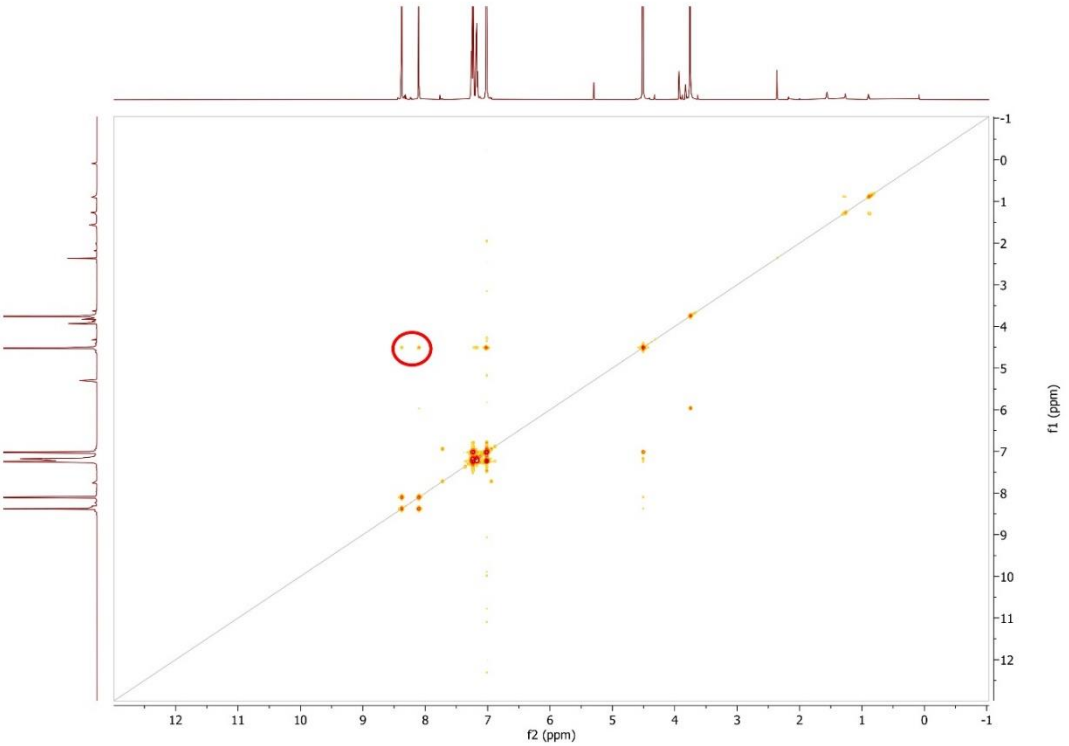

Figure 5.1.21: ^{1}H-^{1}H COSY NMR spectrum of major product **35a**.

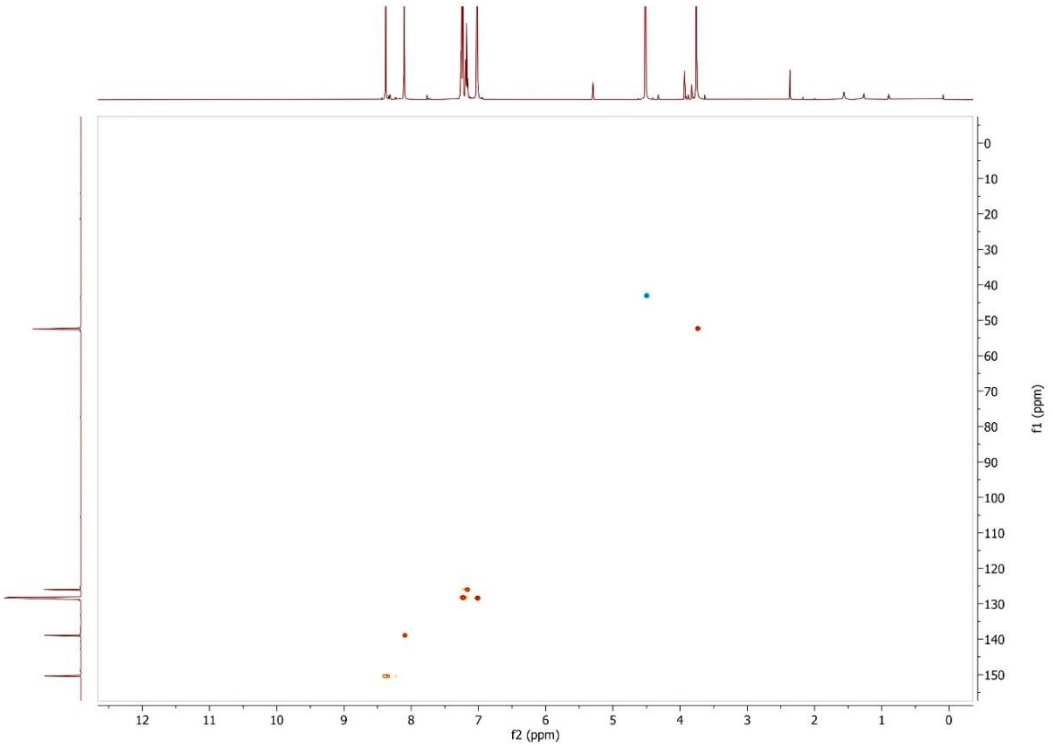

Figure 5.1.22: ^{1}H-^{13}C HSQC NMR spectrum of major product from **35a**

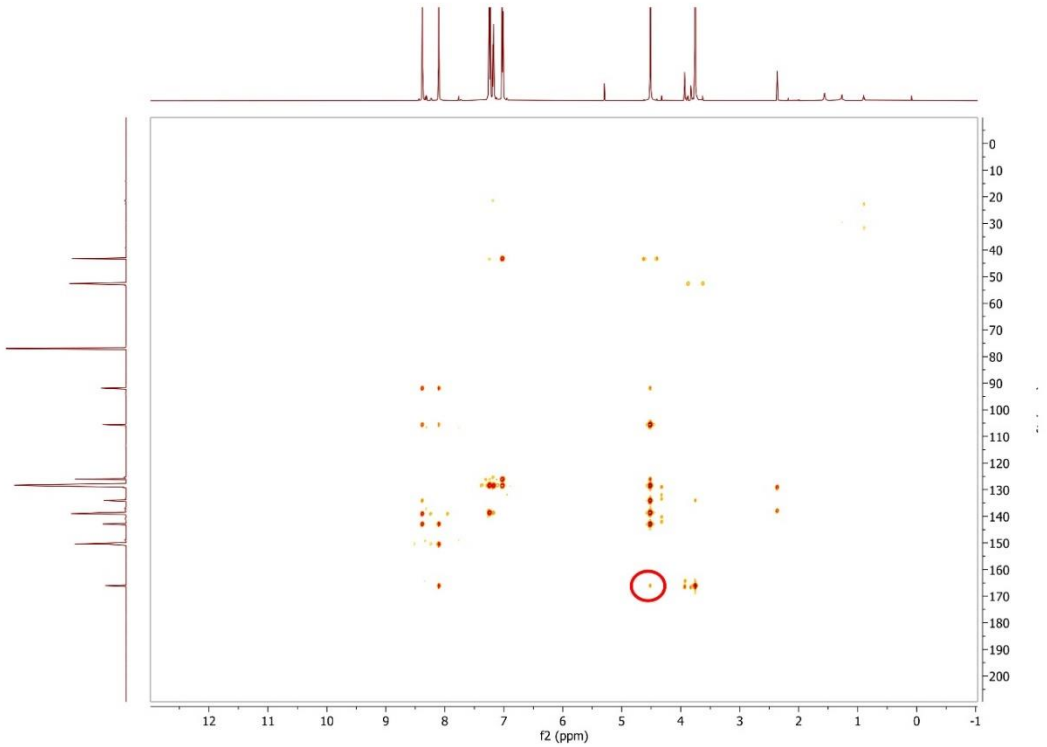

Figure 5.1.23: ^{1}H-^{13}C HMBC NMR spectrum of major product **35a**

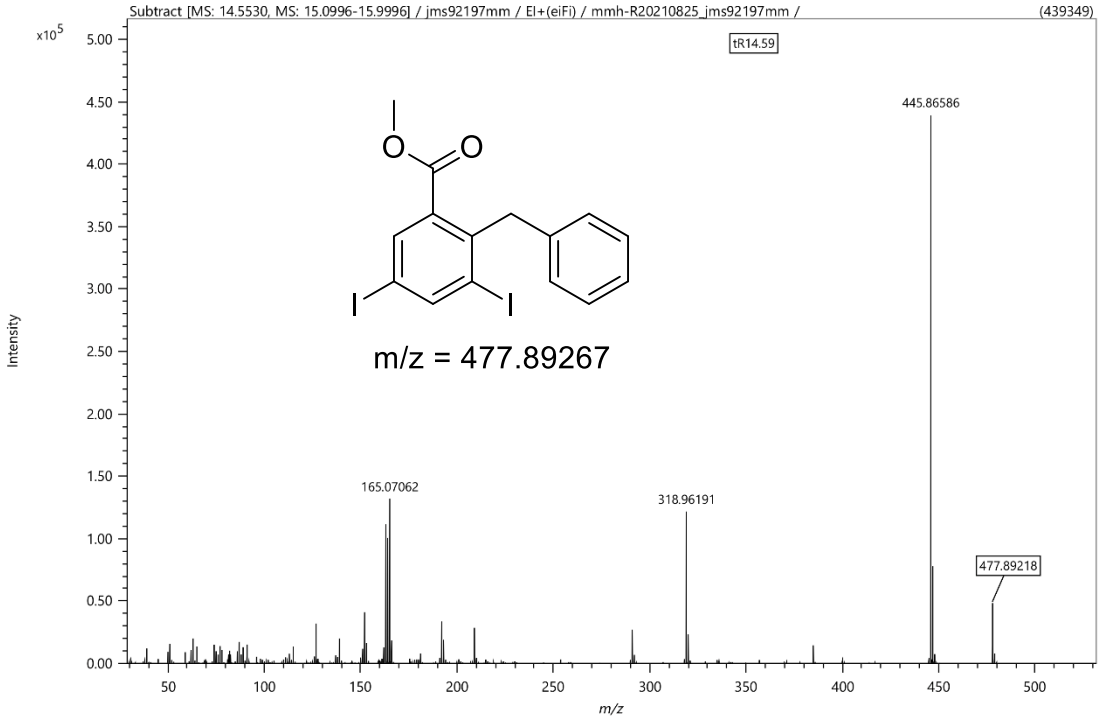

Figure 5.1.24: Electron-ionisation MS spectrum from *ortho*-monosubstituted product **35a**.

5.2 Chapter IV experimental information

5.2.1 General methods

All reagents were purchased from commercial sources unless their preparation is described. All solvents used were HPLC grade. NMR experiments were performed on a JEOL EXC400 spectrometer (operating at 400 MHz for ^{1}H and 100.5 MHz for ^{13}C), The chemical shifts are consecutively reported as position (δ), relative integral, multiplicity (s=singlet, d=doublet, t=triplet, q=quartet, br=broad,), coupling constant (J in Hz) and assignment. ESI-Mass spectrometry measurements were performed on a Bruker microTOF MS (ESI/GC-EI) instrument by Mr. Karl Heaton. Ion detection ranged from 50 to 400 m/z depending on the sample. Elemental analyzes were performed using an Exeter Analytical Inc. CE-440 analyzer by Dr. Graeme McAllister. Samples were analyzed twice for the composition of carbon, hydrogen, and nitrogen. The melting point of the anthraquinone salts were measured in a Stuart SMP30 apparatus. The melting point of the $Tf2N^-$ salts was confirmed with differential scanning calorimetry measurements performed

on a Mettler Toledo DSC822e and analyzed via STARe Software 8.10. Karl Fischer titration was performed using a Mettler Toledo C20S Coulometric KF Titrator. Samples were analyzed via external dissolution using dry acetonitrile according to *Equation 5.2.1* from the equipment's manual. *R* is the water content of the sample in %w/w or ppm, *B* is the water content of the blank solvent, *msol* is the weight of the solvent used to dissolve the sample, *mext* is the sample weight and *C* is the total water content (sample + solvent). If the measurements is given in %w/w then C=C*0.1/m, if it is given in ppm, then C=C*1000/m, where m is the weight of the sample aliquot injected.

$$R(\%, ppm) = (C\frac{msol+mext}{mext} - \frac{B*msol}{mext})/1000$$

Equation 5.2.1: Karl-Fisher water content determination by solid-liquid extraction

The electrochemical cell consisted of a three-electrode cell with a BASi glassy carbon (3 mm diameter) WE, an Innovative Instruments Inc. Leak-free Ag/AgCl in 3 M KCl as RE and platinum wire as CE. For all electrochemical experiments, the concentration of the analyte was 2 mM unless stated otherwise. The scan rate used for all experiments is 100 mV/s unless stated otherwise.

5.2.2 Synthetic preparations

[C_2Mim][Tf_2N]. Methodology adapted from Giernoth and Bankmann.[232] [C_2Mim]Br (10.0 g, 0.05 mol, 1 eq) was added to a round-bottom flask loaded with a stirrer bar and dissolved in in 45 cm^3 of deionised water. Li[Tf_2N] (14.9 g, 0.05 mol, 1 eq) was added to the reaction mixture and stirred at room temperature for 48 h, a biphasic system formed over time. The reaction mixture was transferred to a separation funnel and washed with deionized water until no precipitation was observed when the aqueous phases were mixed with a solution of $AgNO_3$, to test for AgBr precipitates (8x50 cm^3washes were required). The colourless oil was then dried *in vacuo* at 60 °C for 4 days. 8.8 g, 45% yield). ^{1}H NMR resulted in agreement with the literature.

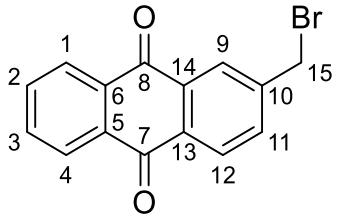

2-Bromomethylanthraquinone (39a). The methodology was adapted from the synthetic procedures by Crozet *et al*. and Zheng *et al*.[206,207] 2-mehtylanthraquinone (4.50 g, 0.02 mol), azobisisobutyronitrile (330 mg, 10 mol %) and N-bromosuccinimide (3.56 g, 0.02 mol, 1 eqs) were dissolved in 30 cm^3 of benzene. The reaction mixture was set to reflux under vigorous stirring for 24 h. Work up: the solvent was removed under vacuum and the product redissolved in 50 cm^3 of ethyl acetate, washed with Na_2CO_3 saturated aqueous solution 3x50 cm^3 dried over $MgSO_4$ and recrystallized from ethyl acetate. 4.2 g, 70% yield of a yellow precipitate was obtained in a 94% purity according to ^{1}H-NMR (d_6-DMSO, 400 MHz). δ 8.32 (m, 4H (aromatic)), 7.81 (m, 3H, (aromatic)), 4.60 (s, 2H, (H15)).

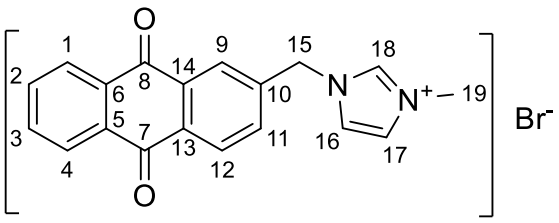

1-Methyl-3-(2-methylanthraquinone)imidazolium bromide ([41]Br). **39a** (200 mg, 0.6 mmol, 1 eq) was added to a round-bottom flask equipped with a magnetic bar, dissolved in 10 cm^3 of toluene and heated to 70 ^oC. 1-methylimidazolium dried over CaH_2 and distilled under pressure (55 μL, 0.66 mmol, 1.1 eqs) was added to the reaction mixture and let under vigorous stirring for 24 h. A yellow precipitate was formed over time. Work up: the precipitate was recovered by filtration, redissolved in 10 cm^3 of dichloromethane and washed with deionized water 3x10 cm^3. The product was recrystallized from dichloromethane with hexane as antisolvent and dried under vacuum in a Schlenk line for 12 h. 210 mg 92% yield of yellow precipitate

was obtained. MP: 236-239 ºC (sample decomposed). Elemental analysis (%) = C(55.87), H(4.13), N(6.57). Theoretical elemental analysis considering AQ:H2O ratio of 3:2, $([C_{19}H_{15}N_2O_2][Br])_2 \bullet (H_2O)_3$ = C(55.62), H(4.42), N(6.83). Water content by Karl-Fisher titration = 42.6 ppm. ESI-MS (m/z): expected for $[C_{19}H_{15}N_2O_2]^+$ = 303.1128, observed = 303.1122 [M^+] (Error = 0.6 mDa). ^{1}H-NMR (d_6-DMSO, 400 MHz). δ 9.41 (s, 1H, (H16)), 8.23 (d, J = 1.3 Hz, 1H, (H9)), 8.18 (d, J = 8.16 Hz, 1H, (H12)), 8.13 (m, 2H, (H2, H3)), 7.96 (dd, J = 8.1 ,1.2, Hz, 1H, (H11)), 7.94 (d, J = 1.4 Hz, 1H, (•H17)), 7.92 (d, J = 5.6 Hz, 1H, (H1 or H4)), 7.91 (d, J =5.6 Hz, 1H, (H1 or H4)), 7.78 (d, J = 1.4 Hz, 1H, (H18)), 5.72 (s, 2H, (H15)), 3.91 (s, 3H, (H19)). ^{13}C{^{1}H}-NMR (d_6-DMSO, 100 MHz). δ 182.15-182.02 (C7, C8), 141.35 (C10), 137.11 (C16), 134.74-134.69 (C1, C4), 134.13 (C12), 133.34-132.92-132.89-132.87 (C5, C6, C13, C14), 127.57 (C11), 126.79-126.77 (C2, C3), 126.55 (C9), 124.24 (C18), 122.49 (C17), 51.12 (C15), 36.03 (C19).

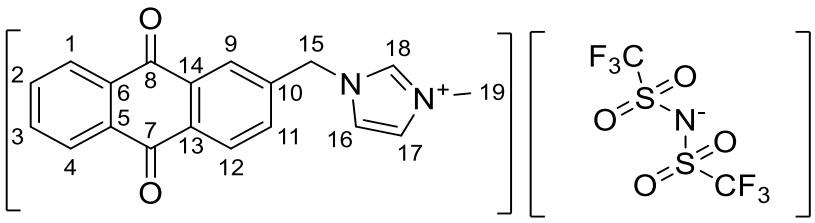

1-Methyl-3-(2-methylanthraquinone)imidazolium bis(trifluoromethanesulfonyl)imide ([41][Tf$_2$N]). In a round-bottom flask quipped with a stirrer bar, salt **[41]Br** (115 mg, 0.3 mmol, 1 eq) was dissolved in 10 cm^3 of ethanol, Li[Tf$_2$N] (86 mg, 0.3 mmol, 1 eq) was added to the reaction mixture and stirred at room temperature for 12 h. A pale-yellow precipitate was formed. The precipitate was redissolved in 10 cm^3 of dichloromethane, transferred to a separation funnel and washed 10 cm^3 of deionized water, an aliquot of the aqueous phase was mixed with an aqueous solution of $AgNO_3$ 1 M to verify if AgBr precipitates were formed. The organic layer was washed four times until no precipitation at the silver test was detected. The product was recrystallized from dichloromethane with hexane as antisolvent and dried under vacuum in a Schlenk line for 12 h. 94 mg 54% yield of pale-yellow precipitate was obtained. MP: 171 ºC. Elemental analysis

(%) = C(43.07), H(2.39), N(6.72). Theoretical elemental analysis considering $[C_{19}H_{15}N_2O_2][C_2F_6NO_4S_2]$ = C(43.23), H(2.59), N(7.20). Water content by Karl-Fisher titration = 1.6 ppm. ESI-MS (m/z): expected for $[C_{19}H_{15}N_2O_2]^+$ = 303.1128, observed = 303.1125 [M^+] (Error = 0.6 mDa); expected for $[C_2F_6NO_4S_2]^-$ = 279.9178, observed = 279.9176 [M^-] (Error = 0.3 mDa). ^{1}H-NMR (d_6-Acetone, 400 MHz). δ 9.37 (s, 1H, (H16)), 8.32 (d, *J* = 2.1 Hz, 1H, (H9)), 8.31 (d, *J* = 7.9 Hz, 1H, (H12)), 8.28 (d, *J* = 5.9 Hz, 1H, (H2 or H3)), 8.27 (d, *J* = 5.9 Hz, 1H, (H2 or H3)), 8.02 (dd, *J* = 8.0, 1.7, Hz, 1H, (H11)), 7.96 (m, 2H, (H1, H4)), 7.94 (d, *J* = 1.8 Hz, 1H, (H17)), 7.83 (d, *J* = 1.8 Hz, 1H, (H18)), 5.91 (s, 2H, (H15)), 4.14 (s, 3H, (H19)). ^{19}F{^{1}H} -NMR (d_6-Acetone, 376 MHz) δ -79.55 (s, 6F).

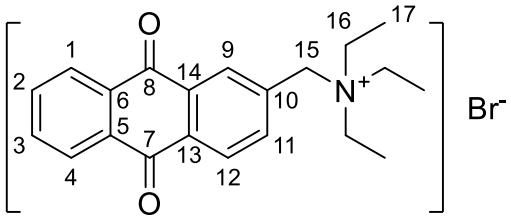

N,N,N-Triethyl(2-methylanthraquinone)ammonium bromide ([42]Br). **39a** (200 mg, 0.6 mmol, 1 eq) was added to a round-bottom flask equipped with a magnetic bar, dissolved in 10 cm^3 of toluene and heated to 70 ºC. Triethylamine dried over CaH_2 and distilled under pressure (68 μL, 0.66 mmol, 1.1 eqs) was added to the reaction mixture and let under vigorous stirring for 24 h. A yellow precipitate was formed over time. Work up: the precipitate was recovered by filtration, redissolved in 10 cm^3 of dichloromethane and washed with deionized water 3x10 cm^3. The product was recrystallized from dichloromethane with hexane as antisolvent and dried under vacuum in a Schlenk line for 12 h. 98 mg 41% yield of a yellow precipitate was obtained. MP: 214-216 ºC (sample decomposed). Elemental analysis (%) = C(57.74), H(6.35), N(3.09). Theoretical elemental analysis considering AQ:H2O ratio of 1:2, $[C_{21}H_{24}NO_2][Br]\bullet(H_2O)_2$ = C(57.54), H(6.44), N(3.20). Water content by Karl-Fisher titration = 93.1 ppm. ESI-MS (m/z): expected for $[C_{21}H_{24}NO_2]^+$ = 322.1802, observed = 322.1794 [M^+] (Error = 0.8 mDa). ^{1}H-NMR (d_6-DMSO, 400 MHz). δ 8.34 (d, *J* = 1.4 Hz, 1H, (H9)), 8.27 (d, *J* = 8.0 Hz, 1H, (H12)),

8.20 (m, 2H, (H2, H3)), 8.08 (dd, *J* = 1.4, 8.0 Hz, 1H, (H11)), 7.96 (d, *J* = 5.7 Hz, 1H, (H1 or H4), 7.95 (d, *J* = 5.8 Hz, 1H, (H1 or H4), 4.80 (s, 2H, (H15)), 3.34 (q, *J* = 7.2 Hz, 6H, (H16)), 1.35 (t, *J* = 7.0 Hz, 9H, (H17)). $^{13}C\{^{1}H\}$-NMR (d_6-DMSO, 100 MHz). δ 182.15-182.02 (C7, C8), 138.4 (C11), 134.89-134.88 (C1, C4), 134.3 (C10), 133.8-133.2-132.9-132.8 (C5, C6, C13, C14), 130.97 (C9), 127.4-126.9 (C2, C3, C12), 59.0 (C15), 52.6 (16) ,7.7 (C17).

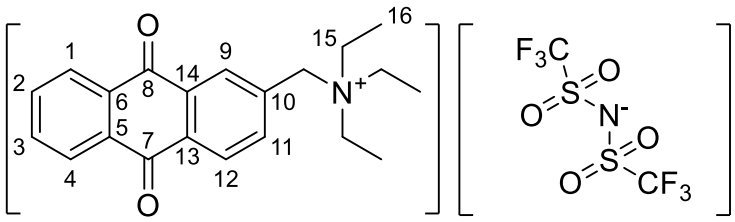

N,N,N-Triethyl(2-methylanthraquinone)ammonium bis(trifluoromethanesulfonyl)imide ([42][Tf_2N]). In a round-bottom flask equipped with a stirrer bar, salt **[42]Br** (120 mg, 0.3 mmol, 1 eq) was dissolved in 10 cm^3 of a dichloromethane/acetone 1:1 mixture, Li[Tf_2N] (86 mg, 0.3 mmol, 1 eq) was added to the reaction mixture and stirred for 12 h. The reaction mixture was transferred to a separation funnel and washed with fractions of 10 cm^3 of deionized water until the aqueous phases did not show precipitates when mixed with an aqueous solution of $AgNO_3$ 1 M (3 washes were required). The product was recrystallized from dichloromethane with hexane as antisolvent and dried under vacuum in a Schlenk line for 12 h. 150 mg 83% yield of a pale-yellow precipitate was obtained. MP: 118 ^{o}C (product decomposed). Elemental analysis (%) = C(46.34), H(3.90), N(4.49). Theoretical elemental analysis considering $[C_{21}H_{24}NO_2][C_2F_6NO_4S_2]$ = C(45.85), H(4.01), N(4.65). Water content by Karl-Fisher titration = 13.7 ppm. ESI-MS (m/z): expected for $[C_{21}H_{24}NO_2]^+$ = 322.1802, observed = 303.1799 $[M^+]$ (Error = 0.3 mDa); expected for $[C_2F_6NO_4S_2]^-$ = 279.9178, observed = 279.9178 $[M^-]$ (Error = 0.0 mDa). ^{1}H-NMR (d_6-Acetone, 400 MHz). δ 8.47 (d, *J* = 1.8 Hz, 1H, (H9)), 8.36 (d, *J* = 7.9 Hz, 1H, (H12)), 8.28 (m, 2H, (H2, H3)), 8.08 (dd, *J* = 2.0, 8.0 Hz, 1H, (H11)), 7.96 (d, *J* = 5.8 Hz, 1H, (H1 or H4), 7.95 (d, *J* = 5.8 Hz, 1H, (H1 or H4), 4.95 (s, 2H, (H15)), 3.57 (q, *J* = 7.2 Hz, 6H,

(H16)), 1.59 (t, *J* = 7.2 Hz, 9H, (H17)). $^{19}F\{^{1}H\}$-NMR (d_6-Acetone, 376 MHz). δ -79.82 (s, 6F).

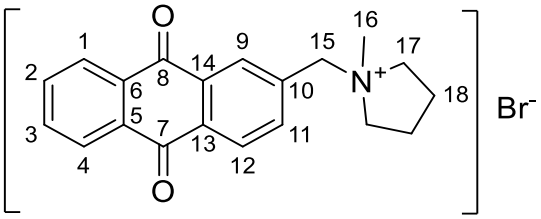

1-Methyl-1-(2-methylanthraquinone)pyrrolidinium bromide ([43]Br). **39a** (200 mg, 0.6 mmol, 1 eq) was added to a round-bottom flask equipped with a magnetic bar, dissolved in 10 cm^3 of toluene and heated to 70 ^oC. N-methylpyrrolidine (68 μL, 0.66 mmol, 1.1 eqs) was added to the reaction mixture and let under vigorous stirring for 24 h. A yellow precipitate was formed over time. Work up: the precipitate was recovered by filtration, redissolved in 10 cm^3 of dichloromethane and washed with deionized water 3x10 cm^3. The product was recrystallized from dichloromethane with hexane as antisolvent and dried under vacuum in a Schlenk line for 12 h. 205 mg 89% yield of a yellow precipitate was obtained. MP: 265-268 ^oC (sample decomposed). Elemental analysis (%) = C(59.41), H(5.08), N(3.70). Theoretical elemental analysis considering AQ:H2O ratio of 1:1, $[C_{20}H_{20}NO_2][Br]•H_2O$ = C(59.42), H(5.48), N(3.46). Water content by Karl-Fisher titration = 58.8 ppm. ESI-MS (m/z): expected for $[C_{20}H_{20}NO_2]^+$ = 306.1489, observed = 306.1488 $[M^+]$ (Error = 0.1 mDa). ^{1}H-NMR (d_6-DMSO, 400 MHz). δ 8.43 (s, 1H, (H9)), 8.30 (d, *J* = 8 Hz, 1H, (12)), 8.23 (m, 2H, (H2, H3)), 8.16 (dd, *J* = 1.2 Hz, 8.0 Hz, (H11)), 7.97 (m, 2H, (H1, H4)), 4.91 (s, 2H, (H15)), 3.68-3.51 (broad, 4H, (H17)), 3.00 (s, 3H, (H16)), 2.17 (broad, 4H, (H18)). $^{13}C\{^{1}H\}$-NMR (d_6-DMSO, 100 MHz). δ 182.21-181.17 (C7, C8), 138.22 (C11), 135.37 (10), 134.75 (2C, (C1, C4)), 133.75-133.21-132.96-132.88 (5, 6, 13, 14), 130.88 (9), 127.48 (12), 126.89 (2C, C2, C3), 64.11 (C15), 63.09 (C17), 47.28 (C16), 20.81 (C18).

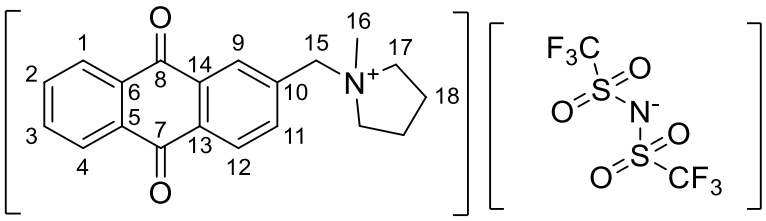

1-Methyl-1-(2-methylanthraquinone)pyrrolidinium bis(trifluoromethanesulfonyl)imide ([43][Tf_2N]). In a round-bottom flask equipped with a stirrer bar, salt **[43]Br** (115 mg, 0.3 mmol, 1 eq) was dissolved in 10 cm^3 of a dichloromethane/acetone 1:1 mixture, Li[Tf_2N] (86 mg, 0.3 mmol, 1 eq) was added to the reaction mixture and stirred for 12 h. The reaction mixture was transferred to a separation funnel and washed with fractions of 10 cm^3 of deionized water until the aqueous phases did not show precipitates when mixed with an aqueous solution of $AgNO_3$ 1 M (3 washes were required). The product was recrystallized from dichloromethane with hexane as antisolvent and dried under vacuum in a Schlenk line for 12 h. 135 mg 77% yield of a pale-yellow precipitate was obtained. MP: 146 ^oC. Elemental analysis (%) = C(44.73), H(3.51), N(4.36). Theoretical elemental analysis considering $[C_{20}H_{20}NO_2][C_2F_6NO_4S_2]$ = C(45.05), H(3.44), N(4.78). Water content by Karl-Fisher titration = 3.5 ppm. ESI-MS (m/z): expected for $[C_{21}H_{24}NO_2]^+$ = 306.1489, observed = 306.1492 [M^+] (Error = 0.3 mDa); expected for $[C_2F_6NO_4S_2]^-$ = 279.9178, observed = 279.9176 [M^-] (Error = 0.2 mDa). ^{1}H-NMR (d_6-Acetone, 400 MHz). δ 8.55 (d, *J* = 1.9 Hz 1H, (H9)), 8.40 (d, *J* = 8 Hz, 1H, (H12)), 8.31 (m, 2H, (H2, H3)), 8.26 (dd, *J* = 8.0, 1.5 Hz, (H11)), 7.99 (m, 2H, (H1, H4)), 5.08 (s, 2H, (H15)), 4.04-3.76 (broad, 4H, (H17)), 3.33 (s, 3H, (H16)), 2.43 (broad, 4H, (H18)). ^{19}F{^{1}H}-NMR (d_6-Acetone, 376 MHz). δ -79.91 (s, 6F).

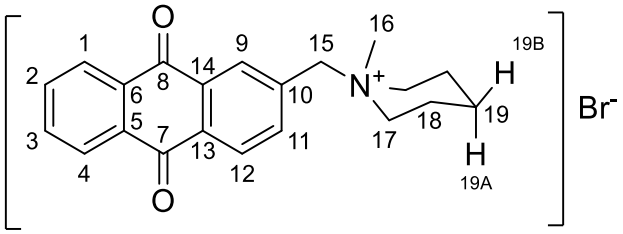

1-Methyl-1-(2-methylanthraquinone)piperidinium bromide ([44]Br). **39a** (200 mg, 0.6 mmol, 1 eq) was added to a round-bottom flask equipped with a magnetic bar, dissolved in 10 cm^3 of toluene and and heated to 70 ^oC. N-methylpiperidine (80 μL, 0.66 mmol, 1.1 eqs) was added to the reaction mixture and let under vigorous stirring for 24 h. A yellow precipitate was formed over time. Work up: the precipitate was recovered by filtration, redissolved in 10 cm^3 of dichloromethane and washed with deionized water 3x10 cm^3. The product was recrystallized from dichloromethane with hexane as antisolvent and dried under vacuum in a Schlenk line for 12 h. 206 mg 78% yield of a yellow precipitate was obtained. MP: 265-268 ^oC (sample decomposed). Elemental analysis (%) = C(58.88), H(5.74), N(3.17). Theoretical elemental analysis considering AQ:H2O ratio of 2:3, $([C_{21}H_{22}NO_2][Br])_2 \bullet (H_2O)_3$ = C(59.02), H(5.90), N(3.28). Water content by Karl-Fisher titration = 42.9 ppm. ESI-MS (m/z): expected for $[C_{21}H_{22}NO_2]^+$ = 320.1645, observed = 320.1649 $[M^+]$ (Error = 0.4 mDa). ^{1}H-NMR (D_2O/d_6-Acetone 1:1, 400 MHz). δ 8.50 (d, *J* = 1.5 Hz, 1H, (H9), 8.42 (d, *J* = 8.0 Hz, 1H, (H12)), 8.31 (m, 2H, (H2, H3)), 8.29 (dd, *J* = 8.0, 1.5 Hz, 1H, (H11), 8.02 (m, 2H, (H1, H4)), 4.98 (s, 2H, (H15)), 3.68 (m, 4H, (H17)), 3.31 (s, 3H, (H16)), 2.19 (m, 4H, (H18)), 1.97 (m, 1H, (H19A or H19B)), 1.83 (m, 1H, (H19A or H19b)). $^{13}C\{^1H\}$-NMR (d_6-DMSO, 100 MHz). δ 182.26-182.21 (C7, C8), 138.80 (C11), 134.94-134.93 (C2, C3), 134.15-133.82-132.97-132.91 (C5, C6, C13, C14), 133.18 (C10), 131.5 (C9), 127.36 (C12), 126.92 (C1, C4), 65.34 (15), 60.10 (C17), 45.98 (C16), 20.76 (C19), 19.36 (C18)

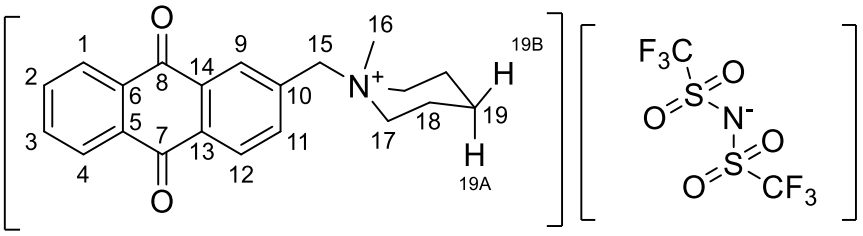

1-Methyl-1-(2-methylanthraquinone)piperidinium bis(trifluoromethanesulfonyl)imide ([44][Tf_2N]). In a round-bottom flask equipped with a stirrer bar, salt **[44]Br** (120 mg, 0.3 mmol, 1 eq) was dissolved in 10 cm^3 of a dichloromethane/acetone 1:1 mixture, Li[Tf_2N] (86 mg, 0.3

mmol, 1 eq) was added to the reaction mixture and stirred for 12 h. The reaction mixture was transferred to a separation funnel and washed with fractions of 10 cm^3 of deionized water until the aqueous phases did not show precipitates when mixed with an aqueous solution of $AgNO_3$ 1 M (3 washes were required). The product was recrystallized from dichloromethane with hexane as antisolvent and dried under vacuum in a Schlenk line for 12 h. 145 mg 81% yield of a pale-yellow precipitate was obtained. MP: 162 ^oC. Elemental analysis (%) = C(46.11), H(3.71), N(4.47). Theoretical elemental analysis considering $[C_{21}H_{22}NO_2][C_2F_6NO_4S_2]$ = C(46.00), H(3.69), N(4.66). Water content by Karl-Fisher titration = 17.3 ppm. ESI-MS (m/z): expected for $[C_{21}H_{24}NO_2]^+$ = 320.1645, observed = 320.1641 $[M^+]$ (Error = 0.4 mDa); expected for $[C_2F_6NO_4S_2]^-$ = 279.9178, observed = 279.9171 $[M^-]$ (Error = 0.7 mDa). ^{1}H-NMR (d_6-Acetone, 400 MHz). δ 8.53 (d, *J* = 1.9 Hz, 1H, (H9), 8.39 (d, *J* = 8.0 Hz, 1H, (H12)), 8.32 (d, *J* = 5.6 Hz 1H, (H2 or H3)), 8.31 (d, *J* = 5.6 Hz 1H, (H2 or H3)), 8.23 (dd, *J* = 1.9, 8.0 Hz, 1H, (H11), 7.99 (d, *J* = 5.8 Hz 1H, (H1 or H4)), 7.98 (d, *J* = 5.8 Hz 1H, (H1 or H4)), 5.07 (s, 2H, (H15)), 3.73 (m, 4H, (H17)), 3.3 (s, 3H, (H16)), 2.14 (m, 4H, (H18)), 1.86 (m, 1H, (H19A or H19B)), 1.73 (m, 1H, (H19A or H19B)). ^{19}F{^{1}H}-NMR (d_6-acetone, 376 MHz). δ -79.83

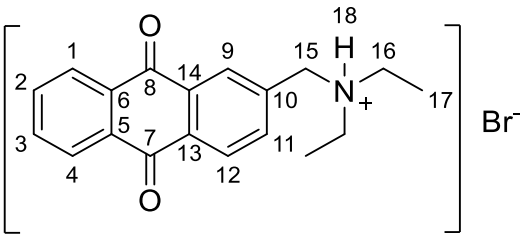

N,N-Diethyl(2-methylanthraquinone)ammonium bromide ([45]Br). **39a** (300 mg, 1 mmol, 1 eq) was added to a round-bottom flask equipped with a magnetic bar, dissolved in 10 cm^3 of toluene and heated to 70 ^oC. Diethylamine dried over CaH_2 and distilled under pressure (310 μL, 3 mmol, 1.1 eqs) was added to the reaction mixture and let under vigorous stirring for 24 h. Work up: the solvent was removed under vacuum and the crude reaction mixture redissolved in 10 cm^3 of methanol. HBr 1M (6 cm^3, 6 mmol, 6 eqs) was added dropwise and the reaction mixture stirred for 10 minutes. The solvent

was removed under vacuum, the crude product was redissolved in 10 cm^3 of dichloromethane and washed with deionized water 3x10 cm^3. The product was recrystallized from dichloromethane with hexane as antisolvent and dried under vacuum in a Schlenk line for 12 h. 295 mg 79% yield of a yellow precipitate was obtained. MP: 218-220 ^oC (sample decomposed). Elemental analysis (%) = C(60.22), H(5.08), N(3.71). Theoretical elemental analysis considering AQ:H2O ratio of 3:1, $([C_{19}H_{20}NO_2][Br])_3 \bullet H_2O$ = C(60.01), H(5.48), N(3.68). Water content by Karl-Fisher titration = 67.4 ppm. ESI-MS (m/z): expected for $[C_{19}H_{20}NO_2]^+$ = 294.1489, observed = 294.1481 $[M^+]$ (Error = 0.8 mDa). ^{1}H-NMR (d_6-DMSO, 400 MHz). δ 9.89 (s, 1H, (18)), 8.72 (d, *J* = 1.4 Hz, 1H, (H9)), 8.24 (d, *J* = 7.9 Hz, 1H, (H12)), 8.17 (broad, 3H, (H2, H3, H11)), 7.94 (d, *J* = 5.9 Hz, 1H, (H1 or H4)), 7.93 (d, *J* = 5.9, 1H, (H1 or H4)), 4.61 (d, *J* = 5.5 Hz, 2H, (H15)), 3.15 (qd, *J* = 7.3, 4.5 Hz, 4H, (H16)), 1.27 (t, *J* = 7.3 Hz, 6H, (H17)). ^{13}C{^{1}H}-NMR (d_6-DMSO, 100 MHz). δ 182.17-182.09 (C7, C8), 136.88 (C10), 136.83 (C12), 134.75-134.74 (C1, C4), 133.37-133.21-132.92-132.89 (C5, C6, C13, C14), 129.42 (C9), 127.30 (C11), 126.82-129.79 (C2, C3), 54.26 (C15), 46.14 (C16), 8.33 (C17).

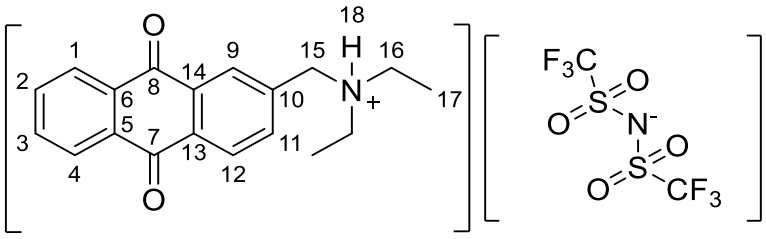

N,N-Diethyl(2-methylanthraquinone)ammonium bis(trifluoromethanesulfonyl)imide ([45][Tf_2N]). **39a** (300 mg, 1 mmol, 1 eq) was added to a round-bottom flask equipped with a magnetic bar, dissolved in 10 cm^3 of toluene and heated to 70 ^oC. Diethylamine dried over CaH_2 and distilled under pressure (310 µL, 3 mmol, 3 eqs) was added to the reaction mixture and let under vigorous stirring for 24 h. The solvent was removed under vacuum, the crude reaction mixture was redissolved in 10 cm^3 of dichloromethane and washed with HCl 1M 3x10 cm^3 and saturated aqueous Na_2CO_3 to obtain the free amine. The amine was dissolved in 5 cm^3 of acetonitrile, H[Tf_2N] (stored in a glovebox filled with

N_2 (511 mg, 1.8 mmol, 6 eqs) was added to the reaction mixture and sonicated for 10 minutes. Work up: the reaction was quenched with 10 cm^3 of deionized water, the product was extracted with 10 cm^3 of dichloromethane and washed with deionized water 3x10 cm^3. The salt was recrystallized from dichloromethane and hexane as antisolvent and dried under vacuum in a Schlenk line for 12 h. 134 mg 78% yield of a yellow precipitate was obtained. MP: 145 ºC. Elemental analysis (%) = C(43.65), H(3.53), N(4.21). Theoretical elemental analysis considering AQ:H2O ratio of 3:1, $([C_{19}H_{20}NO_2][C_2F_6NO_4S_2])_3 \bullet H_2O$ = C(43.45), H(3.59), N(4.83). Water content by Karl-Fisher titration = 8.2 ppm. ESI-MS (m/z): expected for $[C_{19}H_{20}NO_2]^+$ = 294.1489, observed = 284.1486 $[M^+]$ (Error = 0.3 mDa); expected for $[C_2F_6NO_4S_2]^-$ = 279.9178, observed = 279.9178 $[M^-]$ (Error = 0.0 mDa). ^{1}H-NMR (d_6-DMSO, 400 MHz). δ 8.49 (d, *J* = 1.9 Hz, 1H, (H9)), 8.34 (d, *J* = 8.1 Hz, 1H, (H12)), 8.27 (m, 2H, (H2, H3)), 8.16 (dd, *J* = 8.0, 1.9 Hz, 1H, (H11)) 7.95 (d, *J* = 6.0 Hz, 1H, (H1 or H4)), 7.94 (d, *J* = 6.0, 1H, (H1 or H4)), 4.61 (d, *J* = 5.5 Hz, 2H, (H15)), 3.15 (qd, *J* = 7.3, 4.5, Hz, 4H, (H16)), 1.27 (t, *J* = 7.3 Hz, 6H, (H17)). ^{19}F{^{1}H}-NMR (d_6-DMSO, 376 MHz). δ -79.70 (s, 6F)

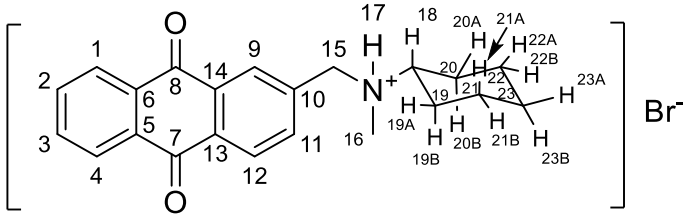

N-cyclohexyl-N-methyl(2-methylanthraquinone)ammonium bromide ([46]Br). **39a** (300 mg, 1 mmol, 1 eq) was added to a round-bottom flask equipped with a magnetic bar, dissolved in 10 cm^3 of toluene and heated to 70 ºC. N-methylcyclohexylamine (390 μL, 3 mmol, 3 eqs) was added to the reaction mixture and let under vigorous stirring for 24 h. Work up: the solvent was removed under vacuum and the crude reaction mixture redissolved in 10 cm^3 of methanol. HBr 1M (6 cm^3, 6 mmol, 6 eqs) was added dropwise and the reaction mixture stirred for 10 minutes. The solvent was removed under vacuum, the crude product was redissolved in 10 cm^3 of dichloromethane and

washed with deionized water 3x10 cm^3. The product was recrystallized from dichloromethane with hexane as antisolvent and dried under vacuum in a Schlenk line for 12 h. 352 mg 85% yield of a yellow precipitate was obtained. MP: 257-259 ºC (sample decomposed). Elemental analysis (%) = C(61.88), H(5.66), N(3.20). Theoretical elemental analysis considering AQ:H2O ratio of 3:2, $([C_{19}H_{20}NO_2][Br])_3 \bullet (H_2O)_2$ = C(61.98), H(5.99), N(3.29). Water content by Karl-Fisher titration = 18.4 ppm. ESI-MS (m/z): expected for $[C_{19}H_{20}NO_2]^+$ = 334.1802, observed = 334.1801 [M^+] (Error = 0.1 mDa). ^{1}H-NMR ($CDCl_3$/acetone 1:1, 400 MHz). δ 11.8 (s, 1H, (H17)), 8.73 (dd, *J* = 1.7, 7.9 Hz, 1H, (H11)), 8.43 (d, *J* = 7.9 Hz, 1H, (H11)), 8.32-8.27 (Broad, 2H, (H2, H3)), 8.29 (d, *J* = 1.7 Hz, 1H, (H9)), 7.86-7.80 (m, 2H, (H1, H4)), 4.42 (dd, *J* = 13.1, 5.4 Hz 1H, ($H15_{60^o\text{-}H17}$)), 4.33 (dd, *J* = 13.1, 5.9 Hz, 1H, ($H15_{180^o\text{-}H17}$)), 3.17 (t, *J* = 12.1 Hz, 1H, (H18)), 2.72 (d, *J* = 4.6 Hz, 3H, (H16)), 2.52 (d, *J* = 12.2 Hz, 1H, (H19A or H20A)), 2.28 (d, *J* = 11.8 Hz, 1H, (H19A or H20A)), 1.95 (t, *J* = 13.5 Hz, 2H, (H21B, H22B)), 1.72 (d, *J* = 12.4, 1H, (H23A)), 1.54 (qd, *J* = 3.4, 11.9 Hz, 2H, (H19B, H20B)), 1.33-1.10 (m, 3H, (H21A, H22A, H23A)).^{13}C{^{1}H}-NMR (d_6-DMSO, 100 MHz). δ 182.31-182.23 (C7, C8), 137.07-136.97 (C10, C11), 134.81-134.79 (C1, C4), 133.49-133.25-133.03-132.99 (C5, C6, C13, C14), 129.69 (C9), 127.31 (C12) 126.88-126.86 (C2, C3), 64.3 (C18), 54.9 (C15), 35.3 (C16), 26.76-25.15 (C19, C20), 24.7-24.5-24.4 (C21, C22, C23).

N-cyclohexyl-N-methyl(2-methylanthraquinone)ammonium bis(trifluoromethanesulfonyl)imide ([46][Tf_2N]). **39a** (300 mg, 1 mmol, 1 eq) was added to a round-bottom flask equipped with a magnetic bar, dissolved in 10 cm^3 of toluene and heated to 70 ºC. N-methylcyclohexylamine (390 μL, 3 mmol, 3 eqs) was added to the reaction mixture and let under vigorous stirring for 24 h. The solvent was removed under vacuum, the crude reaction mixture was redissolved in 10 cm^3 of dichloromethane and washed with HCl 1M 3x10 cm^3 and saturated aqueous Na_2CO_3 to obtain the free amine. The amine was dissolved in 5 cm^3 of acetonitrile, H[Tf_2N] (stored in a glovebox filled with N_2 (511 mg, 1.8 mmol, 6 eqs) was added to the reaction mixture and sonicated for 10 minutes. Work up: the reaction was quenched with 10 cm^3 of deionized water, the product was extracted with 10 cm^3 of

dichloromethane and washed with deionized water 3x10 cm^3. The salt was recrystallized from dichloromethane and hexane as antisolvent and dried under vacuum in a Schlenk line for 12 h. 134 mg 78% yield of a yellow precipitate was obtained. MP: 159 ^oC. Elemental analysis (%) = C(46.36), H(3.94), N(4.48). Theoretical elemental analysis considering AQ:H2O ratio of 3:1, $([C_{22}H_{24}NO_2][C_2F_6NO_4S_2])_3 \bullet H_2O$ = C(46.45), H(4.01), N(4.51). Water content by Karl-Fisher titration = 13.7 ppm. ESI-MS (m/z): expected for $[C_{22}H_{24}NO_2]^+$ = 334.1802, observed = 334.1800 $[M^+]$ (Error = 0.2 mDa); expected for $[C_2F_6NO_4S_2]^-$ = 279.9178, observed = 279.9175 $[M^-]$ (Error = 0.3 mDa). ^{1}H-NMR (d_6-Acetone, 400 MHz). δ 8.54 (d, *J* = 1.9 Hz, 1H, (H9)), 8.36 (d, *J* = 8.0 Hz, 1H, (H12)), 8.29 (ddt, *J* = 7.6 , 4.2, 2.1 Hz, 2H, (H2, H3)), 8.20 (dd, *J* = 8.0, 1.9 Hz, 1H, (H11)), 7.97 (d, *J* = 5.8 Hz, 1H, (H1 or H4)), 7.96 (d, *J* = 5.8 Hz, 1H, (H1 or H4)), 5.15-4.65 (broad, 2H, (H15)), 3.78 (tt, *J* = 12.1, 3.5 Hz, 1H, (H18)), 3.02 (s, 3H, (H16)), 2.50-2.20 (broad, 2H, (H19A, H20A)), 1.95 (m, 2H, (H21B, H22B)), 1.81 (qd, *J* = 12.0, 3.3 Hz, 2H, (H19B, H20B)), 1.69 (dt, *J* = 12.9, 2.5 Hz, 1H, (H23A)), 1.43 (qt, *J* = 13.1, 3.3 Hz, 2H, (H21A, H22A)), 1.25 (qt, *J* = 13.1, 3.6 Hz, 3H, (H23B)). ^{19}F{^{1}H}-NMR (d_6-Acetone, 376 MHz) δ -79.81 (s, 6F)

Appendix I: Miscellaneous experimental and computational data from Chapter IV.

6.1 NMR spectra, mass spectrometry spectra, calorimetry Energy vs temperature diagrams and crystallographic data.

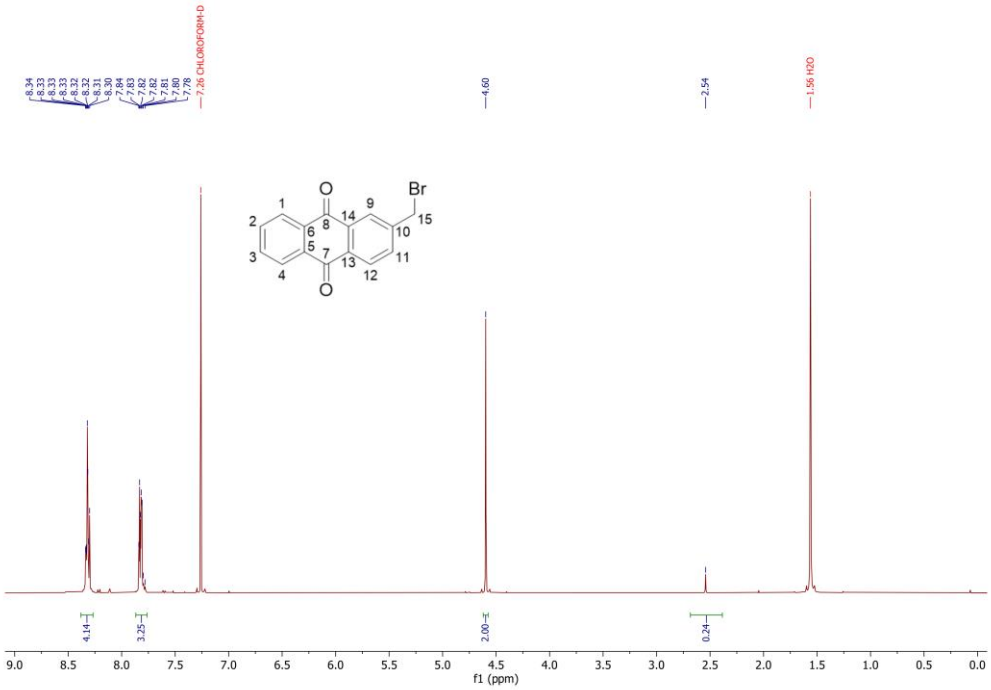

Figure 6.1.1: ^{1}H-NMR spectrum of 2-bromomethylanthraquinone **39a**

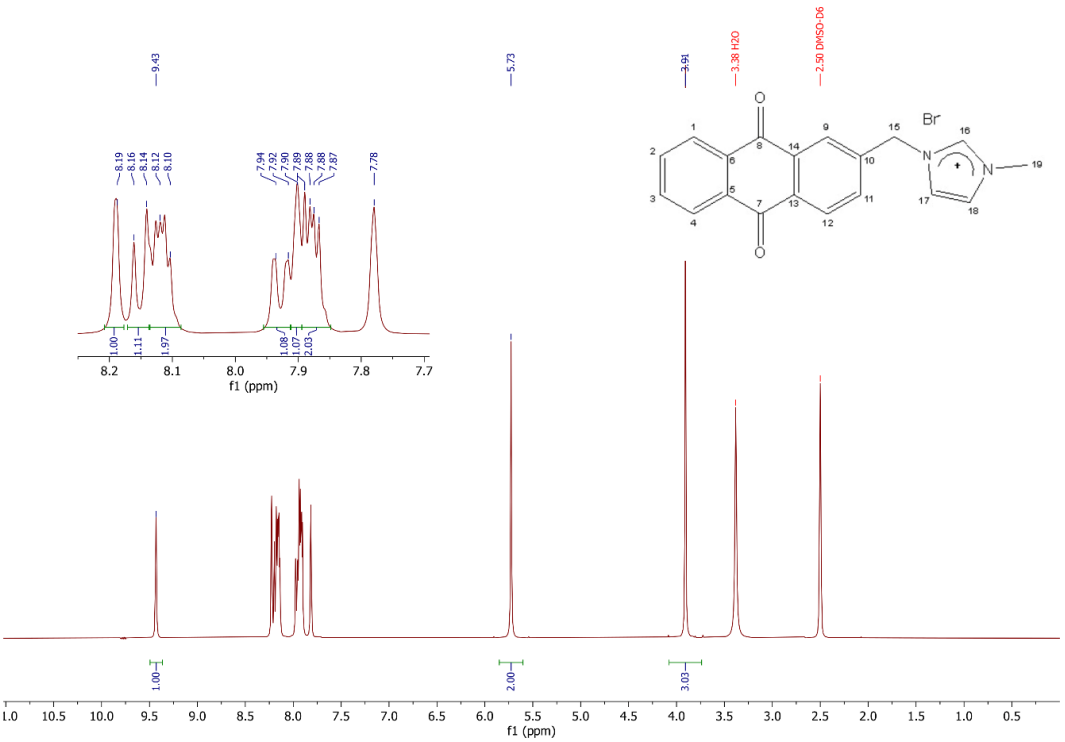

Figure 6.1.2: ^{1}H-NMR spectrum of 1-methyl-3-(2-methylanthraquinone)imidazolium bromide **[41]Br**.

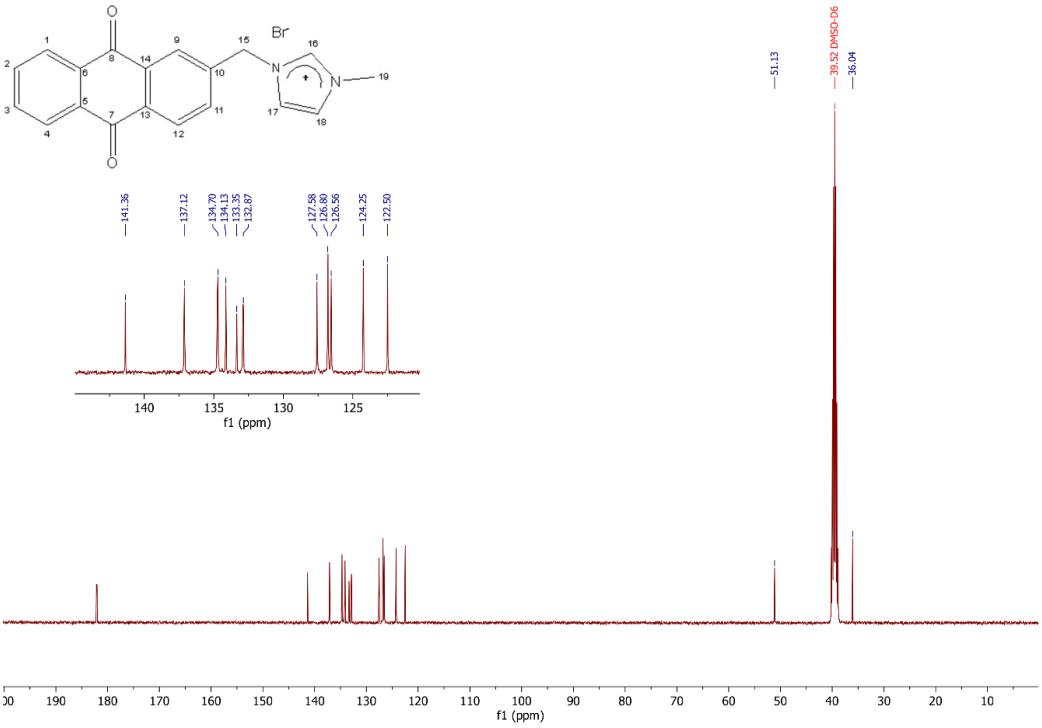

Figure 6.1.3: ^{13}C-NMR spectrum of 1-methyl-3-(2-methylanthraquinone)imidazolium bromide **[41]Br**.

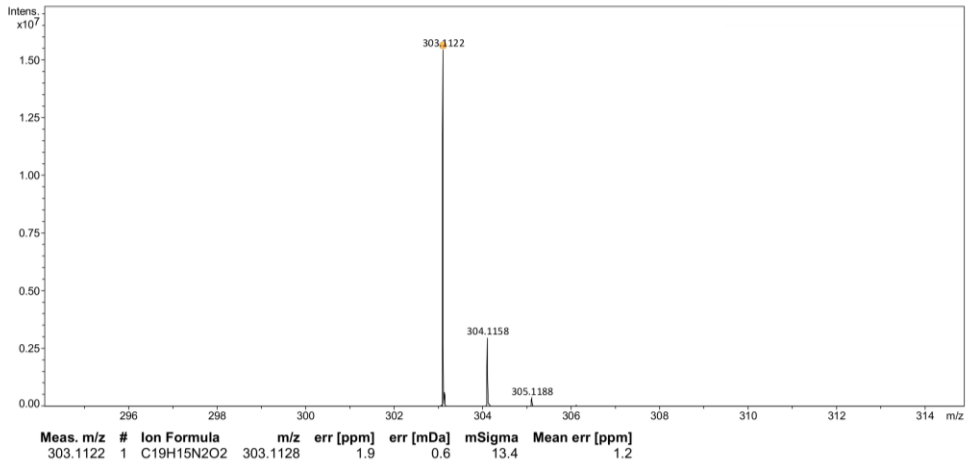

Figure 6.1.4: ESI-MS spectrum (positive channel) of 1-methyl-3-(2-methylanthraquinone)imidazolium bromide **[41]Br**.

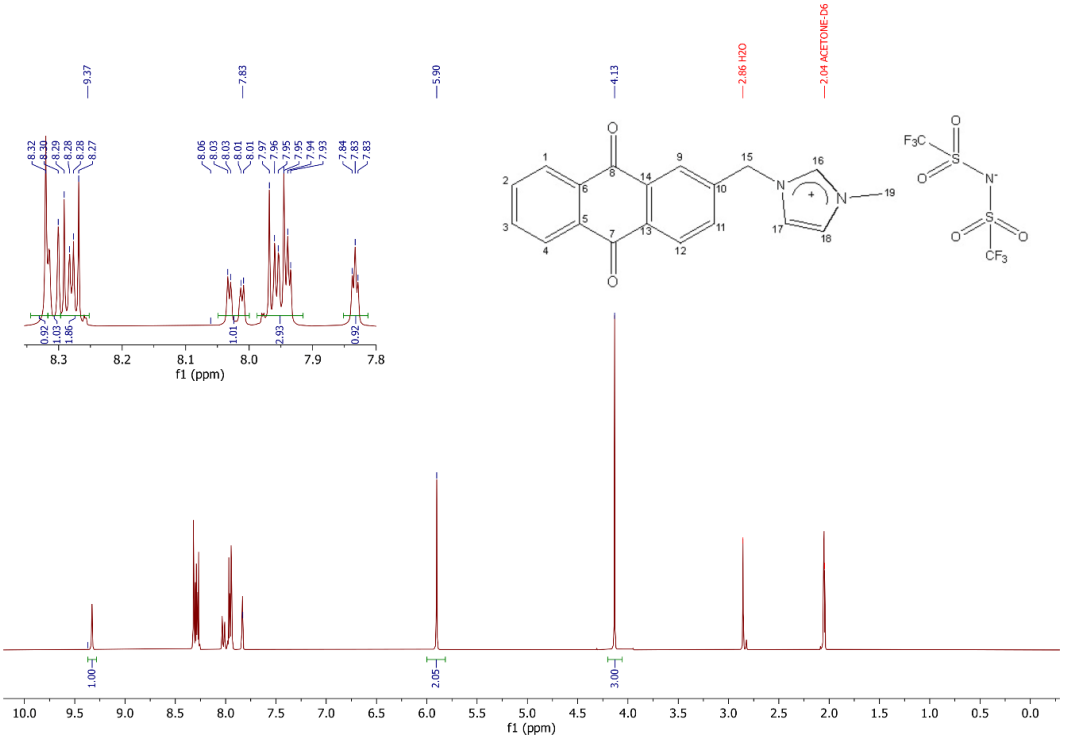

Figure 6.1.5: ^{1}H-NMR spectrum of 1-methyl-3-(2-methylanthraquinone)imidazolium bis(trifluoromethanesulfonyl)imide **[41][Tf$_2$N]**.

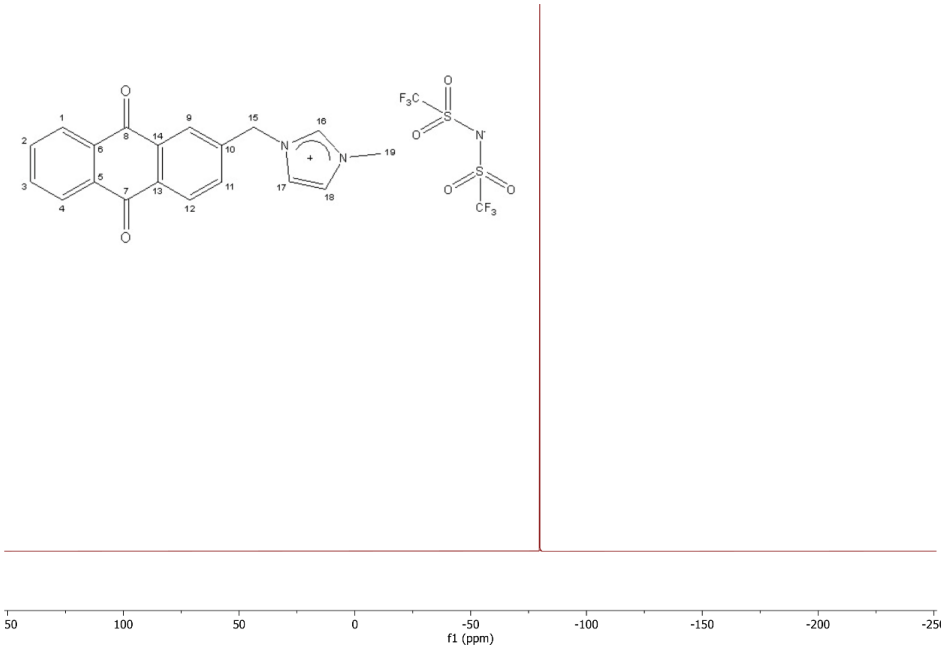

Figure 6.1.6: ^{19}F-NMR spectrum of 1-methyl-3-(2-methylanthraquinone)imidazolium bis(trifluoromethanesulfonyl)imide **[41][Tf$_2$N].**

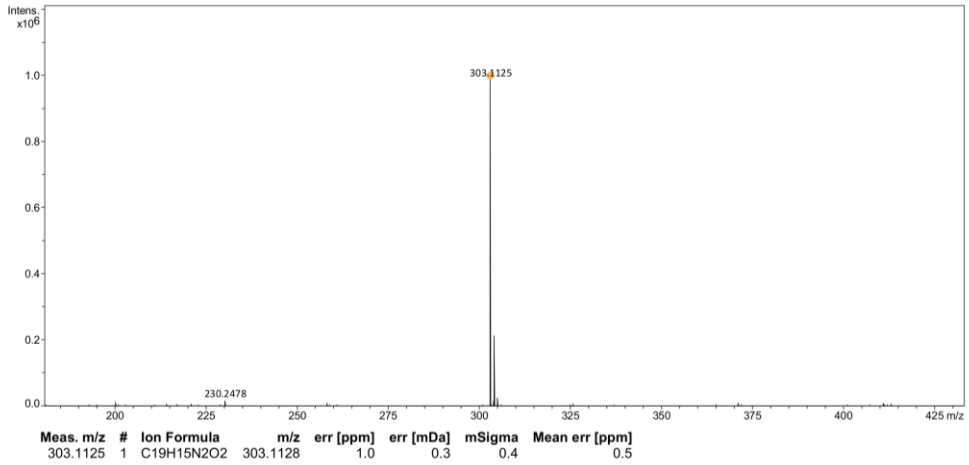

Figure 6.1.7: ESI-MS spectrum (positive channel) of 1-methyl-3-(2-methylanthraquinone)imidazolium bis(trifluoromethanesulfonyl)imide **[41][Tf$_2$N]**.

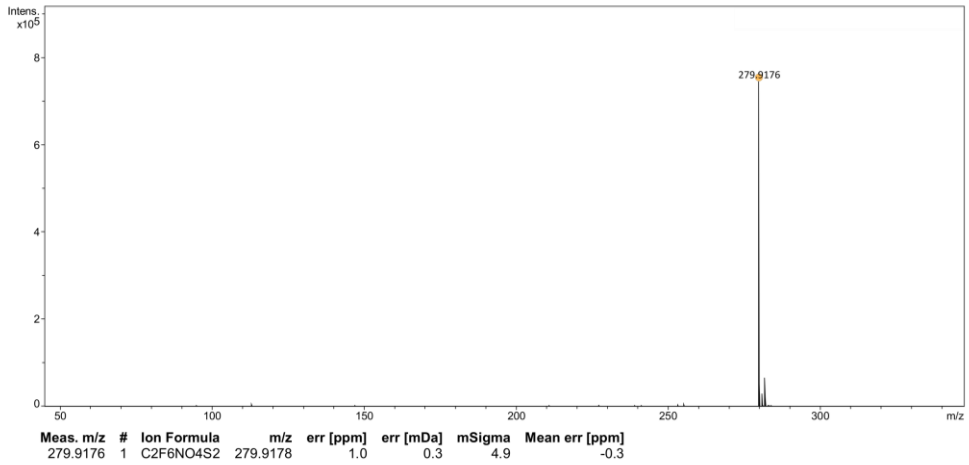

Figure 6.1.8: ESI-MS spectrum (negative channel) of 1-methyl-3-(2-methylanthraquinone)imidazolium bis(trifluoromethanesulfonyl)imide **[41][Tf$_2$N]**.

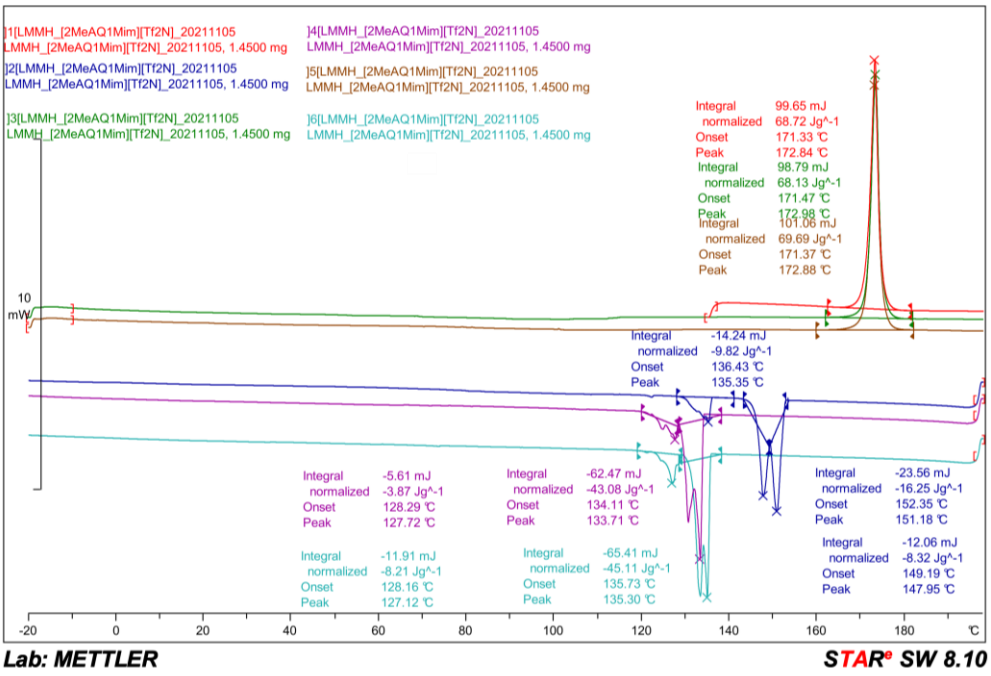

Figure 6.1.9: DSC experiment of 1-methyl-3-(2-methylanthraquinone)imidazolium bis(trifluoromethanesulfonyl)imide **[41][Tf$_2$N]** from -20 °C to 190 °C. MP: 171°C, ΔH_{fus} = 68.8 J/g.

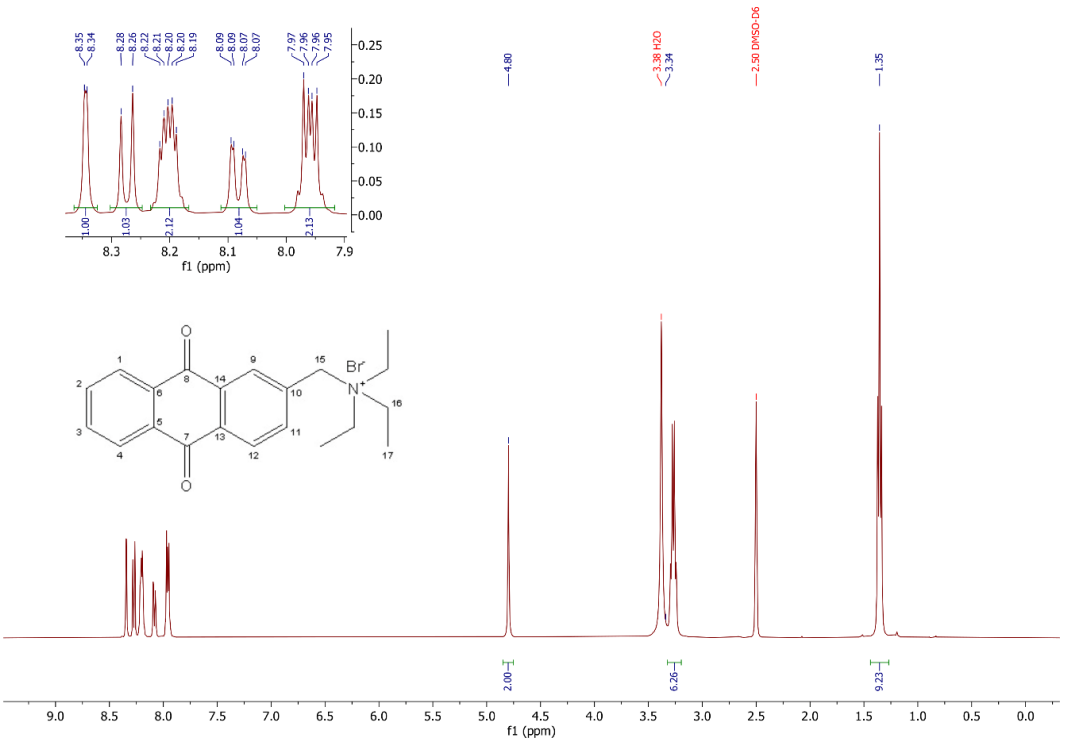

Figure 6.1.10: ^{1}H-NMR spectrum of N,N,N-triethyl(2-methylanthraquinone)ammonium bromide **[42]Br**.

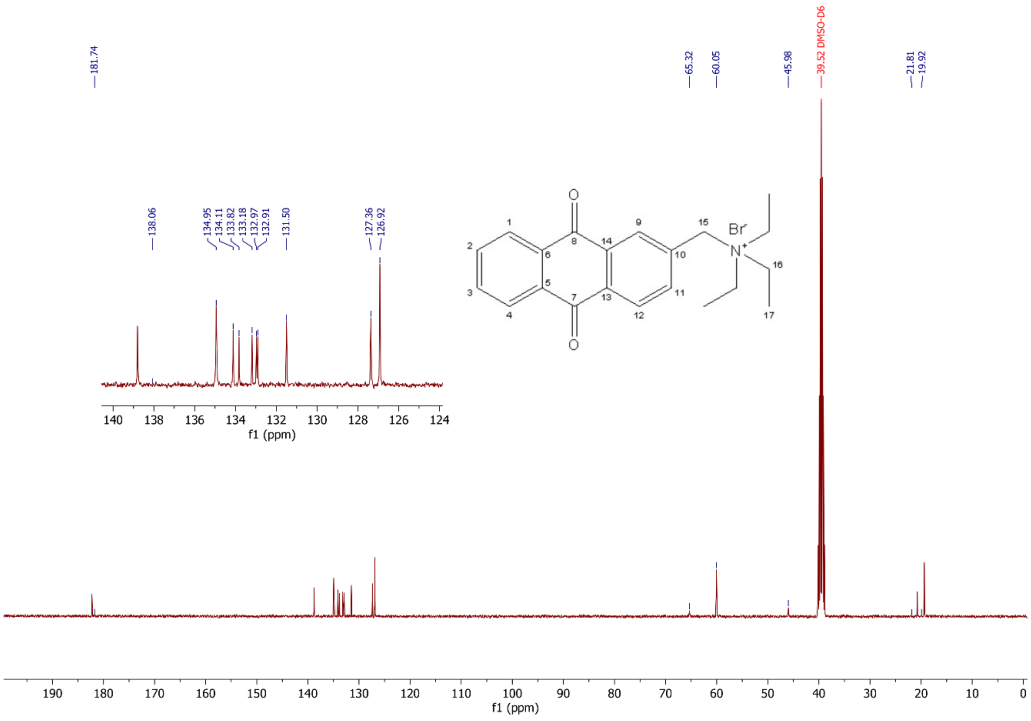

Figure 6.1.11: ^{13}C-NMR spectrum of N,N,N-triethyl(2-methylanthraquinone)ammonium bromide **[42]Br**.

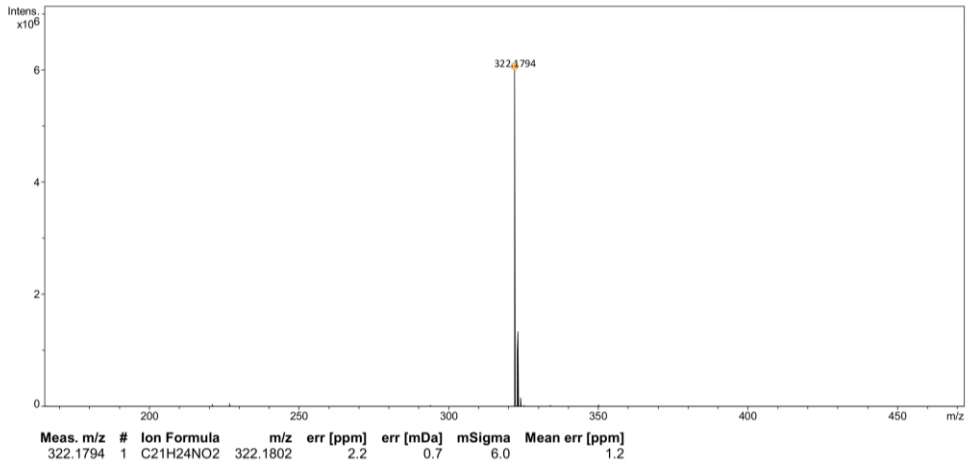

Figure 6.1.12: ESI-MS spectrum (positive channel) of N,N,N-triethyl(2-methylanthraquinone)ammonium bromide **[42]Br**.

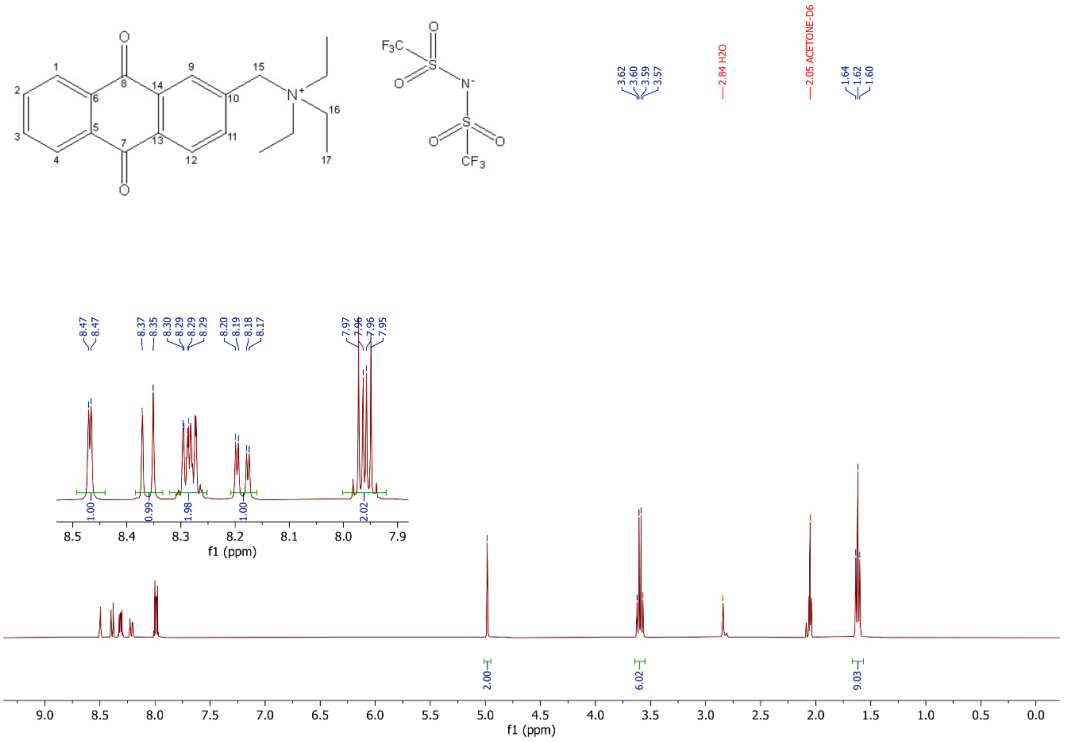

Figure 6.1.13: ^{1}H-NMR spectrum of N,N,N-triethyl(2-methylanthraquinone)ammonium bis(trifluoromethanesulfonyl)imide **[42][Tf$_2$N]**.

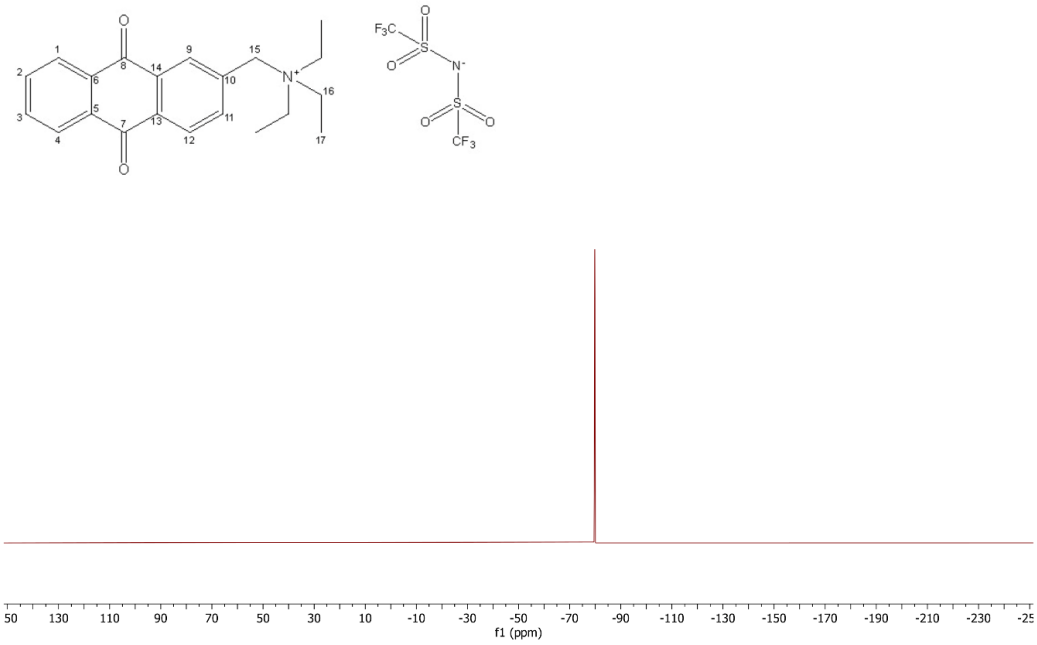

Figure 6.1.14: ^{19}F-NMR spectrum of N,N,N-triethyl(2-methylanthraquinone)ammonium bis(trifluoromethanesulfonyl)imide **[42][Tf$_2$N]**.

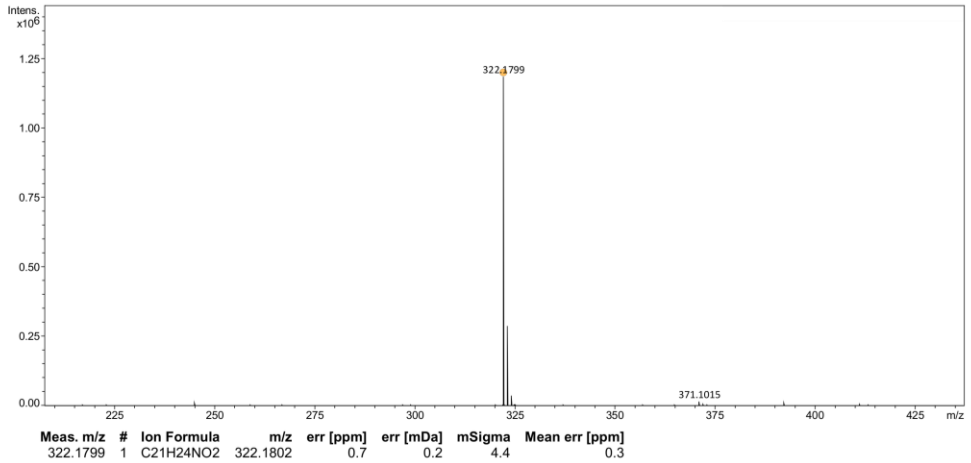

Figure 6.1.15: ESI-MS spectrum (positive channel) of N,N,N-triethyl(2-methylanthraquinone)ammonium bis(trifluoromethanesulfonyl)imide **[42][Tf$_2$N]**.

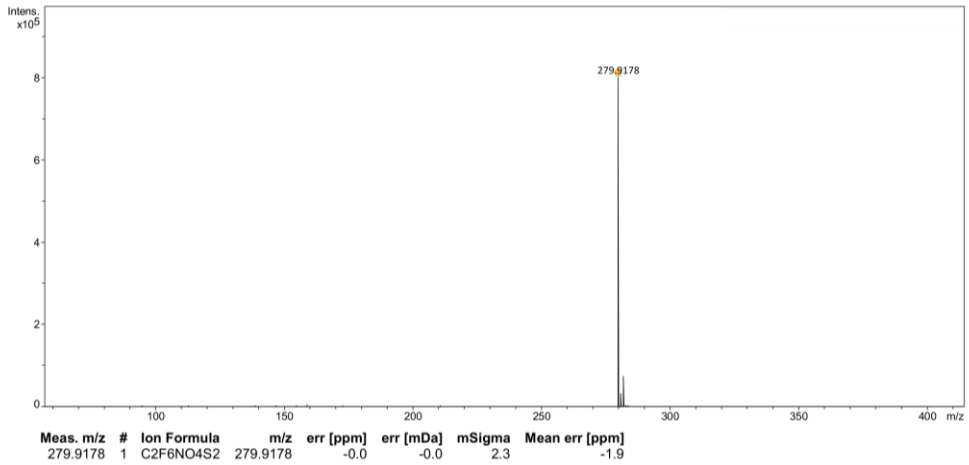

Figure 6.1.16: ESI-MS spectrum (negative channel) of N,N,N-triethyl(2-methylanthraquinone)ammonium bis(trifluoromethanesulfonyl)imide **[42][Tf$_2$N]**.

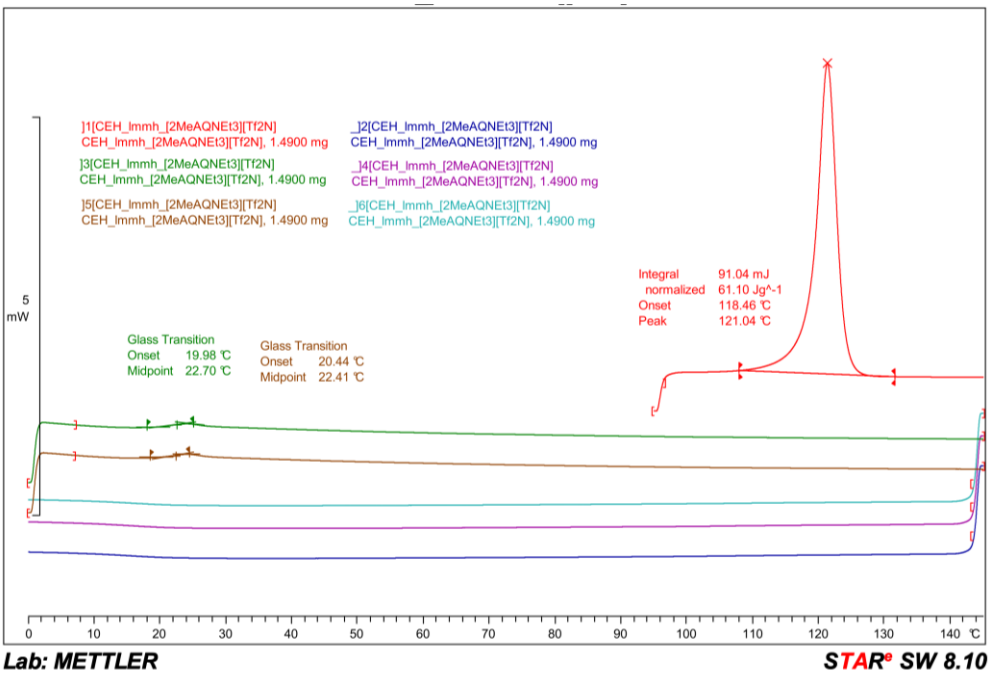

Figure 6.1.17: DSC experiment of N,N,N-triethyl(2-methylanthraquinone)ammonium bis(trifluoromethanesulfonyl)imide **[42][Tf$_2$N]** from -0 °C to 145 °C. MP: 118 °C, ΔH_{fus} = 61.1 J/g. Product decomposed after the first heating cycle

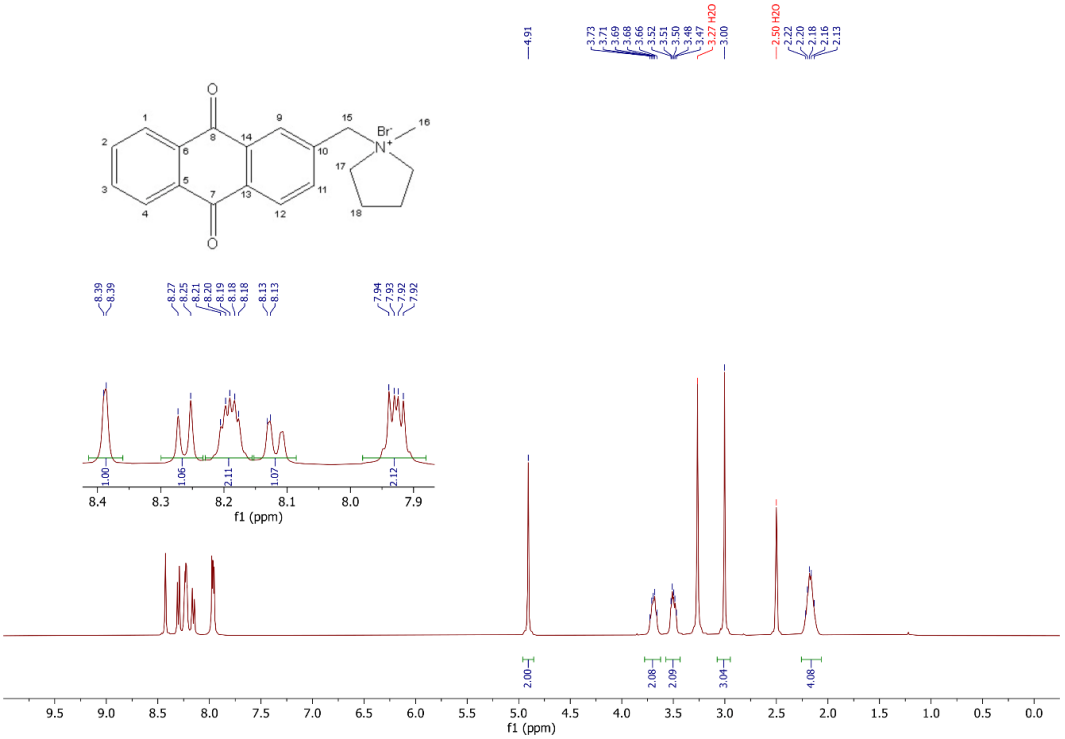

Figure 6.1.18: ^{1}H-NMR spectrum of 1-methyl-1-(2-methylanthraquinone)pyrrolidinium bromide **[43]Br**.

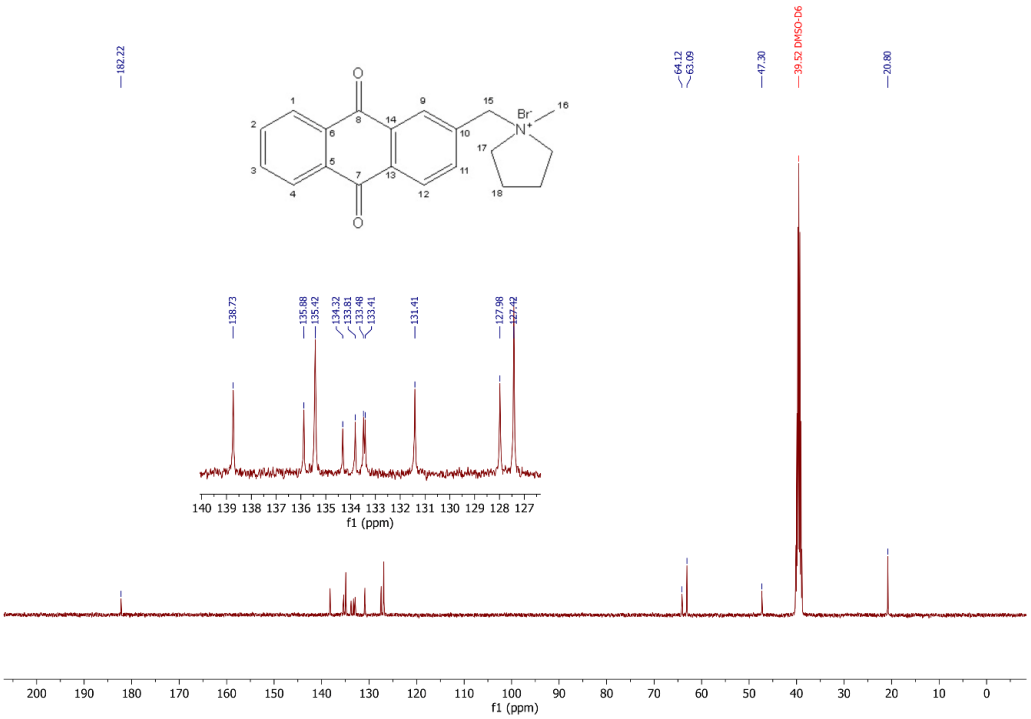

Figure 6.1.19: ^{13}C-NMR spectrum of 1-methyl-1-(2-methylanthraquinone)pyrrolidinium bromide **[43]Br**.

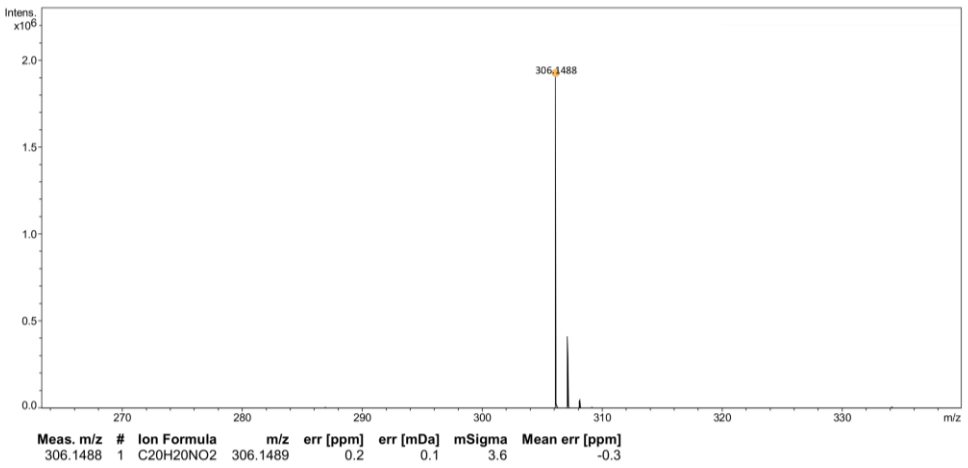

Figure 6.1.20: ESI-MS spectrum (positive channel) of 1-methyl-1-(2-methylanthraquinone)pyrrolidinium bromide **[43]Br**.

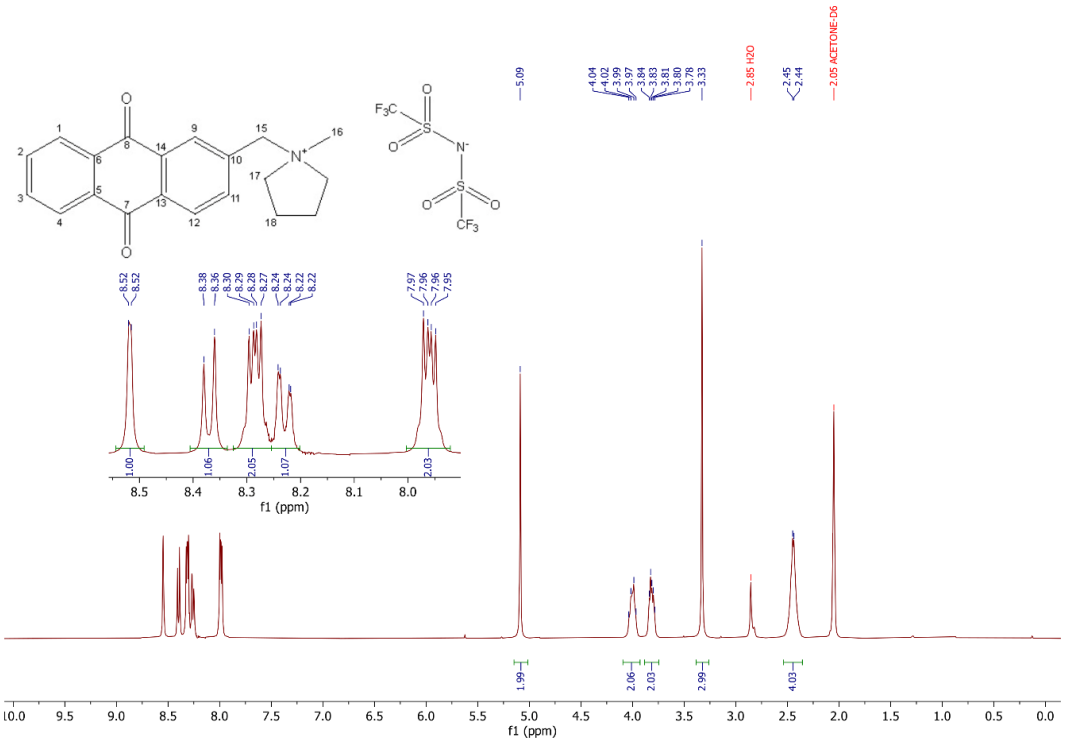

Figure 6.1.21: ^{1}H-NMR spectrum of 1-methyl-1-(2-methylanthraquinone)pyrrolidinium bis(trifluoromethanesulfonyl)imide **[43][Tf$_2$N]**.

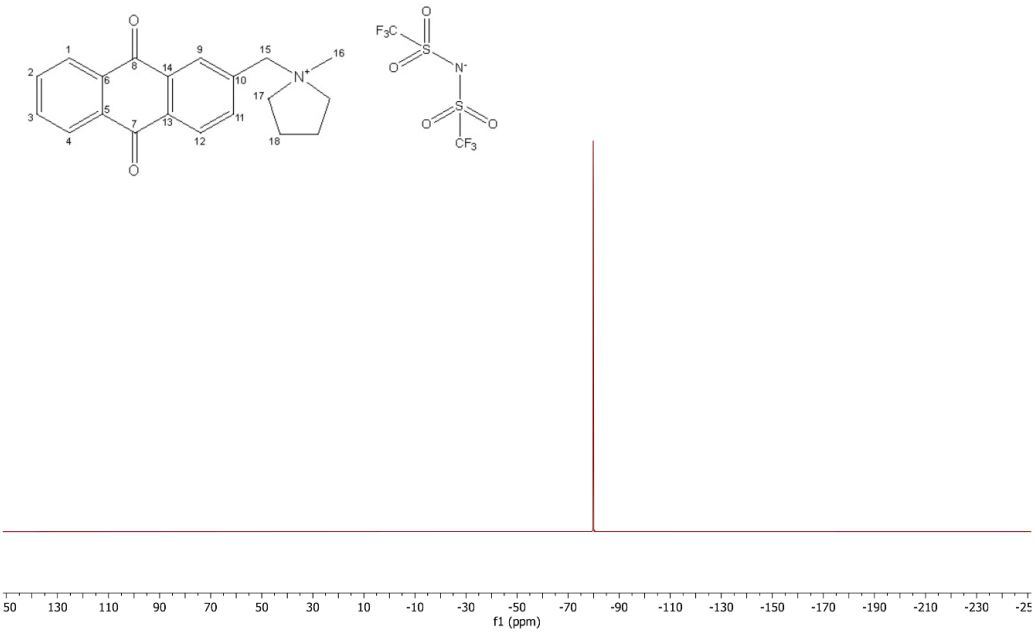

Figure 6.1.22: ^{19}F-NMR spectrum of 1-methyl-1-(2-methylanthraquinone)pyrrolidinium bis(trifluoromethanesulfonyl)imide **[43][Tf$_2$N]**.

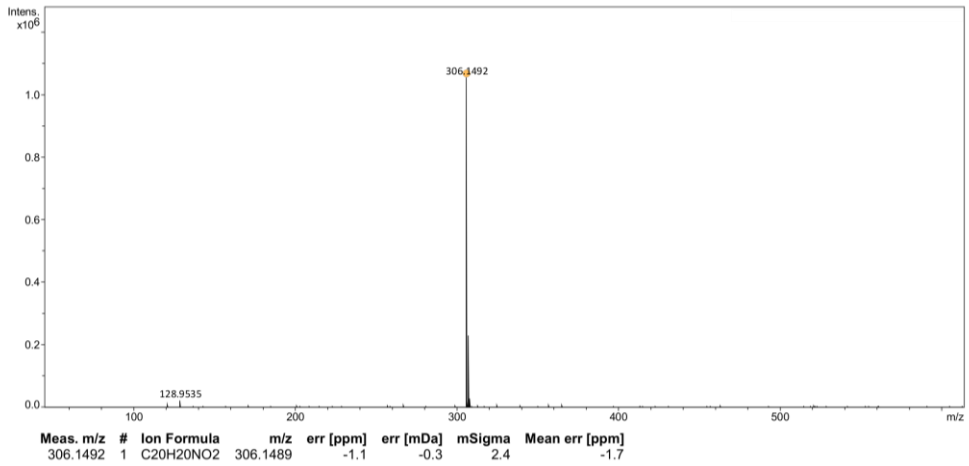

Figure 6.1.23: ESI-MS spectrum (positive channel) of 1-methyl-1-(2-methylanthraquinone)pyrrolidinium bis(trifluoromethanesulfonyl)imide **[43][Tf$_2$N]**.

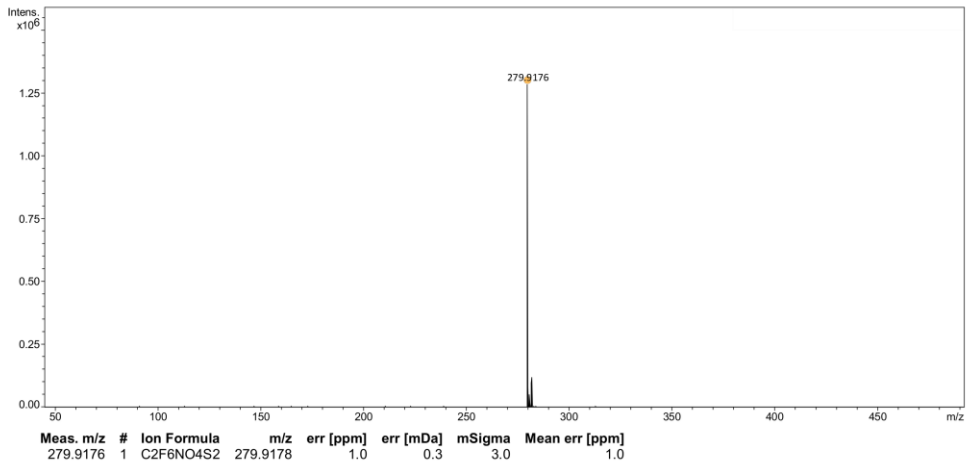

Figure 6.1.24: ESI-MS spectrum (negative channel) of 1-methyl-1-(2-methylanthraquinone)pyrrolidinium bis(trifluoromethanesulfonyl)imide **[43][Tf$_2$N]**.

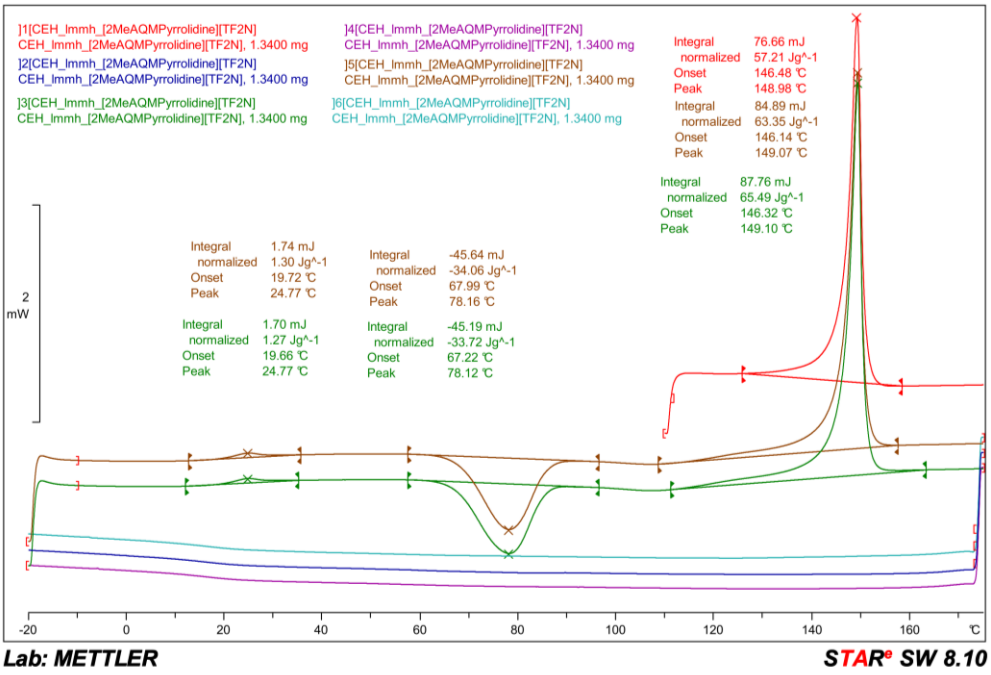

Figure 6.1.25: DSC experiment of 1-methyl-1-(2-methylanthraquinone)pyrrolidinium bis(trifluoromethanesulfonyl)imide **[43][Tf$_2$N]** from -20 °C to 175 °C. MP: 146 °C, ΔH_{fus} = 62.1 J/g.

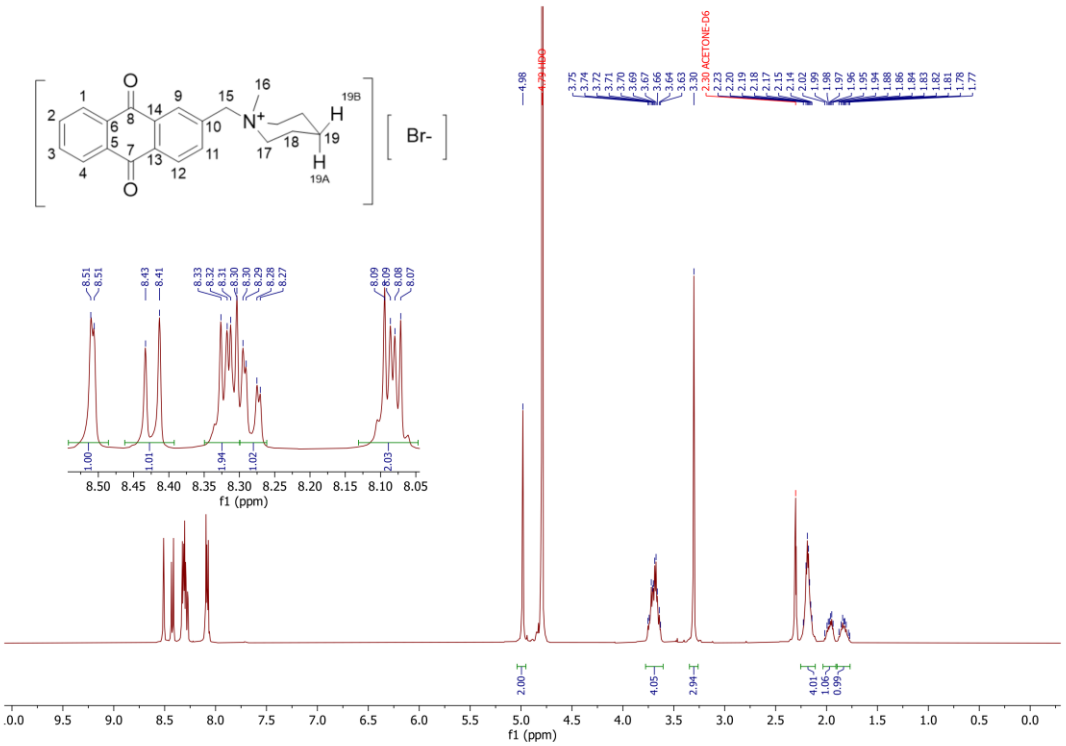

Figure 6.1.26: ^{1}H-NMR spectrum of 1-methyl-1-(2-methylanthraquinone)piperidinium bromide **[44]Br**.

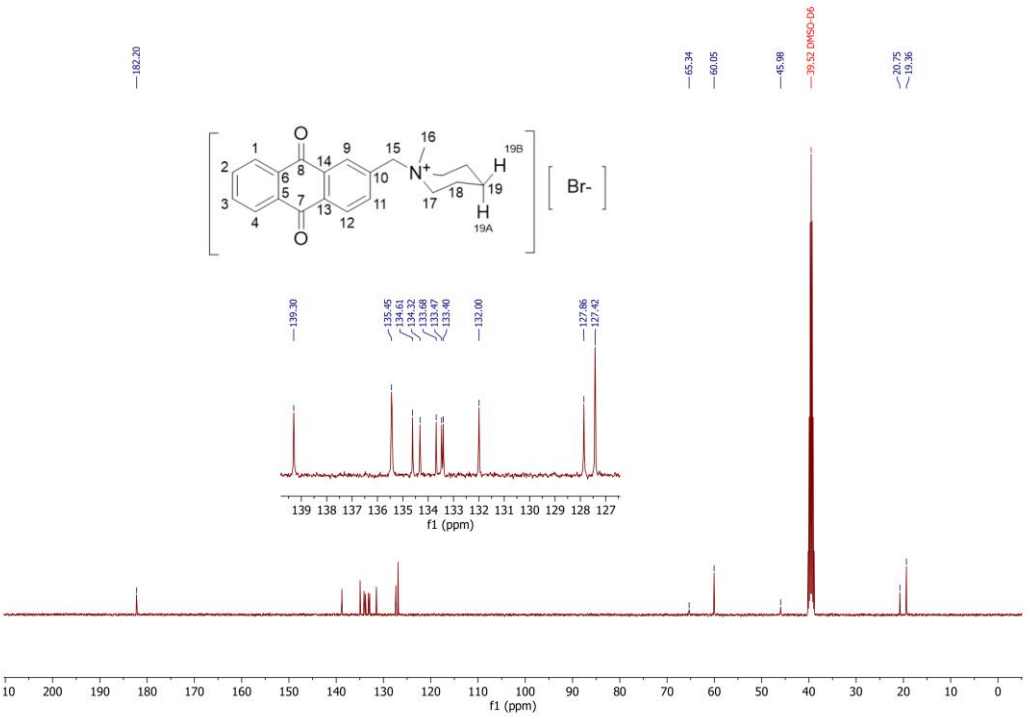

Figure 6.1.27: ^{13}C-NMR spectrum of 1-methyl-1-(2-methylanthraquinone)piperidinium bromide **[44]Br**.

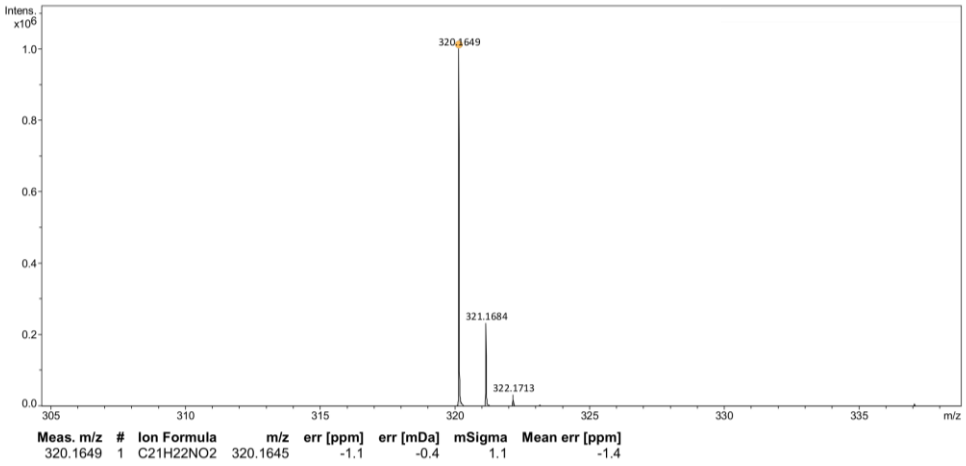

Figure 6.1.28: ESI-MS spectrum (positive channel) of 1-methyl-1-(2-methylanthraquinone)piperidinium bromide **[44]Br**.

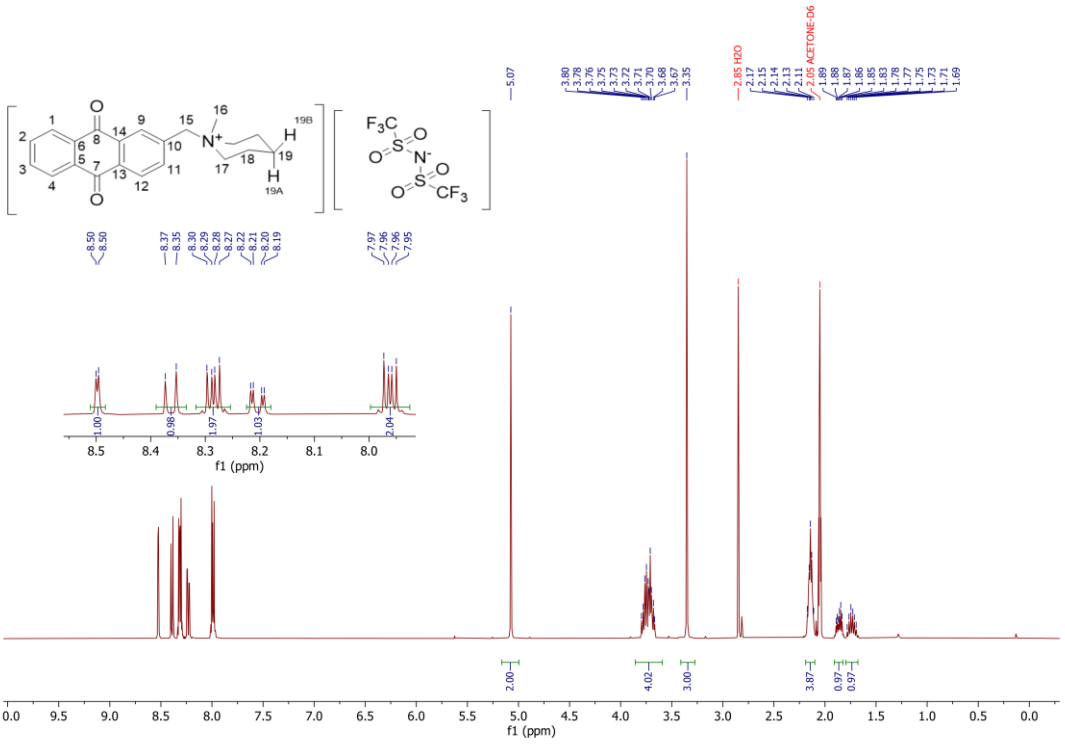

Figure 6.1.29: ^{1}H-NMR spectrum of 1-methyl-1-(2-methylanthraquinone)piperidinium bis(trifluoromethanesulfonyl)imide **[44][Tf$_2$N]**.

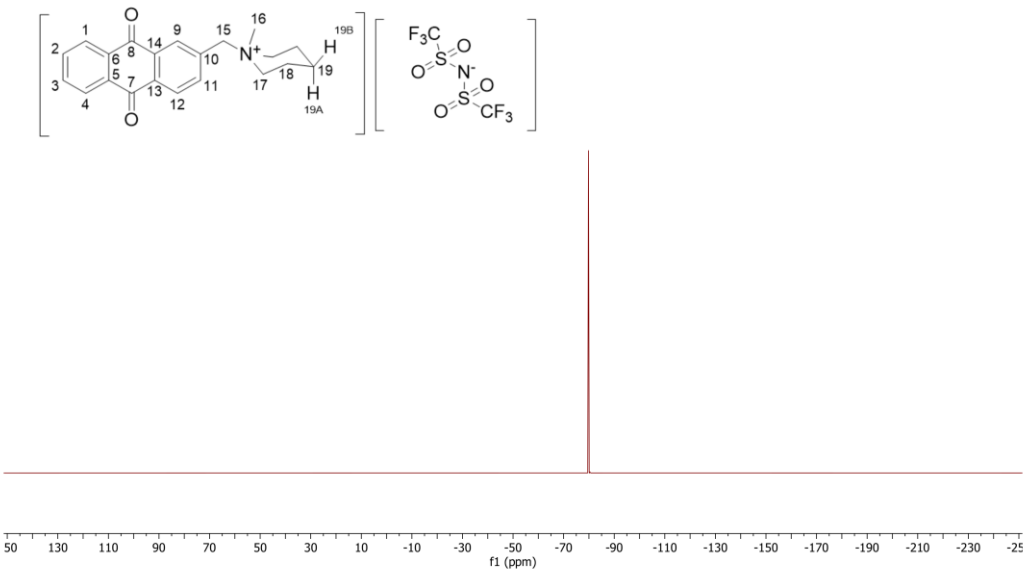

Figure 6.1.30: ^{19}F-NMR spectrum of 1-methyl-1-(2-methylanthraquinone)piperidinium bis(trifluoromethanesulfonyl)imide **[44][Tf$_2$N]**.

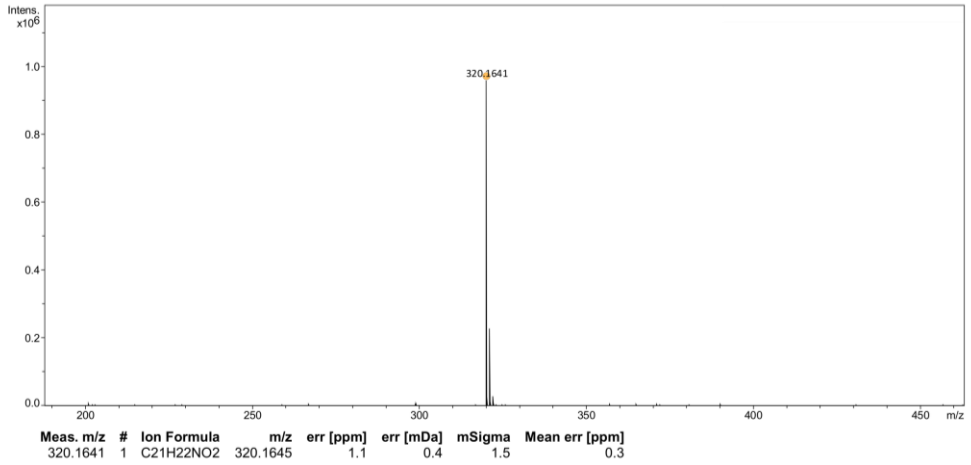

Figure 6.1.31: ESI-MS spectrum (positive channel) of 1-methyl-1-(2-methylanthraquinone)piperidinium bis(trifluoromethanesulfonyl)imide **[44][Tf$_2$N]**.

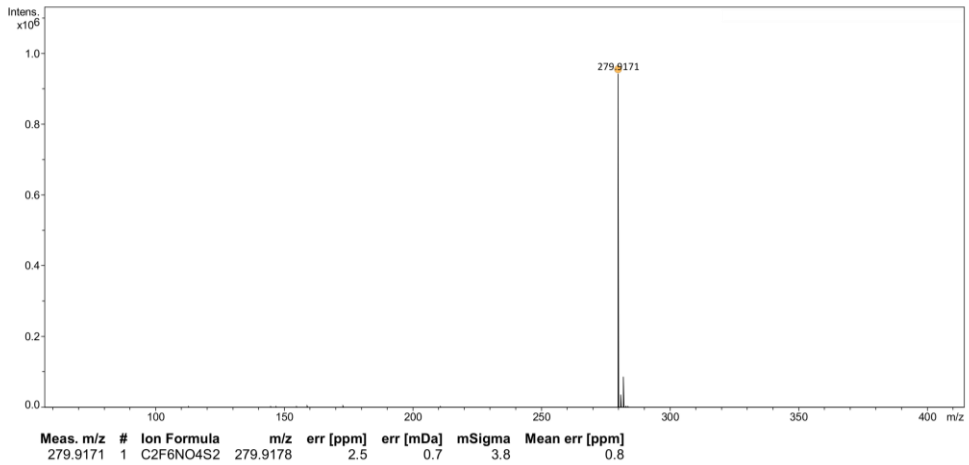

Figure 6.1.32: ESI-MS spectrum (negative channel) of 1-methyl-1-(2-methylanthraquinone)piperidinium bis(trifluoromethanesulfonyl)imide **[44][Tf$_2$N].**

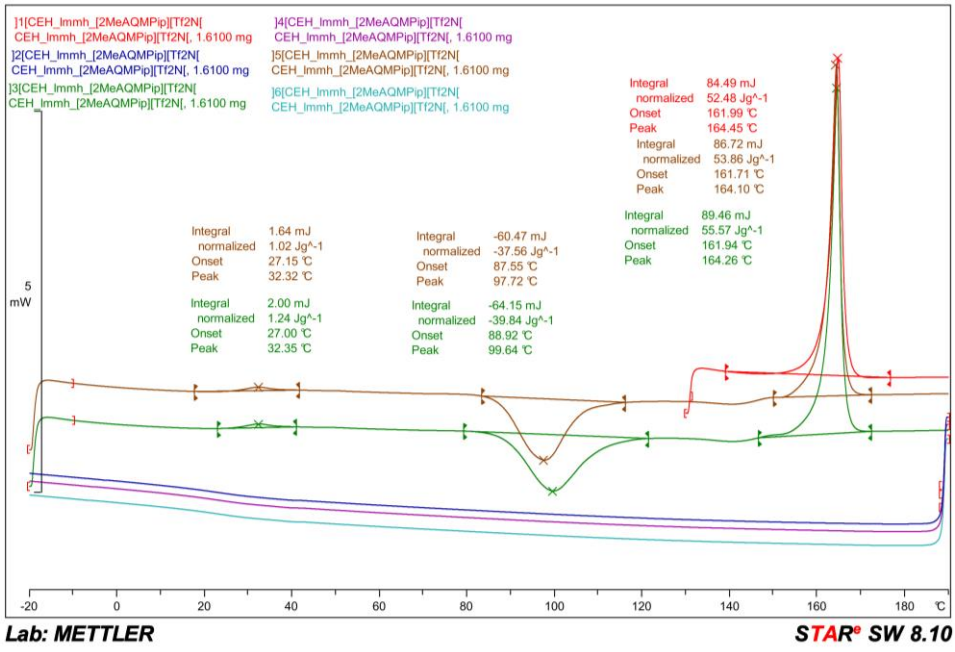

Figure 6.1.33: DSC experiment of 1-methyl-1-(2-methylanthraquinone)piperidinium bis(trifluoromethanesulfonyl)imide **[44][Tf$_2$N]** from -20 °C to 195 °C. MP: 162 °C, ΔH_{fus} = 54.0 J/g.

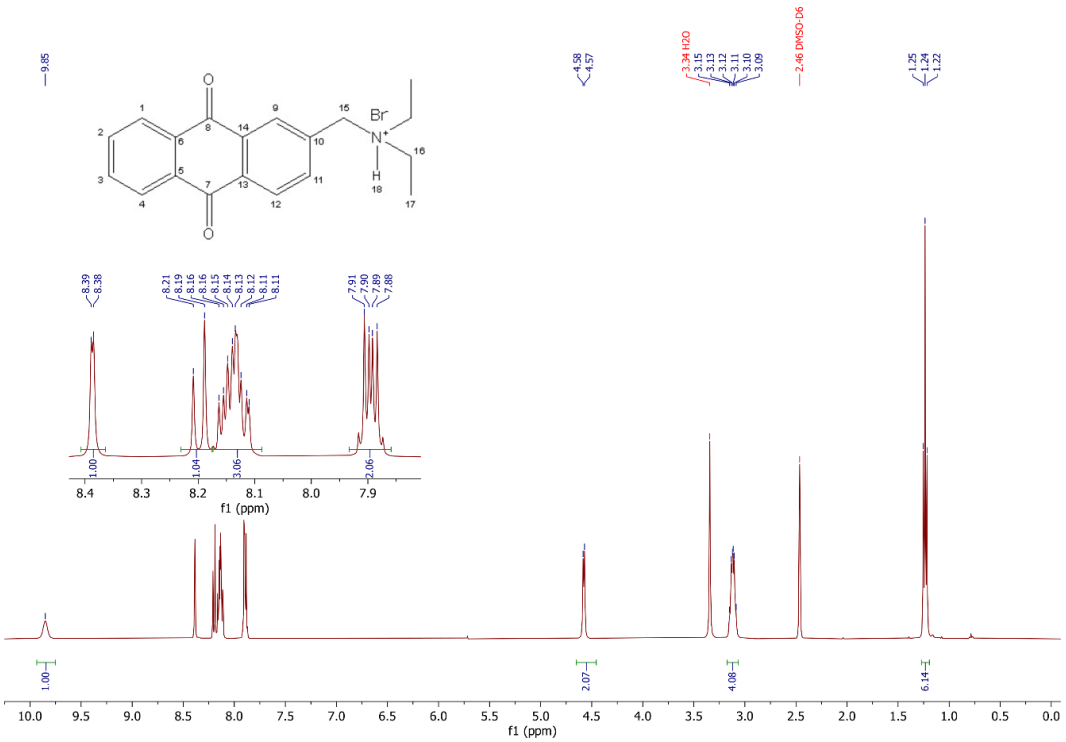

Figure 6.1.34: ^{1}H-NMR spectrum of N,N-diethyl(2-methylanthraquinone)ammonium bromide **[45]Br**.

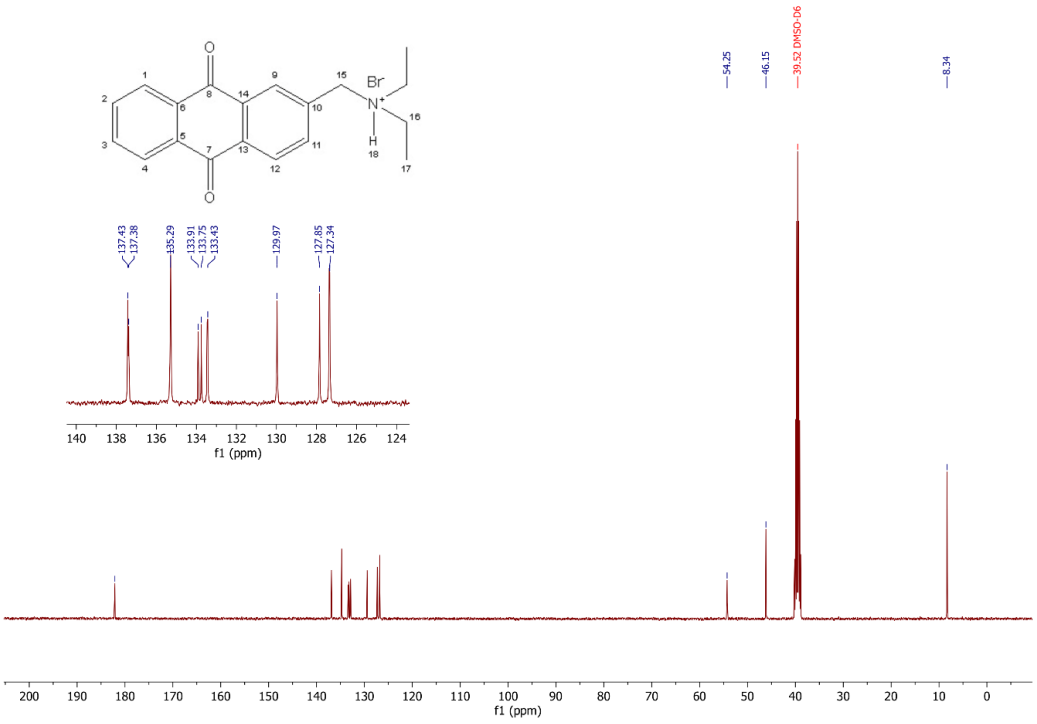

Figure 6.1.35: ^{13}C-NMR spectrum of N,N-diethyl(2-methylanthraquinone)ammonium bromide **[45]Br**.

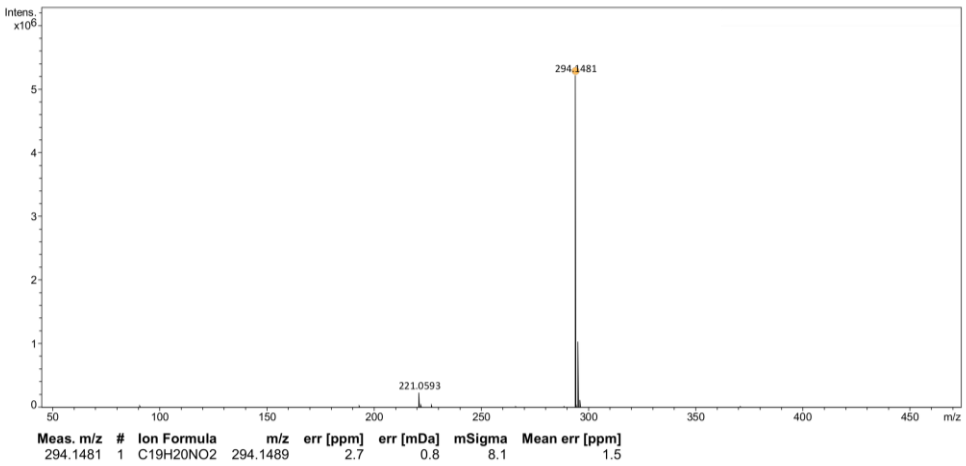

Figure 6.1.36: ESI-MS spectrum (positive channel) of N,N-diethyl(2-methylanthraquinone)ammonium bromide **[45]Br**.

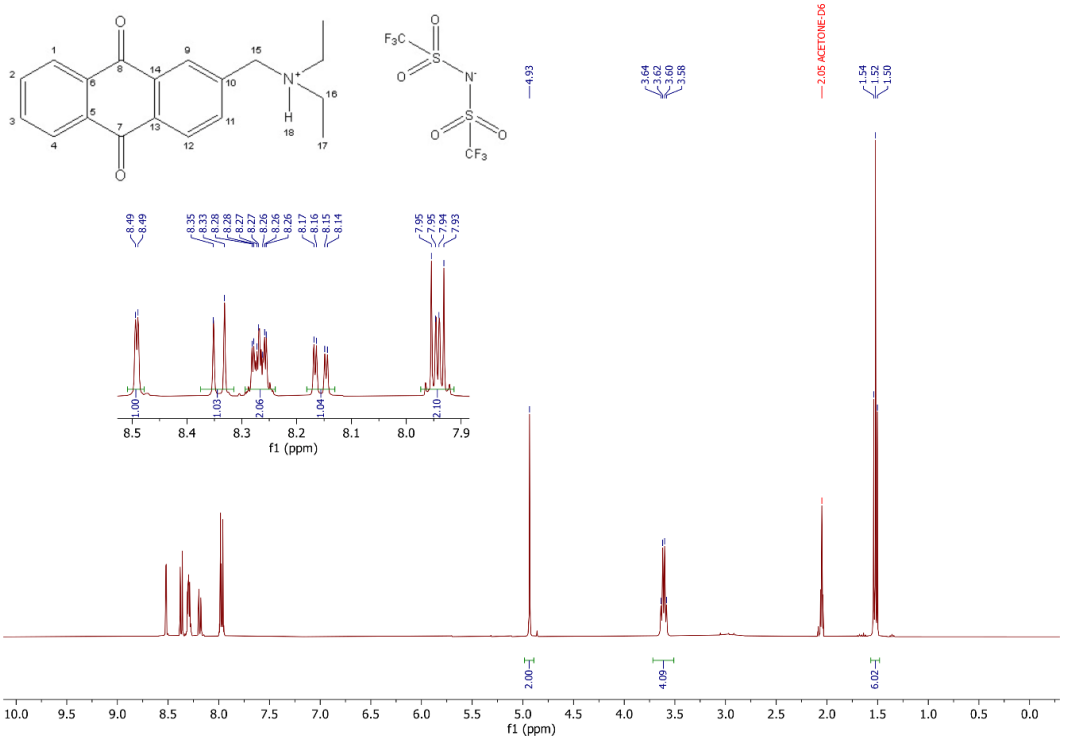

Figure 6.1.37: ^{1}H-NMR spectrum of N,N-diethyl(2-methylanthraquinone)ammonium bis(trifluoromethanesulfonyl)imide **[45][Tf$_2$N]**.

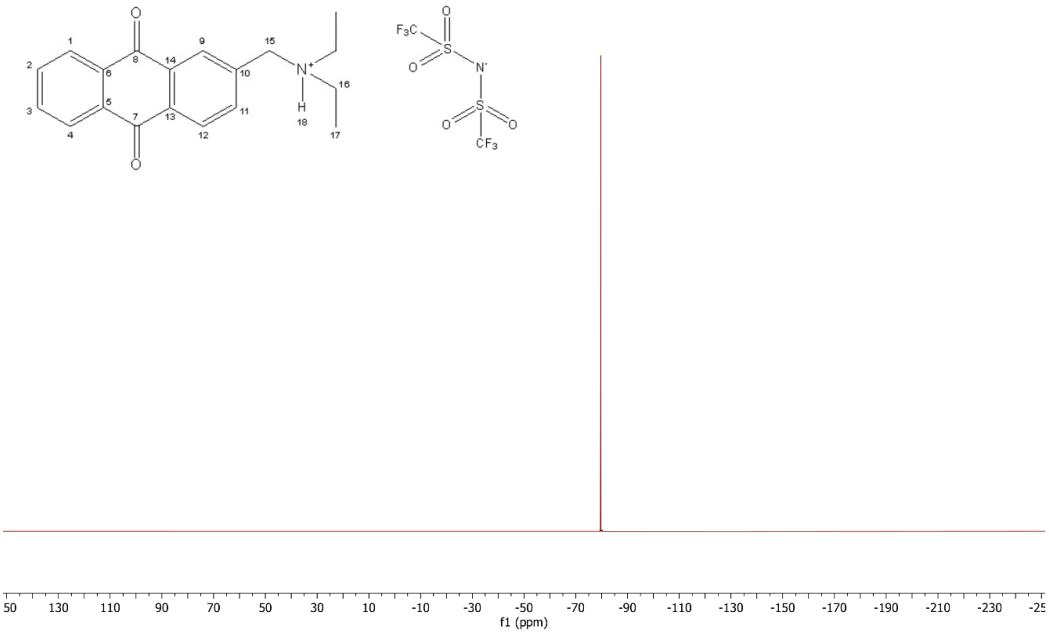

Figure 6.1.38: ^{19}F-NMR spectrum of N,N-diethyl(2-methylanthraquinone)ammonium bis(trifluoromethanesulfonyl)imide **[45][Tf$_2$N]**.

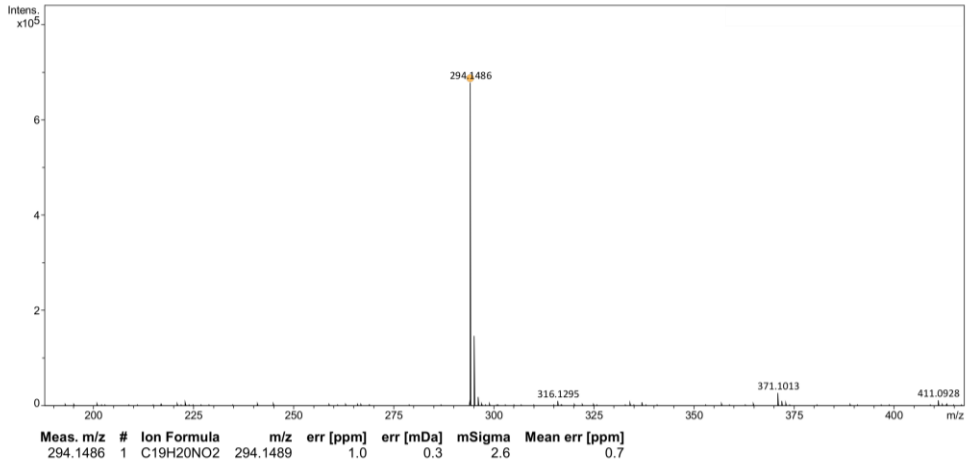

Figure 6.1.39: ESI-MS spectrum (positive channel) of N,N-diethyl(2-methylanthraquinone)ammonium bis(trifluoromethanesulfonyl)mide **[45][Tf$_2$N]**.

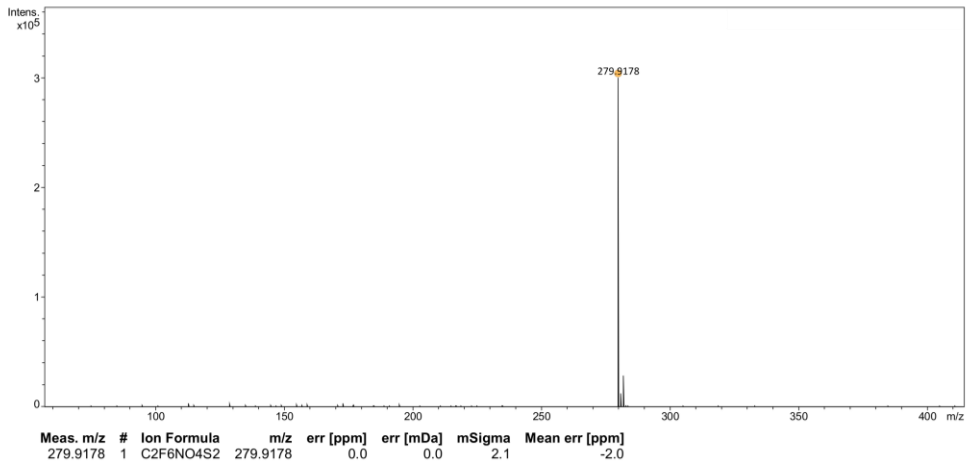

Figure 6.1.40: ESI-MS spectrum (negative channel) of N,N-diethyl(2-methylanthraquinone)ammonium bis(trifluoromethanesulfonyl)imide **[45][Tf$_2$N]**.

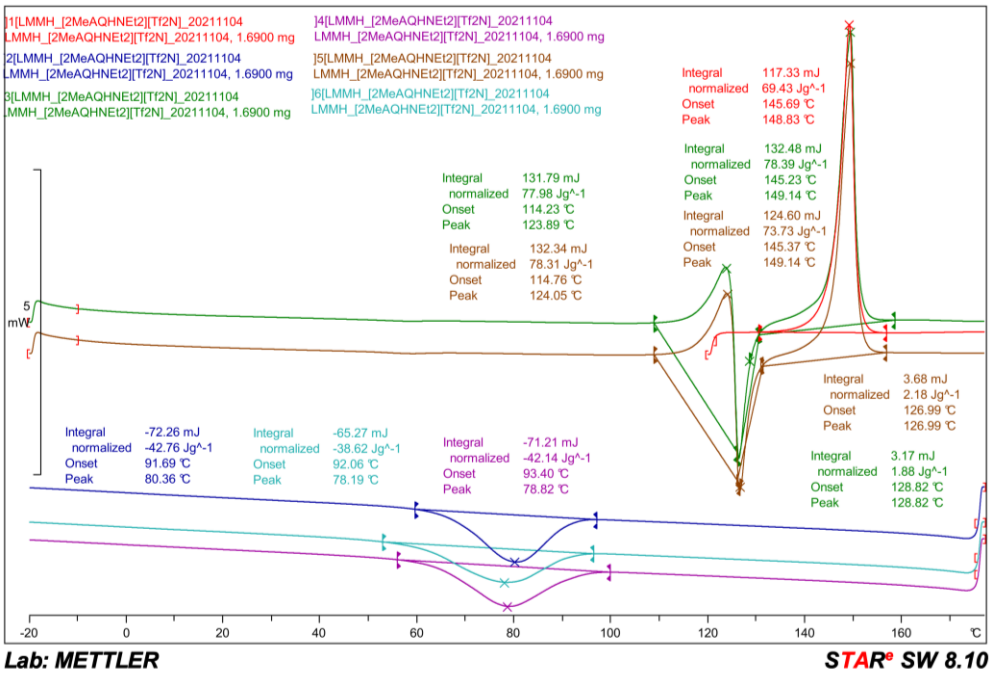

Figure 6.1.41: DSC experiment of N,N-diethyl(2-methylanthraquinone)ammonium bis(trifluoromethanesulfonyl)imide **[45][Tf$_2$N]** from -20 ºC to 175 ºC. MP: 145 ºC, ΔH_{fus} = 73.9 J/g

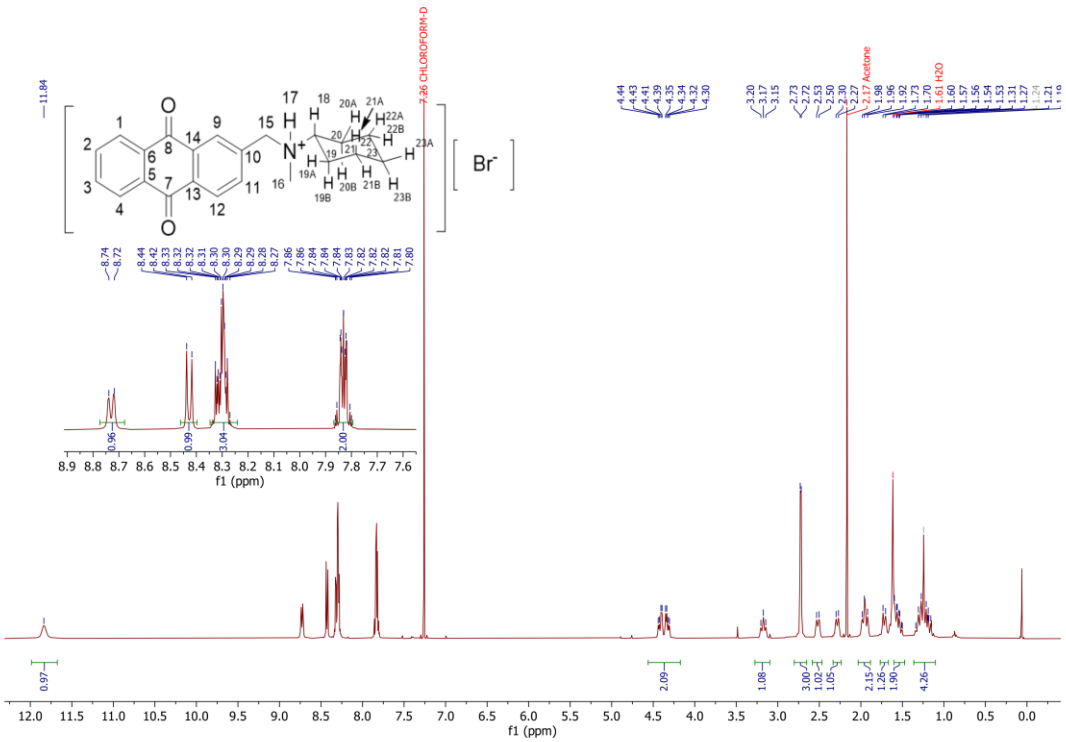

Figure 6.1.42: ^{1}H-NMR spectrum of N-cyclohexyl N-methyl(2-methylanthraquinone)ammonium bromide **[46]Br**.

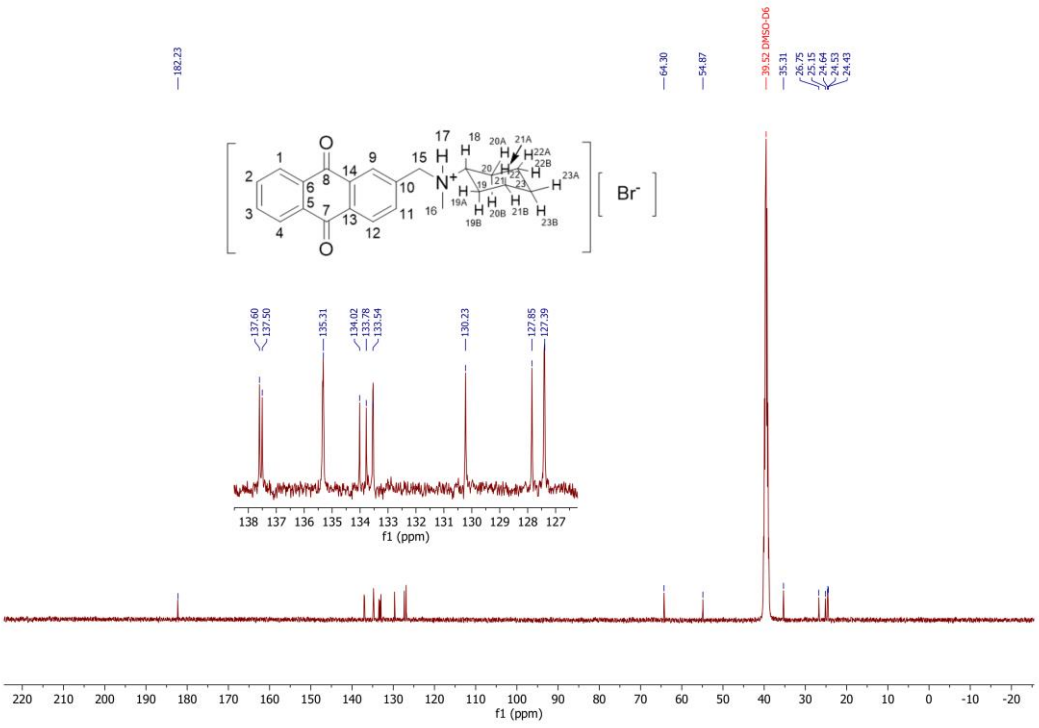

Figure 6.1.43: ^{13}C-NMR spectrum of N-cyclohexyl N-methyl(2-methylanthraquinone)ammonium bromide **[46]Br**.

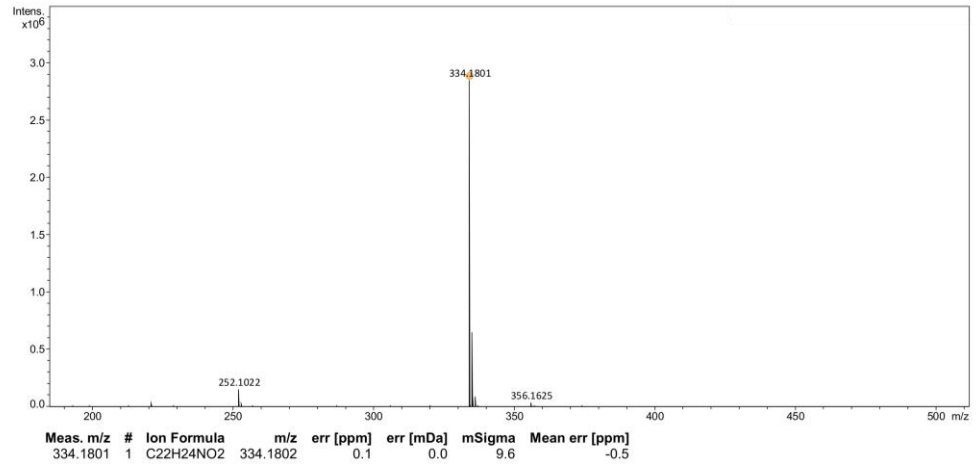

Figure 6.1.44: ESI-MS spectrum (positive channel) of N-cyclohexyl N-methyl(2-methylanthraquinone)ammonium bromide **[46]Br**.

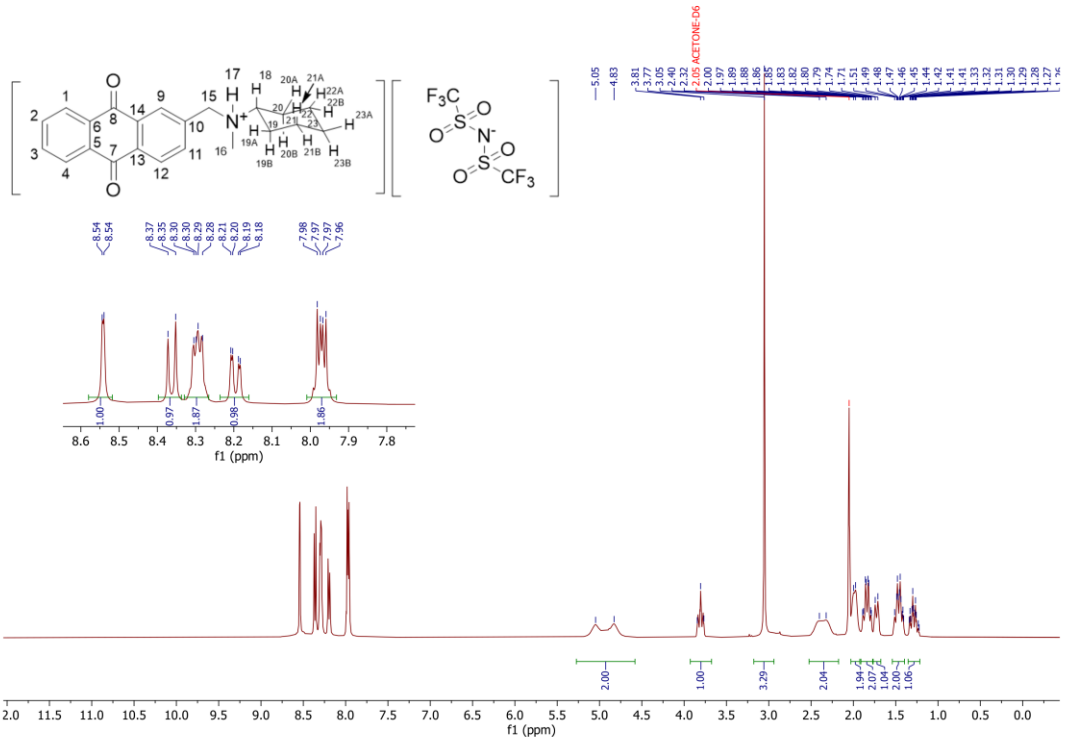

Figure 6.1.45: ^{1}H-NMR spectrum of N-cyclohexyl N-methyl(2-methylanthraquinone)ammonium bis(trifluoromethanesulfonyl)imide **[46][Tf$_2$N]**.

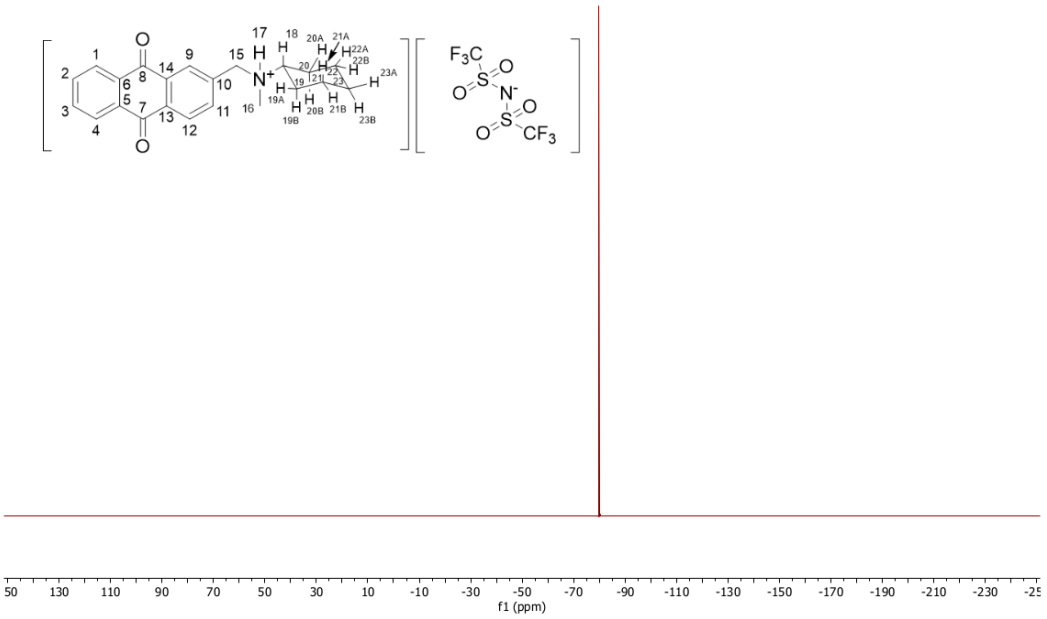

Figure 6.1.46: ^{19}F-NMR spectrum of N-cyclohexyl N-methyl(2-methylanthraquinone)ammonium bis(trifluoromethanesulfonyl)imide **[46][Tf$_2$N]**.

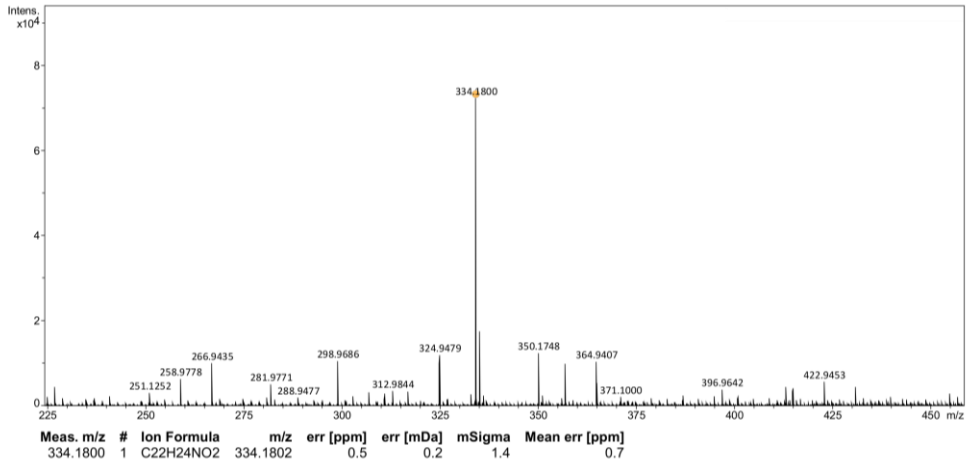

Figure 6.1.47: ESI-MS spectrum (positive channel) of N-cyclohexyl N-methyl(2-methylanthraquinone)ammonium bis(trifluoromethanesulfonyl)imide **[46][Tf$_2$N]**.

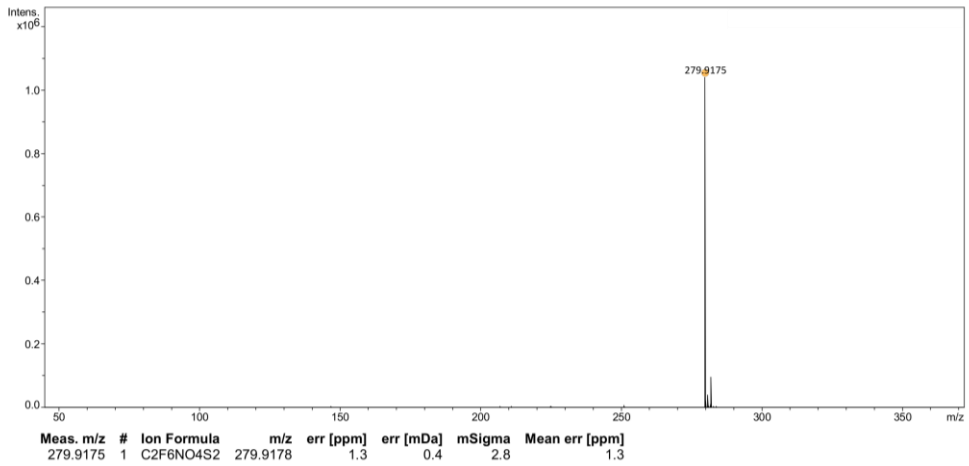

Figure 6.1.48: ESI-MS spectrum (negative channel) of N-cyclohexyl N-methyl(2-methylanthraquinone)ammonium bis(trifluoromethanesulfonyl)imide **[46][Tf$_2$N]**.

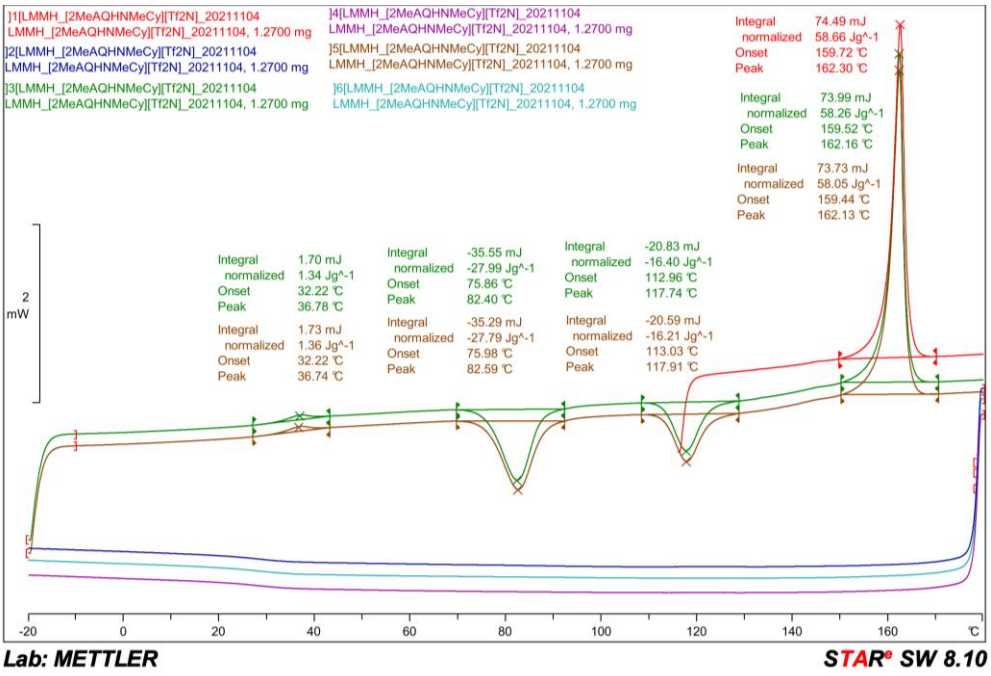

Figure 6.1.49: DSC experiment of N-cyclohexyl N-methyl (2-methylanthraquinone)ammonium bis(trifluoromethanesulfonyl)imide **[46][Tf$_2$N]** from -20 °C to 180 °C. MP: 159 °C, ΔH_{fus} = 58.3 J/g

Table 6.1.1: Crystallographic data and structure refinement for 1-Methyl-3-(2-methylanthraquinone)imidazolium bromide (**[41]Br**). Data collected, solved and refined by Dr Rachel Parker.

Empirical formula	$C_{20}H_{19}BrN_2O_3$
Formula weight	415.28
Temperature/K	110.05(10)
Crystal system	orthorhombic
Space group	$P2_12_12_1$
a/Å	6.74730(10)
b/Å	13.2098(3)
c/Å	20.3423(4)
α/°	90
β/°	90
γ/°	90
Volume/Å^3	1813.12(6)
Z	4
ρ_{calc}g/cm^3	1.521
μ/mm^{-1}	3.280
F(000)	848.0
Crystal size/mm^3	0.245 × 0.078 × 0.063
Radiation	CuKα (λ = 1.54184)
2Θ range for data collection/°	7.98 to 134.146
Index ranges	-7 ≤ h ≤ 8, -14 ≤ k ≤ 15, -22 ≤ l ≤ 24
Reflections collected	11700
Independent reflections	3229 [R_{int} = 0.0303, R_{sigma} = 0.0276]
Data/restraints/parameters	3229/0/249
Goodness-of-fit on F^2	1.114
Final R indexes [I>=2σ (I)]	R_1 = 0.0337, wR_2 = 0.0783
Final R indexes [all data]	R_1 = 0.0360, wR_2 = 0.0795
Largest diff. peak/hole / e Å^{-3}	0.69/-0.55
Flack parameter	-0.010(10)

Table 6.1.2: Crystallographic data and structure refinement for 1-Methyl-3-(2-methylanthraquinone)imidazolium bis(trifluoromethanesulfonyl)imide (**[41][Tf$_2$N]**). Data collected, solved and refined by Mr Theo Tanner.

Empirical formula	$C_{21}H_{15}F_6N_3O_6S_2$
Formula weight	583.48
Temperature/K	110.00(10)
Crystal system	triclinic
Space group	P-1
a/Å	7.4806(3)
b/Å	7.9349(3)
c/Å	20.8904(9)
α/°	81.197(3)
β/°	83.121(4)
γ/°	65.506(4)
Volume/Å^3	1112.93(9)
Z	2
ρ_{calc}g/cm^3	1.741
μ/mm^{-1}	3.085
F(000)	592.0
Crystal size/mm^3	0.298 × 0.148 × 0.051
Radiation	Cu Kα (λ = 1.54184)
2Θ range for data collection/°	8.584 to 142.1
Index ranges	-9 ≤ h ≤ 8, -9 ≤ k ≤ 6, -25 ≤ l ≤ 25
Reflections collected	7221
Independent reflections	4188 [R_{int} = 0.0182, R_{sigma} = 0.0260]
Data/restraints/parameters	4188/0/344
Goodness-of-fit on F^2	1.060
Final R indexes [I>=2σ (I)]	R_1 = 0.0346, wR_2 = 0.0920
Final R indexes [all data]	R_1 = 0.0383, wR_2 = 0.0953
Largest diff. peak/hole / e Å^{-3}	0.56/-0.40

Table 6.1.3: Crystallographic data and structure refinement for N,N,N-triethyl(2-methylanthraquinone)ammonium bis(trifluoromethanesulfonyl)imide (**[42][Tf_2N]**). Data collected, solved and refined by Mr Theo Tanner.

Empirical formula	$C_{23}H_{24}F_6N_2O_6S_2$
Formula weight	602.56
Temperature/K	110.1(2)
Crystal system	triclinic
Space group	P-1
a/Å	10.0909(5)
b/Å	10.7713(7)
c/Å	11.8875(7)
α/°	79.478(5)
β/°	85.290(5)
γ/°	88.533(5)
Volume/$Å^3$	1265.99(13)
Z	2
$\rho_{calc}g/cm^3$	1.581
μ/mm^{-1}	2.714
F(000)	620.0
Crystal size/mm^3	0.22 × 0.08 × 0.05
Radiation	CuKα (λ = 1.54184)
2Θ range for data collection/°	7.588 to 141.92
Index ranges	-12 ≤ h ≤ 10, -12 ≤ k ≤ 12, -13 ≤ l ≤ 14
Reflections collected	8446
Independent reflections	4774 [R_{int} = 0.0237, R_{sigma} = 0.0363]
Data/restraints/parameters	4774/0/355
Goodness-of-fit on F^2	1.040
Final R indexes [I>=2σ (I)]	R_1 = 0.0346, wR_2 = 0.0870

Final R indexes [all data]	R_1 = 0.0424, wR_2 = 0.0930
Largest diff. peak/hole / e Å^{-3}	0.35/-0.43

Table 6.1.4: Crystallographic data and structure refinement for 1-methyl-1-(2-methylanthraquinone)pyrrolidinium bis(trifluoromethanesulfonyl)imide (**[43][Tf$_2$N]**). Data collected, solved and refined by Dr Adrian Whitwood.

Empirical formula	$C_{22}H_{20}F_6N_2O_6S_2$
Formula weight	586.52
Temperature/K	110.00(10)
Crystal system	triclinic
Space group	P-1
a/Å	9.0015(3)
b/Å	15.4010(5)
c/Å	18.3074(7)
α/°	76.454(3)
β/°	78.737(3)
γ/°	78.327(3)
Volume/Å^3	2387.02(15)
Z	4
ρ_{calc}g/cm^3	1.632
μ/mm^{-1}	2.864
F(000)	1200.0
Crystal size/mm^3	0.195 × 0.104 × 0.032
Radiation	Cu Kα (λ = 1.54184)
2Θ range for data collection/°	6.992 to 134.15
Index ranges	-10 ≤ h ≤ 8, -18 ≤ k ≤ 18, -21 ≤ l ≤ 21
Reflections collected	16178
Independent reflections	8529 [R_{int} = 0.0243, R_{sigma} = 0.0330]
Data/restraints/parameters	8529/0/845

Goodness-of-fit on F^2	1.036
Final R indexes [I>=2σ (I)]	R_1 = 0.0354, wR_2 = 0.0894
Final R indexes [all data]	R_1 = 0.0433, wR_2 = 0.0953
Largest diff. peak/hole / e $Å^{-3}$	0.51/-0.44

Table 6.1.5: Crystallographic data and structure refinement for 1-methyl-1-(2-methylanthraquinone)piperidinium bis(trifluoromethanesulfonyl)imide (**[44][Tf_2N]**). Data collected, solved and refined by Dr Adrian Whitwood.

Empirical formula	$C_{23}H_{22}F_6N_2O_6S_2$
Formula weight	600.54
Temperature/K	110.00(10)
Crystal system	triclinic
Space group	P-1
a/Å	8.1191(3)
b/Å	8.6887(5)
c/Å	18.7539(10)
α/°	80.432(4)
β/°	80.562(3)
γ/°	73.952(4)
Volume/$Å^3$	1243.98(11)
Z	2
$\rho_{calc}g/cm^3$	1.603
μ/mm^{-1}	2.762
F(000)	616.0
Crystal size/mm^3	0.261 × 0.208 × 0.024
Radiation	Cu Kα (λ = 1.54184)
2Θ range for data collection/°	9.64 to 134.16
Index ranges	-6 ≤ h ≤ 9, -9 ≤ k ≤ 10, -22 ≤ l ≤ 22
Reflections collected	7788

Independent reflections	4429 [R_{int} = 0.0287, R_{sigma} = 0.0411]
Data/restraints/parameters	4429/0/440
Goodness-of-fit on F^2	1.062
Final R indexes [I>=2σ (I)]	R_1 = 0.0404, wR_2 = 0.1028
Final R indexes [all data]	R_1 = 0.0520, wR_2 = 0.1106
Largest diff. peak/hole / e $Å^{-3}$	0.47/-0.49

Table 6.1.6: Crystallographic data and structure refinement for N-cyclohexyl-N-methyl(2-methylanthraquinone)piperidinium bromide (**[46]Br**). Data collected, solved and refined by Dr Adrian Whitwood.

Empirical formula	$C_{22}H_{24}BrNO_2$
Formula weight	414.33
Temperature/K	109.95(10)
Crystal system	triclinic
Space group	P-1
a/Å	7.7783(6)
b/Å	9.1483(9)
c/Å	13.3981(10)
α/°	86.324(7)
β/°	81.755(6)
γ/°	86.755(7)
Volume/$Å^3$	940.51(14)
Z	2
$\rho_{calc}g/cm^3$	1.463
μ/mm^{-1}	3.099
F(000)	428.0
Crystal size/mm^3	0.255 × 0.033 × 0.018
Radiation	Cu Kα (λ = 1.54184)
2Θ range for data collection/°	9.7 to 134.154

Index ranges	$-9 \leq h \leq 7, -10 \leq k \leq 9, -13 \leq l \leq 15$
Reflections collected	5461
Independent reflections	3322 [R_{int} = 0.0635, R_{sigma} = 0.1099]
Data/restraints/parameters	3322/0/236
Goodness-of-fit on F^2	1.041
Final R indexes [I>=2σ (I)]	R_1 = 0.0763, wR_2 = 0.1933
Final R indexes [all data]	R_1 = 0.1001, wR_2 = 0.2166
Largest diff. peak/hole / e $Å^{-3}$	1.31/-1.28

Table 6.1.7: Crystallographic data and structure refinement for N-cyclohexyl-N-methyl(2-methylanthraquinone)piperidinium bis(trifluoromethanesulfonyl)imide (**[46][Tf_2N]**). Data collected, solved and refined by Dr Adrian Whitwood.

Empirical formula	$C_{24}H_{24}F_6N_2O_6S_2$
Formula weight	614.57
Temperature/K	110.00(10)
Crystal system	triclinic
Space group	P-1
a/Å	8.9673(3)
b/Å	9.0942(3)
c/Å	17.0002(6)
α/°	80.473(3)
β/°	81.320(3)
γ/°	73.657(3)
Volume/$Å^3$	1304.02(7)
Z	2
$\rho_{calc}g/cm^3$	1.565
μ/mm^{-1}	2.649
F(000)	632.0

Crystal size/mm^3	0.242 × 0.1 × 0.075
Radiation	Cu Kα (λ = 1.54184)
2Θ range for data collection/°	10.222 to 134.146
Index ranges	-10 ≤ h ≤ 10, -9 ≤ k ≤ 10, -19 ≤ l ≤ 20
Reflections collected	8820
Independent reflections	4657 [R_{int} = 0.0199, R_{sigma} = 0.0293]
Data/restraints/parameters	4657/0/457
Goodness-of-fit on F^2	1.031
Final R indexes [I>=2σ (I)]	R_1 = 0.0312, wR_2 = 0.0768
Final R indexes [all data]	R_1 = 0.0380, wR_2 = 0.0809
Largest diff. peak/hole / e Å^{-3}	0.39/-0.37

6.2 Data from the electronic structure calculations

Fragment: 2-methylanthraquinone (**38a**)
Imaginary Frequency: None
DFT(PBE0)/def2-TZVPP SCF energies corrected by SMD model in acetonitrile (Hartree/particle):

- Fully oxidized species: -727.494466482
- First reduction species: -727.613775347
- Second reduction species: -727.690127328

Optimised geometry Cartesian coordinates of the fully oxidised species:

0 1

C	-4.14004816	0.37715698	0.00558526
C	-3.00868608	1.20477202	0.00393386
C	-1.71682739	0.64177416	0.00056897
C	-1.56553230	-0.76933813	-0.00133774
C	-2.70899409	-1.59355234	0.00011034
C	-3.98995237	-1.02465521	0.00367461

C	-0.52855903	1.55518526	-0.00030785
C	-0.21137948	-1.41004048	-0.00426126
C	0.97518858	-0.49612840	-0.00303856
C	0.82109347	0.91348386	-0.00173169
C	1.97125478	1.72879712	-0.00427510
H	1.83203658	2.82140686	-0.00633804
C	3.24671257	1.15430057	-0.00743800
C	3.41870740	-0.25261181	-0.00574307
C	2.26574709	-1.05952580	-0.00550350
H	-5.14841539	0.82333335	0.00814292
H	-3.09430446	2.30287925	0.00557735
H	-2.56017522	-2.68496424	-0.00142566
H	-4.88080111	-1.67438830	0.00499304
H	4.13666226	1.80723194	-0.01315786
H	2.34246567	-2.15913313	-0.00904781
O	-0.08087045	-2.63575146	-0.00684607
O	-0.66126779	2.78089572	0.00057661
C	4.80215881	-0.86030663	0.01542482
H	4.77962070	-1.93871097	-0.24714407
H	5.48511168	-0.34274335	-0.69357394
H	5.25960225	-0.77193246	1.02816306

Fragment: 1-Methyl-3-(2-methylanthraquinone)imidazolium **41**$^{+}$ Imaginary Frequency: None
DFT(PBE0)/def2-TZVPP SCF energies corrected by SMD model in acetonitrile (Hartree/particle):

- Fully oxidized species: -992.068564869
- First reduction species: -992.194106231
- Second reduction species: -992. 276901791

Optimised geometry Cartesian coordinates of the fully oxidised species:

1 1

C	-5.71543598	-0.43227452	0.76663544
C	-4.75360086	0.58216631	0.87440874
C	-3.44864440	0.37764069	0.38186069
C	-3.11160328	-0.86615722	-0.22260562
C	-4.08637362	-1.88006829	-0.32314503
C	-5.38184730	-1.66392506	0.16725854
C	-2.45191243	1.47977328	0.51160456
C	-1.74423030	-1.12812761	-0.75305522
C	-0.74483738	-0.00622030	-0.65172015
C	-1.07652780	1.22973651	-0.05094944
C	-0.11136141	2.25513273	0.02038387
H	-0.40213073	3.21066219	0.48508189
C	1.17137379	2.05265336	-0.50126485
C	1.51124950	0.81621819	-1.10430102
C	0.54683397	-0.20455867	-1.17596259
H	-6.73485578	-0.26528881	1.15085030
H	-4.99005557	1.55253246	1.33840200
H	-3.80179949	-2.83352691	-0.79495861
H	-6.14082654	-2.45862008	0.08318802
H	1.91431964	2.86738970	-0.45551986
H	0.75801577	-1.17818641	-1.65059646
O	-1.41834295	-2.20511282	-1.25323857
O	-2.71684691	2.55352254	1.04913344
C	2.89823202	0.59208014	-1.66212158
H	2.88434301	-0.15561631	-2.48306338
H	3.33355683	1.53282169	-2.05802859
C	3.54975339	-0.42420053	0.56871420
C	5.24082530	0.03916235	-0.79151136
H	2.53425271	-0.51632061	0.97124013
C	5.75858826	-0.51924403	0.35522409
H	5.73865257	0.40144382	-1.69850957
H	6.79456857	-0.73307062	0.64318411
N	3.86363185	0.08967331	-0.63618854

N	4.68677712	-0.80077666	1.18982679
C	4.77583354	-1.39779034	2.52881642
H	5.35225343	-0.72842703	3.19976891
H	3.75435201	-1.53188995	2.93350795
H	5.27611956	-2.38543936	2.46320832

Fragment: N,N-diethyl(2-methylanthraquinone)ammonium **[42]**$^{+}$
Imaginary Frequency: None
DFT(PBE0)/def2-TZVPP SCF energies corrected by SMD model in acetonitrile (Hartree/particle):

- Fully oxidized species: -1018.85810531
- First reduction species: -1018.98351280
- Second reduction species: -1019.06634362

Optimised geometry Cartesian coordinates of the fully oxidised species:

1 1

C	6.12049079	0.26174497	0.42600925
C	5.18941384	-0.77032960	0.24189837
C	3.82590019	-0.46961983	0.04826267
C	3.39906048	0.88853234	0.04168691
C	4.34430729	1.91811472	0.22950501
C	5.69777865	1.60666930	0.41987757
C	2.86405362	-1.59385059	-0.14452574
C	1.96908513	1.25269584	-0.15784450
C	0.99864433	0.12101712	-0.36864171
C	1.41847629	-1.22814175	-0.35918989
C	0.47367299	-2.25224325	-0.56997805
H	0.82923031	-3.29482754	-0.57563763
C	-0.87366301	-1.93579677	-0.77753423
C	-1.31046112	-0.58619142	-0.77612049
C	-0.35581776	0.43138391	-0.58709175
H	7.18532310	0.02019916	0.57546793

H	5.49530433	-1.82825048	0.24291245
H	3.99015714	2.96067333	0.22041944
H	6.43256529	2.41530169	0.56438923
H	-1.59576853	-2.74906200	-0.96439181
H	-0.61789678	1.50227716	-0.62001213
O	1.56899269	2.41779708	-0.15014191
O	3.21126065	-2.77327519	-0.13475079
C	-2.75722969	-0.24772208	-1.05490181
H	-2.83329194	0.67286395	-1.66265438
H	-3.25095749	-1.06979069	-1.61204860
N	-3.65870859	-0.00776638	0.18376245
C	-3.18607892	1.20778538	0.98856543
H	-3.77769233	1.18992201	1.92456840
H	-2.13283788	0.98417418	1.25464887
C	-3.29824484	2.58034620	0.33562424
H	-2.81165896	3.30587180	1.02284573
H	-2.76797798	2.66013177	-0.63622889
H	-4.34793282	2.91415827	0.20608135
C	-5.12606114	0.13499872	-0.26968108
H	-5.64905736	0.62879390	0.57410134
H	-5.51487870	-0.90206341	-0.33886176
C	-5.40750535	0.86044307	-1.58459520
H	-6.51322190	0.91892576	-1.68549887
H	-5.02260069	1.89808360	-1.61991953
H	-5.03542194	0.30825064	-2.47144544
C	-3.55227586	-1.24431802	1.09490797
H	-3.73356888	-2.11340308	0.42855625
H	-2.49245598	-1.28655741	1.41632756
C	-4.48639646	-1.29919704	2.30022972
H	-4.27989954	-2.25705840	2.82481738
H	-4.30775199	-0.49042079	3.03906105
H	-5.56167136	-1.30793122	2.02653035

Fragment: 1-methyl-1-(2-methylanthraquinone)pyrrolidinium **43**$^{+}$
Imaginary Frequency: None
DFT(PBE0)/def2-TZVPP SCF energies corrected by SMD model in acetonitrile (Hartree/particle):

- Fully oxidized species: -978.400318946
- First reduction species: -978.525910864
- Second reduction species: -978.608997029

Optimised geometry Cartesian coordinates of the fully oxidised species:

1 1

C	-5.95625856	-0.03972574	0.61785505
C	-4.94866875	0.92454628	0.47297719
C	-3.62721554	0.53115091	0.17942837
C	-3.32074432	-0.85157045	0.03277357
C	-4.34198855	-1.81234282	0.18250936
C	-5.65283896	-1.40874757	0.47237533
C	-2.58189908	1.58451230	0.03068339
C	-1.93896576	-1.31357575	-0.27475492
C	-0.88461063	-0.25119028	-0.44299038
C	-1.18556976	1.12206288	-0.29819031
C	-0.16938002	2.08204774	-0.47740986
H	-0.43634854	3.14602882	-0.37711334
C	1.13356503	1.67846509	-0.79012239
C	1.45035842	0.30232117	-0.92219809
C	0.42669335	-0.64987107	-0.75906003
H	-6.98783532	0.27434475	0.84549744
H	-5.16120956	1.99957487	0.58201941
H	-4.08070076	-2.87558999	0.06465690
H	-6.44765742	-2.16375954	0.58598293
H	1.90969751	2.44470906	-0.95755208
H	0.60402083	-1.73148743	-0.88598893
O	-1.64165955	-2.50314611	-0.38834281

O	-2.82222487	2.78285971	0.16421958
C	2.84975052	-0.13626886	-1.27934702
H	2.84127249	-1.09633252	-1.83557305
H	3.36444853	0.62289702	-1.90388531
C	3.22756587	-1.43499127	0.83091631
H	2.25533490	-1.08943556	1.23122574
H	3.08344869	-2.36725902	0.24999491
H	3.93546269	-1.61902304	1.66125316
C	5.18185352	-0.78297873	-0.56149459
C	4.08384903	0.90055064	0.70798934
H	5.39340093	-0.15931402	-1.45388479
H	5.15663382	-1.84615888	-0.87306842
C	5.40079576	0.62352373	1.45105194
H	4.20134214	1.70550633	-0.04565059
H	3.21440917	1.14209186	1.34978548
C	6.13366576	-0.46152029	0.60398767
H	5.98752220	1.56002462	1.53916780
H	5.21482777	0.27109377	2.48629436
H	6.35386552	-1.36495823	1.20848817
H	7.10515068	-0.10308689	0.20806286
N	3.78917793	-0.37513746	-0.07837234

Fragment: 1-methyl-1-(2-methylanthraquinone)piperidinium **44**$^{+}$
Imaginary Frequency: None
DFT(PBE0)/def2-TZVPP SCF energies corrected by SMD model in acetonitrile (Hartree/particle):

- Fully oxidized species: -1017.67549724
- First reduction species: -1017.80118978
- Second reduction species: -1017.88441934

Optimised geometry Cartesian coordinates of the fully oxidised species:

1 1

C	-6.23605489	-0.05937890	0.68492070
C	-5.24190875	0.91041835	0.49265615
C	-3.92107515	0.52191399	0.18982821
C	-3.60157742	-0.86141816	0.08241758
C	-4.60946650	-1.82770613	0.27969074
C	-5.91989027	-1.42908267	0.57820833
C	-2.89015718	1.58114657	-0.01041856
C	-2.21995893	-1.31819790	-0.23399272
C	-1.18083240	-0.25053256	-0.45461100
C	-1.49471522	1.12334673	-0.34867219
C	-0.49279334	2.08756253	-0.57767970
H	-0.76938944	3.15147081	-0.50686543
C	0.80876877	1.68771251	-0.90091685
C	1.13981751	0.31137448	-0.99413183
C	0.12879180	-0.64530884	-0.78200868
H	-7.26728715	0.25082641	0.91945633
H	-5.46459167	1.98602204	0.57083040
H	-4.33817124	-2.89126183	0.19121361
H	-6.70417017	-2.18848957	0.72908271
H	1.57381141	2.45574419	-1.10678716
H	0.31393653	-1.72843368	-0.87985742
O	-1.91165150	-2.50775706	-0.31496721
O	-3.14205984	2.78049250	0.08879520
C	2.53302473	-0.12273585	-1.37773833
H	2.51328342	-1.07799043	-1.94190374
H	3.03260711	0.64185478	-2.00717704
C	2.96646520	-1.45704894	0.69040160
H	2.00296132	-1.11588233	1.11497092
H	2.80700084	-2.37296874	0.08766591
H	3.68096972	-1.67016559	1.50523466
C	4.85033848	-0.82033826	-0.81459479
C	3.73275634	0.91661813	0.58595729
C	5.98639071	-0.93604458	0.20310047

H	5.09300747	-0.05349784	-1.58053286
H	4.65504980	-1.77946734	-1.33765345
C	4.85214322	0.81929381	1.62452692
H	3.97992254	1.68711821	-0.17509079
H	2.75575722	1.17999822	1.03900162
C	6.17842326	0.36892260	0.99208064
H	6.90410815	-1.19167100	-0.37041718
H	5.81532453	-1.79419536	0.89043355
H	4.95292654	1.82837510	2.08064118
H	4.55938799	0.14347154	2.45880105
H	6.95403502	0.23453676	1.77534118
H	6.55477089	1.16544147	0.30920127
N	3.51621427	-0.37797441	-0.20147960

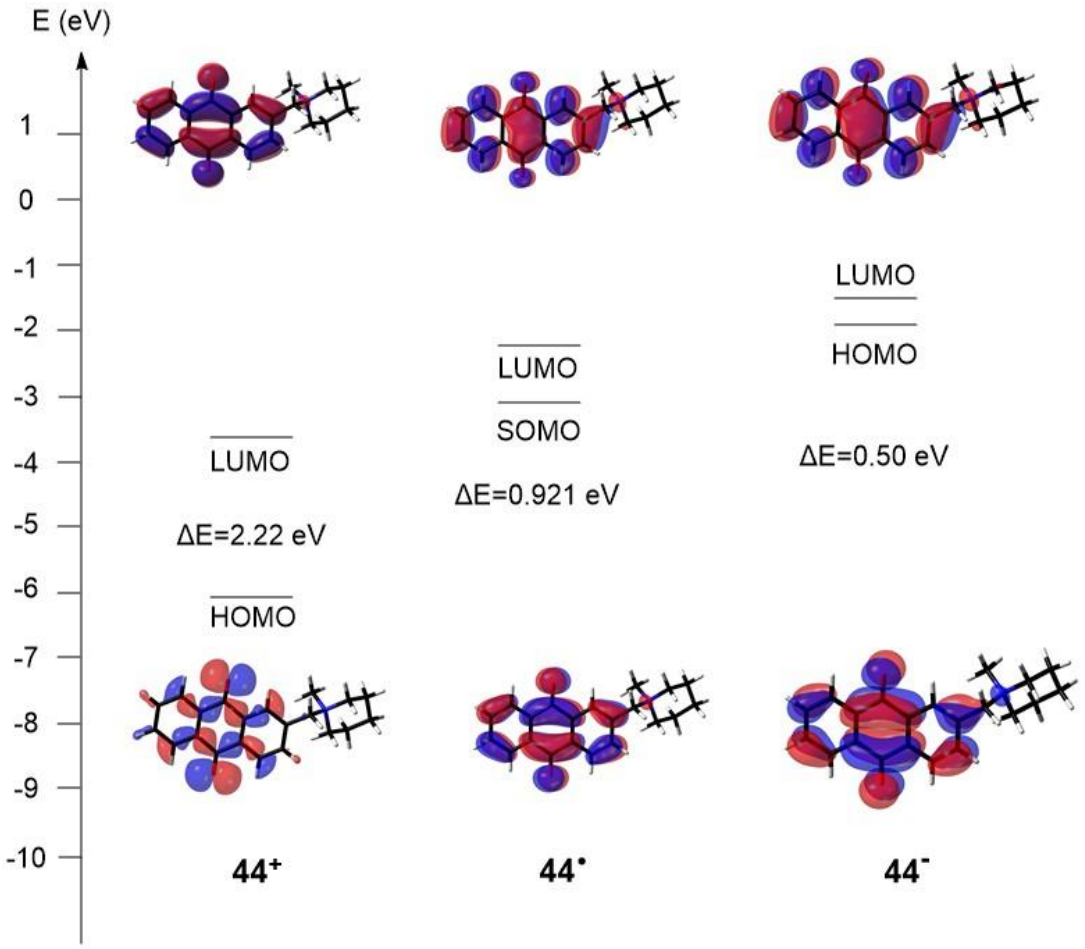

Figure 6.2.1: Calculated HOMO, SOMO and LUMO energy levels of the AQ-methylpiperidinium motif **44**$^{+}$ different oxidation states at the PBE0/def2-TZVPP level of theory in acetonitrile.

Fragment: of N,N-diethyl(2-methylanthraquinone)ammonium **45**$^{+}$
Imaginary Frequency: None
DFT(PBE0)/def2-TZVPP SCF energies corrected by SMD model in acetonitrile (Hartree/particle):

- Fully oxidized species: -940.337209257
- First reduction species: -940.462988571
- Second reduction species: -940.546218802

Optimised geometry Cartesian coordinates of the fully oxidised species:

1 1

C	-5.74285752	-0.22012681	0.53871193

C	-4.77671268	0.79585673	0.51976343
C	-3.43522867	0.49326490	0.20970674
C	-3.06635690	-0.85051435	-0.08260016
C	-4.04662458	-1.86396383	-0.05962253
C	-5.37782856	-1.55060130	0.24866691
C	-2.43522935	1.59946872	0.19894036
C	-1.66149549	-1.21702901	-0.41164760
C	-0.65141832	-0.09954030	-0.43838984
C	-1.01405773	1.23490334	-0.14796281
C	-0.03768570	2.25115040	-0.19048238
H	-0.35331889	3.28431803	0.02485293
C	1.28653739	1.93976694	-0.51755135
C	1.66207417	0.60092387	-0.79828494
C	0.68295722	-0.40781505	-0.76234056
H	-6.79030583	0.02294937	0.78058397
H	-5.03786087	1.84221856	0.74252163
H	-3.73757739	-2.89566083	-0.28961602
H	-6.14013855	-2.34632830	0.26359993
H	2.03309891	2.75203044	-0.57992834
H	0.91405472	-1.46132612	-0.99521874
O	-1.30990790	-2.37262898	-0.65112698
O	-2.72947133	2.76473353	0.45768241
C	3.09639000	0.27560865	-1.13115262
H	3.20114864	-0.69199164	-1.65951862
H	3.55642986	1.06653814	-1.75889249
N	3.98521902	0.18860670	0.12465575
C	3.59897320	-0.95808017	1.06104720
H	4.12203172	-0.75567085	2.01752334
H	2.51116968	-0.83277046	1.23928976
C	3.92037306	-2.35001603	0.53462846
H	3.55899308	-3.08495752	1.28538262
H	3.40074219	-2.58660355	-0.41782248
H	5.00888344	-2.52682591	0.40581547

C	5.46316205	0.23021146	-0.24252495
H	5.58105771	1.12467386	-0.88915413
H	3.78607899	1.05513182	0.66281502
H	5.65637191	-0.66296129	-0.87081639
C	6.39504832	0.30385754	0.96044997
H	6.40058637	-0.62641217	1.56564885
H	7.43032656	0.45740766	0.58832984
H	6.15660872	1.16520332	1.62343860

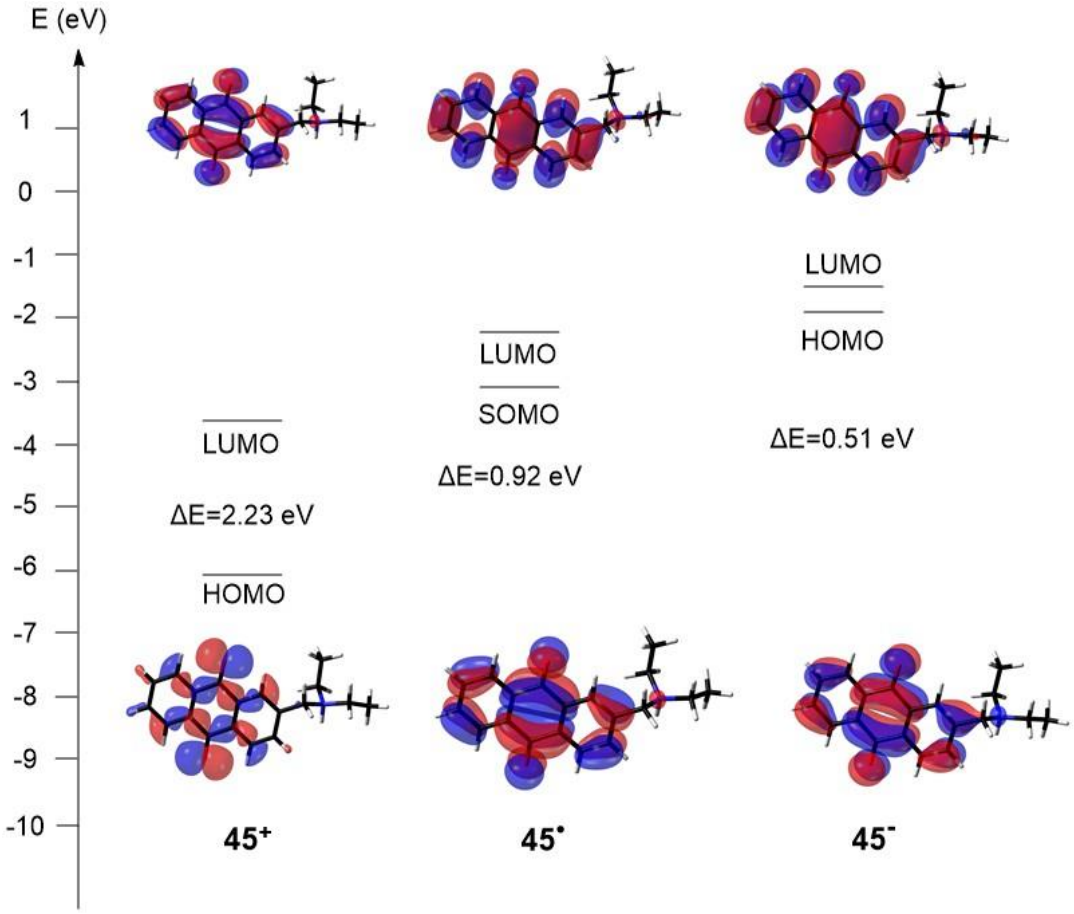

Figure 6.2.2: Calculated HOMO, SOMO and LUMO energy levels of AQ-diethylammonium motif **45**$^{+}$ different oxidation states at the PBE0/def2-TZVPP level of theory in acetonitrile.

Fragment: of N-cyclohexyl-N-methyl(2-methylanthraquinone)ammonium **46**$^{+}$
Imaginary Frequency: None

DFT(PBE0)/def2-TZVPP SCF energies corrected by SMD model in acetonitrile (Hartree/particle):

- Fully oxidized species: -1056.95635907
- First reduction species: -1057.08210782
- Second reduction species: -1057.16531091

Optimised geometry Cartesian coordinates of the fully oxidised species:

1 1

C	-6.84615769	0.12397518	0.48231801
C	-5.77775009	1.03152578	0.51072924
C	-4.46861821	0.59523593	0.22192048
C	-4.23726124	-0.77290917	-0.09686437
C	-5.31930474	-1.67668341	-0.12070806
C	-6.61697181	-1.23061497	0.16644004
C	-3.35695202	1.58853781	0.26029551
C	-2.87133840	-1.27910052	-0.40661726
C	-1.74896799	-0.27433225	-0.38679706
C	-1.97567246	1.08382377	-0.07040228
C	-0.89741466	1.99242905	-0.07198908
H	-1.10723559	3.04782506	0.16372812
C	0.39273752	1.55137774	-0.38534128
C	0.63169647	0.18687198	-0.69155133
C	-0.44777593	-0.71429887	-0.69448494
H	-7.86760943	0.47147130	0.70724623
H	-5.93193689	2.09420160	0.75491878
H	-5.11522997	-2.72968977	-0.37007117
H	-7.45933055	-1.94088952	0.14455865
H	1.22128595	2.28169325	-0.41425915
H	-0.32250376	-1.78049078	-0.94943693
O	-2.63945657	-2.45956578	-0.66780427
O	-3.53217117	2.77192121	0.54464253
C	2.02999186	-0.27943536	-1.01411607

H	2.03899034	-1.26933861	-1.51306030
H	2.55638596	0.44750220	-1.66195479
N	2.90118247	-0.43905812	0.24841947
C	2.44939359	-1.63258814	1.04262712
H	2.92783831	-1.62371338	2.03886970
H	1.34868161	-1.57472348	1.15483608
H	2.72494195	-2.55303740	0.49134256
H	2.71559527	0.40126030	0.83266054
C	4.41849400	-0.40676050	-0.08859366
C	4.83598031	1.03525637	-0.42998895
C	5.28840194	-0.97667003	1.04369882
H	4.50804420	-1.05759281	-0.98679884
C	6.33178163	1.10901077	-0.80113984
H	4.64992614	1.68040458	0.46302537
H	4.23242704	1.45102961	-1.26624514
C	6.78437751	-0.90007579	0.66513948
H	5.11491577	-0.39100408	1.97773125
H	5.02647682	-2.03415221	1.25734486
C	7.21901169	0.52862168	0.30941364
H	6.59647239	2.16782745	-1.00969958
H	6.49987187	0.55121500	-1.75148659
H	7.38380018	-1.29813971	1.51186505
H	6.97561593	-1.57849583	-0.19856409
H	8.28373272	0.53589536	-0.00904912
H	7.15750065	1.17632303	1.21492725

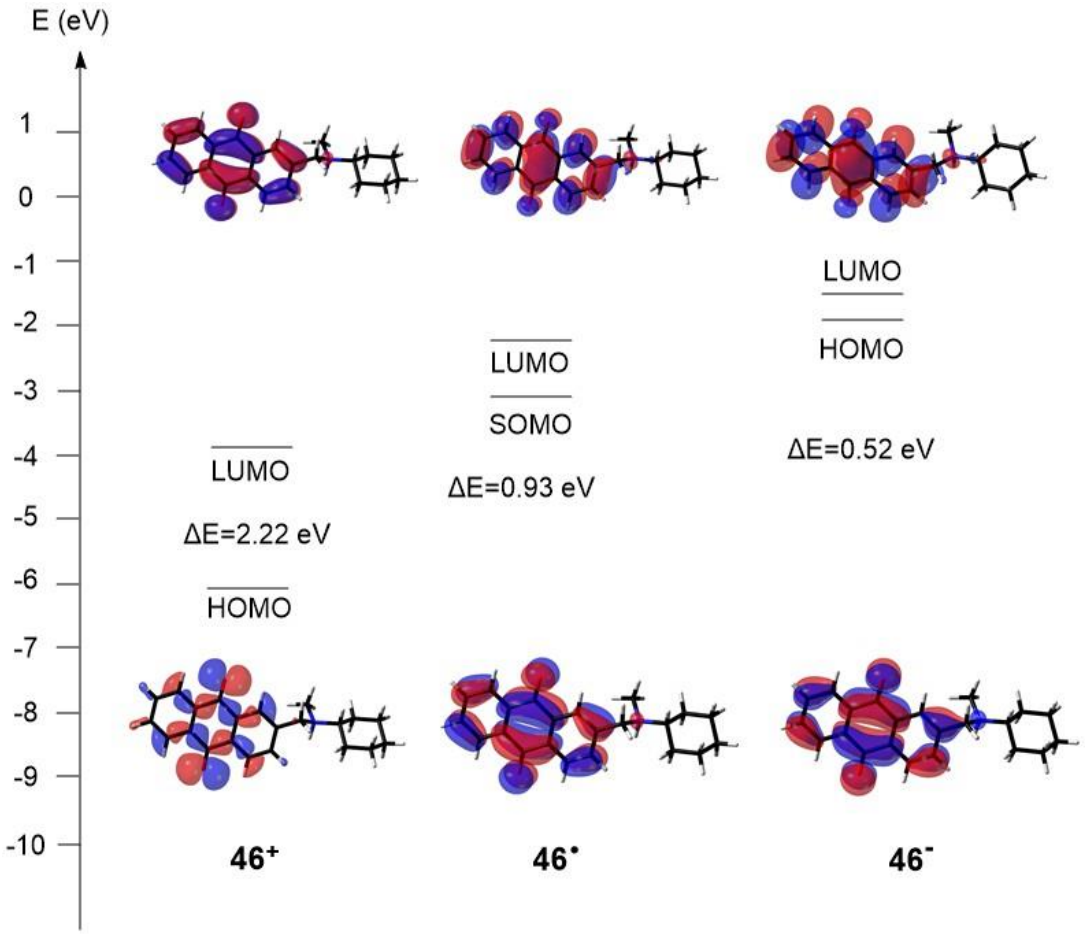

Figure 6.2.3: Calculated HOMO, SOMO and LUMO energy levels of AQ-N-methylcyclohexylammonium motif **46**$^{+}$ different oxidation states at the PBE0/def2-TZVPP level of theory in acetonitrile.

Abbreviations

ILs	Ionic Liquids
MP	Melting Point
DESs	Deep Eutectic Solvents
C_nMim^+	1-metyl-3-alkylimidazolium cation family
$[C_4C_1im][BF_4]$	1-methyl-3-butylimidazolium tetrafluoroborate ionic liquid
HBD	Hydrogen Bond Donor
Ch	Choline
ChCl	Choline Chloride
ChCl/U	DES: 1 equivalent of ChCl per 2 equivalents of urea
ChCl/EG glycol	DES:1 equivalent of ChCl per 2 equivalents of ethylene
ChCl/G	DES: 1 equivalent of ChCl per 2 equivalents of glycerol
ChCl/D-Glu glucose	DES: 1 equivalent of ChCl per 2 equivalents of D-
ChCl/D-Fru fructose	DES: 1 equivalent of ChCl per 2 equivalents of D-
ChCl/D-Sor sorbitol	DES: 1 equivalent of ChCl per 2 equivalents of D-
ChCl/MA acid	DES: 1 equivalent of ChCl per 1 equivalent of malonic
ChCl/H2O	DES: 1 equivalent of ChCl per 2 equivalents of water
DMU	Dimethyl urea
RDF	Radial Distribution Function
QUENS	Quasielastic Neutron Scattering

ChOAcCl	Acetylcholine chloride
ChCl/DMU	DES: 1 equivalent of ChCl per 2 equivalents of dimethylurea
ChCl/$AcNH_2$	DES: 1 equivalent of ChCl per 2 equivalents of acetamide
ChOAcCl/U	DES: 1 equivalent of ChOAc per 2 equivalents of urea
Gly	Glycerol
EtGly	Ethylene glycol
MP	Melting point
SWOT	Strengths, weaknesses, opportunities and threats analysis
DFT	Density functional theory
LDA	Local density approximation
GGA	Generalized gradient approximation
B88	GGA exchange energy functional published by Becke in 1988
PBE	GGA exchange energy functional published by Perdew, Burke and Ernzerhof in 1997
LYP	GGA correlation energy functional published by Lee, Yang and Parr published in 1988
P86	GGA correlation functional published by Perdew in 1986
B3LYP	3 parameters hybrid functional composed by the B88 exchange functional and LYP correlation functional
PBE0	hybrid functional composed by the PBE exchange functional and the PBEc correlation functional.
EWG	Electron-withdrawing group
EDG	Electron-donating group
NHC	*N*-heterocyclic carbene
XPhos	2-Dicyclohexylphosphino-2′,4′,6′-triisopropylbiphenyl

CyJohnPhos	[1,1’-biphenyl]-2-yldicyclohexylphosphine
Amphos	di-tert-butyl(4-dimethylaminophenyl)phosphine
Handaphos	(2R,3R)-3-Tert-butyl-4-(2,6-dimethoxyphenyl)- 2-{[2,4,6-tris(propan-2-yl)phenyl]methyl}-2,3-dihydro-1,3-benzoxaphosphole
TPPTS	3,3′,3″-Phosphanetriyltris(benzenesulfonic acid) trisodium salt
TMEDA	Tetramethylethylenediamine
PdNPs	Palladium Nanoparticles
RADES	Redox-active deep eutectic solvent
WE	Working electrode
RE	Reference electron
CE	Counter electron
SHE	Standard hydrogen electrode
CV	Cyclic voltamperommetry or cyclic voltammogram
DPV	Differential Pulse Voltammetry
DFT	Density functional theory
NBS	N-bromosuccinimide
AIBN	azobisisobutyronitrile
XRD	X-Ray diffraction
HOMO	Highest Occupied Molecular Orbital
LUMO	Lowest Unoccupied Molecular Orbital
SOMO	Singly-occupied Molecular Orbital

References

1 R. Serrano-López, J. Fradera and S. Cuesta-López, *Chem. Eng. Process. Process Intensif.*, 2013, **73**, 87–102.

2 J. D. Holbrey and R. D. Rogers, in *Ionic Liquids in Synthesis*, eds. P. Wasserscheid and T. Welton, Wiley-VCH, Weinheim, Germany, 2002, pp. 41–90.

3 R. D. Rogers and K. R. Seddon, *Science*, 2003, **302**, 792–793.

4 B. Clare, A. Sirwardana and D. R. MacFarlane, in *Topics in Current Chemistry: Ionic Liquids*, ed. B. Kirchner, Heilderbeg, Germany, 2010, pp. 1–40.

5 C. M. Gordon, in *Ionic Liquids in Synthesis*, eds. P. Wasserchied and T. Welton, Wiley-VCH, Mörlenbach, Germany, 2002, pp. 7–33.

6 United Nations Sustainable Development Summit 2015, http://unhabitat.org/wp-content/uploads/2015/10/Statement-ED-Joan-Clos-UN-SDGs-Summit.pdf, (accessed 30 March 2020).

7 T. Welton, *Green Chem.*, 2008, **10**, 483.

8 T. Welton, *Chem. Rev.*, 1999, **99**, 2071–2083.

9 M. Deetlefs and K. R. Seddon, *Green Chem.*, 2010, **12**, 17–30.

10 A. P. Abbott, G. Capper, D. L. Davies, H. L. Munro, R. K. Rasheed and V. Tambyrajah, *Chem. Commun.*, 2001, **1**, 2010–2011.

11 E. L. Smith, A. P. Abbott and K. S. Ryder, *Chem. Rev.*, 2014, **114**, 11060–11082.

12 K. De Oliveira Vigier and F. Jérôme, in *Deep Eutectic Solvents: Synthesis, Properties, and Applications*, eds. D. J. Ramón and G. Guillena, Weinheim, Germany, 2019, pp. 1–23.

13 J. Naser, F. Mjalli, B. Jibril, S. Al-Hatmi and Z. Gano, *Int. J. Chem. Eng. Appl.*, 2013, **4**, 114–118.

14 Y. H. Choi, J. van Spronsen, Y. Dai, M. Verberne, F. Hollmann, I. W.

C. E. Arends, G. J. Witkamp and R. Verpoorte, *Plant Physiol.*, 2011, **156**, 1701–1705.

15 A. P. Abbott, G. Capper and S. Gray, *ChemPhysChem*, 2006, **7**, 803–806.

16 A. P. Abbott, G. Capper, D. L. Davies, R. K. Rasheed and V. Tambyrajah, *Chem. Commun.*, 2003, 70–71.

17 A. P. Abbott, C. D'Agostino, S. J. Davis, L. F. Gladden and M. D. Mantle, *Phys. Chem. Chem. Phys.*, 2016, **18**, 25528–25537.

18 M. Francisco, A. van den Bruinhorst, L. F. Zubeir, C. J. Peters and M. C. Kroon, *Fluid Phase Equilib.*, 2013, **340**, 77–84.

19 A. P. Abbott, D. Boothby, G. Capper, D. L. Davies and R. K. Rasheed, *J. Am. Chem. Soc.*, 2004, **126**, 9142–9147.

20 O. S. Hammond and K. J. Edler, in *Deep Eutectic Solvents: Synthesis, Properties and Applications*, eds. D. J. Ramón and G. Guillena, Wiley-VCH, Weinheim, Germany, 2020, pp. 25–42.

21 M. Francisco, A. Van Den Bruinhorst and M. C. Kroon, *Angew. Chem., Int. Ed*, 2013, **52**, 3074–3085.

22 G. Cuevas and F. Cortés, *Introducción a la Química Computacional*, Fondo de Cultura Económica, Mexico City, Mexico, 2003.

23 H. Sun, Y. Li, X. Wu and G. Li, *J. Mol. Model.*, 2013, **19**, 2433–2441.

24 S. L. Perkins, P. Painter and C. M. Colina, *J. Chem. Eng. Data*, 2014, **59**, 3652–3662.

25 G. García, M. Atilhan and S. Aparicio, *Chem. Phys. Lett.*, 2015, **634**, 151–155.

26 D. V. Wagle, C. A. Deakyne and G. A. Baker, *J. Phys. Chem. B*, 2016, **120**, 6739–6746.

27 C. R. Ashworth, R. P. Matthews, T. Welton and P. A. Hunt, *Phys. Chem. Chem. Phys.*, 2016, **18**, 18145–18160.

28 S. Zahn, *Phys. Chem. Chem. Phys.*, 2017, **19**, 4041–4047.

29 R. Stefanovic, M. Ludwig, G. B. Webber, R. Atkin and A. J. Page, *Phys. Chem. Chem. Phys.*, 2017, **19**, 3297–3306.

30 C. D'Agostino, R. C. Harris, A. P. Abbott, L. F. Gladden and M. D. Mantle, *Phys. Chem. Chem. Phys.*, 2011, **13**, 21383–21391.

31 D. V. Wagle, G. A. Baker and E. Mamontov, *J. Phys. Chem. Lett.*, 2015, **6**, 2924–2928.

32 O. S. Hammond, D. T. Bowron and K. J. Edler, *Green Chem.*, 2016, **18**, 2736–2744.

33 Z. Yang, in *Deep Eutectic Solvents: Synthesis, Properties and Applications*, eds. D. J. Ramon and G. Guilleana, Wiley-VCH, Weinheim, Germany, 2020, pp. 43–60.

34 P. Liu, J.-W. Hao, L.-P. Mo and Z.-H. Zhang, *RSC Adv.*, 2015, **5**, 48675–48704.

35 D. A. Alonso, A. Baeza, R. Chinchilla, G. Guillena, I. M. Pastor and D. J. Ramón, *European J. Org. Chem.*, 2016, **2016**, 612–632.

36 D. Lloyd, T. Vainikka and K. Kontturi, *Electrochim. Acta*, 2013, **100**, 18–23.

37 C. Zhang, Y. Ding, L. Zhang, X. Wang, Y. Zhao, X. Zhang and G. Yu, *Angew. Chem., Int. Ed*, 2017, **56**, 7454–7459.

38 M. H. Chakrabarti, F. S. Mjalli, I. M. Alnashef, M. A. Hashim, M. A. Hussain, L. Bahadori and C. T. J. Low, *Renew. Sustain. Energy Rev.*, 2014, **30**, 254–270.

39 D. A. Skoog, F. J. Holler and S. R. Crouch, *Principles of Instrumental Analysis*, Thomson Brooks Cole, 2006.

40 W. R. Browne, *Electrochemistry*, Oxford University Press, Glasgow, 2018.

41 J. E. Nutting, J. B. Gerken, A. G. Stamoulis, D. L. Bruns and S. S. Stahl, *J. Org. Chem.*, , DOI:10.1021/acs.joc.1c01520.

42 N. Elgrishi, K. J. Rountree, B. D. McCarthy, E. S. Rountree, T. T.

Eisenhart and J. L. Dempsey, *J. Chem. Educ.*, 2018, **95**, 197–206.

43 I. N. Levine, *Introduction to Quantum Chemistry*, Pearson, Hobboken, USA, 2014.

44 F. Jensen, *Introduction to Computational Chemistry*, John Wiley & Sons Inc., Chirchester, England, 2007.

45 P. Popelier, *Atoms in Molecules And Introduction*, Pearson, Harlow, England, 2000.

46 A. Schäfer, H. Horn and R. Ahlrichs, *J. Chem. Phys.*, 1992, **97**, 2571–2577.

47 M. Nonella, G. Mathias and P. Tavan, 2003, 8638–8647.

48 I. Raabe, K. Wagner, K. Guttsche, M. Wang, M. Grätzel, G. Santiso-quiçones and I. Krossing, 2009, 1966–1976.

49 T. Gaudin and J. M. Aubry, *J. Energy Storage*, 2022, **49**, 1–13.

50 M. J. Frisch, G. W. Trucks, H. B. Schlegel, G. E. Scuseria, M. A. Robb, J. R. Cheeseman, G. Scalmani, V. Barone, B. Menucci, G. A. Petersson, H. Nakatsuji, M. Caricato, X. Li, H. P. Hratchian, A. F. Izmaylov, J. Blonio, G. Zheng, J. L. Sonnenberg, M. Hada, M. Ehara, K. Toyota, R. Fukuda, J. Hasegawa, M. Ishida, T. Nakajima, Y. Honda, O. Kitao, H. Nakai, T. Vreven, J. A. Montgomery, J. E. Peralta, F. Ogliaro, M. Beapark, J. J. Heyd, E. Brothers, K. N. Kudin, V. N. Staroverov, T. Keith, R. Kobayashi, J. Normand, K. Raghavachari, A. Rendell, J. C. Burant, S. S. Iyengar, J. Tomasi, M. Cossi, N. Rega, J. M. Millam, M. Klene, J. E. Knox, J. B. Cross, V. Bakken, C. Adamo, J. Jaramillo, R. Gomperts, R. E. Stratmann, O. Yazyev, A. J. Austin, R. Cammi, C. Pomelli, J. W. Ochtersky, R. L. Martin, K. Morokuma, V. G. Zakrzewsky, G. A. Voth, P. Salvador, J. J. Dannenberg, S. Dapprich, A. D. Daniels, O. Farkas, J. B. Foresman, J. V. Ortiz, J. Cioslowski and D. J. Fox, 2013.

51 A. D. Becke, *Phys. Rev. A*, 1988, **38**, 3098–3100.

52 J. P. Perdew, *Phys. Rev. B*, 1986, **34**, 7406.

53 J. P. Perdew, K. Burke and M. Ernzerhof, *Phys. Rev. Lett.*, 1997, **78**, 1396–1396.

54 C. Adamo and V. Barone, *J. Chem. Phys.*, 1999, **110**, 6158–6170.

55 M. Ernzerhof and G. E. Scuseria, *J. Chem. Phys.*, 1999, **110**, 5029–5036.

56 F. Weigend and R. Ahlrichs, *Phys. Chem. Chem. Phys.*, 2005, **7**, 3297–3305.

57 M. Namazian, C. Y. Lin and M. L. Coote, *J. Chem. theory Comput.*, 2010, **6**, 2721–2725.

58 A. Decken, A. Mailman, J. Passmore, J. M. Rautiainen, W. Scherer and E.-W. Scheidt, *Dalt. Trans.*, 2011, **40**, 868–879.

59 Y. Fu, L. Liu, H. Yu, Y. Wang and Q. Guo, 2005, 7227–7234.

60 C. J. Clarke, W. C. Tu, O. Levers, A. Bröhl and J. P. Hallett, *Chem. Rev.*, 2018, **118**, 747–800.

61 R. Martínez, L. Berbegal, G. Guillena and D. J. Ramón, *Green Chem.*, 2016, **18**, 1724–1730.

62 D. Brenna, E. Massolo, A. Puglisi, S. Rossi, G. Celentano, M. Benaglia and V. Capriati, *Beilstein J. Org. Chem.*, 2016, **12**, 2620–2626.

63 N. Azizi, Z. Rahimi and M. Alipour, *Comptes Rendus Chim.*, 2015, **18**, 626–629.

64 V. Krishnakumar, N. G. Vindhya, B. K. Mandal and F. R. Nawaz Khan, *Ind. Eng. Chem. Res.*, 2014, **53**, 10814–10819.

65 E. Massolo, S. Palmieri, M. Benaglia, V. Capriati and F. M. Perna, *Green Chem.*, 2016, **18**, 792–797.

66 A. K. Sanap and G. S. Shankarling, *Catal. Commun.*, 2014, **49**, 58–62.

67 J. Flores-Ferrándiz and R. Chinchilla, *Tetrahedron Asymmetry*, 2017, **28**, 302–306.

68 D. R. Ñíguez, G. Guillena and D. A. Alonso, *ACS Sustain. Chem. Eng.*, 2017, **5**, 10649–10656.

69 Y. A. Sonawane, S. B. Phadtare, B. N. Borse, A. R. Jagtap and G. S. Shankarling, *Org. Lett.*, 2010, **12**, 1456–1459.

70 A. Kumar, R. D. Shukla, D. Yadav and L. P. Gupta, *RSC Adv.*, 2015, **5**, 52062–52065.

71 N. Azizi, M. Khajeh and M. Alipour, *Ind. Eng. Chem. Res.*, 2014, **53**, 15561–15565.

72 N. Azizi, E. Batebi, S. Bagherpour and H. Ghafuri, *RSC Adv.*, 2012, **2**, 2289–2293.

73 D. Y. Dai, L. Wang, Q. Chen and M. Y. He, *J. Chem. Res.*, 2014, **38**, 183–185.

74 S. B. Phadtare and G. S. Shankarling, *Green Chem.*, 2010, **12**, 458–46.

75 G. Imperato, E. Eibler, J. Niedermaier and B. König, *Chem. Commun.*, 2005, 1170–1172.

76 A. P. Abbott, G. Capper, D. L. Davies, R. K. Rasheed and V. Tambyrajah, *Green Chem.*, 2002, **4**, 24–26.

77 S. Handy and M. Wright, *Tetrahedron Lett.*, 2014, **55**, 3440–3442.

78 R. C. Morales, V. Tambyrajah, P. R. Jenkins, D. L. Davies and A. P. Abbott, *Chem. Commun.*, 2004, **4**, 158–159.

79 P. Wang, F. P. Ma and Z. H. Zhang, *J. Mol. Liq.*, 2014, **198**, 259–262.

80 S. Handy and K. Lavender, *Tetrahedron Lett.*, 2013, **54**, 4377–4379.

81 H. Truong Nguyen, D. K. Nguyen Chau and P. H. Tran, *New J. Chem.*, 2017, **41**, 12481–12489.

82 F. Keshavarzipour and H. Tavakol, *Catal. Letters*, 2015, **145**, 1062–1066.

83 X. Meng, K. Ballerat-Busserolles, P. Husson and J. M. Andanson, *New J. Chem.*, 2016, **40**, 4492–4499.

84 S. C. Kuo, F. Chen, D. Hou, A. Kim-Meade, C. Bernard, J. Liu, S. Levy and G. G. Wu, *J. Org. Chem.*, 2003, **68**, 4984–4987.

85 G. Osztrovszky, T. Holm and R. Madsen, *Org. Biomol. Chem.*, 2010, **8**, 3402–3404.

86 E. O. Fetisov, D. B. Harwood, I.-F. W. Kuo, S. E. E. Warrag, M. C. Kroon, C. J. Peters and J. I. Siepmann, *J. Phys. Chem. B*, 2018, **122**, 1245–1254.

87 O. S. Hammond, D. T. Bowron and K. J. Edler, *Angew. Chem., Int. Ed*, 2017, **56**, 9782–9785.

88 L. Sapir and D. Harries, *J. Chem. Theory Comput.*, 2020, **16**, 3335–3342.

89 H. Zong, H. Huang, J. Liu, G. Bian and L. Song, *J. Org. Chem.*, 2012, **77**, 4645–4652.

90 C. Vidal, J. García-Álvarez, A. Hernán-Gõmez, A. R. Kennedy and E. Hevia, *Angew. Chem., Int. Ed*, 2014, **53**, 5969–5973.

91 L. Cicco, S. Sblendorio, R. Mansueto, F. M. Perna, A. Salomone, S. Florio and V. Capriati, *Chem. Sci.*, 2016, **7**, 1192–1199.

92 V. Mallardo, R. Rizzi, F. C. Sassone, R. Mansueto, F. M. Perna, A. Salomone and V. Capriati, *Chem. Commun.*, 2014, **50**, 8655–8658.

93 F. C. Sassone, F. M. Perna, A. Salomone, S. Florio and V. Capriati, *Chem. Commun.*, 2015, **51**, 9459–9462.

94 C. Vidal, J. García-Álvarez, A. Hernán-Gómez, A. R. Kennedy and E. Hevia, *Angew. Chem., Int. Ed*, 2016, **55**, 16145–16148.

95 G. Dilauro, M. Dell'Aera, P. Vitale, V. Capriati and F. M. Perna, *Angew. Chem., Int. Ed*, 2017, **56**, 10200–10203.

96 E. Hevia, M. J. Rodriguez-Alvarez, J. Garcia-Alvarez, M. Uzelac, M. Fairley, C. T. O'Hara, M. J. Rodríguez-Álvarez, J. García-Álvarez, M. Uzelac, M. Fairley, C. T. O'Hara and E. Hevia, *Chem. Eur. J.*, 2018, **24**, 1720–1725.

97 S. Ghinato, G. Dilauro, F. M. Perna, V. Capriati, M. Blangetti and C. Prandi, *Chem. Commun.*, 2019, **55**, 7741–7744.

98 A. F. Quivelli, G. D'Addato, P. Vitale, J. García-Álvarez, F. M. Perna and V. Capriati, *Tetrahedron*, 2021, **81**, 1–7.

99 L. Cicco, A. Salomone, P. Vitale, N. Ríos-Lombardía, J. González-Sabín, J. García-Álvarez, F. M. Perna and V. Capriati, *ChemSusChem*, 2020, **13**, 3583–3588.

100 L. Cicco, A. Fombona-Pascual, A. Sánchez-Condado, G. A. Carriedo, F. M. Perna, V. Capriati, A. Presa Soto and J. García-Álvarez, *ChemSusChem*, 2020, **13**, 4967–4973.

101 J. García-Álvarez, E. Hevia and V. Capriati, *European J. Org. Chem.*, 2015, **2015**, 6779–6799.

102 C. C. C. Johansson Seechurn, M. O. Kitching, T. J. Colacot and V. Snieckus, *Angew. Chem., Int. Ed*, 2012, **51**, 5062–5085.

103 R. H. Crabtree, *The Organometallic Chemistry of the Transition Metals*, John Wiley & Sons Inc., Hoboken, New Jersey, 2009.

104 K. Tamao, Y. Kiso, K. Sumitani and M. Kumada, *J. Am. Chem. Soc.*, 1972, **94**, 9268–9269.

105 K. F. Heck and J. P. Nolley, *J. Org. Chem.*, 1972, **37**, 2320–2322.

106 K. Sonogashira, Y. Tohda and N. Hagihara, *Tetrahedron Lett.*, 1975, **16**, 4467–4470.

107 S. Baba and E. ichi Negishi, *J. Am. Chem. Soc.*, 1976, **98**, 6729–6731.

108 D. Milstein and J. K. Stille, *J. Am. Chem. Soc.*, 1979, **101**, 4992–4998.

109 N. Miyaura, K. Yamada and A. Suzuki, *Tetrahedron Lett.*, 1979, **20**, 3437–3440.

110 E. ichi Negishi, in *Handbook of Organopalladium Chemistry for Organic Synthesis. Vol I*, ed. E. ichi Negishi, New York, 1st Editio., 2002, pp. 39–214.

111 L. Schiavo, G. Carotenuto, L. Aversa, R. Tatti, R. Verucchi and L. Schiavo, *IEEE-NANO 2015 - 15th Int. Conf. Nanotechnol.*, 2015, 282–285.

112 A. E. Díaz-Álvarez and V. Cadierno, *Appl. Sci.*, 2013, **3**, 55–69.

113 M. Moreno-Mañas, M. Pérez and R. Pleixats, *J. Org. Chem.*, 1996, **61**, 2346–2351.

114 J. Sherwood, J. H. Clark, I. J. S. Fairlamb and J. M. Slattery, *Green Chem.*, 2019, **21**, 2164–2213.

115 L. A. Adrio, B. N. Nguyen, G. Guilera, A. G. Livingston and K. K. Hii, *Catal. Sci. Technol.*, 2012, **2**, 316–323.

116 T. Jeffrey, *Tetrahedron*, 1996, **52**, 10113–10130.

117 A. Biffis, P. Centomo, A. Del Zotto and M. Zecca, *Chem. Rev.*, 2018, **118**, 2249–2295.

118 D. Astruc, F. Lu and J. R. Aranzaes, *Angew. Chem., Int. Ed*, 2005, **44**, 7852–7872.

119 J. Liu, Y. Deng, H. Wang, H. H. H. Zhang, G. Yu, B. Wu, H. H. H. Zhang, Q. Li, T. B. Marder, Z. Yang and A. Lei, *Org. Lett.*, 2008, **10**, 2661–2664.

120 G. Dilauro, A. F. Quivelli, P. Vitale, V. Capriati and F. Perna, *Angew. Chem., Int. Ed*, 2019, **58**, 1799–1802.

121 G. Dilauro, C. S. Azzollini, P. Vitale, A. Salomone, F. M. Perna and V. Capriati, *Angew. Chem., Int. Ed*, 2021, **60**, 10632–10636.

122 A. J. Reay and I. J. S. Fairlamb, *Chem. Commun.*, 2015, **51**, 16289–16307.

123 P. J. Ellis, I. J. S. Fairlamb, S. F. J. Hackett, K. Wilson and A. F. Lee, *Angew. Chem., Int. Ed*, 2010, **49**, 1820–1824.

124 A. Leyva-Pérez, J. Oliver-Meseguer, P. Rubio-Márques and A. Corma, *Angew. Chem., Int. Ed*, 2013, **52**, 11554–11559.

125 M. Aufiero, T. Scattolin, F. Proutière and F. Schoenebeck, *Organometallics*, 2015, **34**, 5191–5195.

126 C. Amatore, A. Mohamed and J. Anny, *J. Organomet. Chem.*, 1989, **363**, 41–45.

127 S. Kozuch, C. Amatore, A. Jutand and S. Shaik, *Organometallics*, 2005, **24**, 2319–2330.

128 C. Amatore, M. Azzabi and A. Jutand, *J. Am. Chem. Soc.*, 1991, **113**, 8375–8384.

129 K. Böck, J. E. Feil, K. Karaghiosoff and K. Koszinowski, *Chem. Eur. J.*, 2015, **21**, 5548–5560.

130 C. Amatore and A. Jutand, *Acc. Chem. Res.*, 2000, **33**, 314–321.

131 M. Kolter, K. Böck, K. Karaghiosoff and K. Koszinowski, *Angew. Chem., Int. Ed*, 2017, **56**, 13244–13248.

132 C. Amatore, E. Carré, A. Jutand, M. A. M'Barki, B. O. Kneisel, R. Herbst-Irmer, M. A. Pellinghelli and A. Tiripicchio, *Organometallics*, 1995, **14**, 1818–1826.

133 N. W. J. Scott, M. J. Ford, C. Schotes, R. R. Parker, A. C. Whitwood and I. J. S. Fairlamb, *Chem. Sci.*, 2019, **10**, 7898–7906.

134 WO/2011/012889, 2011.

135 C. C. C. J. Seechurn, T. Sperger, T. G. Scrase, F. Schoenebeck and T. J. Colacot, *J. Am. Chem. Soc.*, 2017, **139**, 5194–5200.

136 A. J. J. Lennox and G. C. Lloyd-Jones, *Chem. Soc. Rev.*, 2014, **43**, 412–443.

137 S. Sharma, J. Das, W. M. Braje, A. K. Dash and S. Handa, *ChemSusChem*, 2020, 2859–2875.

138 M. A. Andrade and L. M. D. R. S. Martins, *Molecules*, 2020, **25**, 1–32.

139 M. Yousaf, A. F. Zahoor, R. Akhtar, M. Ahmad and S. Naheed, *Mol. Divers.*, 2020, **24**, 821–839.

140 C. J. Mathews, P. J. Smith and T. Welton, *Chem. Commun.*, 2000, 1249–1250.

141 C. J. Mathews, P. J. Smith and T. Welton, *J. Mol. Catal. A Chem.*, 2004, **214**, 27–32.

142 C. J. Mathews, P. J. Smith, T. Welton, A. J. P. White and D. J.

Williams, *Organometallics*, 2001, **20**, 3848–3850.

143 F. McLachlan, C. J. Mathews, P. J. Smith and T. Welton, *Organometallics*, 2003, **22**, 5350–5357.

144 C. J. Mathews, P. J. Smith and T. Welton, *J. Mol. Catal. A Chem.*, 2003, **206**, 77–82.

145 G. Imperato, S. Höger, D. Lenoir and B. König, *Green Chem.*, 2006, **8**, 1051–1055.

146 X. Marset, A. Khoshnood, L. Sotorríos, E. Gómez-Bengoa, D. A. Alonso and D. J. Ramón, *ChemCatChem*, 2017, **9**, 1269–1275.

147 X. Marset, B. Saavedra, N. González-Gallardo, A. Beaton, M. M. León, R. Luna, D. J. Ramón and G. Guillena, *Front. Chem.*, 2019, **7**, 1–8.

148 G. Dilauro, S. M. García, D. Tagarelli, P. Vitale, F. M. Perna and V. Capriati, *ChemSusChem*, 2018, **11**, 3495–3501.

149 J. A. Kist, K. R. Mitchell-Koch and G. A. Baker, *J. Mater. Chem. B*, 2021, **9**, 535–566.

150 J. Paris, N. Ríos-Lombardía, F. Morís, H. Gröger and J. González-Sabín, *ChemCatChem*, 2018, **10**, 4417–4423.

151 J. Paris, A. Telzerow, N. Ríos-Lombardía, K. Steiner, H. Schwab, F. Morís, H. Gröger and J. González-Sabín, *ACS Sustain. Chem. Eng.*, 2019, **7**, 5486–5493.

152 S. Chakraborty, M. H. Mruthunjayappa, K. Aruchamy, N. Singh, K. Prasad, D. Kalpana, D. Ghosh, N. Sanna Kotrappanavar and D. Mondal, *ACS Sustain. Chem. Eng.*, 2019, **7**, 14225–14235.

153 T. Jeffery, *J. Chem. Soc., Chem. Commun*, 1984, **19**, 1287–1289.

154 T. J. Sanderson, C. M. Black, J. W. Southwell, E. J. Wilde, A. Pandey, R. Herman, G. H. Thomas, E. Boros, A.-K. Duhme-Klair and A. Routledge, *ACS Infect. Dis.*, 2020, **6**, 2532–2541.

155 S. Tabassum, A. F. Zahoor, S. Ahmad, R. Noreen, S. G. Khan and H. Ahmad, *Cross-coupling reactions towards the synthesis of natural*

products, Springer International Publishing, 2021.

156 A. W. Dombrowski, N. J. Gesmundo, A. L. Aguirre, K. A. Sarris, J. M. Young, A. R. Bogdan, M. C. Martin, S. Gedeon and Y. Wang, *ACS Med. Chem. Lett.*, 2020, **11**, 597–604.

157 S. Xu, E. H. Kim, A. Wei and E. I. Negishi, *Sci. Technol. Adv. Mater.*, 2014, **15**, 1–23.

158 D. Haas, M. Hammann, R. Greiner, P. Knochel, J. M. Hammann, R. Greiner and P. Knochel, *ACS Catal.*, 2016, **6**, 1540–1552.

159 E. ichi Negishi, *Angew. Chem., Int. Ed*, 2011, **50**, 6738–6764.

160 E. I. Negishi, K. Akiyoshi and T. Takahashi, *J. Chem. Soc. Chem. Commun.*, 1987, 477–478.

161 L. Jin and A. Lei, *Org. Biomol. Chem.*, 2012, **10**, 6817–6825.

162 J. Del Pozo, G. Salas, R. Álvarez, J. A. Casares and P. Espinet, *Organometallics*, 2016, **35**, 3604–3611.

163 Q. Liu, Y. Lan, J. Liu, G. Li, Y. Wu and A. Lei, *J. Am. Chem. Soc.*, 2009, **131**, 10201–10210.

164 Y. Yang, N. J. Oldenhuis and S. L. Buchwald, *Angew. Chem., Int. Ed*, 2013, **52**, 615–619.

165 M. Alami, C. Amatore, S. Bensalem, A. Choukchou-brahim and A. Jutand, *Eur. J. Inorg. Chem.*, 2001, **2001**, 2675–2681.

166 T. S. Khaibulova, I. A. Boyarskaya and V. P. Boyarskii, *Russ. J. Org. Chem.*, 2013, **49**, 360–365.

167 C. Dai and G. C. Fu, *J. Am. Chem. Soc.*, 2001, **123**, 2719–2724.

168 S. Çalimsiz, M. Sayah, D. Mallik and M. G. Organ, *Angew. Chemie*, 2010, **122**, 2058–2061.

169 J. Sirieix, M. Oßberger, B. Betzemeier and P. Knochel, *Synlett*, 2000, **10**, 1613–1615.

170 A. Krasovskiy, C. Duplais and B. H. Lipshutz, *J. Am. Chem. Soc.*, 2009, **131**, 15592–15593.

171 C. Duplais, A. Krasovskiy and B. H. Lipshutz, *Organometallics*, 2011, **30**, 6090–6097.

172 A. Krasovskiy, C. Duplais and B. H. Lipshutz, *Org. Lett.*, 2010, **12**, 4742–4744.

173 S. E. García-Garrido, A. Presa Soto, E. Hevia and J. García-Álvarez, *Eur. J. Inorg. Chem.*, 2021, **2021**, 3116–3130.

174 J. García-Álvarez, E. Hevia and V. Capriati, *Chem. Eur. J.*, 2018, **24**, 14854–14863.

175 A. Wolfson and C. Dlugy, *Chem. Pap.*, 2007, **61**, 228–232.

176 A. Krasovskiy, V. Malakhov, A. Gavryushin and P. Knochel, *Angew. Chem., Int. Ed*, 2006, **45**, 6040–6044.

177 A. Krasovskiy and P. Knochel, *Synthesis* , 2006, **5**, 890–891.

178 S. C. Berk, M. C. P. Yen, N. Jeong and P. Knochel, *Organometallics*, 1990, **9**, 3053–3064.

179 P. Eckert, S. Sharif and M. G. Organ, *Angew. Chem., Int. Ed*, 2021, **60**, 12224–12241.

180 G. T. Achonduh, N. Hadei, C. Valente, S. Avola, C. J. O'Brien and M. G. Organ, *Chem. Commun.*, 2010, **46**, 4109–4111.

181 I. N. Houpis, C. Huang, U. Nettekoven, J. G. Chen, R. Liu and M. Canters, *Org. Lett.*, 2008, **10**, 5601–5604.

182 B. Saavedra, N. González-Gallardo, A. Meli and D. J. Ramón, *Adv. Synth. Catal.*, 2019, **361**, 3868–3879.

183 O. Zech, A. Stoppa, R. Buchner and W. Kunz, *J. Chem. Eng. Data*, 2010, **55**, 1774–1778.

184 A. P. Abbott, *ChemPhysChem*, 2005, **6**, 2502–2505.

185 M. Figueiredo, C. Gomes, R. Costa, A. Martins, C. M. Pereira and F. Silva, *Electrochim. Acta*, 2009, **54**, 2630–2634.

186 R. Costa, M. Figueiredo, C. M. Pereira and F. Silva, *Electrochim. Acta*, 2010, **55**, 8916–8920.

187 G. H. Lane, *Electrochim. Acta*, 2012, **83**, 513–528.

188 K. Haerens, E. Matthijs, K. Binnemans and B. Van der Bruggen, *Green Chem.*, 2009, **11**, 1357–1365.

189 Z. Yoshida and F. Takabayashi, *Tetrahedron*, 1968, **24**, 933–943.

190 A. Ohta, K. Hattori, Y. Kusumoto, T. Kawase, T. Kobayashi, H. Naito and C. Kitamura, *Chem. Lett.*, 2012, **41**, 674–676.

191 T. Wolff and H. Görner, *J. Photochem. Photobiol. A Chem.*, 2010, **209**, 219–223.

192 A. Navaz, *J. Photochem. Photobiol. A Chem.*, 1990, **53**, 141–167.

193 D. Zarzeczańska, P. Niedziałkowski, A. Wcisło, L. Chomicz, J. Rak and T. Ossowski, *Struct. Chem.*, 2014, **25**, 625–634.

194 N. Gupta and H. Linschitz, *J. Am. Chem. Soc.*, 1997, **119**, 6384–6391.

195 D. K. Smith, *Chem. Rec.*, 2021, **21**, 2488–2501.

196 P. A. Staley, C. M. Newell, D. P. Pullman and D. K. Smith, *Anal. Chem.*, 2014, **86**, 10917–10924.

197 N. A. Macías-Ruvalcaba and D. H. Evans, *J. Phys. Chem. C*, 2010, **114**, 1285–1292.

198 M. Wu, Y. Jing, A. A. Wong, E. M. Fell, S. Jin, Z. Tang, R. G. Gordon and M. J. Aziz, *Chem*, 2020, **6**, 1432–1442.

199 K. Lin, Q. Chen, M. R. Gerhardt, L. Tong, S. Bok, S. B. Kim, L. Eisenach, A. W. Valle, D. Hardee, R. G. Gordon, M. J. Aziz and M. P. Marshak, *Science*, 2015, **349**, 1529–1532.

200 B. Huskinson, M. P. Marshak, C. Suh, S. Er, M. R. Gerhardt, C. J. Galvin, X. Chen, A. Aspuru-Guzik, R. G. Gordon and M. J. Aziz, *Nature*, 2014, **505**, 195–198.

201 Q. Chen, L. Eisenach and M. J. Aziz, *J. Electrochem. Soc.*, 2016, **163**, 5057–5063.

202 Y. Ding, C. Zhang, L. Zhang, Y. Zhou and G. Yu, *Chem. Soc. Rev.*, 2017, **47**, 69–103.

203 S. Er, C. Suh, M. P. Marshak and A. Aspuru-Guzik, *Chem. Sci.*, 2015, **6**, 885–893.

204 Y. Zhen, C. Zhang, J. Yuan and Y. Li, *J. Mater. Chem. A*, 2021, **9**, 22056–22063.

205 B. Mohan Reddy, V. Venkata Ramana Kumar, N. Chinna Gangi Reddy and S. Mahender Rao, *Chinese Chem. Lett.*, 2014, **25**, 179–182.

206 M. P. Crozet, P. Vanelle, O. Jentzer, S. Donini and J. Maldonado, *Tetrahedron*, 1993, **49**, 11253–11262.

207 Y. Zheng, L. Zhu, L. Fan, W. Zhao, J. Wang, X. Hao, Y. Zhu, X. Hu, Y. Yuan, J. Shao and W. Wang, *Eur. J. Med. Chem.*, 2017, **125**, 902–913.

208 T. L. Greaves and C. J. Drummond, *Chem. Rev.*, 2015, **115**, 11379–11448.

209 P. Wasserscheid, M. Sesing and W. Korth, *Green Chem.*, 2002, **4**, 134–138.

210 M. Baidya, F. Brotzel and H. Mayr, *Org. Biomol. Chem.*, 2010, **8**, 1929–1935.

211 J. Ammer, M. Baidya, S. Kobayashi and H. Mayr, *J. Phys. Org. Chem.*, 2010, **23**, 1029–1035.

212 R. Kingsford-Adaboh and S. Kashino, *Acta Crystallogr. Sect. C Cryst. Struct. Commun.*, 1995, **51**, 2094–2096.

213 L. Yu, X. Jin and G. Z. Chen, *J. Electroanal. Chem.*, 2013, **688**, 371–378.

214 J. Xie and T. L. Riechel, *J. Electrochem. Soc.*, 1998, **145**, 2660–2664.

215 Y. Liang, P. Zhang and J. Chen, *Chem. Sci.*, 2013, **4**, 1330–1337.

216 U. Mahanta, R. P. Venkatesh, S. Sujatha, S. A. Ilangovan and T. Banerjee, *J. Solution Chem.*, 2019, **48**, 1119–1134.

217 H. Matsumoto, H. Sakaebe and K. Tatsumi, *J. Power Sources*, 2005, **146**, 45–50.

218 N. Gamboa-Valero, P. D. Astudillo, M. A. González-Fuentes, M. A. Leyva, M. D. J. Rosales-Hoz and F. J. González, *Electrochim. Acta*, 2016, **188**, 602–610.

219 P. A. Staley, E. M. Lopez, L. A. Clare and D. K. Smith, *J. Phys. Chem. C*, 2015, **119**, 20319–20327.

220 R. K. Emmett and M. E. Roberts, *J. Power Sources*, 2021, **506**, 230087.

221 S. Sowmiah, V. Srinivasadesikan, M. C. Tseng and Y. H. Chu, *On the chemical stabilities of ionic liquids*, 2009, vol. 14.

222 Q. Li, J. Jiang, G. Li, W. Zhao, X. Zhao and T. Mu, *Sci. China Chem.*, 2016, **59**, 571–577.

223 E. Nouri-Nigjeh, M. P. De Vries, A. P. Bruins, R. Bischoff and H. P. Permentier, *Electrochem. commun.*, 2012, **21**, 54–57.

224 M. Piana, J. Wandt, S. Meini, I. Buchberger, N. Tsiouvaras and H. A. Gasteiger, *J. Electrochem. Soc.*, 2014, **161**, A1992–A2001.

225 M. C. Kroon, W. Buijs, C. J. Peters and G. J. Witkamp, *Green Chem.*, 2006, **8**, 241–245.

226 M. Aguilar-Martinez, N. Macias-Ruvalcaba, J. Bautista-Martinez, M. Gomez, F. Gonzalez and I. Gonzalez, *Curr. Org. Chem.*, 2005, **8**, 1721–1738.

227 P. D. Astudillo, J. Tiburcio and F. J. González, *J. Electroanal. Chem.*, 2007, **604**, 57–64.

228 P. D. Astudillo, D. P. Valencia, M. A. González-Fuentes, B. R. Díaz-Sánchez, C. Frontana and F. J. González, *Electrochim. Acta*, 2012, **81**, 197–204.

229 V. S. Chan, R. G. Bergman and F. D. Toste, *J. Am. Chem. Soc.*, 2007, **129**, 15122–15123.

230 A. R. Dick, K. L. Hull and M. S. Sanford, *J. Am. Chem. Soc.*, 2004, **126**, 2300–2301.

231 H. Kinoshita, H. Fukumoto, T. Tohjima and K. Miura, *Tetrahedron Lett.*, 2016, **57**, 3571–3574.

232 R. Giernoth and D. Bankmann, *European J. Org. Chem.*, 2008, **2008**, 2881–2886.